HYDRATE GROWTH MODEL IN THE PRESENCE OF THERMODYNAMIC INHIBITORS OR PROMOTERS

Ingrid Azevedo de Oliveira

Tese de Doutorado apresentada ao Programa de Pós-graduação em Engenharia Civil, COPPE, da Universidade Federal do Rio de Janeiro, como parte dos requisitos necessários à obtenção do título de Doutor em Engenharia Civil.

Orientador(es): Frederico Wanderley Tavares
Amaro Gomes Barreto Júnior

Rio de Janeiro
Outubro de 2020

HYDRATE GROWTH MODEL IN THE PRESENCE OF THERMODYNAMIC INHIBITORS OR PROMOTERS

Ingrid Azevedo de Oliveira

TESE SUBMETIDA AO CORPO DOCENTE DO INSTITUTO ALBERTO LUIZ COIMBRA DE PÓS-GRADUAÇÃO E PESQUISA DE ENGENHARIA DA UNIVERSIDADE FEDERAL DO RIO DE JANEIRO COMO PARTE DOS REQUISITOS NECESSÁRIOS PARA A OBTENÇÃO DO GRAU DE DOUTOR EM CIÊNCIAS EM ENGENHARIA QUÍMICA.

Orientadores: Frederico Wanderley Tavares
Amaro Gomes Barreto Júnior

Aprovada por: Prof. Frederico Wanderley Tavares
Prof. Amaro Gomes Barreto Júnior
Prof. Gabriel Gonçalves da Silva Ferreira
Prof. Pedro de Alcântara Pessôa Filho
Prof. Paulo Couto
Prof. Amadeu Kun Wan Sum

RIO DE JANEIRO, RJ - BRASIL
OUTUBRO DE 2020

Oliveira, Ingrid Azevedo de

Hydrate Growth Model in the Presence of Thermodynamic Inhibitors or Promoters / Ingrid Azevedo de Oliveira. – Rio de Janeiro: UFRJ/COPPE, 2020.

XLIII, 293 p.: il.; 29,7cm.

Orientadores: Frederico Wanderley Tavares

Amaro Gomes Barreto Júnior

Tese (doutorado) – UFRJ/ COPPE/ Programa de Engenharia Química, 2020.

Referências Bibliográficas: p. 134-160

1. Hidrato. 2. Crescimento. 3. Inibidores termodinâmicos. 4.Promotores termodinâmicos. 5. Termodinâmica de não-equilíbrio. I. Tavares, Frederico Wanderley *et al.* II. Universidade Federal do Rio de Janeiro, COPPE, Programa de Engenharia Química. III. Título.

“É preciso que eu suporte duas ou três larvas

se quiser conhecer as borboletas...”

Antoine de Saint-Exupéry

Agradecimentos

Começo esses agradecimentos citando um trecho do livro *O Pequeno Príncipe*, de Antoine de Saint-Exupéry: “Cada um que passa em nossa vida passa sozinho, mas não vai só, nem nos deixa sós. Leva um pouco de nós mesmos, deixa um pouco de si mesmo. Há os que levam muito; mas não há os que não levam nada. Há os que deixam muito; mas não há os que não deixam nada.” Sem sombra de dúvidas todos que serão aqui citados deixaram muito de si na minha vida nesses últimos quatro anos ou mais.

Agradeço a Deus, que na sua infinita bondade me permitiu chegar até aqui. Ele foi o meu sustento, o meu refúgio e a minha força em todo esse tempo. Hoje afirmo que até aqui me sustentou o Senhor e o seu Amor.

Agradeço aos meus país, Marcelo e Adriana, e à minha irmã, Iasmim; que foram motivadores na minha vida mesmo quando eu não conseguia achar motivação; que acreditaram em mim, quando eu mesma não consegui acreditar. Obrigada pelo amor que me dedicaram, que não foi pouco, mas foi essencial para eu me tornar quem sou hoje.

Agradeço ao meu noivo, André; que todos os dias desses quatro anos me fez lembrar que eu era capaz. Obrigada por sempre enxergar o melhor em mim. Te agradeço imensamente pelo seu suporte, amor e amparo. Meus dias, tanto os ensolarados quanto os nublados, são mais felizes desde que você chegou. Obrigada por sonhar junto comigo.

Agradeço, com muito carinho, a todos os meus amigos da vida. É muito bom cativar e se deixar cativar. A vida é muito mais bela quando se tem amigos para compartilhá-la.

Agradeço aos meus orientadores, Professor Amaro e Professor Fred. Vocês me ensinaram muito nesses anos. Passo a passo vocês me conduziram de uma caloura da graduação, que nem sabia o que era fazer pesquisa, a uma Doutora. Obrigada por cada oportunidade, cada reunião, cada correção e cada conselho. Obrigada por me apresentarem o mundo da ciência e pela oportunidade que me deram de ser uma cientista.

Agradeço muito a toda a equipe do ATOMS. Se eu citar nomes sem dúvida esquecerei algum, por isso vou me abster deles. Gostaria apenas de dizer que encontrei nesse grupo muito mais que colegas de profissão, encontrei amigos. Encontrei ajuda, solidariedade, carinho e respeito. No ATOMS encontrei cientistas que me motivaram e motivam a seguir essa carreira tão desafiadora. Vocês são incríveis.

Agradeço à UFRJ, ao PEQ, a todos os professores, pesquisadores e profissionais dessa instituição. O trabalho que vejo sendo realizado me enche de orgulho e da certeza de que escolhi a profissão certa. Mesmo com todos os desafios de fazer ciência no Brasil, principalmente nos últimos tempos, vocês se superam diariamente. Todo o meu orgulho e admiração pela ciência nacional.

Agradeço aos membros da banca, que prontamente aceitaram fazer parte deste trabalho e contribuir para minha formação. Me sinto honrada de ter em minha banca nomes tão valiosos para a ciência brasileira. Em especial, agradeço ao professor Amadeu Sum, que me recebeu para um doutorado sanduíche em seu grupo no Colorado.

Agradeço à PETROBRÁS, ao CNPq e à CAPES pelo apoio financeiro a este trabalho e à ciência brasileira.

Resumo da Tese apresentada à COPPE/UFRJ como parte dos requisitos necessários para a obtenção do grau de Doutor em Ciências (D.Sc.)

MODELO DE CRESCIMENTO DE HIDRATO NA PRESENÇA DE INIBIDORES OU PROMOTORES TERMODINÂMICOS

Ingrid Azevedo de Oliveira

Outubro/2020

Orientadores: Frederico Wanderley Tavares
Amaro Gomes Barreto Jr.

Programa: Engenharia Química

Existem cenários em que a formação de hidrato é desejada, como na sua aplicação tecnológica para armazenamento de gás ou em reservas naturais com potencial energético. Existem outros cenários em que a formação desses sólidos é indesejada, como na formação de hidratos em tubulações, dificultando a garantia de escoamento na indústria de petróleo e gás. Em ambos os casos, a compreensão da termodinâmica e da dinâmica de formação desses sólidos na presença de aditivos químicos é essencial. Neste trabalho propõe-se aperfeiçoar o cálculo de equilíbrio de hidratos na presença de um inibidor termodinâmico, etanol (EtOH), ou de um promotor termodinâmico, tetrahidrofurano (THF). O conhecimento sobre o equilíbrio é usado para desenvolver um modelo de crescimento capaz de contabilizar os efeitos desses aditivos, baseado na teoria da termodinâmica de não-equilíbrio e usando a afinidade química como força motriz. Como resultado, obteve-se adequada modelagem do hidrato duplo de CH_4 com THF com desvio máximo de 0.27% na temperatura de equilíbrio. Além disso, 15% em peso de EtOH na fase líquida foi definido como o limite para sua aplicação apenas como um inibidor, combinando resultados experimentais com cálculos de equilíbrio de fases. Os efeitos de acoplamento entre difusão e reação no crescimento de hidrato de CH_4 em água pura se mostraram dependentes principalmente da pressão. O crescimento de hidrato de CH_4 na presença de EtOH, incluindo os efeitos de não-idealidade, permitiram descrever o comportamento duplo desse álcool, normalmente observado na literatura, como inibidor termodinâmico e como potencial inibidor cinético.

Abstract of Thesis presented to COPPE/UFRJ as a partial fulfillment of the requirements for the degree of Doctor of Science (D.Sc.)

HYDRATE GROWTH MODEL IN THE PRESENCE OF THERMODYNAMIC INHIBITORS OR PROMOTERS

Ingrid Azevedo de Oliveira

October/2020

Advisors: Frederico Wanderley Tavares

Amaro Gomes Barreto Júnior

Department: Chemical Engineering

There are scenarios in which hydrate formation is desired, such as in its technological application for gas storage or in natural reserves with potential sources of energy. There are other scenarios in which these solids formation is undesirable, as hydrate precipitation in pipelines causing flow assurance problems in the oil and gas industry. In both cases, an understanding of the thermodynamics and dynamics of the hydrate formation in the presence of chemical additives is essential. In this work, it is proposed to improve the calculation of hydrate equilibrium in the presence of a thermodynamic inhibitor, ethanol (EtOH), or a thermodynamic promoter, tetrahydrofuran (THF). The knowledge about hydrate equilibria is used to develop a kinetic model of growth capable of accounting the effects of additives, based on the non-equilibrium thermodynamics theory, and using chemical affinity as a driving force. As a result, adequate modeling of the double CH_4/THF hydrate was obtained with a maximum deviation of 0.27% in the equilibrium temperature. Besides, 15 wt% of EtOH in the liquid phase was defined as the limited for its application only as an inhibitor by combining experimental results with equilibrium calculations. The effects of coupling diffusion and reaction on the CH_4 hydrate growth in freshwater were mainly dependent on pressure. The kinetic model of CH_4-hydrate growth in the presence of EtOH, including the effects of non-ideality, can describe the behavior of EtOH as a thermodynamic inhibitor and as a potential kinetic inhibitor, observed in the literature.

Summary

Summary ..... **ix**

List of Figures ..... **xv**

List of Tables ..... **xlii**

Chapter 1. Introduction **1**

1.1 Background and relevance 1

1.1.1 Gas hydrate 1

1.1.2 Gas hydrate as an issue, a resource or a potential technology 3

1.1.3 Gas hydrate formation 5

1.2 Motivation and objectives 8

1.3 Thesis structure 10

Chapter 2. Hydrate equilibria with promoter (THF) **12**

2.1 Introduction 13

2.2 Thermodynamic modeling 14

2.2.1 Equilibrium criteria and algorithms 15

2.2.2 Non-ideal liquid phase model 17

2.2.3 Hydrate phase model 17

2.3 Parameter regression methodology 19

2.3.1 NRTL 21

2.3.2 Kihara 22

2.3.3 Optimization methodology 23

2.4 Results and discussion 23

2.4.1 Liquid-vapor equilibria of the THF/water system 24

2.4.2 Infinite dilution activity coefficient of the THF/water system 26

2.4.3 Solid-liquid equilibria of the THF/water system 27

2.4.4 Thermodynamic prediction of promoted gas hydrate systems 30

2.5 Partial conclusions 33

List of symbols 34

Chapter 3. Hydrate equilibria with inhibitor (EtOH) 36

3.1 Introduction 37

3.2 Experimental section 39

3.2.1 Materials 39

3.2.2 Experimental apparatus 40

3.2.3 Experimental procedure 40

3.3 Thermodynamic analysis and models 43

3.3.1 Thermodynamic consistency analysis 43

3.3.2 Prediction tool 45

3.3.2.1 Hu-Lee-Sum correlation 45

3.3.2.2 Thermodynamic modeling 46

3.4 Results and discussion 47

3.5 Partial conclusions 60

List of symbols 61

Chapter 4. Hydrate growth in freshwater 63

4.1 Introduction 64

4.2 Kinetic model 67

4.2.1 Driving force 68

4.2.2 Growth rate 70

4.2.3 System modeling 74

4.3 Results and discussion 79
4.3.1 Diffusion/reaction coupling effect 79
4.3.2 Effect of water activity on driving force 86
4.3.3 Pressure effect 89
4.3.4 Temperature effect 91
4.4 Partial conclusions 93
List of symbols 94

Chapter 5. Hydrate growth in an inhibited system 96

5.1 Introduction 97
5.2 Kinetic model 99
5.2.1 Growth Model 100
5.2.2 System modeling 101
5.3 Results and discussion 105
5.3.1 Hydrate growth with a thermodynamic hydrate inhibitor (EtOH) 105
5.3.1.1 Thermodynamic hydrate inhibitor (EtOH) effect 105
5.3.1.2 Thermodynamic inhibitor (EtOH) concentration effect 110
5.3.2 The effect of water activity in the driving force in an inhibited system 114
5.3.2.1 Thermodynamic hydrate inhibitor (EtOH) effect 114
5.3.2.2 Thermodynamic inhibitor (EtOH) concentration effect 117
5.3.3 Pressure effect in an inhibited system 122
5.3.4 Temperature effect in an inhibited system 125
5.4 Partial conclusions 128
List of symbols 129

Chapter 6. Conclusion and future work suggestions 131

6.1 Conclusions 131

6.2 Future work suggestions 132

References..... 134

Appendix 1. Supporting information for Chapter 2 161

Appendix 2. Supporting information for Chapter 3 166

S.1 Gas hydrate equilibrium model for systems containing ethanol..... 174

S.1.1 Liquid Phase 175

S.1.2 Vapor Phase 175

S.1.3 Hydrate Phase 176

S.2 Methodology of parameter estimation 178

S.3 Result of parameter estimation 180

S.3.1 Liquid-vapor equilibrium..... 180

S.3.2 Infinite Dilution 182

S.3.3 Gas hydrate phase equilibria for pure water systems 183

Appendix 3. Supporting information for Chapter 4 188

S.4 Excess Gibbs Free Energy Model (NRTL)..... 188

S.5 Calculation of the equilibrium composition at the H-L interface 189

S.6 Growth Kinetics 190

S.6.1 Liquid phase molar balance 190

S.6.2 Gas phase molar balance..... 191

S.6.3 Solid phase molar balance 191

S.6.4 Constitutive relations 191

S.6.5 Volumes and Molar Densities of the Phases..... 193

S.6.6 Population balance 194

S.6.7 Numerical solution of dynamic..... 196

S.7 System property variable profiles 198

S.7.1 System at 276 K and 70.9 bar with water activity in the driving force . 198

S.7.2 System at 276 K and 48.6 bar with water activity in the driving force . 202

S.7.3 System at 274 K and 76.0 bar with water activity in the driving force . 209

S.7.4 System at 276 K and 70.9 bar without water activity in the driving force 216

S.8 System property derivative profiles 222

S.8.1 System at 276 K and 70.9 bar with water activity in the driving force . 222

S.8.2 System at 276 K and 48.6 bar with water activity in the driving force . 227

S.8.3 System at 274 K and 76.0 bar with water activity in the driving force . 232

S.8.4 System at 276 K and 70.9 bar without water activity in the driving force 237

S.9 Correlation of the parameters A_{int}^{GL} e k_d^{GL} 242

S.10 - Krichevsky e Kasarnovsey (1935) correlation 244

S.11 - Fugacity correlation of the light gases hypothetical liquid phase at 101.32 Pa 245

S.12 - NRTL model adjustment with LVE and solubility experimental data of the $CH_4 + H_2O$ system 247

Appendix 4. Supporting information for Chapter 5 250

S.13 Excess Gibbs Free Energy Model (NRTL) 250

S.14 Calculation of the equilibrium composition at the H-L interface 252

S.15 Growth Kinetics 253

S.15.1 Liquid phase mole balance 253

S.15.2 Gas-phase mole balance 254

S.15.3 Solid-phase mole balance 254

S.15.4 Constitutive relations 254

S.15.5 Volumes and Molar Densities of the Phases 256

S.15.6 Numerical solution of dynamic 256

S.16 System property variable profiles 257

S.16.1 The system at 276 K and 70.9 bar with water activity in the driving force for 0 and 5 wt% 258

S.16.2 The system at 276 K and 70.9 bar with water activity in the driving force for 5, 10 and 15 wt% 260

S.16.3 The system at 276 K and 70.9 bar without water activity in the driving force for 0 and 5 wt% 262

S.16.4 The system at 276 K and 70.9 bar without water activity in the driving force for 5, 10, and 15 wt% 264

S.16.5 The system at 276 K and 74.9 bar with water activity in the driving force for 5, 10 and 15 wt% 266

S.16.6 The system at 274 K and 70.9 bar with water activity in the driving force for 5, 10, and 15 wt% 269

S.17 System property derivative profiles 271

S.17.1 The system at 276 K and 70.9 bar with water activity in the driving force for 0 and 5 wt% 272

S.17.2 The system at 276 K and 70.9 bar with water activity in the driving force for 5, 10, and 15 wt% 275

S.17.3 The system at 276 K and 70.9 bar without water activity in the driving force for 0 and 5 wt% 278

S.17.4 The system at 276 K and 70.9 bar without water activity in the driving force for 5, 10 and 15 wt% 281

S.17.5 The system at 276 K and 74.9 bar with water activity in the driving force for 5, 10 and 15 wt% 284

S.17.6 The system at 274 K and 70.9 bar with water activity in the driving force for 5, 10 and 15 wt% 287

S.18 Correlation of the parameters A_{int}^{GL} e k_d^{GL} 290

S.19 NRTL model adjustment with LVE experimental data of the CH_4 + EtOH system 291

List of Figures

Figure 1 - Block diagram of the parameters estimation methodology with the proposed approach. All experimental data for estimation are in Appendix 1. 20

Figure 2 - Vapor-liquid equilibrium diagram for isobaric systems of THF/H_2O. Continuous curves represent modeling results at: ○, p=101.33/kPa [151]; ◊, p=93/kPa [138]; □, p=80/kPa [138]; Δ, p=67/kPa [138]; ●, p=53.3/kPa [1]; ♦, p=40/kPa [138]. . 25

Figure 3 - Vapor-liquid equilibrium diagram for isothermal systems of THF/H_2O. Continuous curves represent modeling results at: □, T=343.15/K [149]; ○, T=323.15/K [149]; Δ, T=298.15/K [150]. 26

Figure 4 - Coefficient of activity in infinite dilution for different temperatures at 101.33 kPa. The symbols represent the experimental data and the continuous curves represent the values calculated by the NRTL model for: □, infinite dilution of THF in H_2O (γ_{THF}^{∞}) [152]; ○, infinite dilution of H_2O in THF (γ_w^{∞}) [153,154]. 27

Figure 5 - Complete diagram for isobaric systems of THF/H2O at 101.33 kPa. Continuous curves represent modeling results for: ◊, VLE [151]; ○, HLE [9,127,128,134–137]; □, HILE [128]; Δ, ILE [128]. 29

Figure 6 - Pressure, p, vs. temperature, T, diagram for the THF/H_2O/CH_4 system. Continuous curves represent equilibrium temperature calculations with the proposed approach for THF molar fractions of: ◊, x=0.0107 [119]; ○, x=0.03 [129]; □, x=0.05 [119]; Δ, x=0.06 [130]; ▲, x=0.1[119]. And p-T diagram for the THF/CH_4 system, ■, x=0.0 [158]. 31

Figure 7 - Pressure, p, vs. temperature, T, diagram for the THF/H_2O/CH_4 system. Continuous curves represent equilibrium temperature calculations with the proposed approach for THF molar fractions of (literature data): ■, x=0.0 [158]; ◊, x=0.0107 [119]; □, x=0.05 [119]. Dashed curves represent equilibrium temperature calculations with the proposed approach for THF molar fractions of: dotted line, x=0.2; dashed line, x=0.6; dotted-dashed line, x=0.8, that do not present literature data. 31

Figure 8 - Pressure, p, vs. temperature, T, diagram for the THF/H_2O/CO_2 system. Continuous curves represent equilibrium temperature calculations with the proposed approach for THF molar fractions of: □, x=0.012 [159]; ◊, x=0.016 [128]; ○, x=0.029 [128,159]; Δ, x=0.05 [159]. 32

Figure 9 - Pressure, p, vs. temperature, T, diagram for the THF/H_2O/H_2 system.

Continuous curves represent equilibrium temperature calculations with the proposed approach for THF molar fractions of: □, *x*=0.01 [127,160]; ◊, *x*=0.0113[161]; ○, *x*=0.024 [160,161]; ■, *x*=0.0351 [161]; ●, *x*=0.05 [162]; Δ, *x*=0.13 [160]..... 33

Figure 10 - Illustration of the experimental procedure for hydrate phase equilibrium measurements with high ethanol concentration [168]. (a) Pressure vs. temperature trace for hydrate formation and dissociation in the 40 wt% of ethanol system with the four steps procedure. (1) Fast cooling step - black, (2) hydrate formation step - blue, (3) fast heating step - red, (4) slow stepwise heating - green. The circled area shows the slope change of the heating curve as the phase equilibrium point is reached. (b) Time traces for the pressure (continuous black) and temperature (dashed red) during slow step-wise temperature increase. Temperature steps are maintained for about 5 hours until the pressure stabilizes. Circled area shows the reduction in the increase in pressure after reaching the phase equilibrium point..... 42

Figure 11 - Methane (CH_4) hydrate phase equilibrium data with ethanol. (a) x for 0 wt% EtOH [158,180–186]. ■ for 5 wt% EtOH [52]. ● for 10 wt% EtOH [52]. ♦ for 13.2 wt% EtOH [10]. (b) ■ for 15 wt% EtOH [169]. ● for 20 wt% EtOH [187]. ♦ for 26.2 wt% EtOH [187]. ▲ for 30 wt% EtOH [10]. (c) ■ for 39.6 wt% EtOH [187]. ● for 44.6 wt% EtOH [187]. ♦ for 52.3 wt% EtOH [10]. ▲ for 63 wt% EtOH [10]. The lines show the predictive calculations of the models: continuous for the adapted model of Oliveira et al. [123], dashed to PVTsim® software and dotted to Hu-Lee-Sum Correlation [176]. (d) The relationship between $\Delta T/T_0T$ and temperature T for methane hydrate systems with ethanol. The lines correspond to the constant value of the best fit that represents the constant value of the water activity for a small temperature range. 49

Figure 12 - Carbon dioxide (CO_2) hydrate phase equilibrium data with ethanol. (a) x for 0 wt% EtOH [188]. ■ for 2 wt% EtOH [171]. ● for 5 wt% EtOH [52]. ♦ for 10 wt% EtOH [52,170,172]. ▲ for 15 wt% EtOH [170,171]. ▼ for 20 wt% EtOH [172]. The lines show the predictive calculations of the models: dashed-dotted for CO_2 liquefy pressure (PVTsim®), continuous for the adapted model of Oliveira et al. [123], dashed to PVTsim® software and dotted to Hu-Lee-Sum Correlation [176]. (b) The relationship between $\Delta T/T_0T$ and temperature T for carbon dioxide hydrate systems with ethanol. The lines correspond to the constant value of the best fit that represents the constant value of the water activity for a small temperature range. 51

Figure 13 - Propane (C_3H_8) hydrate phase equilibrium data with ethanol. (a) x for 0 wt% EtOH [181,186,189–192]. ■ for 5 wt% EtOH [52,172]. ● for 10 wt% EtOH [52,172]. ♦

for 15 wt% EtOH [172]. The lines show the predictive calculations of the models: dashed-dotted for C_3H_8 liquefy pressure (PVTsim®), continuous for the adapted model of Oliveira et al. [123], dashed to PVTsim® software and dotted to Hu-Lee-Sum Correlation [176]. (b) The relationship between $\Delta T/T_0T$ and temperature T for propane hydrate systems with ethanol. The lines correspond to the constant value of the best fit that represents the constant value of the water activity for a small temperature range. 53
Figure 14 - Ethane (C_2H_6) hydrate phase equilibrium conditions with ethanol. (a) x for 0 wt% EtOH [181,182,193]. ▼ for 5 wt% EtOH [52]. ▶ for 10 wt% EtOH [52]. ■ for 10 wt% EtOH (this work). ● for 26 wt% EtOH (this work). ♦ for 35 wt% EtOH (this work). ▲ for 40 wt% EtOH (this work). ▲ for 45 wt% EtOH (this work). The lines show the predictive calculations of the models: dashed-dotted for C_2H_6 liquefy pressure (PVTsim®), continuous for the adapted model of Oliveira et al. [123], dashed to PVTsim® software and dotted to Hu-Lee-Sum Correlation [176]. (b) The relationship between $\Delta T/T_0T$ and temperature T for propane hydrate systems with ethanol. The lines correspond to the constant value of the best fit that represents the constant value of the water activity for a small temperature range. 56
Figure 15 - Mixture of methane and ethane (73.8 mol%CH_4/26.2 mol%C_2H_6) hydrate phase equilibrium data with ethanol. (a) x for 0 wt% EtOH (this work). ■ for 9 wt% EtOH (this work). ● for 25 wt% EtOH (this work). ♦ for 30 wt% EtOH (this work). ▲ for 40 wt% EtOH (this work). The lines show the predictive calculations of the models: continuous for the adapted model of Oliveira et al. [123], dashed to PVTsim® software and dotted to Hu-Lee-Sum Correlation [176]. (b) The relationship between $\Delta T/T_0T$ and temperature T for a mixture of methane and ethane (73.8 mol%CH_4/26.2 mol%C_2H_6) hydrate systems with ethanol. The lines correspond to the constant value of the best fit that represents the constant value of the water activity for a small temperature range.. 58
Figure 16 - Illustrative image of the liquid film surrounding the hydrate solid surface.71
Figure 17 - Block diagram of the hydrate growth dynamic modeling. The blocks represent a set of models and equations, while the arrows represent the direction of the input and output variables between these sets, like the growth rate, *G*, that is proportional to the chemical affinity, *A*. The molar volume of the liquid phase, $\overline{V_L}$, of the vapor phase $\overline{V_V}$; the gas-liquid interface equilibrium, $x_{eq}^{G/L}$, the liquid-hydrate interface equilibrium, $x_{eq}^{H/L}$, and the liquid bulk, x_i^L, composition; the activity of the hydrate compounents

formers at the hydrate-liquid equilibrium, a_i^{eq} and at the liquid bulk, a_i^b; and the order-three moment, $\mu_3^{'}$. In this way we can see how the mass and population balances, the growth rate and the thermodynamic models relate to each other. 75
Figure 18 - *DR* scale. Coupling scale between diffusion and reaction. A growth hydrate profile limited by diffusion has a *DR* equal to 0.0, while a limited by reaction profile has a *DR* equal to 1.0. A complete coupling profile between diffusion and reaction is described by a *DR* equal to 0.5. 80
Figure 19 – The comparation of the methane molar consumption (Δn_G) over time at 276 K and 70.9 bar (a) between the limited by diffusion rate, equation (36), and the profile using the diffusion-reaction coupling rate for a *DR* equal to 0.01, equation (35), (black dotted line) and (b) between limited by reaction rate, equation (37), and the profile using the diffusion-reaction coupling rate for a *DR* equal to 0.99, equation (35) (black dashed-dotted line). The continuous gray line represents the 45 degree line expected for this comparison. The insertion shows the temporal variation of the methane number of moles in the gas phase (n_G). The continuous line represented the profile with the adjusted *DR* factor, while the dotted line represented the profile limited by diffusion and the dotted-dashed line the profile limited by reaction. 81
Figure 20 - The hydrate number of moles (n_H) temporal profile at 276 K and 70.9 bar. The dotted line describes the limited by diffusion profile (*DR*=0.01), the continue line the diffusion-reaction coupling profile (*DR*=0.5) and the dotted-dashed line, in the 2nd time axis, the limited by reaction profile (*DR*=0.99). The insertion shows the hydrate growth rate (G) temporal profile with a zoom in the limited by reaction profile also at 276 K and 70.9 bar. 82
Figure 21 - The methane number of moles in the bulk liquid phase ($n_{L,}CH4$) temporal profile at 276 K and 70.9 bar. The dotted line describes the limited by diffusion profile (*DR*=0.01), the continue line the diffusion-reaction coupling profile (*DR*=0.5) and the dotted-dashed line, in the 2nd time axis, the limited by reaction profile (*DR*=0.99). The insertion on the left shows the methane in water saturation profile, the one in the bottom-right shows the methane mole fraction ($x_{L,}CH_4$) profile in the bulk liquid phase (dark lines), in the gas-liquid equilibria interface (gray continus line) and in the liquid-hydrate equilibrium interface (gray dotted-dashed line) and the one in the top right shows the water number of moles in the bulk liquid phase (n_L,H2O)..... 84
Figure 22 - The methane molar consumption (Δn_G) temporal profile at 276 K and 70.9

bar. The insertion shows the temporal variation of the methane number of moles in the gas phase (n_G). The dotted line describes the limited by diffusion profile (*DR*=0.01), the continue line the diffusion-reaction coupling profile (*DR*=0.5) and the dotted-dashed line, in the 2nd time axis, the limited by reaction profile (*DR*=0.99). The black big circles are the Englezos et al. [42] experimental data at 276 K and 70.9 bar. 85
Figure 23 - (a) The diffusion-reaction coupling temporal profile (*DR*=0.5) of the methane number of moles in the bulk liquid phase ($n_{L,}CH_4$) at 276 K and 70.9 bar. The insertion on the left shows the methane in the water saturation profile. In constrast, the insertion in the top right shows the water number of moles in the bulk liquid phase ($n_{L,}H2O$) and the insertion in the bottom right shows the methane mole fraction ($x_{L,}CH4$) profile in the bulk liquid phase (dark lines), in the gas-liquid equilibria interface (gray continuous line) and the liquid-hydrate equilibria interface (gray dotted-dashed line). (b) The hydrate number of moles (n_H) temporal profile. The insertion shows the hydrate growth rate (G) temporal profile. The continuous line represents the profile with the water activity, while the dashed line represents the profile without the water activity in the growth rate driving force. . 87
Figure 24 - (a) The diffusion-reaction coupling temporal profile (*DR*=0.5) of the product reagents' activities weighted by their stoichiometric coefficients in the bulk phase variable (K_b) and in the liquid-hydrate equilibrium interface variable (K_{eq}) at 276 K and 70.9 bar. The variable in the bulk liquid phase (K_b) are the ones with the the highest value, while the variable in the liquid-hydrate equilibrium (K_{eq}) are the ones constant. The insertion on the right shows the methane mole fraction ($x_{L,CH4}$) profile in the bulk liquid phase (dark line), in the gas-liquid equilibria interface (gray line), and the liquid-hydrate equilibria interface (gray dotted-dashed line). The continuous line represents the profile with the water activity, while the dashed line represents the profile without the water activity in the growth rate driving force. 88
Figure 25 - The diffusion-reaction coupling temporal profile of the methane molar consumption (Δn_G). The insertion shows the temporal variation of the methane number of moles in the gas phase (n_G). The dark gray line is the calculated profile (*DR* = 0.5), and the dark gray circles are the Englezos et al. [42] data at 276 K and 70.9 bar. The black line is the calculated profile (*DR* = 0.1), and the black circles are the Englezos et al. [42] data at 276 K and 48.6 bar. 90
Figure 26 - The diffusion-reaction coupling temporal profile of the methane molar consumption (Δn_G). The insertion shows the temporal variation of the methane number of moles in the gas phase (n_G). The dark gray line is the calculated profile (*DR* = 0.5), and

the dark gray circles are the Englezos et al. [42] data at 276 K and 70.9 bar. The light gray line is the calculated profile (*DR* = 0.6), and the light gray circles are the Englezos et al. [42] data at 274 K and 76.0 bar. 92
Figure 27 - Block diagram of the algebraic-differential equation system explaining the variables that account for the effect of adding ethanol on hydrate growth. The molar volume of the liquid phase, $\overline{V_L}$, the gas-liquid interface equilibrium, $x_{eq}^{G/L}$, and the hydrate-liquid interface equilibrium, $x_{eq}^{H/L}$; and activity of the hydrate compounents formers at the hydrate-liquid equilibrium, a_i^{eq} and at the bulk, a_i^b. And also, the growth rate, *G*. and its diving force the chemical affinity, *A*. 105
Figure 28 - (a) The number of moles of methane (n_L,CH_4) and (b) the H_2O (x_L,H_2O) and EtOH (x_L,EtOH, in gray) mass fractions in the bulk liquid phase temporal profiles at 276 K and 70.9 bar (*DR* = 0.5). The lines describe the time profiles for the following ethanol compositions of the initial liquid phase: 0 wt% (dotted line) and 5 wt% (continuous line) of EtOH. The insertion (a) in the left shows the methane in water saturation profile and the one in the right shows the number of moles of water (n_L,H_2O) profile in the bulk liquid phase. The insertion (b) in the left is a zoom in the H_2O mass fraction temporal profile for 0 wt% of EtOH, and the one in the right is the methane mass fraction (x_L,CH_4) profile in the bulk liquid phase (continuous black lines), in the gas-liquid equilibrium (GLE) interface (continuous gray line) and in the hydrate-liquid equilibrium (HLE) interface (gray dotted-dashed line). 107
Figure 29 - (a) The number of moles of hydrate (n_H), (b) the hydrate growth rate (G), the activity coefficient (γ) for (c) H_2O and (d) CH_4 temporal profile at 276 K and 70.9 bar (*DR* = 0.5). The lines describe the time profiles for the following ethanol compositions of the initial liquid phase: 0 wt% (dotted line) and 5 wt% (continuous line) of EtOH. The insertion (a) in the right is the hydrate volume temporal profile (V_H). The insertion (b) shows the parameters of the product reagents' activities weighted by their stoichiometric coefficients in the bulk phase (K_b) and in the hydrate-liquid equilibrium interface (K_{eq}) at 0 wt% (1st axis) and 5 wt% (2nd axis). The gray lines represent the variable temporal profiles at the hydrate-liquid equilibrium ($_{eq}$) and the black ones at the bulk conditions ($_b$). 109
Figure 30 - (a) The number of moles of methane (n_L,CH_4) and (b) the EtOH (x_L,EtOH) and H_2O (x_L,H_2O) mass fractions in the bulk liquid phase temporal profile at 276 K and 70.9 bar (*DR* = 0.5). The lines describe the time profiles for the following ethanol

compositions of the initial liquid phase: 5 wt% (continuous line), 10 wt% (dashed line) and 15 wt% (dotted-dashed line) of EtOH. The insertion (a) in the left shows the methane in the water saturation profile, and the one in the right shows the water number of moles (n_L,H_2O) profile in the bulk liquid phase. The insertion (b) in the left is a zoom in the H_2O mass fraction temporal profile for 0 wt% of EtOH, and the one in the right is the methane mass fraction (x_L,CH_4) profile in the bulk liquid phase (continuous black lines), in the gas-liquid equilibrium (GLE) interface (continuous gray line) and the hydrate-liquid equilibrium (HLE) interface (gray dotted-dashed line). 111

Figure 31 – (a) The number of moles of hydrate (n_H), (b) the hydrate growth rate (G), the activity coefficient (γ) for (c) H_2O and (d) CH_4 temporal profiles at 276 K and 70.9 bar (*DR* = 0.5). The lines describe the time profiles for the following ethanol compositions of the initial liquid phase: 5 wt% (continuous line), 10 wt% (dashed line) and 15 wt% (dotted-dashed line) of EtOH. The insertion (a) in the left is the hydrate volume temporal profile (V_H). The insertion (b) shows the parameters of the product reagents' activities weighted by their stoichiometric coefficients in the bulk phase (K_b) and the hydrate-liquid equilibrium interface (K_{eq}) at 0 wt% for the one in the bottom, and at 10 wt% (1st axis) and 15 wt% (2nd axis) for the one in the top. The gray lines represent the variable temporal profiles at the hydrate-liquid equilibrium ($_{eq}$) and the black ones at the bulk conditions ($_b$). 113

Figure 32 - (a) The number of moles of methane (n_L,CH_4) and (b) the H_2O (x_L,H_2O) and EtOH (x_L,EtOH in gray and light yellow) mass fractions in the bulk liquid phase temporal profiles at 276 K and 70.9 bar (*DR* = 0.5). The lines describe the time profiles for the following ethanol compositions of the initial liquid phase: 0 wt% (dotted line) and 5 wt% (continuous line) of EtOH, with (black or gray) and without (yellow or light yellow) water activity in the driving force. The insertion (a) in the right shows the number of moles of water (n_L,H_2O) profile in the bulk liquid phase. The insertion (b) in the left is a zoom in the H_2O mass fraction temporal profile for 0 wt% of EtOH, and the one in the right is the methane mass fraction (x_L,CH_4) profile in the bulk liquid phase (black or yellow continuous lines), in the gas-liquid equilibrium (GLE) interface (gray or light yellow continuous lines) and in the hydrate-liquid equilibrium (HLE) interface (gray or light yellow dotted-dashed lines). 115

Figure 33 - (a) The number of moles of hydrate (n_H), (b) the hydrate growth rate (G), the activity coefficient (γ) for (c) H_2O and (d) CH_4 temporal profiles at 276 K and 70.9 bar (*DR* = 0.5). The lines describe the time profiles for the following ethanol compositions of

the initial liquid phase: 0 wt% (dotted line) and 5 wt% (continuous line) of EtOH, with (black) and without (yellow) water activity in the driving force. The insertion (a) in the right is the hydrate volume temporal profile (V_H). The insertion (b) shows the parameters of the product reagents' activities weighted by their stoichiometric coefficients in the bulk phase (K_b) and in the hydrate-liquid equilibrium interface (K_{eq}) at 0 wt% (1^{st} axis) and 5 wt% (2^{nd} axis). The gray and light yellow lines represent the variable temporal profiles at the hydrate-liquid equilibrium ($_{eq}$) and the black and yellow ones at the bulk conditions ($_b$). 117

Figure 34 - (a) The number of moles of methane (n_L,CH_4) and (b) the H_2O (x_L,H_2O) and EtOH (x_L,EtOH, in gray and light yellow) mass fractions in the bulk liquid phase temporal profiles at 276 K and 70.9 bar (*DR* = 0.5). The lines describe the time profiles for the following ethanol compositions of the initial liquid phase: 5 wt% (continuous line), 10 wt% (dashed line) and 15 wt% (dotted-dashed line) of EtOH, with (black) and without (yellow) water activity in the driving force. The insertion (a) in the right shows the number of moles of water (n_L,H_2O) profile in the bulk liquid phase. The insertion (b) in the right is the methane mass fraction (x_L,CH_4) profile in the bulk liquid phase (black and yellow continuous lines), in the gas-liquid equilibrium (GLE) interface (gray and light yellow continuous lines) and in the hydrate-liquid equilibrium (HLE) interface (gray and light yellow dotted-dashed lines)..... 119

Figure 35 - (a) The number of moles of hydrate (n_H), (b) the hydrate growth rate (G), the activity coefficient (γ) for (c) H_2O and (d) CH_4 temporal profiles at 276 K and 70.9 bar (*DR* = 0.5). The lines describe the time profiles for the following ethanol compositions of the initial liquid phase: 5 wt% (continuous line), 10 wt% (dashed line) and 15 wt% (dotted-dashed line) of EtOH, with (black) and without (yellow) water activity in the driving force. The insertion (a) in the left is the hydrate volume temporal profile (V_H). The insertion (b) shows the parameters of the product reagents' activities weighted by their stoichiometric coefficients in the bulk phase (K_b) and in the hydrate-liquid equilibrium interface (K_{eq}) at 0 wt% for the one in the bottom, and at 10 wt% and 15 wt% for the one in the top, without (1^{st} axis) and with (2^{nd} axis) water activity. The gray and light yellow lines represent the variable temporal profiles at the hydrate-liquid equilibrium ($_{eq}$) and the black and yellow ones at the bulk conditions ($_b$). 121

Figure 36 - (a) The H_2O (x_L,H_2O) and EtOH (x_L,EtOH, in gray and light yellow) mass fractions in the bulk liquid phase, (b) the number of moles of methane gas (n_G), (c) the number of moles of hydrate (n_H) and (d) the hydrate growth rate (G) temporal profiles at

276 K (*DR* = 0.5). The lines describe the time profiles for the following ethanol compositions of the initial liquid phase: 5 wt% (continuous line), 10 wt% (dashed line) and 15 wt% (dotted-dashed line) of EtOH, at 70.9 bar, θ = 72% (black and gray), and at 74.9 bar, θ = 75% (yellow and light yellow). The insertion (a) is the methane mass fraction (x_L,CH_4) profile in the bulk liquid phase (black and continuous yellow lines), in the gas-liquid equilibrium (GLE) interface (gray and light yellow continuous lines), and in the hydrate-liquid equilibrium (HLE) interface (gray and light yellow dotted-dashed lines). The insertion (d) shows the parameters of the product reagents' activities weighted by their stoichiometric coefficients in the bulk phase (K_b) and in the hydrate-liquid equilibrium interface (K_{eq}) at 0 wt% for the one in the top-left, and at 10 wt% (1st axis) and 15 wt% (2nd axis) for the one in the bottom-right. The gray and light yellow lines represent the variable temporal profiles at the hydrate-liquid equilibrium ($_{eq}$) and the black and yellow ones at the bulk conditions ($_b$)..... 124

Figure 37 - (a) The H_2O (x_L,H_2O) and EtOH (x_L,EtOH, in gray and light yellow) mass fractions in the bulk liquid phase, (b) the number of moles of methane gas (n_G), (c) the number of moles of hydrate (n_H) and (d) the hydrate growth rate (G) temporal profiles at 70.9 bar (*DR* = 0.5).The lines describe the time profiles for the following ethanol compositions of the initial liquid phase: 5 wt% (continuous line), 10 wt% (dashed line), and 15 wt% (dotted-dashed line) of EtOH, at 276 K, θ = 72% (black and gray), and at 274 K, θ = 68% (yellow and light yellow). The insertion (a) is the methane mass fraction (x_L,CH_4) profile in the bulk liquid phase (black and continuous yellow lines), in the gas-liquid equilibrium (GLE) interface (gray and light yellow continuous lines), and in the hydrate- liquid equilibrium (HLE) interface (gray and light yellow dotted-dashed lines). The insertion (d) shows the parameters of the product reagents' activities weighted by their stoichiometric coefficients in the bulk phase (K_b) and the hydrate-liquid equilibrium interface (K_{eq}) at 0 wt% for the one in the top-left, and at 10 wt% (1st axis) and 15 wt% (2nd axis) for the one in the bottom-right. The gray and light yellow lines represent the variable temporal profiles at the hydrate- liquid equilibrium ($_{eq}$) and the black and yellow ones at the bulk conditions ($_b$). 127

Figure S1 - Block diagram of the thermodynamic model used to calculate the LHV equilibrium pressure of systems with additives [123]. 174

Figure S2 - Isothermal curves of liquid-vapor equilibrium of H_2O + Ethanol at: (a) 323.15 K, 328.15 K, 333.15 K and 343.15 K; (b) 298.15 K and 303.15 K; (c) 363.15 K. The experimental data are represented by the squares for the dew point curves and circles for

the bubble point curves [227–232]. The continuous curves represent the calculation with the adjusted NRTL model. 181
Figure S3 - Isobaric equilibrium liquid-vapor equilibria of H_2O + Ethanol. The experimental data are represented by the squares for the dew point curves and circles for the bubble point curves [227–232]. The continuous curves represent the calculation with the adjusted NRTL model. 182
Figure S4 - Activity coefficient in the condition of infinite dilution of ethanol in H_2O. The squares represent the experimental data with their respective errors [152,157] and the continuous curve is the model prediction. 183
Figure S5 - P vs. T hydrate phase equilibrium curve for the CH_4 + H_2O system. The squares, ■, represent the experimental data [158,180–186]. The curve represents the calculation of the hydrate dissociation pressure with the model [123]. 184
Figure S6 - P vs. T hydrate phase equilibrium curve for the CO_2 + H_2O system. The squares, ■, represent the experimental data [188]. The curve represents the calculation of the hydrate dissociation pressure with the model [123]. 185
Figure S7 - P vs. T hydrate phase equilibrium curve for the C_2H_6 + H_2O system. The squares, ■, represent the experimental data [181,182,193]. The curve represents the calculation of the hydrate dissociation pressure with the model [123]. 186
Figure S8 - P vs. T hydrate phase equilibrium curve for the C_3H_8 + H_2O system. The squares, ■, represent the experimental data [181,186,189–192]. The curve represents the calculation of the hydrate dissociation pressure with the model [123]. 187
Figure S9 - The temporal profile of the liquid phase volume (V_L). The insertion shows the liquid density (ρ_L) profile with a zoom in the methane in water saturation (the first 2 hours). The dotted line describes the limited by diffusion profile (*DR*=0.01), the continuous line the diffusion-reaction coupling profile (*DR*=0.5), and the dotted-dashed line, in the 2nd time axis, the limited by reaction profile (*DR*=0.99). All profiles are at 276 K and 70.9 bar. 198
Figure S10 - The temporal profile of the methane number of moles in the pure vapor phase (n_G). The insertion shows the vapor phase volume (V_G) with the constant vapor density (ρ_G) profile. The dotted line describes the limited by diffusion profile (*DR*=0.01), the continue line the diffusion-reaction coupling profile (*DR*=0.5), and the dotted-dashed line, in the 2nd time axis, the limited by reaction profile (*DR*=0.99). All profiles are at 276 K and 70.9 bar. 199
Figure S11 - The temporal profile of the product reagents' activities weighted by their

stoichiometric coefficients in the bulk phase variable (K_b) and in the liquid-hydrate equilibrium interface variable (K_{eq}). The variable in the bulk liquid phase (K_b) is the one with the the highest value, while the variable in the liquid-hydrate equilibrium interface (K_{eq}) is the one constant. The insertion shows the hydrate phase volume (V_H). The dotted line describes the limited by diffusion profile (*DR*=0.01), the continuous line the diffusion-reaction coupling profile (*DR*=0.5), and the dotted-dashed line, in the 2nd time axis, the limited by reaction profile (*DR*=0.99). All profiles are at 276 K and 70.9 bar. 200

Figure S12 - (a) The temporal profile of the population balance moment of order zero, number of particles per liquid volume (μ_0), (b) moment of order one, particle diameter per liquid volume (μ_1), (c) moment of order two, particle surface area per liquid volume (μ_2) and (d) moment of order three, particle volume per liquid volume (μ_3). The inserts are a zoom in the limited by reaction profile. The dotted line describes the limited by diffusion profile (*DR*=0.01), the continue line the diffusion-reaction coupling profile (*DR*=0.5), and the dotted-dashed line, in the 2nd time axis, the limited by reaction profile (*DR*=0.99). All profiles are at 276 K and 70.9 bar. 201

Figure S13 - The temporal profile of the methane number of moles in the bulk liquid phase ($n_{L,}CH4$). The insertion on the left shows the methane in water saturation profile, the one in the bottom-right shows the methane mole fraction ($x_{L,}CH4$) profile in the bulk liquid phase (dark lines), in the gas-liquid equilibria interface (continuous gray line), and the liquid-hydrate equilibrium interface (gray dotted-dashed line) and the one in the top right shows the water number of moles in the bulk liquid phase ($n_{L,}H2O$). The dotted line describes the limited by diffusion profile (*DR*=0.01), the continuous line the diffusion-reaction coupling profile (*DR*=0.1), and the dotted-dashed line, in the 2nd time axis, the limited by reaction profile (*DR*=0.99). All profiles are at 276 K and 48.6 bar. 202

Figure S14 - The temporal profile of the liquid phase volume (V_L). The insertion shows the liquid density (ρ_L) profile with a zoom in the methane in water saturation (the first 2 hours). The dotted line describes the limited by diffusion profile (*DR*=0.01), the continue line the diffusion-reaction coupling profile (*DR*=0.1), and the dotted-dashed line, in the 2nd time axis, the limited by reaction profile (*DR*=0.99). All profiles are at 276 K and 48.6 bar. 203

Figure S15 - The temporal profile of the methane number of moles in the pure vapor phase (n_G). The insertion shows the vapor phase volume (V_G) with the constant vapor

density (ρ_G) profile. The dotted line describes the limited by diffusion profile (*DR*=0.01), the continuous line the diffusion-reaction coupling profile (*DR*=0.1), and the dotted-dashed line, in the 2nd time axis, the limited by reaction profile (*DR*=0.99). All profiles are at 276 K and 48.6 bar..... 204

Figure S16 - The temporal profile of the hydrate number of moles (n_H). The insertion shows the hydrate growth rate (G) temporal profile with a zoom in the limited by reaction profile. The dotted line describes the limited by diffusion profile (*DR*=0.01), the continuous line the diffusion-reaction coupling profile (*DR*=0.1), and the dotted-dashed line, in the 2nd time axis, the limited by reaction profile (*DR*=0.99). All profiles are at 276 K and 48.6 bar. 205

Figure S17 - The temporal profile of the product reagents' activities weighted by their stoichiometric coefficients in the bulk phase variable (K_b) and in the liquid-hydrate equilibrium interface variable (K_{eq}). The variable in the bulk liquid phase (K_b) is the one with the the highest value, while the variable in the liquid-hydrate equilibrium interface (K_{eq}) is the one constant. The insertion shows the hydrate phase volume (V_H). The dotted line describes the limited by diffusion profile (*DR*=0.01), the continuous line the diffusion-reaction coupling profile (*DR*=0.1), and the dotted-dashed line, in the 2nd time axis, the limited by reaction profile (*DR*=0.99). All profiles are at 276 K and 48.6 bar. 206

Figure S18 - (a) The temporal profile of the population balance moment of order zero, number of particles per liquid volume (μ_0), (b) moment of order one, particle diameter per liquid volume (μ_1), (c) moment of order two, particle surface area per liquid volume (μ_2) and (d) moment of order three, particle volume per liquid volume (μ_3). The inserts are a zoom in the limited by reaction profile. The dotted line describes the limited by diffusion profile (*DR*=0.01), the continuous line the diffusion-reaction coupling profile (*DR*=0.1), and the dotted-dashed line, in the 2nd time axis, the limited by reaction profile (*DR*=0.99). All profiles are at 276 K and 48.6 bar. 207

Figure S19 - The temporal profile of the methane molar consumption (Δn_G). The insertion shows the temporal variation of the methane number of moles in the gas phase (n_G). The dotted line describes the limited by diffusion profile (*DR*=0.01), the continue line the diffusion-reaction coupling profile (*DR*=0.1), and the dotted-dashed line, in the 2nd time axis, the limited by reaction profile (*DR*=0.99). All profiles are at 276 K and 48.6 bar. The black circles are the Englezos et al. [42] data also at 276 K and 48.6 bar. 208

Figure S20 - The temporal profile of the methane number of moles in the bulk liquid phase ($n_{L,}CH4$). The insertion on the left shows the methane in water saturation profile, the one in the bottom-right shows the methane mole fraction ($x_{L,}CH4$) profile in the bulk liquid phase (dark lines), in the gas-liquid equilibria interface (gray continus line), and in the liquid-hydrate equilibrium interface (gray dotted-dashed line) and the one in the top right shows the water number of moles in the bulk liquid phase ($n_{L,}H2O$). The dotted line describes the limited by diffusion profile (*DR*=0.01), the continuous line the diffusion-reaction coupling profile (*DR*=0.6), and the dotted-dashed line, in the 2nd time axis, the limited by reaction profile (*DR*=0.99). All profiles are at 274 K and 76.0 bar. 209
Figure S21 - The temporal profile of the liquid phase volume (V_L). The insertion shows the liquid density (ρ_L) profile with a zoom in the methane in water saturation (the first 2 hours). The dotted line describes the limited by diffusion profile (*DR*=0.01), the continuous line the diffusion-reaction coupling profile (*DR*=0.6), and the dotted-dashed line, in the 2nd time axis, the limited by reaction profile (*DR*=0.99). All profiles are at 274 K and 76.0 bar. 210
Figure S22 - The temporal profile of the methane number of moles in the pure vapor phase (n_G). The insertion shows the vapor phase volume (V_G) with the constant vapor density (ρ_G) profile. The dotted line describes the limited by diffusion profile (*DR*=0.01), the continuous line the diffusion-reaction coupling profile (*DR*=0.6), and the dotted-dashed line, in the 2nd time axis, the limited by reaction profile (*DR*=0.99). All profiles are at 274 K and 76.0 bar..... 211
Figure S23 - The temporal profile of the hydrate number of moles (n_H). The insertion shows the hydrate growth rate (G) temporal profile with a zoom in the limited by reaction profile. The dotted line describes the limited by diffusion profile (*DR*=0.01), the continuous line the diffusion-reaction coupling profile (*DR*=0.6), and the dotted-dashed line, in the 2nd time axis, the limited by reaction profile (*DR*=0.99). All profiles are at 274 K and 76.0 bar. 212
Figure S24 - The temporal profile of the product reagents' activities weighted by their stoichiometric coefficients in the bulk phase variable (K_b) and in the liquid-hydrate equilibrium interface variable (K_{eq}). The variable in the bulk liquid phase (K_b) is the one with the the highest value, while the variable in the liquid-hydrate equilibrium interface (K_{eq}) is the one constant. The insertion shows the hydrate phase volume (V_H). The dotted line describes the limited by diffusion profile (*DR*=0.01), the continuous line the diffusion-reaction coupling profile (*DR*=0.6), and the dotted-dashed line, in the 2nd time

axis, the limited by reaction profile (*DR*=0.99). All profiles are at 274 K and 76.0 bar. 213
Figure S25 - (a) The temporal profile of the population balance moment of order zero, number of particles per liquid volume (μ_0), (b) moment of order one, particle diameter per liquid volume (μ_1), (c) moment of order two, particle surface area per liquid volume (μ_2) and (d) moment of order three, particle volume per liquid volume (μ_3). The inserts are a zoom in the limited by reaction profile. The dotted line describes the limited by diffusion profile (*DR*=0.01), the continuous line the diffusion-reaction coupling profile (*DR*=0.6), and the dotted-dashed line, in the 2nd time axis, the limited by reaction profile (*DR*=0.99). All profiles are at 274 K and 76.0 bar. 214
Figure S26 - The temporal profile of the methane molar consumption (Δn_G). The insertion shows the temporal variation of the methane number of moles in the gas phase (n_G). The dotted line describes the limited by diffusion profile (*DR*=0.01), the continuous line the diffusion-reaction coupling profile (*DR*=0.6), and the dotted-dashed line, in the 2nd time axis, the limited by reaction profile (*DR*=0.99). All profiles are at 274 K and 76.0 bar. The black circles are the Englezos et al. (1987) [42] data also at 274 K and 76.0 bar.215
Figure S27 - The diffusion-reaction coupling (*DR*=0.5) temporal profile of the methane number of moles in the bulk liquid phase ($n_{L,}CH4$). The insertion on the left shows the methane in water saturation profile, the one in the bottom-right shows the methane mole fraction ($x_{L,}CH4$) profile in the bulk liquid phase (dark lines), in the gas-liquid equilibria interface (gray continus line) and in the liquid-hydrate equilibrium interface (gray dotted-dashed line) and the one in the top right shows the water number of moles in the bulk liquid phase ($n_{L,}H2O$). The continuous line represents the profile with the water activity, while the dashed line represents the profile without the water activity in the growth rate driving force. All profiles are at 276 K and 70.9 bar. 216
Figure S28 - The diffusion-reaction coupling (*DR*=0.5) temporal profile of the liquid phase volume (V_L). The insertion shows the liquid density (ρ_L) profile with a zoom in the methane in water saturation (the first 2 hours). The continuous line represents the profile with the water activity, while the dashed line represents the profile without the water activity in the growth rate driving force. All profiles are at 276 K and 70.9 bar. 217
Figure S29 - The diffusion-reaction coupling (*DR*=0.5) temporal profile of the methane number of moles in the pure vapor phase (n_G). The insertion shows the vapor phase volume (V_G) with the constant vapor density (ρ_G) profile. The continuous line represents

the profile with the water activity, while the dashed line represents the profile without the water activity in the growth rate driving force. All profiles are at 276 K and 70.9 bar. 218
Figure S30 - The diffusion-reaction coupling (*DR*=0.5) temporal profile of the hydrate number of moles (n_H). The insertion shows the hydrate growth rate (G) temporal profile with a zoom in the limited by reaction profile. The continuous line represents the profile with the water activity, while the dashed line represents the profile without the water activity in the growth rate driving force. All profiles are at 276 K and 70.9 bar. 219
Figure S31 - The diffusion-reaction coupling (*DR*=0.5) temporal profile of the product reagents' activities weighted by their stoichiometric coefficients in the bulk phase variable (K_b) and in the liquid-hydrate equilibrium interface variable (K_{eq}). The variable in the bulk liquid phase (K_b) is the one with the the highest value, while the variable in the liquid-hydrate equilibrium interface (K_{eq}) is the one constant. The insertion shows the hydrate phase volume (V_H). The continuous line represents the profile with the water activity, while the dashed line represents the profile without the water activity in the growth rate driving force. All profiles are at 276 K and 70.9 bar. 220
Figure S32 - (a) The diffusion-reaction coupling (*DR*=0.5) temporal profile of the population balance moment of order zero, number of particles per liquid volume (μ_0), (b) moment of order one, particle diameter per liquid volume (μ_1), (c) moment of order two, particle surface area per liquid volume (μ_2) and (d) moment of order three, particle volume per liquid volume (μ_3). The inserts are a zoom in the limited by reaction profile. The continuous line represents the profile with the water activity, while the dashed line represents the profile without the water activity in the growth rate driving force. All profiles are at 276 K and 70.9 bar. 221
Figure S33 - The differential profile of methane number of moles in the bulk liquid phase ($dn_{L,}CH4$). The insertion on the top-left shows a zoom in the limited by reaction profile, while the one in the top-right shows the methane in water saturation profile (the first 2 hours). The insertion in the bottom-right shows the differential profile of the water number of moles in the bulk liquid phase ($dn_{L,}H2O$). The dotted line describes the limited by diffusion profile (*DR*=0.01), the continuous line the diffusion-reaction coupling profile (*DR*=0.5), and the dotted-dashed line, in the 2nd time axis, the limited by reaction profile (*DR*=0.99). All profiles are at 276 K and 70.9 bar. 222
Figure S34 - The differential profile of the liquid phase volume (dV_L). The insertion

shows the differential profile of the liquid density ($d\rho_L$) with a zoon in the methane in water saturation (the first 2 hours) and in the limited by reaction profile. The dotted line describes the limited by diffusion profile (*DR*=0.01), the continuous line the diffusion-reaction coupling profile (*DR*=0.5), and the dotted-dashed line, in the 2nd time axis, the limited by reaction profile (*DR*=0.99). All profiles are at 276 K and 70.9 bar. 223
Figure S35 - The differential profile of the methane number of moles in the pure vapor phase (dn_G). The insertion shows the vapor phase volume (dV_G) with the constant vapor density ($d\rho_G$) differential profile. The dotted line describes the limited by diffusion profile (*DR*=0.01), the continuous line the diffusion-reaction coupling profile (*DR*=0.5), and the dotted-dashed line, in the 2nd time axis, the limited by reaction profile (*DR*=0.99). All profiles are at 276 K and 70.9 bar. 224
Figure S36 - The differential profile of the hydrate number of moles (dn_H). The insertion shows the hydrate phase volume (dV_H) differential profile. The dotted line describes the limited by diffusion profile (*DR*=0.01), the continuous line the diffusion-reaction coupling profile (*DR*=0.5), and the dotted-dashed line, in the 2nd time axis, the limited by reaction profile (*DR*=0.99). All profiles are at 276 K and 70.9 bar. 225
Figure S37 - (a) The differential profile of the population balance moment of order zero, number of particles per liquid volume ($d\mu_0$), (b) moment of order one, particle diameter per liquid volume ($d\mu_1$), (c) moment of order two, particle surface area per liquid volume ($d\mu_2$) and (d) moment of order three, particle volume per liquid volume ($d\mu_3$). The inserts are a zoom in the limited by reaction differential profile. The dotted line describes the limited by diffusion profile (*DR*=0.01), the continuous line the diffusion-reaction coupling profile (*DR*=0.5), and the dotted-dashed line, in the 2nd time axis, the limited by reaction profile (*DR*=0.99). All profiles are at 276 K and 70.9 bar. 226
Figure S38 - The differential profile of methane number of moles in the bulk liquid phase ($dn_{L,}CH4$). The insertion on the top-left shows a zoom in the limited by reaction profile, while the one in the top-right shows the methane in water saturation profile (the first 2 hours). The insertion in the bottom-right shows the differential profile of the water number of moles in the bulk liquid phase ($dn_{L,}H2O$). The dotted line describes the limited by diffusion profile (*DR*=0.01), the continuous line the diffusion-reaction coupling profile (*DR*=0.1), and the dotted-dashed line, in the 2nd time axis, the limited by reaction profile (*DR*=0.99). All profiles are at 276 K and 48.6 bar. 227
Figure S39 - The differential profile of the liquid phase volume (dV_L). The insertion

shows the differential profile of the liquid density ($d\rho_L$) with a zoon in the methane in water saturation (the first 2 hours) and in the limited by reaction profile. The dotted line describes the limited by diffusion profile (*DR*=0.01), the continuous line the diffusion-reaction coupling profile (*DR*=0.1), and the dotted-dashed line, in the 2nd time axis, the limited by reaction profile (*DR*=0.99). All profiles are at 276 K and 48.6 bar. 228
Figure S40 - The differential profile of the methane number of moles in the pure vapor phase (dn_G). The insertion shows the vapor phase volume (dV_G) with the constant vapor density ($d\rho_G$) differential profile. The dotted line describes the limited by diffusion profile (*DR*=0.01), the continuous line the diffusion-reaction coupling profile (*DR*=0.1), and the dotted-dashed line, in the 2nd time axis, the limited by reaction profile (*DR*=0.99). All profiles are at 276 K and 48.6 bar. 229
Figure S41 - The differential profile of the hydrate number of moles (dn_H). The insertion shows the hydrate phase volume (dV_H) differential profile. The dotted line describes the limited by diffusion profile (*DR*=0.01), the continuous line the diffusion-reaction coupling profile (*DR*=0.1), and the dotted-dashed line, in the 2nd time axis, the limited by reaction profile (*DR*=0.99). All profiles are at 276 K and 48.6 bar. 230
Figure S42 - (a) The differential profile of the population balance moment of order zero, number of particles per liquid volume ($d\mu_0$), (b) moment of order one, particle diameter per liquid volume ($d\mu_1$), (c) moment of order two, particle surface area per liquid volume ($d\mu_2$) and (d) moment of order three, particle volume per liquid volume ($d\mu_3$). The inserts are a zoom in the limited by reaction differential profile. The dotted line describes the limited by diffusion profile (*DR*=0.01), the continuous line the diffusion-reaction coupling profile (*DR*=0.1), and the dotted-dashed line, in the 2nd time axis, the limited by reaction profile (*DR*=0.99). All profiles are at 276 K and 48.6 bar. 231
Figure S43 - The differential profile of methane number of moles in the bulk liquid phase ($dn_{L,}CH4$). The insertion on the top-left shows a zoom in the limited by reaction profile, while the one in the top-right shows the methane in water saturation profile (the first 2 hours). The insertion in the bottom-right shows the differential profile of the water number of moles in the bulk liquid phase ($dn_{L,}H2O$). The dotted line describes the limited by diffusion profile (*DR*=0.01), the continuous line the diffusion-reaction coupling profile (*DR*=0.6), and the dotted-dashed line, in the 2nd time axis, the limited by reaction profile (*DR*=0.99). All profiles are at 274 K and 76.0 bar. 232
Figure S44 - The differential profile of the liquid phase volume (dV_L). The insertion

shows the differential profile of the liquid density ($d\rho_L$) with a zoon in the methane in water saturation (the first 2 hours) and in the limited by reaction profile. The dotted line describes the limited by diffusion profile (*DR*=0.01), the continuous line the diffusion-reaction coupling profile (*DR*=0.6), and the dotted-dashed line, in the 2nd time axis, the limited by reaction profile (*DR*=0.99). All profiles are at 274 K and 76.0 bar. 233
Figure S45 - The differential profile of the methane number of moles in the pure vapor phase (dn_G). The insertion shows the vapor phase volume (dV_G) with the constant vapor density ($d\rho_G$) differential profile. The dotted line describes the limited by diffusion profile (*DR*=0.01), the continuous line the diffusion-reaction coupling profile (*DR*=0.6), and the dotted-dashed line, in the 2nd time axis, the limited by reaction profile (*DR*=0.99). All profiles are at 274 K and 76.0 bar. 234
Figure S46 - The differential profile of the hydrate number of moles (dn_H). The insertion shows the hydrate phase volume (dV_H) differential profile. The dotted line describes the limited by diffusion profile (*DR*=0.01), the continuous line the diffusion-reaction coupling profile (*DR*=0.6), and the dotted-dashed line, in the 2nd time axis, the limited by reaction profile (*DR*=0.99). All profiles are at 274 K and 76.0 bar. 235
Figure S47 - (a) The differential profile of the population balance moment of order zero, number of particles per liquid volume ($d\mu_0$), (b) moment of order one, particle diameter per liquid volume ($d\mu_1$), (c) moment of order two, particle surface area per liquid volume ($d\mu_2$) and (d) moment of order three, particle volume per liquid volume ($d\mu_3$). The inserts are a zoom in the limited by reaction differential profile. The dotted line describes the limited by diffusion profile (*DR*=0.01), the continuous line the diffusion-reaction coupling profile (*DR*=0.6), and the dotted-dashed line, in the 2nd time axis, the limited by reaction profile (*DR*=0.99). All profiles are at 274 K and 76.0 bar. 236
Figure S48 - The diffusion-reaction coupling (*DR*=0.5) differential profile of methane number of moles in the bulk liquid phase ($dn_{L,}CH4$). The insertion on the top-left shows a zoom in the limited by reaction profile, while the one in the top-right shows the methane in water saturation profile (the first 2 hours). The insertion in the bottom-right shows the differential profile of the water number of moles in the bulk liquid phase ($dn_{L,}H2O$). The continuous line represents the profile with the water activity, while the dashed line represents the profile without the water activity in the growth rate driving force. All profiles are at 276 K and 70.9 bar. 237
Figure S49 - The diffusion-reaction coupling (*DR*=0.5) differential profile of the liquid

phase volume (dV_L). The insertion shows the differential profile of the liquid density ($d\rho_L$) with a zoom in the methane in water saturation (the first 2 hours) and in the limited by reaction profile. The continuous line represents the profile with the water activity, while the dashed line represents the profile without the water activity in the growth rate driving force. All profiles are at 276 K and 70.9 bar. 238
Figure S50 - The diffusion-reaction coupling (*DR*=0.5) differential profile of the methane number of moles in the pure vapor phase (dn_G). The insertion shows the vapor phase volume (dV_G) with the constant vapor density ($d\rho_G$) differential profile. The continuous line represents the profile with the water activity, while the dashed line represents the profile without the water activity in the growth rate driving force. All profiles are at 276 K and 70.9 bar. 239
Figure S51 - The diffusion-reaction coupling (*DR*=0.5) differential profile of the hydrate number of moles (dn_H). The insertion shows the hydrate phase volume (dV_H) differential profile. The continuous line represents the profile with the water activity, while the dashed line represents the profile without the water activity in the growth rate driving force. All profiles are at 276 K and 70.9 bar. 240
Figure S52 - (a) The diffusion-reaction coupling (*DR*=0.5) differential profile of the population balance moment of order zero, number of particles per liquid volume ($d\mu_0$), (b) moment of order one, particle diameter per liquid volume ($d\mu_1$), (c) moment of order two, particle surface area per liquid volume ($d\mu_2$) and (d) moment of order three, particle volume per liquid volume ($d\mu_3$). The inserts are a zoom in the limited by reaction differential profile. The continuous line represents the profile with the water activity, while the dashed line represents the profile without the water activity in the growth rate driving force. All profiles are at 276 K and 70.9 bar. 241
Figure S53 - Fugacy profile of the hypothetical liquid phase for light gases by the correlation of Prausnitz and Shair [244] with the temperature at 101.32 Pa. The points, ●, represent the calculation of the correlation and the curve the calculation performed by the function used in this work. 246
Figure S54 - H_2O+CH_4 liquid-vapor equilibrium isothermal curves. The experimental data are represented by the filled circles for (a) the dew point and for (b) the bubble point [234–236]. The empty circles represent the points calculated with the NRTL model. 248
Figure S55 - Isothermal curves of CH_4 solubility in H_2O. The experimental data is represented by the filled circles [237–242]. The empty circles represent the points

calculated with the NRTL model..... 248
Figure S56 - (a) The liquid phase volume (V_L) and (b) the methane number of moles in the pure vapor phase (n_G) temporal profiles at 276 K and 70.9 bar (*DR* = 0.5). The insertion (a) shows the liquid density (ρ_L) profile. The insertion (b) in the left is the gas density (ρ_G) profile, and the one in the right is the vapor phase volume (V_G). The lines describe the time profiles for the following ethanol compositions of the initial liquid phase: 0 wt% (dotted line) and 5 wt% (continuous line) of EtOH. 258
Figure S57 - (a) The temporal profile of the population balance moment of order zero, number of particles per liquid volume (μ_0), (b) moment of order one, particle diameter per liquid volume (μ_1), (c) moment of order two, particle surface area per liquid volume (μ_2) and (d) moment of order three, particle volume per liquid volume (μ_3) at 276 K and 70.9 bar (*DR* = 0.5). The lines describe the time profiles for the following ethanol compositions of the initial liquid phase: 0 wt% (dotted line) and 5 wt% (continuous line) of EtOH. 259
Figure S58 - (a) The liquid phase volume (V_L) and (b) the methane number of moles in the pure vapor phase (n_G) temporal profiles at 276 K and 70.9 bar (*DR* = 0.5). The insertion (a) shows the liquid density (ρ_L) profile. The insertion (b) in the left is the gas density (ρ_G) profile, and the one in the right is the vapor phase volume (V_G). The lines describe the time profiles for the following ethanol compositions of the initial liquid phase: 5 wt% (continuous line), 10 wt% (dashed line) and 15 wt% (dotted-dashed line) of EtOH. 260
Figure S59 - (a) The temporal profile of the population balance moment of order zero, number of particles per liquid volume (μ_0), (b) moment of order one, particle diameter per liquid volume (μ_1), (c) moment of order two, particle surface area per liquid volume (μ_2) and (d) moment of order three, particle volume per liquid volume (μ_3) at 276 K and 70.9 bar (*DR* = 0.5). The lines describe the time profiles for the following ethanol compositions of the initial liquid phase: 5 wt% (continuous line), 10 wt% (dashed line) and 15 wt% (dotted-dashed line) of EtOH. 261
Figure S60 - (a) The liquid phase volume (V_L) and (b) the methane number of moles in the pure vapor phase (n_G) temporal profiles at 276 K and 70.9 bar (*DR* = 0.5). The insertion (a) shows the liquid density (ρ_L) profile. The insertion (b) in the left is the gas density (ρ_G) profile, and the one in the right is the vapor phase volume (V_G). The lines describe the time profiles for the following ethanol compositions of the initial liquid

phase: 0 wt% (dotted line) and 5 wt% (continuous line) of EtOH, with (black) and without (yellow) water activity in the driving force. 262
Figure S61 - (a) The temporal profile of the population balance moment of order zero, number of particles per liquid volume (μ_0), (b) moment of order one, particle diameter per liquid volume (μ_1), (c) moment of order two, particle surface area per liquid volume (μ_2) and (d) moment of order three, particle volume per liquid volume (μ_3) at 276 K and 70.9 bar (*DR* = 0.5). The lines describe the time profiles for the following ethanol compositions of the initial liquid phase: 0 wt% (dotted line) and 5 wt% (continuous line) of EtOH, with (black) and without (yellow) water activity in the driving force. 263
Figure S62 - (a) The liquid phase volume (V_L) and (b) the methane number of moles in the pure vapor phase (n_G) temporal profiles at 276 K and 70.9 bar (*DR* = 0.5). The insertion (a) shows the liquid density (ρ_L) profile. The insertion (b) in the left is the gas density (ρ_G) profile, and the one in the right is the vapor phase volume (V_G). The lines describe the time profiles for the following ethanol compositions of the initial liquid phase: 5 wt% (continuous line), 10 wt% (dashed line) and 15 wt% (dotted-dashed line) of EtOH, with (black) and without (yellow) water activity in the driving force. 264
Figure S63 - (a) The temporal profile of the population balance moment of order zero, number of particles per liquid volume (μ_0), (b) moment of order one, particle diameter per liquid volume (μ_1), (c) moment of order two, particle surface area per liquid volume (μ_2) and (d) moment of order three, particle volume per liquid volume (μ_3) at 276 K and 70.9 bar (*DR* = 0.5). The lines describe the time profiles for the following ethanol compositions of the initial liquid phase: 5 wt% (continuous line), 10 wt% (dashed line) and 15 wt% (dotted-dashed line) of EtOH, with (black) and without (yellow) water activity in the driving force. 265
Figure S64 - (a) The number of moles of methane (n_L,CH_4) and (b) the liquid phase volume (V_L) temporal profiles at 276 K (*DR* = 0.5). The insertion (a) shows the number of moles of water (n_L,H_2O) profile in the bulk liquid phase. The insertion (b) shows the liquid density (ρ_L) profile. The lines describe the time profiles for the following ethanol compositions of the initial liquid phase: 5 wt% (continuous line), 10 wt% (dashed line) and 15 wt% (dotted-dashed line) of EtOH, at 70.9 bar, θ = 72% (black), and at 74.9 bar, θ = 75% (yellow). 266
Figure S65 - The activity coefficient (γ) for (a) H_2O and (b) CH_4, (c) the hydrate volume temporal profile (V_H) and (d) the vapor phase volume (V_G) temporal profile at 276 K (*DR*

= 0.5). The insertion (d) shows the the gas density (ρ_G) profile. The lines describe the time profiles for the following ethanol compositions of the initial liquid phase: 5 wt% (continuous line), 10 wt% (dashed line) and 15 wt% (dotted-dashed line) of EtOH, at 70.9 bar, θ = 72% (black), and at 74.9 bar, θ = 75% (yellow). 267
Figure S66 - (a) The temporal profile of the population balance moment of order zero, number of particles per liquid volume (μ_0), (b) moment of order one, particle diameter per liquid volume (μ_1), (c) moment of order two, particle surface area per liquid volume (μ_2) and (d) moment of order three, particle volume per liquid volume (μ_3) at 276 K (*DR* = 0.5). The lines describe the time profiles for the following ethanol compositions of the initial liquid phase: 5 wt% (continuous line), 10 wt% (dashed line) and 15 wt% (dotted-dashed line) of EtOH, at 70.9 bar, θ = 72% (black), and at 74.9 bar, θ = 75% (yellow). 268
Figure S67 - (a) The number of moles of methane (n_L,CH_4) and (b) the liquid phase volume (V_L) temporal profiles at 70.9 bar (*DR* = 0.5). The insertion (a) shows the number of moles of water (n_L,H_2O) profile in the bulk liquid phase. The insertion (b) shows the liquid density (ρ_L) profile. The lines describe the time profiles for the following ethanol compositions of the initial liquid phase: 5 wt% (continuous line), 10 wt% (dashed line) and 15 wt% (dotted-dashed line) of EtOH, at 276 K, θ = 72% (black), and at 274 K, θ = 68% (yellow). 269
Figure S68 - The activity coefficient (γ) for (a) H_2O and (b) CH_4, (c) the hydrate volume temporal profile (V_H) and (d) the vapor phase volume (V_G) temporal profile at 70.9 bar (*DR* = 0.5). The insertion (d) shows the the gas density (ρ_G) profile. The lines describe the time profiles for the following ethanol compositions of the initial liquid phase: 5 wt% (continuous line), 10 wt% (dashed line) and 15 wt% (dotted-dashed line) of EtOH, at 276 K, θ = 72% (black), and at 274 K, θ = 68% (yellow)..... 270
Figure S69 - (a) The temporal profile of the population balance moment of order zero, number of particles per liquid volume (μ_0), (b) moment of order one, particle diameter per liquid volume (μ_1), (c) moment of order two, particle surface area per liquid volume (μ_2) and (d) moment of order three, particle volume per liquid volume (μ_3) at 70.9 bar (*DR* = 0.5). The lines describe the time profiles for the following ethanol compositions of the initial liquid phase: 5 wt% (continuous line), 10 wt% (dashed line) and 15 wt% (dotted-dashed line) of EtOH, at 276 K, θ = 72% (black), and at 274 K, θ = 68% (yellow). 271

Figure S70 - The differential profile of (a) the methane number of moles in the bulk liquid phase ($dn_{L,CH4}$) and (b) the liquid phase volume (dV_L) at 276 K and 70.9 bar (*DR* = 0.5). The insertion (a) in the left shows the methane saturation profile and the one in the right shows the water number of moles (n_L,H_2O) profile in the bulk liquid phase. The insertion (b) shows the liquid density (ρ_L) profile with a zoom in the profile at 0 wt% of EtOH. The lines describe the time profiles for the following ethanol compositions of the initial liquid phase: 0 wt% (dotted line) and 5 wt% (continuous line) of EtOH. 272
Figure S71 - The differential profile of (a) the methane number of moles in the pure vapor phase (dn_G) and (b) the hydrate number of moles (dn_H) at 276 K and 70.9 bar (*DR* = 0.5). The insertion (a) shows the vapor phase volume (dV_G) with the constant vapor density ($d\rho_G$) differential profile. The insertion (b) shows the hydrate phase volume (dV_H) differential profile. The lines describe the time profiles for the following ethanol compositions of the initial liquid phase: 0 wt% (dotted line) and 5 wt% (continuous line) of EtOH. 273
Figure S72 - (a) The differential profile of the population balance moment of order zero, number of particles per liquid volume ($d\mu_0$), (b) moment of order one, particle diameter per liquid volume ($d\mu_1$), (c) moment of order two, particle surface area per liquid volume ($d\mu_2$) and (d) moment of order three, particle volume per liquid volume ($d\mu_3$) at 276 K and 70.9 bar (*DR* = 0.5). The lines describe the time profiles for the following ethanol compositions of the initial liquid phase: 0 wt% (dotted line, 2nd axis) and 5 wt% (continuous line, 1st axis) of EtOH. 274
Figure S73 - The differential profile of (a) the methane number of moles in the bulk liquid phase ($dn_{L,CH4}$) and (b) the liquid phase volume (dV_L) at 276 K and 70.9 bar (*DR* = 0.5). The insertion (a) in the left shows the methane saturation profile and the one in the right shows the water number of moles (n_L,H_2O) profile in the bulk liquid phase. The insertion (b) shows the liquid density (ρ_L) profile with a zoom in the methane saturation profile. The lines describe the time profiles for the following ethanol compositions of the initial liquid phase: 5 wt% (continuous line), 10 wt% (dashed line) and 15 wt% (dotted-dashed line) of EtOH. 275
Figure S74 - The differential profile of (a) the methane number of moles in the pure vapor phase (dn_G) and (b) the hydrate number of moles (dn_H) at 276 K and 70.9 bar (*DR* = 0.5). The insertion (a) shows the vapor phase volume (dV_G) and the constant vapor density ($d\rho_G$) differential profile. The insertion (b) shows the hydrate phase volume (dV_H)

differential profile. The lines describe the time profiles for the following ethanol compositions of the initial liquid phase: 5 wt% (continuous line), 10 wt% (dashed line) and 15 wt% (dotted-dashed line) of EtOH. 276
Figure S75 - (a) The differential profile of the population balance moment of order zero, number of particles per liquid volume ($d\mu_0$), (b) moment of order one, particle diameter per liquid volume ($d\mu_1$), (c) moment of order two, particle surface area per liquid volume ($d\mu_2$) and (d) moment of order three, particle volume per liquid volume ($d\mu_3$) at 276 K and 70.9 bar (*DR* = 0.5). The lines describe the time profiles for the following ethanol compositions of the initial liquid phase: 5 wt% (continuous line), 10 wt% (dashed line) and 15 wt% (dotted-dashed line) of EtOH. 277
Figure S76 - The differential profile of (a) the methane number of moles in the bulk liquid phase ($dn_{L,CH4}$) and (b) the liquid phase volume (dV_L) at 276 K and 70.9 bar (*DR* = 0.5). The insertion (a) in the left shows the methane saturation profile and the one in the right shows the water number of moles (n_L,H_2O) profile in the bulk liquid phase. The insertion (b) shows the liquid density (ρ_L) profile with a zoom in the profile at 0 wt% of EtOH. The lines describe the time profiles for the following ethanol compositions of the initial liquid phase: 0 wt% (dotted line) and 5 wt% (continuous line) of EtOH, with (black) and without (yellow) water activity in the driving force. 278
Figure S77 - The differential profile of (a) the methane number of moles in the pure vapor phase (dn_G) and (b) the hydrate number of moles (dn_H) at 276 K and 70.9 bar (*DR* = 0.5). The insertion (a) shows the vapor phase volume (dV_G) with the constant vapor density ($d\rho_G$) differential profile. The insertion (b) shows the hydrate phase volume (dV_H) differential profile. The lines describe the time profiles for the following ethanol compositions of the initial liquid phase: 0 wt% (dotted line) and 5 wt% (continuous line) of EtOH, with (black) and without (yellow) water activity in the driving force. 279
Figure S78 - (a) The differential profile of the population balance moment of order zero, number of particles per liquid volume ($d\mu_0$), (b) moment of order one, particle diameter per liquid volume ($d\mu_1$), (c) moment of order two, particle surface area per liquid volume ($d\mu_2$) and (d) moment of order three, particle volume per liquid volume ($d\mu_3$) at 276 K and 70.9 bar (*DR* = 0.5). The lines describe the time profiles for the following ethanol compositions of the initial liquid phase: 0 wt% (dotted line, 2nd axis) and 5 wt% (continuous line, 1st axis) of EtOH, with (black) and without (yellow) water activity in the driving force..... 280

Figure S79 - The differential profile of (a) the methane number of moles in the bulk liquid phase ($dn_{L,CH4}$) and (b) the liquid phase volume (dV_L) at 276 K and 70.9 bar (*DR* = 0.5). The insertion (a) in the left shows the methane saturation profile and the one in the right shows the water number of moles (n_L,H_2O) profile in the bulk liquid phase. The insertion (b) shows the liquid density (ρ_L) profile with a zoom in the methane saturation profile. The lines describe the time profiles for the following ethanol compositions of the initial liquid phase: 5 wt% (continuous line), 10 wt% (dashed line) and 15 wt% (dotted-dashed line) of EtOH, with (black) and without (yellow) water activity in the driving force.. 281
Figure S80 - The differential profile of (a) the methane number of moles in the pure vapor phase (dn_G) and (b) the hydrate number of moles (dn_H) at 276 K and 70.9 bar (*DR* = 0.5). The insertion (a) shows the vapor phase volume (dV_G) and the constant vapor density ($d\rho_G$) differential profile. The insertion (b) shows the hydrate phase volume (dV_H) differential profile. The lines describe the time profiles for the following ethanol compositions of the initial liquid phase: 5 wt% (continuous line), 10 wt% (dashed line) and 15 wt% (dotted-dashed line) of EtOH, with (black) and without (yellow) water activity in the driving force. 282
Figure S81 - (a) The differential profile of the population balance moment of order zero, number of particles per liquid volume ($d\mu_0$), (b) moment of order one, particle diameter per liquid volume ($d\mu_1$), (c) moment of order two, particle surface area per liquid volume ($d\mu_2$) and (d) moment of order three, particle volume per liquid volume ($d\mu_3$) at 276 K and 70.9 bar (*DR* = 0.5). The lines describe the time profiles for the following ethanol compositions of the initial liquid phase: 5 wt% (continuous line), 10 wt% (dashed line) and 15 wt% (dotted-dashed line) of EtOH, with (black) and without (yellow) water activity in the driving force. 283
Figure S82 - The differential profile of (a) the methane number of moles in the bulk liquid phase ($dn_{L,CH4}$) and (b) the liquid phase volume (dV_L) at 276 K (*DR* = 0.5). The insertion (a) in the left shows the methane saturation profile and the one in the right shows the water number of moles (n_L,H_2O) profile in the bulk liquid phase. The insertion (b) shows the liquid density (ρ_L) profile with a zoom in the methane saturation profile. The lines describe the time profiles for the following ethanol compositions of the initial liquid phase: 5 wt% (continuous line), 10 wt% (dashed line) and 15 wt% (dotted-dashed line) of EtOH, at 70.9 bar, θ = 72% (black), and at 74.9 bar, θ = 75% (yellow)..... 284
Figure S83 - The differential profile of (a) the methane number of moles in the pure vapor

phase (dn_G) and (b) the hydrate number of moles (dn_H) at 276 K (*DR* = 0.5). The insertion (a) shows the vapor phase volume (dV_G) and the constant vapor density ($d\rho_G$) differential profile. The insertion (b) shows the hydrate phase volume (dV_H) differential profile. The lines describe the time profiles for the following ethanol compositions of the initial liquid phase: 5 wt% (continuous line), 10 wt% (dashed line) and 15 wt% (dotted-dashed line) of EtOH, at 70.9 bar, θ = 72% (black), and at 74.9 bar, θ = 75% (yellow). 285

Figure S84- (a) The differential profile of the population balance moment of order zero, number of particles per liquid volume ($d\mu_0$), (b) moment of order one, particle diameter per liquid volume ($d\mu_1$), (c) moment of order two, particle surface area per liquid volume ($d\mu_2$) and (d) moment of order three, particle volume per liquid volume ($d\mu_3$) at 276 (*DR* = 0.5). The lines describe the time profiles for the following ethanol compositions of the initial liquid phase: 5 wt% (continuous line), 10 wt% (dashed line) and 15 wt% (dotted-dashed line) of EtOH, at 70.9 bar, θ = 72% (black), and at 74.9 bar, θ = 75% (yellow). 286

Figure S85 - The differential profile of (a) the methane number of moles in the bulk liquid phase ($dn_{L,CH4}$) and (b) the liquid phase volume (dV_L) at 70.9 bar (*DR* = 0.5). The insertion (a) in the left shows the methane saturation profile and the one in the right shows the water number of moles (n_L,H_2O) profile in the bulk liquid phase. The insertion (b) shows the liquid density (ρ_L) profile with a zoom in the methane saturation profile. The lines describe the time profiles for the following ethanol compositions of the initial liquid phase: 5 wt% (continuous line), 10 wt% (dashed line) and 15 wt% (dotted-dashed line) of EtOH, at 276 K, θ = 72% (black), and at 274 K, θ = 68% (yellow). 287

Figure S86 - The differential profile of (a) the methane number of moles in the pure vapor phase (dn_G) and (b) the hydrate number of moles (dn_H) at 70.9 bar (*DR* = 0.5). The insertion (a) shows the vapor phase volume (dV_G) and the constant vapor density ($d\rho_G$) differential profile. The insertion (b) shows the hydrate phase volume (dV_H) differential profile. The lines describe the time profiles for the following ethanol compositions of the initial liquid phase: 5 wt% (continuous line), 10 wt% (dashed line) and 15 wt% (dotted-dashed line) of EtOH, at 276 K, θ = 72% (black), and at 274 K, θ = 68% (yellow).... 288

Figure S87 - (a) The differential profile of the population balance moment of order zero, number of particles per liquid volume ($d\mu_0$), (b) moment of order one, particle diameter per liquid volume ($d\mu_1$), (c) moment of order two, particle surface area per liquid volume ($d\mu_2$) and (d) moment of order three, particle volume per liquid volume ($d\mu_3$) at 70.9 bar

(*DR* = 0.5). The lines describe the time profiles for the following ethanol compositions of the initial liquid phase: 5 wt% (continuous line), 10 wt% (dashed line) and 15 wt% (dotted-dashed line) of EtOH, at 276 K, θ = 72% (black), and at 274 K, θ = 68% (yellow). 289

Figure S88- Comparison between experimental values, y-axis, and calculated values, x-axis, in the estimation of NRTL model parameters using data reconciliation for the CH_4+EtOH system [165,253,254] and the matrix of the parameters correlation coefficients. The input variables reconciled using the reported experimental errors were (a) the methane composition in the liquid phase, x_{CH4}, and (b) the equilibrium temperature. The output variable calculated through the NRTL model in the estimation process was (c) the pressure. 292

Figure S89 - CH_4(2) + EtOH(3) liquid-vapor equilibrium isothermal curves. The experimental data are represented by the filled circles for (a) 253.15 K, 263.15 K, 273.15 K, 298.15 K, and (b) 280.15 K, 313.4 K, and 333.4 K. The empty circles are calculated with the NRTL model..... 293

List of Tables

Table 1 - Relationship between the diameter of the molecule and the diameter of the cavity. 2

Table 2 - NRTL model parameters, and their respective parameter errors, obtained by adjusting the liquid-vapor equilibrium data and infinite dilution data of the THF(1)/H_2O(2) system. 24

Table 3 - Kihara potential cavity parameters for THF, and their respective parameter errors, obtained by adjusting the hydrate-liquid equilibrium data of the THF/H_2O system. And the Kihara potential cavity parameters for CH_4, CO_2 e H_2. 24

Table 4 - Purity and supplier of materials used in the experimental study. 40

Table 5 - Input data for the calculation of isothermal-isobaric single hydrate (sI) growth of the CH_4 + H_2O system. 76

Table 6 – Additional input data for the calculation of isothermal-isobaric single hydrate (sI) growth of the CH_4 + H_2O + EtOH system. 102

Table S1 – Literature THF/H_2O vapor-liquid equilibria experimental data. 161

Table S2 – Literature THF/H_2O hydrate-liquid-vapor equilibria (HLE) experimental data. 163

Table S3 - Calculated data properties from the liquid-hydrate-vapor equilibrium data for H_2O + EtOH + CH_4 system. 166

Table S4 - The average absolute deviation (AAD) for the CH_4 hydrate phase equilibria data with ethanol for the three tested models. 167

Table S5 - Calculated data properties from the liquid-hydrate-vapor equilibria data for H_2O + EtOH + CO_2 system. 168

Table S6 - The average absolute deviation (AAD) for the CO_2 hydrate phase equilibria data with ethanol for the three tested models. 169

Table S7 - Calculated data properties from the liquid-hydrate-vapor equilibria data for H_2O + EtOH + C_3H_8 system. 169

Table S8 - The average absolute deviation (AAD) for the C_3H_8 hydrate phase equilibria data with ethanol for the three tested models. 170

Table S9 - Liquid-hydrate-vapor equilibrium data with ethanol of C_2H_6 gas. 170

Table S10 - Calculated data properties from the liquid-hydrate-vapor equilibria data for

H_2O + EtOH + C_2H_6 system. 171
Table S11 - The average absolute deviation (AAD) for the C_2H_6 hydrate phase equilibria data with ethanol for the three tested models. 172
Table S12 - Liquid-hydrate-vapor equilibrium data with ethanol of the gas mixture of 73.8 wt.% CH_4 and 26.2 wt.% C_2H_6..... 172
Table S13 - Calculated data properties from the liquid-hydrate-vapor equilibria data for H_2O + EtOH + CH_4/C_2H_6 system. 173
Table S14 - The average absolute deviation (AAD) for the gas mixture of 73.8 mol% CH_4 and 26.2 mol% C_2H_6 hydrate phase equilibria data with ethanol for the two tested models..... 173
Table S15 - Parameters of the NRTL model, and their respective errors, obtained by adjusting the liquid-vapor equilibrium data and infinite dilution data of the Ethanol (1) + H_2O (2) system. 180
Table S16 - Kihara parameters adjusted for the hydrate phase equilibrium data of the Gas + H_2O systems. 184
Table S17 - Parameters of the NRTL model, and their respective errors, obtained by adjusting the liquid-vapor equilibrium and solubility data of the system CH_4 (1) + H_2O (2). 189
Table S18 - Correlation parameters of the hypothetical liquid phase for light gases at 101.32 Pa and their respective deviations. 245
Table S19 - Parameters of the ternary NRTL model for the system H_2O(1) + CH_4(2) + EtOH(3), and their respective errors, obtained by adjusting experimental data from binary systems. 251

Chapter 1. Introduction

This chapter will pass through the background and contextualization of the hydrate research field, focusing on the relevance of modeling the hydrate growth in non-ideal systems using the literature thermodynamic knowledge. We will then present what motivated this work and its objectives, and the structure, that compose this thesis.

1.1 Background and relevance

Gas hydrate formation and decomposition processes are critical in flow assurance for the oil and gas industry [1], which boosted research to comprehend and avoid these solids formation from 1930 until the present [2]. However, research on gas hydrates has also progressed over the past several decades as a technology enabler for several innovative applications in the areas of energy storage, energy transport, gas separation, desalination, and others [3].

1.1.1 Gas hydrate

Hydrates are crystalline-solid structures formed by water and a guest molecule, an organic light molecule, under high-pressure and low-temperature conditions [4]. The hydrophobic effect causes the ordering of water molecules forming structured cavities by hydrogen bonds interaction, while the guest is trapped inside the water-cavity framework by van der Waals forces [2].

Hydrate crystals were characterized through X-ray methods, and the three main crystalline structures of these solids were determined [5,6]. The structures I, II and H are differentiated by the size of the cavities formed and by different amounts of pentagonal and hexagonal faces with varied conformations and arrangements for each type [4].

The main characteristics that distinguish these structures are:

a) The number of small and large cavities that a hydrate structure has per unit cell;

b) The type of cavity represented by the powers of 5 and 6 to describe the number of pentagonal and hexagonal faces, respectively;

c) The average radius of each cavity, that is, the average distance between the centers of the water molecules present in the edges that form the cavity; and

d) The coordination number, which is the quantity of water molecules on the periphery of each cavity.

These characteristics of hydrate structures are specified for the three structures mentioned in the paper Sloan Jr. [4].

The crystalline hydrate structure is defined mainly by the characteristics of the guest molecule. Such definition is a function of two factors: a) the chemical nature of the guest and b) its size and shape [2,4]. The ratio between the size of the guest and the cavity-average radius is fundamental to determine the stability of the crystalline structure. It is defined that the closer to one (between 0.75 and 1.00) is the relationship between the guest molecule diameter and the cavity diameter, the more stable is the structure [4].

With the literature information of the CH_4 [4], tetrahydrofuran (THF) [7] and ethanol (EtOH) [8], average radii, and the structures I and II average cavity radii [4], the relationship between the guest molecule radius and the cavity radius are calculated, Table 1, for the molecules of interest in this study.

Table 1 - Relationship between the diameter of the molecule and the diameter of the cavity.

Guest Molecule	**The average radius of the guest molecule (Å)**	**Structure I**		**Structure II**	
		Small	**Large**	**Small**	**Large**
Mean cavity radius (Å)		2.55[a]	2.93[a]	2.51[a]	3.33[a]
CH_4	2.18[c]	0.855	0.744	0.869	0.655
THF	3.15[d]	1.235	1.075	1.255	0.946
EtOH	3.25[e]	1.275	1.109	1.295	0.976

[a] Cavity radius minus the water radius of 1.4 Å [4]. [b] Cavities occupied by a single guest. [c] [4] [d] [7] [e] [8]

However, the type of structure formed is not just a function of the guest molecule size, but more specifically of a) the relationship between the molecule diameter and the cavity diameter; b) the number of small and large cavities in a structure, and c) the percentage of cavity occupation. It is important mention that organic additives such as THF or EtOH are potential hydrate formers of structure II, with occupation of large cavities. Some experimental studies reaffirm these characteristics [8–11].

Another classification is according to the cavities occupation by the guest molecules [1,2]. This classification helps to understand the role of chemical additives in altering or not the hydrate structures. The hydrates can be classified as:

a) Simple: one guest and one molecule per cavity;

b) Mixed: cavities are occupied by more than one type of molecule;

c) Double: each type of cavity is mainly occupied by a type of molecule;

d) *Hilfgase* or "help gas": system with a small guest assisting the formation of a hydrate with a larger guest;

e) Multiple occupancies: cavities occupied by more than one molecule at the same time.

The use of chemical additives, such as THF and EtOH, and the understanding of how they alter the crystalline structure formed and its formation mechanism, are motivated by the different applications they have in the industry and in the technological development that involves hydrate formation.

1.1.2 Gas hydrate as an issue, a resource or a potential technology

For decades, hydrates have been seen only as unwanted solids due to flow assurance in the oil and gas industry, i.e., as a problem to be avoided [1]. However, hydrate have recently gained prominence as solidified natural gas (SNG) technology due to its ability to store light gases and the attempt to explore its natural reserves. That is, scenarios in which the controlled formation or dissociation of this solid are desired to make use of their technological and energetic potential [3].

The conditions for oil and gas exploration, mainly offshore, are incredibly favorable for hydrate formation. Hydrates formation in pipelines can lead to blockages along with the flow and cause significant damage in terms of economy and security. Conventional hydrate inhibition methods are based mainly on dehydration of the gas mixtures, temperature control, and chemical additives [12]. Since the physical options are neither applicable nor economical, the use of additives is the most common method to prevent the occurrence of blockages [13]. Between the chemical additives, there are thermodynamic hydrate inhibitors (THIs) and low-dosage hydrate inhibitors (LDHIs) [14]. The LDHIs are kinetic hydrate inhibitors (KHIs) or anti-agglomerates (AAs) that

slow down the growth and/or agglomeration. Although the industry has already used LDHIs, the understanding of its effects and the guarantee of its application are still under study [1,2,13]. Besides, THIs have been used for a longer time by the industry and have greater understanding and guarantee of their inhibitory effect [15]. THIs are defined as chemical additives, mainly alcohols or glycols, such as methanol, ethanol and monoethylene glycol (MEG) [16]. Its addition shifts the equilibrium condition to conditions of higher temperatures and/or lower pressures in order to ensure that the production lines are outside the hydrate formation region [17].

The occurrence of CH_4 hydrate reserves in nature came to be seen as a potential renewable energy source [18]. Natural reserves have not only become a potential source of energy with the largest carbon source on the planet [19]. It is also a renewable energy source, and studies are under development to enable the replacement of CH_4, which is useful, by CO_2, a polluting gas, through chemical additives [20]. The environmental impact of the global warming effects on natural hydrate reserves has driven the exploration of these reserves, which may have a lesser impact in the long term [21].

Advances in the applications for using these crystalline structures, due to their capacity to store gases, have been recently developed [3,22,23]. The researches in solidified natural gas (SNG) technology concluded that the requirement of high pressure for hydrate formation is one of the decisive obstacles for the commercialization of the process [13,23]. The use of chemical additives, mainly thermodynamic promoters, enables hydrates production and control for storage and separation of gases, assuaging the thermodynamic hydrate formation conditions [24]. Thermodynamic hydrate promoters are defined as co-formers, which participate in a double hydrate formation process and stabilize the crystalline structure at higher temperatures and/or lower pressures [25].

The first requirement for hydrate stabilization is the size limitation. The molecule must not be larger than the cavity. THF has a 0.946 ratio between its radius and the structure II large cavity radius, while CH_4 has a ratio of 0.869 to occupy the structure II small cavities, Table 1. Consequently, the THF/CH_4 double hydrate with this cavity's occupation has high stability [9]. Therefore, in principle, alcohol can stabilize the hydrate, as long as it has an adequate diameter to be kept encapsulated in a cavity. Ethanol can form double hydrates with light gases with a 0.976 ratio between its radius and the structure II large cavity radius. It should be noted that the relationship between

the size of the cavity and the diameter of the guest molecule does not determine whether a compound can form hydrates or not [26], but it is a factor of significant influence. However, more studies are still necessary to define under which temperature, pressure or composition conditions the co-former effect predominates over the inhibitory effect [8,27–29].

Chemical additives are required to prevent the formation of blockages in the oil and gas industry, assist the exploration of natural hydrate reserves, or facilitate the SNG technology. The formation of hydrates in mixtures containing water-soluble organic compounds has ambiguous characteristics. Theoretically, some of THIs can stabilize the hydrate structure under certain conditions [8,10,28,30]. Besides, hydrate-promoting species can also alter water activity, changing the hydrate equilibrium condition [9,26,31]. Because of the inhibitor/promoter present double behavior, it is necessary to know and to model these effects to improve the use of this type of compound as a blocking-prevention agent to assure flow, or hydrate promoting agent to enable a new storage technology.

1.1.3 Gas hydrate formation

Water, light organic molecules, high pressure, and low temperature are considered primary factors for the hydrate formation [4]. Although these factors are necessary to guarantee formation, they are not decisive. Hydrate formation is a crystallization process influenced by the dynamics that involve mainly two distinct stages: nucleation and growth. These two hydrate formation stages must be understood to build a dynamic model, and it is essential to establish considerations under the limitations imposed by mass and/or energy transport [32]. Because the focus here is the hydrate growth kinetics, only a summary of the nucleation theory is presented.

The stochastic nature of hydrate nucleation, confounding cause-effect relations, and spatial-temporal scales has made it challenging to understand [33,34]. Because the guest species is usually in the gas phase, the process starts with the dissolution into the liquid phase. After that, supersaturation begins when the pressure and temperature are thermodynamically favorable to hydrate formation. It occurs by forming light gases and water pre-nuclei until the formation of critical-size hydrate nuclei. This reorganization creates small gas-water clusters which form the sites for nucleation to begin. Reorganization to create a new surface reduces the system entropy, leading to a positive

in the surface excess Gibbs free energy [11,35]. A critical nucleus of the hydrate phase can be defined as the minimum amount of hydrate capable of existing independently [34]. The time interval between the supersaturation establishment and critical nuclei formation is called induction time [36]. Despite efforts to describe the hydrate nucleation mechanism, the nucleation pathways themselves are still debated, and there are opinions that nucleation is likely to occur through multiple competing pathways [34,37,38]. Khurana, Yin, and Linga carried out a compilation of the main hydrate nucleation mechanisms in the literature [34].

On the other side, the hydrate growth process involves hydrate core [32]. The literature presents mechanisms on macroscopic, mesoscopic, and microscopic scales to describe the hydrate growth phenomenon. While the macroscopic mechanisms are based on the gas consumption profile [39], the mesoscopic and microscopic mechanisms are mostly molecular and boundary layers [2].

The boundary layer theory, which is the fluid layer in the bounding surface, is subject to diffusive effects, that is, the mass transfer of the guest from the bulk liquid phase to the hydrate crystal interface [2,40]. Two regions are generally considered in the hydrate growth mechanism: the region of stagnant film at the interface between the crystal and the liquid phase, and the region corresponding to the adsorption layer [16]. Consequently, two driving forces can govern the phenomenon:

(1) the diffusion of the light organic gas dissolved in the solution to the liquid-crystal interface through a laminar diffusion layer around the particle;

(2) the "reaction" at the crystal interface occurs when the gas molecules are incorporated into the water structure, providing stability.

Hydrate growth models are based mainly on this two-steps mechanism and have been in the literature since 1897 [41], including the model proposed by Englezos et al. [42,43], which is the most notorious hydrate growth model in the past years, until the most recent work by Bassani et al. [44–46].

From a microscopic point of view, Sloan and Koh [2] combined the conceptual mechanism of Elwell and Sheel [47] for crystal growth with the Labile Cluster Hypothesis (LCH) theory or the local structuring hypothesis (Local Structuring Mechanism-LSM) [48,49] for nucleation and thus presented a molecular mechanism to

describe the phenomenon of hydrate crystal growth. As in the Elwell and Sheel mechanism, the integration of the atoms in the crystal occurs more readily in the crystalline surface faults.

Some molecular simulation studies use this mechanism conceptually [50,51]. However, unlike nucleation, growth, although also a stochastic process, has a high probability of occurring and is an easier phenomenon to be experimentally measured. For this reason, growth models developed more through boundary layer mechanisms than through molecular mechanisms.

The literature has kinetic models that differ mainly in terms of the growth rate driving force. According to Mohammadi et al. [52], the literature presents several driving forces; however, the most common types are related to the equilibrium curve. Hydrate growth models are classified by the literature [15,32] according to the phenomena involved in growth and its driving force.

The empirical or semi-empirical kinetic growth models [53,54,63,64,55–62] are based on mechanisms proposed to describe the hydration formation "reaction", considering the factors that favor these crystals formation. Among these factors are subcooling, pressure, and solubility of the gas in the liquid phase, which can be measured along with the growth process. Models based on subcooling [65–74], the temperature difference between the system condition and the hydrate equilibrium temperature, are typical because hydrate formation is an exothermic process. Models limited by mass transfer [33,42,82–90,43,75–81] are basically divided into three categories of driving force: in chemical potential or fugacity differences, in concentration difference, and chemical affinity. Chemical affinity as a driving force is recently proposed in the literature, and most models that use this approach tend to simplify the driving force and be limited to describe systems without additives. However, these simplifications are no longer valid when chemical additives are added, as in the case of inhibited or promoted systems. Therefore, models based on chemical affinity need improvements. Models combine driving forces, such as mass transfer and chemical reaction [91–96], and subcooling and chemical reaction [40,97] are presented in the literature, as well.

1.2 Motivation and objectives

Understanding the vital role of chemical additives in the hydrates field advances and in what stage are the development of the hydrate growth models, this work proposes a growth model with chemical affinity as a driving force capable of accounting for the non-ideal effect of these systems. The objective is to incorporate the hydrate equilibrium modeling knowledge in the growth kinetics, mainly for non-ideal systems.

The classical thermodynamic modeling of hydrate equilibrium in systems with chemical additives is developed based on the theory of van der Waals and Platteeuw. Van der Waals and Platteeuw [98] model is based on statistical thermodynamics. This model expresses the water chemical potential difference between the hydrate phase and the liquid phase, passing through the empty-hydrate hypothetical structure, as a function of the cavity occupation fraction. The fraction of occupied cavities is obtained according to the Langmuir theory of localized adsorption. Advances in the van der Waals and Platteeuw model occur through the different models for the chemical potential of water in the empty structure [99–102], and suitable models for calculating the Langmuir constants [103–108].

The effects of chemical additives require consistent models for the fluid phases in order to simultaneously describe the conditions of liquid-vapor (LVE), hydrate-liquid (HLE) and hydrate-liquid-vapor (HLVE) equilibria. The equilibrium condition is obtained directly by the equality between the water potentials in the liquid and solid phases and indirectly by the criterion of fugacity equality between the fluid and the hydrate phase for both gas and polar formers. Therefore, the literature presents, in general, two approaches to calculate water activity and the hydrate former or co-former fugacity. The first one consists of calculating the vapor and liquid phase fugacity of the former and the co-former, and the water activity using an equation of state like CPA or SAFT [109–113]. In the second approach, the water activity and the co-former fugacity in the liquid phase are calculated by an excess Gibbs free energy model, like NRTL or UNIQUAC, and the fugacity of the former in the vapor phase with a equation of state, like Peng-Robinson [114–118].

However, the main difficulty in obtaining models capable of predicting the complete diagram of systems containing hydrate inhibitors or promoters is to obtain parameters that show good correlation of data and good transferability between the

different conditions involving LVE, HLE and HLVE. Most of the thermodynamic models available in the literature are restricted to narrow ranges of system composition, temperature, and pressure [13]. The first objective here is to improve the equilibria understanding and modeling of promoted or inhibited systems. The development of a growth model for these systems requires proper calculation for different equilibrium conditions and thermodynamic properties over time.

The hydrate thermodynamic promoter studied here is tetrahydrofuran (THF). THF is a well-known and used hydrate promoter in the literature [119]. Our objective in this work is to provide a consistent thermodynamic modeling strategy capable of representing the equilibrium of THF and water mixtures, and that also has the potential for extrapolation to scenarios with light gases. The hydrate thermodynamic inhibitor studied here is ethanol (ETOH). However, the literature presents limited equilibrium data for EtOH, especially for high concentrated solutions [120]. Brazil is one of the biggest producers of ethanol. Because of the price, it has become increasingly more common in the Brazilian oil and gas industries. However, there are experimental data in the literature showing that EtOH can work as a co-former for hydrates [8,27,28]. As such, there is a need to understand the hydrate phase equilibrium with ethanol [8,27,28] better. For the development of the equilibrium modeling, systems of different light gases were studied, such as methane, ethane, carbon dioxide and others, most present in the usually natural gas composition.

Exploring natural gas reserves, flow assurance, and the development of the SNG technology require a predictive model for the formation of hydrates at non-ideal systems to ensure the economic and safety requirements [13]. Therefore, the main objective here is to develop a hydrate growth model to include thermodynamic knowledge. Non-equilibrium thermodynamics [121,122] is the theoretical approach used in the model development. A new driving force, based on the Prigogine Chemical Affinity [121], is stablished to account for the effect of the thermodynamic factor in the kinetics and to be able to describe the non-ideal systems adequately. With this model, we intend to describe the growth considering the diffusion and reaction steps.

The developed model was first used to simulate the methane hydrate formation in freshwater. We compared the CH_4 hydrate growth system with and without the ethanol addition. Even more, we evaluated the effect of increasing the ethanol concentration, comparing systems with 5, 10 and 15 wt% of EtOH initial composition. The effect of

temperature and pressure, important properties for the hydrate formation, were also studied. Because most of the hydrate growth models in the literature [15,33,84,85,93] use only the guest properties in the driving force, we evaluated the effect of including the water activity on the driving force with and without ethanol.

In summary, the objectives of this work are:

a) To provide consistent thermodynamic modeling for hydrate formation systems with THF. The model can predict different equilibrium conditions consistently, and that could be transferred to non-equilibrium conditions.
b) To obtain a better understanding of the EtOH effect as a hydrate inhibitor or promoter, thus being able to distinguish this behavior and to better model the hydrate equilibrium and kinetics in its presence.
c) To develop a hydrate growth model considering the thermodynamic knowledge already well established in the literature and propose a driving force that accounts for the chemical additives effect through the inclusion of the thermodynamic factor.
d) To calculate the formation rate of methane hydrate in pure water and ethanol inhibited systems, we tested the model quantitative and qualitative capacity and the importance of including the thermodynamic factor for inhibited systems.

1.3 Thesis structure

Besides the present chapter, this thesis is structured with five more chapters. Each chapter, from 2 to 5, is prepared based on an article published or in preparation.

Chapter 2 corresponds to the proposed "Accurate thermodynamic description of vapor-liquid and solid-liquid equilibria of THF, water and gas hydrates with a unique set of parameters" [123]. In this chapter, the hydrate equilibrium modeling with THF is discussed.

Chapter 3 presents the experimental study on "Phase Equilibria Data and Thermodynamic Analysis for Liquid-Hydrate-Vapor (LHV) with High Ethanol Concentrations" [124]. This chapter focus on the understanding and modeling of the hydrate equilibrium with EtOH.

Chapter 4 present the "Hydrate growth model based on non-equilibrium thermodynamics using Prigogine chemical affinity: Applied to CH_4 hydrate in freshwater". The chapter presents the development of the proposed growth model and its simulations for methane hydrate in fresh water. The corresponded article is in preparation.

Chapter 5 corresponds to the study on the "Hydrate growth model based on non-equilibrium thermodynamics using Prigogine chemical affinity: Applied to CH_4 hydrate in EtOH inhibited system". This chapter presents the proposed model, and its application to a hydrate inhibited system with simulated results for the methane hydrate growth in the presence of ethanol. The corresponded article is in preparation.

Chapter 6 contains general conclusions and suggestions for future work.

In this document, there are additional and complementary information in terms of Appendixes 1 to 4. **Appendix 1** is the supporting information of the second chapter and presented VLE and HLE experimental data of H_2O+THF collected from the literature, which were used to estimate parameters. **Appendix 2** is the supporting information of the third chapter. It presented the tables of the literature thermodynamic analysis for the gas hydrate experimental data with ethanol. And also, the HLVE experimental data obtained and the adjustments in the previously modeling for its application in hydrate systems with ethanol.

Appendix 3 and **Appendix 4** are the supporting information of the fourth and fifth chapter, respectively. Appendixes 3 and 4 presented the thermodynamic models used, the phase balances, the rates constitutive relationships, the interfaces equilibrium compositions calculations, the numerical solution methods, and the parameters adjustment necessary to describe the methane hydrate growth without and with ethanol, respectively. The time profiles of the secondary variables for each simulated system are also present in the Appendixes 3 and 4, as well as the time profiles of all derivatives computed in the growth calculation, respectively.

Chapter 2. Hydrate equilibria with promoter (THF)

In the context of gas hydrates technology for gas storage and separation processes, tetrahydrofuran (THF) has a recognized performance as a thermodynamic promoter. The literature presents a large amount of phase equilibrium experimental data for the THF hydrates systems. However, consistent thermodynamic modeling capable of describing vapor-liquid, liquid-hydrate, and liquid-ice equilibria of THF and water is still needed. To obtain this needed modeling, we propose a strategy for estimating a unique set of parameters for suitable thermodynamic models for THF and water mixtures in the conditions of vapor, liquid, and hydrate. We selected the NRTL model, the Peng-Robinson equation of state, and the van der Waals and Platteeuw hydrate model with the Kihara potential to correlate phase equilibrium calculations independent properties. We regressed parameters for the NRTL and Kihara models in two sequential steps using experimental data at conditions with pressure from 40 kPa to 101.33 kPa and temperature from 272 K to 343.15 K. The first steps determine optimal parameters for NRTL with, simultaneously, vapor-liquid equilibria and infinite dilution activity coefficient data. The second determines optimal Kihara parameters with liquid-hydrate equilibria data using a data reconciliation methodology. We verified the potential of the model for extrapolation by accurately describing phase equilibria scenarios involving liquid and vapor mixtures not included in the regression procedure, in addition to scenarios involving conventional ice and hydrates of THF with some industrial gas or natural gas components: H_2, CO_2 or CH_4.

2.1 Introduction

Thermodynamics of hydrates is a matter of special relevance for some technological applications involving industrial or natural gas components of interest. A few of such are the storage of H_2 and CH_4 or the separation of CO_2 from gas lines [125]. These exploit the nature of hydrates as solid phases with a molecular structure consisting of a host lattice of water molecules and enculturated molecules of guest components [2]. According to Sun et al. [23], the requirement of high pressure for hydrate formation is one of the decisive obstacles to the viability of such separation processes.

The thermodynamic stability of hydrates depends on the guest components. While said components of interest form hydrate at relatively immoderate conditions of high pressure and low temperature [2], tetrahydrofuran (THF) hydrate can form at atmospheric pressure and temperature around 277 K [126]. Hydrates of THF occur in structure II, where THF occupies the large cavities due to its relatively big molecular size [9]. Moreover, in systems containing both THF and other component of interest, double hydrates, where THF primarily occupies the large cavities while the smaller component occupies the small cavity, form at conditions of higher temperature and lower pressure than single hydrates would form whether only one of the guest components was present. With that in mind, THF is a potential guest component that has a recognized performance as a thermodynamic promoter [31,127–133].

At moderate conditions, THF is soluble in water. Increasing the concentration of THF in the liquid phase contributes to hydrate stability in two opposite ways. It increases its activity, which contribute to occupancy of hydrate cavities, and reduce chemical potential of water there, thus stabilizing the hydrate phase, while at the same time activity of water in the liquid phase decreases, granting more relative stability to the liquid phase, in relation to the hydrate. At low concentration (up to 0.0556 mole fraction, 1 atm), the former contribution is dominant, and this component will show its promoter effect on hydrate stability. On the other hand, at higher THF concentration, the water activity effect becomes dominant and THF will show an inhibitor effect.

Literature presents a large amount of phase equilibrium experimental data for the THF hydrates systems [9,126–128,134–137]. Most notably phase behavior of pure THF and mixtures thereof with water at atmospheric pressure is summarized as follows: This a volatile cyclic ether, with boiling point of 339 K and melting point of 164.8 K [138].

The solution of THF in water is highly non-ideal, with its vapor-liquid equilibria (VLE) showing an azeotrope in the region of high THF concentration (around 0.82 mole fraction). This solution's solid-liquid equilibria shows a congruent melting point hydrate-liquid-equilibria (HLE) at 277.55 K and 0.0556 mole fraction of THF [126], and an eutectic point hydrate-ice-liquid-equilibria (HILE) at 272.0 K and 0.01 mole fraction [127,128]. In order to be able to perform design and optimization of processes, a thermodynamic model capable of representing these varying behaviors is of practical importance. Moreover, descriptions of hydrate growth rate, adopting Gibbs energy difference as driving force [139], further motivate the search for consistent description of thermodynamic properties.

A few studies [111,140,141] have proposed modelings with varying combinations of equations of states (EoS), excess Gibbs energy (G^{E}) models and modifications of the van der Waals and Platteeuw theory [98,101,106] to describes these behaviors of THF and water mixtures. These were able to correlate properly only the hydrate phase equilibria in the THF concentration range with promoter effect, while the modeling of the inhibitory region has been neglected. Therefore, a consistent thermodynamic modeling capable of describing all of vapor-liquid, liquid-hydrate in both concentration ranges and liquid-ice equilibria of THF and water is still needed.

Our objective is to provide a consistent thermodynamic modeling capable of representing both liquid-vapor and solid-liquid equilibria of THF and water mixtures, while also having potential for extrapolation to different scenarios. For that purpose, we select models of current engineering relevance. Then, we propose a strategy for the estimation of a unique set of parameters to represent THF and water in the conditions of vapor, liquid, hydrate and ice. We discuss the correlations obtained with the optimal parameter set and, furthermore, verify the extrapolation potential by describing different scenarios. We are able to describe phase equilibria involving ice and double hydrates with all components of interest.

2.2 Thermodynamic modeling

In order to perform phase equilibrium calculations of broad applicability and with potential for extrapolations, we need consistent equilibrium criteria and well-known thermodynamic models. The underlying criteria basing the algorithms used here is the

classical thermodynamics condition for equilibrium: temperature (T), pressure (p) and the chemical potential (μ_i) of each component is the same for every present phase.

The phases of interest here are liquid (L) mixtures of water and THF, hydrates (H) of THF with or without H_2, CO_2 or CH_4, vapor (V) mixtures of water and THF (for VLE scenarios), pure vapor of H_2, CO_2 or CH_4 for (HLVE scenarios), and conventional ice (I). We implemented an algorithm for the specific scenario of VLE and expressed the equilibrium criteria for HLE in a way suited for fast iterative usage in the parameter estimation methodology.

2.2.1 Equilibrium criteria and algorithms

Our algorithm for VLE of water and THF is based on the equilibrium criteria expressed from using fugacities $\hat{f}_i$, equations (1).

$$\hat{f}_{\mathrm{w}}^{\mathrm{L}} = \hat{f}_{\mathrm{w}}^{\mathrm{V}} \qquad (1)$$

$$\hat{f}_{\mathrm{THF}}^{\mathrm{L}} = \hat{f}_{\mathrm{THF}}^{\mathrm{V}}$$

Where, for the liquid phase, we choose an G^{E} approach, thus expressing fugacities in the mixture from the activity coefficients (γ_i), as function of liquid phase composition ($\underline{x}$), and the pure liquid fugacities (f_i^{L}), equation (2).

$$\hat{f}_i^{\mathrm{L}} = x_i \, \gamma_i \left(T, p, \underline{x}\right) f_i^{\mathrm{L}} \left(T, p\right) \qquad (2)$$

Where f_i^{L} are calculated from pure VLE saturation pressure (p_i^{sat}) and pure liquid molar volume (v_i^{L}) correlations, equation (4).

$$f_i^{\mathrm{L}} = p_i^{\mathrm{sat}}\left(T\right) \phi_i^{\mathrm{sat}}(T) \exp\left(\int_{p_i^{sat}}^{p} \frac{v_i^{\mathrm{L}}\left(T, p\right)}{RT} dp \right) \qquad (3)$$

For THF, we were unable to find a correlation in literature, therefore using experimental data of THF density at different temperatures [142,143], we fit an empirical equation for the liquid molar volume of THF, $v_i^{L}(T)$, equation (4).

$$v_{\mathrm{THF}}^{\mathrm{L}} / \mathrm{m^3 mol^{-1}} = 7.0\ 10^{-10} (T/\mathrm{K})^2 - 4.0\ 10^{-7} (T/\mathrm{K}) + 10^{-4} \qquad (4)$$

While, for the vapor phase, we express fugacities from pressure and the fugacity coefficients (ϕ_i^{V}), equation (5).

$$f_i^{\mathrm{V}} = \phi_i^{\mathrm{V}}(p,T)\,p \tag{5}$$

we use the usual approximation for low pressure and temperature conditions for these VLE calculations of THF and water, equation (6).

$$\frac{\phi_i^{\mathrm{V}}(p,T)}{\phi_i^{\mathrm{sat}}(T)\exp\left(\int_{p_i^{sat}}^{p}\frac{v_i^{\mathrm{L}}(T,p)}{RT}dp\right)} \cong 1 \tag{6}$$

We expressed the equilibrium criteria for HLE in a convenient approach under the van der Waals and Platteeuw theory: using chemical potential difference, for water, with respect to the standard theoretical reference of an empty lattice ($\Delta\mu_{\mathrm{w}}^{\mathrm{H\text{-}EL}}$ and $\Delta\mu_{\mathrm{w}}^{\mathrm{L\text{-}EL}}$), equation (7).

$$\begin{gathered}\hat{f}_{\mathrm{THF}}^{\mathrm{H}} = \hat{f}_{\mathrm{THF}}^{\mathrm{L}}\left(T,p,\underline{x}\right)\\ \Delta\mu_{\mathrm{w}}^{\mathrm{H\text{-}EL}}\left(T,p,\hat{f}_{\mathrm{THF}}^{\mathrm{H}}\right)/\Delta\mu_{\mathrm{w}}^{\mathrm{L\text{-}EL}}\left(T,p\right)=1\end{gathered} \tag{7}$$

We calculate $\hat{f}_{\mathrm{THF}}^{\mathrm{L}}$ using equations (2) and (3) with the accurate correlation developed here and with the low-temperature approximation of $\phi_{\mathrm{THF}}^{\mathrm{sat}}(T)\cong 1$.

Only after finding the optimal parameters, HLVE diagrams are calculated using a specific scenario algorithm based on Parrish and Prausnitz's [103], assuming THF is not present in gas and H_2, CO_2 and CH_4 are not present in the liquid phase. Therefore, in addition to the criteria in equation (7), we also consider the fugacities for the gas phase guest components ($f_{\mathrm{g}}^{\mathrm{V}}$), provided by the Peng-Robinson EoS for a pure component, equation (8).

$$\hat{f}_{\mathrm{g}}^{\mathrm{H}} = f_{\mathrm{g}}^{\mathrm{V}}\left(T,p\right) \tag{8}$$

The Segtovich et al. [144] methodology, adapted to work with the modeling approach used here, was used to predict phase stability and generate complete phase diagrams of water and THF mixtures, including V, L, H, and I phases.

2.2.2 Non-ideal liquid phase model

Our reason for choosing an G^{E} approach to describe the non-ideal liquid phase was motivated by results from literature where EoS based approaches using the CPA [145] and SAFT-VR [146] were not able to quantitatively predict the vapor-liquid equilibrium of the THF/H_2O system. At the same time, other authors presented a good prediction capability of the equilibrium using G^{E} approach with Wilson [147] and NRTL [148] models. However, the adjusted VLE data in [148] comprised only compositions above 0.3 moles fraction of THF. Therefore, with selected the modified NRTL [148] model, and together with a wider set of VLE experimental data for the mixture raised in literature [138,149–151], we were able to re-evaluate the parameters of that model.

The activity coefficient expression from NRTL for a binary mixture of THF (1) and H_2O (2) is given by equation (9).

$$\gamma_i = \exp\left(\frac{\sum_{j=1}^{n} x_j \tau_{j,i} G_{j,i}}{\sum_{k=1}^{n} x_k G_{\mathrm{k},i}}\right) + \sum_{j=1}^{n} \frac{x_j G_{\mathrm{i,j}}}{\sum_{k=1}^{n} x_k G_{\mathrm{k,j}}} \left(\tau_{i,j} - \frac{\sum_{m=1}^{n} x_m \tau_{\mathrm{m,j}} G_{\mathrm{m,j}}}{\sum_{k=1}^{n} x_k G_{\mathrm{k,j}}}\right) \tag{9}$$

$$G_{i,\mathrm{j}} = \exp(\alpha \tau_{i,\mathrm{j}})$$

Where α is the symmetrical nonrandomness factor.

In addition, the binary interaction parameters ($\tau_{i,\mathrm{j}}$) are temperature dependent and were described by equation (10) for T_{ref} = 283.15 K.

$$\tau_{i,\mathrm{j}} = A_{\mathrm{i,j}} + B_{i,\mathrm{j}} \left(\frac{T_{ref}}{T} - 1\right) \tag{10}$$

Then, $A_{i,\mathrm{j}}$ $B_{i,\mathrm{j}}$ and α are the first of two subsets of parameters that require regression here.

2.2.3 Hydrate phase model

The original theory of van der Waals and Platteeuw [98] provides an expression for the difference in the chemical potential of H_2O between the hydrate (H) phase and the hypothetical phase of the empty lattice (EL), where *j* is the type of the cavity, i is

the type of the guest and ν_j is the number of cavities of the type j per water molecule of the unit cell, equation (11).

$$\Delta\mu_{\mathrm{w}}^{\mathrm{H\text{-}EL}} = -RT\sum_j \nu_j \ln\left(1-\sum_i \frac{CL_{i,j} f_i^{\mathrm{H}}}{1+CL_{i,j} f_i^{\mathrm{H}}}\right) \tag{11}$$

According to the theory of Lennard-Jones-Devonshire, Langmuir constants ($CL_{i,j}$), that quantify the affinity between the guest molecule (i) and the host structure, can be calculated with the assumption of spherical symmetry making use of the pair interaction potential of Kihara, equation (12).

$$CL_{i,j} = \frac{4\pi}{k_B T}\int_0^{R_j - a_i} \exp\left(\frac{-\omega(r)}{k_B T}\right) r^2 dr$$

$$\omega(r) = 2Z_j\varepsilon_i\left[\frac{\sigma_i^{12}}{R_j^{11}}\left(\Delta_{10}(r)+\frac{a_i}{R_j}\Delta_{11}(r)\right)-\frac{\sigma_i^{6}}{R_j^{5}}\left(\Delta_{4}(r)+\frac{a_i}{R_j}\Delta_{5}(r)\right)\right]\frac{1}{r} \tag{12}$$

$$\Delta_N = \frac{\left[\left(1-\frac{r}{R_j}-\frac{a_i}{R_j}\right)^{-N}-\left(1+\frac{r}{R_j}-\frac{a_i}{R_j}\right)^{-N}\right]}{N}$$

Where σ_i is the intermolecular radius, a_i is the soft radius of the spherical core for the guest component, and ε_i is the well depth for the Kihara potential. These, for THF, constitute the second subset of parameters, the model parameters, which require regression here. In this work, it was admitted that the parameter referring to the radius of the structure cavity is equal to the size of the radius of the THF molecule that occupies the cavity, σ_{THF} = 0.315 nm [7]. Those used for CH_4, CO_2, and H_2 are taken from Sloan and Koh [2].

Single and double hydrates with THF only form structure II, and the characteristic data of each cavity of this structure (ν_j, number of cavities of type j per water molecule of the unit cell; R_j, cavity radius of type j; Z_j, the coordination number of cavity-type j) were obtained from the work of van der Waals and Platteeuw [98].

From the description of the chemical potential by classical thermodynamics of a pure substance, it is possible to express the chemical potential difference of H_2O in the

empty lattice (EL) and the liquid phase coexisting with the hydrate phase. Where $\Delta\mu_w^0$ is the variation of the chemical potential of water in the reference conditions, $\Delta h_w^{EL\text{-}L}$ is the enthalpy variation of water between phases, and $\Delta v_w^{EL\text{-}L}$ is the variation of the molar volume of water between phases. Assuming that the difference of the molar volumes constant and enthalpy calculated from specific heat depending linearly with temperature, equation (13).

$$\frac{\Delta\mu_w^{L\text{-}EL}}{RT} = \frac{\Delta\mu_w^0}{RT_0} - \int_{T_0}^{T} \frac{\Delta h_w^{L\text{-}EL}(T, p_0)}{RT^2} dT + \int_{p_0}^{p} \frac{\Delta v_w^{L\text{-}EL}(T, p)}{RT} dp - ln(\gamma_w x_w)$$

$$\Delta h_w^{L\text{-}EL}(T, p_0) = \Delta h_w^{L\text{-}EL}(T_0, p_0) + \int_{T_0}^{T} \Delta Cp_w^{L\text{-}EL}(T, p_0)\, dT \tag{13}$$

$$\Delta C_{Pw}^{L\text{-}EL}(T, p_0) = \Delta Cp_w^{L\text{-}EL}(T_0, p_0) + a_1(T - T_0)$$

In this work, the reference pressure and temperature adopted were those of the triple point of the water (p_0 = 612.62 Pa and T_0 = 273.15 K), and the macroscopic thermodynamic parameters of equation 13 were those presented in the work of John et al. [105].

2.3 Parameter regression methodology

We seek a unique set of parameters for the NRTL and the Kihara models that is able to correlate a wide range of data, provide reliable extrapolations and parameter transferability. We make use of a parameter estimation framework to find the parameters that best represent the available data. This consists on establishing a measure of the distance between experimental data and predictions of the model and finding parameter values that minimize this metric. The underlying metric used here is the maximum like hood metric, in the absence of reported experimental uncertainties, we approximated it to the least weighted squares function. Thus our matches the general weighted least squares form below, for *Ne* experimental conditions indexed (e), in which Nc types of variables were measured (m) such that we can calculate them (c), with our model, as a function of parameters ($\underline{\beta}$), other measurements ($\underline{X}$), and Nr types of reconciled variables ($\underline{R}$), equation (14).

$$F\left(\underline{\beta},\underline{R}\right)=\sum_{e=1}^{Ne}\left[\begin{array}{l}\sum_{t=1}^{Nc_e}\left[\left(w_{e,t}^{\mathrm{c}}\left(Y_{e,t}^{\mathrm{c}}\left(\underline{X}_{e,t},\underline{\beta},\underline{R}_{e,t}^{\mathrm{r}}\right)-Y_{e,t}^{\mathrm{m}}\right)\right)^2\right]+\\ +\sum_{t=1}^{Nr_e}\left[\left(w_{e,r}^{\mathrm{r}}\left(R_{e,r}^{t,\mathrm{r}}-R_{e,r}^{t,\mathrm{m}}\right)\right)^2\right]\end{array}\right] \quad (14)$$

For the goal depicted, we propose the parameter regression in two separate steps. In the first step, we obtain optimal NRTL parameters using VLE and infinite dilution activity coefficients (γ_i^{∞}) data. While in the second step, we extrapolate the NRTL model and obtain optimal Kihara parameters using HLE data. The block diagram of Figure 1 outlines the methodology proposed here.

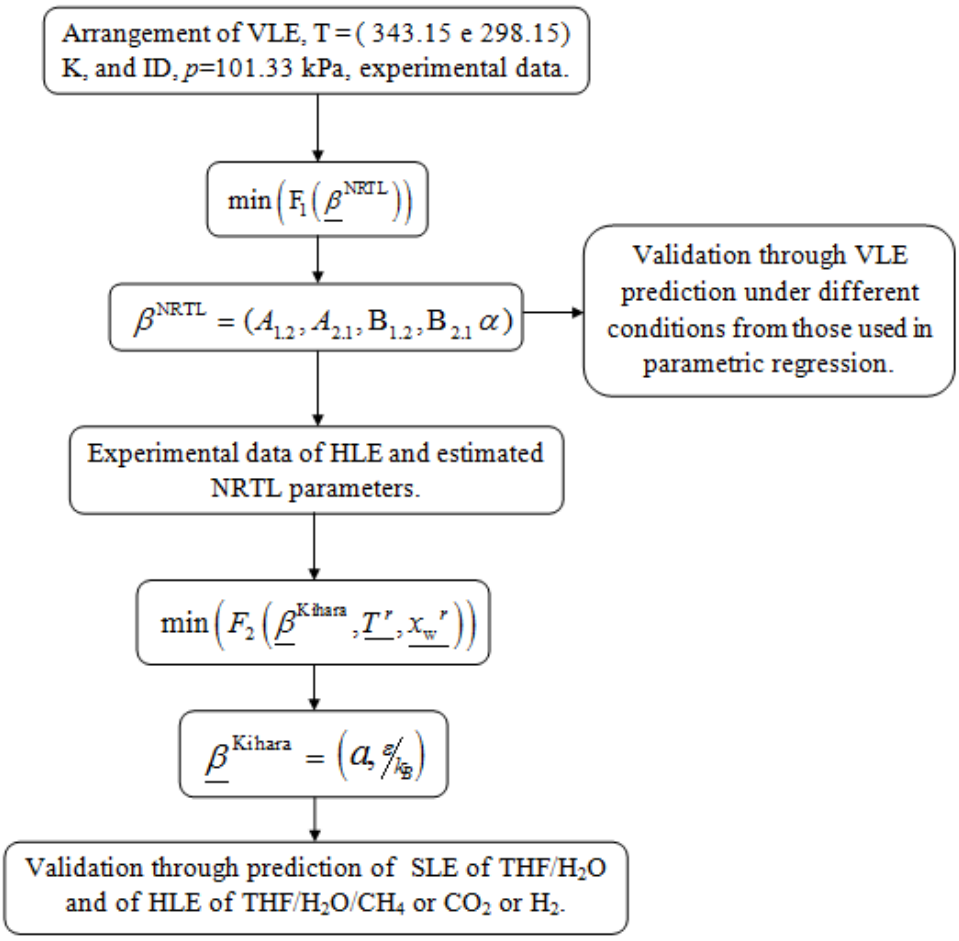

Figure 1 - Block diagram of the parameters estimation methodology with the proposed approach. All experimental data for estimation are in Appendix 1.

Previous works have taken varying strategies towards the parameterization of thermodynamic models for water and THF systems. Our two-step-parameterization strategy is similar to Herslund et al. [141], De Deugd et al. [119], Yoon [111], and Strobel et al. [140], in that a model for liquid and a model for hydrate are parameterized

with independent experimental data. However, while, in a first step to parameterize a model for liquid, Herslund et al.[141] used VLE and LLE data, Strobel et al. [140] and De Deugd et al. [119] use infinite dilution data, and Yoon [111] use a group contribution-based approach, here, we parameterize our model for liquid with both VLE and infinite dilution (ID) data. Then, in a second step, to model equilibria involving hydrates, Strobel et al. [140] evaluated a Kihara model with a parameter set from literature, while Herslund et al. [141], Yoon [111] and De Deugd et al.[119] regressed their own set of Kihara parameters using hydrate experimental data. While Herslund et al. [141] used data at varying pressures, De Deugd et al. [119] used data with CH_4 (double hydrates), and Yoon [111] used data for single hydrate at constant pressure, but up to THF mole fraction of 0.1. Here we used single HLE data at constant pressure with additional experimental points in the inhibition region (up to THF mole fraction of 0.2).

2.3.1 NRTL

For step 1, in Figure 1, data types (Y) for N_1 experiments correspond to VLE pressure (p) and mole fraction of water in vapor (y_{w}), as a function of the input (X) corresponding to temperature and liquid phase composition; and for additional N_2 and N_3 experiments, Y corresponds to infinite dilution activity coefficients for water and THF ($\gamma_{\mathrm{w}}^{\infty}$ and $\gamma_{\mathrm{THF}}^{\infty}$), and X to temperature. Being all these data calculated through our VLE algorithm and NRTL model as a function of a subset of parameters $\underline{\beta}_1$, corresponding to $A_{1,2}$, $A_{2,1}$, $B_{1,2}$, $\mathrm{B}_{2,1}$, and α. No variables were set for reconciliation in this first step. In this step, the objective function is given by equation (15).

$$
\begin{aligned}
\mathrm{F}_1\left(\underline{\beta}^{\mathrm{NRTL}}\right) = \sum_{e=1}^{N_1}\left[\begin{array}{l}\left(w_e^{\mathrm{p}}\left(P_e^{\mathrm{c}}\left(T,x,\underline{\beta}^{\mathrm{NRTL}}\right)-P_l^{\mathrm{m}}\right)\right)^2+\\ +\left(w_e^{\mathrm{y_{THF}}}\left(y_{THF,e}^{\mathrm{c}}\left(T,x,\underline{\beta}^{\mathrm{NRTL}}\right)-y_{THF,l}^{\mathrm{m}}\right)\right)^2\end{array}\right]+\\
+\sum_{e=N_1+1}^{N_1+N_2}\left[\left(w_e^{\gamma_{\mathrm{w}}^{\infty}}\left(\gamma_{\mathrm{w},e}^{\infty\ \mathrm{c}}\left(T,\underline{\beta}^{\mathrm{NRTL}}\right)-\gamma_{\mathrm{w},e}^{\infty\ \mathrm{m}}\right)\right)^2\right]+\\
+\sum_{e=N_1+N_2+1}^{N_1+N_2+N_3}\left[\left(w_e^{\gamma_{\mathrm{THF}}^{\infty}}\left(\gamma_{\mathrm{THF},e}^{\infty\ \mathrm{c}}\left(T,\underline{\beta}^{\mathrm{NRTL}}\right)-\gamma_{\mathrm{THF},e}^{\infty\ \mathrm{m}}\right)\right)^2\right]
\end{aligned}
\tag{15}
$$

We used weights (w) so that for each experimental condition, the value of the inverse of the weight (w^{-1}) was 1% of the measured variable. These weights were

stipulated to establish similar deviations for all points in the absence of reports of experimental uncertainties in the data obtained from the literature.

The case addressed involved regression of the following arrangement of the experimental data from the THF/H_2O system: vapor-liquid equilibrium data at a constant temperature of 343.15 K and 298.15 K, in a total of 34 different experimental points, and infinite dilution data at atmospheric pressure (101.33 kPa), which encompass 5 points are at infinite dilution conditions of THF in H_2O [152] and 5 of H_2O in THF [153,154], between temperatures of 293.15 K and 343.15 K at 101.33 kPa. These literature data are available in Appendix 1.

The NRTL model parameters are valid in the thermodynamic condition range of temperature pressure and composition in which they were estimated. For this reason, some VLE data were deliberately not included in the estimation to allow for posterior parameter validation.

2.3.2 Kihara

Now, for step 2, in Figure 1, the first and only data type is the explicit equilibrium criteria for HLE already described ($\Delta\mu_{w,l}^{\text{H-EL}}$ / $\Delta\mu_{w,l}^{\text{L-EL}}$), which can be calculated from input condition of temperature, pressure, and liquid phase composition; and that at an experimental measurement of phase equilibria correspond to a measured value of 1 to this variable, while the model will calculate slightly higher or lower values, depending on how accurate it is. In addition, we use temperature (T) and mole fraction of water (x_w) in a data reconciliation approach. The equilibrium criteria are furthermore a function of the second subset of parameters: a_{THF} and ε_{THF}. In this step, the objective function is given by equation (16).

$$F_2\left(\underline{\beta}^{\text{Kihara}}, \underline{T}^{r}, \underline{x_w}^{r}\right) = \sum_e^{N_3} \left[\begin{array}{l} \left(w_e^{\Delta\mu_w} \left(\dfrac{\Delta\mu_{w,e}^{\text{H-EL}}\left(P_e^{\text{m}}, \underline{\beta}^{\text{Kihara}}, T_e^{r}, x_{w,e}^{r}\right)}{\Delta\mu_{w,e}^{\text{L-EL}}\left(P_e^{\text{m}}, \underline{\beta}^{\text{Kihara}}, T_e^{r}, x_{w,e}^{r}\right)} - 1 \right) \right)^2 + \\ + \left(w_e^{\text{T}} \left(T_e^{\text{r}} - T_e^{m} \right) \right)^2 + \\ + \left(w_e^{x_w} \left(x_{w,e}^{\text{r}} - x_{w,e}^{m} \right) \right)^2 \end{array} \right] \quad (16)$$

In the strategy we propose for the estimation of the Kihara potential parameters, we imposed the equilibrium criteria as a function of measured variables in the objective

function, instead of using one of the measured variables itself as a function of another by means of an algorithm. In this way we are saving the computational cost that would be required by algorithm of the hydrate dissociation pressure at given temperature, by iterative usage of the equilibrium criteria, such as Parrish and Prausnitz [103] algorithm, also we are safe, through the regression methodology, from running the algorithm with parameter such that there would be no solution for given input, the equilibrium criteria will always yields some value to be compared with 1 in the objective function. Moreover, the reason for reconciliation in this step, and the choice of value for weights , w, was to obtain, empirically, a compromise between enforcing that the equilibrium criteria is met with satisfactory tolerance while allowing for slightly variations of the reconciled variables in relation to measurements in the absence of reports of experimental uncertainties in the data obtained from the literature. We used the values of 10^7 for the chemical potential difference ration term and the inverse of 0.001% of the measured variable for the reconciliation terms.

We used experimental data of hydrate-liquid equilibrium of THF/H_2O at 101.33 kPa [9,127,128,134–137] in the temperature range of 272 K to 280 K, with 69 experimental points up to the composition of 0.2 mole fraction of THF. These literature data are in Appendix 1.

2.3.3 Optimization methodology

For conducting the minimization procedure, we use a particle swarm optimization method [155] coupled to a Quasi-Newton [156] method, where the former provides a global optimization characteristics while the latter provides improvement to the precision of the final solution.

2.4 Results and discussion

Through the approach proposed here, we obtain, in the first step, optimal parameter values and error analysis for NRTL ($A_{i,j}$, $B_{i,j}$ and α), these results are summarized in Table 2.

Table 2 - NRTL model parameters, and their respective parameter errors, obtained by adjusting the liquid-vapor equilibrium data and infinite dilution data of the THF(1)/H_2O(2) system.

NRTL parameters	
$A_{1,2}$	1.7545 ± 0.0009
$A_{2,1}$	1.9684 ± 0.0009
$B_{1,2}$	2.1355 ± 0.0062
$B_{2,1}$	-3.7664 ± 0.0098
α	0.4404 ± 0.0001

[a]The standard error was calculated by making three times the standard deviation.

In the second step, we obtain the Kihara potential cavity parameters for THF (a_{THF} and $\varepsilon_{\mathrm{THF}}$), Table 3 shows these values together with literature values for H_2, CH_4, and CO_2.

Table 3 - Kihara potential cavity parameters for THF, and their respective parameter errors, obtained by adjusting the hydrate-liquid equilibrium data of the THF/H_2O system. And the Kihara potential cavity parameters for CH_4, CO_2 e H_2.

Component	**Kihara potential cavity parameters**			
	a / nm	σ / nm	ε/k_B / K	Ref.
THF	0.0635 ± 0.0002[a]	0.315 (set)	320.16 ± 0.33[a]	This work
CH_4	0.0383	0.314	155.59	[2]
CO_2	0.0681	0.298	175.40	[2]
H_2	0.0353	0.314	127.43	[2]

[a]The standard error was calculated by making three times the standard deviation.

We compare the model results with the experimental data establishing the Average Absolute Relative Deviation (AARD%) metric, equation (17). Where, Y corresponds to either p^{VLE}, $\gamma^{\infty}{}_{\mathrm{w}}$, $\gamma^{\infty}{}_{\mathrm{THF}}$, or $\Delta\mu_{\mathrm{w}}^{\mathrm{H\text{-}EL}}$ / $\Delta\mu_{\mathrm{w}}^{\mathrm{L\text{-}EL}}$ for each scenario under consideration.

$$AARD\% = 100 \times \frac{\sum_{e=1}^{Ne} \left| \frac{Y_e^{\mathrm{c}} - Y_e^{\mathrm{m}}}{Y_e^{\mathrm{m}}} \right|}{Ne} \tag{17}$$

2.4.1 Liquid-vapor equilibria of the THF/water system

We compared the predictions of boiling point and dew point temperatures with experimental data. The model is able to adequately calculate equilibrium at different pressures (101.33 kPa, 93 kPa, 80 kPa, 67 kPa, 53.3 kPa and 40 kPa), and the formation of the minimum-in-temperature azeotrope at 0.82 THF mole fraction at 101.33 kPa [138]. We achieved satisfactory fit of the model for the entire composition range, including the narrow envelope region, with THF mole fraction greater than at the azeotrope concentration. The proposed model yielded an AARD% of 2.8% for the calculation of the equilibrium temperature of the THF/H_2O system. These results are shown in Figure 2.

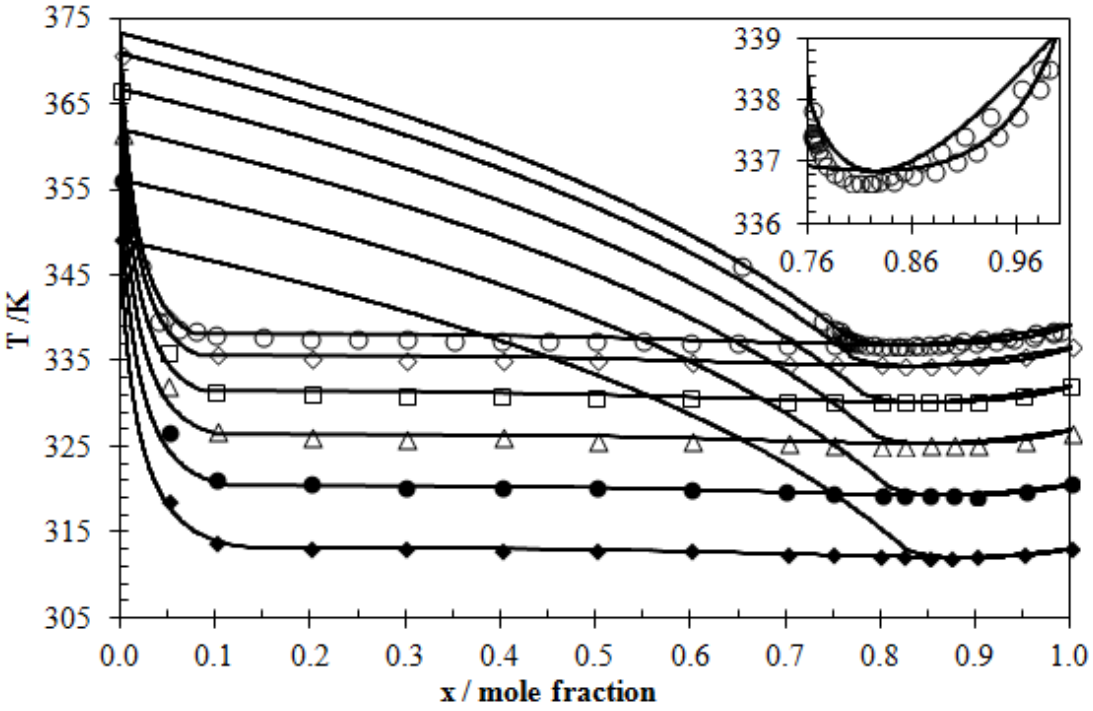

Figure 2 - Vapor-liquid equilibrium diagram for isobaric systems of THF/H_2O. Continuous curves represent modeling results at: ○, *p*=101.33/kPa [151]; ◊, *p*=93/kPa [138]; □, *p*=80/kPa [138]; Δ, *p*=67/kPa [138]; ●, *p*=53.3/kPa [1]; ♦, *p*=40/kPa [138].

We used the resulting model in flash calculations to predict vapor-liquid equilibrium at temperatures of 343.15 K, 323.15 K and 298.15 K. We achieved satisfactory fit throughout the whole range of composition, as shown in Figure 3, with an AARD% of 0.8% for the calculations of the equilibrium pressure of the THF/H_2O system.

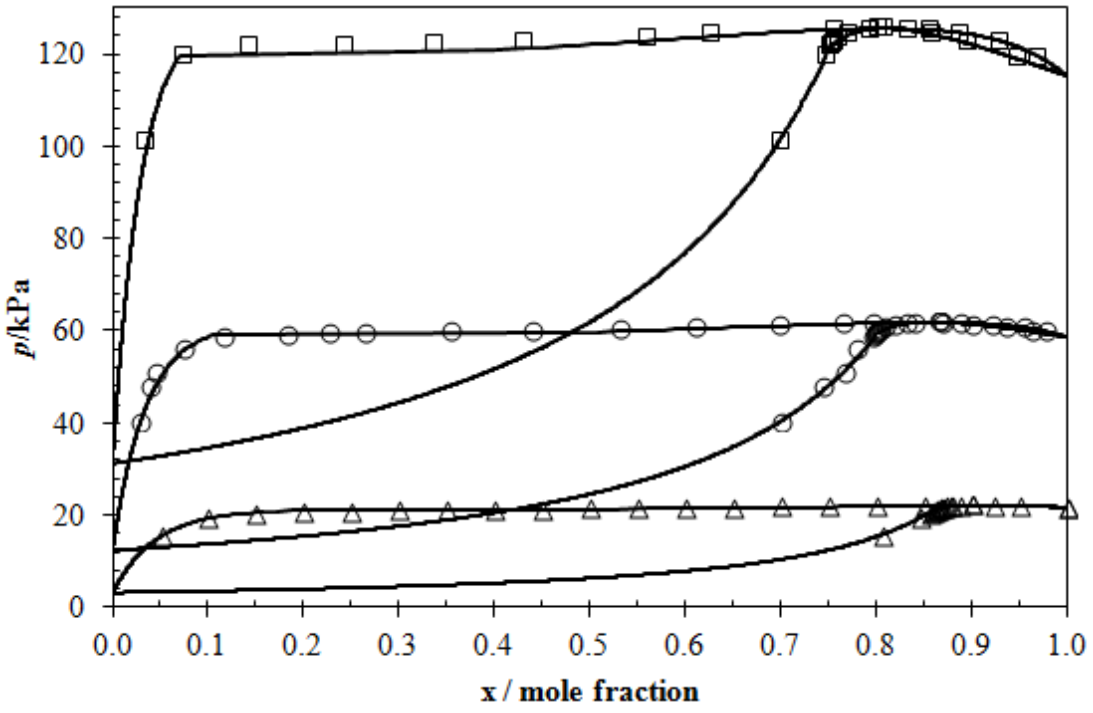

Figure 3 - Vapor-liquid equilibrium diagram for isothermal systems of THF/H_2O. Continuous curves represent modeling results at: □, *T*=343.15/K [149]; ○, *T*=323.15/K [149]; Δ, *T*=298.15/K [150].

2.4.2 Infinite dilution activity coefficient of the THF/water system

Studies involving infinite dilution activity coefficient data are relevant in the analysis of the THF/H_2O system due to the increased sensitivity of the model in regions with low THF mole fraction, relevant for the study of promoter effect in hydrate-liquid equilibria. Figure 4 shows the calculation of the activity coefficient by the resulting NRTL model at infinite dilution conditions. The model yielded an AARD% of 8.5% for these data, it adequately correlates the experimental data of infinite dilution of H_2O in THF, while for THF in H_2O, reproducing only qualitative behavior. Note that infinite dilution data reported by literature for the THF/H_2O system are scarce and that data at infinite dilution conditions is obtained by extrapolation of liquid-vapor equilibrium data, due to limitations of experimental apparatus, a methodology which yields data with standard error in the same order of magnitude as the data itself [157]. For these reasons, such data are unreliable for methodology validation. All this makes it difficult to evaluate the prediction error.

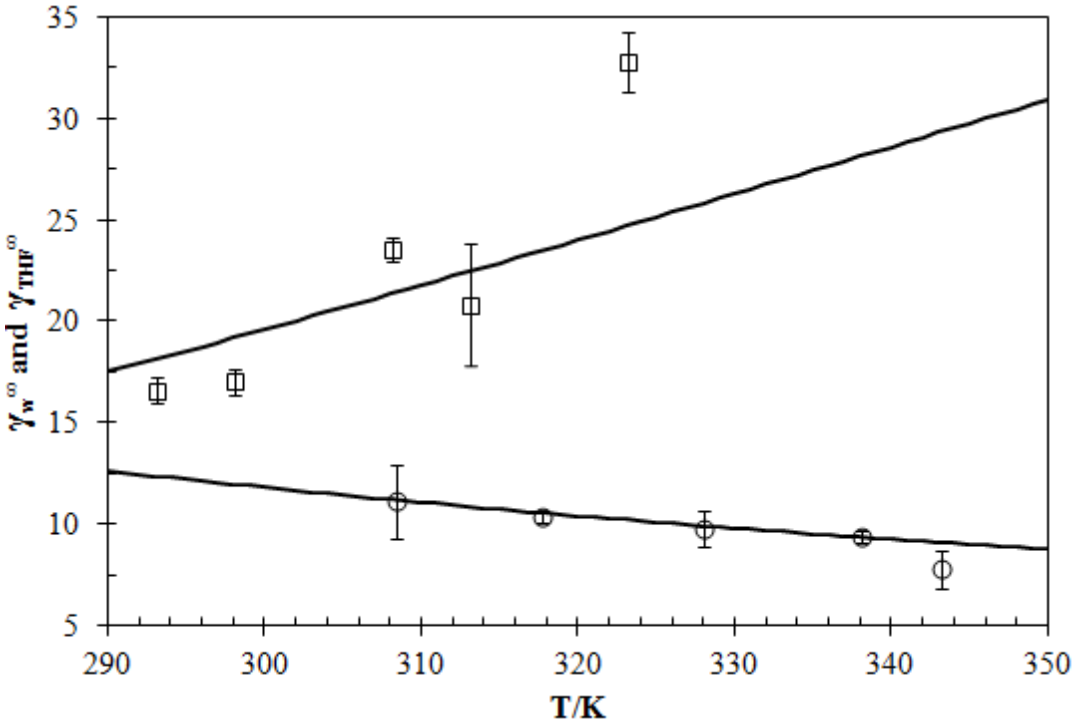

Figure 4 - Coefficient of activity in infinite dilution for different temperatures at 101.33 kPa. The symbols represent the experimental data and the continuous curves represent the values calculated by the NRTL model for: □, infinite dilution of THF in H_2O (γ_{THF}^{∞}) [152]; ○, infinite dilution of H_2O in THF (γ_w^{∞}) [153,154].

2.4.3 Solid-liquid equilibria of the THF/water system

Using the optimal parameter set we were able to predict the solid-liquid diagram for the THF/H_2O system. This is shown in Figure 5. The model adequately correlates the hydrate-liquid equilibrium with the experimental data throughout the evaluated composition range, including points with higher than 0.1 mole fraction. The AARD% was of 0.01%. We obtained prediction for the hydrate-ice-liquid equilibrium temperature at 272.7 K, a result which is 0.5 K below the experimental data (272.0 ± 0.2 K, [128]). However, in the congruent melting composition, the experimental results described are within a range of 0.8 K of variation, which is attributed to the fact that the measurement of melting temperature of a THF hydrate is influenced by the presence of air in the sample [126]. Note that our predictions are inside this range of experimental uncertainty.

The ice-liquid equilibrium data [128] is reproduced within experimental error range of 0.1 K. The eutectic at 0.01 THF mole fraction is also observed. In Figure 5, the

adequate simultaneous prediction of vapor-liquid equilibrium, hydrate-liquid equilibrium, hydrate-ice-liquid equilibrium and ice-liquid equilibrium at pressure of 101.33 kPa and low THF compositions is observed. The model is able to predict equilibria over the entire composition range; however, there is no experimental data on solid-liquid equilibrium of THF/H_2O above 0.2 mole fraction of THF.

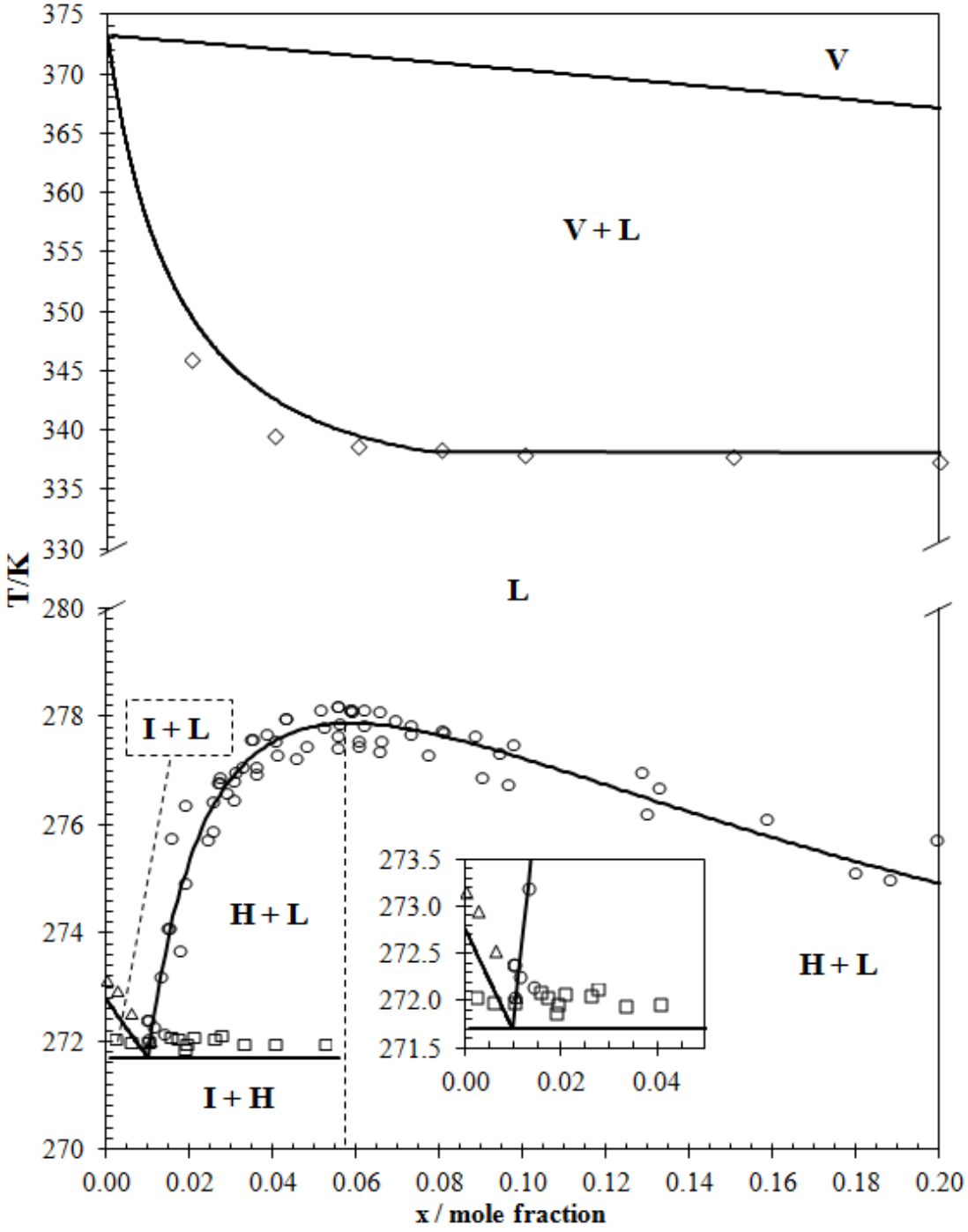

Figure 5 - Complete diagram for isobaric systems of THF/H2O at 101.33 kPa. Continuous curves represent modeling results for: ◊, VLE [151]; ○, HLE [9,127,128,134–137]; □, HILE [128]; Δ, ILE [128].

2.4.4 Thermodynamic prediction of promoted gas hydrate systems

So far, we showed consistent modeling of VLE and SLE equilibrium conditions of the THF/H_2O system, under conditions of hydrate formation. Then, in this section, we show the transferability potential of the parameters. We tested the optimized parameters in double hydrate formation conditions.

Figure 6 shows the *p* versus T diagram for the THF/H_2O/CH_4 system at different liquid phase composition (THF mole fraction of 0.0107, 0.03, 0.05, 0.06 and 0.1008 with deviations of 0.25%, 0.27%, 0.16%, 0.78% and 0.09% in the calculated temperature, respectively), and the diagram for the H_2O/CH_4 system, which forms structure I, modeled with Kihara parameters of Sloan and Koh [2] with 3.38% deviation in pressure. The hydrate promoter effect of THF is observed in comparison to the pure methane hydrate formation system. However, there is a limit to the THF promoter effect. Above 0.03 mole fraction, a temperature increase is no longer significant and THF has a slightly inhibitory effect. As the equilibrium curve at 0.05 mole fraction is at temperatures slightly higher than 0.1008 mole fraction, the effect is reproduced by the proposed model, but it was not previously observed by literature models.

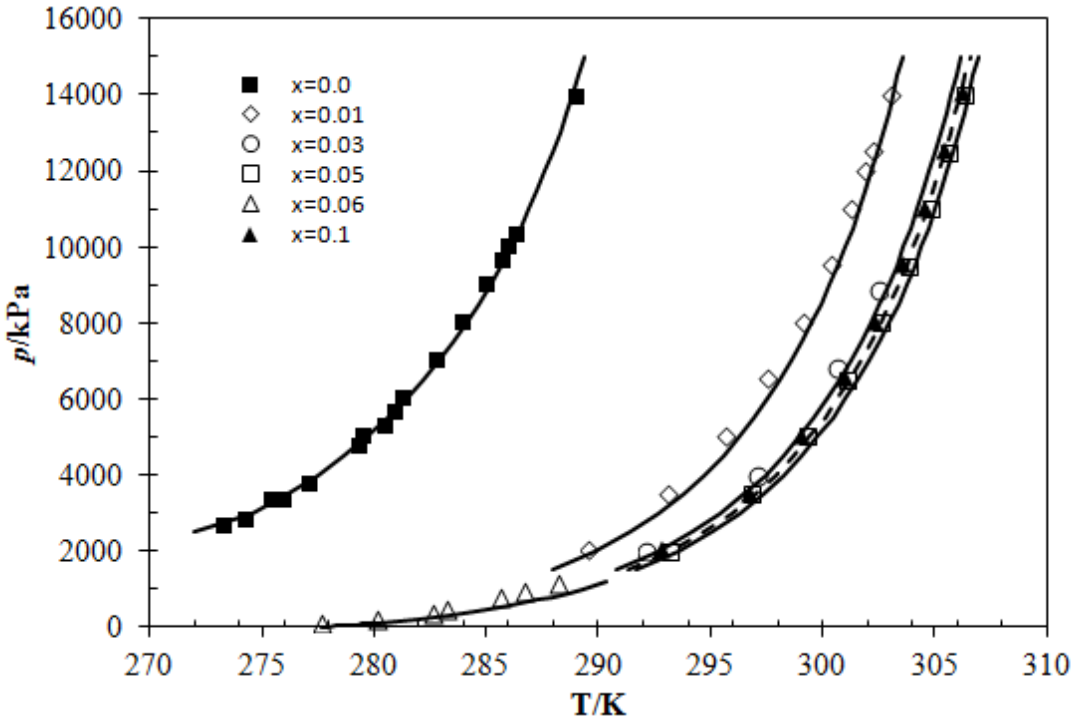

Figure 6 - Pressure, *p*, vs. temperature, *T*, diagram for the THF/H_2O/CH_4 system. Continuous curves represent equilibrium temperature calculations with the proposed approach for THF molar fractions of: ◊, *x*=0.0107 [119]; ○, *x*=0.03 [129]; □, *x*=0.05 [119]; Δ, *x*=0.06 [130]; ▲, *x*=0.1[119]. And *p*-*T* diagram for the THF/CH_4 system, ■, *x*=0.0 [158].

The observation of the hydrate inhibitory effect at high concentrations of THF, reported by the solid-liquid diagram of the THF/H_2O system (Figure 5), motivated equilibrium calculations at high compositions of THF for double hydrates. We show, in Figure 7, a smaller set of experimental data for the *p* versus *T* diagram of the THF/H_2O/CH_4 system, together with calculations for higher THF concentrations. It is noted that at 0.2 THF mole fraction, the curve is dislocated to temperatures less than those for 0.05 mole fraction of THF, as well as at 0.6 mole fraction it presents a behavior similar to the curve at 0.0107 mole fraction. At 0.8 mole fraction, the curve is closest to the pure CH_4 hydrate formation conditions. However, these equilibrium conditions lack experimental data confirmation.

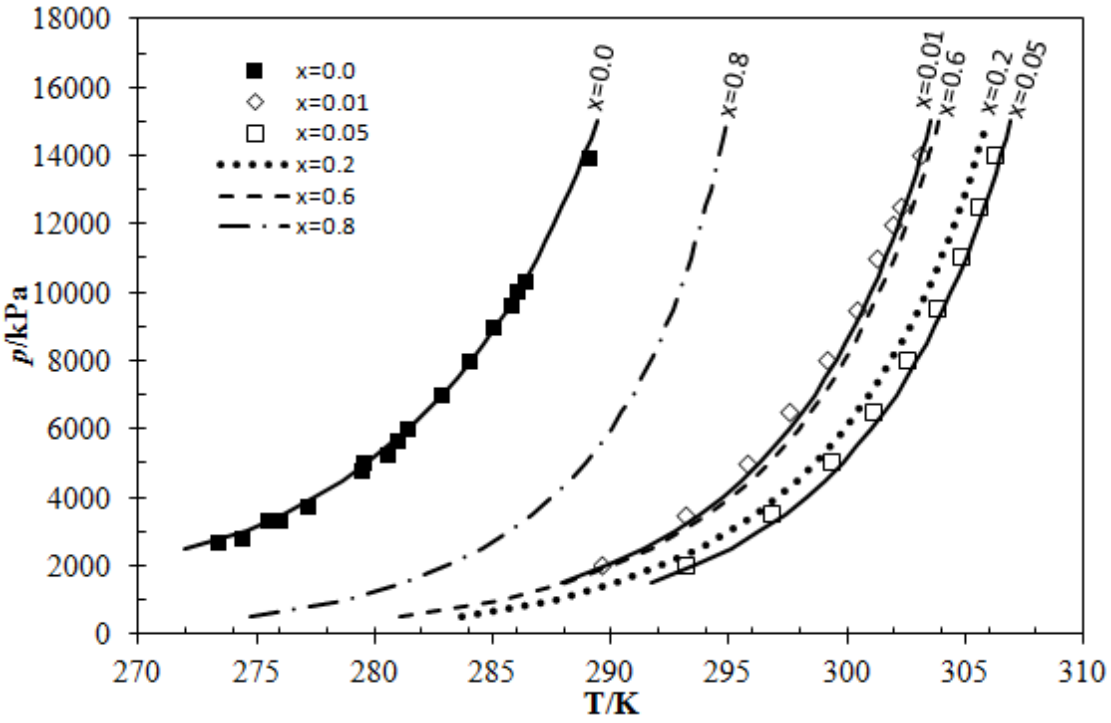

Figure 7 - Pressure, *p*, vs. temperature, *T*, diagram for the THF/H_2O/CH_4 system. Continuous curves represent equilibrium temperature calculations with the proposed approach for THF molar fractions of (literature data): ■, *x*=0.0 [158]; ◊, *x*=0.0107 [119]; □, *x*=0.05 [119]. Dashed curves represent equilibrium temperature calculations with the proposed approach for THF molar fractions of: dotted line, *x*=0.2; dashed line, *x*=0.6; dotted-dashed line, *x*=0.8, that do not present literature data.

We also performed calculations for double hydrate with H_2 or CO_2. Figure 8 shows the *p* versus T diagram for the THF/H_2O/CO_2 system for different THF mole fraction (0.012, 0.016, 0.029 and 0.05). The model adequately reproduced the experimental data and the promoting effect of THF present in this composition range. This diagram was reproduced only at low pressures.

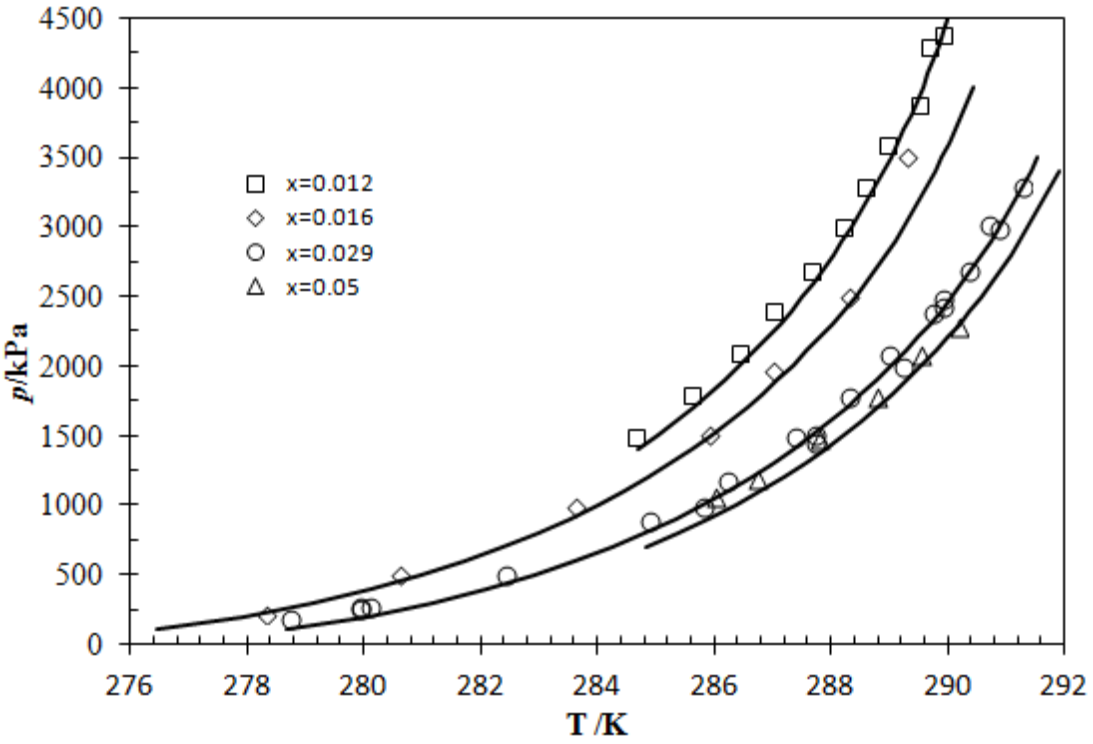

Figure 8 - Pressure, *p*, vs. temperature, *T*, diagram for the THF/H_2O/CO_2 system. Continuous curves represent equilibrium temperature calculations with the proposed approach for THF molar fractions of: □, *x*=0.012 [159]; ◊, *x*=0.016 [128]; ○, *x*=0.029 [128,159]; Δ, *x*=0.05 [159].

Figure 9 shows the *p* versus T diagram for the THF/H_2O/H_2 system for different THF mole fraction, *x* = (0.01, 0.0113, 0.024, 0.0351, 0.05 and 0.13) mole fraction. The adjustment of the hydrate dissociation pressure of double hydrate of THF/H_2, through the proposed modeling, was adequate to the experimental data and the THF promoter effect, from 0 to around 0.05 mole fraction was well predicted, the THF inhibitor effect observed at 0.13 THF mole fraction was also predicted.

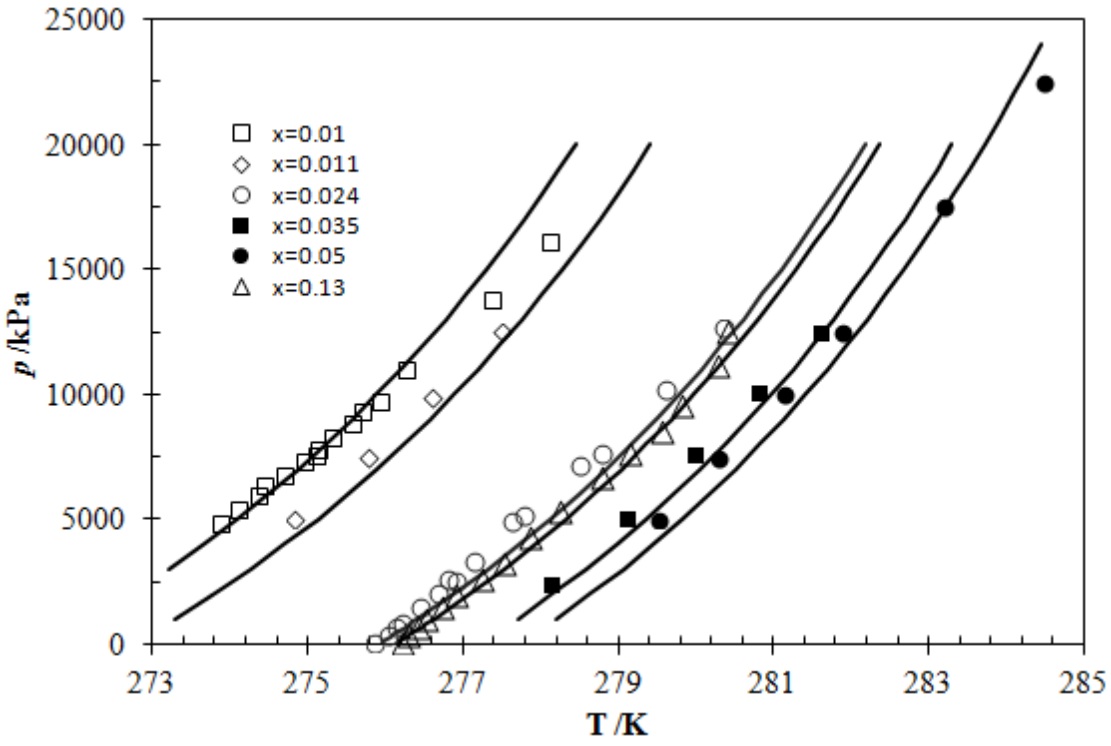

Figure 9 - Pressure, *p*, vs. temperature, *T*, diagram for the THF/H_2O/H_2 system. Continuous curves represent equilibrium temperature calculations with the proposed approach for THF molar fractions of: □, *x*=0.01 [127,160]; ◊, *x*=0.0113[161]; ○, *x*=0.024 [160,161]; ■, *x*=0.0351 [161]; ●, *x*=0.05 [162]; Δ, *x*=0.13 [160].

2.5 Partial conclusions

In this work, we proposed a strategy for parameter estimation of a thermodynamic modeling of the THF/H_2O system, using the classical van der Waals and Platteeuw theory, with Kihara potential (hydrate phase), and a NRTL model, with temperature dependent interaction parameter for calculation of the liquid phase, using VLE, HLE, γ_w^∞ and γ_{THF}^∞ data. We obtained consistent and accurate calculations of VLE and SLE with a unique set of parameters. We were able to generate satisfactory results for hydrate-liquid equilibrium conditions of the THF/H_2O system at concentrations above 0.1 mole fraction of THF, which had not been possible with the models previously available in literature [111,140,141].

The diversity of experimental data of THF and light organic compounds (CO_2, H_2, CH_4) hydrate formation systems in literature and the consistent modeling for the THF/H_2O system allowed the transferability of this model to systems containing double hydrates formation with accuracy at low pressures. The equilibrium calculations of these

systems reproduced both the promoter effect at low concentrations of THF and the inhibitory effect of THF in compositions greater than 0.1 mole fraction.

List of symbols

T - Temperature [K]

p - Pressure [kPa]

R - Universal gas constant [J mol / K]

f - Fugacity [Pa]

$\underline{x}$ - Liquid phase composition

$\underline{y}$ - Vapor phase composition

γ - Activity coefficients

v - Molar volume [m³ / mol]

ϕ - Fugacity coefficients

μ - Chemical potential [J / mol]

Δ - Variation

α - Symmetrical nonrandomness factor

$\tau_{i,j}$ - Binary interaction parameter

A and B - NRTL parameters

ν_j - Number of cavities of the type j

R_j - Cavity radius of type j

Z_j - Coordination number of cavity type j

CL - Langmuir constant

σ - Intermolecular radius [nm]

a - Soft radius of the spherical core [nm]

ε - Well depth [K]

k_b - Boltzmann constant [m^2 kg / s K]

h - Enthalpy [J / mol]

C_p - Specific heat [J / mol K]

$\underline{\beta}$ - Function of parameters

w - Weights

N - Number counter

1 - THF

2 - H_2O

AARD% - Average Absolute Relative Deviation

HLE - Hydrate liquid equilibrium

VLE - Vapor liquid equilibrium

HILE - Hydrate ice liquid equilibrium

ILE - Ice liquid equilibrium

HLVE – Hydrate liquid vapor equilibrium

^{L} - Liquid phase

^{V} - Vapor phase

^{H} - Hydrate phase

^{EL}- Empty lattice phase

^{sat} – saturation

^{c} – calculated

^{m}- measured

$_{e}$ – experiments

$_{r}$- reconciled

Chapter 3. Hydrate equilibria with inhibitor (EtOH)

Significant portions of the oil reserves in Brazil are located in deep or ultra-deep waters. Oil production from these reservoirs implies a constant awareness of gas hydrates formation. The petroleum industry uses thermodynamic inhibitors to reduce the temperature/increase the pressure of hydrate formation to ensure hydrate-free production. As ethanol is abundant in Brazil and works as a hydrate thermodynamic inhibitor, its use is more common. However, experimental data of hydrate phase equilibria (HPE) at high ethanol concentrations are scarce, and there is a limited characterization of the existing data. This study reports LHV equilibrium data for C_2H_6 and a mixture of CH_4/C_2H_6 at high ethanol concentrations and compiles the equilibrium data with ethanol from the literature to evaluate their consistency hydrate inhibited systems, as well as to present a comparison between predictive approaches for hydrates with ethanol. We apply a consistency test with three criteria to characterize all HPE data with ethanol in the literature data. The experimental data were measured up to 45 wt% of ethanol. The used hydrate data, such as CH_4, CO_2, and C_2H_6, deviate from the average behavior established by the criteria for 5 and 15 wt%, 2 and 5 wt%, and 5 wt%, respectively. The C_3H_8 hydrate data from the literature obeys the average behavior of the test criteria as well as the C_2H_6 and CH_4/C_2H_6 data measured. In general, all predictions were in agreement with the experimental data for ethanol concentrations up to 15 wt%.

3.1 Introduction

Gas hydrates are crystalline compounds formed at low temperatures and high pressures in systems with water and low molecular weight molecules, mainly light gases [2]. Such conditions, typical of hydrate formation, are present in offshore oil and gas production. In those systems, the occurrence of hydrates can lead to blockages along the flowline. Among the conventional methods for hydrates inhibition, there is the prevention of the occurrence of blockages by altering the thermodynamic equilibrium condition through the addition of thermodynamic inhibitors [12]. Thermodynamic inhibitors of hydrates are usually organic chemical additives, mainly alcohols and glycols. The presence of inhibitors usually reduces the activity of water in the aqueous phase, which shifts hydrate phase boundaries to higher pressures and lower temperatures without inclusion in the hydrate crystalline structure [16].

Significant portions of the oil reserves in Brazil are located in deep or ultra-deep waters, in which the oil production occurs at high pressures and low temperatures, suitable conditions for the formation of hydrates. In this scenario, flow assurance actions are crucial production factors, especially for large natural gas production scenarios such as the exploration of the pre-salt layer [163]. Therefore, to ensure production is free of hydrates in those scenarios, where the conditions are more favorable to hydrate formation, i.e., the conditions of oil production are more rigorous, requirement larger amounts of thermodynamic inhibitor to shift the hydrate equilibrium curve [17].

Desirable properties for a thermodynamic inhibitor include miscibility in water, efficient recovery, stability, and low vapor pressure [164]. Based on these criteria, the most common industrial thermodynamic inhibitors are methanol (MeOH), ethanol (EtOH) and monoethylene glycol (MEG) [165]. Although many experimental data have been reported for equilibrium conditions of gas hydrates in the presence of methanol, information for hydrate equilibria in the presence of other alcohols, like ethanol, is limited, especially for high concentrated solutions [166]. Brazil is one of the biggest producers of ethanol, so its use is cheaper than the use of methanol or MEG for the Brazilian oil and gas production scenarios. For this reason, the use of ethanol as a thermodynamic inhibitor is increasingly more common. As such, there is a need to better understand the hydrate phase equilibria for high concentrations of ethanol.

However, experimental studies on the thermodynamics of hydrate formation in the presence of alcohols show that they may act as co-formers of double hydrate with light gases [167]. The thermodynamically inhibited systems with ethanol have characteristics of also promoting the formation of double hydrate with light gases, such as methane [31]. The experimental studies to characterize the hydrate structure and composition for those systems are challenging to perform, for this reason, the literature presents only a few studies for the concentrations of 13.2 and 15 wt% of ethanol [8,27,28]. In these studies, the participation of ethanol in the crystalline structure is identified but with low occupation in the cavities. However, due to the methodological difficulty of the execution of these experiments, it is not possible to affirm such participation. We must evaluate this hypothesis. Therefore, more equilibrium data at high ethanol concentration and better characterization are needed to define the conditions at which this behavior occur [168].

The literature presents a few Liquid-Hydrate-Vapor (LHV) equilibrium data with ethanol, mostly for single gas hydrate and even fewer data above 15 wt% of ethanol [120]. Among the experimental data present in the literature, hydrates formed with CH_4 for concentrations up to 63 wt% of ethanol [27,30,52,169], CO_2 for concentrations up to 20 wt% of ethanol [170–172], C_2H_6 for concentrations up to 10 wt% of ethanol [52], and C_3H_8 for concentrations up to 15 wt% of ethanol [52,172]. As apparent from the literature collected data, the availability of hydrate phase equilibrium data with high concentrations of ethanol is limited.

In the petroleum industry, operating the production lines outside the hydrate zone is a common practice to prevent the formation of hydrates. For this reason, proper modeling of these systems for predicting the hydrate dissociation condition is essential for the industry to ensure production is free of hydrates. Nevertheless, extra efforts are needed before these models can reliably be applied for the cases when ethanol is present at high concentrations [173].

The development of thermodynamic methods to calculate hydrate equilibrium conditions requires accurate experimental data [171]. It is crucial to perform the measurements considering that in systems with chemical additives at high concentrations, the concentration of the solution is continuously changing during the hydrate formation and dissociation processes [174]. We frequently apply this consideration in the development of the methodologies present in the literature to obtain

experimental data at high concentrations of salts and thermodynamic inhibitors [168]. More than an adequately measured data at high ethanol concentration, the development of a model to predict the hydrate zone needs consistent thermodynamic data with a defined behavior of ethanol as an inhibitor or a potential hydrate co-former. Rigorous thermodynamic analysis are rarely used to validate the data in the literature with thermodynamic inhibitors at high concentrations [120,175].

This study reports hydrate phase equilibria data with ethanol, for C_2H_6 and a mixture of CH_4 and C_2H_6, at high ethanol concentrations, up to 45 wt% EtOH, applying the methodology for an isochoric system and the thermodynamic consistency analysis of the data. Here, we compile and apply the consistency test for inhibited systems proposed by Sa et al. [175] to the hydrate phase equilibria data with ethanol. With this test, it is possible to define a standard average established by the three criteria and define which sets of experimental data deviate from the average behavior for each gas hydrate system. We also tested a correlation based on the three thermodynamic criteria of the consistency test, a thermodynamic model, and a commercial software to evaluate their predictive reliability at high ethanol concentrations. All three approaches to describe inhibited hydrate systems are used to determine the conditions that ethanol behaves predominantly as a thermodynamic inhibitor. Moreover, we test whether the traditional thermodynamic modeling is still applicable without including alcohol as a hydrate co-former [123].

3.2 Experimental section

3.2.1 Materials

Table 4 presents the suppliers and purities of the chemicals used to obtain the experimental data in this study. Appropriate amounts of the chemicals and distilled water were weighed on an electronic balance with a resolution of 0.01 g and mixed thoroughly at room temperature. Solutions up to 0.45 mass fraction of ethanol (45 wt% EtOH) were prepared by keeping the cell cooled to prevent evaporation. The uncertainties in the composition of the solutions were less than ± 0.001 on a mass fraction basis of the balance.

Table 4 - Purity and supplier of materials used in the experimental study.

Chemical		CAS Reg. No.	Source	Purity (mass fraction)	Analysis method
Pure C_2H_6		74-84-0	Praxair	0.98	GC[a]
Mixture	73.8 mol% CH_4	74-82-8	American Gas Group	0.98	GC[a]
	Balance C_2H_6	74-84-0		0.98	GC[a]
Ethanol		64-17-5	Greenfield	≥0.99	SG[b]

[a]Gas chromatograph.

[b]Specific gravity.

3.2.2 Experimental apparatus

The experimental setup used was a 275 mL stainless steel cylindrical cell. The limit working condition of this cell is 50 bar for the pressure in the range of 258.15 K to 298.15 K for the temperature. The cell has a sapphire window which allows phase transition observations and a mechanical stirrer used to maintain uniform and homogenous conditions in the cell. The three temperature sensors are T-type thermocouples (OMEGA®) with a precision of ± 0.1 K. They are used to measure the temperature of the liquid phase inside the cell, the temperature of the cooling fluid in the thermostatic bath, and the room temperature. The cell is immersed in a glycol-water bath, in which the temperature is controlled by an external refrigeration unit. The relative pressure measurements are made with a pressure transducer (WIKA®) sensor with an uncertainty of ± 0.08 bar. A separate pressure transducer measures the absolute pressure at the standard atmospheric pressure, with the precision of ± 0.001 bar.

3.2.3 Experimental procedure

It is essential to perform hydrate phase equilibria measurements, mainly at high ethanol concentrations, considering that in systems with chemical additives, the concentration of the solution is continuously changed during the hydrate formation and dissociation processes. Therefore, for precise measurements, in the isochoric procedure with the step-wise temperature increase methodology, with sufficient equilibration time at every step, is used to ensure that the measurements of samples with a high concentration of ethanol are properly equilibrated [168,174].

At first, before assembling the apparatus, the equilibrium cell is carefully cleaned. The cell is loaded with 60 mL of the solution at ambient pressure and cooled, to be around 2 K above the 10 K of the expected subcooling (predicted by the PVTsim®), to prevent evaporation. With the cell cooled we cleaned the air inside. The air cleaning process is doing filling the cell with the gas up to 2 bar and depressurizing slowly twice. After that, we pressurized the cell up to 0.5 bar above the expected equilibrium pressure (predicted by the PVTsim®). These procedures are previously done to prepare the cell to begin the experimental process to obtain the phase equilibrium point [2], which increases accuracy and speeds up the attainment of each experimental point.

Figure 10 shows an example of the experimental process utilized to obtain the phase equilibrium points, which consists of four steps: (1) fast cooling step – linear line of pressure-temperature data with no hydrate (around 10 degrees of subcooling); (2) hydrate formation step – the amount of hydrate formation is controlled by increasing the temperature after about 3 bars of large pressure decrease; (3) fast heating step – heating up to 1 K below the expected equilibrium condition; and (4) slow stepwise heating – the temperature is increased stepwise by 0.2 K in 1 hour and held for 5 hours so that the system pressure stabilizes at each temperature. The five hours time per step ensures complete equilibration at each step. The hydrate phase equilibrium point corresponds to the inflection point, the intersection of the hydrate dissociation line and the expansion/contraction line, as shown in Figure 10 (a), and at the same time the reduction on the increasing rate of the pressure per step, as in Figure 10 (b).

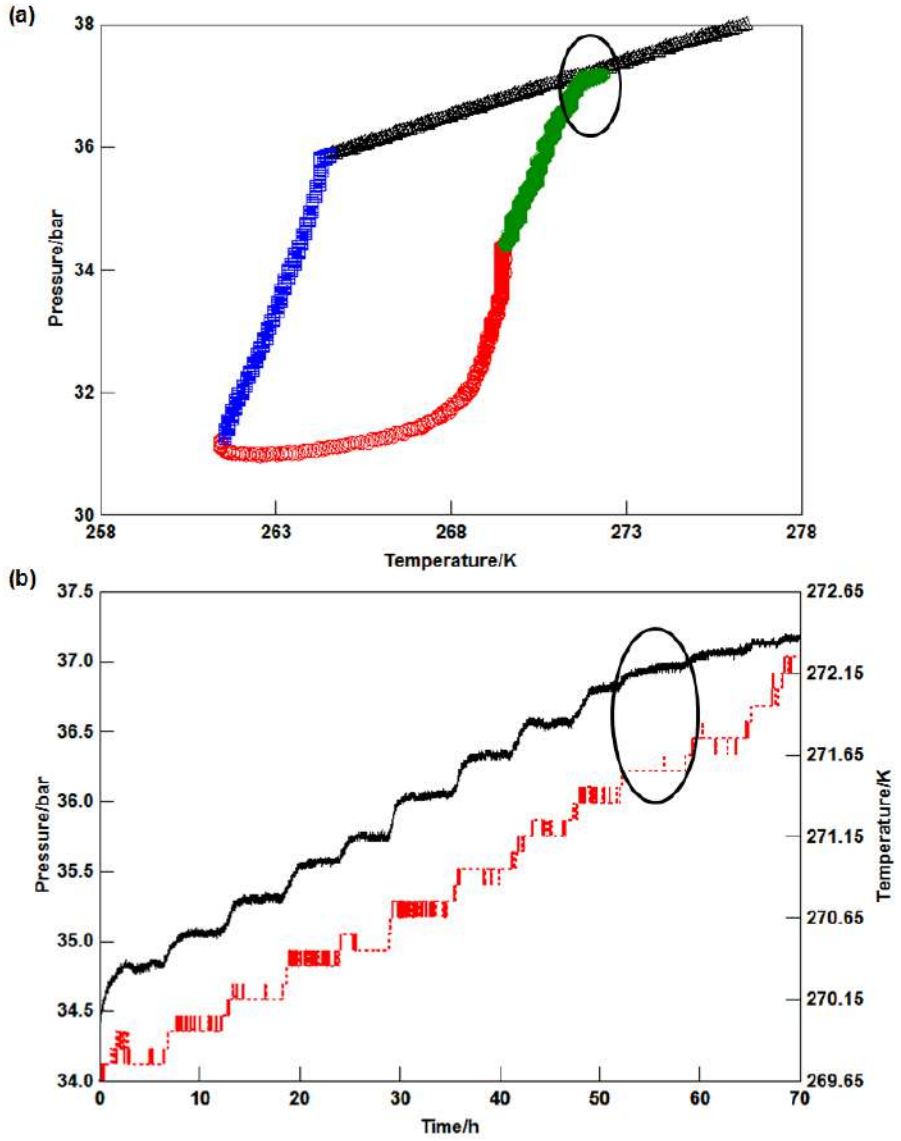

Figure 10 - Illustration of the experimental procedure for hydrate phase equilibrium measurements with high ethanol concentration [168]. (a) Pressure vs. temperature trace for hydrate formation and dissociation in the 40 wt% of ethanol system with the four steps procedure. (1) Fast cooling step - black, (2) hydrate formation step - blue, (3) fast heating step - red, (4) slow stepwise heating - green. The circled area shows the slope change of the heating curve as the phase equilibrium point is reached. (b) Time traces for the pressure (continuous black) and temperature (dashed red) during slow step-wise temperature increase. Temperature steps are maintained for about 5 hours until the pressure stabilizes. Circled area shows the reduction in the increase in pressure after reaching the phase equilibrium point.

3.3 Thermodynamic analysis and models

3.3.1 Thermodynamic consistency analysis

Sa et al. [175] proposed a methodology to assess the thermodynamic consistency of hydrate phase equilibrium data for inhibited systems. In this methodology, thermodynamic relations are used to derive the criteria for assessment, including linear regression of data according to the Clausius-Clapeyron equation, consistency of the hydrate dissociation enthalpy, and water activity. The authors applied this methodology for numerous cases of hydrate phase equilibria from the literature with salts.

Hu et al. [176] applied the same methodology to test the thermodynamic consistency of hydrate phase equilibrium data from the literature with several salts (NaCl, KCl, $CaCl_2$, $MgCl_2$, NH_4Cl, NaBr, KBr, and $CaBr_2$) and organic inhibitors (methanol, monoethylene glycol, ethanol, glycerol, diethylene glycol and triethylene glycol). However, the data with ethanol was only for CH_4 hydrates up to 26.9 wt%.

This methodology consists in the application of three criteria. The first criterion of thermodynamic consistency is to check how close the phase equilibrium data are to the linear fitting regression equation given by the Clausius-Clapeyron equation. A relation which adopts the hypothesis that the hydrate dissociation enthalpy and the gas compressibility do not significantly change in a narrow temperature range of about 10-20 K. The statistical parameter used to evaluate the linearity of phase equilibrium data is the 1-R^2 (R-squared) value. With this criterion, we can check if the hydrate structure changes with the temperature and pressure condition for each concentration, because the slope changes with a change in the hydrate structure.

The second criterion tests the consistency of the hydrate dissociation enthalpy, which only depends on the hydrate structure and the guest species. The hydrate dissociation enthalpy (ΔH_{diss}) values are relatively constant regardless of the type and concentration of the thermodynamic hydrate inhibitor. The hydrate dissociation enthalpy can be calculated through the linear slope of the phase equilibrium curves plotted as log P vs. $1/T$ as expected by the Clausius-Clapeyron equation with the gas compressibility (z) and the universal gas constant (R). We applied the relative standard deviation (RSD) in ΔH_{diss} for each ethanol concentration, which is defined as the deviation of the ΔH_{diss} at a concentration from the average ΔH_{diss} of all concentrations for each gas hydrate divided by the average ΔH_{diss}. This criterion allows us to check if

the hydrate structure can change with the thermodynamic inhibitor concentration because, with the change in the hydrate structure, the slope used to calculate the enthalpy also changes. So, if the enthalpy varies significantly from one concentration to the other, there is a possibility that the hydrate structure is changing with the thermodynamic inhibitor concentration.

The last criterion is based on the suppression temperature ($\Delta T = T_0 - T$), that is, at a given concentration of a specific thermodynamic inhibitor, the activity of liquid water does not significantly change over a relatively narrow temperature range (20-30 K). The thermodynamic consistency of the water activity in the liquid phase is only determined by the type and concentration of the thermodynamic inhibitor. So, if the concentration of the thermodynamic inhibitor in the liquid phase does not change, i.e., the thermodynamic inhibitor does not participate in the hydrate structure and/or do not evaporate to the vapor phase, the water activity in the liquid phase will be constant.

The quantity $\Delta T/T_0T$ is proportional to the water activity at each concentration and independent of the temperature in the typical range of hydrate phase equilibrium data and depends only on the thermodynamic hydrate inhibitor concentration. To quantify the thermodynamic consistency in terms of water activity invariance, we also applied the relative standard deviation (RSD) for $\Delta T/T_0T$ – the sum, divided by the number of data, of the difference between the $\Delta T/T_0T$ for each data at the same concentration from the average $\Delta T/T_0T$ of that concentration divided by concentration average of $\Delta T/T_0T$. The β ($= -nR/\Delta H_{diss}$) term depends on the hydrate structure, the guest species and hydration number (n), and it can be also calculated through the suppression temperature ($\Delta T/T_0T$) and the hydrate dissociation enthalpy (ΔH_{diss}). This criterion evaluates if the thermodynamic inhibitor concentration does not change with a small variation in temperature. The parameter will be constant if the inhibitor is not participating in the hydrate structure or evaporating.

In this work, those three criteria were applied for the literature data of CH_4, CO_2, C_2H_6, and C_3H_8 hydrates with ethanol concentrations up to 63 wt%. Moreover, for the measured data of C_2H_6 and the mixture of 73.8 mol% of CH_4 and C_2H_6, with ethanol concentrations up to 45 wt%.

We also used the classification proposed by Sa et al.[175] to evaluate the data according to good (< 5%), acceptable (between 5% and 10%) and fail (> 10%) based on

the relative standard deviation (RSD). This classification allows us to evaluate in which conditions hydrate equilibrium data with ethanol differs from the average that characterizes all the data. That is, under which conditions inhibition and/or ethanol inclusion into hydrate phase may cause changes in the water activity. Consequently, for those conditions, experimental investigations for hydrate characterization are most needed.

3.3.2 Prediction tool

PVTsim® is a commercial package for general phase equilibria calculation that is also equipped with predictions for hydrate phase equilibria with and without inhibitors. The software is distributed by Calsep A/S (Nova 4 version). For the hydrate calculations, the Peng-Robinson equation of state, coupled with NRTL model and the Huron and Vidal mixing rules[177,178]. PVTsim® is widely used in the oil and gas industry for hydrate predictions.

3.3.2.1 Hu-Lee-Sum correlation

Hu et al. [120,176,179] developed a correlation based on the colligative properties and thermodynamic consideration for the effect of inhibitors (salts and organic inhibitors) in the hydrate phase equilibria. That correlation is based on the fundamental principle of freezing point depression, which for hydrate is equivalent to the suppression temperature from the uninhibited (fresh water) system.

The correlation considers that at the equilibrium hydrate dissociation, the fugacity of water in the hydrate (solid) phase and the liquid phase have to be equal (isofugacity condition). The assumptions for this condition are that the system pressure is constant; the hydrate is a pure phase (the inhibitor is not part of the hydrate structure); the composition of the hydrocarbon-rich vapor or liquid phase is constant; and the composition of the hydrate is constant.

The correlation expresses the hydrate depression temperature in terms of the water activity in the liquid phase, which is strongly dependent on the thermodynamic inhibitor species and concentration. Based on published literature data, the regression of data based on the effective mole fraction of inhibitors resulted in a general correlation for the water activity. The correlation considers the water activity for salts and organic inhibitors.

3.3.2.2 Thermodynamic modeling

Oliveira et al. [123] proposed a strategy for the estimation of a unique set of parameters for suitable thermodynamic models for THF and water mixtures in the conditions of LHV equilibrium. To perform phase equilibrium calculations, the authors selected the NRTL G^E model (for the liquid phase, L), the Peng-Robinson equation of state (for the vapor phase, V), and the van der Waals and Platteeuw hydrate model with the Kihara potential (for the hydrate phase, H) to correlate independent properties. They regressed optimal parameters for the NRTL model with, simultaneously, vapor-liquid equilibria and infinite dilution activity coefficient data, and determined optimal Kihara parameters with liquid-hydrate equilibrium data, using data reconciliation. The method used a strategy to obtain parameters through independent experiments.

Following a similar strategy, the NRTL parameters were estimated in this study using infinite dilution and liquid-vapor equilibrium data of ethanol/water from the literature to predict phase equilibria scenarios with ethanol involving liquid, hydrate, and vapor mixtures (see Appendix 2).

The hydrate phase equilibria conditions evaluated were the ones with the following natural gas components: CH_4, CO_2, C_2H_6, and C_3H_8, whose LHV equilibrium data with ethanol are present in the literature [27,30,52,169–172]. In those conditions, it was considered that the ethanol only act as a thermodynamic inhibitor and only change the water activity in the bulk phase, i.e., it is not part of the hydrate structure. More details about the NRTL parameters set and the methodology used to adapt the model for the systems with ethanol instead of THF are in the Appendix 2.

Here, we used the average absolute deviation (AAD) to evaluate the accuracy of each model. For the pressure, the absolute deviation accepted for the prediction is 2 bar, and 0.5 K for the temperature. Since all three models were tested to calculate the equilibrium condition for inhibited systems, we can use these results with the consistency test to characterize the data.

If the same gas, water, and inhibitor system exhibit different behavior between the data sets at different concentrations, this is an indication that the inhibitor may be participating in the hydrate structure depending on the concentration. It is possible to show, by applying the consistency analysis, that higher concentrations present higher deviation from the average behavior, in separate data sets. With the analysis of the

deviation presented by the models, for the cases in which the ethanol only behaves as an inhibitor (no inclusion in the hydrate), it is possible to define which of those concentration sets are better adjusted by this hypothesis. In this way, we define the conditions in which experimental characterization data, which are expensive and challenging to perform, are still needed.

3.4 Results and discussion

Figure 11 shows the evaluation of the consistency analysis test for the methane hydrate equilibrium data from the literature with ethanol concentrations up to 63 wt%. The methane hydrate equilibrium data showed an excellent linear fit to the Clausius-Clapeyron equation for all the concentrations. The statistical parameter ($1\text{-}R^2$) are in Table S3 of Appendix 2. For almost all the sets, ($1\text{-}R^2$) is below 1%, with only two sets having higher statistical parameters: 2.43% and 1.65% for 13.2 wt% and 44.6 wt% EtOH, respectively. However, they are still adequate (< 5%), according to the criterion. For the same concentration, the hydrate structure (sI) is the same for the temperature and pressure ranges considered.

The second criterion is the independence of the hydrate dissociation enthalpy on the type and concentration of the thermodynamic inhibitor. Using the Clausius-Clapeyron equation and the linear slope of the experimental data of CH_4 hydrate with ethanol, the ΔH_{diss} was calculated for each set of concentration (see Table S3 in Appendix 2), as well as the relative standard deviation (RSD) of ΔH_{diss} for each concentration. Only the sets with 5 wt% and 15 wt% had RSD of ΔH_{diss} higher than 10% and were not in agreement with the average of the data. The data sets with 10 wt%, 20 wt%, 26.2 wt%, and 44.6 wt% showed an acceptable RSD of ΔH_{diss}, however, higher than 5%, which shows that they also have a deviation from the average behavior. The other data sets had RSD lower than 5% and were characterized as the sets that follow the average behavior.

Figure 11 (d) shows the thermodynamic consistency of the water activity in the liquid phase ($\Delta T/T_0T$) which is only determined by the type and concentration of the thermodynamic inhibitor for the methane hydrate equilibrium data with ethanol. The relative standard deviation (RSD) in $\Delta T/T_0T$ for all the methane hydrate equilibrium data (see Table S3 in Appendix 2), was acceptable, except for the case with 15 wt% EtOH. However, in general, the data sets up to 20 wt% and the set with 52.3 wt% had an RSD

in $\Delta T/T_0T$ higher than 5% showing some deviation from the average behavior of each concentration.

With this analysis, we can characterize that, in general, the data sets higher than 26.2 wt% ethanol appear to have different behavior from the data sets at lower concentrations. It shows that these two collections of data have different hydrate dissociation enthalpy, which can be an indication of different hydrate structure. We can also infer that for lower concentrations of ethanol, the values of $\Delta T/T_0T$ have a strong temperature dependence.

The predictions of the methane hydrate phase equilibrium for each model are shown in Figure 11 (a), (b) and (c) for each concentration. Based on the average absolute deviation (see Table S4 in Appendix 2) PVTsim® showed adequate AAD up to 15 wt% and for 30, 52, and 63 wt% in temperature prediction. For pressure predictions, the AAD was adequate up to 10 wt%. For the HLS correlation, the AAD was adequate for temperature prediction up to 13.2 wt% and for 20 and 39.6 wt%. For the Oliveira et al. thermodynamic model, the pressure prediction showed an adequate AAD up to 10 wt%.

The different models implicitly assume that ethanol is only a thermodynamic hydrate inhibitor, showing better predictions at lower concentrations. The result of the consistency test separates the data sets in two different predominant groups depending on the ethanol concentration. With these two analyses, we can infer that it is possible that the ethanol is participating in the hydrate structure by changing the structure at high ethanol concentration. The literature already showed a few results of X-ray diffraction for the methane hydrate formed in the presence of ethanol at concentrations of 13.2 and 20 wt% [8,10]. The analysis of those experimental data showed that in these conditions, ethanol was part of the hydrate with a lower occupation in the hydrate structure. Moreover, the hydrate was structure II, unlike the expected structure I for a methane hydrate [2]. Then, it is probable that ethanol has an ambiguous behavior. Ethanol can act as a thermodynamic hydrate inhibitor, altering the water activity in the liquid phase, and also as a thermodynamic hydrate promoter, participating in the hydrate structure. In systems containing CH_4/water/ethanol, the behavior that will have a predominant effect is then defined from the ethanol concentration in the liquid phase.

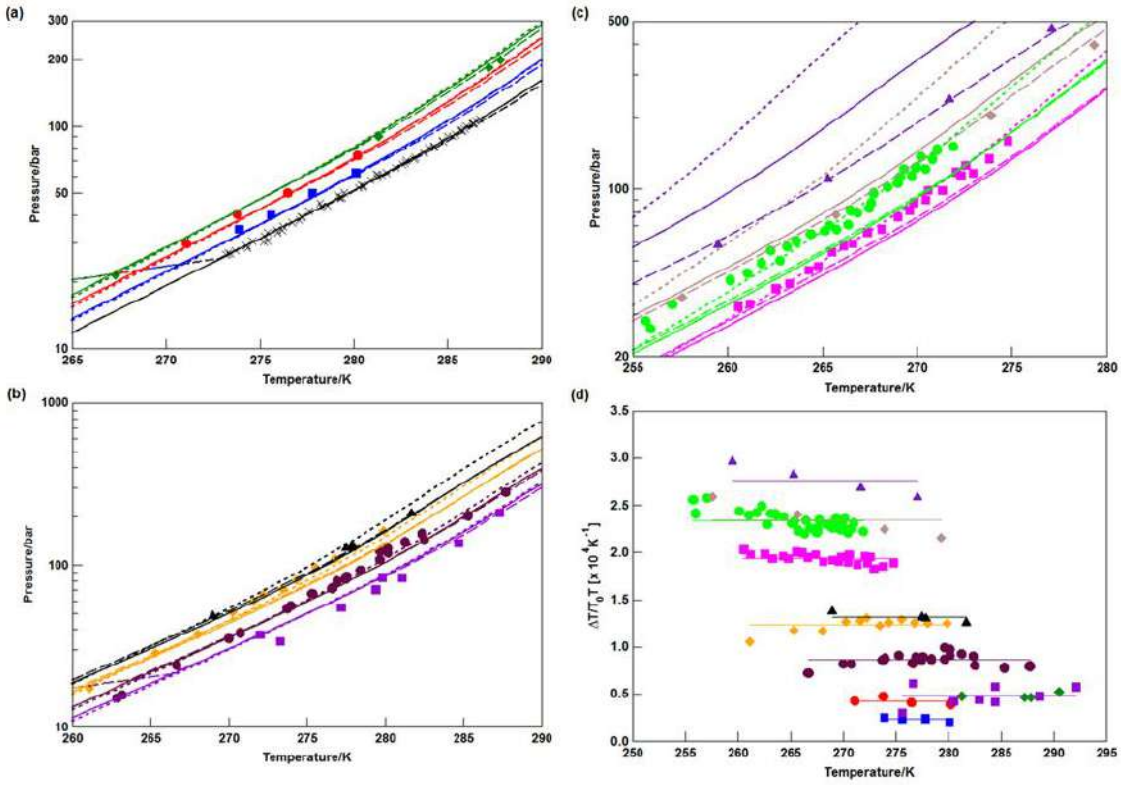

Figure 11 - Methane (CH_4) hydrate phase equilibrium data with ethanol. (a) x for 0 wt% EtOH [158,180–186]. ■ for 5 wt% EtOH [52]. ● for 10 wt% EtOH [52]. ♦ for 13.2 wt% EtOH [10]. (b) ■ for 15 wt% EtOH [169]. ● for 20 wt% EtOH [187]. ♦ for 26.2 wt% EtOH [187]. ▲ for 30 wt% EtOH [10]. (c) ■ for 39.6 wt% EtOH [187]. ● for 44.6 wt% EtOH [187]. ♦ for 52.3 wt% EtOH [10]. ▲ for 63 wt% EtOH [10]. The lines show the predictive calculations of the models: continuous for the adapted model of Oliveira et al. [123], dashed to PVTsim® software and dotted to Hu-Lee-Sum Correlation [176]. (d) The relationship between $\Delta T/T_0T$ and temperature T for methane hydrate systems with ethanol. The lines correspond to the constant value of the best fit that represents the constant value of the water activity for a small temperature range.

It is possible that the behavior observed for systems with methane also occur for other gases. With the analysis presented here, we can identify conditions in which that behavior is more likely to occur and will be worth to perform additional experimental characterization since these data are expensive and challenging to perform [10].

Equilibrium data for carbon dioxide hydrate are shown in Figure 12 (a), including a linear fit of the data to the Clausius-Clapeyron equation for all the concentrations. The highest statistical parameters ($1\text{-}R^2$) is 1.20% for the 10 wt% EtOH (see Table S5 in Appendix 2). All of the CO_2 hydrate phase equilibria data passed the first criterion. For the temperature and pressure range, the hydrate structure does not change at each concentration.

The hydrate dissociation enthalpy was calculated for each concentration of the CO_2 hydrate phase equilibria data (see Table S5 in Appendix 2). Here, the relative standard deviation (RSD) of ΔH_{diss} was calculated comparing each concentration with the average ΔH_{diss}. All of the CO_2 hydrate phase equilibrium data have RSD of ΔH_{diss} lower than 5%, passing in the second criterion. This criterion confirms that the ΔH_{diss} are independent of the thermodynamic inhibitor type and concentration up to 20 wt% EtOH having the same hydrate structure.

The evaluation of the third criterion for the CO_2 data is shown in Figure 12 (b). The relative standard deviation (RSD) in $\Delta T/T_0T$ for those data at each concentration is reported in Table S5 in Appendix 2. The CO_2 data for concentrations higher than 5 wt% were adequate according to the third criterion, with an RSD in $\Delta T/T_0T$ lower than 10%. So, for the data with 2 and 5 wt%, the $\Delta T/T_0T$ shows higher sensibility in the temperature range. However, for 10 wt% the RSD in $\Delta T/T_0T$ is 6.27%, which is adequate according to the criterion (< 10%) but still higher than the 5% observed for the other data sets. The water activity in the liquid phase has a higher deviation from the average at lower concentration.

The predictions with PVTsim® for the CO_2 hydrate phase equilibria have an adequate AAD in pressure for concentrations up to 15 wt%. The highest AAD is 2.45 bar for 20 wt% of EtOH. For the AAD in temperature, PVTsim® gives an adequate prediction for all the concentrations except at 20 wt%, which has an AAD of 0.83 K, higher than the accepted AAD for a good prediction. Similar to the result by PVTsim® for temperature prediction, the HLS correlation has an AAD in temperature higher than 0.5 K only for the 20 wt% of EtOH, for which the AAD is 1.22 K. The Oliveira et al. thermodynamic model showed an AAD higher than 2 bars only for the concentration of 20 wt% (AAD = 2.63 bar), similar to the PVTsim® result. Figure 12 (a) shows all the calculations for each model for each concentration, with the AADs are reported in Table S6 in Appendix 2.

The analysis showed that for the CO_2 hydrate systems with ethanol up to 15 wt% the inhibitor behavior is predominant. The literature reported experimental data characterizing the CO_2 hydrate as structure I for the system with 13.2 wt% EtOH [16]. However, the RSD of ΔH_{diss} increases with the increase in the concentration, and the modeling approach for inhibited hydrate systems shows large deviations for the highest concentration (20 wt%). This can be an indication of the changing behavior of ethanol

from an inhibitor (altering only the water activity in the liquid phase) to a promoter (participating in the hydrate phase). We can also notice that the $\Delta T/T_0T$ for the carbon dioxide hydrate data at lower ethanol concentration have higher variation for a narrow temperature range. As such, there is a need for additional experimental characterization of CO_2 hydrate for ethanol concentrations higher than 15 wt% EtOH.

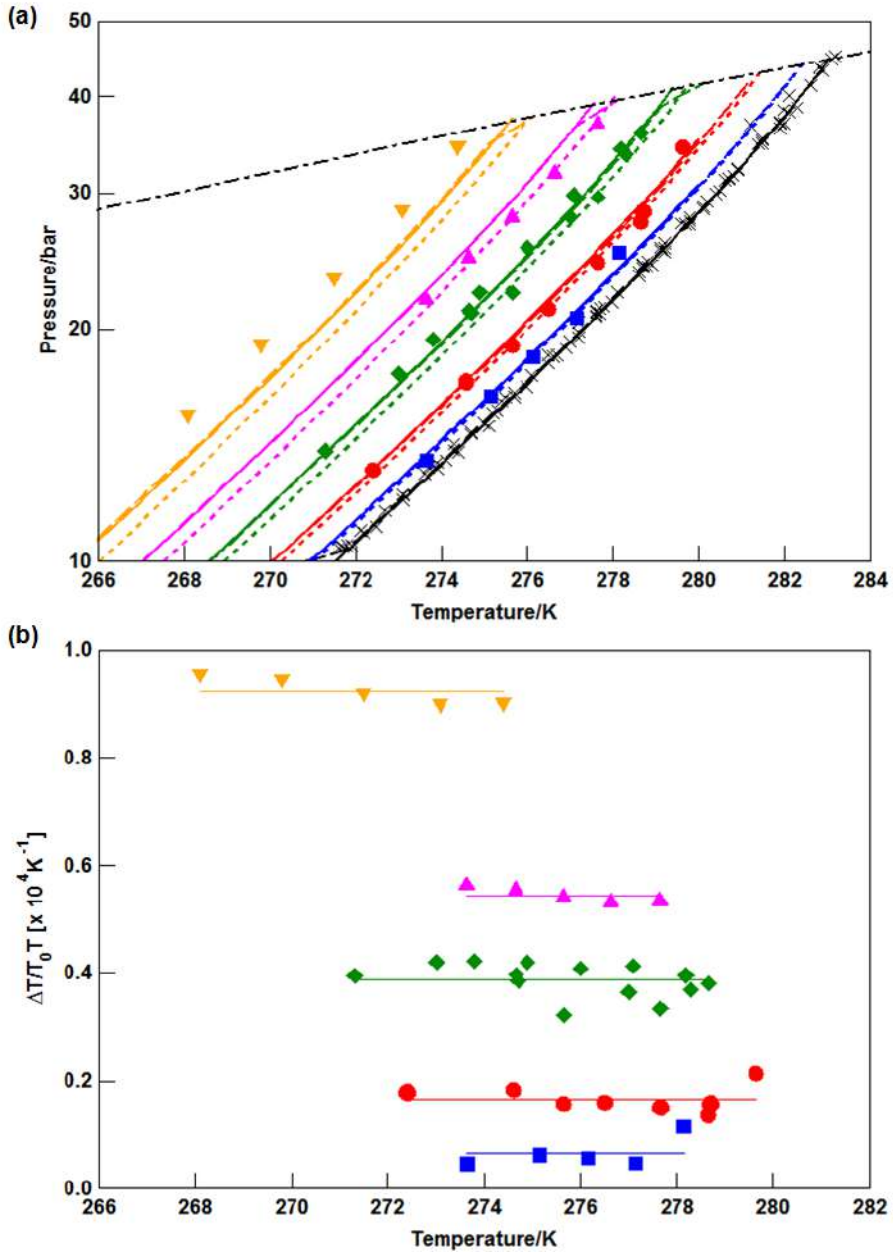

Figure 12 - Carbon dioxide (CO_2) hydrate phase equilibrium data with ethanol. (a) x for 0 wt% EtOH [188]. ■ for 2 wt% EtOH [171]. ● for 5 wt% EtOH [52]. ♦ for 10 wt% EtOH [52,170,172]. ▲ for 15 wt% EtOH [170,171]. ▼ for 20 wt% EtOH [172]. The lines show the predictive calculations of the models: dashed-dotted for CO_2 liquefy pressure (PVTsim®), continuous for the adapted model of Oliveira et al. [123], dashed to PVTsim® software and

dotted to Hu-Lee-Sum Correlation [176]. (b) The relationship between $\Delta T/T_0T$ and temperature T for carbon dioxide hydrate systems with ethanol. The lines correspond to the constant value of the best fit that represents the constant value of the water activity for a small temperature range.

The evaluation of the consistency of the propane hydrate equilibrium data as an inhibited system is shown in Figure 13. Figure 13 (a) shows the linear fit of those data to the Clausius-Clapeyron equation. The statistical parameter ($1\text{-}R^2$) for the propane hydrate phase equilibria showed a proper linear fitting, lower than 2%, as showed in Table S7 in Appendix 2.

The second criterion of the consistency test for the C_3H_8 hydrate equilibrium data is tested through the RSD of ΔH_{diss} (see Table S7 in Appendix 2). The C_3H_8 hydrate phase equilibria data up to 15 wt% EtOH presented good RSD of ΔH_{diss} below 4%. So, the hydrate structure (sII) is the same for all the three data sets. However, we only had three concentration sets to evaluate the deviation from the average behavior. The third criterion is evaluated through the RSD in $\Delta T/T_0T$ for each concentration (Table S7 Appendix 2). All the C_3H_8 data presented good agreement, with the highest RSD in $\Delta T/T_0T$ of 4.75% for the 10 wt% data, lower than 5%. Therefore, for all data, the water activity in the liquid phase does not significantly change with temperature in the studied range.

The calculation of the three models used in this work is also showed in Figure 13 (a). The AAD for each concentration and model are in Table S8 in Appendix 2. The three models presented adequate AAD in pressure and temperature, besides the average absolute deviation in temperature for the ethanol concentration of 15 wt%, that is 1.1 K, obtained with the PVTsim® software.

Since the data passed the consistency test and the modeling approach for inhibited systems showed adequate prediction, we can infer that for a propane hydrate system with ethanol up to 15 wt%, the ethanol predominantly behaves as inhibitor. However, propane is a gas that forms single gas hydrate of structure II [2]. For these systems, the calculation already defines the same hydrate structure, in which the ethanol can occupy the large cavity. Therefore, if the ethanol occupancy is lower for lower concentration in the liquid phase, as the literature reported [8,16,27,28], the model approach will predict

better the equilibrium in those systems. Then, there is a need in the literature for more propane hydrate equilibrium data with ethanol concentrations higher than 15 wt%.

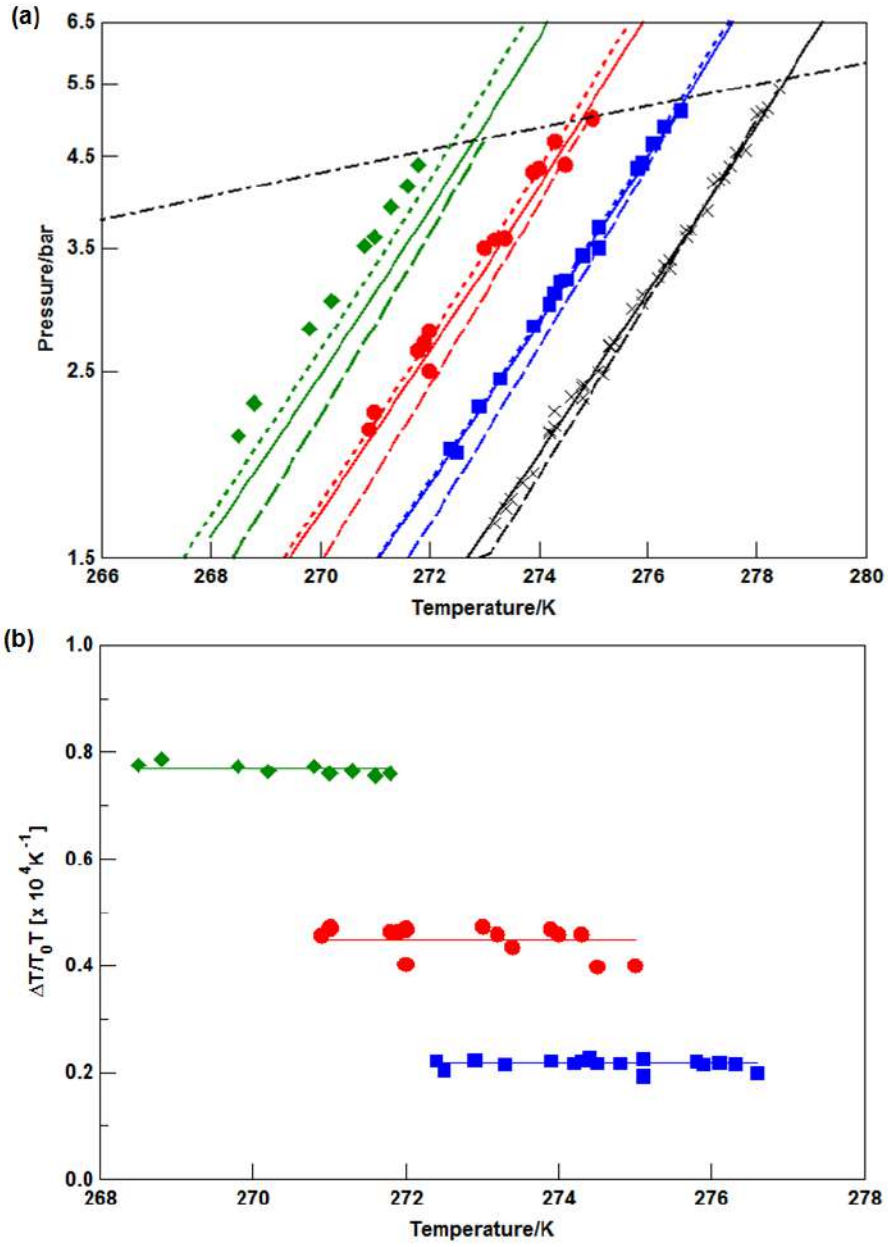

Figure 13 - Propane (C_3H_8) hydrate phase equilibrium data with ethanol. (a) x for 0 wt% EtOH [181,186,189–192]. ■ for 5 wt% EtOH [52,172]. ● for 10 wt% EtOH [52,172]. ♦ for 15 wt% EtOH [172]. The lines show the predictive calculations of the models: dashed-dotted for C_3H_8 liquefy pressure (PVTsim®), continuous for the adapted model of Oliveira et al. [123], dashed to PVTsim® software and dotted to Hu-Lee-Sum Correlation [176]. (b) The relationship between $\Delta T/T_0T$ and temperature T for propane hydrate systems with ethanol. The lines correspond to the constant value of the best fit that represents the constant value of the water activity for a small temperature range.

The literature presents only two sets of ethane hydrate equilibrium data with ethanol for concentrations of 5 and 10 wt% EtOH [52]. In this work, we increase the ethane hydrate equilibrium data in the literature presenting data with concentrations up to 45 wt% EtOH. These data are shown in Table S9 in Appendix 2. The C_2H_6 data was tested for consistency as a hydrate inhibited system. Figure 14 (a) shows all those data and present the linear fit as well as the predictive calculation of the three models.

The first criterion of the consistency test for the C_2H_6 data is evaluated through the statistical parameter ($1\text{-}R^2$), shown in Table S10 in Appendix 2. All the data from the literature and the ones presented in this work showed adequate statistical parameter below 0.4% and passed the first criterion. For each concentration, there is no higher variation in the slope of the curve for that temperature and pressure range.

The second criterion to be evaluated is the consistency of the relative standard deviation of ΔH_{diss}, also shown in Table S10 in Appendix 2. The C_2H_6 hydrate phase equilibria data were acceptable according to the criterion, presenting an RSD of ΔH_{diss} below 10%. However, the experimental data sets of 10, 35, 45 wt% of ethanol, from this work, presented RSD of 9.36%, 5.52%, and 5.52%, respectively, higher than the good classification of 5%. The ΔH_{diss} is between 71.05 kJ/mol and 76.74 kJ/mol for the data higher than 10 wt% and the set of 5 wt%, but for the set of 10 wt% the ΔH_{diss} is 65.92 kJ/mol, having the highest RSD. The hydrate dissociation enthalpy at 10 wt% is the one with the highest deviation from the average, which can be an indication of a different hydrate structure (sII). This concentration will be the best condition for future experimental hydrate characterization data.

Figure 14 (b) shows the independency of the water activity in the liquid phase with the temperature range for C_2H_6 data. The RSD in $\Delta T/T_0T$ for those data are shown in Table S10 in Appendix 2. Except for the set of 5 wt% of ethanol, that showed an RSD in $\Delta T/T_0T$ of 10.38%, all the sets were accepted in the third criterion of the test. However, the set of 10 wt% showed an RSD in $\Delta T/T_0T$ of 5.28%, slightly higher than a good deviation (< 5%). So, for the lower concentrations datasets, the water activity in the liquid phase has higher sensitivity with the temperature. They show similar results as for the hydrate-forming gases (CH_4, CO_2, C_2H_6) that formed single hydrate of structure I[1].

The accuracy of the models for the C_2H_6 data was evaluated through the average absolute deviation (AAD) in Table S11 in Appendix 2. The Oliveira et al. thermodynamic model had an AAD below 2 bars for the data sets up to 10 wt%. The PVTsim® showed an adequate AAD in pressure up to 26 wt% and for 45 wt% EtOH. For the AAD in temperature the PVTsim® had good AADs up to 10 wt% EtOH and for 45 wt% EtOH, below 0.5 K. For the HLS correlation, the AADs in temperature were adequate up to 10 wt% and for 40 wt%. All the models showed a higher AAD for concentrations from 26 wt% to 40 wt% EtOH. Using any approach to model inhibited hydrate system, in general, the models show consistency with the data up to 10 wt% for the C_2H_6 hydrate system with ethanol.

The predictive results and the consistency test showed that the ethane hydrate equilibrium data with ethanol appears to have different behavior between the sets of 10 wt% or lower and 26 wt% or higher. This is an indication that a probable different hydrate structure (i.e., sII) forms for concentrations larger than 26 wt%, giving further evidence that ethanol can act as a hydrate co-former, changing the expecting single gas hydrate of structure I to a double hydrate of structure II [10]. Therefore, more experimental investigation is needed in these conditions to better understand the role of ethanol.

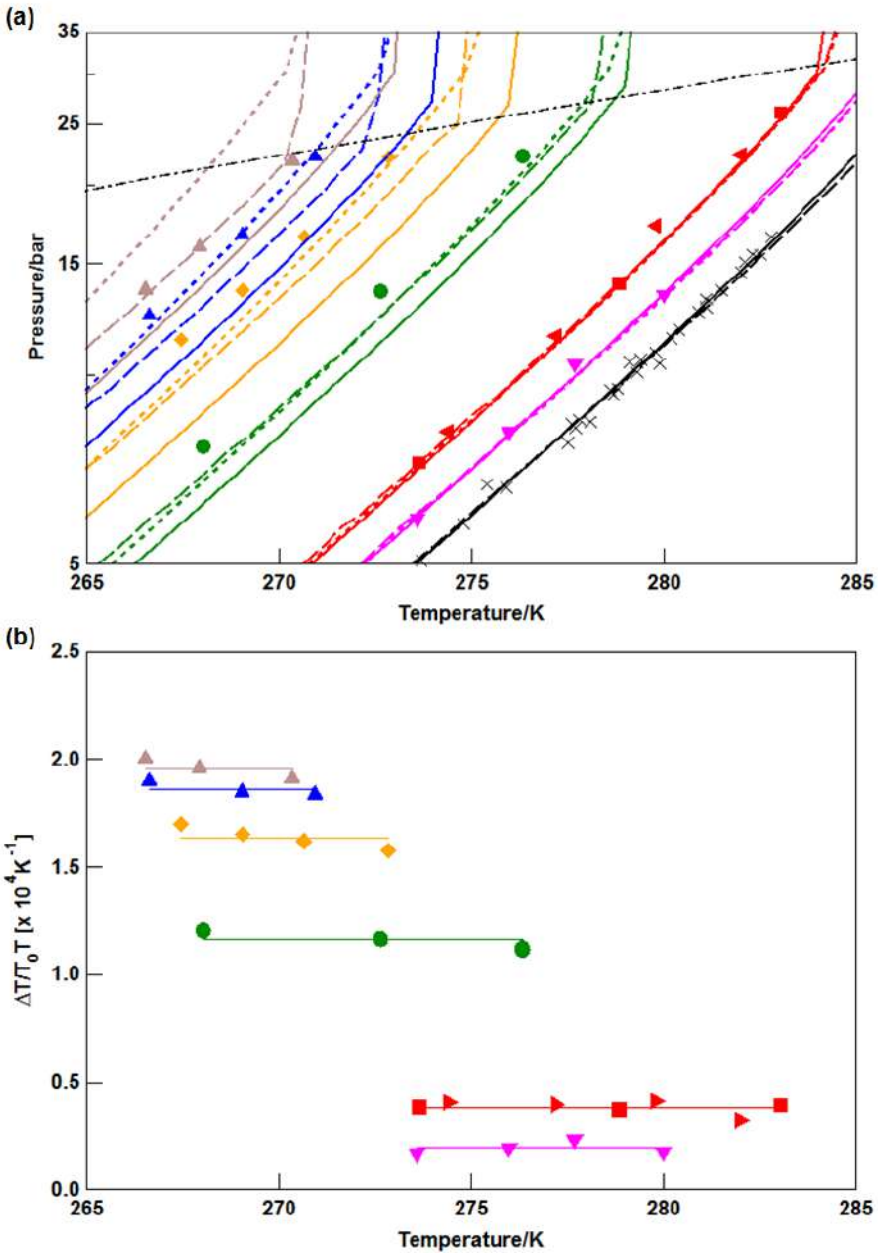

Figure 14 - Ethane (C_2H_6) hydrate phase equilibrium conditions with ethanol. (a) x for 0 wt% EtOH [181,182,193]. ▼ for 5 wt% EtOH [52]. ► for 10 wt% EtOH [52]. ■ for 10 wt% EtOH (this work). ● for 26 wt% EtOH (this work). ♦ for 35 wt% EtOH (this work). ▲ for 40 wt% EtOH (this work). ▲ for 45 wt% EtOH (this work). The lines show the predictive calculations of the models: dashed-dotted for C_2H_6 liquefy pressure (PVTsim®), continuous for the adapted model of Oliveira et al. [123], dashed to PVTsim® software and dotted to Hu-Lee-Sum Correlation [176]. (b) The relationship between $\Delta T/T_0T$ and temperature T for propane hydrate systems with ethanol. The lines correspond to the constant value of the best fit that represents the constant value of the water activity for a small temperature range.

Because there are no liquid-hydrate-vapor equilibria data with ethanol for a gas mixture in the literature [194], this study presents the first set of hydrate equilibria data with ethanol. Hydrate phase equilibria data were measured up to 40 wt% ethanol for a gas mixture composed of 73.8 mol% of methane and 26.2 mol% of ethane, as given in Table S12 in Appendix 2.

Figure 15 (a) shows the CH_4/C_2H_6 hydrate phase equilibria data as well as their linear fit and the equilibrium conditions predicted with two models (PVTsim® and HLS correlation). The linear regression evaluated through the statistical parameter ($1\text{-}R^2$) are in Table S13 in Appendix 2 for the CH_4/C_2H_6 hydrate data. The CH_4/C_2H_6 data obtained in this study passed the first criterion with a statistical parameter lower than 0.45%. For each concentration, there is no variation in the slope for the temperature and pressure ranges.

The relative standard deviation of ΔH_{diss} for the CH_4/C_2H_6 data are in Table S13 in Appendix 2. The CH_4/C_2H_6 data were acceptable by the second criterion of the test. However, the 9 wt% presented the highest RSD of ΔH_{diss} of 7.82%, below the 10% acceptable, but higher than a good deviation of less than 5%. For the sets from 25 wt% up to 40 wt% EtOH, the value of the ΔH_{diss} is between 57.72 kJ/mol and 58.46 kJ/mol, which are in good agreement. However, the set at 9 wt% had a ΔH_{diss} of 63.88 kJ/mol. The ΔH_{diss} is independent from the type and concentration of the thermodynamic inhibitor for the same gas hydrate structure. Therefore, we can infer that the sets at 25 wt% or higher probably correspond to a hydrate structure with a different composition from the structure of the set at 9 wt%, since the mixture CH_4/C_2H_6 forms structure II.

Figure 15 (b) shows the evaluation of the average $\Delta T/T_0T$ for the CH_4/C_2H_6 data. The RSD in $\Delta T/T_0T$ was calculated for each concentration to analyze the third criterion, with values given in Table S13 in Appendix 2. The CH_4/C_2H_6 data obtained in this study showed a good RSD in $\Delta T/T_0T$, below 4%, and passed the third criterion.

The prediction from the PVTsim® and the HLS correlation, shown in Figure 15 (a), were analyzed through the AAD from the CH_4/C_2H_6 data and they are given in Table S14 in Appendix 2. PVTsim® had an adequate AAD for the pressure, below 2 bar, and for the temperature, below 0.5 K, for the sets up to 25 wt% EtOH, while the HLS correlation had an AAD for the temperature below 0.5 K up to 30 wt% EtOH. These two approaches assume that ethanol is only a hydrate inhibitor. The evaluation of the

consistency test for an inhibited system and the deviation from the calculation of the models show different behaviors for the set at 9 wt% and the sets at 25 wt% or higher.

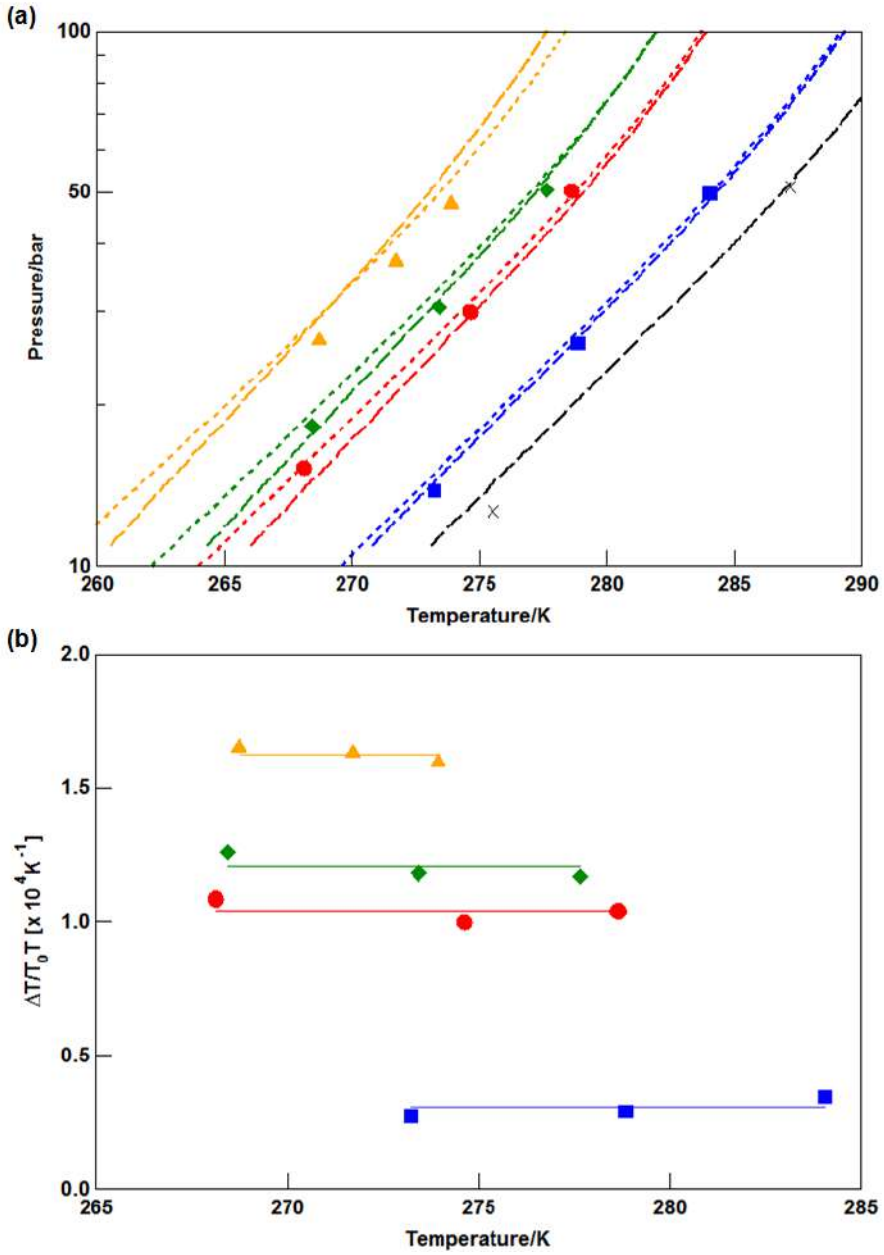

Figure 15 - Mixture of methane and ethane (73.8 mol%CH_4/26.2 mol%C_2H_6) hydrate phase equilibrium data with ethanol. (a) x for 0 wt% EtOH (this work). ■ for 9 wt% EtOH (this work). ● for 25 wt% EtOH (this work). ♦ for 30 wt% EtOH (this work). ▲ for 40 wt% EtOH (this work). The lines show the predictive calculations of the models: continuous for the adapted model of Oliveira et al. [123], dashed to PVTsim® software and dotted to Hu-Lee-Sum Correlation [176]. (b) The relationship between $\Delta T/T_0T$ and temperature T for a mixture of methane and ethane (73.8 mol%CH_4/26.2 mol%C_2H_6) hydrate systems with ethanol. The lines

correspond to the constant value of the best fit that represents the constant value of the water activity for a small temperature range.

We apply the three criteria of the consistency test proposed by Sa et al. [175] for inhibited systems to all the hydrate equilibria data with ethanol. Applying this test, we could verify the consistency of the data in the literature and also the data obtained in this study to be characterized as a hydrate inhibited system. Since there is limited validation to characterize the existing data with ethanol and there is an indication in the literature that ethanol can have an ambiguous behavior as either a hydrate thermodynamic inhibitor or promoter [8,27,28], this analysis has great importance to define conditions in which hydrate experimental characterization data are needed.

For the set of CH_4 hydrate phase equilibria with ethanol, only the 15 and 5 wt% of ethanol fails the third criterion of the consistency test. Among the sets of CO_2 hydrate phase equilibria with ethanol, only the data of 2 and 5 wt% of ethanol fail the third criterion. For all the other data of C_3H_8, C_2H_6, CH_4/C_2H_6 hydrate phase equilibria, only the C_2H_6 hydrate equilibria data of 5 wt% from the literature fails the third criterion of the test. The hydrate structure for all of those systems is supposed to be a single hydrate forming structure I. However, we could notice in the evaluation of the second criterion that the hydrate dissociation enthalpy of those conditions showed higher deviation from the other sets, giving some indication that the hydrate structure may be changed. Coupling this information with the three predictive models for inhibited hydrate systems and the literature reports that ethanol could behave as a hydrate thermodynamic promoter, we can define experimental conditions in which more information about the hydrate structure are needed. The definition of these experimental conditions is of high relevance because the experimental data to characterize the hydrate structure are expensive and challenging to perform [27].

For the sets of C_3H_8 and CH_4/C_2H_6 hydrate phase equilibrium data, the hydrate is already characterized as structure II [2]. So, the transformation that could occur on the hydrate will not change the hydrate structure but include a competition between the ethanol and the gases to occupy the large cavity of structure II. In these conditions, the hydrate dissociation enthalpy will also change because of the changing hydrate composition, as it was shown with the evaluation of the experimental CH_4/C_2H_6 hydrate phase equilibrium data.

The predictive potential of the three models was tested here, mainly for high ethanol concentrations. In general, all the three models showed good predictions for lower ethanol concentrations, up to 10 wt%, while for high concentrations the accuracy varied. PVTsim® shows lower accuracy between 15 wt% and 44.6 wt%, with some exceptions. The HLS correlation has an accuracy lower than 0.5 K for almost all the data up to 30 wt% ethanol. The exceptions are for the 26 and 40 wt% for the C_2H_6, the 20 wt% for the CO_2, and the 39.6 wt% for the CH_4, that had the AAD above 0.5 K. The thermodynamic model of Oliveira et al. [123] showed an AAD lower than 2 bar for all the HPE data with ethanol for 10 wt% or lower. However, all three models were developed with an approach to model a hydrate inhibitor system. As such, if ethanol is a co-guest in the hydrate structure (solid phase), there may be structural change in some system, and a different approach is needed to develop a model that will properly account for the changes under the proper conditions. Between the three models presented here, the thermodynamic model of Oliveira et al. [123] is the one that allows adaptation to describe the equilibrium condition in systems where the chemical additive behaves both as thermodynamic hydrate promoter and inhibitor. This modeling approach has already been done to calculate the equilibrium condition of hydrate systems with THF [123].

3.5 Partial conclusions

Knowing that the hydrate phase equilibria data at high concentrations of ethanol are scarce in the literature, this study presents a comprehensive summary of ethane hydrate equilibrium data with ethanol, up to 45 wt% EtOH. Here we also show sets of hydrate phase equilibrium data with ethanol, up to 40 wt%, for a gas mixture of 73.8 mol% methane and 26.2 mol% ethane, which was not available before in the literature.

In addition to experimental data for hydrate phase equilibria at high ethanol concentrations, we tested the consistency of all the hydrate equilibria data with ethanol as an inhibited hydrate system. The predictive potential to determine the gas hydrate equilibrium temperature or pressure of three different modeling approaches were tested for the systems, defined as inhibited hydrate systems, with ethanol. With this result and the literature reports [8,27,28] that ethanol has ambiguous behavior, as a hydrate thermodynamic inhibitor and promoter, we could infer the condition in which inhibitor or promoter was predominant. For concentrations up to 10 wt%, ethanol is predominantly a hydrate thermodynamic inhibitor, and for higher concentrations, the

promoter behavior begins to compete with the inhibitor behavior, reducing the thermodynamic inhibition effect of ethanol, mainly for systems that in fresh water the gas forms hydrate structure I (CH_4, CO_2 and C_2H_6). However, for systems that in fresh water the gas forms structure II hydrate, we also see an indication that the ethanol could participate as a hydrate co-former, as for the CH_4/C_2H_6 data.

The hydrate phase equilibrium data with ethanol collected and measured here contribute to increasing body of knowledge for hydrates with high ethanol concentration. The methodology presented to evaluate the potential for ethanol to behave as a hydrate thermodynamic inhibitor or promoter allowed to define conditions at which a full experimental characterization of the hydrate structure and guest's occupancy are needed, which can be determined from x-ray diffraction and spectroscopy measurements. Further improvements to predictive model will require even more data with well-defined characterization of the hydrate structure and composition.

List of symbols

T - Temperature [K]

P - Pressure [bar]

R - Universal gas constant [J mol / K]

wt% - massa fraction [g / g]

ΔHdiss - hydrate dissociation enthalpy [J / mol]

z - gas compressibility

RSD - relative standard deviation

$\Delta T = T_0 - T$ - suppression temperature

n - number of moles

T_0 - equilibrium temperature without additive

LHVE - liquid hydrate vapor equiibrium

AAD - average absolute deviation

sI - Hydrate structure I

sII - Hydrate structure II

EtOH - Ethanol

Chapter 4. Hydrate growth in freshwater

Gas hydrates are crystalline solids formed in systems with water and light components at low temperatures and high pressures. Those conditions are present in natural gas offshore production, where it can lead to blockages. Although there are consolidated operating procedures to avoid these blockages, there are also limitations to their use. Similar conditions led to the formation of natural reserves of CH_4 hydrate on the seafloor, which came to be seen as a potential source of renewable energy. Therefore, studies are under development to allow the exploration of the CH_4 present in those reserves. On the other hand, different applications for using these crystalline structures are under development due to their capacity to store gases. Thus, a better understanding of the growing phenomenon can allow the development of alternative operational procedures to avoid blockages, adequately explore natural reserves, and develop a new gas storage technology. The objective here is to develop a new model for the hydrate growth kinetics with chemical affinity as a driving force. The use of the Prigogine affinity allows the inclusion of the thermodynamic factor of all hydrate-forming components in the growth model. This model is based on non-equilibrium thermodynamics, which can clarify some conceptually relevant and rarely investigated problems. Besides, it enables the inclusion of the thermodynamic behavior of hydrate formation in the kinetics. Here, we evaluate the diffusion and reaction steps and their limiting condition on the growth rate of CH_4 hydrate in freshwater. The hydrate growth model can describe the growth behavior quantitatively and qualitatively, showing good agreement with the experimental data. Because the model considers both reaction and diffusion, it shows that hydrate growth is governed by both mechanisms depending on the pressure.

4.1 Introduction

Gas hydrates are crystalline solids formed in systems containing water and light-guest molecules at low temperatures and high pressures [4]. The interactions between the guest components and water molecules are controlled by the weak hydrogen bonds [32]. These guest molecules are usually light gases, mainly natural gas components, trapped inside the hydrogen-bond framework of water molecules [2]. Between natural gas components, methane (CH_4) is not only the gas usually in the highest concentration, but also it is the most common gas in hydrate natural reserves. However, other gases may also be included in hydrate structures, particularly in areas close to conventional oil and gas reservoirs [195].

The conditions of hydrate formation are present in offshore oil and gas production. In these systems, the formation of hydrates can lead to blockages along the flowline. Conventional methods of hydrate preventions include physical and chemical interventions. Limited physical options are available to prevent gas hydrate formation, and, in most cases, the techniques are neither applicable nor economical [196]. The conventional methods of chemical hydrate inhibition are the addition of thermodynamic (THI) and low-dosage (LDHI) hydrate inhibitors [14]. However, the recent increase in natural gas production started to require high volumes of THI [24]. As an alternative, the use of LDHI, whether kinetic and/or anti-agglomerate, has become of greater interest [196]. So, flow assurance requires an adequate predictive model for the formation of solids to guarantee financial and safety requirements. Therefore, it is necessary to understand the thermodynamic effects of hydrate formation in the presence of chemical additives and the kinetic effect of the THIs and LDHIs on hydrate formation to guarantee their use efficiency as hydrate blockage prevention methods [15].

The CH_4 hydrate reserves in nature became a potential renewable energy source, and studies are under development to explore these reserves [18]. According to the review of Chong et al.[197], natural gas hydrates are one of the largest carbon sources on earth and a potential source of clean carbon-based energy in the near future [195]. The exploration of this solid in geological formations requires the hydrate formation and dissociation dynamics knowledge [19] to guarantee an efficient and economically viable gas production [198] without causing environmental impacts [21,199]. On the other hand, there is a great interest in developing hydrate technology applications due to their

capacity to store gases. Among these applications are gas separation, energy storage, energy transport, CO_2 sequestration, and desalination [3]. However, the requirement of high pressure is one of the decisive obstacles for the process commercialization [23]. The use of chemical additives eases the thermodynamic conditions and enables the hydrate production for gas storage [200] and separation [196]. Therefore, developing a model capable of describing hydrate growth will allow its process to be controlled, making this new technology physically and economically viable [14].

Thermodynamic modeling for the phase equilibrium calculation with hydrate has been in development since the 1960s with the van der Waals and Platteeuw model [98]. This model is based on statistical thermodynamics to describe the equilibrium between hydrate, liquid, and vapor phases. The review of advances in modeling the phase equilibrium with hydrate shows that this development occurred mainly around improving the van der Waals and Platteeuw model. Although we still need some improvements in the hydrate equilibrium calculations, this modeling is already sufficiently consolidated for some systems such as the methane hydrate system [201]. Meanwhile, this solid-formation dynamic modeling still presents a large gap, as shown in the literature [19].

The formation of gas hydrate is similar to the crystallization process and can be described in three stages: nucleation, growth, and agglomeration [2]. Kinetic experimentation and molecular simulation are used to understand the nucleation mechanism [11,35]. However, due to the difficulty of obtaining nucleation direct experimental evidence, molecular simulations have been preferred over experimental studies [33,34]. The agglomeration is the stage with more evidence in the literature studies because it is the main stage responsible for blocking oil and gas production lines [19]. According to Yin et al. [15], that reviewed the gas hydrate growth kinetic models, the gap still exists in understanding the controlling mechanism of gas hydrate growth, which is further augmented by the dynamic behavior of multiphase fluids flow, the thermodynamics of the hydrate-forming system, and the compounding interfacial phenomena. Most of the hydrate growth models in the literature are based on the guest molecule dynamics only and are unable to describe non-ideal systems [33,42–44,84–87,95,96].

This work focuses on the hydrate growth kinetics, mainly because studies show that, after the beginning of the appearance of the first crystals, the growth effect overlaps

the nucleation just as agglomeration overlaps the growth in the particle size scale. However, it is possible to separate these effects in the time scale to understand those mechanisms [44,202,203]. The models that include water or some additive effect do not account for the host molecule effect or the interaction between those compounds [80,83,204,205]. Therefore, there is still a need for a model capable of explaining the effect of all components participating in the hydrate formation "reaction" and the non-ideality effects of the systems. Here, we are proposing the use of the Prigogine affinity as the driving force. Changes in thermodynamic potentials for chemical reactions produce affinity [122]. The affinity allows evaluating all the components involved in the hydrate formation and evaluates the growth accounting for non-ideal effects. The affinity is already used in the literature [88–90]. However, as far as we know, all the models that use affinity in the driving force adopted simplifications that did not take into account the essential effects of the thermodynamic factor.

The reaction rate is the change in the extent of the reaction over time, and it can be proved that, from non-equilibrium thermodynamics, the driving force and its conjugated flow establish a linear relationship. More details on the thermodynamics of non-equilibrium are on Demirel [121] and Lebon et al. [122].

The coupling of the diffusion effects from the gas-liquid interface to the bulk phase, with the reaction effect, due to the host movement from the bulk phase to the liquid-solid interface, is a mechanism widely used in the literature [33,41,42,86,206]. However, in ideal systems, the solubility of methane in water is low, and its diffusion will be slower than the reaction to form the solid phase. Thus, a variety of models only account for the diffusion effect for the hydrate growth in the literature [33,81,83–87]. Then, there are still questions about the competition between reaction and diffusion in systems that deviate from this ideal scenario due to using an additive or systems at very high pressures [93–96].

A better understanding of the dynamic hydrate growth behavior is necessary to facilitate the exploration of natural gas hydrate reserves, develop the hydrate technology to store or separate gases, and allow the safer use of KHI and LDHI. Therefore, this work aimed to develop a hydrate growth model based on the non-equilibrium thermodynamics and applied to CH_4 hydrate in freshwater. With this model, we intend to describe the growth considering the diffusion and reaction steps. To establish a new

driving force to account for the effect of the thermodynamic factor in the kinetic for both water and guest molecule (CH_4).

4.2 Kinetic model

Although hydrate formation does not involve breaking or forming new bonds between the atoms involved, characterizing the transformation of molecules, the term "reaction" is used to refer to the formation of hydrate [2]. The hydrate formation reaction modeled here is the methane hydrate formation reaction in systems containing methane and pure water. This reaction is shown in equation (35), where H is the symbol representing the hydrate phase, with the molar composition ξ of methane and τ of water.

$$\xi CH_4 + \tau H_2O \rightleftharpoons H \rightleftharpoons \xi CH_4 \cdot \tau H_2O \tag{18}$$

The stoichiometric coefficients of each component are defined depending on the hydrate structure formed. For water, this is obtained by the number of water molecules present in a unit cell, that is, it is the sum of the product between the number of cavities per unit cell and the coordination number of each unit cell for large and small cavities. Therefore, for structure I, $\tau = 184$, and for structure II, $\tau = 544$. The stoichiometric coefficient of the guest is given by the sum of the number of large and small cavities per unit cell of the structure. Then, for the methane hydrate unit, $\xi = 8$, as it forms structure I [2].

In order to describe the growth, some hypotheses were adopted. First, it is assumed that growth occurs separately from nucleation. The growth process will take place at the solid-liquid interface. Therefore, the mass and energy balances will be applied to the liquid, vapor, and hydrate phases, given the following considerations:

(a) nucleation and growth occur sequentially, and, in this work, we will focus only on the growth stage, so there is no nucleation after the beginning of the growth;
(b) the liquid phase consists of water and solubilized methane;
(c) the liquid provides water and methane for the hydrate growth process in the solid-liquid interface;
(d) the vapor phase provides methane for the liquid phase;
(e) the amount of water present in the vapor phase is despised;
(f) in the vapor phase there is no hydrate growth;

(g) the gas-liquid interface is in local equilibrium.

4.2.1 Driving force

In this sense, for constant P and T systems, the mass balance for each phase, the population balance to obtain properties of the solid phase, and the reaction rate with a driving force that accounts for both water and hydrate forms' activity are necessary. In addition to this algebraic-differential equations system, thermodynamic models proposed by Oliveira et al. [123,207] were structured and validated to calculate the equilibrium conditions and thermodynamic properties (Appendix 3). The main equation of the model will be presented in the following topics. The experimental hydrate formation systems are a high-pressure reactor with a mechanical stirrer filled with pure methane (CH_4) gas, representing the gas phase, and pure water (H_2O), representing the liquid phase.

For chemical reactions, analysis in terms of Gibbs free energy is convenient. For the constant temperature, *T*, and pressure, *P*, the variation of Gibbs' free energy, G_b, can be related to the degree of extent of the reaction, ε, according to the Donder thermodynamic theory of affinity. Then, the Prigogine's Affinity, *A*, defined by equation (19), is introduced [121]. Where ν_i is the stoichiometric coefficient and μ_i is the chemical potential of component *i* in the reaction.

$$\left(\frac{dG_b}{d\varepsilon}\right)_{T,P} = \sum_i \nu_i \mu_i = -A \tag{19}$$

Describing the chemical potential in terms of the activity, a, the affinity can be obtained in terms of the activity of each component according to the equation (20).

$$A = -\sum_i \nu_i \left(\mu_i^0 + RT \ln\left(a_i\right)\right) = -\sum_i \nu_i \mu_i^0 - RT \ln\left(\prod_i \left(a_i\right)^{\nu_i}\right) \tag{20}$$

Because the Gibbs free energy is minimal at equilibrium $\left({}^{dG}\!/_{d\varepsilon} = 0\right)$, the affinity at equilibrium is zero. Applying the chemical equilibrium condition in equation (20) leads to equation (21).

$$A^{eq} = -\sum_i \nu_i \mu_i^{eq} = 0 \rightarrow \sum_i \nu_i \mu_i^0 = -RT \ln\left(\prod_i \left(a_i^{eq}\right)^{\nu_i}\right) \tag{21}$$

Substituting equation (21) into equation (20), affinity can be defined as the distance from the equilibrium in terms of activity, according to equation (22).

$$A = RT \ln\left(\frac{\prod_i \left(a_i^{eq}\right)^{v_i}}{\prod_i \left(a_i\right)^{v_i}}\right) = RT \ln\left(\frac{K'_{eq}}{K'}\right) \tag{22}$$

The chemical equilibrium constant is the geometric mean of the activities weighted by the stoichiometric reaction coefficients, $K'_{eq} = \prod_i \left(a_i^{eq}\right)^{v_i}$.

The calculation of affinity requires the description of each species' activities in the liquid and hydrate phases. For the proposed reaction, equation (35), the activity of the components in the liquid phase is obtained by the excess Gibbs energy model, NRTL [123], with the parameters estimated for the H_2O and CH_4 system (Appendix 3).

The literature does not contain consolidated models that describe the difference in the chemical potential of the components in the hydrate phase-out of equilibrium. However, with the hypothesis of the solid phase in equilibrium, the activity of the components in the hydrate phase is only necessary to define the equilibrium curve of the system, that can be obtained through the traditional modeling of van der Waals and Platteeuw theory [98]. We used the modeling proposed by Oliveira et al. [207] to describe the hydrate-liquid equilibrium conditions.

Adopting the hypothesis that the solid phase is in equilibrium, the activities in the solid phase are the activities of the components in the equilibrium condition. Therefore, the K' is calculated according to equation (23) and K'_{eq} according to equation (24).

$$K' = \frac{\left(a_{CH_4}^{H}\right)_{eq}^{\xi} \left(a_{H_2O}^{H}\right)_{eq}^{\tau}}{\left(a_{CH_4}^{L}\right)^{\xi} \left(a_{H_2O}^{L}\right)^{\tau}} \tag{23}$$

$$K'_{eq} = \frac{\left(a_{CH_4}^{H}\right)_{eq}^{\xi} \left(a_{H_2O}^{H}\right)_{eq}^{\tau}}{\left(a_{CH_4}^{L}\right)_{eq}^{\xi} \left(a_{H_2O}^{L}\right)_{eq}^{\tau}} \tag{24}$$

The affinity is then described by equation (25), where K is the product of activities, weighted by stoichiometric coefficients, in the liquid phase, out of the equilibrium, and K_{eq} is the same product but in equilibrium with the solid phase.

$$A = RT \ln\left(\frac{\left(a_{CH_4}^{L}\right)^{\xi}\left(a_{H_2O}^{L}\right)^{\tau}}{\left(a_{CH_4}^{L}\right)_{eq}^{\xi}\left(a_{H_2O}^{L}\right)_{eq}^{\tau}} \right) = RT \ln\left(\frac{K}{K_{eq}} \right) \quad (25)$$

The advantage of using affinity as a driving force is to incorporate water or co-formers in the hydrate growth kinetics automatically. Therefore, this driving force allows us to account for the non-ideality effect of hydrate formation systems.

4.2.2 Growth rate

Non-equilibrium thermodynamics can clarify some conceptually relevant problems that are rarely investigated in other formalisms, mainly the non-ideality effect of the systems. According to Lebon et al. [39], chemical kinetics is a rich but complex topic, understood by the non-equilibrium thermodynamics by a linear regime between the flow and the driving force in the proximity to equilibrium.

For a single reaction, the system's entropy, S, can be obtaining by the substitution of the mass balance and the energy balance in the time differential Gibbs relationship per molar unit [121,122]. Comparing it with a generic entropy balance defined by the non-equilibrium thermodynamics the system entropy generation term, σ^S, is defined by equation (26). Where, J_r is the reaction flow.

$$\sigma^S = \frac{A}{T} J_r \quad (26)$$

According to the second law of thermodynamics, $\sigma^S \geq 0$, that is, the entropy generation term is always positive or null in equilibrium. Therefore, the affinity and the reaction flow must show the same signal. Known the condition of proximity to equilibrium, for the approach of non-equilibrium thermodynamics applied to chemical reactions, the driving force and its conjugated flow establish a linear relationship. Therefore, considering these conditions, the reaction flow can then be calculated by equation (27).

$$J_r = L_{rr} \frac{A}{T} \quad (27)$$

where $L_{rr} > 0$ is the phenomenological coefficient of the reaction.

Figure 16 outlines the hydrate growth phenomenon stages based on the hypothesis of diffusion with reversible heterogeneous reaction. This approach is already used in mathematical models found in the literature, such as the model by Englezos et al. [42,43]. By the liquid film theory, the hydrate growth process is treated with consideration of the following steps: a) diffusion of the solute from the bulk of the liquid phase ($z = \delta$) to the solid surface ($z = 0$), and b) hydrate formation reaction on the surface ($z = 0$).

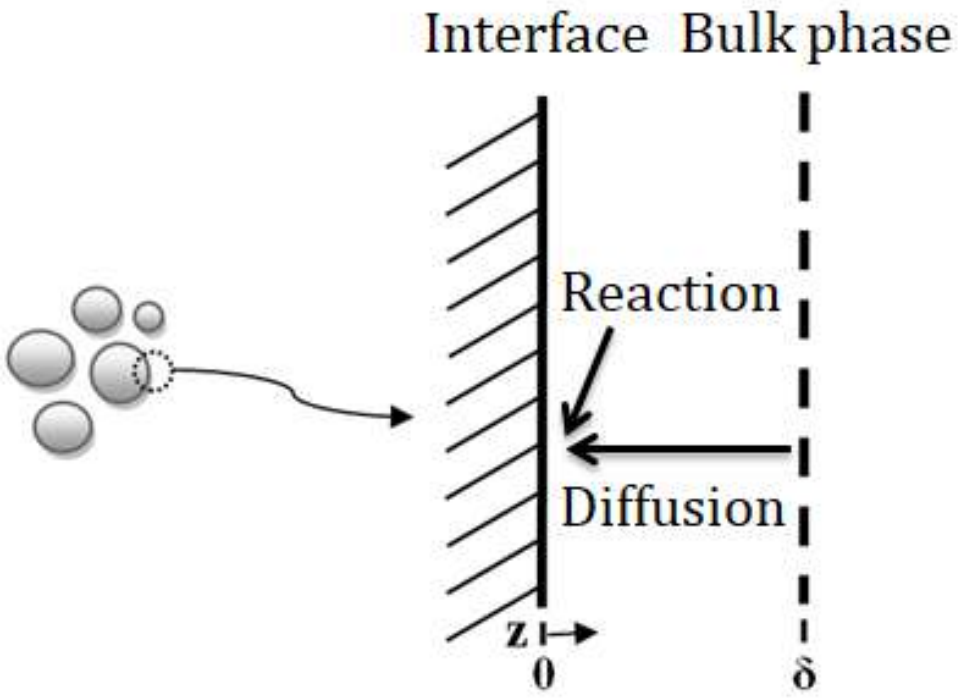

Figure 16 - Illustrative image of the liquid film surrounding the hydrate solid surface.

For the description of the two stages, the following hypotheses are adopted: a) in the liquid film, the system is in a steady state; b) absence of convection in the liquid film; c) unidirectional transport; d) isothermal system, e) reversible heterogeneous reaction, occurring only at the liquid-solid interface and f) there is no chemical reaction in the liquid film. According to the considered hypotheses, the mass balance can be represented by equation (28). The diffusive mass flow can be written in terms of each component's chemical potential, and the solution is linear with the z-axis, equation (28), considering that the methane concentration slightly changes in the liquid film.

$$J_i^z = 0 \rightarrow \frac{d}{dz}\left(-c_i \frac{L_i^{'}}{RT}\frac{\partial \mu_i}{\partial z}\right) = 0 \rightarrow \mu_i = C_1 z + C_2 \quad (28)$$

The following boundary conditions are also assumed: a) diffusive flow equal to the reaction rate per area, J_r^z, on the crystal surface, $z = 0 \rightarrow J_i^z = J_r^z$, and b) chemical potential in $z = \delta$ equal to the chemical potential in the bulk of the liquid phase, $z = \delta \rightarrow \mu_i = \mu_i^b$.

With the defined reaction flow, equation (27), it is possible to obtain the parameters of the chemical potential profile of each species in the liquid film, equation (28), using the boundary conditions, where $J_i^z = -c_i L_i^{'} / RT\left(\partial \mu'_i / \partial z\right)$ and $J_r^z = -L_{rr}\, A\big|_{z=0} / T$ for reagents. Therefore, the chemical potential in the liquid film for methane and water are given by equations (29) and (30), respectively, where $L_i = L_i^{'} \overline{c}_i$.

$$\mu_{CH_4} = R\frac{L_{rr}}{L_{CH_4}} A\big|_{z=0}\left(z - \delta\right) + \mu_{CH_4}^0 + RT\ln\left(a_{CH_4}^b\right) \quad (29)$$

$$\mu_{H_2O} = R\frac{L_{rr}}{L_{H_2O}} A\big|_{z=0}\left(z - \delta\right) + \mu_{H_2O}^0 + RT\ln\left(a_{H_2O}^b\right) \quad (30)$$

Adding the chemical potentials of the reagents weighted by their respective stoichiometric coefficients, $\tau\ \mu_{H_2O} + \xi\ \mu_{CH_4}$, described by equation (31). And then, equaling it to the same sum, but using the profiles of the equations (29) and (30) we get the expression of equation (32).

$$\tau\ \mu_{H_2O} + \xi\ \mu_{CH_4} = \tau\left(\mu_{H_2O}^0 + RT\ln(a_{H_2O})\right) + \xi\left(\mu_{CH_4}^0 + RT\ln(a_{CH_4})\right) \quad (31)$$

$$RL_{rr}\, A\big|_{z=0}\left(z - \delta\right)\left(\frac{\xi}{L_{CH_4}} + \frac{\tau}{L_{H_2O}}\right) = RT\ln\left(\frac{\left(a_{CH_4}\right)^{\xi}\left(a_{H_2O}\right)^{\tau}}{\left(a_{CH_4}^b\right)^{\xi}\left(a_{H_2O}^b\right)^{\tau}}\right) \quad (32)$$

Defining the product of the reagents' activities weighted by their stoichiometric coefficients as $K = \left(a_{CH_4}\right)^{\xi}\left(a_{H_2O}\right)^{\tau}$ and the diffusion constant of the system as $\frac{1}{L_D} = \left(\frac{\xi}{L_{CH_4}} + \frac{\tau}{L_{H_2O}}\right)$, equation (32) became the equation (33) by applying the definition of affinity given by equation (25) on the surface of the solid. Thus, an expression is obtained for the description of K profile over the liquid film.

We know from the Viges equation [208] that $L_{\mathrm{CH_4/H_2}O} = \left(L^0_{\mathrm{CH_4/H_2}O}\right)^{n_{H_2O}} + \left(L^0_{\mathrm{H_2}O/\mathrm{CH_4}}\right)^{n_{CH_4}}$. As the system is mostly water, $n_{H_2O} \gg n_{CH_4}$, $L_{\mathrm{CH_4/H_2}O} \cong \left(L^0_{\mathrm{CH_4/H_2}O}\right)$. So, L_{CH_4} is basically the diffusion coefficient of methane in water and can be described according to the relation $L_{CH_4} = \overline{c_{CH_4}} D \exp\left(E_a/RT\right)$ [87,209], where $\overline{c_{CH_4}}$ is the methane average concentration in the liquid film, E_a is the activation energy (J/mol) of the water diffusion process, R is the universal gases constant and D is a parameter that depends on the molecule that is diffusing in the aqueous phase. Then, the diffusion constant is $L_D = L_{CH_4} \big/ \xi$.

$$\frac{K}{K_b} = \left(\frac{K\big|_{z=0}}{K_{eq}} \right)^{R\frac{L_{rr}}{L_D}(z-\delta)} \tag{33}$$

As equation (33) is valid throughout the liquid film, it can be applied to the surface of the solid to obtain $K\big|_{z=0}$ according to equation (34).

$$K\big|_{z=0} = \left(K_{eq}\right)^{\frac{RL_{rr}\delta}{L_D + RL_{rr}\delta}} \left(K_b\right)^{\frac{L_D}{L_D + RL_{rr}\delta}} \tag{34}$$

The diffusion and reaction coefficients presented different dimensions, [L_D] = mol/m s and [L_{rr}] = mol² K/m² J s. However, the exponents $L_D \big/ (L_D + RL_{rr}\delta)$ or $RL_{rr}\delta \big/ (L_D + RL_{rr}\delta)$ are dimensionless. Therefore, a more accurate comparison is made between L_D and $RL_{rr}\delta$.

The equation (34) allows to evaluate the coupling between diffusion and reaction. If $L_D >>> RL_{rr}\delta$ the exponent of K_{eq} tends to zero while the exponent of K_b tends to one, then $K\big|_{z=0} = K_b$. In other words, diffusion is the fast stage, reaction is the limiting stage of the system and on the surface of the crystal the reagents are in the condition of the bulk liquid phase. However, if $RL_{rr}\delta >>> L_D$, by the same analysis of the exponents, $K\big|_{z=0} = K_{eq}$. In this case, the reaction is the fast stage, diffusion is the limiting stage of the system and the reagents are in equilibrium on the crystal surface. Then, the model is capable to describe the coupling between diffusion and reaction, but also the limiting conditions of the system where the growth is limited by reaction or limited by diffusion.

Known the $K\big|_{z=0}$ profile, it is possible to describe the reaction rate of hydrate formation on the crystal surface, that can couple the reaction with the diffusion, equation (35), according to the conditions of the reagents in the liquid phase bulk and in equilibrium in the crystal surface.

$$G = A_{\text{sup}}\, J_{rr}\big|_{z=0} = A_{\text{sup}} RL_{rr} \ln\left(\left(\frac{K_b}{K_{eq}}\right)^{\frac{L_D}{L_D + RL_{rr}\delta}}\right) \tag{35}$$

4.2.3 System modeling

The mathematical modeling of the hydrate formation dynamics was developed according to the block diagram shown in Figure 17, for a high-pressure batch reactor with a mechanical stirrer. In the dynamic modeling, conservation principles coupled with constitutive equations were used, representing kinetic and thermodynamic relationships. The mass balance for each component in each phase, the population balance to obtain properties of the solid phase, and the reaction rate with its driving force that accounts for water activity and hydrate formation activity was used. In addition to the algebraic-differential equations, thermodynamic modeling is structured and validated to calculate the equilibrium conditions [207]. The thermodynamic properties and the detailed equations for all the modeling are in the Appendix 3.

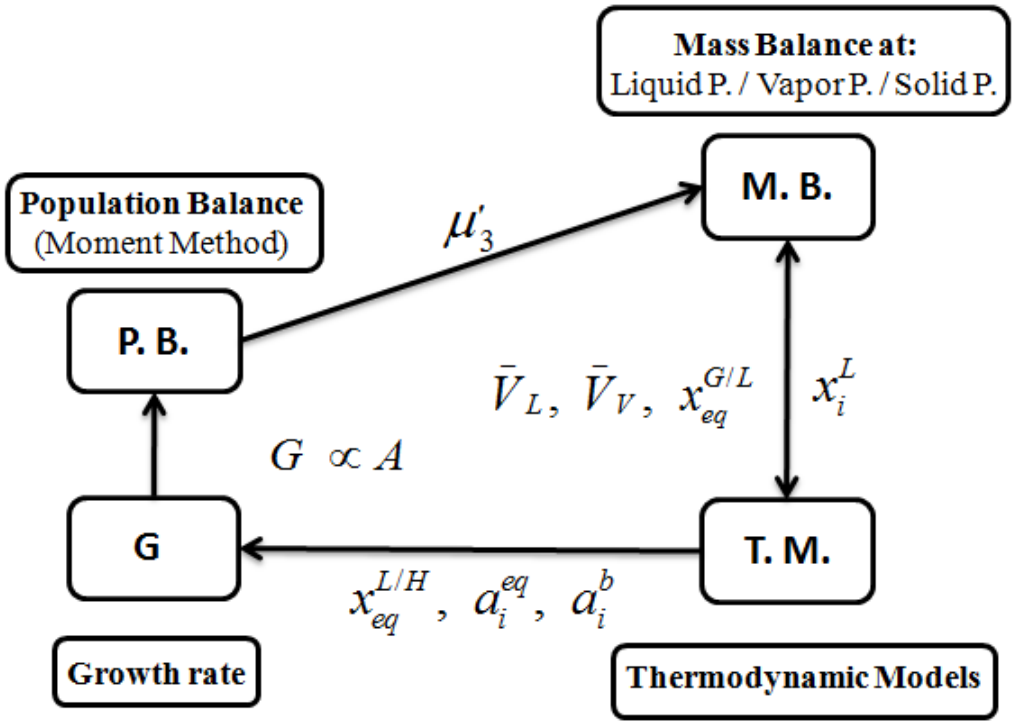

Figure 17 - Block diagram of the hydrate growth dynamic modeling. The blocks represent a set of models and equations, while the arrows represent the direction of the input and output variables between these sets, like the growth rate, *G*, that is proportional to the chemical affinity, *A*. The molar volume of the liquid phase, $\overline{V_L}$, of the vapor phase $\overline{V_V}$; the gas-liquid interface equilibrium, $x_{eq}^{G/L}$, the liquid-hydrate interface equilibrium, $x_{eq}^{H/L}$, and the liquid bulk, x_i^L, composition; the activity of the hydrate compounents formers at the hydrate-liquid equilibrium, a_i^{eq} and at the liquid bulk, a_i^b; and the order-three moment, $\mu_3^{'}$. In this way we can see how the mass and population balances, the growth rate and the thermodynamic models relate to each other.

The theoretical modeling of the dynamic system was developed and implemented in FORTRAN language. The system of differential-algebraic equations (DAE's) was integrated through the use of the DASSL routine. Further details on the numerical solution of the dynamic calculation are in the Appendix 3.

The dynamic experimental data of Englezos et al. [42] of the $CH_4 + H_2O$ system at 276 K and pressures of 70.9 bar and 48.6 bar, and 274 K at the pressure of 76.0 bar were compared with the proposed modeling prediction. The properties and initial conditions of the systems, as well as the parameters of the thermodynamic models (Appendix 3), are input data, reported in Table 5.

Table 5 - Input data for the calculation of isothermal-isobaric single hydrate (sI) growth of the $CH_4 + H_2O$ system.

Input data		
Component and System Properties		
Liquid Phase		
Molar mass of component [g/mol]		
H_2O	18.015	[210]
CH_4	16.043	[210]
Critical component temperature [K]		
H_2O	647.14	[210]
CH_4	190.56	[210]
Critical component pressure [bar]		
H_2O	220.64	[210]
CH_4	45.99	[210]
Critical component volume [cm³/mol]		
H_2O	55.95	[210]
CH_4	98.60	[210]
Component dynamic viscosity [mol/m s]		
H_2O	$\upsilon_{H_2O} = \frac{10^3}{MM_{H_2O}} \exp\left(-3.7188 + \frac{578.918}{T - 137.546}\right)$	Liquid Dynamic Viscosity (Vogel equation by online Dortmund Data Bank) http://www.ddbst.com/
CH_4	$\upsilon_{CH_4} = \frac{10^3}{MM_{CH_4}} \exp\left(-25.5947 + \frac{25392.0}{T - 969.306}\right)$	
Component density [kg/m³]		
H_2O	997.0	[210]
CH_4	0.656	[210]
Solid Phase		
Density [kg/m³]	917.8	[2,87]

Volumetric parameter	$4\pi/3$	spherical shape [211]
Superficial parameter	4π	spherical shape [211]
Number of molecules of each component in structure I completely occupied		
H_2O	184	[2]
CH_4	8	[2]
Film thickness around the particle [m]	10% of the minimum growth diameter	[211,212]
CH_4 Hydrate Occupancy Factor	Dependent on system temperature and pressure (72% at 276 and 70.9 bar; 56% at 276 and 48.6 bar; and 68% at 274 and 76.0 bar)	Ajusted acording to the experimental data of Uchida et al. [213]. [214–216]
Constants		
Universal gas constant [J/mol K]	8.314	[210]
Avogadro number [molecules/mol]	$6.022\ 10^{23}$	[210]
Reactor properties		
Volume [L]	1.5	[87]
Internal reactor radius [cm]	54	[87]
Stirrer diameter [m]	Two thirds of the reactor internal radius	[87]
Stirrer rate [rpm]	400	[42]
Agitator power number	200	[87]
Methane diffusion constants		
Diffusivity of methane in water [m^2/s]	$0.347\ 10^{-5}$	[87,209]

Activation energy of the methane diffusion process in water [kJ/mol]	18.36	[87,209]
Initial Conditions		
Liquid Phase		
Number of moles		
H_2O	16.6	[42]
CH_4	10^{-5}	Minimum amount to start solubilization without numerical issues
Solid Phase		
Relative hydrate fraction (hydrate volume/water volume)	0.0001%	[24,79,87]
Average diameter of hydrate crystals (d) [m]	10^{-6}	[33,42,79]
Volume of a medium-sized particle [m^3]	$4\pi/3 \times (d/2)^3$	spherical shape [211]
Surface area of a medium-sized particle [m^2]	$4\pi \times (d/2)^3$	spherical shape [211]

In order to predict the kinetic data obtained by Englezos et al. [42] with the proposed model, the conditions used to obtain these data were used as input data. Some extra information necessary to calculate the growth with the proposed model was obtained mainly from the study proposed by Sampaio et al. [87], who described hydrate growth using population balance.

It is important to note that the properties of the solid phase, Table 5, were imposed to define the initial moments, based on spherical particles, for the calculation of the population balance of the modeling (Appendix 3). We thus defined an average hydrate crystal diameter based on the critical radius values used in nucleation models based on the theory of primary homogeneous nucleation [11,34,42,87].

4.3 Results and discussion

Calculations of the simple methane hydrate growth with the proposed model and conditions were performed. We evaluated the coupling effect between the diffusion and reaction phenomena incorporated in the growth rate, the effect of the non-ideality that the driving force incorporates to the hydrate growth, as well as the effect of adding the water activity with the guest molecule activity of the hydrate phase in the driving force. The effect of the pressure and temperature on the growth dynamics was also observed here.

4.3.1 Diffusion/reaction coupling effect

The growth rate proposed in this work, equation (35), allows evaluating the coupling effect between the solid phase growth reaction and the guest molecule diffusion from the gas phase to the bulk liquid phase. For this evaluation, the *DR* factor is defined as the degree of coupling between those two phenomena. The *DR* factor is given by the ratio $L_D/(L_D+RL_{rr}\delta)$, which is the exponent of the growth rate driving force.

The *DR* factor represents a scale that goes from 0.0 to 1.0, Figure 18. *DR* equal to 0.0 describes a growth limited by diffusion only of the host molecule from the gas phase to the bulk liquid phase. Meanwhile, *DR* factor equal to 1.0 describes a growth limited by reaction only of the solid phase growth. The *DR* = 0.5 describes a growth with total coupling between the diffusion and the reaction. Therefore, a *DR* = 0.1 describes a growth where the diffusion is the slow stage and the reaction the quick stage; that is, the diffusion rate corresponds to about 10% of the growth rate. For a *DR* = 0.6, the diffusion is the quick stage, and the reaction is the slow stage, i.e., the diffusion rate corresponds to about 60% of the growth rate.

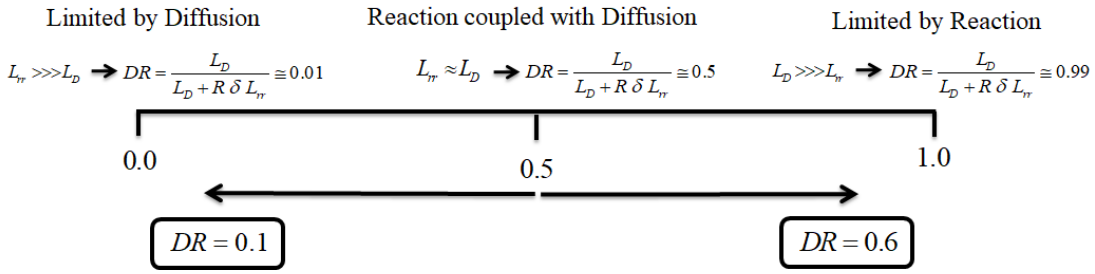

Figure 18 - *DR* scale. Coupling scale between diffusion and reaction. A growth hydrate profile limited by diffusion has a *DR* equal to 0.0, while a limited by reaction profile has a *DR* equal to 1.0. A complete coupling profile between diffusion and reaction is described by a *DR* equal to 0.5.

The imposition of these limit values for the *DR* factor in developing of the proposed growth model generates two rates. The growth rate limited by diffusion, equation (36), and the growth rate limited by reaction, equation (37).

$$G = A_{sup} \frac{L_D}{\delta} \ln\left(\frac{K_b}{K_{eq}}\right) \tag{36}$$

$$G = A_{sup} R L_{rr} \ln\left(\frac{K_b}{K_{eq}}\right) \tag{37}$$

In this work, we used to describe the limiting conditions with the factors of 0.01, limited by diffusion, or 0.99, limited by reaction. Therefore, it is not necessary to impose a rate to describe the system's limiting conditions. The proposed rate allows describing systems in limit conditions or not from the adjustment of the *DR* factor. These factors were sufficient to describe behavior similar to the profiles obtained from the limit rates imposition. The comparisons between *DR* = 0 or 0.01 and equal to 1 or 0.99, close to the limiting conditions, are shown in the Figure 19. Through this comparison it is noted that is not necessary to impose a reaction rate in the limit condition, the proposed model is able to describe through the *DR* adjustment whether or not the system is in the limit condition. In addition, we observed that the limit condition does not occur by imposing a *DR* = 0 or *DR* = 1 only, but in a range of *DR* that approaches that limit condition.

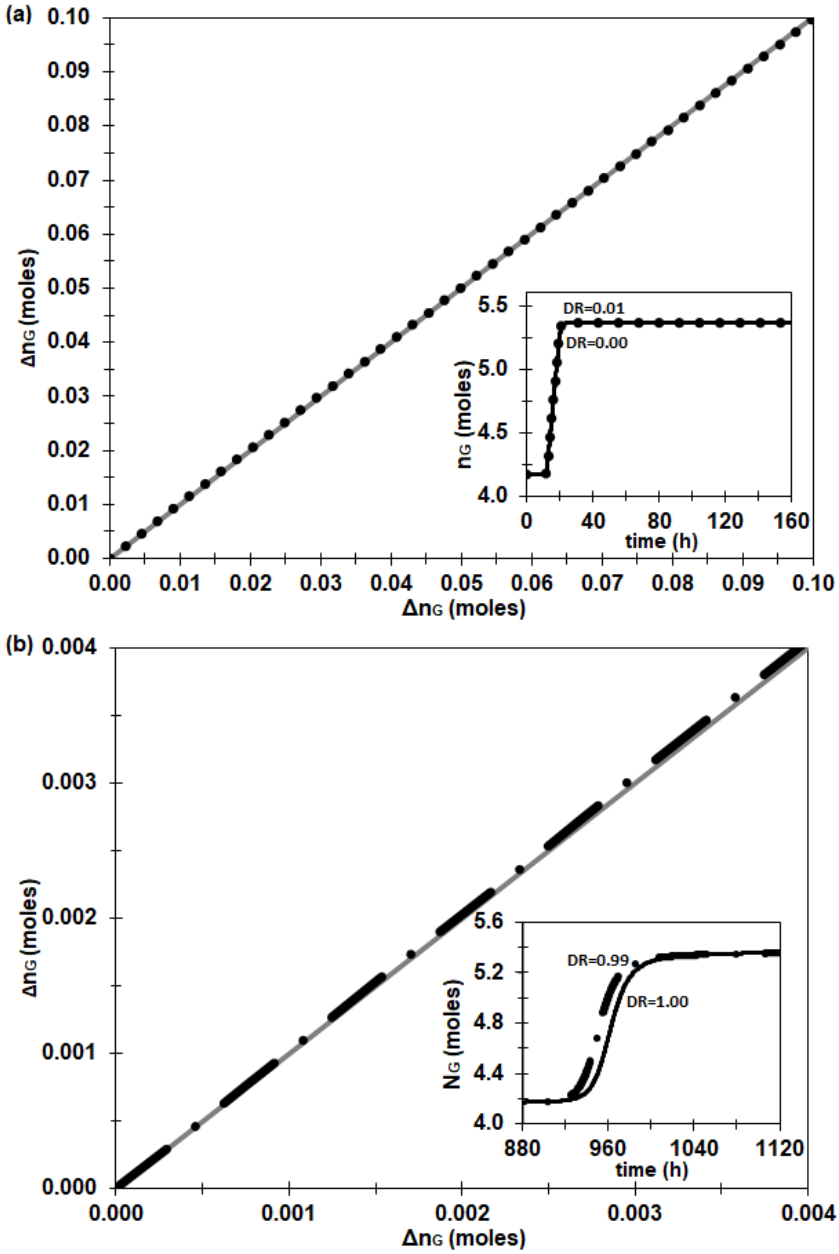

Figure 19 – The comparation of the methane molar consumption (Δn_G) over time at 276 K and 70.9 bar (a) between the limited by diffusion rate, equation (36), and the profile using the diffusion-reaction coupling rate for a *DR* equal to 0.01, equation (35), (black dotted line) and (b) between limited by reaction rate, equation (37), and the profile using the diffusion-reaction coupling rate for a *DR* equal to 0.99, equation (35) (black dashed-dotted line). The continuous gray line represents the 45 degree line expected for this comparison. The insertion shows the temporal variation of the methane number of moles in the gas phase (n_G). The continuous line represented the profile with the adjusted *DR* factor, while the dotted line represented the profile limited by diffusion and the dotted-dashed line the profile limited by reaction.

The profiles of Figure 20 and Figure 21 were calculated for the limiting conditions using the values of the DR factor appropriate to each limiting condition and a *DR* factor of total coupling between diffusion and reaction. Comparing these three profiles, limited by diffusion (*DR* = 0.01), diffusion and reaction fully coupled (*DR* = 0.5) and limited by reaction (*DR* = 0.99), it is observed that this factor will only influence the dynamics of the system, i.e., the equilibrium conditions remain independent of the path, as expected. Among the kinetic effects, it is noted that the more limited by diffusion the growth, the shorter is the induction time to start particles growth, Figure 20, and the higher and faster is the growth rate, that is, the particles grow more quickly until reaching the stationary condition, Figure 20 insertion. It is also noted in Figure 20 insertion that the growth rate reaches the stationary state and not the thermodynamic equilibrium. As there is a constant supply of methane in the gas phase, to maintain the system pressure constant, growth occurs until practically all the water is consumed, shown in the Figure 21 top right insertion.

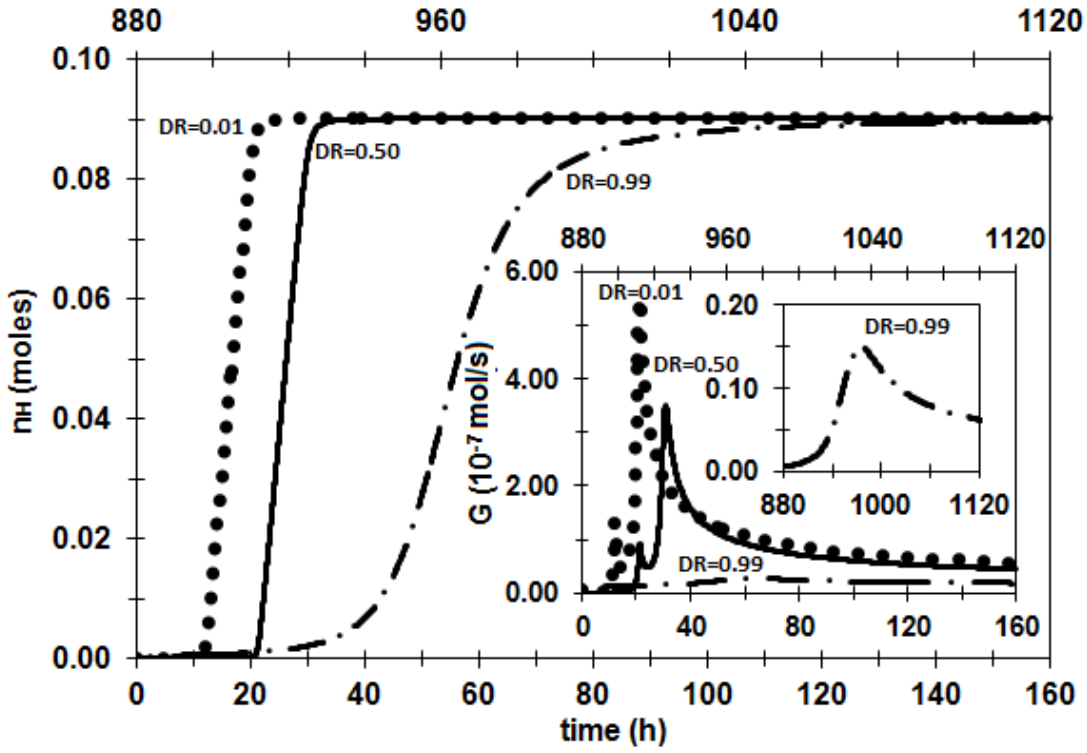

Figure 20 - The hydrate number of moles (n_H) temporal profile at 276 K and 70.9 bar. The dotted line describes the limited by diffusion profile (*DR*=0.01), the continue line the diffusion-reaction coupling profile (*DR*=0.5) and the dotted-dashed line, in the 2nd time axis, the limited by reaction profile (*DR*=0.99). The insertion shows the hydrate growth rate (G) temporal profile with a zoom in the limited by reaction profile also at 276 K and 70.9 bar.

The growth phenomenon described by the proposed model can be understood by the behavior of the host molecule, CH_4, mole fraction in the liquid phase, Figure 21. We observed that the methane solubilization in water occurs in the first two hours, as seen in the Figure 21 left insertion, and the gas saturates in the liquid phase after this time. It is observed that the solubilization effect occurs more quickly than the growth, which will only start hours after depending on the *DR* factor value and the initial conditions, Table 5. The CH_4 mole fraction profile in the liquid phase is limited by the gas-liquid (G-L) and the liquid-hydrate (L-H) interfaces equilibrium conditions, as seen in the Figure 21 bottom-right insertion. In 276 K and 70.9 bar conditions, methane compositions in the interfaces G-L and L-H in equilibrium are 0.24% and 0.15%, respectively.

Further details on the calculation of the equilibrium compositions are in the Appendix 3. This limitation allowed us to adjust the methane occupation factor in the hydrate phase. Some experimental works in the literature show possible occupancy factors depending on temperature and pressure [213–216]. Within these ranges, we used the maximum occupancy factor for which the methane mole fraction profile in the liquid phase had the greatest possible variation limited by the equilibrium conditions. For the system at 276 K and 70.9 bar, the occupancy factor was 72% given these criteria.

The methane number of moles profile, Figure 21, and water, Figure 21 bottom-right insertion, in the liquid phase allows us to conclude that practically the entire liquid phase converts to a solid phase in these systems. The number of moles of methane starts in practically zero (10^{-5} moles), reaches the maximum solubility of methane in the liquid phase, about 0.04 moles, and at the end of the growth, it returns to practically zero (10^{-6} moles). In contrast, the water came from 16.6 moles (300 mL), a condition of the Englezos et al. [42] experiments, to practically zero ($5\ 10^{-4}$ moles). These values result in similar initial, after the saturation, and final compositions. Note that the water is the limiting factor for the system to reach steady-state because although the gas supply remains, the amount of water is not enough to continue the hydrate structures growth.

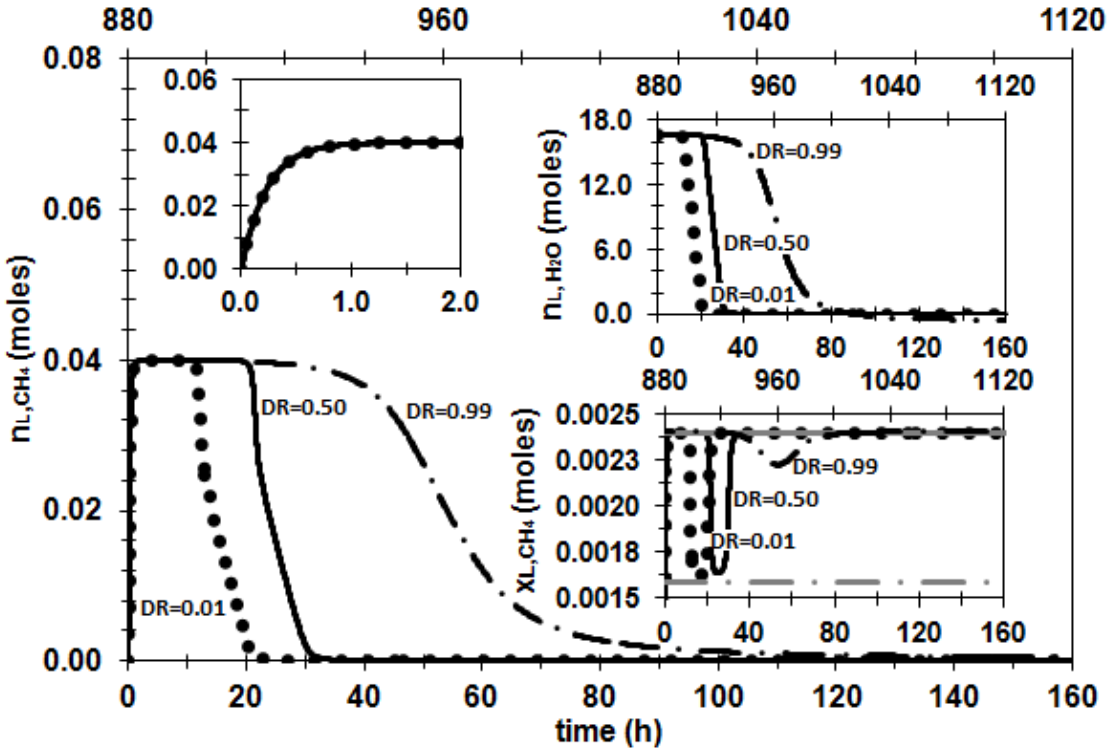

Figure 21 - The methane number of moles in the bulk liquid phase ($n_{L,}CH_4$) temporal profile at 276 K and 70.9 bar. The dotted line describes the limited by diffusion profile (*DR*=0.01), the continue line the diffusion-reaction coupling profile (*DR*=0.5) and the dotted-dashed line, in the 2nd time axis, the limited by reaction profile (*DR*=0.99). The insertion on the left shows the methane in water saturation profile, the one in the bottom-right shows the methane mole fraction ($x_{L,}CH_4$) profile in the bulk liquid phase (dark lines), in the gas-liquid equilibria interface (gray continus line) and in the liquid-hydrate equilibrium interface (gray dotted-dashed line) and the one in the top right shows the water number of moles in the bulk liquid phase (n_L,H_2O).

The methane molar consumption (Δn_G) from the gas phase during the hydrate growth is the most accessible measurement variable in these experiments [2,15,39,217]. Therefore, the comparison and validation of the proposed model were performed using this variable, as seen in Figure 22, for that we had to normalize the time scale. Comparing the growth data given by Englezos et al. [42] with the model description, we can understand how coupling is the diffusion and reaction. At 276 K, 70.9 bar, and the initial conditions, Table 5, Figure 22 shows that the diffusion and reaction are coupled and better described by a *DR* = 0.5.

The beginning of the growth (up to 0.2 hours in Figure 22) seems to be better adjusted by the limited by diffusion profile; however, because our populational balance does not include a nucleation model yet, this can be the primary nucleation effect, that

is more prevalent at the beginning of the formation [34]. So, to include a nucleation model in the populational balance will allow us to understand better if the beginning of the growth is limited by diffusion or the primary nucleation effect. However, the modeling is already able for this inclusion in future work. We also noted that after the beginning of the formation (0.2 hours), the growth is prevalent, and the experimental data can be adequately described by the growth model only. These results allow us to know that, at a certain point, the nucleation, growth, and agglomeration hydrate phenomena can be studied separated.

The time profiles of all other variables were also calculated during the growth. The molar and volume phase density reproduce an adequate and expected behavior. Moreover, the moments of the population balance were adequate for all the systems studied. The profiles of these other variables and their derivatives are in the Appendix 3.

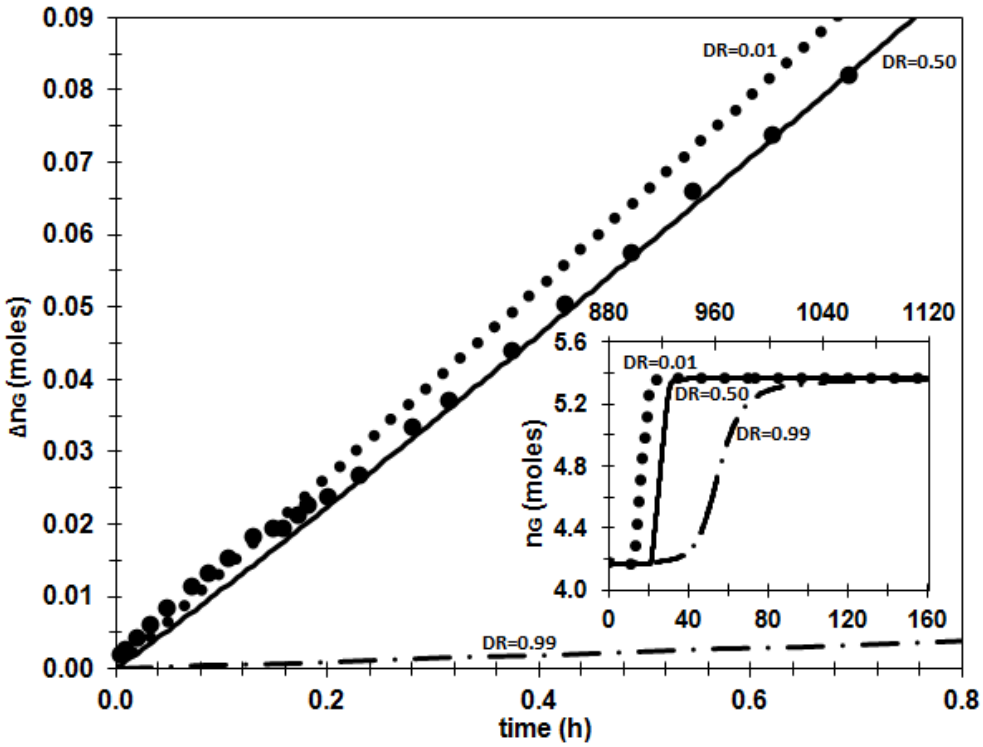

Figure 22 - The methane molar consumption (Δn_G) temporal profile at 276 K and 70.9 bar. The insertion shows the temporal variation of the methane number of moles in the gas phase (n_G). The dotted line describes the limited by diffusion profile (*DR*=0.01), the continue line the diffusion-reaction coupling profile (*DR*=0.5) and the dotted-dashed line, in the 2nd time axis, the limited by reaction profile (*DR*=0.99). The black big circles are the Englezos et al. [42] experimental data at 276 K and 70.9 bar.

Therefore, in a broadway, we can describe and understand what occurs in a hydrate growth experiment for the CH_4 + H_2O system at constant pressure and temperature, given the initial conditions, Table 5. The experiment starts with the gas solubilization in the aqueous phase until it reaches saturation because solubilization occurs faster than growth. After the induction time, growth begins by consuming the gas and water present in the liquid phase. As methane is consumed in the liquid phase, the gas phase replaces this solubilized methane, as the system continues to be pressurized by the addition of methane in the gas phase (constant pressure). This growth occurs until the amount of water present in the liquid phase is no longer sufficient for the hydrate crystalline structure formation, so the system reaches the stationary state if it is given sufficient time. The induction time and the growth rate are related to the level of coupling between diffusion and reaction (*DR*). The hydrate occupancy is likely to be related to the difference between the equilibrium compositions at the G-L and L-H interfaces.

4.3.2 Effect of water activity on driving force

Most of the literature hydrate growth models did not account for the water effect in the growth [33,42–44,84–87,95,96], mainly because hydrate formation systems without additives reproduce an ideal liquid phase because the guest molecule is usually a gas with low solubility in water, such as CH_4. However, this is an approximation, and for systems with additives, it does not reproduce the reality, i.e., it is not possible to extend the model for an inhibited or promoted hydrate system. Therefore, to better understand this effect, we use the Prigogine Affinity that allows the non-ideal effect for the guest, CH_4, and the water in the liquid phase. With this approach, we can include the non-ideal effect of all the hydrate formation compounds, given by the thermodynamic modeling, in the kinect behavior.

Figure 23 shows the comparison for the model proposed included the water activity in the driving force, continuous line, or without it (only with the methane activity) in the driving force, dashed line. As expected, the equilibrium conditions do not change; however, the driving force with water activity shifts the beginning of the growth about 2 hours after.

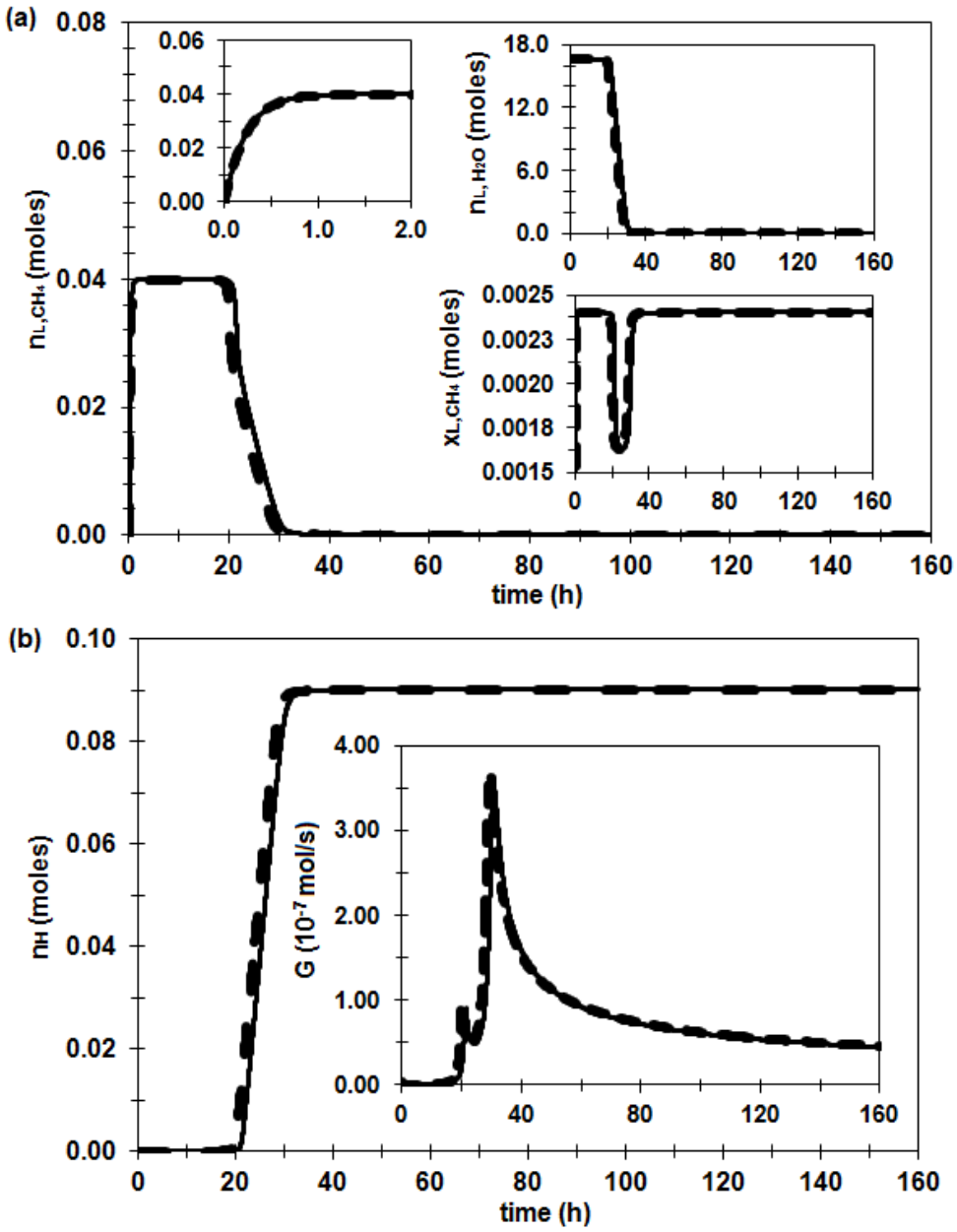

Figure 23 - (a) The diffusion-reaction coupling temporal profile (*DR*=0.5) of the methane number of moles in the bulk liquid phase ($n_{L,}CH_4$) at 276 K and 70.9 bar. The insertion on the left shows the methane in the water saturation profile. In constrast, the insertion in the top right shows the water number of moles in the bulk liquid phase ($n_{L,}H_2O$) and the insertion in the bottom right shows the methane mole fraction ($x_{L,}CH_4$) profile in the bulk liquid phase (dark lines), in the gas-liquid equilibria interface (gray continuous line) and the liquid-hydrate equilibria interface (gray dotted-dashed line). (b) The hydrate number of moles (n_H) temporal profile. The insertion shows the hydrate growth rate (G) temporal profile. The continuous line represents the profile with the water activity, while the dashed line represents the profile without the water activity in the growth rate driving force.

To better understand why the addition of the water activity in the driving force for a $CH_4 + H_2O$ hydrate formation system changed the beginning of the growth in 2 hours, we look at the K_b and the K_{eq} variables the product of the compound activities weighted by the stoichiometric coefficient.

Figure 24 compares K_b and K_{eq} variables using the water activity, continuous line, or not, dashed line. Since the equilibrium condition for the $CH_4 + H_2O$ system does not change with the growth, the K_{eq} is constant with the growth and still basically the same with the water activity or not. It is expected because, for the equilibrium condition in water and gas systems, the literature modeling has considering the water an ideal liquid phase because of the low solubility and describes adequate the equilibria using this assumption. In the K_b profile the beginning of the growth is shifting in 2 hours after. It occurs because, without the water activity in the driving force, $a^{L}_{H_2O} = 1.0$ is imposed in the calculation. While, with the water activity in the driving force, the thermodynamic modeling is used to calculate the water activity, that is equal to 0.999. This difference is the reason for the growth begging delay in 2 hours.

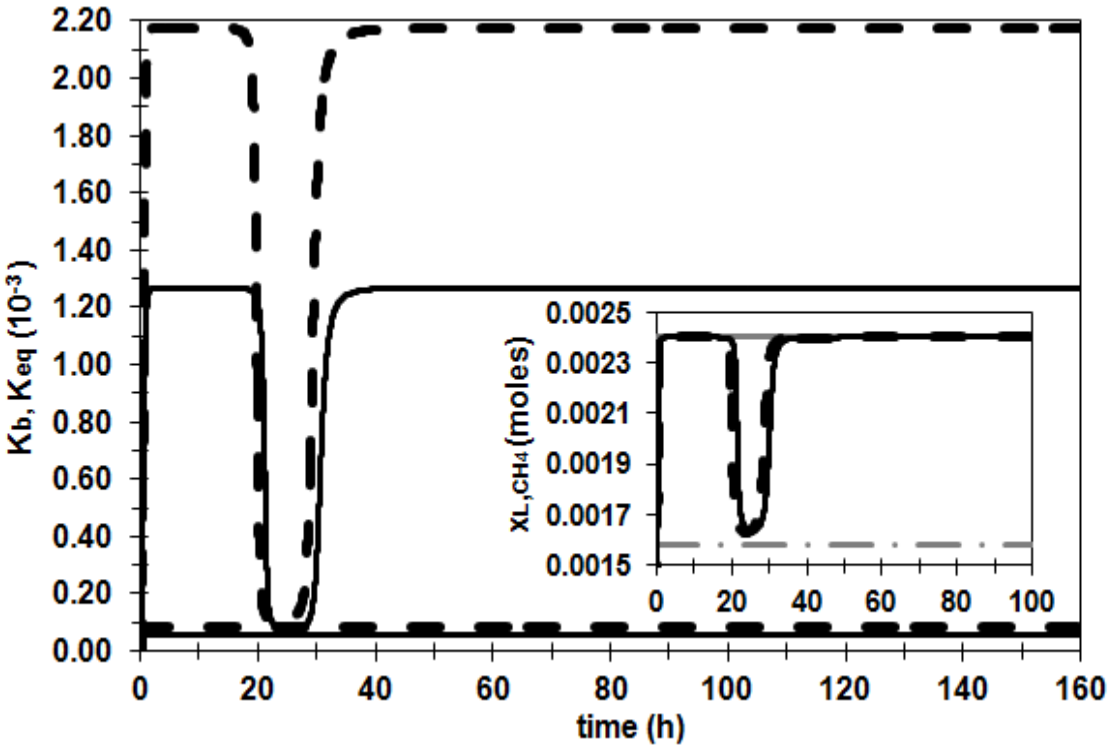

Figure 24 - (a) The diffusion-reaction coupling temporal profile (*DR*=0.5) of the product reagents' activities weighted by their stoichiometric coefficients in the bulk phase variable (K_b) and in the liquid-hydrate equilibrium interface variable (K_{eq}) at 276 K and 70.9 bar. The variable in the bulk liquid phase (K_b) are the ones with the the highest value, while the variable in the

liquid-hydrate equilibrium (K_{eq}) are the ones constant. The insertion on the right shows the methane mole fraction ($x_{L,CH4}$) profile in the bulk liquid phase (dark line), in the gas-liquid equilibria interface (gray line), and the liquid-hydrate equilibria interface (gray dotted-dashed line). The continuous line represents the profile with the water activity, while the dashed line represents the profile without the water activity in the growth rate driving force.

We can understand looking for that result that the assumption of the water as an ideal phase in systems without additives is acceptable. However, we know that for systems with addictive in water, as salts, hydrate inhibitors, or promoters, the growth behavior could change, since the little change between the assumption of ideal liquid phase or allows the modeling to calculate this proximity with an ideal liquid phase already delayed the growth in 2 hours. Another interesting observation is that for this system in proximity to the ideality, the K behavior is the same behavior of the CH_4 liquid mole fraction, as shown in the insertion in Figure 24. This justifies the use of the CH_4 liquid mole fraction as a reasonable driving force for systems without additives, as we can see being used in the literature [15,84,85,93,218].

4.3.3 Pressure effect

Because with the proposed model, we can evaluate how coupled is the diffusion and reaction through the *DR* factor, we analyze the pressure and temperature effect in the *DR* factor and the growth rate.

Figure 25 shows the methane temporal consumption (molar) for *DR* factor that best adjusted both data sets (276 K) at 70.9 bar, dark gray, and 48.6 bar, black. Both systems are at the same temperature so that we can infer the pressure effect with this result. At the higher pressure, the model showed the best adjust for *DR* = 0.5, while for the lower pressure, the best adjust is for *DR* = 0.1. The conclusion is that for lower pressures, the system presents a behavior closer to the limited by diffusion behavior, i.e., methane diffusion from the bulk liquid phase to the liquid-hydrate interface is the slow growth stage. This behavior is justified because of the lower the pressure, the lower the mobility of this gas, CH_4, in the liquid phase, since it has low water solubility. The equation of the diffusion coefficient, L_D, described in the topic 2.2, does not depend on the pressure, so this effect is given only by the growth rate. As shown in Figure 25, if higher the pressure, higher the growth curve inclination.

It is also interesting to note that for the system at a lower pressure (48.6 bar), the nucleation effect, which is not accounted in this modeling, appears to be more prevalent over the growth. At the beginning of the black data, Figure 25, there is a curvature that cannot be reproduced by the diffusion-limited profile, just as the dark gray data appeared to be correlated as shown in Figure 22. We can also conclude that the lower the pressure, the more prevalent the primary nucleation effect at the beginning of the growth is, that it is less accurate to separately describe these two phenomena.

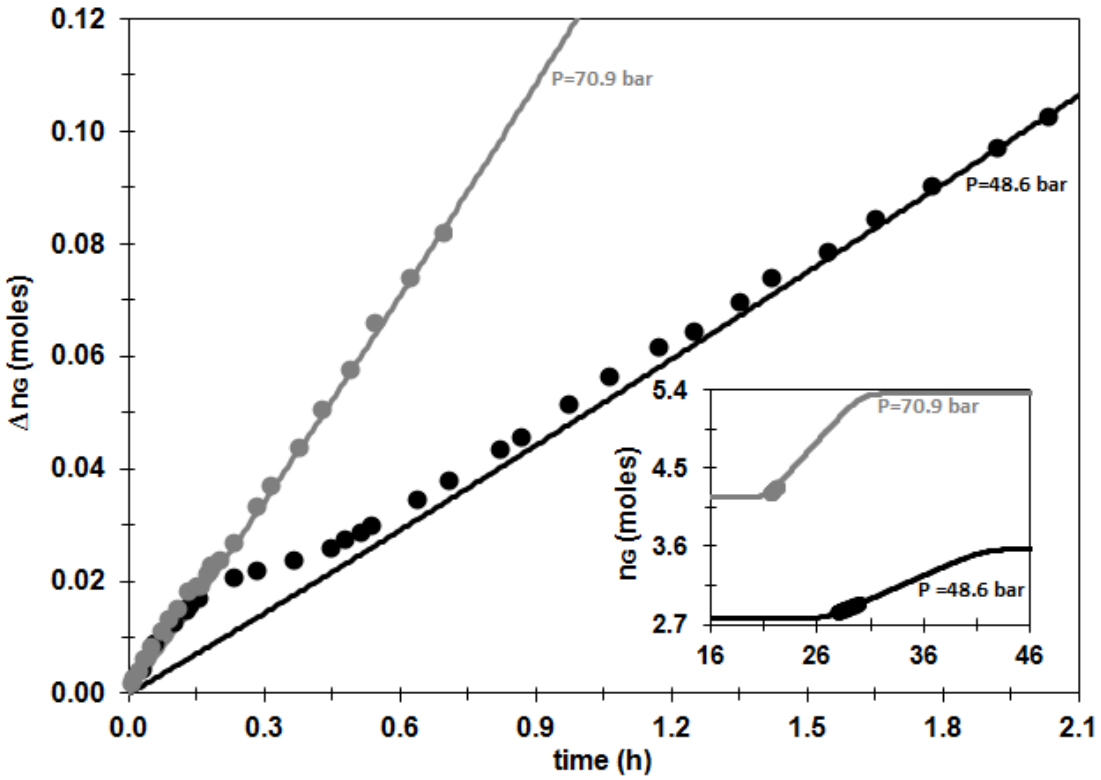

Figure 25 - The diffusion-reaction coupling temporal profile of the methane molar consumption (Δn_G). The insertion shows the temporal variation of the methane number of moles in the gas phase (n_G). The dark gray line is the calculated profile (*DR* = 0.5), and the dark gray circles are the Englezos et al. [42] data at 276 K and 70.9 bar. The black line is the calculated profile (*DR* = 0.1), and the black circles are the Englezos et al. [42] data at 276 K and 48.6 bar.

It is crucial to mention that only the hydrate occupancy factor was changed to model those data besides pressure and the *DR* factor. Almost all the Englezoss et al. [42] data had the same initial conditions. However, if we change the pressure or temperature, we will change the equilibrium conditions. Therefore, keeping the same criteria for all the data sets, we defined the maximum occupancy factor for which the methane mole

fraction in the bulk liquid phase uses the entire delta between the composition interfaces. For 48.6 bar and 276 K it was 56%.

We can conclude that if we increase the pressure, we accelerated the hydrate growth, changing the growth rate inclination and reducing the time to start the growth, as seen in Figure 25 insertion. Then, less limited by diffusion is the growth, i.e., more coupled are diffusion and reaction, and more separated can be modeled the nucleation and growth phenomena.

4.3.4 Temperature effect

In the same way that we evaluated the effect of pressure, we evaluated the effect of temperature on the *DR* factor and the possibility of modeling the nucleation and growth phenomena separately. Among the data obtained by Englezos et al. (1987) [42] we did not find data at the same pressure, so we compared two data sets at close pressures (70.9 and 76 bar) and different temperatures (276 K and 274 K).

Figure 26 shows the temporal profile of the methane molar consumption for 276 K (70.9 bar), dark gray, and 274 K (76.0 bar), light gray. Considering that the increase in the pressure increases the *DR* factor and accelerates the beginning of the growth, we can say that the decrease of the temperature only slows down the beginning of the growth. It slightly effects the *DR* factor or compensates part of the increase by the pressure, as it changes little with the variation in the temperature. The *DR* factor adjusted to get the best correlation between the experimental data and the model for the lower temperature set is the same as the high-temperature data, *DR* =0.6, because the increase of the pressure compensates the reduction of the temperature.

The decrease of the temperature slows down the growth beginning, and the same logic can understand that the increase in pressure accelerates the growth beginning, as seen in Figure 26 insertion. With the increase in the pressure, the arrival of methane molecules at the liquid-hydrate interface accelerates. The reduction in temperature makes it difficult for methane to reach the interface where the reaction occurs.

However, since the hydrate formation condition is favorable, the higher the hydrate growth rate inclination, i.e., the faster this particle growth. The equation of the diffusion coefficient, L_D, described in the topic 2.2, depends on the temperature, but when the *DR* factor is adjusted, the system will automatically calculate a new value of

the reaction constant, L_{rr}, for which its relation with this new L_D follows the same proportion.

At the beginning of the growth, the data set at 274 K and 76.0 bar also reproduce the same behavior as the other sets showing some curvature, Figure 26. For this case, data can be described by the limited by diffusion as the data set at 276 and 70.6 bar, Figure 22. The limiting by diffusion profile for the system at 274 K and 76.0 bar is in the Appendix 3. So, we can say that the temperature does not affect the possibility of modeling the growth separately from the nucleation; however, we know that future improvement, as the addition of a nucleation model in the DAE system proposed in this work, could improve the adjustment of this growth beginning.

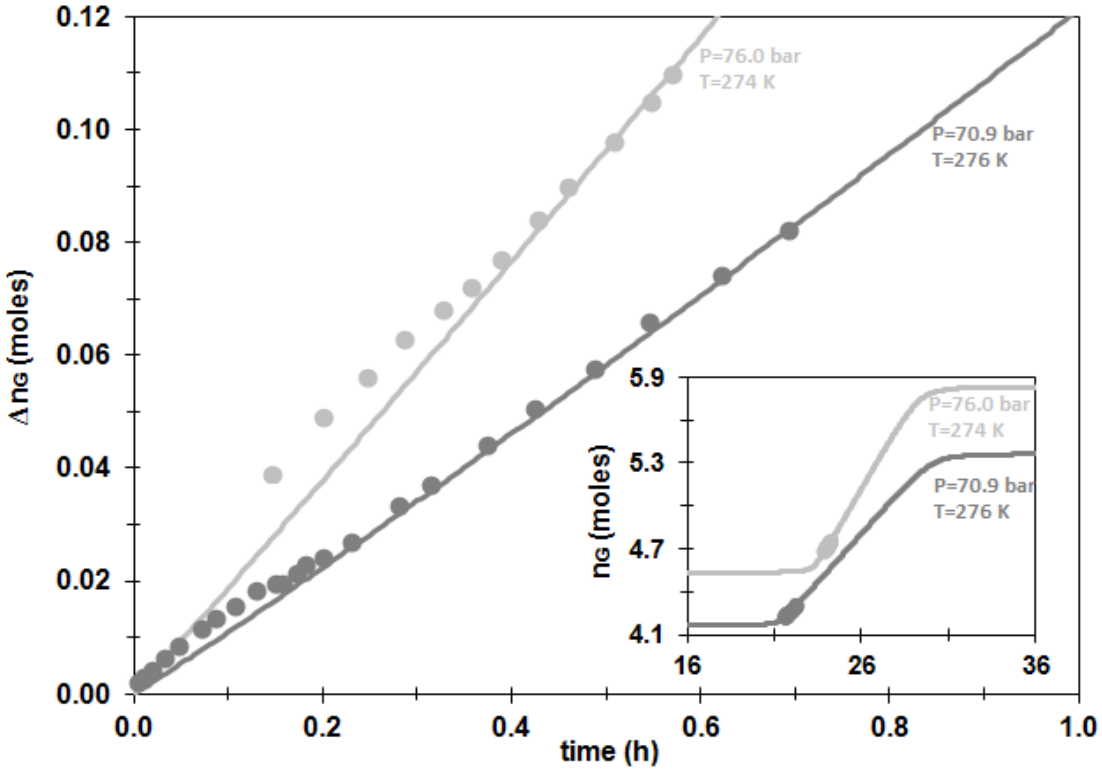

Figure 26 - The diffusion-reaction coupling temporal profile of the methane molar consumption (Δn_G). The insertion shows the temporal variation of the methane number of moles in the gas phase (n_G). The dark gray line is the calculated profile (*DR* = 0.5), and the dark gray circles are the Englezos et al. [42] data at 276 K and 70.9 bar. The light gray line is the calculated profile (*DR* = 0.6), and the light gray circles are the Englezos et al. [42] data at 274 K and 76.0 bar.

To keep the same criteria, we defined the maximum occupancy factor as 68% for 76.0 bar and 274 K, for which the methane mole fraction in the bulk liquid phase used the entire delta between the composition of the G-L and L-H interfaces. Note that is

higher than in the system at 276 K and 48.6 bar, but lower than in the system at 276 K and 70.9 bar. It occurs because, even if the decrease in the temperature and increase in the pressure facilitated the hydrate formation, the reduction in the temperature and pressure also decrease the methane solubility in the liquid phase, so even more favorable the 76.0 bar and 274 K system will contain a hydrate with less methane in the structure than the system with 276 K and 70.9 bar.

We can conclude that the effect of temperature on the *DR* factor and the separation of the nucleation and growth to model the formation is of little significance than the pressure effect. Temperature basically only increases the start of the growth time, since the temperature reduction slows down the molecules' movement.

4.4 Partial conclusions

The model proposed in this work allows the evaluating the coupling between the diffusion and reaction phenomena in the hydrate growth. The definition of a coupling factor, *DR*, makes it unnecessary to estimate a constant reaction for each system as in most growth models in the literature [33,42–44,84–87,95,96]. The *DR* factor has a scale of 0.0 to 1.0 and can represent both conditions of limiting diffusion or limiting reaction and the coupling between them using a single growth rate. Therefore, to adequately describe different sets of experimental data, it is only necessary to adjust the *DR* factor that best represents the data. We also note that this *DR* factor is mainly related to the system pressure. The higher the system pressure, the lower the limiting diffusion effect, and the more coupled is the diffusion and reaction. In contrast, the temperature has little influence on *DR* factor. Besides, the pressure and temperature influence the time for the beginning of the growth.

Another significant contribution here is in the terms of the driving force. It was shown that for systems without chemical additives, with a liquid phase close to ideality, there are driving forces in the literature that account for the host molecule effect, such as CH_4. However, these models cannot provide satisfactory results for non-ideal systems and additive effects.

The proposed model can adequately model experimental hydrate formation data, measuring methane consumption in the vapor phase at constant temperature and pressure. Besides, the inclusion of the thermodynamic factor in the driving force and thermodynamic modeling, which is already more consolidated than the dynamics in the

literature, allows us to understand how to describe more complete systems. Here, we provide a growth model capable of describing simple systems (gas and water) at low pressures, limited by diffusion, and more complex systems (gas, water, and chemical additive) at high pressures, with diffusion and reaction coupled.

List of symbols

T - Temperature [K]

P - Pressure [bar]

R - Universal gas constant [J mol / K]

ξ - Stoichiometric coefficient for CH_4

τ - Stoichiometric coefficient for H_2O

H - Hydrate

t - Time [h]

G_b - Free Gibbs energy [J / mol]

ε - Extent of reaction [mol]

ν - Stoichiometric coefficient

μ - Chemical potencial [J / mol]

A - Affinity

α - Activity

ρ - Density [mol / m³]

c - concentration [mol / m³]

M - Molar mass [g / mol]

S - Entropy [J / K]

σ^s - Entropy generation [J / K s]

J_r - Reaction flow [mol / m² s]

G - Growth rate [mol/ s]

A_{sup} - Surface area [m²]

δ - Liquid film thickness [m]

N_c - Number of compounds

L_{rr} - Reaction coefficient [mol^2 K / m^2 J s]

L'_i - Diffusion coefficient for the component *i* [m^2 / s]

L_D- Diffusion coefficient [mol / m s]

K - Activity product weighted by Stoichiometric coefficient

n - Number of moles [mol]

V - Volume [m^3]

x - Mole fraction

μ'_i - Moment of order *i* [m^i / m^3]

DR - Coupling factor

υ - Dynamic viscosity [mol / m s]

$_{eq}$ - Equilibrium condition

$_b$ - Bulk condition

^{L} - Liquid phase

^{G} - Gas phase

^{H} - Hydrate phase

^{0}- Reference

Chapter 5. Hydrate growth in an inhibited system

Gas hydrates can lead to blockages in natural gas offshore production. Among the conventional methods for hydrates inhibition, there is the prevention of blockage occurrence through thermodynamic hydrate inhibitors (THI). Although there are consolidated operating procedures to avoid these blockages, its limitations are well-known. As ethanol is abundant in Brazil and works as a THI, its use is becoming more common. Besides the thermodynamic effect, it is experimentally known that the hydrate inhibitor species alter the hydrate formation dynamics. Therefore, it is necessary to understand such effects, to enable better usage of those chemicals. Here, we propose a new model to simulate the hydrate growth kinetics with chemical affinity as a driving force. The use of the Prigogine affinity allows the inclusion of the thermodynamic factor in the growth. With this model based on non-equilibrium thermodynamics, we can better understand the role of the THI on the hydrate growth. We evaluated the CH_4 hydrate growth with ethanol as a THI and concluded that the ethanol delays the hydrate growth beginning, acting as a kinetic hydrate inhibitor, and reduces the amount of hydrate formed, acting as a THI. The inclusion of the water activity in the driving force is key to better understanding the kinetic inhibitor effect of ethanol.

5.1 Introduction

Gas hydrates are crystalline structures formed at low temperatures and high pressures, in systems containing water and guest molecules [4]. These guest molecules are usually light gases, mainly natural gas components, such as methane [219]. The hydrophobic effect causes the ordering of water molecules forming structured cavities by hydrogen bonds interaction, and the guest molecules are trapped inside the water hydrogen-bond framework by van der Waals forces [2].

Offshore oil and gas productions present favorable conditions for hydrate formation. In these systems, the formation of hydrates can lead to blockages along the flowline. Conventional methods of hydrate preventions include physical and chemical interventions. Limited physical options are available to prevent gas hydrate formation, and, in most cases, the techniques are neither applicable nor economical [196]. The conventional methods of chemical hydrate inhibition are the addition of thermodynamic (THI) and low-dosage (LDHI) hydrate inhibitors [14]. Among the LDHI, there are the kinetic hydrate inhibitors (KHI), that delay the formation of the crystals (increase the hydrate induction time), and the anti-agglomerate (AA), which prevent blockages formation through the formation of a suspension of the solid phase in the liquid phase [1,2,13]. Therefore, it is necessary to understand the thermodynamic effects of hydrate formation in the presence of chemical additives and the kinetic effect of the THIs and LDHIs on hydrate formation to guarantee the efficiency of their use as hydrate blockage prevention methods [15]. We focus on understanding the thermodynamic hydrate inhibitors (THIs) in the hydrate growth in this work.

The chemicals, THIs, are usually organic additives, mainly alcohols and glycols. The presence of inhibitors usually reduces water activity in the aqueous phase, which shifts hydrate phase boundaries without participation in the hydrate crystalline structure [16]. Significant portions of the oil reserves in Brazil are located in deep or ultra-deep waters, in which the oil production occurs at high pressures and low temperatures, suitable conditions for the formation of hydrates. In this scenario, flow assurance actions are crucial production factors, especially for large natural gas production scenarios, such as exploring the pre-salt layer [163]. Therefore, to ensure production is free of hydrates in those scenarios, larger amounts of the thermodynamic inhibitors are required to shift the hydrate equilibrium curve [17].

A thermodynamic hydrate inhibitor's desired properties include miscibility in water, efficient recovery, and stability [164]. Based on these criteria, the most common industrial THIs are methanol (MeOH), ethanol (EtOH), and monoethylene glycol (MEG) [165]. Brazil is one of the largest ethanol producers, so its use is cheaper than methanol or MEG for the Brazilian oil and gas production scenarios. For this reason, the use of ethanol as a THI is increasingly more frequent. However, the literature presents a few modeling hydrate equilibrium studies with ethanol [120] and even fewer dynamic modeling and experimental studies for this system [196,220]. Thus, there is still a lack of information to better understand the hydrate formation in ethanol systems as THI. Mainly because experimental studies of the hydrate growth with ethanol have showed that ethanol can also act as a kinetic hydrate inhibitor, that has not yet been modeled [220].

The review of advances in modeling phase equilibrium with hydrates shows that this development mainly improved details in the van der Waals and Platteeuw model and is consolidated [98]. However, we still need improvements in the hydrate equilibrium calculations, mainly for systems with additives [120]. Many experimental data and proposed models have been reported for gas hydrates equilibrium conditions in the presence of methanol, but for hydrate equilibria in other alcohols, like ethanol, it is limited, especially for highly concentrated solutions [166]. Recently, we studied in the work of Oliveira et al. [207] hydrate systems with ethanol as an inhibitor and we got a set of experimental data in a broad range of ethanol concentration, up to 45 wt%. In the same work, we proposed thermodynamic modeling that shown better accuracy for the equilibrium condition for systems up to 15 wt% of EtOH [124]. The reduction in the performance of the modeling at high ethanol concentrations can be understood because ethanol can be a hydrate co-host trapped in the large cages of the hydrate structure II with methane [8,27,124]. However, some questions still need to be answered for hydrate systems with ethanol at high concentrations. Meanwhile, the dynamic modeling still presents a large gap in the literature, even for low ethanol concentrations [19].

According to Yin et al. [15], who reviewed the gas hydrate growth kinetic models, there is still a gap in the understanding of the gas hydrate growth control mechanism, which is further augmented by the dynamic behavior of multiphase fluids flow, the thermodynamics of the hydrate-forming system, and the compounding interfacial phenomena. In the literature, most of the hydrate growth models are based on the guest

molecule behavior only and cannot describe non-ideal systems [33,42–44,84–87,95,96]. The ones that include water or some additive effect do not account for the interaction between those compounds [80,83,204,205]. Nasir et al. [13], who reviewed conventional and novel additives used to promote or inhibit hydrate formation in different chemical processes, said that we still have challenges and need further development to understand better the promoter/inhibitor hydrate role in the industry. Therefore, there is still a need for a model capable of explaining the non-ideality effects in the hydrate formation "reaction" for systems with additives is still required.

The Prigogine chemical affinity allows the evaluation of all the components involved in the hydrate formation and evaluates the growth accounting for non-ideal effects. The affinity is already used in the literature [88–90]. However, most models that use this property adopted simplifications that result in the number of mols as the driving force, without including the thermodynamic factor [89,90]. In our previous work (Chapter 4), we proposed a model to describe the hydrate growth keeping the activity of the components in the chemical affinity, i.e., including the thermodynamic factor in the driving force in order to describe non-ideal systems.

The objective here is to apply the hydrate growth model based on the non-equilibrium thermodynamics proposed previously to describe CH_4 hydrate growth with EtOH as an inhibitor. We compared the CH_4 hydrate growth system with and without the ethanol addition. Besides, the effect of increasing the concentration of ethanol comparing systems with 5, 10, and 15 wt% of EtOH was also evaluated at different temperatures and pressures. The effect of including the water activity on the growth driving force and not only the guest molecule was studied [15,33,84,85,93].

5.2 Kinetic model

The dynamic model proposed previously (Chapter 4), used proper balances and the reaction rate with the Prigogine chemical affinity driving force that accounts for the non-ideal effect. In addition to the differential-algebraic equations, thermodynamic models were used [124] to calculate the equilibrium conditions and thermodynamic properties (Appendix 4). The simulated hydrate formation systems are based on the experimental apparatus of the work of Englezos et al. [42]. It is a high-pressure reactor with a mechanical stirrer contain methane (CH_4), water (H_2O), and ethanol (EtOH). The gas phase is pure methane.

5.2.1 Growth Model

We assume the hydrate formation in terms of "reaction" [2]. The hydrate formation is described as a reaction in a mixture containing methane, water, and ethanol. Because we are considering that the ethanol does not participate in the hydrate structure, the reaction is shown by equation (38), where H is the symbol that holds for the hydrate phase, with the molar composition ξ of methane and τ of water.

$$\xi CH_4 + \tau H_2O \rightleftharpoons H \rightleftharpoons \xi CH_4 \cdot \tau H_2O \tag{38}$$

The stoichiometric coefficients of each component are defined according to the hydrate structure formed. So, for the single CH_4 hydrate, it is defined according to the structure I [4], because, in the modeled systems, ethanol acts only as a thermodynamic hydrate inhibitor and do not participate in the structure.

Similar hypotheses used to describe the CH_4 hydrate growth phenomenon in freshwater were adopted here (Chapter 4). However, to consider the presence of the additive, some changes in the hypotheses were included:

(h) the liquid phase consists of a water-ethanol mixture with solubilized methane;
(i) the liquid provides only water and methane for the hydrate growth process in the solid-liquid interface, i.e., ethanol is not consumed in the growth process;
(j) the ethanol composition in the liquid phase does not vary spatially, only temporally;
(k) there is no ethanol in the solid phase;
(l) the vapor phase provides methane for the liquid phase;
(m) the amount of water or ethanol present in the vapor phase is neglected;
(n) in the vapor phase, there is no hydrate growth;
(o) the gas-liquid and solid-liquid interfaces are in local equilibrium.

Using the non-equilibrium thermodynamics theory, we clarify some relevant hydrate growth problems rarely investigated in other formalisms, mainly for the non-ideality effect of inhibited hydrate systems. The reaction rate of hydrate growth was developed in our previous work (Chapter 4), coupling reaction, L_{rr}, with diffusion, L_D, equation (39), and allows the inclusion of the non-ideal effect in the growth caused by the addition of ethanol. This model calculated the growth according to the ratio between

the hydrate-reagents conditions in the bulk liquid phase, K_b, and in the equilibrium, K_{eq}, at the crystal surface, without imposing an ideality condition.

$$G = A_{sup} RL_{rr} \ln\left(\left(\frac{K_b}{K_{eq}}\right)^{\frac{L_D}{L_D + RL_{rr}\delta}}\right) \tag{39}$$

The model uses the Prigogine chemical affinity as the driving force, equation (40), where the K_b factor is defined according to the activity of the components in the bulk liquid phase and K_{eq} in the liquid phase in equilibrium with the solid phase.

$$A = RT \ln\left(\frac{K_b}{K_{eq}}\right) = RT \ln\left(\frac{\left(a^L_{CH_4}\right)^{\xi}_b \left(a^L_{H_2O}\right)^{\tau}_b}{\left(a^L_{CH_4}\right)^{\xi}_{eq} \left(a^L_{H_2O}\right)^{\tau}_{eq}}\right) \tag{40}$$

The advantage of using affinity as a driving force is to incorporate water activity in the hydrate growth kinetics automatically. Therefore, this driving force allows us to account for the non-ideality effect throughout each reagent activity coefficient.

The activity in the liquid phase for the methane-water-ethanol system is calculated using the ternary NRTL model. The NRTL parameters for the CH_4 + H_2O + EtOH system were adjusted and validated according to the binary mixtures experimental data (CH_4 + H_2O, H_2O + EtOH and CH_4 + EtOH) and are in the Appendix 4. The equilibrium calculation was performed based on the theory of van der Waals and Platteew [98], following the same approach as in Oliveira et al. [124], but calculating the equilibrium composition for a given T and P, and are also in the Appendix 4.

5.2.2 System modeling

The dynamic modeling uses conservation principles coupled with constitutive equations, which represent kinetic and thermodynamic relationships. The mass balance for each component in each phase, the population balance to obtain properties of the solid phase, and the reaction rate with its driving force were applied to the CH_4 + H_2O + EtOH system (more details in the Appendix 4).

The theoretical modeling of the dynamic system was implemented in FORTRAN language. The system of differential-algebraic equations (DAE's) was integrated through the use of the DASSL routine. Further details on the numerical solution of the dynamic calculation are in our previous work (Chapter 4).

It is essential to know previously, through the equilibrium calculation, if at the chosen condition, when we add ethanol to the system, hydrate will form or not, since the presence of the inhibitor will shift the equilibrium condition [1]. Because of that, we used the model to describe the dynamic of the $CH_4 + H_2O$ + EtOH system at 276 K and 70.9 bar to compare with the model prediction of the Englezos et al. [42] experimental data for $CH_4 + H_2O$ system, that got good accuracy in our previous work (Chapter 4). Since there is no dynamic data available for the system with ethanol in the literature, the coupling effect between the diffusion and reaction (*DR* factor) incorporated in the growth rate was admitted the same as the one that provides the best adjustment with the experimental data for the methane hydrate growth in freshwater (*DR* = 0.5). The pressure increasing and temperature reduction effects are of primary importance for the hydrate formation; consequently, their effects on growth dynamics are also observed here for the same properties, initial conditions of the system's phases, and parameters. The ethanol parameters and the thermodynamic models' parameters for methane and water with ethanol (Appendix 4) were included in the input data and are reported in Table 6.

Table 6 – Additional input data for the calculation of isothermal-isobaric single hydrate (sI) growth of the $CH_4 + H_2O$ + EtOH system.

Input data		
Ethanol (EtOH) Properties		
Molar mass of component [g/mol]		
EtOH	46.069	[210]
Acentric Factor		
EtOH	0.649	[210]
Critical component temperature [K]		
EtOH	513.92	[210]
Critical component pressure [bar]		
EtOH	61.48	[210]
Critical component volume [cm³/mol]		
EtOH	167.00	[210]

Component dynamic viscosity [mol/m s]		
EtOH	$\upsilon_{EtOH} = \frac{10^3}{MM_{EtOH}} \exp\left(-7.37146 + \frac{2770.25}{T + 74.6787}\right)$	Liquid Dynamic Viscosity (Vogel Equation by online Dortmund Data Bank) http://www.ddbst.com/
Component density [kg/m³]		
EtOH	789.0	[210]
Initial Conditions		
Liquid Phase		
Number of moles		
H_2O	16.6	[42]
CH_4	10^{-5}	Minimum amount to start solubilization without numerical issues
EtOH	0.353 (5 wt%), 0.721 (10 wt%) and 1.110 (15 wt%)	Calculated for the initial ethanol mass fraction of 5, 10 and 15 wt%.
Solid Phase		
Relative hydrate fraction (hydrate volume/water volume)	0.0001%	[24,79,87]
Average diameter of hydrate crystals (d) [m]	10^{-6}	[33,42,79]
Volume of a medium-sized particle [m³]	$4\pi/3 \times (d/2)^3$	spherical shape [211]

The surface area of a medium-sized particle [m²]	$4\pi \times (d/2)^3$	spherical shape [211]

We use the same criteria to define the CH_4 hydrate occupancy factor used for the freshwater system, as the maximum occupancy for which the methane mole fraction profile in the liquid phase had the greatest possible variation within the limits given by the gas-liquid and hydrate-liquid interfaces equilibrium condition [213,215,216,221]. We also used the same reactor, and methane diffusion properties from the first work (Chapter 4). The only change in the input data table refers to the ethanol addition in the simulated system, Table 6. The initial ethanol number of moles was calculated to obtain the ethanol initial mass fraction of 5, 10, and 15 wt%. According to a previous study, a maximum of 15 wt% was defined, Oliveira et al. [124], where we compare the accuracy of three different thermodynamic approaches to predict the hydrate equilibrium condition for systems with ethanol. In that paper, we concluded that it is probable that above 15 wt% of ethanol, this alcohol is present in the hydrate structure [8,27,124], and that is why the traditional equilibrium modeling for inhibited hydrate systems does not present good accuracy.

The presence of ethanol was accounted in the liquid phase obeying the hypotheses adopted here that the inhibitor does not participate in the hydrate structure [87]. All properties of the liquid phase and the equilibrium conditions at the gas-liquid and hydrate-hydrate interfaces consider ethanol. Figure 27 shows the block diagram of the system of differential equations explaining the variables that were modified with the inclusion of ethanol in the liquid phase of the system. The generalized Rackett equation [222–226] is used to calculate the liquid volumetric properties. The ternary NRTL equation (Appendix 4) was used to calculate the activity coefficient of water and methane in the growth rate and calculate the equilibrium composition at the interfaces. The ethanol number of moles was kept spatially constant, to allow the interactive calculation of the methane mole fraction and, by balance, to obtain the water mole fraction (Appendix 4). However, the mole fraction of ethanol in the liquid phase varies over time due to water and methane consumption to form the solid phase.

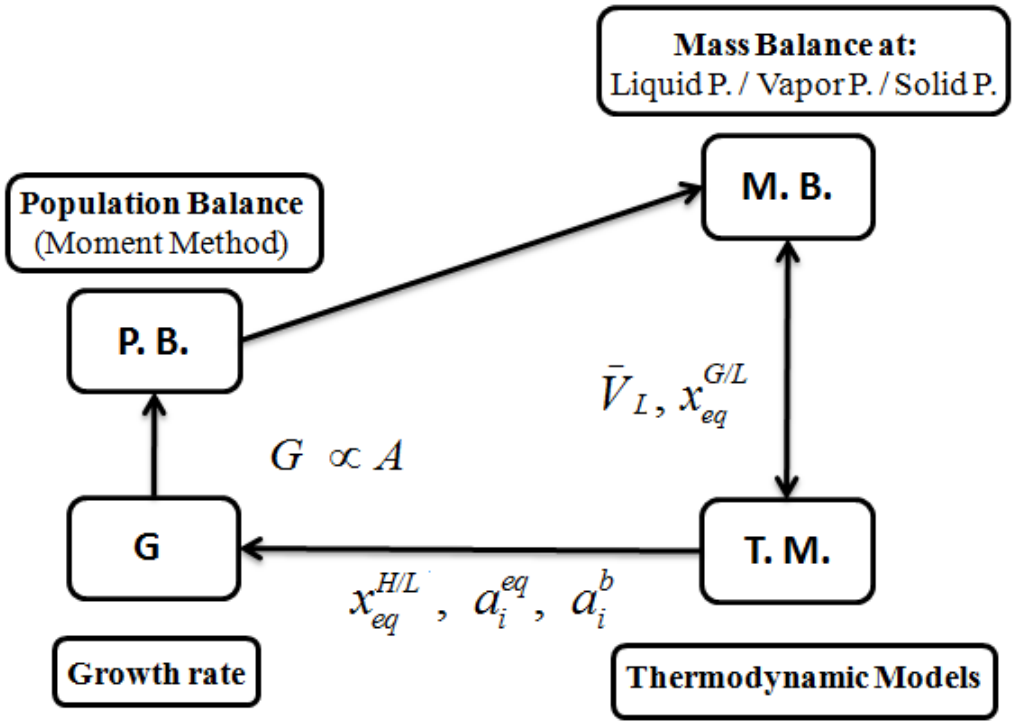

Figure 27 - Block diagram of the algebraic-differential equation system explaining the variables that account for the effect of adding ethanol on hydrate growth. The molar volume of the liquid phase, $\overline{V_L}$, the gas-liquid interface equilibrium, $x_{eq}^{G/L}$, and the hydrate-liquid interface equilibrium, $x_{eq}^{H/L}$; and activity of the hydrate compounents formers at the hydrate-liquid equilibrium, a_i^{eq} and at the bulk, a_i^b. And also, the growth rate, *G*. and its diving force the chemical affinity, *A*.

5.3 Results and discussion

5.3.1 Hydrate growth with a thermodynamic hydrate inhibitor (EtOH)

5.3.1.1 Thermodynamic hydrate inhibitor (EtOH) effect

To study the ethanol influence, we used the 276 K and 70.9 bar system, with the *DR* factor of 0.5, the coupling between diffusion and reaction, and an occupancy factor of 72%. In this system, we compare simulation results for compositions of 0 and 5 wt% of ethanol. Whereas the solid phase formed is in equilibrium and the vapor phase is formed by only pure methane, to understand the ethanol effect on the methane hydrate growth, it is crucial to observe the methane, water, and ethanol time profiles in the liquid phase, Figure 28.

Figure 28 (a), the ethanol addition increases the methane solubilization in the liquid phase in the first 2 hours. The CH_4 composition in the liquid phase changes slightly in the system without ethanol, from 0 wt% to the maximum of 0.214 wt% or 0.04 moles, Figure 28 (a) insertion on the left, as the CH_4 has low solubility in water. In the system with ethanol, the compositions change more along with the growth. The CH_4 composition changes from 0 wt% to a maximum of 0.477 wt% during the first 2 hours, related to the time for solubilization. It occurs because the CH_4 solubility increases with the addition of ethanol. We can also notice that the ethanol addition shifts the beginning of the growth. Moreover, the growth finished when all water and almost all methane are consumed for the system without ethanol as can be observed at 30h, approximately. With ethanol, the growth finished nearly to 25h, before the hydrate reagents are consumed.

Following the methane mass fraction (x_L,CH_4) profile, in Figure 28 (b) right insertion, we can understand why the growth finished before the reagents ended in the system with ethanol. During the growth, the methane mass fraction for the freshwater system (dotted line) in the gas-liquid equilibrium interface and the hydrate-liquid equilibrium interface are kept constant, Figure 28 (b) right insertion, so the growth keeps going until all the water is consumed, Figure 28 (a) right insertion, because the methane feed in the gas phase is maintained to keep the pressure constant. Meanwhile, for ethanol systems (continuous line), the methane mass fraction in the gas-liquid and hydrate-liquid equilibrium interfaces varies during the growth, Figure 28 (b) right insertion. It occurs because, with the water, Figure 28 (a) right insertion, and methane consumption, Figure 28 (a), for the solid-phase formation, the liquid phase becomes more concentrated in ethanol, from 5 wt% to 22 wt% of EtOH, gray line in Figure 28 (b). Then, the bulk liquid phase CH_4 composition is changing until it matches the composition of the hydrate-liquid equilibrium interface, Figure 28 (b) right insertion, changing with the growth. So, the equilibrium condition of the system is achieved before the hydrate reagents formers ended.

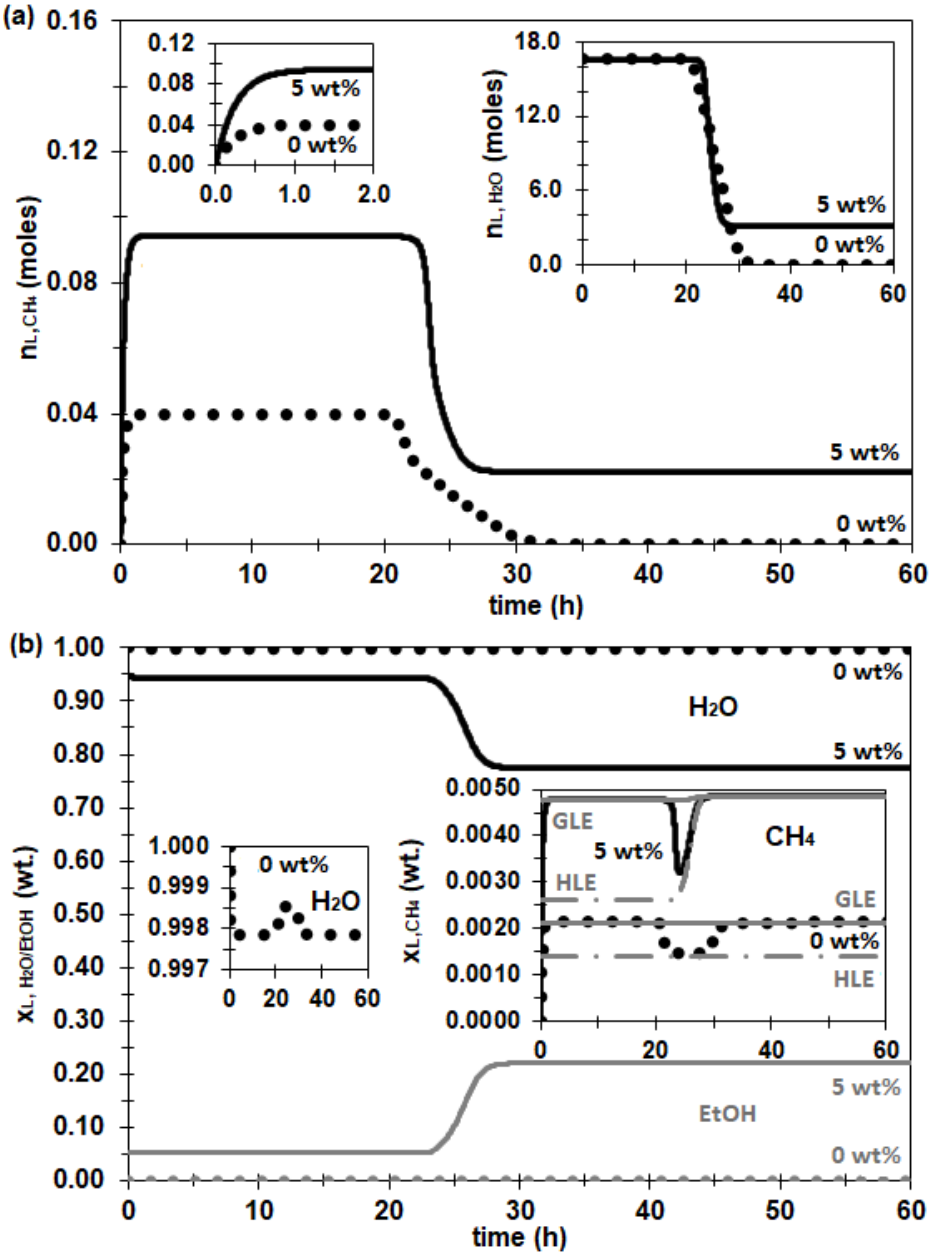

Figure 28 - (a) The number of moles of methane (n_L,CH_4) and (b) the H_2O (x_L,H_2O) and EtOH (x_L,EtOH, in gray) mass fractions in the bulk liquid phase temporal profiles at 276 K and 70.9 bar (*DR* = 0.5). The lines describe the time profiles for the following ethanol compositions of the initial liquid phase: 0 wt% (dotted line) and 5 wt% (continuous line) of EtOH. The insertion (a) in the left shows the methane in water saturation profile and the one in the right shows the number of moles of water (n_L,H_2O) profile in the bulk liquid phase. The insertion (b) in the left is a zoom in the H_2O mass fraction temporal profile for 0 wt% of EtOH, and the one in the right is the methane mass fraction (x_L,CH_4) profile in the bulk liquid phase (continuous black lines), in the gas-liquid equilibrium (GLE) interface (continuous gray line) and in the hydrate-liquid equilibrium (HLE) interface (gray dotted-dashed line).

To understand the non-ideal effect in the hydrate growth, Figure 29 shows the solid properties and the activity coefficient calculated by the NRTL model. Figure 29 (a) shows the hydrate number of moles formed during the growth and, consequently, the hydrate volume increase. The first observation is that the ethanol addition reduces the hydrate amount formed during the growth. Without ethanol (Figure 29 (a) dotted line), 0.09 mole of hydrate is formed, while ethanol 0.07 mole is formed (Figure 29 (a) continuous line), i.e., 0.02 mole less. This is because the addition of ethanol to the system causes, throughout the growth, not only the system conditions to approach the equilibrium, but also the equilibrium to approach the bulk condition, Figure 28 (b) right insertion. The difference between the conditions of equilibrium and bulk reduces, so less hydrate is formed. We can also notice a significant difference in the growth curve inclination, between 20h and 30h, approximately: the systems with ethanol (Figure 29 (a) continuous line) presented higher inclination, which means that the growth occurs faster than without ethanol (Figure 29 (a) dotted line). In conclusion, the growth with ethanol (Figure 29 (a) continuous line) occurs later, beginning at 23h, but faster, finishing at 27h, than without ethanol (Figure 29 (a) dotted line), that begins at 21h and finished at 31h, approximately.

Figure 29 (b) shows the growth rate, G, and parameters K_b and K_{eq} profiles. That profiles show the ethanol systems going to the equilibrium condition, $G = 0$, while the system without ethanol only achieves the steady-state, G = Constant. We can also notice that the displacement of the growth beginning is slight between the systems at 0 and 5 wt% EtOH. The difference is approximately 2 hours. Looking at the growth rate profile without ethanol, we can see two peaks. The first peak occurs at the beginning of the growth (21.2h), and it is probably the reason for the growth to start quicker than one with ethanol. The second peak occurs at 30.6 h, and it is probably the reason for forming more hydrate without ethanol than with it. On the other hand, the growth rate with ethanol presented one small peak at 23.5 h.

The parameters K_b and K_{eq}, equation (40), representing the product the reagents activities weighted by their stoichiometric coefficients, presented different profiles for the system without ethanol (dotted line) and with ethanol (continuous line) each system present different orders of magnitude. More than that, the profile without ethanol (0 wt% of EtOH) is similar to the methane mole fraction profile in Figure 28 (b) right insertion. It occurs because the water activity coefficient is close to the freshwater, Figure 29 (c)

dotted black line. The methane activity coefficient profile, Figure 29 (d) dotted black line, also presented a profile similar to the methane mole fraction, Figure 28 (b) right insertion dotted black line, while the parameters profiles with ethanol (5 wt% of EtOH) are closer to the water activity coefficient profile, Figure 29 (c) continuous black line, up to the beginning of the growth, and similar to the methane activity coefficient profile, Figure 29 (d) continuous black line, when the growth starts to decrease. THI changes the driving force because of the change in the water and the methane activities even for lower ethanol concentration. It is then essential to use thermodynamic and dynamic models capable of accounting for the non-ideal effect in the growth and utilizing all its inhibiting capacity, whether in the equilibrium or the kinetics.

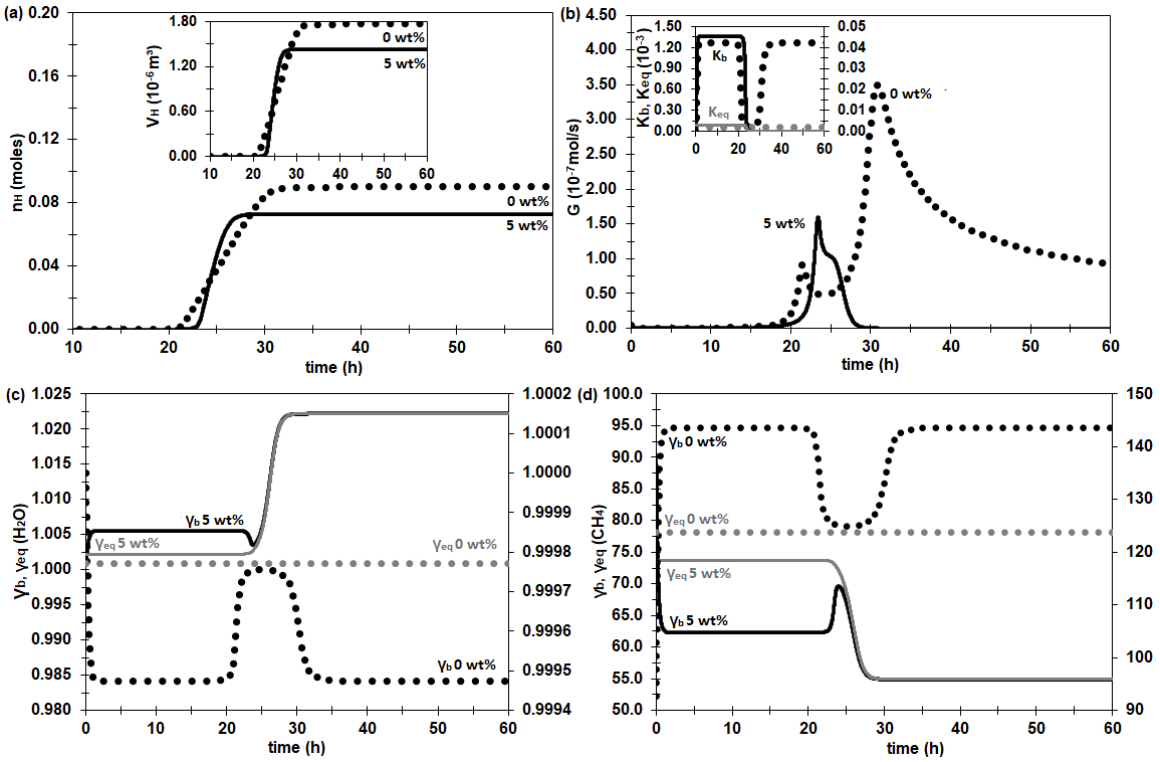

Figure 29 - (a) The number of moles of hydrate (n_H), (b) the hydrate growth rate (G), the activity coefficient (γ) for (c) H_2O and (d) CH_4 temporal profile at 276 K and 70.9 bar (*DR* = 0.5). The lines describe the time profiles for the following ethanol compositions of the initial liquid phase: 0 wt% (dotted line) and 5 wt% (continuous line) of EtOH. The insertion (a) in the right is the hydrate volume temporal profile (V_H). The insertion (b) shows the parameters of the product reagents' activities weighted by their stoichiometric coefficients in the bulk phase (K_b) and in the hydrate-liquid equilibrium interface (K_{eq}) at 0 wt% (1st axis) and 5 wt% (2nd axis). The gray lines represent the variable temporal profiles at the hydrate-liquid equilibrium ($_{eq}$) and the black ones at the bulk conditions ($_b$).

This first evaluation allows us to understand that the THI effect in the hydrate formation changes the equilibrium condition, but it also changes the growth dynamics. More than that, the use of a THI will provide not only a thermodynamic inhibitor effect. It can also act as a kinetic hydrate inhibitor, delaying the start of solid-phase growth, as some experimental studies have shown [220]. This potential needs to be better understood and explored to take advantage of the alcohol inhibiting capacity that has already been used as additives in the oil and gas exploration systems with possible hydrate formation [163].

5.3.1.2 Thermodynamic inhibitor (EtOH) concentration effect

In deep or ultra-deep waters, oil production presents even more favorable conditions for the hydrate formation. In this scenario, flow assurance actions are crucial production factors, especially for large natural gas production scenarios, such as the pre-salt layer [163]. So, to ensure production is free of hydrates in those scenarios, a larger amount of thermodynamic hydrate inhibitor is necessary to shift the hydrate equilibrium curve [17]. An alternative is to use kinetic hydrate inhibitors (KHI). The KHI can delay nucleation and/or reduce the growth rate [1]. Looking to the increases in THI volume used to explore those reserves without hydrate blockages and the alternative that is the use of KHI, we search for the ethanol capacity to act also as a KHI with the increase in its concentration.

Figure 30 shows the methane, water, and ethanol liquid phase behavior with the increase in the initial ethanol concentration. We can notice that the CH_4 composition, Figure 30 (a), changes from 0 wt% to a maximum of 0.477 wt%, 0.478 wt%, and 0.480 wt% (0.094, 0.099, 0.105 moles) for 5, 10, and 15 wt% of EtOH, respectively, in the first 2 hours, that is the solubilization time. For higher ethanol concentration, slightly more methane can be solubilized in the liquid phase. However, the ethanol composition change with the water consumption from 5 wt%, 10 wt% or 15 wt% to 22 wt%, Figure 30 (b) grey line, that is the system equilibrium composition at 276 K and 70.9 bar (0.485 wt% of CH_4 and 22 wt% of EtOH). Since the system conditions are kept the same, the equilibrium condition will also be the same. The higher the initial concentration of ethanol in the system, the faster the system reaches equilibrium because closer to the equilibrium condition the system is, since the beginning. So, methane and water consumption during hydrate growth is lower with the increase in the initial ethanol

concentration. That is, the amount of hydrate formed is going to be also lower. However, the increase in ethanol concentration shifts the beginning of the growth.

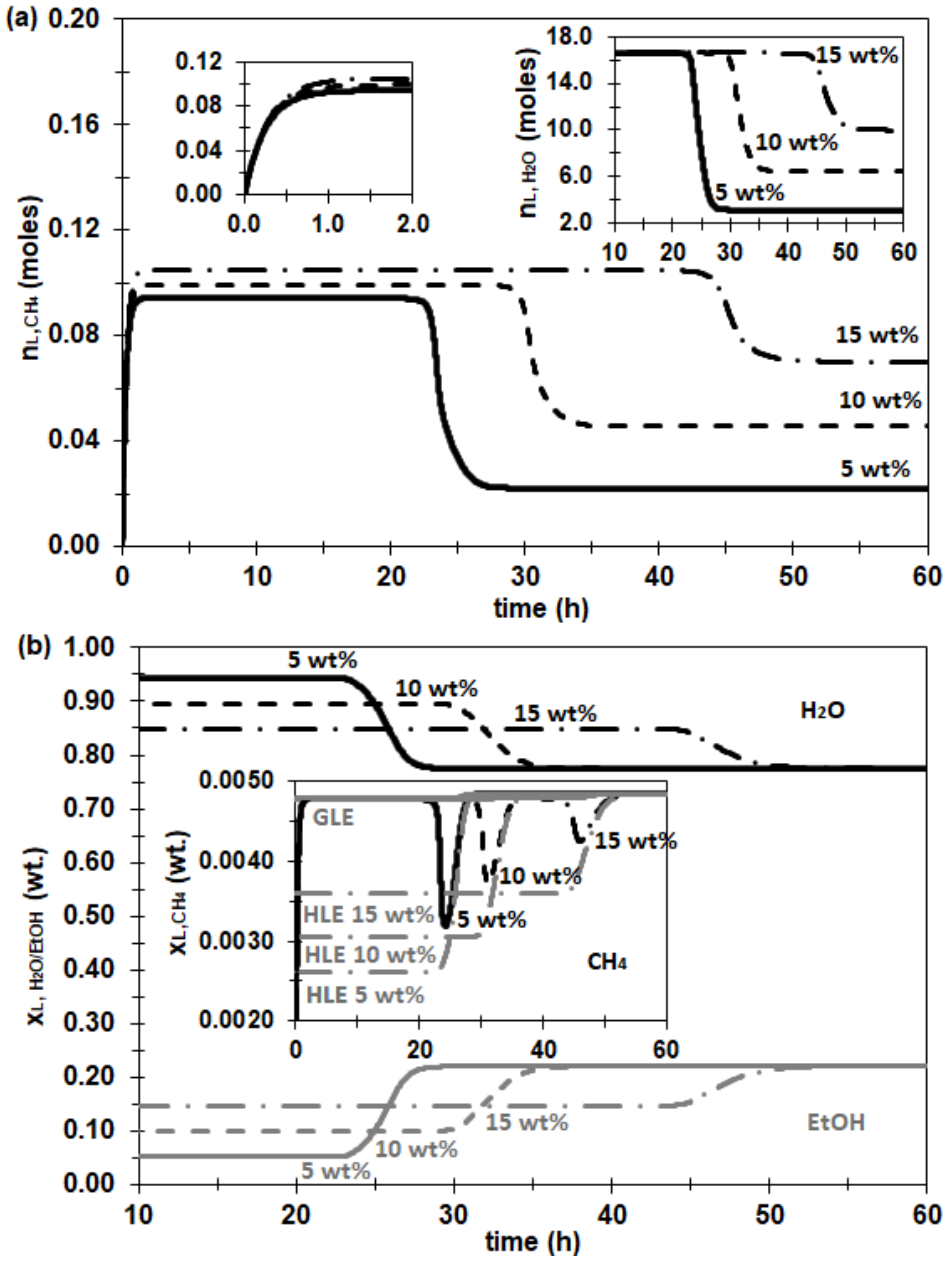

Figure 30 - (a) The number of moles of methane (n_L,CH_4) and (b) the EtOH (x_L,EtOH) and H_2O (x_L,H_2O) mass fractions in the bulk liquid phase temporal profile at 276 K and 70.9 bar (*DR* = 0.5). The lines describe the time profiles for the following ethanol compositions of the initial liquid phase: 5 wt% (continuous line), 10 wt% (dashed line) and 15 wt% (dotted-dashed line) of EtOH. The insertion (a) in the left shows the methane in the water saturation profile, and the one in the right shows the water number of moles (n_L,H_2O) profile in the bulk liquid phase. The insertion (b) in the left is a zoom in the H_2O mass fraction temporal profile for 0 wt% of EtOH, and the one in the right is the methane mass fraction (x_L,CH_4) profile in the bulk

liquid phase (continuous black lines), in the gas-liquid equilibrium (GLE) interface (continuous gray line) and the hydrate-liquid equilibrium (HLE) interface (gray dotted-dashed line).

Figure 31 shows the solid properties and the activity coefficient temporal profiles. The amount of hydrate formed is reduced due to the increase in ethanol concentration, shown in Figure 31 (a). In the mole base, the amount moles of hydrate formed are 0.07, 0.05, and 0.04 for 5, 10, and 15 wt% of EtOH, respectively, Figure 31 (a). It can also be seen in the growth rate behavior, Figure 31 (b), the higher is the initial ethanol concentration, the lower is the peak of growth rate. However, the longer it takes for the growth to begin. The increase in the ethanol concentration increases the growth beginning time in 8 and 22 hours, approximately 10 and 15 wt% of EtOH, comparing the system without ethanol, Figure 31 (b). We can also notice that the higher the concentration of ethanol, the more the time to start growing, and this increase is getting bigger. In other words, the performance of ethanol as a kinetic hydrate inhibitor is enhanced. Parameters K_b and K_{eq} presented similar profiles for all the ethanol initial concentration systems, but they present different orders of magnitude for each system, decreasing ethanol concentration, Figure 31 (b) insertions. The same behavior is observed for the water and methane activity temporal profile, Figure 31 (c), and (d).

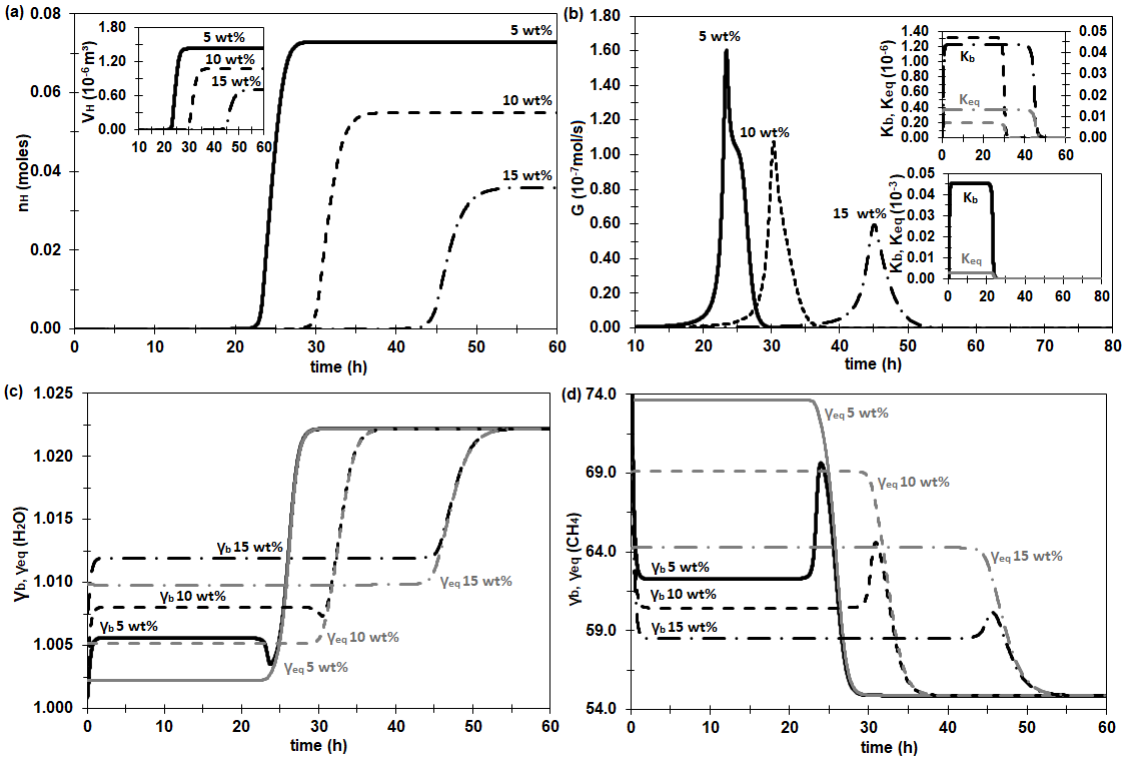

Figure 31 – (a) The number of moles of hydrate (n_H), (b) the hydrate growth rate (G), the activity coefficient (γ) for (c) H_2O and (d) CH_4 temporal profiles at 276 K and 70.9 bar (*DR* = 0.5). The lines describe the time profiles for the following ethanol compositions of the initial liquid phase: 5 wt% (continuous line), 10 wt% (dashed line) and 15 wt% (dotted-dashed line) of EtOH. The insertion (a) in the left is the hydrate volume temporal profile (V_H). The insertion (b) shows the parameters of the product reagents' activities weighted by their stoichiometric coefficients in the bulk phase (K_b) and the hydrate-liquid equilibrium interface (K_{eq}) at 0 wt% for the one in the bottom, and at 10 wt% (1st axis) and 15 wt% (2nd axis) for the one in the top. The gray lines represent the variable temporal profiles at the hydrate-liquid equilibrium ($_{eq}$) and the black ones at the bulk conditions ($_b$).

These results show that the thermodynamic hydrate inhibitor has the potential to behave as a kinetic hydrate inhibitor. Even more, that the increase in the THI concentration potentialize the KHI behavior of that additive and reduces the risk of hydrate blockage by delaying the beginning of the growth and reducing the amount of hydrate formed. A behavior observed previous experimentally [220], but that could not be predicted trough calculations before.

5.3.2 The effect of water activity in the driving force in an inhibited system

Basically, all the hydrate growth models in the literature use a driving force that only accounts for the guest molecule properties and does not account for the water effect directly in the driving force [15]. This occurs because for systems without additives, the water does not affect the growth rate, as we demonstrated in our previous work using the proposed model (Chapter 4), because in this condition, the system is close to the ideality and consequently the water activity is close to one. However, in systems with additives, the inclusion of the water activity in the driving force affects the dynamics because the system is no more ideal. Then here, we evaluate how the increasing in the inhibitor concentration will further distance the system from the ideality.

5.3.2.1 Thermodynamic hydrate inhibitor (EtOH) effect

First, to understand the effect of adding the water activity in the driving force in the system with ethanol, we compare systems with (black) and without (yellow) water activity for the ethanol concentration of 0 wt% (dotted) and 5 wt% (continuous).

Figure 32 shows the same qualitative behavior of the system, in the liquid phase, and the equilibrium conditions, with (black) and without (yellow) the water activity in the driving force. However, the temporal behavior of the methane number of moles in the liquid phase presents a displacement of 1.7 hours less in the system without ethanol, difference between the curves of the methane consumption in the black and yellow dotted lines, Figure 32 (a) from 21h to 31h, approximately, and 1.3 hours more in the system with ethanol, difference between the curves of the methane consumption in the black and yellow continuous lines, Figure 32 (a) from 22h to 30h, approximately. The growth occurs before but slower in the system without ethanol than with ethanol. Therefore, the inclusion of the water activity in the driving force changes the kinetic rate, showing the effect of the THI in the kinetic.

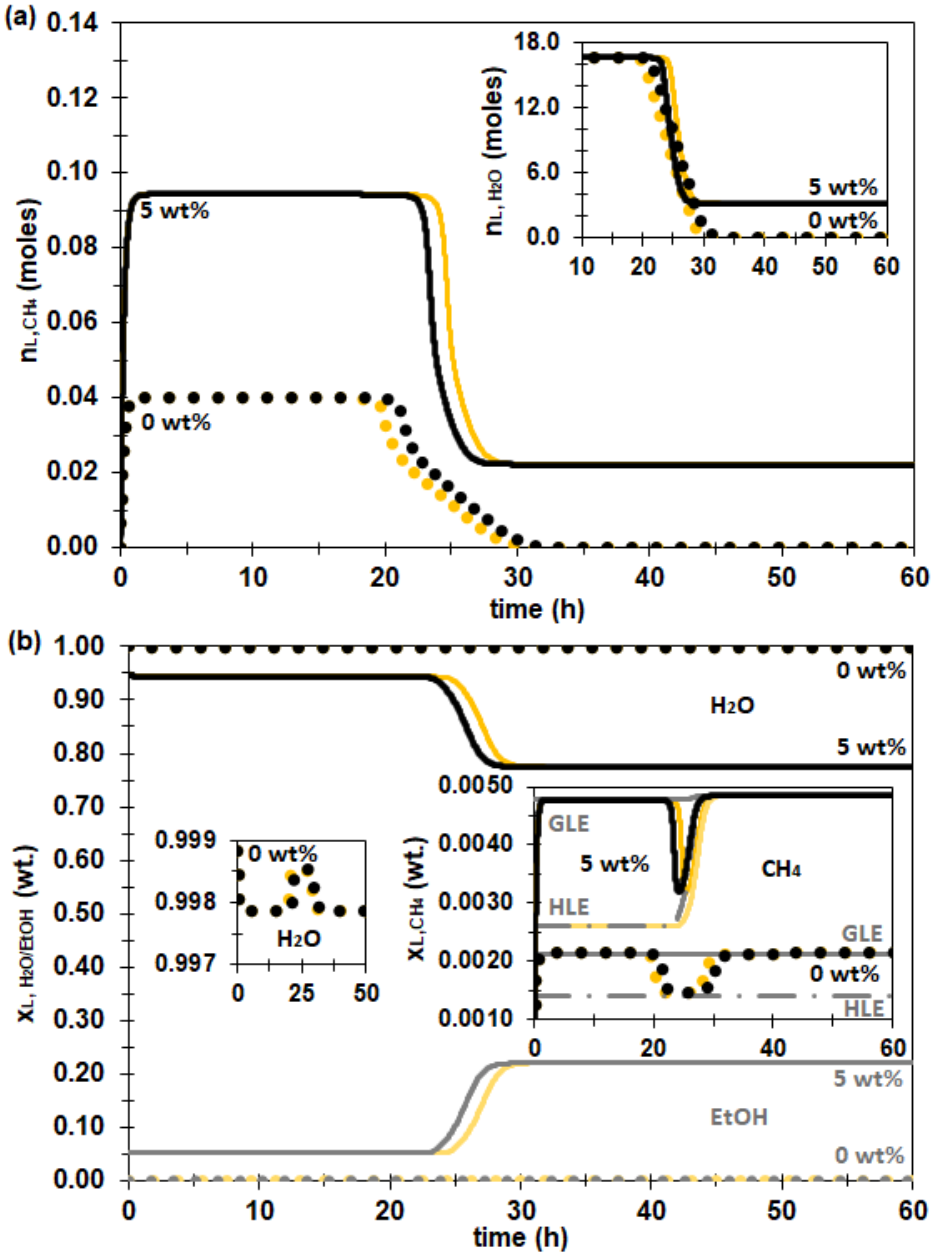

Figure 32 - (a) The number of moles of methane (n_L,CH_4) and (b) the H_2O (x_L,H_2O) and EtOH (x_L,EtOH in gray and light yellow) mass fractions in the bulk liquid phase temporal profiles at 276 K and 70.9 bar (*DR* = 0.5). The lines describe the time profiles for the following ethanol compositions of the initial liquid phase: 0 wt% (dotted line) and 5 wt% (continuous line) of EtOH, with (black or gray) and without (yellow or light yellow) water activity in the driving force. The insertion (a) in the right shows the number of moles of water (n_L,H_2O) profile in the bulk liquid phase. The insertion (b) in the left is a zoom in the H_2O mass fraction temporal profile for 0 wt% of EtOH, and the one in the right is the methane mass fraction (x_L,CH_4) profile in the bulk liquid phase (black or yellow continuous lines), in the gas-liquid equilibrium (GLE)

interface (gray or light yellow continuous lines) and in the hydrate-liquid equilibrium (HLE) interface (gray or light yellow dotted-dashed lines).

To better understand why the addition of the water activity in the growth driving force presented an opposite temporal behavior without (dotted lines) and with ethanol (continuous lines), Figure 33 shows the solid phase properties, like the growth rate. The hydrate number of moles formed is kept the same, which means that the inclusion or not of the water activity does not affect the equilibrium condition, as expected, Figure 33 (a). However, the systems presented the same temporal displacement that was shown before. It is possible to understand why this displacement occurs, looking to the parameters of the product reagents' activities weighted by their stoichiometric coefficients in the bulk phase (K_b) and the hydrate-liquid equilibrium interface (K_{eq}), equation (40), Figure 33 (b) insertion. In Figure 33 (b), we can see that the growth rate moves in time, and it happened mainly due to the behavior of parameters K_b and K_{eq}. As we have seen before, without the water activity in the driving force these parameters reproduce the temporal behavior of the methane composition in the bulk liquid phase, Figure 33 (a) right insertion. In contrast, with the water activity in the driving force, these parameters present a temporal behavior similar to activity coefficients, Figure 33 (c), and (d).

However, if we look at the activity coefficient of water in Figure 33 (c) and (d), we can see that the addition of ethanol in the liquid phase changes the water activity coefficient. For the system without ethanol, dotted lines, the water activity coefficient changes over time for values smaller than one. However, for systems with ethanol, continuous lines, the water activity coefficient changes over time (slightly for 5 wt% of ethanol), but values higher than 1.0 are observed. The increase in the water activity coefficient due to the ethanol addition in the system is why the growth rate to start decreases, Figure 33 (b). So, it is the non-ideal effect of the system that changes the beginning of the growth. Moreover, the non-ideal effect of the system is critical to understand ethanol as a kinetic inhibitor.

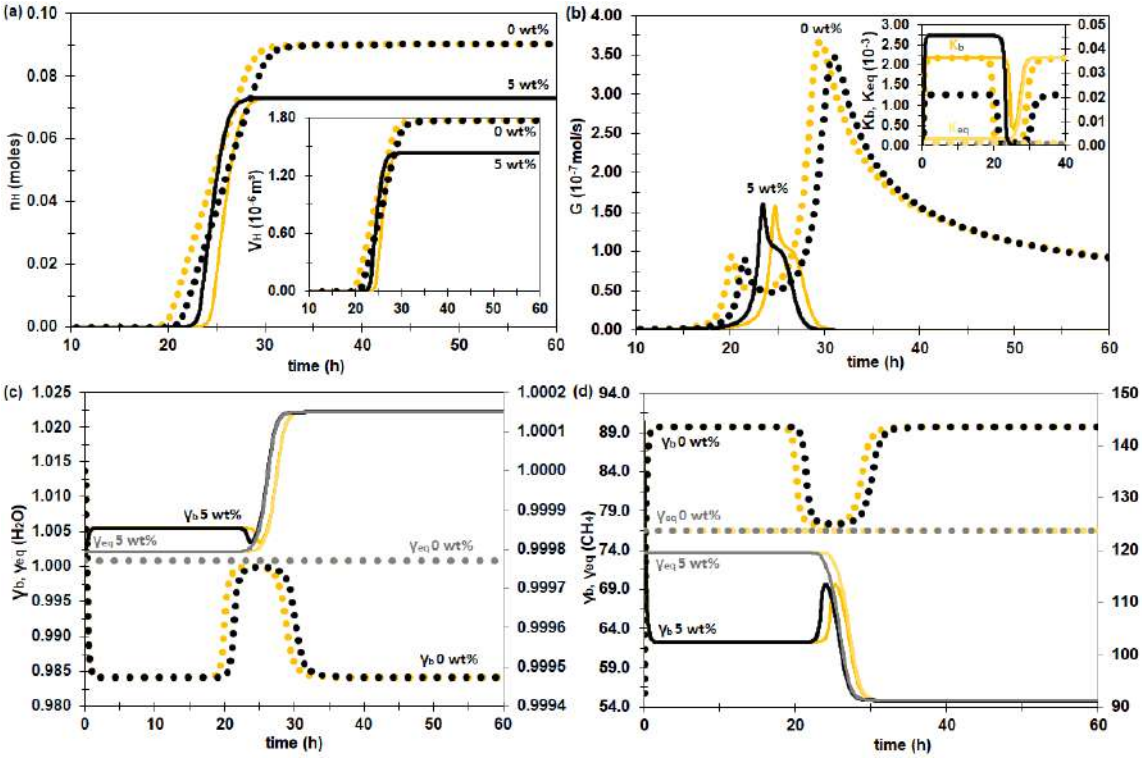

Figure 33 - (a) The number of moles of hydrate (n_H), (b) the hydrate growth rate (G), the activity coefficient (γ) for (c) H_2O and (d) CH_4 temporal profiles at 276 K and 70.9 bar (*DR* = 0.5). The lines describe the time profiles for the following ethanol compositions of the initial liquid phase: 0 wt% (dotted line) and 5 wt% (continuous line) of EtOH, with (black) and without (yellow) water activity in the driving force. The insertion (a) in the right is the hydrate volume temporal profile (V_H). The insertion (b) shows the parameters of the product reagents' activities weighted by their stoichiometric coefficients in the bulk phase (K_b) and in the hydrate-liquid equilibrium interface (K_{eq}) at 0 wt% (1st axis) and 5 wt% (2nd axis). The gray and light yellow lines represent the variable temporal profiles at the hydrate-liquid equilibrium ($_{eq}$) and the black and yellow ones at the bulk conditions ($_b$).

The inclusion of the non-ideal effect in the driving force through the water activity coefficient is the main factor in using the kinetic hydrate inhibitor potential of the thermodynamic hydrate inhibitors.

5.3.2.2 Thermodynamic inhibitor (EtOH) concentration effect

Before that, we concluded that the ethanol kinetic inhibitor effect increases with the increase in the initial ethanol concentration. Moreover, the addition of the water activity in the driving force decreases the time to start the growth. To better understand

the contribution of water activity, we compare systems with 5, 10, and 15 wt% of EtOH with and without the water activity in the driving force.

Figure 34 shows the properties of the components in the liquid phase behavior with (black) and without (yellow) water activity in the driving force. It is shown that the addition of water activity reduces the kinetic inhibitor behavior of ethanol. The equilibrium conditions for all component's concentrations are kept the same, Figure 34 (b); however, the time to start the growth changes for less 1.3 h, 2.1 h, and 3.8 h for 5, 10, and 15 wt%, respectively, Figure 34 (a). So, the increase in ethanol concentration increases the displacement caused by adding water activity to the driving force. As the ethanol concentration increases, the addition of the water activity in the driving force became even more relevant because it reduces the kinetic inhibitor effect that the ethanol can have in the hydrate growth.

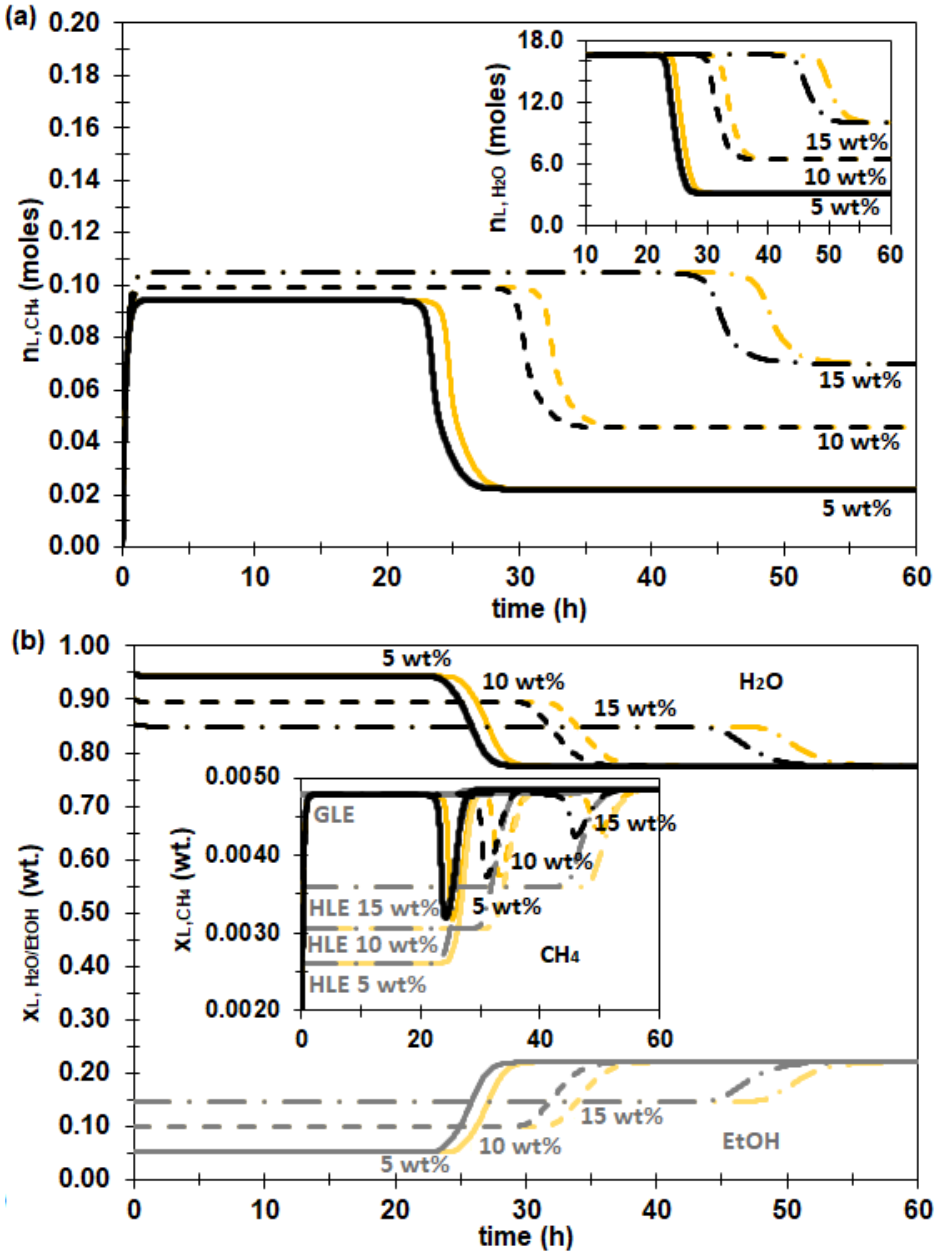

Figure 34 - (a) The number of moles of methane (n_L,CH_4) and (b) the H_2O (x_L,H_2O) and EtOH (x_L,EtOH, in gray and light yellow) mass fractions in the bulk liquid phase temporal profiles at 276 K and 70.9 bar (*DR* = 0.5). The lines describe the time profiles for the following ethanol compositions of the initial liquid phase: 5 wt% (continuous line), 10 wt% (dashed line) and 15 wt% (dotted-dashed line) of EtOH, with (black) and without (yellow) water activity in the driving force. The insertion (a) in the right shows the number of moles of water (n_L,H_2O) profile in the bulk liquid phase. The insertion (b) in the right is the methane mass fraction (x_L,CH_4) profile in the bulk liquid phase (black and yellow continuous lines), in the gas-liquid equilibrium (GLE) interface (gray and light yellow continuous lines) and in the hydrate-liquid equilibrium (HLE) interface (gray and light yellow dotted-dashed lines).

Figure 35 shows the solid phase properties and the activity coefficient behavior of the hydrate reagents. We can understand why the water activity effect of reducing the ethanol kinetic inhibitor behavior increases with the increase in ethanol concentration. The hydrate number of moles, Figure 35 (a), and the growth rate, Figure 35 (b), presented the same time displacement observed before, but the qualitative behavior and equilibrium conditions are kept the same. It is also possible to see that the inclusion of the water activity in the driving force changes the behavior of the product reagents' activities weighted by their stoichiometric coefficients parameters, K_b and K_{eq}, Figure 35 (b) insertions, equation (40). These parameters also reproduce the methane composition behavior if we do not include the water activity for all the initial ethanol concentration systems (yellow lines). However, the ethanol concentration increase changes the water and methane activity coefficients, Figure 35 (c) and (d). We can see that the increase in the ethanol concentration increases the water activity coefficient for values each time more distant from the ideality condition, $\gamma_{H_2O} = 1.0$, Figure 35 (c). So, the water activity coefficient becomes greater with the increase in the system ethanol concentration. This is the reason why the effect of reducing the ethanol kinetic inhibition potential becomes more pronounced with the increase in concentration.

Therefore, there is probably an specific concentration point for a thermodynamic inhibitor to reach its maximum kinetic inhibition effect, as ethanol also presents a thermodynamic hydrate promoter behavior, participating in the solid structure, in concentrations greater than 15 wt% [8,27]. In this system, 15 wt% is probably the concentration with the highest kinetic/thermodynamic inhibition efficiency for the ethanol without participation in the hydrate structure. However, other thermodynamic inhibitors, like methanol, which do not have this characteristic, may have an even more pronounced combined thermodynamic and kinetic inhibition effect at higher concentrations. It is also worth mentioning that experimental investigations of the ethanol behavior at higher concentrations are still necessary for better use of its potential as a thermodynamic or kinetic promoter or inhibitor [8,27,28,124].

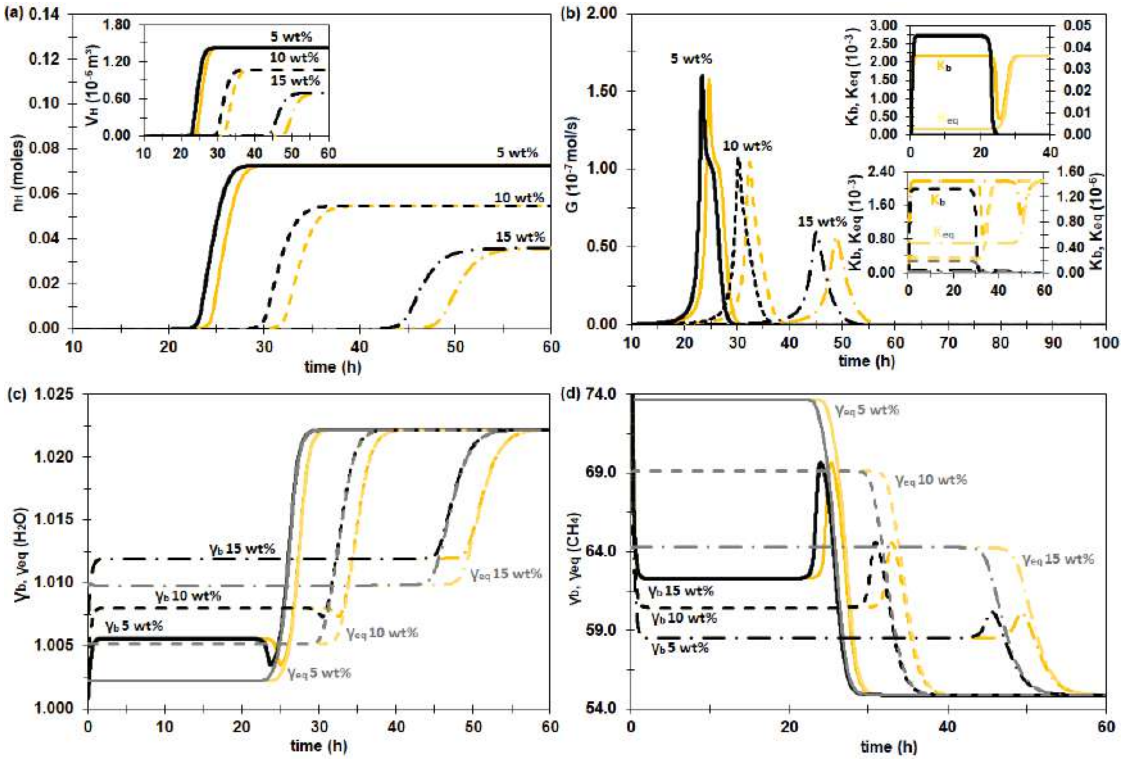

Figure 35 - (a) The number of moles of hydrate (n_H), (b) the hydrate growth rate (G), the activity coefficient (γ) for (c) H_2O and (d) CH_4 temporal profiles at 276 K and 70.9 bar (*DR* = 0.5). The lines describe the time profiles for the following ethanol compositions of the initial liquid phase: 5 wt% (continuous line), 10 wt% (dashed line) and 15 wt% (dotted-dashed line) of EtOH, with (black) and without (yellow) water activity in the driving force. The insertion (a) in the left is the hydrate volume temporal profile (V_H). The insertion (b) shows the parameters of the product reagents' activities weighted by their stoichiometric coefficients in the bulk phase (K_b) and in the hydrate-liquid equilibrium interface (K_{eq}) at 0 wt% for the one in the bottom, and at 10 wt% and 15 wt% for the one in the top, without (1st axis) and with (2nd axis) water activity. The gray and light yellow lines represent the variable temporal profiles at the hydrate-liquid equilibrium ($_{eq}$) and the black and yellow ones at the bulk conditions ($_b$).

The increase in ethanol concentration enhances the effect of the kinetic inhibitor of this thermodynamic hydrate inhibitor. However, on the other hand, the inclusion of water activity in the driving force reduces this effect compared to the driving force with only the host activity. Here we showed the relevance of considering the water non-ideality in the driving force. In this way, we can measure each THI inhibition potential and use the THI not only to change the equilibrium condition, but also to increase the induction time because of its kinetic inhibitor effect.

5.3.3 Pressure effect in an inhibited system

We studied a system similar to the one used by Englezos et al. [42] to obtain hydrate growth experimental data and use the parameters, like the *DR* factor and the hydrate occupancy factor adjusted to represent those data better. However, when we simulate an experimental system adding a thermodynamic hydrate inhibitor, we have to make sure that the system will form hydrate in that new condition because we know that the THI will shift the hydrate formation curve to more severe conditions [2]. Because of that, to make sure that the hydrate will form in all the ethanol concentration range studied in this work, up to 15 wt%, to evaluate the pressure effect, we increase the system pressure from 70.9 bar to 74.9 bar, to guarantee that we still are in a hydrate formation region. For the evaluation, we kept the *DR* factor equal to 0.5. Furthermore, we adjusted the hydrate occupancy factor, θ, using the same criteria used before: the maximum occupancy factor for which the methane mole fraction profile in the liquid phase had the greatest possible variation within limits given by the gas-liquid and hydrate-liquid interfaces equilibrium condition [213]. The system at 276 K and 70.9 bar was θ = 72%, while for the system at 276 K and 74.9 bar, it was 75%. We can see that the increase in the pressure increases the hydrate occupancy factor, which is expected and observed in experimental studies in the literature [213,215,216,221].

In Figure 36 it is shown the pressure effect in all the system phases: liquid phase, gas phase, and solid phase, and also the growth rate behavior. As expected, the methane equilibrium condition increases with the increase in the pressure, Figure 36 (a) insertion. So, the equilibrium composition of 0.485 wt% of CH_4 and 22.0 wt% of EtOH at 70.9 bar became 0.52 wt% of CH_4 and 23.6 wt% of EtOH at 74.9 bar, Figure 36 (a). The increase in the pressure also accelerates the hydrate formation. The increase of 4 bars accelerate in 2.5, 4.2, and 8.8 hours the beginning of the growth for 5, 10, and 15 wt%, respectively, Figure 36 (d). So, the equilibrium condition is increased with the pressure, but the growth is accelerated. The higher the initial inhibitor concentration, the more the growth beginning accelerates with an increase in the pressure.

Figure 36 (a) shows that the liquid phase components are consumed faster at 74.9 bar than at 70.9 bar. It is shown that the increase in the pressure increases the methane solubilization in the liquid phase for all systems. That comes from an average of 0.478 wt% to 0.507 wt% of CH_4 for the ethanol concentration range of 5 wt% to 15 wt%,

Figure 36 (a) insertion. We presented here the average values because the methane solubilization slightly changes with the ethanol concentration. The methane saturation is 0.477 wt%, 0.478 wt% and 0.480 wt% at 70.9 bar and 0.506 wt%, 0.507 wt% and 0.508 wt% at 74.9 bar for 5, 10 and 15 wt% of EtOH, respectively.

The addition of ethanol in the system, keeping the same amount of water, increases the liquid phase volume. To achieve the same pressure, it is necessary less methane in the gas phase: 5.07, 4.74, and 4.41 moles of CH_4 for 5, 10, and 15 wt% of EtOH, respectively at 70.9 bar, Figure 36 (b). The same occurs at 74.9 bar, where the number of moles of methane in the gas phase is 5.38, 5.07, and 4.74 for 5, 10, and 15 wt% of EtOH, respectively. Moreover, the number of moles in the gas phase increases with the pressure increase. It increases around 0.33 mole with the 4 bars increase in the pressure for each ethanol concentration system.

As it was shown before, the increase in the concentration reduces the amount of hydrate formed because the initial condition became closer to the equilibrium condition. So, the system achieves equilibrium quicker. In Figure 36 (c) this effect is shown, but it is also shown that the increase in the pressure increases the amount of hydrate formed. So, the hydrate number of moles at 70.9 bar is 0.073, 0.055, and 0.036 for 5, 10, and 15 wt% of EtOH, respectively, while at 74.9 bar the numbers are 0.074, 0.058 and 0.040 for 5, 10 and 15 wt% of EtOH, respectively. The 4 bars increase in the pressure increases the number of hydrate moles in 0.001, 0.003 and 0.004 for 5, 10, and 15 wt% of EtOH, respectively. This means that the increase in the pressure increases the amount of hydrate formed and that this increase is more significant for the higher initial concentration of ethanol in the system.

The growth behavior observed before can be understood throughout the growth rate and its parameters, Figure 36 (d). The growth rate is accelerated and has its peak increased with the increase in the pressure, which explains why the growth starts faster and more hydrate is formed. The parameters order of magnitude decreases with the increase in the ethanol concentration, but it is basically maintained with increased pressure. Then, the increase in the growth rate peak occurs because the water activity coefficient increases with the pressure as all the solid phase (in Appendix 4).

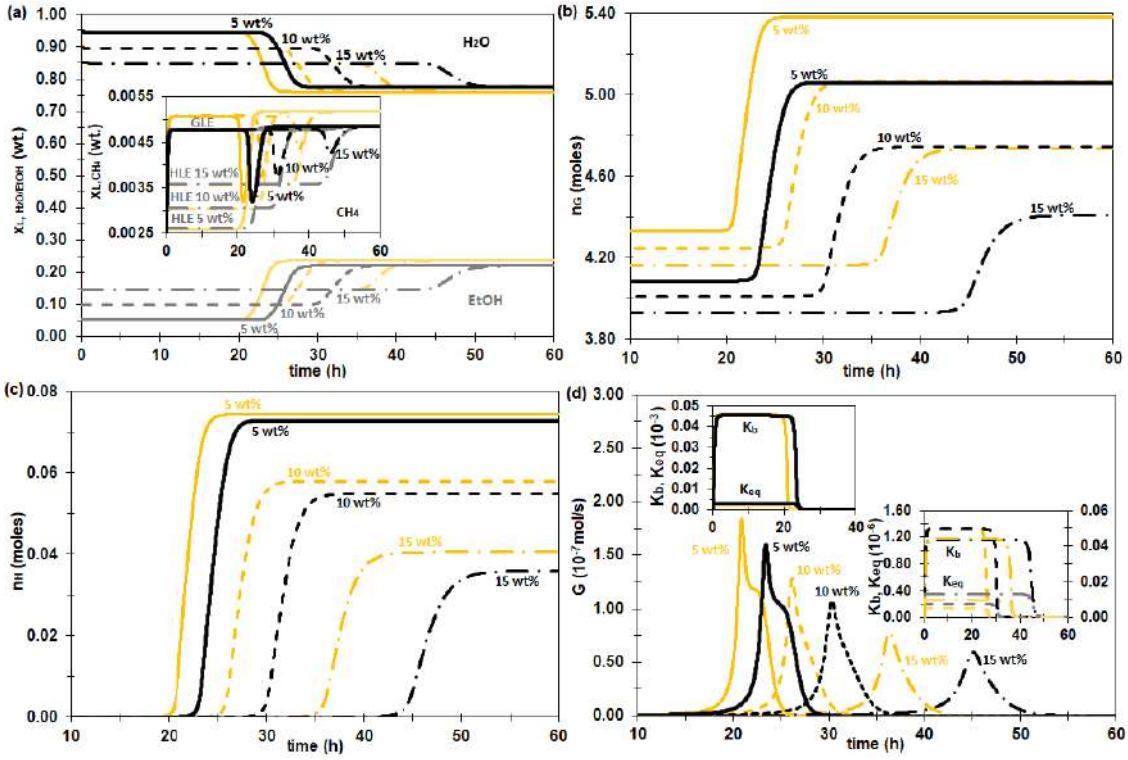

Figure 36 - (a) The H_2O (x_L,H_2O) and EtOH (x_L,EtOH, in gray and light yellow) mass fractions in the bulk liquid phase, (b) the number of moles of methane gas (n_G), (c) the number of moles of hydrate (n_H) and (d) the hydrate growth rate (G) temporal profiles at 276 K (*DR* = 0.5). The lines describe the time profiles for the following ethanol compositions of the initial liquid phase: 5 wt% (continuous line), 10 wt% (dashed line) and 15 wt% (dotted-dashed line) of EtOH, at 70.9 bar, θ = 72% (black and gray), and at 74.9 bar, θ = 75% (yellow and light yellow). The insertion (a) is the methane mass fraction (x_L,CH_4) profile in the bulk liquid phase (black and continuous yellow lines), in the gas-liquid equilibrium (GLE) interface (gray and light yellow continuous lines), and in the hydrate-liquid equilibrium (HLE) interface (gray and light yellow dotted-dashed lines). The insertion (d) shows the parameters of the product reagents' activities weighted by their stoichiometric coefficients in the bulk phase (K_b) and in the hydrate-liquid equilibrium interface (K_{eq}) at 0 wt% for the one in the top-left, and at 10 wt% (1st axis) and 15 wt% (2nd axis) for the one in the bottom-right. The gray and light yellow lines represent the variable temporal profiles at the hydrate-liquid equilibrium ($_{eq}$) and the black and yellow ones at the bulk conditions ($_b$).

The pressure increases, changing the equilibrium condition of the system and the dynamic of the growth. Because with the increase in the pressure, the system changes to a more favorable hydrate formation condition, the growth occurs faster and more hydrate is formed, as expected [13,42,220], and it was observed through the proposed

model. The new observation that our model allowed is that the increase in the initial ethanol concentration affects the amount of hydrate formed with the increase in the pressure. Therefore, for inhibited systems, the greater the amount of inhibitor more important it is to account for the non-ideal effect in the simulation to quantify the amount of hydrate that will be formed and prevent blockages.

5.3.4 Temperature effect in an inhibited system

A system similar to the one used by Englezos et al. [42] to obtain hydrate growth experimental data at 70.9 bar and 276 K or 274 K were simulated to evaluate the temperature effect in hydrate inhibited systems, keeping the same *DR* factor of 0.5, and the same hydrate occupancy factor, θ, adjusted to represent those data better. For the system at 276 K and 70.9 bar it was θ = 72%. In comparison, for the system at 274 K and 70.9 bar it was 68%, obeying the criterion of the maximum occupancy factor for which the methane mole fraction profile in the liquid phase had the greatest possible variation within limits given by the interfaces equilibrium condition at those temperature and pressure [213]. We can see that the temperature decrease decreases the hydrate occupancy factor, as it was observed experimentally in the literature [213,215,216,221].

Figure 37 shows the temperature effect in hydrate inhibited systems. The temperature decrease puts the system in a more favorable hydrate formation condition, accelerating the hydrate formation and increasing the methane and ethanol equilibrium composition, Figure 37 (a). The equilibrium composition of 0.485 wt% of CH_4 and 22.0 wt% of EtOH at 276 K became 0.54 wt% of CH_4 and 27.8 wt% of EtOH at 274 K. The decrease of 2 K accelerates in 5.7, 9.3, and 18.7 hours the beginning of the growth for 5, 10 and 15 wt%, respectively. It is noticed that the increase in ethanol concentration accelerates, even more, the start of growth due to the temperature reduction.

The liquid phase behavior is shown in Figure 37 (a). The temperature reduction increases the methane solubilization in the liquid phase, as expected. The methane saturation is 0.477 wt%, 0.478 wt% and 0.480 wt% at 276 K and 0.544 wt%, 0.530 wt% and 0.519 wt% at 274 K for 5, 10 and 15 wt% of EtOH, respectively. The cooling of the system makes an increase in methane solubility. However, at a lower temperature, 274 K, the methane mass fraction in the liquid phase decreases with the ethanol concentration increase. It occurs not because the methane solubility reduces, but because the molecular weight of ethanol is greater than that of methane and, as both are

increasing, the methane mass fraction reduces. The amount of methane solubilized in the liquid phase increases with increasing ethanol concentration at 274 K, 0.108, 0.110, and 0.114 moles for 5, 10, and 15 wt% of EtOH, respectively (in Appendix 4).

When cooling the system, to reach the same pressure, it is necessary to increase the amount of gas present in the gas phase; therefore, the methane number of moles in the gas phase increases, as we can see in Figure 37 (b). The methane gas number of moles goes from 5.07, 4.74 and 4.41 for 276 K to 5.18, 4.93 and 4.66 for 274 K at 5, 10 and 15 wt% of EtOH, respectively. So, the higher the ethanol initial concentration, higher is the increase in the methane number of moles in the gas phase with cooling: 0.11, 0.19 and 0.25 moles at 5, 10 and 15 wt% of EtOH, respectively.

Figure 37 (c) shows that cooling the system increases the amount of hydrate formed. The hydrate number of moles at 276 K come from 0.073, 0.055 and 0.036 to 0.078, 0.064 and 0.050 at 274 K for 5, 10 and 15 wt% of EtOH, respectively. The 2 K cooling increases the hydrate number of moles in 0.005, 0.009 and 0.014 moles. This means that the temperature decrease increases the amount of hydrate formed, and that this increase is greater the higher is the initial ethanol concentration. We can see that there is almost an increase of 0.005 in the hydrate number of moles for each system ethanol initial concentration due to the cooling. It occurs because the temperature reduction puts the system in an even more favorable hydrate formation condition. It increases the distance between the bulk and equilibrium conditions, causing more hydrate to form.

Cooling accelerates the growth rate and increases its peak, making growth start faster and form more hydrate, Figure 37 (d). The order of magnitude of parameters K_b and K_{eq} decreases with the increase in the ethanol concentration and increases with the temperature reduction, Figure 37 (d) insertions. The increase in the growth occurs because the distance between the gas-liquid and hydrate-liquid interfaces equilibrium conditions and the water activity coefficient (Appendix 4) increases with the cooling. Therefore, the equilibrium condition and water activity change accelerate the growth and increase the number of hydrates.

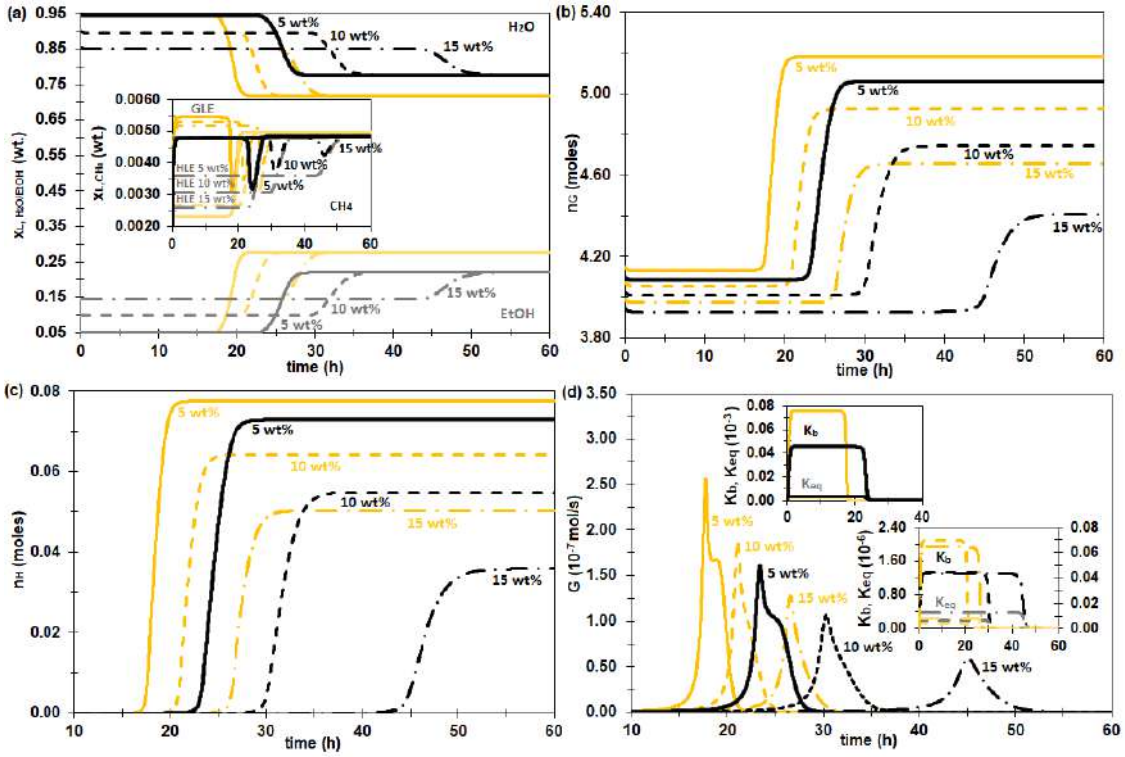

Figure 37 - (a) The H_2O (x_L,H_2O) and EtOH (x_L,EtOH, in gray and light yellow) mass fractions in the bulk liquid phase, (b) the number of moles of methane gas (n_G), (c) the number of moles of hydrate (n_H) and (d) the hydrate growth rate (G) temporal profiles at 70.9 bar (*DR* = 0.5).The lines describe the time profiles for the following ethanol compositions of the initial liquid phase: 5 wt% (continuous line), 10 wt% (dashed line), and 15 wt% (dotted-dashed line) of EtOH, at 276 K, θ = 72% (black and gray), and at 274 K, θ = 68% (yellow and light yellow). The insertion (a) is the methane mass fraction (x_L,CH_4) profile in the bulk liquid phase (black and continuous yellow lines), in the gas-liquid equilibrium (GLE) interface (gray and light yellow continuous lines), and in the hydrate- liquid equilibrium (HLE) interface (gray and light yellow dotted-dashed lines). The insertion (d) shows the parameters of the product reagents' activities weighted by their stoichiometric coefficients in the bulk phase (K_b) and the hydrate-liquid equilibrium interface (K_{eq}) at 0 wt% for the one in the top-left, and at 10 wt% (1st axis) and 15 wt% (2nd axis) for the one in the bottom-right. The gray and light yellow lines represent the variable temporal profiles at the hydrate- liquid equilibrium ($_{eq}$) and the black and yellow ones at the bulk conditions ($_b$).

The higher the ethanol concentration and temperature, the greater the inhibitory effect, thermodynamic and kinetic, of ethanol. A few experimental studies [220] have already shown this result, but now with this model, we could simulate this kind of system, predict and quantify the ethanol inhibitory capacity.

5.4 Partial conclusions

The proposed model is capable to adequately calculate the qualitative dynamic behavior of the methane hydrate growth in systems [15,32,196] contain inhibitor. The model was used to calculate the growth of methane hydrate in an ethanol-inhibited system at different concentrations. We showed that the higher the ethanol concentration, the slower it is for the growth to start. In other words, ethanol can act as a thermodynamic hydrate inhibitor and as a kinetic inhibitor. Besides, when there is no inhibitor, the system reaches a steady-state with the total consumption of water. However, with the inhibitor, the system reaches equilibrium. The higher the initial inhibitor concentration, the faster the equilibrium is achieved, as the system is closer to the equilibrium concentration. The higher the inhibitor concentration, the slower the growth starts, but when growth begins, the faster the system reaches equilibrium. The thermodynamic hydrate inhibitor can then delay the beginning of the growth and reduce the solid amount. At higher initial inhibitor concentration [220], these effects are more pronounced. These results agree with experimental observation.

The inclusion of the water activity in the driving force is the key contribution to the kinetic inhibitor behavior of ethanol better. The increase in ethanol concentration enhances the kinetic inhibitor effect of this THI, but on the other hand, the inclusion of water activity in the driving force reduces this effect concerning the driving force that accounts only for the host activity. This evaluation shows the relevance of considering the water non-ideality in the driving force to account for the real kinetic inhibition potential. In this way, we can measure each THI's inhibition potential, use the ethanol to change the equilibrium condition, delay the hydrate formation, and prevent blockages.

The increase in the pressure and the temperature decrease presented similar changes in the ethanol inhibited hydrate system. It occurs because the higher the pressure and the lower the temperature, the more favorable is the hydrate formation, so it is expected that the growth occurs faster and forms more hydrate [42,196,220]. Calculations of systems in more favorable conditions responded adequately, making the beginning of growing faster and forming a more solid phase. However, 2 K cooling the system pronounced more than the pressure increase by 4 bar. It is possible to conclude

that temperature has an even more pronounced kinetic and equilibrium effect in the hydrate growth than pressure for inhibited systems.

The new model showed that the increases in the initial ethanol concentration affect the amount of hydrate formed. So, for inhibited systems, the greater the amount of inhibitor, the more important it is to account for the non-ideal effect in the simulation to quantify the amount of hydrate that will be formed.

List of symbols

T - Temperature [K]

p - Pressure [bar]

R - Universal gas constant [J mol / K]

ξ - Stoichiometric coefficient for CH_4

τ - Stoichiometric coefficient for H_2O

H - Hydrate

t - Time [h]

ν - Stoichiometric coefficient

A - Affinity

α - Activity

ρ - Density [mol / m³]

c - concentration [mol / m³]

M - Molar mass [g / mol]

J_{rr} - Reaction flow [mol / m^2 s]

G - Growth rate [mol / s]

A_{sup} - Surface area [m²]

δ - Liquid film thickness [m]

N_c - Number of compounds

L_{rr} - Reaction coefficient [mol^2 K / m^2 J s]

L_D- Diffusion coefficient [mol / m s]

K - Activity product weighted by stoichiometric coefficient

n - Number of moles [mol]

V - Volume [m^3]

x - Mole fraction

μ_i - Moment of order *i* [m^i / m^3]

DR - Coupling factor

Θ – Hydrate occupancy factor

υ - Dynamic viscosity [mol / m s]

$_{eq}$ - Equilibrium condition

$_{b}$ - Bulk condition

^{L} - Liquid phase

^{G} - Gas phase

^{H} - Hydrate phase

^{0}- Reference

Chapter 6. Conclusion and future work suggestions

6.1 Conclusions

From the proper understanding of the gas hydrate equilibria in the presence of promoters (THF) and inhibitors (EtOH), we define modeling with a broader application range or with its applicability range well-established. The proper equilibrium calculation of these systems allowed developing a hydrate growth model capable of including thermodynamic effects in freshwater systems and systems with chemical additives (EtOH).

The hydrate-liquid-vapor equilibria calculation with the proposed equilibrium modeling is adequate for the systems of H_2O+THF, H_2O+Gas, and H_2O+Gas+THF. The parameter estimation strategy provides adequate and transferable parameters to be used in different conditions. The traditional equilibrium modeling shows an adequate deviation of up to 15 wt% of ethanol for the H_2O+Gas+EtOH system. We obtained thermodynamically consistent data of C_2H_6 and a mixture of C_2H_6/CH_4 up to 45 wt% of ethanol. Those measured data are valuable to test and improve hydrate prediction tools. Besides, a qualitative assessment of the literature data with high ethanol concentration was made to understand ethanol behavior as a THI better. However, a future experimental investigation is still needed to better understand the ethanol concentration limit as a thermodynamic hydrate inhibitor or a promoter. The presented methodology allowed to define conditions at which a full experimental characterization data of the hydrate structure is needed to hydrate formation with ethanol.

A driving force based on Prigogine's affinity was proposed and applied to the new hydrate growth model developed according to the non-equilibrium thermodynamic fundamental theory. With the proposed hydrate growth model and adequate balances, the growth system properties behavior was quantitatively and qualitatively reproduced for the CH_4 hydrate growth in freshwater and ethanol-inhibited systems. We could conclude first that the hydrate growth phenomenon is governed by both stages: reaction and diffusion. Second, at lower pressures, the growth behavior is close to the limiting diffusion behavior, while at high pressures, the diffusion and the reaction compete to

drive the growth. Moreover, it is possible to describe the growth phenomenon separated from the nucleation step. However, the lower the pressure, the greater the nucleation effect on the growth. The addition of an inhibitor alters the induction time, the kinetic rate, and the equilibrium condition. The simulations showed that THI presents a kinetic inhibition potential. So, ethanol can be used to change the equilibrium condition and delay the hydrate formation to prevent blockages. This effect can be simulated by adding the H_2O activity in the driving force, which is purely kinetic and increases with the increase in the inhibitor concentration.

6.2 Future work suggestions

To expand and continue this study, we suggest the following subjects for future work:

- Experimental investigation on the gas hydrate formation at high ethanol concentration. Hydrate-liquid-vapor equilibrium data, as well as the hydrate crystalline structure data and hydrate occupancy factor data in the presence of ethanol are still needed to better understand and model the ethanol behavior, mainly at high concentrations.
- Adaptation and application of the hydrate growth model to describe the growth of the double hydrate promoted by THF, since the equilibrium is already properly modeled. The proposed model can include the change in the water activity due to the addition of THF, but it is also capable of including another hydrate guest property in the driving force, through its activity, and account both effects caused by the THF addition.
- As hydrate formation is an exothermic reaction, it is important to include an energy balance in growth modeling. Theoretical development of the hydrate growth energy balance is already made. However, more experimental data on the hydrate thermal properties is still needed to describe the system temperature changes better. Previous studies [24,87] show that the spatial thermal variation in a hydrate formation system can be neglected concerning the temporal thermal variation. Therefore, an energy balance of the system can consider that the thermal exchange between the phases occurs instantly, such that the temperature of the entire system is the same spatially, although it varies temporally.

- An experimental study for the theoretical model validation, mainly for application in systems with chemical additives, is critical. It will compare the calculated temporal profiles with those measured and then obtain the model's precision level. Besides, this experimental analysis can also be used to define the induction time and the boundaries between the phenomena involved in the hydrate formation process, so that the comparison is made in an adequate time range. The initial conditions of the population balance moments by a particle size distribution can also be obtained from experimental studies. These results will allow the calculation of a more precise hydrate formation kinetic constant by reconciling dynamic data to make the model more robust. It is the same methodology that Clarke and Bishnoi [77] proposed for the Englezoss et al.[42,43] model. It is interesting to note that this methodology will allow detaching the model from the experimental apparatus.
- The approach of using a population balance to describe the solid phase, even a simple one, allows future inclusion of both the nucleation rate and the aggregation/breakage rate. Thus, we can describe with even more precision all stages of formation or dissociation of hydrates.

References

[1] E.D. Sloan, C. Koh, K.A. Sum, Natural Gas Hydrates in Flow Assurance, 1st ed., Elsevier, 2011.

[2] E.D. Sloan, C.A. Koh, Clathrate Hydrates of Natural Gases, 3rd ed., CRC Press, New York, 2008.

[3] H.P. Veluswamy, A. Kumar, Y. Seo, J.D. Lee, P. Linga, A review of solidified natural gas (SNG) technology for gas storage via clathrate hydrates, Appl. Energy. 216 (2018) 262–285. https://doi.org/10.1016/j.apenergy.2018.02.059.

[4] E.D. Sloan Jr, Fundamental principles and applications of natural gas hydrates, Nature. 426 (2003) 353–359.

[5] V.M. V Stackelberg, Feste Gashydrate., Naturwissenschaften. 36 (1949) 359–362.

[6] J.A. Ripmeester, J.S. Tse, C.I. Ratcliffe, B.M. Powell, A new clathrate hydrate structure, Nature. 325 (1987) 135–136.

[7] J.Y. Lee, T.S. Yun, J.C. Santamarina, C. Ruppel, Observations related to tetrahydrofuran and methane hydrates for laboratory studies of hydrate-bearing sediments, Geochemistry, Geophys. Geosystems. 8 (2007) 1–10. https://doi.org/10.1029/2006GC001531.

[8] K. Yasuda, S. Takeya, M. Sakashita, H. Yamawaki, R. Ohmura, Binary Ethanol - Methane Clathrate Hydrate Formation in the System CH4 - C2H5OH - H2O : Confirmation of Structure II Hydrate Formation, J.Phys. Chem. C. 113 (2009) 12598–12601.

[9] T. Makino, T. Sugahara, K. Ohgaki, Stability boundaries of tetrahydrofuran + water system, J. Chem. Eng. Data. 50 (2005) 2058–2060. https://doi.org/10.1021/je0502694.

[10] R. Anderson, A. Chapoy, H. Haghighi, B. Tohidi, Binary Ethanol−Methane Clathrate Hydrate Formation in the System CH4-C2H5OH-H2O: Phase Equilibria and Compositional Analyses, J. Phys. Chem. C. 113 (2009) 12602–12607. https://doi.org/10.1021/jp9021536.

[11] S. Sun, X. Peng, Y. Zhang, J. Zhao, Y. Kong, Stochastic nature of nucleation and growth kinetics of THF hydrate, J. Chem. Thermodyn. 107 (2017) 141–152. https://doi.org/10.1016/j.jct.2016.12.026.

[12] Z. Vatani, G. Amini, M. Samadi, A.M. Fuladgar, Prediction of gas hydrate formation in the presence of methanol, ethanol, (ethylene, diethylene and triethylene) glycol thermodynamic inhibitors, Pet. Sci. Technol. 36 (2018) 1150–1157. https://doi.org/10.1080/10916466.2018.1465960.

[13] Q. Nasir, H. Suleman, Y.A. Elsheikh, A review on the role and impact of various additives as promoters/ inhibitors for gas hydrate formation, J. Nat. Gas Sci. Eng. (2020) 103211. https://doi.org/10.1016/j.jngse.2020.103211.

[14] B. Lal, O. Nashed, Chemical Additives for Gas Hydrates, 1st ed., Springer, 2020.

[15] Z. Yin, M. Khurana, H.K. Tan, P. Linga, A review of gas hydrate growth kinetic models, Chem. Eng. J. 342 (2018) 9–29. https://doi.org/10.1016/j.cej.2018.01.120.

[16] T. Makiya, T. Murakami, S. Takeya, A.K. Sum, S. Alavi, R. Ohmura, Synthesis and characterization of clathrate hydrates containing carbon dioxide and ethanol., Phys. Chem. Chem. Phys. 12 (2010) 9927–9932. https://doi.org/10.1039/c002187c.

[17] H. Mozaffar, R. Anderson, B. Tohidi, Fluid Phase Equilibria Effect of alcohols and diols on PVCap-induced hydrate crystal growth patterns in methane systems, Fluid Phase Equilib. 425 (2016) 1–8. https://doi.org/10.1016/j.fluid.2016.05.005.

[18] X. Sen Li, C.G. Xu, Y. Zhang, X.K. Ruan, G. Li, Y. Wang, Investigation into gas production from natural gas hydrate: A review, Appl. Energy. 172 (2016) 286–322. https://doi.org/10.1016/j.apenergy.2016.03.101.

[19] Z. Yin, Z.R. Chong, H.K. Tan, P. Linga, Review of gas hydrate dissociation kinetic models for energy recovery, J. Nat. Gas Sci. Eng. 35 (2016) 1362–1387. https://doi.org/10.1016/j.jngse.2016.04.050.

[20] S. Horii, R. Ohmura, Continuous separation of CO2from a H2 + CO2gas mixture using clathrate hydrate, Appl. Energy. 225 (2018) 78–84. https://doi.org/10.1016/j.apenergy.2018.04.105.

[21] J. Zhao, Y. Song, X. Le Lim, W.H. Lam, Opportunities and challenges of gas hydrate policies with consideration of environmental impacts, Renew. Sustain. Energy Rev. 70 (2017) 875–885. https://doi.org/10.1016/j.rser.2016.11.269.

[22] J. Zheng, N.K. Loganathan, P. Linga, Natural gas storage via clathrate hydrate formation: Effect of carbon dioxide and experimental conditions, Energy Procedia. 158 (2019) 5535–5540. https://doi.org/10.1016/j.egypro.2019.01.590.

[23] C. Sun, W. Li, X. Yang, F. L i, Q. Yuan, L. Mu, J. Chen, B. Liu, G. Chen, Progress in Research of Gas Hydrate, Chinese J. Chem. Eng. 19 (2011) 151–162. https://doi.org/10.1016/S1004-9541(09)60192-0.

[24] C.P. Ribeiro, P.L.C. Lage, Modelling of hydrate formation kinetics: State-of-the-art and future directions, Chem. Eng. Sci. 63 (2008) 2007–2034. https://doi.org/10.1016/j.ces.2008.01.014.

[25] P.J. Herslund, N. Daraboina, K. Thomsen, J. Abildskov, N. Von Solms, Measuring and modelling of the combined thermodynamic promoting effect of tetrahydrofuran and cyclopentane on carbon dioxide hydrates, Fluid Phase Equilib. 381 (2014) 20–27. https://doi.org/10.1016/j.fluid.2014.08.015.

[26] A. Chapoy, R. Anderson, H. Haghighi, T. Edwards, B. Tohidi, Can n-propanol form hydrate?, Ind. Eng. Chem. Res. 47 (2008) 1689–1694. https://doi.org/10.1021/ie071019e.

[27] R. Anderson, A. Chapoy, H. Haghighi, B. Tohidi, Binary Ethanol - Methane Clathrate Hydrate Formation in the System CH4 -C2H5OH-H2O : Phase Equilibria and Compositional Analyses, J.Phys. Chem. C. 113 (2009) 12602–12607.

[28] K. Yasuda, R. Ohmura, A.K. Sum, Guest-guest and guest-host interactions in ethanol, propan-1-ol, and propan-2-ol clathrate hydrate forming systems, New J. Chem. 42 (2018) 7364–7370. https://doi.org/10.1039/c8nj00750k.

[29] J. Javanmardi, S. Babaee, A. Eslamimanesh, A.H. Mohammadi, Experimental Measurements and Predictions of Gas Hydrate Dissociation Conditions in the Presence of Methanol and Ethane-1,2-diol Aqueous Solutions, J. Chem. Eng. Data. 57 (2012) 1474–1479.

[30] F. V Zhurko, A. Yu, V.I. Kosyakov, Formation of gas hydrates in the systems methane – water – ROH (ROH = ethanol , n -propanol , i -propanol , i -butanol), Chem. Eng. Sci. 65 (2010) 900–905. https://doi.org/10.1016/j.ces.2009.09.040.

[31] I.L. Moudrakovski, K.A. Udachin, S. Alavi, C.I. Ratcliffe, J.A. Ripmeester, Facilitating guest transport in clathrate hydrates by tuning guest-host interactions, J. Chem. Phys. 142 (2015) 074705-01-074705–10. https://doi.org/10.1063/1.4907720.

[32] W. Ke, T.M. Svartaas, D. Chen, A review of gas hydrate nucleation theories and growth models, J. Nat. Gas Sci. Eng. 61 (2019) 169–196. https://doi.org/10.1016/j.jngse.2018.10.021.

[33] M.S. Khatami, A. Shahsavand, Application Of Population Balance Theory For Dynamic Modeling Of Methane And Ethane Hydrate Formation Processes, 2018. https://doi.org/10.1021/acs.energyfuels.8b01351.

[34] M. Khurana, Z. Yin, P. Linga, A review of clathrate hydrate nucleation, ACS Sustain. Chem. Eng. 5 (2017) 11176–11203. https://doi.org/10.1021/acssuschemeng.7b03238.

[35] P. Warrier, M.N. Khan, V. Srivastava, C.M. Maupin, C.A. Koh, Overview: Nucleation of clathrate hydrates, J. Chem. Phys. 145 (2016) 211705. https://doi.org/10.1063/1.4968590.

[36] J.W. Mullin, Crystallization, 4th ed., Butterworth-Heinemann, 2001. https://doi.org/https://doi.org/10.1016/B978-0-7506-4833-2.X5000-1.

[37] Y. Bi, A. Porras, T. Li, Free energy landscape and molecular pathways of gas hydrate nucleation, J. Chem. Phys. 145 (2016) 211909. https://doi.org/10.1063/1.4961241.

[38] C. Moon, P.C. Taylor, P.M. Rodger, Molecular dynamics study of gas hydrate formation, J. Am. Chem. Soc. 125 (2003) 4706–4707. papers3://publication/uuid/D1804CE2-6160-461B-B684-215F438CC26D.

[39] J.P. Lederhos, J.P. Long, A. Sum, R.L. Christiansen, E.D. Sloan, Effective kinetic inhibitors for natural gas hydrates, Chem. Eng. Sci. 51 (1996) 1221–1229. https://doi.org/10.1016/0009-2509(95)00370-3.

[40] E.M. Freer, M.S. Selim, E.D. Sloan Jr, Methane hydrate film growth kinetics, Fluid Phase Equilib. 185 (2001) 65–75.

[41] A.A. Noyes, W.R. Whitney, THE RATE OF SOLUTION OF SOLID SUBSTANCES IN THEIR OWN SOLUTIONS, Solut. SOLID Subst. (1897) 930–934. https://doi.org/CMU/SEI-2006-TR-008 ESC-TR-2006-008.

[42] P. Englezos, N. Kalogerakis, P.D.D. Dholabhai, P.R.R. Bishnoi, Kinetics of formation of methane and ethane gas hydrates, Chem. Eng. Sci. 42 (1987) 2647–2658. https://doi.org/10.1016/0009-2509(87)87015-X.

[43] P. Englezos, N. Kalogerakis, P.D. Dholabhai, P.R. Bishnoi, Kinetics of gas hydrate formation from mixtures of metane and ethane, Chem. Eng. Sci. 42 (1987) 2659–2666.

[44] C.L. Bassani, A.K. Sum, J. Herri, R.E.M. Morales, A. Cameira, A Multiscale Approach for Gas Hydrates Considering Structure , Agglomeration , and Transportability under Multiphase Flow Conditions : II . Growth Kinetic Model, Ind. Eng. Chem. Res. 59 (2020) 2123–2144. https://doi.org/10.1021/acs.iecr.9b04245.

[45] C.L. Bassani, C. Kakitani, J.-M. Herri, A.K. Sum, R.E.M. Morales, A. Cameirão, A Multiscale Approach for Gas Hydrates Considering Structure, Agglomeration, and Transportability under Multiphase Flow Conditions: III. Agglomeration Model, Ind. Eng. Chem. Res. (2020). https://doi.org/10.1021/acs.iecr.0c02633.

[46] C.L. Bassani, A.M. Melchuna, A. Cameiraõ, J.M. Herri, R.E.M. Morales, A.K. Sum, A multiscale approach for gas hydrates considering structure, agglomeration, and transportability under multiphase flow conditions: I. phenomenological model, Ind. Eng. Chem. Res. 58 (2019) 14446–14461. https://doi.org/10.1021/acs.iecr.9b01841.

[47] D. Elwell, H.J. Sheel, Crystal Growth from High-Temperature Solutions, Academic Press, New York, 1975.

[48] E.D. Sloan, F. Fleyfel, A Molecular Mechanism for Gas Hydrate Nucleation from Ice, AIChE J. 37 (1991) 1281–1292.

[49] R.L. Christiansen, E.D. Sloan Jr., Mechanisms and Kinetics of Hydrate

Formation., 284 Ann. NEW YORK Acad. Sci. (1994) 283–305.

[50] L.A. Baez, P. Clancy, Computer simulation of the crystal growth and dissolution of natural gas hydrates, Ann. N. Y. Acad. Sci. 715 (1994) 177–186. https://doi.org/10.1111/j.1749-6632.1994.tb38833.x.

[51] M.R. Walsh, C.A. Koh, D.E. Sloan, A.K. Sum, D.T. Wu, Microsecond Simulations of Spontaneous Methane Hydrate Nucleation and Growth, Science (80-.). 326 (2009) 1095–1098. https://doi.org/10.1126/science.1174010.

[52] A.H. Mohammadi, I. Kraouti, D. Richon, Experimental data and predictions of dissociation conditions for methane, ethane, propane, and carbon dioxide simple hydrates in the presence of glycerol aqueous solutions, Ind. Eng. Chem. Res. 47 (2008) 8492–8495. https://doi.org/10.1021/ie801018e.

[53] a. Vysniauskas, P.R. Bishnoi, A kinetic study of methane hydrate formation, Chem. Eng. Scince. 38 (1983) 1061–1072. https://doi.org/10.1016/0009-2509(83)80027-X.

[54] a. Vysniauskas, P.R. Bishnoi, Kinetics of ethane hydrate formation, Chem. Eng. Sci. 40 (1985) 299–303. https://doi.org/10.1016/0009-2509(85)80070-1.

[55] D.R. Topham, THE MODELLING OF HYDROCARBON BUBBLE PLUMES TO INCLUDE GAS HYDRATE FORMATION, Chem. Eng. Sci. 39 (1984) 1613–1622.

[56] D.R. Topham, The Formation of Gas Hydrates on Bubbles of Hydrocarbon Gases Rising in Seawater, Chem. Eng. Sci. 39 (1984) 821–828.

[57] T. Elperin, A. Forminykh, MODEL OF GAS HYDRATE FORMATION ON THE SURFACE OF A SLUG OF A PURE GAS, Int. Commun. Heat Mass Transf. 22 (1995) 435–443.

[58] J. Boxall, S. Davies, C. Koh, E.D. Sloan, Predicting When and Where Hydrate Plugs Form in Oil-Dominated Flowlines, SPE Proj. Facil. Constr. 4 (2009) 80–86. https://doi.org/10.2118/129538-PA.

[59] T.B. Charlton, M. Di Lorenzo, L.E. Zerpa, C.A. Koh, M.L. Johns, E.F. May, Z.M. Aman, Simulating Hydrate Growth and Transport Behaviour in Gas-Dominant Flow, Energy & Fuels. 32 (2018) 1012–1023.

https://doi.org/10.1021/acs.energyfuels.7b02199.

[60] L.E. Zerpa, E.D. Sloan, A.K. Sum, C.A. Koh, Overview of CSMHyK: A transient hydrate formation model, J. Pet. Sci. Eng. 98–99 (2012) 122–129. https://doi.org/10.1016/j.petrol.2012.08.017.

[61] K. Lekvam, P. Ruoff, A Reaction Kinetic Mechanism for Methane Hydrate Formation in Liquid Water, J. Am. Chem. Soc. 115 (1993) 8565–8569.

[62] K. Lekvam, P. Ruoff, Kinetics and mechanism of methane hydrate formation and decomposition in liquid water description of hysteresis, J. Cryst. Growth. 179 (1997) 618–624.

[63] D. Yang, L.A. Le, R.J. Martinez, R.P. Currier, D.F. Spencer, Kinetics of CO2 hydrate formation in a continuous flow reactor, Chem. Eng. J. 172 (2011) 144–157. https://doi.org/10.1016/j.cej.2011.05.082.

[64] E. Chaturvedi, K. Patidar, M. Srungavarapu, S. Laik, A. Mandal, Thermodynamics and kinetics of methane hydrate formation and dissociation in presence of calcium carbonate, Adv. Powder Technol. 29 (2018) 1025–1034. https://doi.org/10.1016/j.apt.2018.01.021.

[65] D.N. Glew, M.L. Haggett, Kinetics of formation of ethylene oxide hydrate. Part I. Experimental method and congruent solutions, Can. J. Chem. 46 (1968) 3857–3865.

[66] D.N. Glew, M.L. Haggett, Kinetics of formation of ethylene oxide hydrate. Part II. Incongruent solutions and discussion, Can. J. Chem. 46 (1968) 3867–3877. https://doi.org/10.1139/v68-640.

[67] J.B. Pangborn, A.J. Barduhn, THE KINETICS OF METHYL BROMIDE HYDRATE FORMATION, Dcsalinarion. 8 (1970) 35–68.

[68] T. Uchida, I.Y. Ikeda, S. Takeya, T. Ebinuma, J. Nagao, H. Narita, CO2 hydrate film formation at the boundary between CO2 and water: Effects of temperature, pressure and additives on the formation rate, J. Cryst. Growth. 237–239 (2002) 383–387. https://doi.org/10.1016/S0022-0248(01)01822-X.

[69] T. Uchida, T. Ebinuma, J. Kawabata, H. Narita, Microscopic observations of formation processes of clathrate-hydrate films at an interface between water and

carbon dioxide, J. Cryst. Growth. 204 (1999) 348–356. https://doi.org/10.1016/S0022-0248(99)00178-5.

[70] Y.H. Mori, Estimating the thickness of hydrate films from their lateral growth rates: Application of a simplified heat transfer model, J. Cryst. Growth. 223 (2001) 206–212. https://doi.org/10.1016/S0022-0248(01)00614-5.

[71] T. Mochizuki, Y.H. Mori, Clathrate-hydrate film growth along water/hydrate-former phase boundaries-numerical heat-transfer study, J. Cryst. Growth. 290 (2006) 642–652. https://doi.org/10.1016/j.jcrysgro.2006.01.036.

[72] B.Z. Peng, A. Dandekar, C.Y. Sun, H. Luo, Q.L. Ma, W.X. Pang, G.J. Chen, Hydrate film growth on the surface of a gas bubble suspended in water, J. Phys. Chem. B. 111 (2007) 12485–12493. https://doi.org/10.1021/jp074606m.

[73] R.-E. Meindinyo, T. Svartaas, Gas Hydrate Growth Kinetics: A Parametric Study, Energies. 9 (2016) 1021. https://doi.org/10.3390/en9121021.

[74] R.T. Meindinyo, Gas Hydrate Growth Kinetics, Faculty of Science and Technology, 2017.

[75] F. Chen, P.D. Yapa, Estimating hydrate formation and decomposition of gases released in a deepwater ocean plume, J. Mar. Syst. 30 (2001) 21–32. https://doi.org/10.1016/S0924-7963(01)00032-X.

[76] M.B. Malegaonkar, P.D. Dholabhai, P.R. Bishnoi, Kinetics of carbon dioxide and methane hydrate formation, Can. J. Chem. Eng. 75 (1997) 1090–1099. https://doi.org/10.1002/cjce.5450750612.

[77] M.A. Clarke, P.R. Bishnoi, Determination of the intrinsic kinetics of CO2gas hydrate formation using in situ particle size analysis, Chem. Eng. Sci. 60 (2005) 695–709. https://doi.org/10.1016/j.ces.2004.08.040.

[78] F. Al-Otaibi, M. Clarke, B. Maini, P.R. Bishnoi, Kinetics of structure II gas hydrate formation for propane and ethane using an in-situ particle size analyzer and a Raman spectrometer, Chem. Eng. Sci. 66 (2011) 2468–2474. https://doi.org/10.1016/j.ces.2011.03.012.

[79] F. Al-Otaibi, M. Clarke, B. Maini, P.R. Bishnoi, Formation kinetics of structure I clathrates of methane and ethane using an in situ particle size analyzer, Energy

and Fuels. 24 (2010) 5012–5022. https://doi.org/10.1021/ef100560f.

[80] D. Kashchiev, A. Firoozabadi, Driving force for crystallization of gas hydrates, J. Cryst. Growth. 241 (2002) 220–230. https://doi.org/10.1016/S0022-0248(02)01134-X.

[81] Y.T. Luo, J.H. Zhu, S.S. Fan, G.J. Chen, Study on the kinetics of hydrate formation in a bubble column, Chem. Eng. Sci. 62 (2007) 1000–1009. https://doi.org/10.1016/j.ces.2006.11.004.

[82] N. Gnanendran, R. Amin, Modelling hydrate formation kinetics of a hydrate promoter-water-natural gas system in a semi-batch spray reactor, Chem. Eng. Sci. 59 (2004) 3849–3863. https://doi.org/10.1016/j.ces.2004.06.009.

[83] A. V. Palodkar, S. Mandal, A.K. Jana, Modeling Growth Kinetics of Gas Hydrate in Porous Media: Experimental Validation, Energy & Fuels. 30 (2016) 7656–7665. https://doi.org/10.1021/acs.energyfuels.6b01397.

[84] P. Skovborg, P. Rasmussen, A Mass Transport Limited Model for the Growth of Methane and Ethane Gas Hydrates, Chem. Eng. Prog. 49 (1993) 1131–1143.

[85] H. Zhou, C.I. Ferreira, Investigation Of Hydrate Growth Rate On The Interface Between Liquid and Solid Film Investigation of hydrate growth rate on the interface between liquid and solid film, in: 16 Th Int. Refrig. Air Cond. Conf., 2016: pp. 1672 1–10. http://docs.lib.purdue.edu/iracc%5Cnhttp://docs.lib.purdue.edu/iracc/1672.

[86] J.M. Herri, J.S. Pic, F. Gruy, M. Cournil, Methane Hydrate Crystallization Mechanism from In- Situ Particle Sizing, AIChE J. 45 (1999) 590–602. https://doi.org/10.1002/aic.690450316.

[87] T.P. Sampaio, F.W. Tavares, P.L.C. Lage, Non-isothermal population balance model of the formation and dissociation of gas hydrates, Chem. Eng. Sci. 163 (2017) 234–254. https://doi.org/10.1016/j.ces.2016.12.012.

[88] B. Zarenezhad, F. Varaminian, A generalized macroscopic kinetic model for description of gas hydrate formation processes in isothermal-isochoric systems, Energy Convers. Manag. 57 (2012) 125–130. https://doi.org/10.1016/j.enconman.2011.12.015.

[89] H. Roosta, S. Khosharay, F. Varaminian, Experimental and modeling investigation on mixed carbon dioxide-tetrahydrofuran hydrate formation kinetics in isothermal and isochoric systems, J. Mol. Liq. 211 (2015) 411–416. https://doi.org/10.1016/j.molliq.2015.07.065.

[90] M. Gudala, S.K. Govindarajan, A. Mandal, CHEMICAL AFFINITY MODELING OF METHANE HYDRATE FORMATION AND DISSOCIATION IN PRESENCE OF SURFACTANTS, Energy & Fuels. 34 (2019) 319–331. https://doi.org/10.1021/acs.energyfuels.9b03777.

[91] Y. Shindo, P.C. Lund, Y. Fuhioka, H. Komiyama, KINETICS OF FORMATION OF CO 2 HYDRATE Y., Energy Convers. Mgmt. 34 (1993) 1073–1079.

[92] H. Teng, C.M. Kinoshita, Hydrate Formation on the Surface of a CO2 Droplet in High Pressure Low Temperature Wwater.pdf, Chem. Eng. Sci. 50 (1995) 559–564.

[93] S. Hashemi, A. Macchi, P. Servio, Gas Hydrate Growth Model in a Semibatch Stirred Tank Reactor, Ind. Eng. Chem. Res. 46 (2007) 5907–5912.

[94] S. Bergeron, P. Servio, Reaction rate constant of propane hydrate formation, Fluid Phase Equilib. 265 (2008) 30–36. https://doi.org/10.1016/j.fluid.2007.12.001.

[95] H. Tajima, T. Nagata, Y. Abe, A. Yamasaki, F. Kiyono, K. Yamagiwa, HFC-134a hydrate formation kinetics during continuous gas hydrate formation with a kenics static mixer for gas separation, Ind. Eng. Chem. Res. 49 (2010) 2525–2532. https://doi.org/10.1021/ie901613h.

[96] S. Babaee, H. Hashemi, A.H. Mohammadi, P. Naidoo, D. Ramjugernath, Kinetic study of hydrate formation for argon + TBAB + SDS aqueous solution system, J. Chem. Thermodyn. 116 (2018) 121–129. https://doi.org/10.1016/j.jct.2017.08.030.

[97] L. Mu, S. Li, Q.L. Ma, K. Zhang, C.Y. Sun, G.J. Chen, B. Liu, L.Y. Yang, Experimental and modeling investigation of kinetics of methane gas hydrate formation in water-in-oil emulsion, Fluid Phase Equilib. 362 (2014) 28–34. https://doi.org/10.1016/j.fluid.2013.08.028.

[98] J.H. van der Waals, J.C. Platteeuw, Clathrate solutions, Adv. Chem. Phys. 2 (1959) 1–57. https://doi.org/10.1002/9780470143483.ch1.

[99] S. Saito, D.R. Marshall, R. Kobayashi, High Application of Statistical Mechanics to the Study of the Hydrates of Methane , Argon , and Nitrogen, AIChE J. (1964) 734–740.

[100] E.D. Sloan, F.M. Khoury, R. Kobayashi, Water Content of Methane Gas in Equilibrium with Hydrates, Ind. Eng. Chem., Fundam. 15 (1976) 318–323.

[101] G.D. Holder, G. Corbh, K.D. Papadopoulos, Prediction of high-pressure gas solubilities in aqueous mixtures of electrolytes, Ind. Eng. Chem. Res. 19 (1980) 282–286. https://doi.org/10.1021/ie00057a019.

[102] J. Munck, S. Skjold-Jørgensen, P. Rasmussen, Computations of the formation of gas hydrates, Chem. Eng. Sci. 43 (1988) 2661–2672. https://doi.org/10.1016/0009-2509(88)80010-1.

[103] W.R. Parrishl, J.M. Prausnitz, Dissociation Pressures of Gas Hydrates Formed by Gas Mixtures, Ind. Eng. Chem. Process Des. Dev. 11 (1972) 26–35.

[104] V.T. John, D. Holder, Contribution of Second and Subsequent Water Shells to the Potential Energy of Guest-Host Interactions in Clathrate Hydrates, J. Phys. Chem. 86 (1982) 455–459.

[105] V.T. John, K.D. Papadopoulos, G.D. Holder, A Generalized Model for Predicting Equilibrium Conditions for Gas Hydrates, AIChE J. 31 (1985) 252–259. https://doi.org/10.1002/aic.690310212.

[106] A.L. Ballard, E.D. Sloan Jr, The next generation of hydrate prediction I . Hydrate standard states and incorporation of spectroscopy, Fluid Phase Equilib. 194–197 (2002) 371–383.

[107] J.B. Klauda, S.I. Sandler, Phase behavior of clathrate hydrates: A model for single and multiple gas component hydrates, Chem. Eng. Sci. 58 (2003) 27–41. https://doi.org/10.1016/S0009-2509(02)00435-9.

[108] A. Lakhlifi, P. Richard, S. Picaud, O. Mousis, A simple van ' t Hoff law for calculating Langmuir constants in clathrate hydrates, Chem. Phys. 448 (2015) 53–60. https://doi.org/10.1016/j.chemphys.2015.01.004.

[109] R. Burgass, A. Chapoy, X. Li, Gas hydrate equilibria in the presence of monoethylene glycol, sodium chloride and sodium bromide at pressures up to 150 MPa, J. Chem. Thermodyn. 118 (2018) 193–197. https://doi.org/10.1016/j.jct.2017.10.007.

[110] M.A. Mahabadian, A. Chapoy, R. Burgass, B. Tohidi, Fluid Phase Equilibria Development of a multiphase fl ash in presence of hydrates : Experimental measurements and validation with the CPA equation of state, Fluid Phase Equilib. 414 (2016) 117–132. https://doi.org/10.1016/j.fluid.2016.01.009.

[111] J.H. Yoon, A theoretical prediction of cage occupancy and heat of dissociation of THF-CH4 hydrate, Korean J. Chem. Eng. 29 (2012) 1670–1673. https://doi.org/10.1007/s11814-012-0137-6.

[112] X. Li, H. Wu, P. Englezos, Prediction of Gas Hydrate Formation Conditions in the Presence of Methanol, Glycerol, Ethylene Glycol, and Triethylene Glycol with the Statistical Associating Fluid Theory Equation of State, Ind. Eng. Chem. Res. 45 (2006) 2131–2137.

[113] M. Abolala, M. Karamoddin, F. Varaminian, Fluid Phase Equilibria Thermodynamic modeling of phase equilibrium for gas hydrate in single and mixed refrigerants by using sPC-SAFT equation of state, Fluid Phase Equilib. 370 (2014) 69–74. https://doi.org/10.1016/j.fluid.2014.02.013.

[114] A.H.S. Dehaghani, B. Karami, A new predictive thermodynamic framework for phase behavior of gas hydrate, Fuel. 216 (2018) 796–809. https://doi.org/10.1016/j.fuel.2017.11.128.

[115] A. Beheshtimaal, A. Haghtalab, Thermodynamic modeling of hydrate formation conditions using different activity coefficient models in the presence of tetrahydrofuran (THF), Chem. Eng. Res. Des. 129 (2018) 150–159. https://doi.org/10.1016/j.cherd.2017.11.015.

[116] G. Moradi, E. Khosravani, Fluid Phase Equilibria Modeling of hydrate formation conditions for CH 4 , C 2 H 6 , C 3 H 8 , N 2 , CO 2 and their mixtures using the PRSV2 equation of state and obtaining the Kihara potential parameters for these components, Fluid Phase Equilib. 338 (2013) 179–187. https://doi.org/10.1016/j.fluid.2012.11.010.

[117] G.D. Holder, N. Pradhan, P. Equilibria, T. Model, Phase Behavior in Systems Containing Clathrate Hydrates, Rev. Chem. Eng. 5 (1988) 1–70.

[118] A. Saberi, A. Alamdari, A. Shariati, A.H. Mohammadi, Experimental measurement and thermodynamic modeling of equilibrium condition for natural gas hydrate in MEG aqueous solution, Fluid Phase Equilib. 459 (2018) 110–118. https://doi.org/10.1016/j.fluid.2017.11.034.

[119] R.M. De Deugd, M.D. Jager, J. De Swaan Arons, Mixed Hydrates of Methane and Water-Soluble Hydrocarbons Modeling of Empirical Results, AIChE J. 47 (2001) 693–704. https://doi.org/10.1002/aic.690470316.

[120] Y. Hu, J.H. Sa, B.R. Lee, A.K. Sum, Universal correlation for gas hydrates suppression temperature of inhibited systems: III. salts and organic inhibitors, AIChE J. 64 (2018) 4097–4109. https://doi.org/10.1002/aic.16369.

[121] Y. Demirel, Nonequilibrium Thermodynamics: Transport and Rate Processes in Physical and Biological Systems, 2nd ed., Elsevier, Lincoln, 2014. https://doi.org/10.1115/1.1579462.

[122] G. Lebon, D. Jou, J. Casas-Vazquez, Understanding Understanding Non-equilibrium Thermodynamics, 1 ed, Springer, Catalonia, 2008.

[123] I.A. de Oliveira, I.S. V Segtovich, A.G. Barreto, F.W. Tavares, Accurate thermodynamic description of vapor–liquid and solid–liquid equilibria of THF, water and gas hydrates with a unique set of parameters, J. Chem. Thermodyn. 117 (2018) 60–67. https://doi.org/10.1016/j.jct.2017.08.003.

[124] I.A. De Oliveira, A.G. Barreto, F.W. Tavares, A.K. Sum, Phase Equilibria Data and Thermodynamic Analysis for Liquid − Hydrate − Vapor (LHV) with High Ethanol Concentrations, J. Chem. Eng. Data. 65 (2020) 349–359. https://doi.org/10.1021/acs.jced.9b00691.

[125] A. Eslamimanesh, A.H. Mohammadi, D. Richon, P. Naidoo, D. Ramjugernath, Application of gas hydrate formation in separation processes: A review of experimental studies, J. Chem. Thermodyn. 46 (2012) 62–71. https://doi.org/10.1016/j.jct.2011.10.006.

[126] S.R. Gough, D.W. Davidson, Composition of Tetrahydrofuran Hydrate and the

Effect of Pressure on the Decomposition, Can. J. Chem. 49 (1971) 2691–2699. https://doi.org/10.1139/v71-447.

[127] R. Anderson, A. Chapoy, B. Tohidi, Phase Relations and Binary Clathrate Hydrate Formation in the System H2 - THF - H2O, Langmuir. 23 (2007) 3440–3444.

[128] A. Delahaye, L. Fournaison, S. Marinhas, I. Chatti, J.P. Petitet, D. Dalmazzone, W. Fürst, Effect of THF on equilibrium pressure and dissociation enthalpy of CO2 hydrates applied to secondary refrigeration, Ind. Eng. Chem. Res. 45 (2006) 391–397. https://doi.org/10.1021/ie050356p.

[129] Y.T. Seo, S.P. Kang, H. Lee, Experimental determination and thermodynamic modeling of methane and nitrogen hydrates in the presence of THF, propylene oxide, 1,4-dioxane and acetone, Fluid Phase Equilib. 189 (2001) 99–110. https://doi.org/10.1016/S0378-3812(01)00580-5.

[130] Q. Zhang, G. Chen, Q. Huang, C. Sun, X. Guo, Q. Ma, Hydrate Formation Conditions of a Hydrogen + Methane Gas Mixture in Tetrahydrofuran + Water, J. Chem. Eng. Data. 50 (2005) 234–236.

[131] A.H. Mohammadi, D. Richon, Phase Equilibria of Clathrate Hydrates of Tetrahydrofuran + Hydrogen Sulfide and Tetrahydrofuran + Methane, Ind. Eng. Chem. Res. 48 (2009) 7838–7841.

[132] C. Sun, G. Chen, L. Zhang, Hydrate phase equilibrium and structure for (methane + ethane + tetrahydrofuran + water) system, J. Chem. Thermodyn. 42 (2010) 1173–1179. https://doi.org/10.1016/j.jct.2010.04.021.

[133] Q. Sun, X. Guo, W.G. Chapman, A. Liu, L. Yang, J. Zhang, Vapor–hydrate two-phase and vapor–liquid–hydrate three-phase equilibrium calculation of THF/CH4/N2 hydrates, Fluid Phase Equilib. 401 (2015) 70–76. https://doi.org/10.1016/j.fluid.2015.05.024.

[134] K. Otake, T. Tsuji, I. Sato, T. Akiya, T. Sako, M. Hongo, A proposal of a new technique for the density measurement of solids, Fluid Phase Equilib. 171 (2000) 175–179. https://doi.org/10.1016/S0378-3812(00)00358-7.

[135] H.J.M. Hanley, G.J. Meyers, J.W. White, E.D. Sloan, The melting curve of

tetrahydrofuran hydrate in D2O, Int. J. Thermophys. 10 (1989) 903–909. https://doi.org/10.1007/BF00514485.

[136] D.G. Leaist, J.J. Murray, M.L. Post, D.W. Davidson, Enthalpies of Decomposition and Heat Capacities of Ethylene Oxide and Tetrahydrofuran Hydrate, J. Phys. Chem. 26 (1982) 4175–4178.

[137] Y.A. Dyadin, P.N. Kuznetsov, I.I. Yakovlev, A. V. Pyrinova, The system water-tetrahydrofuran in the crystallization region at pressures up to 9 kbar., Dokl. Chem. 208 (1973) 9–12.

[138] H. Matsuda., N. Kamihana, K. Kurihara, K. Tochigi, K. Yokayama, Measurement of isobaric vapor-liquid equilibria for binary systems contining tetrahydrofuran using an automatic apparatus, J. Chem. Eng. Jpn. 44 (2011) 131–139.

[139] Q. Sun, Y.T. Kang, Experimental correlation for the formation rate of CO2 hydrate with THF (tetrahydrofuran) for cooling application, Energy. 91 (2015) 712–719. https://doi.org/10.1016/j.energy.2015.08.089.

[140] T.A. Strobel, C.A. Koh, E.D. Sloan, Thermodynamic predictions of various tetrahydrofuran and hydrogen clathrate hydrates, Fluid Phase Equilib. 280 (2009) 61–67. https://doi.org/10.1016/j.fluid.2009.02.012.

[141] P.J. Herslund, K. Thomsen, J. Abildskov, N. Von Solms, Modelling of tetrahydrofuran promoted gas hydrate systems for carbon dioxide capture processes, Fluid Phase Equilib. 375 (2014) 45–65. https://doi.org/10.1016/j.fluid.2014.04.031.

[142] T.M. Letcher, U. Domanska, The excess volumes of (tributylamine + an ether) at the temperature 298.15 K, J. Chem. Thermodyn. 26 (1994) 1241–1247.

[143] R. Francesconi, F. Comelli, Excess Molar Volumes of Binary Mixtures Containing Dimethyl Carbonate Linear and Cyclic Ethers, J. Chem. Eng. Data. 39 (1994) 106–107.

[144] I.S. V. Segtovich, A.G. Barreto Jr., F.W. Tavares, Simultaneous multiphase flash and stability analysis calculations including hydrates, Fluid Phase Equilib. 413 (2016) 196–208. https://doi.org/10.1016/j.fluid.2015.10.030.

[145] P.J. Herslund, K. Thomsen, J. Abildskov, N. Von Solms, Application of the cubic-plus-association (CPA) equation of state to model the fluid phase behaviour of binary mixtures of water and tetrahydrofuran, Fluid Phase Equilib. 356 (2013) 209–222. https://doi.org/10.1016/j.fluid.2013.07.036.

[146] J.M. Míguez, M.M. Piñeiro, J. Algaba, B. Mendiboure, J.P. Torré, F.J. Blas, Understanding the Phase Behavior of Tetrahydrofuran + Carbon Dioxide, + Methane, and + Water Binary Mixtures from the SAFT-VR Approach, J. Phys. Chem. B. 119 (2015) 14288–14302. https://doi.org/10.1021/acs.jpcb.5b07845.

[147] J. Lee, J. Cho, D.M. Kim, S. Park, Separation of tetrahydrofuran and water using pressure swing distillation: Modeling and optimization, Korean J. Chem. Eng. 28 (2011) 591–596. https://doi.org/10.1007/s11814-010-0467-1.

[148] G.M. Bollas, P.I. Barton, A. Mitsos, Bilevel optimization formulation for parameter estimation in vapor-liquid(-liquid) phase equilibrium problems, Chem. Eng. Sci. 64 (2009) 1768–1783. https://doi.org/10.1016/j.ces.2009.01.003.

[149] J. Matouš, J.. Novák, J. Šobr, J. Pick, Phase equilibria in the system tetrahydrofuran (1) + water (2), Collect. 'Czechoslov. Chem. Commun. 37 (1972) 2653–2663. https://doi.org/10.1007/s11669-014-0326-6.

[150] R. Signer, H. Arm, H. Daeniker, Dampfdrucke, Dichten, thermodynamische Mischungsfunktionen und Brechungsindices der binaren Systeme Wasser-Tetrahydrofuran und Wasser-Diathylather bei 25°, Helv. Chim. Acta. 52 (1969) 2347–2351.

[151] V.B. Kogan, Liquid-Vapor Equilibrium in the Systems Tetrahydrofuran-Water and Tetrahydrofuran-Ethylene Glycol and a Method for Dehydration of Tetrahydrofuran, J.Appl.Chem.USSR. 41 (1968) 1236–1242.

[152] K.A. Pividal, A. Birtigh, S.I. Sandler, Infinite Dilution Activity Coefficients for Oxygenate Systems Determined Using a Differential Static Cell, J. Chem. Eng. Data. 37 (1992) 484–487.

[153] D.L. Bergmann, C.A. Eckert, Measurement of limiting activity coefficients for aqueous systems by differential ebulliometry, Fluid Phase Equilib. 63 (1991) 141–150.

[154] G.S. Shealy, S.I. Sandler, The Excess Gibbs Free Energy of Aqueous Nonelectrolyte Solutions, AIChE J. 34 (1988) 1065–1074.

[155] M. Schwaab, J.C. Pinto, Análise de Dados Experimentais - Volume I Fundamentos de Estatística, first ed., Rio de Janeiro, 2007.

[156] W.H. Press, S.A. Teukolsky, W.T. Vetterling, B.P. Flannery, Numerical Recipes in Fortran, first ed., Cambidge University Press, New York, 1992.

[157] K. Kojima, S. Zhang, T. Hiaki, Measuring methods of infinite dilution activity coefficients and a database for systems including water, Fluid Phase Equilib. 131 (1997) 145–179. https://doi.org/10.1016/S0378-3812(96)03210-4.

[158] J.L. De Roo, C.J. Peters, R.N. Lichtenthaler, G.A.M. Diepen, Occurrence of Methane Hydrate in Saturated and Unsaturated Solutions of Sodium Chloride and Water in Dependence of Temperature and Pressure, AIChE J. 29 (1983) 651–657.

[159] K.M. Sabil, C.J. Peters, Phase equilibrium data of mixed carbon dioxide and tetrahydrofuran clathrate hydrate in aqueous electrolyte solutions, in: 11th Int. Conf. Prop. Phase Equilibria PPEPPD, Crete, Greece, 2007.

[160] S. Hashimoto, T. Sugahara, H. Sato, K. Ohgaki, Thermodynamic Stability of H2 + Tetrahydrofuran Mixed Gas Hydrate in Nonstoichiometric Aqueous Solutions, J. Chem. Eng. Data. 52 (2007) 517–520.

[161] L.J. Rovetto, J. Schoonman, C.J. Peters, Phase Behavior of Low-pressure Hydrogen Clathrate Hydrate, in: 5th Int. Conf. Gas Hydrates, Trondheim, Norway, 2005.

[162] L.J. Florusse, C.J. Peters, J. Schoonman, K.C. Hester, C.A. Koh, S.F. Dec, K.N. Marsh, E.D. Sloan, Stable Low-Pressure Hydrogen Clusters Stored in a Binary Clathrate Hydrate, Science (80-.). 306 (2004) 469–471.

[163] C.M.M. Antunes, C. Kakitani, M.A.M. Neto, R.R.M. Morales, A.K. Sum, An Examination of tge prediction of hydrate formation conditions in the presence of thermodynamic inhibitors, Brazilian J. Chem. Eng. 35 (2018) 265–274.

[164] M. Dastanian, A.A. Izadpanah, M. Mofarahi, Phase Equilibria of Carbon Dioxide Hydrates in the Presence of Methanol / Ethylene Glycol and KCl Aqueous

Solutions, J. Chem. Eng. Data. 62 (2017) 1701–1707. https://doi.org/10.1021/acs.jced.7b00146.

[165] M.H. Kapateh, A. Chapoy, R. Burgass, B. Tohidi, Experimental Measurement and Modeling of the Solubility of Methane in Methanol and Ethanol, J. Chem. Eng. Data. 61 (2015) 666–673. https://doi.org/10.1021/acs.jced.5b00793.

[166] T. Maekawa, Equilibrium Conditions of Xenon Hydrates in the Presence of Aqueous Solutions of Alcohols, Glycols, and Glycerol, J. Chem. Eng. Data. 61 (2016) 662–665. https://doi.org/10.1021/acs.jced.5b00791.

[167] A.D. Potts, D.W. Davidson, Ethanol Hydrate, J. Phys. Chem. 69 (1965) 996–1000.

[168] Y. Hu, B.R. Lee, A.K. Sum, Insight into increased stability of methane hydrates at high pressure from phase equilibrium data and molecular structure, Fluid Phase Equilib. 450 (2017) 24–29. https://doi.org/10.1016/j.fluid.2017.07.003.

[169] R. Kobayashil, D.L. Katz, Vapor-Liquid Equilibria for Binary sn-water Systems, Ind. Eng. Chem. 45 (1953) 440–446.

[170] P.F. Ferrari, A.Z. Guembaroski, M.A. Marcelino Neto, R.E.M. Morales, A.K. Sum, Experimental measurements and modelling of carbon dioxide hydrate phase equilibrium with and without ethanol, Fluid Phase Equilib. 413 (2015) 1–8. https://doi.org/10.1016/j.fluid.2015.10.008.

[171] A.Z. Guembaroski, A.M. Neto, D. Bertoldi, R.E.M. Morales, Phase Behavior of Carbon Dioxide Hydrates : A Comparison of Inhibition Between Sodium Chloride and Ethanol, J. Chem. Eng. Data. 62 (2017) 3445–3451. https://doi.org/10.1021/acs.jced.7b00463.

[172] T. Maekawa, Equilibrium Conditions of Propane Hydrates in Aqueous Solutions of Alcohols , Glycols , and Glycerol, J. Chem. Eng. Data. 53 (2008) 2838–2843.

[173] A. Mohammadi, M. Manteghian, A.H. Mohammadi, Chemical Engineering Research and Design Thermodynamic modeling of the dissociation conditions of hydrogen sulfide clathrate hydrate in the presence of aqueous solution of inhibitor (alcohol , salt or ethylene glycol), Chem. Eng. Res. Des. 92 (2014) 2283–2293. https://doi.org/10.1016/j.cherd.2014.01.010.

[174] M. Cha, Y. Hu, A.K. Sum, Methane Hydrate Phase Equilibria for Systems Containing NaCl, KCl, and NH4Cl, Fluid Phase Equilib. 413 (2016) 2–9. https://doi.org/10.1016/j.fluid.2015.08.010.

[175] J. Sa, Y. Hu, A.K. Sum, Assessing thermodynamic consistency of gas hydrates phase equilibrium data for inhibited systems, Fluid Phase Equilib. 473 (2018) 294–299. https://doi.org/10.1016/j.fluid.2018.06.012.

[176] Y. Hu, J. Sa, B.R. Lee, A.K. Sum, Universal Correlation for Gas Hydrates Suppression Temperature of Inhibited Systems: III. Salts and Organic Inhibitors, AIChE J. 64 (2018) 4097–4109. https://doi.org/10.1002/aic.16369.

[177] M.-J. Huron, J. Vidal, New mixing rules in simple equations of state for representing vapor-liquid equilibria of strongly non-ideal mixtures, Fluid Phase Equilib. 3 (1979) 255–271. https://doi.org/https://doi.org/10.1016/0378-3812(79)80001-1.

[178] J. Vidal, Mixing rules and excess properties in cubic equations of state, Chem. Eng. Res. Des. 33 (1978) 787–791. https://doi.org/ttps://doi.org/10.1016/0009-2509(78)80059-1.

[179] Y. Hu, B.R. Lee, A.K. Sum, Universal correlation for gas hydrates suppression temperature of inhibited systems: II. Mixed salts and structure type, AIChE J. 64 (2018) 2240–2250. https://doi.org/10.1002/aic.16116.

[180] S. Adisasmito, R.J. Frank, E.D. Sloan, Hydrates of Carbon Dioxide and Methane Mixtures, J. Chem. Eng. Data. 36 (1991) 68–71.

[181] W.M. Deaton, E.M.J. Frost, Gas Hydrates and Their Relation to the Operation of Natural-Gas Pipe Lines, U.S. Bur. Mines Monogr. 8 (1946) 101.

[182] T.J. Galloway, W. Ruska, P.S. Chappelear, R. Kobayashi, Experimental Measurement of Hydrate Numbers for Methane and Ethane and Comparison with Theoretical Values, Ind. Eng. Chem., Fundam. 9 (1970) 237–243.

[183] J. Jhaveri, D.B. Robinson, Hydrates in the MethaneyNitrogen System, Can. J. Chem. Eng. 4 (1980) 75–78.

[184] A.H. Mohammadi, B. Tohidi, A Novel Predictive Technique for Estimating the Hydrate Inhibition Effects of Single and Mixed Thermodynamic Inhibitors, Can.

J. Chem. Eng. 83 (2005) 951–961.

[185] T. Nakamura, T. Makino, T. Sugahara, K. Ohgaki, Stability boundaries of gas hydrates helped by methane — structure-H hydrates of methylcyclohexane and cis -1 , 2-dimethylcyclohexane, Chem. Eng. Sci. 58 (2003) 269–273.

[186] J.L. Thakore, G.D. Holder, Solid-Vapor Azeotropes in Hydrate-Forming Systems, (1987) 462–469.

[187] F. V. Zhurko, A.Y. Manakov, V.I. Kosyakov, Formation of gas hydrates in the systems methane-water-ROH (ROH=ethanol, n-propanol, i-propanol, i-butanol), Chem. Eng. Sci. 65 (2010) 900–905. https://doi.org/10.1016/j.ces.2009.09.040.

[188] S.D. Larson, Phase Studies of the Two-Component Carbon Dioxide-Water System, Involving the Carbon Dioxide Hydrate, University of Illinois, 1955.

[189] D.B. Robinson, B.R. Mehta, Hydrate formation in systems containing methane, hydrogen, sulphide, and carbon dioxide, J. Can. Pet. Technol. 10 (1940) 33.

[190] V.K. Verma, Gas Hydrates from Liquid Hydrocarbon–Water Systems, University of Michigan, University Microfilms, 1974.

[191] H. Kubota, K. Shimizu, Y. Tanaka, T. Makita, Thermodynamic properties of R13 (CHF3), R152a (C2H4F2), and propane hydrates for desalination of sea water, J. Chem. Eng. Japan. 17 (1984) 423–429.

[192] S.L. Patil, Measurements of Multiphase Gas Hydrates Phase Equilibria: Effect of Inhibitors and Heavier Hydrocarbon Components, University of Alaska, 1987.

[193] G.D. Holder, G.C. Grigoriou, Hydrate dissociation pressures of (methane + ethane + water) Existence of a locus of minimum pressures, J. Chem. Thermodyn. A-150 (1980) 1093–1104.

[194] Y. Hu, B.R. Lee, A.K. Sum, Universal correlation for gas hydrates suppression temperature of inhibited systems: I. Single salts, AIChE J. 63 (2017) 5111–5124. https://doi.org/10.1002/aic.15846.

[195] C.D. Ruppel, Gas Hydrate in Nature, U.S. Geol. Surv. Fact Sheet (2018) 4. https://doi.org/https://doi.org/10.3133/fs20173080.

[196] Q. Nasir, H. Suleman, Y.A. Elsheikh, A review on the role and impact of various

additives as promoters/ inhibitors for gas hydrate formation, J. Nat. Gas Sci. Eng. (2020) 103211. https://doi.org/10.1016/j.jngse.2020.103211.

[197] Z.R. Chong, S. Hern, B. Yang, P. Babu, P. Linga, X. Li, Review of natural gas hydrates as an energy resource : Prospects and challenges q, Appl. Energy. 162 (2016) 1633–1652. https://doi.org/10.1016/j.apenergy.2014.12.061.

[198] K. Yamamoto, X.X. Wang, M. Tamaki, K. Suzuki, The second o ff shore production of methane hydrate in the Nankai Trough and gas production behavior from a heterogeneous methane hydrate reservoir, R. Soc. Chem. 9 (2019) 25987–26013. https://doi.org/10.1039/c9ra00755e.

[199] R. Braga, R.S. Iglesias, C. Romio, D. Praeg, D.J. Miller, A. Viana, J.M. Ketzer, Modelling methane hydrate stability changes and gas release due to seasonal oscillations in bottom water temperatures on the Rio Grande cone, offshore southern Brazil, Mar. Pet. Geol. 112 (2019) 104071. https://doi.org/10.1016/j.marpetgeo.2019.104071.

[200] C. Cheng, F. Wang, Y. Tian, X. Wu, J. Zheng, J. Zhang, L. Li, P. Yang, J. Zhao, Review and prospects of hydrate cold storage technology, Renew. Sustain. Energy Rev. 117 (2020) 109492. https://doi.org/10.1016/j.rser.2019.109492.

[201] M.N. Khan, P. Warrier, C.J. Peters, C.A. Koh, Advancements in hydrate phase equilibria and modeling of gas hydrates systems, Fluid Phase Equilib. 463 (2018) 48–61. https://doi.org/10.1016/j.fluid.2018.01.014.

[202] C.L. Bassani, A.M. Melchuna, A. Cameira, J. Herri, R.E.M. Morales, A.K. Sum, A Multiscale Approach for Gas Hydrates Considering Structure , Agglomeration , and Transportability under Multiphase Flow Conditions : I . Phenomenological Model, Ind. Eng. Chem. Res. 58 (2019) 14446−14461. https://doi.org/10.1021/acs.iecr.9b01841.

[203] G. Song, Y. Li, W. Wang, K. Jiang, Z. Shi, S. Yao, Numerical simulation of pipeline hydrate particle agglomeration based on population balance theory, J. Nat. Gas Sci. Eng. 51 (2018) 251–261. https://doi.org/10.1016/j.jngse.2018.01.009.

[204] Y. Sun, S. Jiang, S. Li, G. Zhang, W. Guo, Growth kinetics of hydrate formation from water – hydrocarbon system, Chinese J. Chem. Eng. 27 (2019) 2164–2179.

https://doi.org/10.1016/j.cjche.2019.03.022.

[205] V.W.S. Lim, P.J. Metaxas, P.L. Stanwix, M.L. Johns, D. Crosby, Z.M. Aman, E.F. May, Gas Hydrate Formation Probability and Growth Rate as a Function of Kinetic Hydrate Inhibitor (KHI) Concentration, Chem. Eng. J. 388 (2020) 124177. https://doi.org/10.1016/j.cej.2020.124177.

[206] C.L. Bassani, A.K. Sum, J. Herri, R.E.M. Morales, A. Cameira, A Multiscale Approach for Gas Hydrates Considering Structure , Agglomeration , and Transportability under Multiphase Flow Conditions : II . Growth Kinetic Model, Ind. Eng. Chem. Res. 59 (2020) 2123–2144. https://doi.org/10.1021/acs.iecr.9b04245.

[207] I.A. De Oliveira, A.G. Barreto, F.W. Tavares, A.K. Sum, Phase Equilibria Data and Thermodynamic Analysis for Liquid − Hydrate − Vapor (LHV) with High Ethanol Concentrations, J. Chem. Eng. Data. (2019). https://doi.org/10.1021/acs.jced.9b00691.

[208] A. Vignes, Diffusion in binary solutions: Variation of Diffusion Coefficient with Composition, Ind. Eng. Chem. Fundam. 5 (1966) 189–199. https://doi.org/10.1021/i160018a007.

[209] B.J. Jahne, G. Heinz, W. Dietrich, Measurment of the diffusion coefficients of sparkling soluble gases in water, J. Geophys. Res. 92 (1987) 10767–10776. https://doi.org/10.1029/JC092iC10p10767.

[210] B.E. Polling, J.M. Prausnitz, J.P. O'Connell, The properties of gases and liquids, 1st ed., McGRAW-HILL, New York, 2001.

[211] D. Ramkrishna, Population balances, 1st ed., Academic Press, Indiana, 2000. https://doi.org/10.1016/B978-012576970-9/50000-X.

[212] B. V Balakin, A.C. Hoffmann, P. Kosinski, Population Balance Model for Nucleation , Growth , Aggregation , and Breakage of Hydrate Particles in Turbulent Flow, AIChE J. 56 (2010). https://doi.org/10.1002/aic.

[213] T. Uchida, T. Hirano, T. Ebinuma, H. Narita, K. Gohara, S. Mae, Raman Spectroscopic Determination of Hydration Number of Methane Hydrates, AIChE J. 45 (1999) 2641–2645.

[214] H. Henley, A. Lucia, Journal of Natural Gas Science and Engineering Constant pressure Gibbs ensemble Monte Carlo simulations for the prediction of structure I gas hydrate occupancy, J. Nat. Gas Sci. Eng. 26 (2015) 446–452. https://doi.org/10.1016/j.jngse.2015.05.038.

[215] J. Qin, W.F. Kuhs, A. Kristallographie, Quantitative Analysis of Gas Hydrates Using Raman Spectroscopy, 00 (2013). https://doi.org/10.1002/aic.

[216] W.F. Kuhs, B. Chazallon, A. Klapprothl, F. Pauer, Filling-Isotherms in Clathrate-Hydrates, Rev. High Press. Sci. Technol. 7 (1998) 1147–1149.

[217] A.Y. Manakov, N. V Penkov, T. V Rodionova, A.N. Nesterov, E.E. Fesenko Jr, Kinetics of formation and dissociation of gas hydrates, Russ. Chem. Rev. 86 (2017) 845–869. https://doi.org/10.1070/RCR4720.

[218] M.S. Khatami, A. Shahsavand, Application Of Population Balance Theory For Dynamic Modeling Of Methane And Ethane Hydrate Formation Processes, Energy & Fuels. 32 (2018) 8131–8144. https://doi.org/10.1021/acs.energyfuels.8b01351.

[219] A.K. Sum, Gas Hydrates in Flow Assurance, in: Workshop, Curitiba - PR/Brazil, 2003.

[220] S. Renato, E. Vinicius, R. Castro, A. Teixeira, R. Rosa, T. Rodrigues, S. Renato, Effects of ethanol on the performance of kinetic hydrate inhibitors, Fluid Phase Equilib. 476 (2018) 112–117. https://doi.org/10.1016/j.fluid.2018.07.036.

[221] H. Henley, A. Lucia, Journal of Natural Gas Science and Engineering Constant pressure Gibbs ensemble Monte Carlo simulations for the prediction of structure I gas hydrate occupancy, J. Nat. Gas Sci. Eng. 26 (2015) 446–452. https://doi.org/10.1016/j.jngse.2015.05.038.

[222] H.G. Rackett, Equation of State for Saturated Liquids, J. Chem. Eng. Data. 15 (1970) 514–517. https://doi.org/10.1021/je60047a012.

[223] F.S. Mjalli, K. Shahbaz, I.M. Alnashef, Thermochimica Acta Modi fi ed Rackett equation for modelling the molar volume of deep eutectic solvents, Thermochim. Acta. 614 (2015) 185–190. https://doi.org/10.1016/j.tca.2015.06.026.

[224] T. Yamada, R.D. Gunn, Saturated Liquid Molar Volumes . The Rackett Equation,

J. Chem. Eng. Data. 18 (1973) 234–236. https://doi.org/10.1021/je60057a006.

[225] O. Iulian, I. Nita, O. Ciocirlan, M. Catrinciuc, A. Fedeles, Property Prediction for Binary and Ternary Systems with Water , 1 , 4-Dioxane , Ethyleneglycol and Diethyleneglycol, REV. CHIM. 60 (2009) 7–10.

[226] J. Wang, V.N. Kabadi, Generalized Method for Prediction of Saturated Liquid Volumes Using Van der Waals Volumes, AIChE J. 42 (1996) 595–598.

[227] H.J.E. Dobson, The partial pressures of aqueous ethyl alcohol, J. Chem. Soc. Trans. 127 (1925) 2866–2873. https://doi.org/10.1039/ct9252702866.

[228] J. Gmehling, U. Onken, W. Arlt, P. Grenzheuser, U. Weidlich, B. Kolbe, J. Rarey, VAPOR-LIQUID EQUILIBRIUM DATA COLLECTION, 1st ed., DECHEMA, Chemische Technik und Biotechnologie, 1977.

[229] K. Kuriharaj, T. Minoura, K. Takedaj, Water, Methanol + Water, and Ethanol Isothermal Vapor-Liquid Equilibria for Methanol + Ethanol + Water, J. Chem. Eng. Data. 40 (1996) 679–684.

[230] D.F. Othmer, W.P. Moeller, S.W. Englund, R.G. Christopher, Composition of Vapors from Boiling Binary Solutions - Recirculation-type Still and Equilibria under Pressure for Ethyl Alcohol-Water System, Ind. Eng. Chem. 43 (1951) 707–711. https://doi.org/10.1021/ie50495a038.

[231] R.C. Pemberton, C.J. Mash, Thermodynamic properties of aqueous mixtures II . Vapour pressuresand excessGibbsenergies for water + ethanol at 303 . 15 to 363 . 15 K determined by an accurate static method, J. Chem. Thermodyn. 10 (1978) 867–888.

[232] R.C. Phutela, Z.S. Kooner, D. V Fenby, Vapour Pressure Study of Deuterium Exchange Reactions in Water-Ethanol Systems : Equilibrium Constant Determination, Aust. J. Chem. 32 (1979) 2353–2362.

[233] M. Schwaab, E.C. Biscaia, J.L. Monteiro, J.C. Pinto, Nonlinear parameter estimation through particle swarm optimization, Chem. Eng. Sci. 63 (2008) 1542–1552. https://doi.org/10.1016/j.ces.2007.11.024.

[234] M. Frost, E. Karakatsani, N. Von Solms, D. Richon, G.M. Kontogeorgis, Vapor − Liquid Equilibrium of Methane with Water and Methanol . Measurements and

Modeling, J. Chem. Eng. Data. 59 (2013) 961–967.

[235] S.O. Yang, S.H. Cho, H. Lee, C.S. Lee, Measurement and prediction of phase equilibria for water + methane in hydrate forming conditions, Fluid Phase Equilib. 185 (2001) 53–63.

[236] J. Qin, R.J. Rosenbauer, Z. Duan, Experimental Measurements of Vapor – Liquid Equilibria of the H 2 O + CO 2 + CH 4 Ternary System, J. Chem. Eng. Data. 53 (2008) 1246–1249.

[237] A. Chapoy, C. Coquelet, D. Richon, Corrigendum to " Revised solubility data and modeling of water in the gas phase of the methane / water binary system at temperatures from 283 . 08 to 318 . 12 K and pressures up to 34 . 5 MPa " [Fluid Phase Equilibria 214 (2003) 101 – 117], Fluid Phase Equilib. 230 (2005) 210–214. https://doi.org/10.1016/j.fluid.2004.07.005.

[238] A.H. Mohammadi, A. Chapoy, B. Tohidi, D. Richon, Gas Solubility : A Key to Estimating the Water Content of Natural Gases, Ind. Eng. Chem. Res. 45 (2006) 4825–4829.

[239] O.L. Culberson, D. Co, J.J.M. Jr, Phase Equilibria In Hydrocarbon-Water Systems IV - Vapor-Liquid Equilibrium Constants in the Methane-Water and Ethane-Water Systems, Pet. Trans. AIME. 192 (1951) 297–300.

[240] Y.S. Kim, S.K. Ryu, S.O. Yang, C.S. Lee, Liquid Water - Hydrate Equilibrium Measurements and Unified Predictions of Hydrate-Containing Phase Equilibria for Methane , Ethane , Propane , and Their Mixtures, Ind. Eng. Chem. Res. 42 (2003) 2409–2414.

[241] J. Kiepe, S. Horstmann, K. Fischer, J. Gmehling, Experimental Determination and Prediction of Gas Solubility Data for Methane + Water Solutions Containing Different Monovalent, Ind. Eng. Chem. Res. 42 (2003) 5392–5398.

[242] W. Lu, I.M. Chou, R.C. Burruss, Determination of methane concentrations in water in equilibrium with sI methane hydrate in the absence of a vapor phase by in situ Raman spectroscopy, Geochim. Cosmochim. Acta. 72 (2008) 412–422. https://doi.org/10.1016/j.gca.2007.11.006.

[243] J.M. Prausnitz, R.N. Lichtenthaler, E.G. De Azevedo, Molecular

thermodynamics of fluid-phase equilibria, 3rd ed., Prentice Hall PTR, New Jersey, 1999. https://doi.org/10.1016/0021-9614(70)90078-9.

[244] J.M. Prausnitz, F.H. Shair, Thermodynamic Correlation of G as Solubilities, AIChE J. 7 (1961) 682–687.

[245] R. Lemoine, B.I. Morsi, An algorithm for predicting the hydrodynamic and mass transfer parameters in agitated reactors, Chem. Eng. J. 114 (2005) 9–31. https://doi.org/10.1016/j.cej.2005.08.015.

[246] I.R. Krichevsky, J.S. Kasarnovsey, Thermodynamical Calculations of Solubilities of Nitrogen and Hydrogen in Water at High Pressures, Contrib. from D. I. Mendeleyeff Chem. Inst. (1935) 2168–2171.

[247] A. Chianese, H.J.. Kramer, Industrial Crystallization Process Monitoring and Control, 1st ed., Wiley-VCH, Weinheim, 2012.

[248] L.R. Petzold, A description of DASSL : A Differential/Algebraic System Solver, in: IMACS World Congr., Montreal, Canada, 1982.

[249] M. Mooney, THE VISCOSITY OF A CONCENTRATED SUSPENSION OF SPHERICAL PARTICLES, J. Colloid Sci. 6 (1951) 162–170.

[250] A. Firoozabadi, H.J.J. Ramey, Surface-Tension of Water-Hydrocarbon Systems at Reservoir Conditions, J. Can. Pet. Technol. 27 (1988) 41–48.

[251] S. Taniguchi, S. Kawaguchi, A. Kikuchi, Fluid flow and gas – liquid mass transfer in gas-injected vessels, Appl. Math. Model. 26 (2002) 249–262.

[252] P.T. Spicer, S.E. Pratsinis, Coagulation and Fragmentation: Universal Steady-State Particle-Size Distribution, AIChE J. 42 (1996) 1612–1620. https://doi.org/10.1002/aic.690420612.

[253] T. Ukai, D. Kodama, J. Miyazaki, M. Kato, Solubility of methane in alcohols and saturated density at 280.15 K, J. Chem. Eng. Data. 47 (2002) 1320–1323. https://doi.org/10.1021/je020108p.

[254] K. Suzuki, H. Sue, M. Itou, R.L. Smith, H. Inomata, K. Arai, S. Saito, Isothermal Vapor-Liquid Equilibrium Data for Binary Systems at High Pressures: Carbon Dioxide-Methanol, Carbon Dioxide-Ethanol, Carbon Dioxide-1-Propanol,

Methane-Ethanol, Methane-1-Propanol, Ethane-Ethanol, and Ethane-1-Propanol Systems, J. Chem. Eng. Data. 35 (1990) 63–66. https://doi.org/10.1021/je00059a020.

[255] F.S. Mjalli, K. Shahbaz, I.M. Alnashef, Thermochimica Acta Modi fi ed Rackett equation for modelling the molar volume of deep eutectic solvents, Thermochim. Acta. 614 (2015) 185–190. https://doi.org/10.1016/j.tca.2015.06.026.

Appendix 1. Supporting information for Chapter 2

Table S1 – Literature THF/H_2O vapor-liquid equilibria experimental data.

Reference	**Experimental data of VLE of THF/H_2O system**		
Matouš et al. [34]	**T = 343.15/K**		
	***p*/kPa**	**THF mole fraction in liquid phase, x**	**THF mole fraction in vapor phase, y**
	102.05	0.032	0.697
	120.59	0.072	0.745
	122.71	0.141	0.749
	122.66	0.241	0.75
	123	0.335	0.751
	123.35	0.429	0.754
	124.32	0.558	0.758
	125.26	0.625	0.768
	126.22	0.754	0.79
	126.44	0.8	0.805
	126.06	0.854	0.83
	125.26	0.886	0.855
	123.39	0.928	0.893
	120.1	0.966	0.945
Signer et al. [35]	**T = 298.15/K**		
	p/kPa	**THF mole fraction in liquid phase, x**	**THF mole fraction in vapor phase, y**
	15.47	0.05	0.805
	19.32	0.1	0.847
	20.34	0.15	0.856

	20.72	0.2	0.859
	20.92	0.25	0.86
	21.04	0.3	0.862
	21.14	0.35	0.863
	21.24	0.4	0.863
	21.33	0.45	0.864
	21.42	0.5	0.866
	21.54	0.55	0.868
	21.64	0.6	0.869
	21.74	0.65	0.872
	21.84	0.7	0.874
	21.96	0.75	0.877
	22.05	0.8	0.88
	22.16	0.85	0.887
	22.25	0.9	0.9
	22.22	0.95	0.923
	21.6	1,000	1,000
Condition	**Experimental data of ID of THF/H_2O system**		
Infinite dilution of THF in H_2O	***p*= 101.33/kPa**		
	T/K	**Coefficient of activity, $\gamma_{i,k}^{\infty}$**	**Ref.**
	293.15	16.6	[40]
	298.15	17	[40]
	308.15	23.5	[40]
	313.15	20.8	[40]
	323.15	32.8	[40]
Infinite dilution of H_2O in THF	***p*= 101.33/kPa**		
	T/K	**Coefficient of activity, $\gamma_{i,k}^{\infty}$**	**Ref.**

	308.35	11.1	[41]
	317.65	10.4	[41]
	328.05	9.8	[41]
	338.05	9.4	[41]
	343.15	7.8	[42]

Table S2 – Literature THF/H_2O hydrate-liquid-vapor equilibria (HLE) experimental data.

Experimental data of HLE of THF/H_2O system		
Reference	***p*= 101.33/kPa**	
	T/K	**THF mole fraction in liquid phase, x**
Makino et al. [5]	272.27	0.011
	275.73	0.024
	277.26	0.045
	277.45	0.056
	277.37	0.065
	276.9	0.09
	276.21	0.13
	275.14	0.18
	275.02	0.188
Anderson et al. [6]	272.4	0.01
	274.1	0.015
	276.8	0.027
	277.6	0.035
	278	0.043
	278.2	0.056
	278.1	0.059
Delahaye et al. [7]	275.79	0.015
	276.39	0.019

	276.45	0.026
	276.91	0.027
	277.09	0.033
	277.57	0.04
	277.81	0.052
	277.88	0.056
	277.86	0.062
	277.69	0.073
	277.73	0.081
	277.51	0.098
Otake et al. [14]	272.06	0.01
	273.2	0.013
	274.95	0.019
	275.9	0.026
	276.82	0.03
	276.99	0.031
	276.97	0.036
	277.09	0.037
	277.32	0.041
	277.48	0.048
	277.65	0.055
	277.46	0.061
	277.57	0.062
	277.57	0.066
	277.32	0.077
	277.76	0.097
Hanley et al. [15]	273.69	0.017
	276.49	0.03

	278.1	0.066
	276.99	0.129
Leaist et al. [16]	272.41	0.01
	274.1	0.015
	276.8	0.027
	277.61	0.035
	278	0.043
	278.21	0.055
	278.14	0.059
Dyadin et al. [17]	272.16	0.014
	276.6	0.029
	277.69	0.039
	278.14	0.051
	278.14	0.059
	278.14	0.062
	277.94	0.07
	277.86	0.073
	277.75	0.08
	277.65	0.088
	277.34	0.095
	276.72	0.133
	276.14	0.159
	275.75	0.2

Appendix 2. Supporting information for Chapter 3

Table S3 - Calculated data properties from the liquid-hydrate-vapor equilibrium data for H_2O + EtOH + CH_4 system.

CH_4 Hydrate Data Properties							
Concentration	**1-R^2**	**ΔH_{diss} / kJ mol^{-1}**	**RSD ΔH_{diss}**	**n[a]**	**β[b]**	**RSD $\Delta T/T_0T$**	**References**
63 wt.%	0.09 %	60.56	2.75 %	3.71	0.510	4.77 %	Anderson et al. [10]
52.3 wt.%	0.26 %	57.40	2.61 %	4.20	0.608	6.28 %	Anderson et al. [10]
44.6 wt.%	1.65 %	53.15	9.82 %	5.01	0.784	3.29 %	Zhurko et al. [187]
39.6 wt.%	0.59 %	57.52	2.42 %	5.38	0.778	2.13 %	Zhurko et al. [187]
30 wt.%	0.03 %	61.53	4.39 %	5.73	0.774	2.49 %	Anderson et al. [10]
26.2 wt.%	0.13 %	61.91	5.04 %	6.48	0.870	4.08 %	Zhurko et al. [187]
20 wt.%	0.28 %	63.37	7.52 %	5.90	0.774	5.79 %	Zhurko et al. [187]
15 wt.%	0.42 %	65.21	10.64 %	5.19	0.662	17.29 %	Kobayashi et al. [169]
13.2 wt.%	2.43 %	61.70	4.68 %	5.75	0.774	4.43 %	Anderson et al. [10]
10 wt.%	0.20 %	53.70	8.88 %	5.98	0.925	5.46 %	Mohammadi et al. [52]
5 wt.%	0.06 %	52.29	11.28 %	6.70	1.064	6.79 %	Mohammadi et al. [52]

[a] n is the hydration number

[b] β $(= -nR/\Delta H_{diss})$

Table S4 - The average absolute deviation (AAD) for the CH_4 hydrate phase equilibria data with ethanol for the three tested models.

CH_4 Hydrate Data AAD					
Concentration	**HLS correlation** [120,176,194]	**PVTsim®**		**Thermodynamic model Oliveira et al.** [123]	**References**
	AAD *T*/K	**AAD *T*/K**	**AAD *P*/bar**	**AAD *P*/bar**	
63 wt.%	8.40	0.24	6.81	155.23	Anderson et al. [10]
52.3 wt.%	4.24	0.28	9.45	35.32	Anderson et al. [10]
44.6 wt.%	0.53	2.09	17.58	19.06	Zhurko et al. [187]
39.6 wt.%	0.33	1.11	10.11	13.04	Zhurko et al. [187]
30 wt.%	0.51	0.33	4.59	7.84	Anderson et al. [10]
26.2 wt.%	0.62	1.10	10.29	11.72	Zhurko et al. [187]
20 wt.%	0.42	0.64	7.25	3.40	Zhurko et al. [187]
15 wt.%	0.73	0.14	4.11	4.87	Kobayashi et al. [169]
13.2 wt.%	0.37	0.50	4.90	5.00	Anderson et al. [10]
10 wt.%	0.25	0.40	1.79	1.30	Mohammadi et al. [52]
5 wt.%	0.34	0.49	2.11	1.61	Mohammadi et al. [52]

[a]AAD $T \leq 0.5$ K

[b] AAD $P \leq 2$ bar

Table S5 - Calculated data properties from the liquid-hydrate-vapor equilibria data for H_2O + EtOH + CO_2 system.

CO_2 Hydrate Data Properties							
Concentration	**1-R^2**	**ΔH_{diss} / kJ mol^{-1}**	**RSD ΔH_{diss}**	**n[a]**	**β[b]**	**RSD $\Delta T/T_0T$**	**References**
20 wt.%	1.05 %	71.30	4.90 %	7.81	0.911	2.36 %	Maekawa [172]
15 wt.%	1.00 %	76.54	2.08 %	6.92	0.751	2.13 %	Guembaroski et al. [171], Ferrari et al. [170]
10 wt.%	1.20 %	73.89	1.45 %	7.48	0.841	6.27 %	Mohammadi et al. [52], Maekawa [172], Ferrari et al. [170]
5 wt.%	0.16 %	74.72	0.35 %	6.80	0.756	10.95 %	Mohammadi et al. [52]
2 wt.%	0.15 %	78.45	4.63 %	7.18	0.760	30.47 %	Guembaroski et al. [171]

[a] n is the hydration number

[b] β $(= -nR/\Delta H_{diss})$

Table S6 - The average absolute deviation (AAD) for the CO_2 hydrate phase equilibria data with ethanol for the three tested models.

CO_2 Hydrate Data AAD					
Concentration	**HLS correlation** [120,176,194]	**PVTsim®**		**Thermodynamic model Oliveira et al.** [123]	**References**
	AAD *T*/K	**AAD *T*/K**	**AAD *P*/bar**	**AAD *P*/bar**	
20 wt.%	1.23	0.83	2.45	2.63	Maekawa [172]
15 wt.%	0.09	0.32	1.37	1.55	Guembaroski et al. [171], Ferrari et al. [170]
10 wt.%	0.32	0.20	0.65	0.63	Mohammadi et al. [52], Maekawa [172], Ferrari et al. [170]
5 wt.%	0.14	0.15	0.56	0.64	Mohammadi et al. [52]
2 wt.%	0.16	0.15	0.41	0.41	Guembaroski et al. [171]

[a]AAD $T \leq 0.5$ K

[b] AAD $P \leq 2$ bar

Table S7 - Calculated data properties from the liquid-hydrate-vapor equilibria data for H_2O + EtOH + C_3H_8 system.

C_3H_8 Hydrate Data Properties							
Concentration	**1-R^2**	**ΔH_{diss} / kJ mol^{-1}**	**RSD ΔH_{diss}**	**n[a]**	**β[b]**	**RSD $\Delta T/T_0T$**	**References**
15 wt.%	0.32 %	123.86	2.31 %	15.77	1.058	1.07 %	Maekawa [172], Mohammadi et al. [52]
10 wt.%	1.95 %	125.09	1.35 %	14.62	0.972	4.75 %	Maekawa [172], Mohammadi et al. [52]
5 wt.%	0.15 %	131.43	3.66 %	15.52	0.981	3.05 %	Maekawa [172]

[a]n is the hydration number

[b] β $(= -nR/\Delta H_{diss})$

Table S8 - The average absolute deviation (AAD) for the C_3H_8 hydrate phase equilibria data with ethanol for the three tested models.

C_3H_8 Hydrate Data AAD					
Concentration	**HLS correlation** [120,176,194]	**PVTsim®**		**Thermodynamic model Oliveira et al.** [123]	**References**
	AAD *T*/K	**AAD *T*/K**	**AAD *P*/bar**	**AAD *P*/bar**	
15 wt.%	0.42	1.06	0.75	0.54	Maekawa [172], Mohammadi et al. [52]
10 wt.%	0.13	0.40	0.30	0.22	Maekawa [172], Mohammadi et al. [52]
5 wt.%	0.05	0.24	0.17	0.06	Maekawa [172]

[a]AAD $T \leq 0.5$ K

[b] AAD $P \leq 2$ bar

Table S9 - Liquid-hydrate-vapor equilibrium data with ethanol of C_2H_6 gas.

C_2H_6 Hydrate Data									
45 wt%		**40 wt%**		**35 wt%**		**26 wt%**		**10 wt%**	
***T*/K**	***P*/bar**	***T*/K**	***P*/bar**	***T*/K**	***P*/bar**	***T*/K**	***P*/bar**	***T*/K**	***P*/bar**
266.55	13.65	266.65	12.40	267.45	11.33	268.05	7.66	273.65	7.24
267.95	15.94	269.05	16.66	269.05	13.57	272.65	13.54	278.85	13.91
270.35	21.89	270.95	22.17	270.65	16.52	276.35	22.21	283.05	26.05
				272.85	22.08				

Table S10 - Calculated data properties from the liquid-hydrate-vapor equilibria data for H_2O + EtOH + C_2H_6 system.

C_2H_6 Hydrate Data Properties							
Concentration	**1-R^2**	**ΔH_{diss} / kJ mol^{-1}**	**RSD ΔH_{diss}**	**n[a]**	**β[b]**	**RSD $\Delta T/T_0T$**	**References**
45 wt.%	0.20 %	76.74	5.52 %	6.05	0.655	1.67 %	This work
40 wt.%	0.33 %	71.05	2.30 %	6.30	0.737	1.34 %	This work
35 wt.%	0.14 %	76.74	5.52 %	7.24	0.785	3.09 %	This work
26 wt.%	0.05 %	73.13	0.56 %	7.28	0.827	2.55 %	This work
10 wt.%	0.34 %	65.92	9.36 %	6.57	0.829	5.28 %	This work, Mohammadi et al. [52]
5 wt.%	0.24 %	72.77	0.06 %	7.59	0.867	10.89 %	Mohammadi et al. [52]

[a] n is the hydration number

[b] β $(= -nR/\Delta H_{diss})$

Table S11 - The average absolute deviation (AAD) for the C_2H_6 hydrate phase equilibria data with ethanol for the three tested models.

C_2H_6 Hydrate Data AAD					
Concentration	**HLS correlation** [120,176,194]	**PVTsim®**		**Thermodynamic model Oliveira et al.** [123]	**References**
	AAD *T*/K	**AAD *T*/K**	**AAD *P*/bar**	**AAD *P*/bar**	
45 wt.%	1.06	0.11	0.26	2.41	This work
40 wt.%	0.16	1.04	2.26	4.03	This work
35 wt.%	0.60	1.12	2.14	4.26	This work
26 wt.%	0.67	0.69	1.23	2.51	This work
10 wt.%	0.27	0.20	0.46	0.60	This work, Mohammadi et al. [52]
5 wt.%	0.16	0.16	0.18	0.15	Mohammadi et al. [52]

[a]AAD $T \leq 0.5$ K

[b] AAD $P \leq 2$ bar

Table S12 - Liquid-hydrate-vapor equilibrium data with ethanol of the gas mixture of 73.8 wt.% CH_4 and 26.2 wt.% C_2H_6.

73.8 mol% CH_4/26.2 mol% C_2H_6 Hydrate Data									
40 wt%		**30 wt%**		**25 wt%**		**9 wt%**		**0 wt%**	
***T*/K**	***P*/bar**	***T*/K**	***P*/bar**	***T*/K**	***P*/bar**	***T*/K**	***P*/bar**	***T*/K**	***P*/bar**
268.75	26.39	268.45	18.24	268.15	15.24	273.25	13.82	275.55	12.65
271.75	37.12	273.45	30.45	274.65	29.82	278.85	26.05	287.15	51.18
273.95	47.49	277.65	50.38	278.65	50.25	284.05	49.84		

Table S13 - Calculated data properties from the liquid-hydrate-vapor equilibria data for H_2O + EtOH + CH_4/C_2H_6 system.

73.8 mol% CH_4/26.2 mol% C_2H_6 Hydrate Data Properties							
Concentration	**1-R^2**	**ΔH_{diss} / kJ mol^{-1}**	**RSD ΔH_{diss}**	**n[a]**	**β[b]**	**RSD $\Delta T/T_0T$**	**References**
40 wt.%	0.00 %	57.72	2.58 %	4.47	0.644	1.34 %	This work
30 wt.%	0.20 %	56.93	3.91 %	4.87	0.711	3.15 %	This work
25 wt.%	0.41 %	58.46	1.33 %	5.46	0.778	2.97 %	This work
9 wt.%	0.22 %	63.88	7.82 %	5.67	0.738	3.25 %	This work

[a] n is the hydration number

[b] β $(= -nR/\Delta H_{diss})$

Table S14 - The average absolute deviation (AAD) for the gas mixture of 73.8 mol% CH_4 and 26.2 mol% C_2H_6 hydrate phase equilibria data with ethanol for the two tested models.

73.8 mol% CH_4/26.2 mol% C_2H_6 Hydrate Data AAD				
Concentration	**HLS correlation** [120,176,194]	**PVTsim®**		**References**
	AAD T/K	**AAD T/K**	**AAD P/bar**	
40 wt.%	1.02	0.92	4.06	This work
30 wt.%	0.31	0.62	2.45	This work
25 wt.%	0.27	0.22	0.81	This work
9 wt.%	0.24	0.38	0.87	This work

[a] AAD $T \leq 0.5$ K

[b] AAD $P \leq 2$ bar

S.1 Gas hydrate equilibrium model for systems containing ethanol.

The model used here to calculate the equilibrium pressure of the gas hydrate studied systems, with or without addictive, was based on Oliveira et al. [123].

In Figure S1, the thermodynamic model fitted to calculate the equilibrium pressure of the Gas + H_2O + Ethanol systems is shown in the block diagram. In this proposal will be adopted the NRTL excess Gibbs energy model (liquid phase), the Peng-Robinson equation of state (vapor phase) and the theory of van der Waals and Platteeuw [98] and Holder et al.[101], with the Kihara potential (hydrate phase).

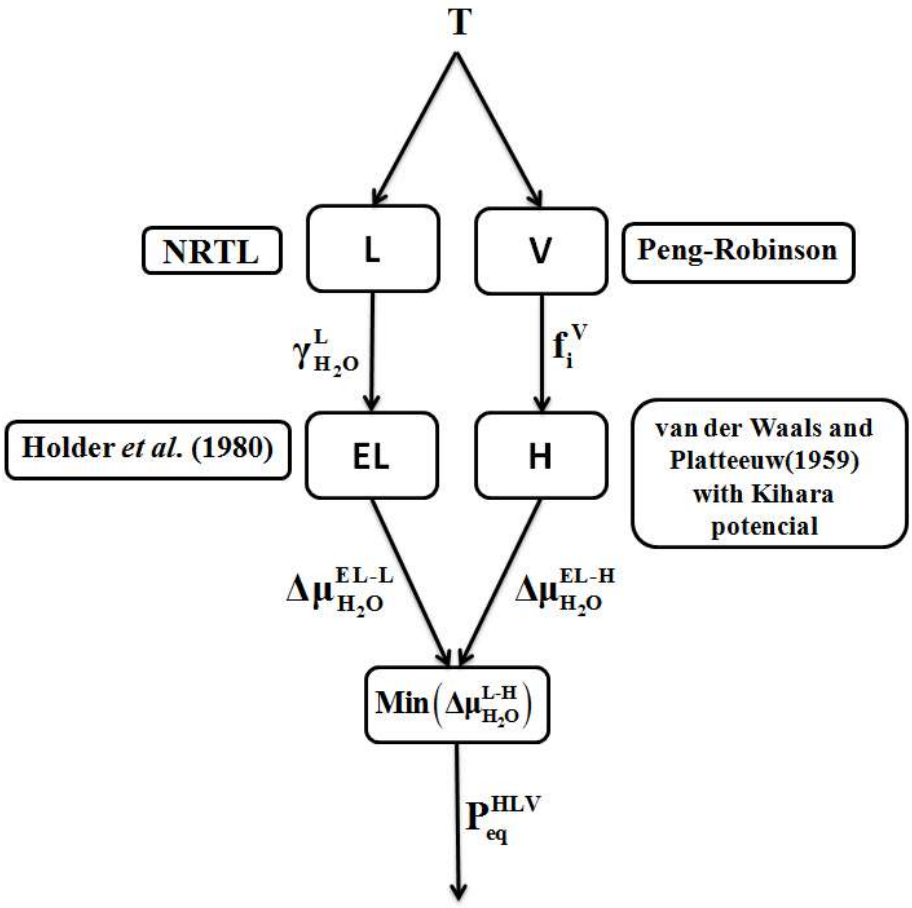

Figure S1 - Block diagram of the thermodynamic model used to calculate the LHV equilibrium pressure of systems with additives [123].

The parameterization of this model for the systems Gas + H_2O and Gas + H_2O + THF was carried out in the work of Oliveira *et al* [123] and the parameterization of the

same model for the Gas + H_2O + Ethanol system as a inhibited system is presented in this work.

S.1.1 Liquid Phase

In this work, we investigated the influence of the model and the parameters that describe the non-ideality of the liquid phase, specifically the NRTL excess Gibbs free energy model, in the calculation of liquid-vapor equilibrium (LVE) and infinite dilution (ID) of H_2O + Ethanol (Dalton and Raoult laws) and consequently in the calculation of single gas hydrate phase equilibria with ethanol.

A large set of LVE experimental data for the H_2O + Ethanol system was raised from literature [227–232]. The binary interaction parameters were estimated by the equation (S1), for T_{ref} = 283.15 K. The coefficients of the binary interaction parameters were estimated in the conditions of LVE at T = 298.15, 323.15, 343.15 and 363.15 K and infinite dilution at P = 1 atm[152,157].

$$\tau_{i,\mathrm{j}} = A_{i,\mathrm{j}} + B_{i,\mathrm{j}}\left(\frac{T_{ref}}{T} - 1\right) \tag{S1}$$

The activity coefficients of the excess Gibbs free energy model, NRTL, for a binary mixture of Ethanol (1) + H_2O (2) were calculated by equation (S2), for $c = 2$.

$$\gamma_i = \exp\left(\frac{\sum_{j=1}^{c} x_j \tau_{j,i} G_{j,i}}{\sum_{k=1}^{c} x_k G_{\mathrm{k},i}}\right) + \sum_{j=1}^{c} \frac{x_j G_{\mathrm{i,j}}}{\sum_{k=1}^{c} x_k G_{\mathrm{k,j}}}\left(\tau_{i,j} - \frac{\sum_{m=1}^{c} x_m \tau_{\mathrm{m,j}} G_{\mathrm{m,j}}}{\sum_{k=1}^{c} x_k G_{\mathrm{k,j}}}\right) \tag{S2}$$

The non-randomness factor, α, was considered symmetric and $G_{i,\mathrm{j}} = \exp(\alpha\tau_{i,\mathrm{j}})$.

S.1.2 Vapor Phase

The fugacity coefficient of the gas in the vapor phase, considered pure, was modeled according to the Peng-Robinson equation of state for pure substances.

S.1.3 Hydrate Phase

The hydrate phase was modeled with the theory of van der Waals and Platteeuw [98], which presents an expression for the difference in chemical potential of water between the hydrate phase and the hypothetical phase of the empty hydrate lattice, equation (S3). ν_j is the number of cavities of type j per water molecule in the unit cell, $CL_{i,j}$ is Langmuir constants of the guest molecule i in the cavity of type j, and f_i^H is the fugacity of the guest molecule i in the hydrate phase.

$$\frac{\Delta\mu_{H_2O}^{EL-H}}{RT} = \sum_j \nu_j \ln\left(1 - \sum_i \frac{CL_{i,j} f_i^H}{1 + CL_{i,j} f_i^H}\right) \tag{S3}$$

The criterion of fugacity equality is adopted for the gas hydrate formers. It will be adopted the hypothesis of gas present only in the vapor phase and ethanol present only in the liquid phase. For the gaseous hydrate former, the fugacity equality will be assumed between the hydrate phase and the vapor phase. Also, it is considered that ethanol acts only as an inhibitor altering water activity, without participation in the hydrate structure. This criterion appears embedded in the van der Waals and Platteeuw [98] model.

Therefore, the fugacity of the gas in the hydrate phase is equal to the vapor phase, as explained in the equilibrium criterion, and calculated by equation (S4), adopting the hypothesis of the pure gas in the vapor phase, y_i = 1,0.

$$f_i^V(T, \mathrm{P}, \mathbf{y}) = \hat{\phi}_i(T, \mathrm{P}, \mathbf{y}) P \; y_i \tag{S4}$$

According to the Lennard-Jones-Devonshire theory, the Langmuir constants ($CL_{i,j}$), which quantify the attractiveness between the guest molecule (i) and the host structure, that can be calculated with spherical symmetry making use of the Kihara pair interaction potential, equation (S5).

$$CL_{i,j} = \frac{4\pi}{k_B T} \int_0^{R_j - a_i} \exp\left(\frac{-X(r)}{k_B T}\right) r^2 dr$$

$$X(r) = 2Z_j \varepsilon_i \left[\frac{\sigma_i^{12}}{R_j^{11}} \left(\Delta_{10}(r) + \frac{a_i}{R_j} \Delta_{11}(r) \right) - \frac{\sigma_i^{6}}{R_j^{5}} \left(\Delta_4(r) + \frac{a_i}{R_j} \Delta_5(r) \right) \right] \frac{1}{r} \qquad \text{(S5)}$$

$$\Delta_N(r) = \frac{\left[\left(1 - \frac{r}{R_j} - \frac{a_i}{R_j} \right)^{-N} - \left(1 + \frac{r}{R_j} - \frac{a_i}{R_j} \right)^{-N} \right]}{N} \quad N = 4,\ 5,\ 10\ e\ 11.$$

Where σ [Å] is the intermolecular radius of Kihara; a [Å] is the soft radius of the spherical core for the guest component; and ε/k_B [K] is the Kihara's maximum attraction potential. The parameters of this model for the CH_4, CO_2, C_2H_6, C_3H_8 gases were fitted directly to the hydrate-liquid-vapor equilibrium experimental data of the gas and fresh water system [158,180,190–193,181–186,188,189].

The difference of the chemical potential of water in the empty hydrate lattice in relation to the liquid phase can be obtained from the classical thermodynamic theory, equation (S6). Assuming the differences of the constant molar volumes and taking into account the classical thermodynamic theory of enthalpy dependence with the temperature, equation (S7), in detriment of its constancy, and linear dependence of the specific heat on temperature, equation (S8), we obtain the equation (S9):

$$\frac{\Delta\mu_{H_2O}^{EL-L}}{RT} = \frac{\Delta\mu_{H_2O}^{0}}{RT_0} - \int_{T_0}^{T} \frac{\Delta h_{H_2O}^{EL-L}(\mathrm{P}_0)}{RT^2} dT + \int_{P_0}^{P} \frac{\Delta \upsilon_{H_2O}^{EL-L}(T)}{RT} dP - ln(\gamma_{H_2O}^{L} x_{H_2O}^{L}) \qquad \text{(S6)}$$

$$\Delta h_{H_2O}^{EL-L}\left(P_0\right) = \Delta h_{H_2O}^{EL-L}\left(T_0, \mathrm{P}_0\right) + \int_{T_0}^{T} \Delta Cp_{H_2O}^{EL-L}\left(P_0\right) dT \qquad \text{(S7)}$$

$$\Delta Cp_{H_2O}^{EL-L}\left(P_0\right) = \Delta Cp_{H_2O}^{EL-L}\left(T_0, \mathrm{P}_0\right) + q_{H_2O}^{EL-L}\left(T - T_0\right) \qquad \text{(S8)}$$

$$\frac{\Delta\mu_{H_2O}^{EL-L}}{RT} = \frac{\Delta\mu_{H_2O}^{0}}{RT_0} + \frac{\Delta h_{H_2O}^{0}}{R}\left(\frac{1}{T} - \frac{1}{T_0}\right) - \left(\frac{2\Delta Cp_{H_2O}^{0} T_0 + q_{H_2O}^{0}}{2R}\right)\left(\frac{1}{T} - \frac{1}{T_0}\right) + \left(\frac{\Delta Cp_{H_2O}^{0} + q_{H_2O}^{0} T_0}{R}\right) \ln\left(\frac{T_0}{T}\right) - \frac{q_{H_{2\partial}O}^{0}\left(T_0 - T\right)}{2R} + \frac{\Delta \upsilon_{H_2O}^{0}\left(P - P_0\right)}{RT} - \ln(\gamma_{H_2O}^{L} x_{H_2O}^{L}) \qquad \text{(S9)}$$

Where $\Delta\mu_{H_2O}^{0}$ is the chemical potential variation for water in the reference conditions, $\Delta h_{H_2O}^{EL-L}$ the enthalpy change for water between the phases, $\Delta \upsilon_{H_2O}^{EL-L}$ the

variation of the molar volume for water between the phases and the term of non-ideality of the liquid phase, considering the water activity, $a_{H_2O}^{L} = \gamma_{H_2O}^{L} x_{H_2O}^{L}$, is obtained by the NRTL model. Water activity was considered one for systems without additives.

In this work, the pressure and temperature of reference adopted were P_0 = 612,61 Pa and T_0 = 273.15 K, and the macroscopic thermodynamic parameters were those presented in the work of John, Papadopoulos and Holder [105].

The hydrate-liquid-vapor balance criterion is described by the equality between water potentials in both hydrate and liquid phases, given the intermediate phase of the empty hydrate lattice structure (EL).

S.2 Methodology of parameter estimation

The equilibrium of the Gas + H_2O + Ethanol system requires adjustment of the parameters of the NRTL model to the H_2O-Ethanol pair, which describes the non-ideality of the liquid phase.

The objective function was minimized for the set of parameters of the NRTL model using data of infinite dilution and liquid-vapor equilibrium of H_2O + Ethanol, similar to the work published for THF [123].

The parameters of the NRTL model were estimated by minimizing the sum of the quadratic residuals of the output variables for each experiment (l), according to equation (S10).

$$F_1^{\text{obj}}\left(\underline{\beta}\right) = \sum_{l}^{N_{\text{exp}}} \left(\begin{array}{l} \left(w\left(P_l^{\text{calc}}\left(\underline{\beta}\right) - P_l^{\text{exp}}\right)\right)^2 + \left(w\left(y_l{}^{\text{calc}}\left(\underline{\beta}\right) - y_l{}^{\text{exp}}\right)\right)^2 + \\ + \left(w\left(\gamma_{1,l}^{\infty\,\text{calc}}\left(\underline{\beta}\right) - \gamma_{1,\,l}^{\infty\ \text{exp}}\right)\right)^2 \end{array} \right) \qquad \text{(S10)}$$

For each type of experimental data, the implemented routine allows different calculations with the NRTL model: for infinite dilution data, the activity coefficients are calculated directly using the temperature as input variable; and for liquid-vapor equilibrium data, the pressure and composition of the vapor phase at equilibrium are calculated using as input variables the temperature and composition of the liquid phase. $\underline{\beta}$ is the set of parameters to be estimated. For the NRTL model, it was defined as:

$\underline{\beta} = (A_{1,2}, A_{2,1}, \mathrm{B}_{1,2}, \mathrm{B}_{2,1}, \alpha)$. The inverse of the weights allowed for each output variable was 0.01% of the measured variable. These weights were defined with the purpose of establishing similar deviations for all points

The case involved regression of the following arrangement of the experimental data of the H_2O + Ethanol system: liquid-vapor equilibrium data at constant temperatures of 298.15 K, 323.15 K, 343.15 K and 363.15 K, in a total of 142 different experimental points, and infinite dilution data at atmospheric pressure (101.33 kPa), which are 10 experimental points between 283.15 K and 373.15 K.

In the estimation strategy of the Kihara parameters the equilibrium criterion is imposed in the objective function, equation (S11).

$$F_2^{\mathrm{obj}}\left(\underline{\beta}\right) = \sum_{l}^{N_{exp}} \left(\frac{\left(\frac{\Delta\mu_{H_2O}^{EL-H}\left(P = p_l^{\exp}, T = T_l^{\exp}, x = x_l^{\exp}, \underline{\beta}\right)}{\Delta\mu_{H_2O}^{EL-L}\left(P = p_l^{\exp}, T = T_l^{\exp}, x = x_l^{\exp}, \underline{\beta}\right)} \right) - 1}{w} \right)^2 \qquad \text{(S11)}$$

where $\underline{\beta} = \left(a, \sigma, \varepsilon/k_B\right)$. These parameters were estimated from the hydrate-liquid-vapor equilibrium experimental data set of the pure water and gas systems. The data collected from the literature were used in the estimation of Kihara parameters for CH_4 gases (273.2 K at 289.9 K and 26.50 bar at 158.37 bar), CO_2 (271.8 K at 279.8 K and 10.48 bar at 27.30 bar), C_2H_6 (273.7 K 282.8 K and 5.03 bar at 16.66 bar) and C_3H_8 (273.4 K at 278.4 K and 1.72 bar and 5.42 bar). The inverse of the weight adopted, empirically, for the difference between the potentials, in order to increase its accuracy, was 10^{-10}.

In this work we used the particle swarm optimization method [233] as the stochastic method to obtain a good initial estimate to be submitted to a Quasi-Newton algorithm, a deterministic method that makes use of techniques of differential calculation.

S.3 Result of parameter estimation

S.3.1 Liquid-vapor equilibrium

The parameters of the NRTL model, Table S15, were estimated for liquid-vapor equilibrium data of H_2O (2) + Ethanol (1) at the temperatures of 298.15 K, 323.15 K, 343.15 K and 363.15 K and infinite dilution data at atmospheric pressure (101.33 kPa) between 283.15 K and 373.15 K.

Table S15 - Parameters of the NRTL model, and their respective errors, obtained by adjusting the liquid-vapor equilibrium data and infinite dilution data of the Ethanol (1) + H_2O (2) system.

$\boldsymbol{A_{1,2}}$	-1.57715 ± 0.06830
$\boldsymbol{A_{2,1}}$	3.07850 ± 0.07670
$\boldsymbol{B_{1,2}}$	7.19352 ± 0.16113
$\boldsymbol{B_{2,1}}$	-11.38690 ± 0..22354
α	0.0609696 ± 0.0019712

The calculated values for molar fraction and pressure were well adjusted and showed absolute average deviations of 0.56% and 0.45%, respectively.

Figure S2 (a), (b) and (c) show the calculated diagrams within the temperature and pressure conditions for which the parameters of the NRTL model were estimated, including the data that were correlated (298.15 K, 323.15 K, 343.15 K and 363.15 K). The correlation of the data used in the estimation was adequate and the model presented satisfactory predictive capacity within the range of temperature and pressure studied.

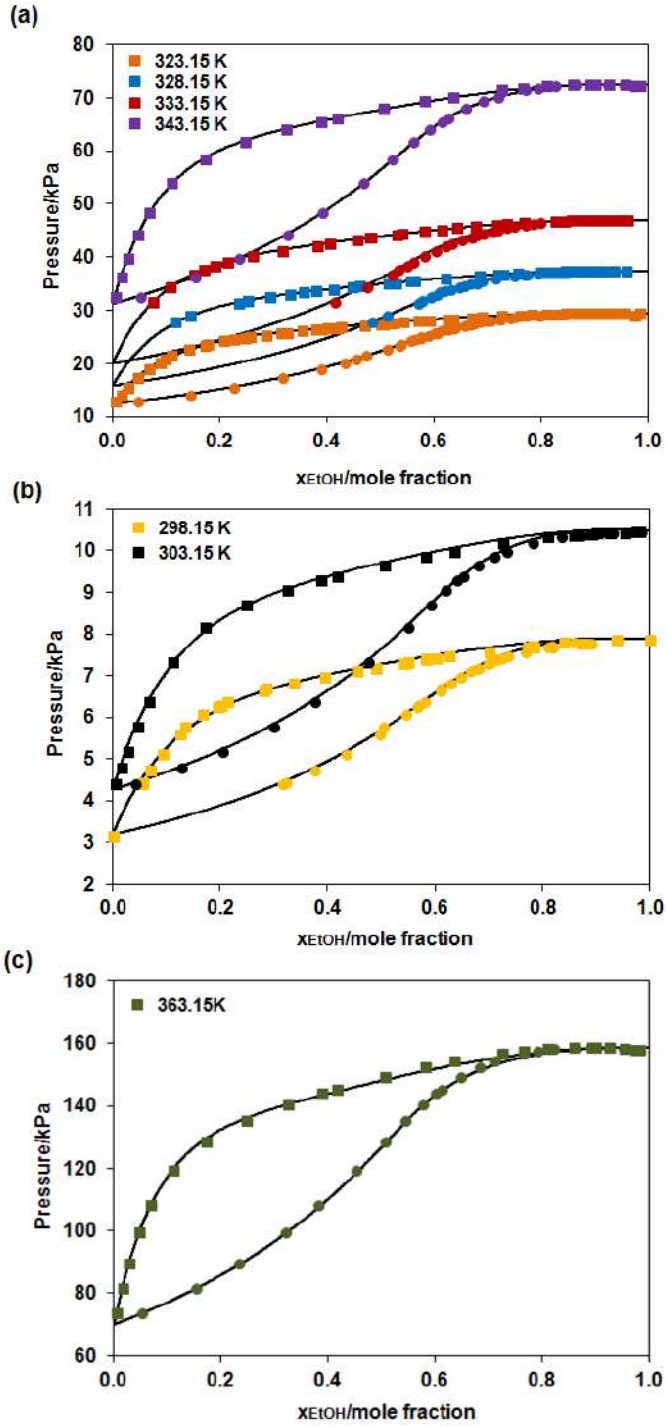

Figure S2 - Isothermal curves of liquid-vapor equilibrium of H_2O + Ethanol at: (a) 323.15 K, 328.15 K, 333.15 K and 343.15 K; (b) 298.15 K and 303.15 K; (c) 363.15 K. The experimental data are represented by the squares for the dew point curves and circles for the bubble point curves [227–232]. The continuous curves represent the calculation with the adjusted NRTL model.

Figure S3 illustrates the predictive calculation of the liquid-vapor equilibrium diagram at constant pressures with the proposed model. The model was able to predict the liquid-vapor equilibrium of the H_2O + Ethanol system within the correlated range and presented an adequate prediction when extrapolated to higher temperatures and pressures (up to 430 K and 666.85 kPa) and lower temperatures and pressures (up to 290 K and 6.7 kPa).

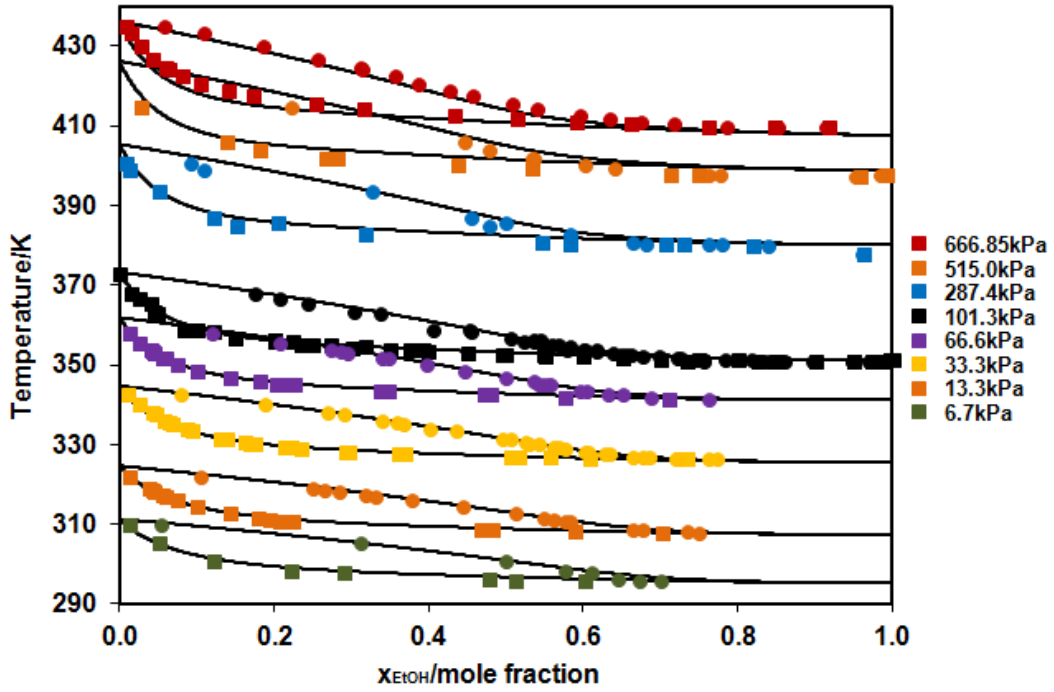

Figure S3 - Isobaric equilibrium liquid-vapor equilibria of H_2O + Ethanol. The experimental data are represented by the squares for the dew point curves and circles for the bubble point curves [227–232]. The continuous curves represent the calculation with the adjusted NRTL model.

S.3.2 Infinite Dilution

In addition to the LVE data, infinite dilution data of ethanol in H_2O at atmospheric pressure (101.33 kPa) between 283.15 K and 373.15 K were used in the NRTL model estimation process to reduce correlation between the NRTL parameters.

Figure S4 shows the correlation of the NRTL model with the experimental data of infinite dilution of ethanol in H_2O and their respective experimental deviations. The

calculation of the infinite dilution coefficient showed an absolute average deviation of 8.19%. This calculation had less precision than the LVE calculation, but it remained within the experimental error of these data. Therefore, the model is able to correlate the data within the presented experimental errors.

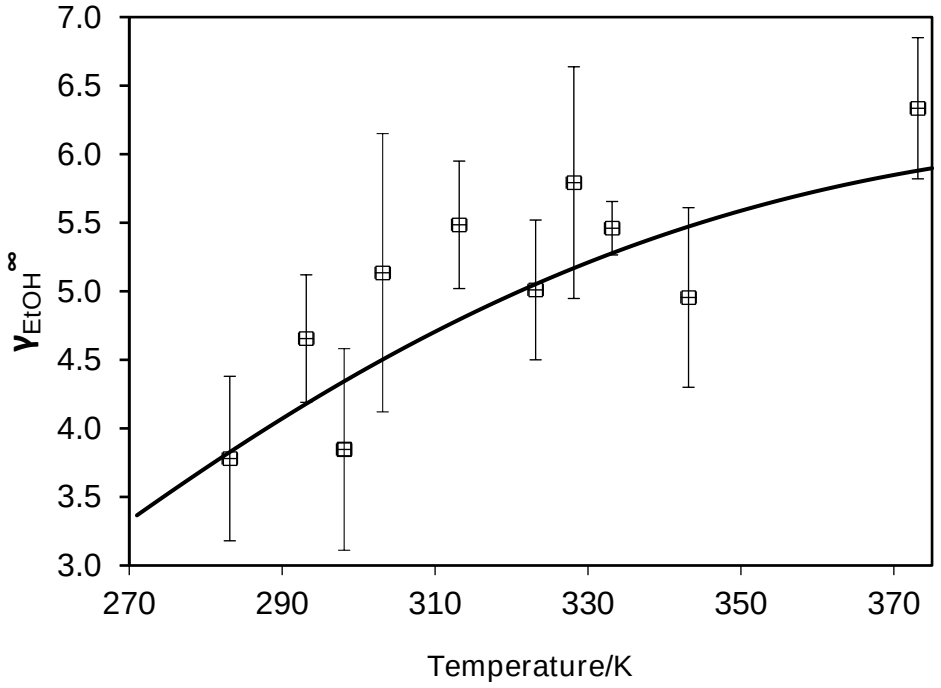

Figure S4 - Activity coefficient in the condition of infinite dilution of ethanol in H_2O. The squares represent the experimental data with their respective errors [152,157] and the continuous curve is the model prediction.

S.3.3 Gas hydrate phase equilibria for pure water systems.

The Kihara parameters re-estimated for the gases studied in this work are presented in Table S16 for pure water condition and were applied in this article in the calculation of hydrate-liquid-vapor equilibrium with ethanol. With an error lower than 10^{-3} for the parameters σ [Å], which is the intermolecular radius of Kihara, and a [Å], which is the soft radius of the spherical core for the guest component; and lower than 10^{-1} for ε/k_B [K], which is the Kihara's maximum attraction potential.

Table S16 - Kihara parameters adjusted for the hydrate phase equilibrium data of the Gas + H_2O systems.

	σ [Å]	a [Å]	ε/k_B [K]
CH_4	0.252	3.431	143.181
CO_2	0.561	3.361	164.532
C_2H_6	1.351	2.762	224.999
C_3H_8	1.535	3.084	360.878

The Oliveira et al.[123] model adjustment for the hydrate phase equilibrium data of the methane system with fresh water showed an absolute average deviation of 1.47% and it is shown in Figure S5.

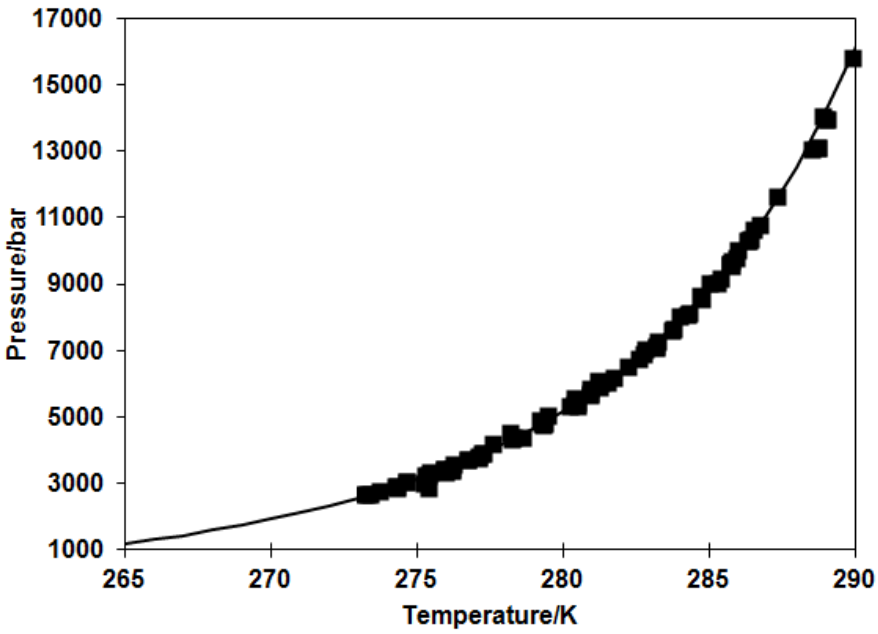

Figure S5 - P vs. T hydrate phase equilibrium curve for the CH_4 + H_2O system. The squares, ■, represent the experimental data [158,180–186]. The curve represents the calculation of the hydrate dissociation pressure with the model [123].

Figure S6 shows the fit of the model to the hydrate phase equilibrium data of the system with CO_2 and fresh water. The model presented an absolute average deviation of 0.69% in relation to the literature data for this system.

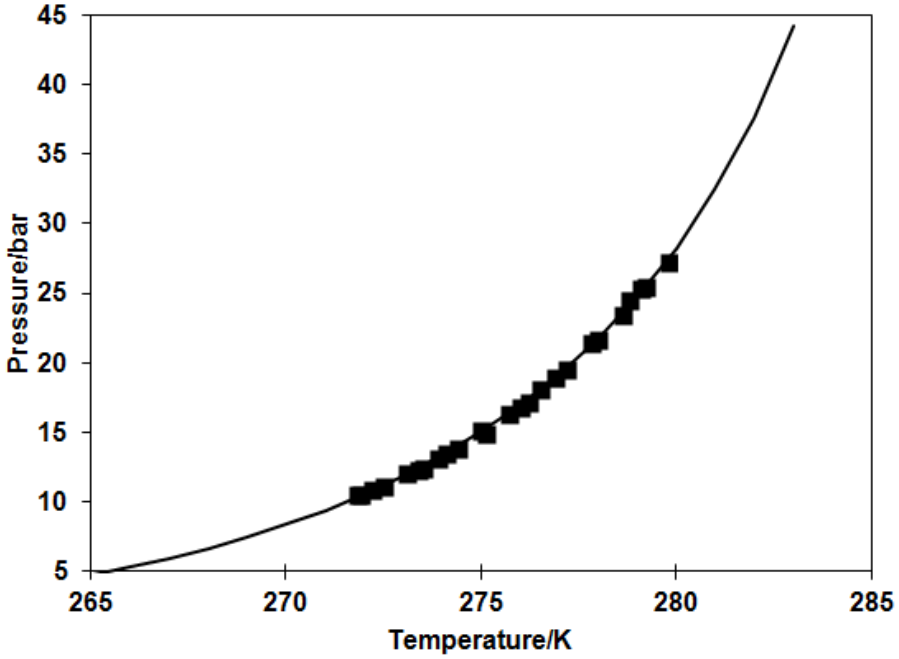

Figure S6 - P vs. T hydrate phase equilibrium curve for the CO_2 + H_2O system. The squares, ■, represent the experimental data [188]. The curve represents the calculation of the hydrate dissociation pressure with the model [123].

For the hydrate phase equilibria experimental data of the system C_2H_6 in fresh water the model presented absolute average deviation of 1.85% in relation to the experimental data of the literature and the adjustment is presented in Figure S7.

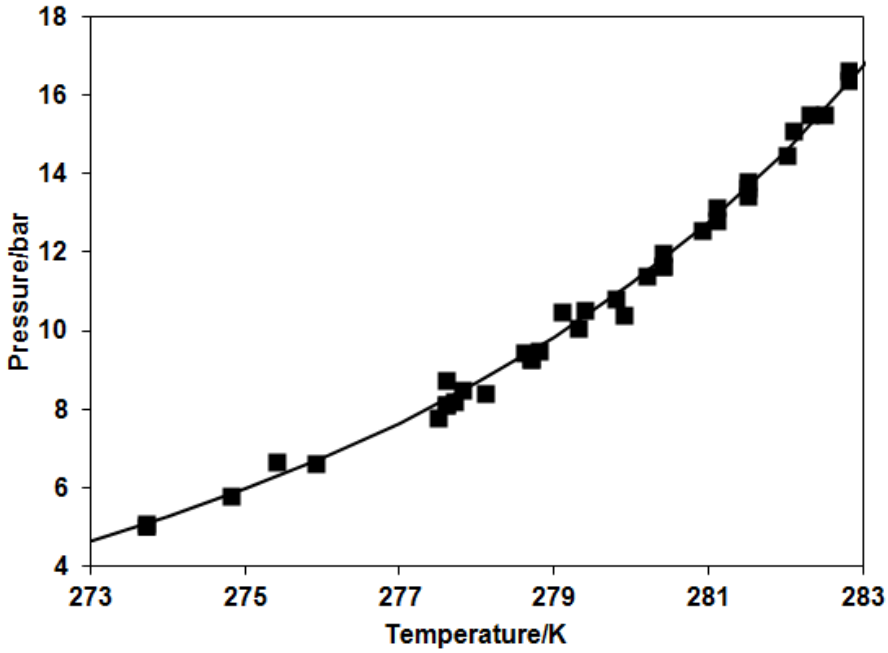

Figure S7 - P vs. T hydrate phase equilibrium curve for the C_2H_6 + H_2O system. The squares, ■, represent the experimental data [181,182,193]. The curve represents the calculation of the hydrate dissociation pressure with the model [123].

For the C_3H_8 system in fresh water the model was correlated with the hydrate phase equilibrium data of the literature as shown in Figure S8. The absolute mean deviation of the model for those data without additives was 2.16%.

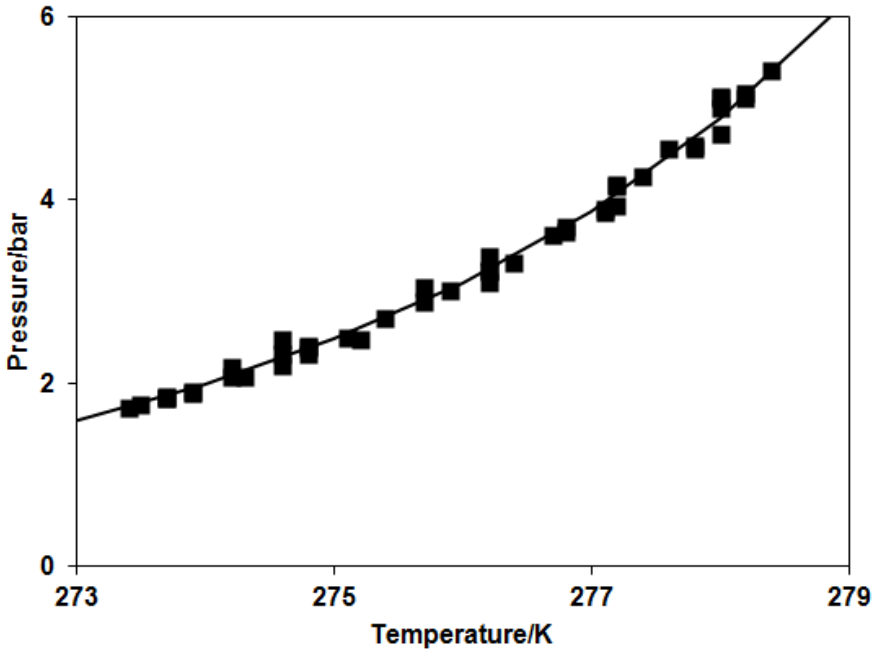

Figure S8 - P vs. T hydrate phase equilibrium curve for the C_3H_8 + H_2O system. The squares, ■, represent the experimental data [181,186,189–192]. The curve represents the calculation of the hydrate dissociation pressure with the model [123].

Appendix 3. Supporting information for Chapter 4

S.4 Excess Gibbs Free Energy Model (NRTL)

In this work, we use the excess Gibbs energy model, NRTL, to describe the non-ideality of the liquid phase in both conditions in the bulk liquid phase and in the local equilibria of the gas-liquid and hydrate-liquid interfaces. The parameters model were estimated by adjusting the liquid-vapor equilibrium (LVE) data of the H_2O + CH_4 system and CH_4 solubility data in H_2O (Dalton and Raoult laws).

A vast set of experimental data on LVE [234–236] and solubility [237–242] for the H_2O + CH_4 system has been drawn from the literature. The temperature-dependent binary interaction parameters in this work were described by equation (S12), for T_{ref} = 330.15 K. The coefficients of the binary interaction parameters and the non-randomness factor were estimated for the temperature range of 275.11 K to 444.26 K and pressure range of 0.0073 MPa to 68.95 MPa.

$$\tau_{i,\mathrm{j}} = A_{i,\mathrm{j}} + B_{i,\mathrm{j}}\left(\frac{T_{ref}}{T} - 1\right) \tag{S12}$$

The activity coefficients of the excess Gibbs free energy model, NRTL, for a binary mixture of CH_4(1) + H_2O(2) were calculated by equation (S13), for $n = 2$.

$$\gamma_i = \exp\left(\frac{\sum_{j=1}^{n} x_j \tau_{j,i} G_{j,i}}{\sum_{k=1}^{n} x_k G_{\mathrm{k},i}}\right) + \sum_{j=1}^{n} \frac{x_j G_{\mathrm{i,j}}}{\sum_{k=1}^{n} x_k G_{\mathrm{k,j}}}\left(\tau_{i,j} - \frac{\sum_{m=1}^{n} x_m \tau_{\mathrm{m,j}} G_{\mathrm{m,j}}}{\sum_{k=1}^{n} x_k G_{\mathrm{k,j}}}\right) \tag{S13}$$

The non-randomness factor, α, was considered symmetric and $G_{i,\mathrm{j}} = \exp(\alpha \tau_{i,\mathrm{j}})$. The parameters of the NRTL model are in the Table S17 and the methodology and results of the estimation are in Item S.12.

Table S17 - Parameters of the NRTL model, and their respective errors, obtained by adjusting the liquid-vapor equilibrium and solubility data of the system CH_4 (1) + H_2O (2).

NRTL Parameters	
$A_{1,2}$	879.302 ± 0.011
$A_{2,1}$	-208.760 ± 0.007
$B_{1,2}$	-430.631 ± 0.013
$B_{2,1}$	-41.891 ± 0.006
α	0.00161 ± 0.00001

The calculation of the activity of the hydrate-forming components in the liquid phase, both in the hydrate-liquid equilibrium and in the bulk liquid phase are obtained by equation (S14) for the CH_4+H_2O system.

$$a\left(T,\mathrm{P},\mathbf{x}\right)=\gamma_i^L\left(T,\mathrm{P},\mathbf{x}\right)x_i^L \tag{S14}$$

S.5 Calculation of the equilibrium composition at the H-L interface

The work approach by Oliveira et al. [207], although adequate for the equilibrium calculation, does not calculate the light organics fugacity, such as CH_4, in the liquid aqueous phase. Most hydrate equilibrium calculations in the literature assume that these compounds are not present in the aqueous phase as they have low water solubility [2].

In this work, to calculate the equilibrium methane composition, at the hydrate-liquid interface, we use the same approach as Oliveira et al. [207]. The minimization of the water chemical potential difference between the liquid phase and the hydrate phase. However, the iterative calculation was carried out at constant pressure and temperature, varying the equilibrium composition at the hydrate-liquid interface (H-L), and we used the bulk methane composition as the initial guess.

Therefore, it was necessary to describe the CH_4 fugacity in the liquid phase, $f_{CH_4}^L$. For this, equation (S15) was used, incorporating non-ideality through the activity coefficient obtained by the excess Gibbs free energy model, NRTL, Item S.4.

$$f_{CH_4}^L\left(T,P\right)=x_{CH_4}^L\gamma_{CH_4}^L f_{puro}^{L,0}\left(T,P\right) \tag{S15}$$

The fugacity of pure CH_4 in the hypothetical liquid phase, $f_{CH_4}^{L,0}$, was calculated by the equation of Prausnitz, Lichtenthaler and Azevedo (1999) [243], where P_0 = 101300 [Pa] and $v_{CH_4}^L$ = 5.21 10-5 [m³ / mol], equation (S16).

$$f_{CH_4}^{L,0}(T,P) = f_{puro}^{L,0}(T,P_0)\exp\left(\frac{v_{CH_4}^{L}(P-P_0)}{RT}\right) \quad \text{(S16)}$$

The fugacity of pure CH_4 in the condition of P_0, $f_{puro}^{L,0}(T,P_0)$, was obtained by a T_r correlation presented by Prausnitz and Shair (1961) [244], adjusted for experimental data of solubility of several light gases in H_2O. However, as this correlation is not explicit in the referenced work, a function similar to the one described by Prausnitz and Shair (1961) [244] was adjusted and correlated with the data presented in the article, as described in Item S.11.

S.6 Growth Kinetics

With the hypotheses adopted for the hydrate growth model development and the proposed hydrate formation reaction, the mass balance of each species *i* in each phase *j* is represented generically by equation (S17) and the number of moles by equation(S18). For the hydrate formation systems studied in this work, we will use the balance in molar terms, the index *"sol"* being used for entry or exit mass, $\dot{m}$, or molar, $\dot{n}$, rates of the solubilization of methane in phase *j*, the "*e* " used for the methane input variables in the gas phase through the feed and the" *c* "for the input or output rates of component *i* due to the growth of the hydrate phase.

$$\frac{dm_i^j}{dt} = \pm\dot{m}_{sol,i} \pm \dot{m}_{e,i} \pm \dot{m}_{c,i} \quad \text{(S17)}$$

$$\frac{dn_i^j}{dt} = \pm\dot{n}_{sol,i} \pm \dot{n}_{e,i} \pm \dot{n}_{c,i} \quad \text{(S18)}$$

S.6.1 Liquid phase molar balance

Applying the molar balance for the liquid phase, equation (S18), with the assumptions previously assumed, we get to equations (S19) and (S20).

$$\frac{dn_{H_2O}^{L}}{dt} = -\frac{\tau}{\xi}\dot{n}_{c,CH_4} \quad \text{(S19)}$$

$$\frac{dn_{CH_4}^{L}}{dt} = \dot{n}_{sol,CH_4} - \dot{n}_{c,CH_4} \quad \text{(S20)}$$

Therefore, the global molar balance in the liquid phase is given by equation (S21).

$$\frac{dn^L}{dt} = \left[\frac{dn^L_{H_2O}}{dt} + \frac{dn^L_{CH_4}}{dt} \right] = \dot{n}_{sol,CH_4} - \left(\frac{\tau}{\xi} + 1 \right) \dot{n}_{c,CH_4} \quad \text{(S21)}$$

Where, $\dot{n}_{sol,CH_4}$ is the methane solubilization rate in the liquid phase and $\dot{n}_{c,CH_4}$ is the hydrate growth rate in terms of the methane moles, Item S.6.4.

S.6.2 Gas phase molar balance

Considering that there is no water evaporation for the gas phase, the mass balance of the pure methane gas phase is described by equation (S22) in mole terms.

$$\frac{dn^G}{dt} = \frac{dn^G_{CH_4}}{dt} = \dot{n}_{e,CH_4} - \dot{n}_{sol,CH_4} \quad \text{(S22)}$$

Where, $\dot{n}_{e,CH_4}$ is the methane molar rate entering the reactor and $\dot{n}_{sol,CH_4}$ is the methane solubilization rate in the liquid phase according to Item S.6.4.

S.6.3 Solid phase molar balance

For the solid phase, with the hypotheses adopted, considering the hydrate crystal a homogeneous solid, equation (S23) is given the mole balance.

$$\frac{dn^S}{dt} = \frac{dn^S_H}{dt} = \dot{n}_{c,H} = \frac{1}{\xi} \dot{n}_{c,CH_4} \quad \text{(S23)}$$

Where $\dot{n}_{c,CH_4}$ is the hydrate growth rate in terms of the methane moles, Item S.6.4

S.6.4 Constitutive relations

The methane solubilization molar rate (methane molar rate entering in the liquid phase), $\dot{n}_{sol,CH_4}$, is defined by the methane diffusion from the gas-liquid interface into the liquid phase, equation (S24), as in Sampaio et al. [87] work, where $A^{GL}_{int}\left[m^2\right]$ is the gas-liquid interface area and $k^{GL}_d\left[m/s\right]$ is the mass transfer coefficient at the gas-liquid interface. Both parameters are obtained by correlations founded in the literature [87,245], which are presented in Item S.9.

$$\dot{n}_{sol,CH_4} = \frac{A^{GL}_{int} k^{GL}_d}{V^L} \left(n^L_{eq,CH_4} - n^L_{CH_4} \right) \quad \text{(S24)}$$

Using the equilibrium hypothesis at the gas-liquid interface, the methane mole fraction at the interface is obtained iteratively by the methane fugacity equality in the

phases, equation (S25). The Peng-Robinson equation of state is applied to obtain the methane fugacity coefficient the CH_4 pure vapor phase, $\phi_{CH_4}^V$, while for the methane fugacity coefficient in the equilibrium liquid phase, $\phi_{CH_4}^L$, equation (S15) divided by system pressure was used. For this iterative calculation, the Krichevsky and Kasarnovsey [246] correlation, shown in Item S.10, is used as an initial guess.

$$f_{CH_4}^V = f_{CH_4}^L \rightarrow x_{CH_4}^{eq} = \frac{\hat{\phi}_{CH_4}^V\left(T, \mathrm{P}, \mathbf{y}\right)}{\hat{\phi}_{CH_4}^L\left(T, \mathrm{P}, \mathbf{x}^{eq}\right)} \tag{S25}$$

Therefore, the methane number of moles solubilized in the liquid phase, n_{eq,CH_4}^L, is given by $n_{\mathrm{eq},CH_4}^L = x_{CH_4}^{eq} n^L$, where $n^L = \sum_i n_i^L = \overline{\rho^L} V^L$.

The methane molar rate consumed by the hydrate phase growth can be obtained from the number of moles temporal variation in the particulate phase according to equation (S26).

$$\dot{n}_{c,CH_4} = \xi \dot{n}_{c,\mathrm{H}} = \xi \frac{dn_H^s}{dt} \tag{S26}$$

The hydrate phase number of moles is equal to the product between the molar density and the phase volume, equation (S27).

$$n_H^s = \overline{\rho^H} V^H \tag{S27}$$

The methane gas number of moles in the reactor is given by equation (S28), where $\overline{\rho_{CH_4}^G}$ is the molar density of the pure methane gas phase. The methane feed rate to maintain the system pressure can be obtained from the vapor phase molar balance, equation (S22). Applying the chain rule in Equation (S28), we arrive at equation (S29) to describe the methane rate entering the reactor.

$$n_{CH_4}^G = \overline{\rho_{CH_4}^G}\left(T_{sist.}\right) V^G \tag{S28}$$

$$\dot{n}_{e,CH_4} = \frac{dn_{CH_4}^G}{dt} + \dot{n}_{\mathrm{sol},CH_4} = \frac{dV^G}{dt}\overline{\rho_{CH_4}^G}\left(T_{sist.}\right) + \frac{d\,\overline{\rho_{CH_4}^G}\left(T_{sist.}\right)}{dt} V^G + \dot{n}_{\mathrm{sol},CH_4} \tag{S29}$$

S.6.5 Volumes and Molar Densities of the Phases

The vapor phase molar density, $\overline{\rho^G}$, is calculated with the Peng-Robinson EoS for pure substances, adopting pure CH_4 in the vapor phase. Meanwhile, the liquid phase molar density, $\overline{\rho^L}$, is calculated by the generalized Rackett equation [222–226]. In this work, the hydrate phase molar density, $\overline{\rho^H}$, is considered constant and is obtained by the product between the hydrate phase mass density of Sloan and Koh [2] and the hydrate phase molecular mass, MM_H. It is obtained through the weighted sum of the molecular masses of the components, by the number of water molecules and guests present in the hydrate phase.

The gas volume inside the reactor can be obtained by the difference of the tank volume, V^r, and the volumes of the liquid, V^L, and solid phases, V^S, equation (S30).

$$V^G = V^r - V^L - V^S \tag{S30}$$

The liquid phase volume is obtained by defining the liquid phase number of moles, the product between molar density and the phase volume, equation (S31).

$$n^L = \overline{\rho^L}(T_{sist.})V^L \rightarrow V^L = \frac{n^L}{\overline{\rho^L}(T_{sist.})} \tag{S31}$$

Its size distribution characterizes the crystalline population that comes out of a crystallizer. Because the hydrate phase is a crystalline phase, its properties can be obtained through its size distribution. The density distribution function, $n(t,l)$, refers to the number, mass or volume of crystals per unit volume of liquid in a size range, whose average size is *l*. The cumulative variable of the density distribution function expresses the number, volume or mass of crystals per unit volume of liquid in a size range [247].

By definition, the third-order moment, μ_3, is the cumulative variable of the density distribution function that express the volume of crystals per unit volume of liquid for the entire range of system particle size, according to the equation (S32). Therefore, the third-order moment is proportional to the particulate solid phase volume given a volumetric form factor, k_V^H, considered constant for the solid phase, if the liquid phase volume is known, as shown in equation (S33) [247].

$$\mu_3 = \int_0^\infty l^3 n(t,l)dl \tag{S32}$$

$$V^S = k_H \mu_3 V^L \tag{S33}$$

In this work, we assumed that the shape of the hydrate phase is spherical. The calculation of the third-order moment of the particulate phase will be discussed below in Item S.6.6.

S.6.6 Population balance

To understand the polydispersed systems growth kinetics and to compare the modeling with experimental data, the use of a population balance equation, equation (S34), is necessary to describe the hydrate particles temporal evolution. The population balance equation is the conservation equation for the number of particles in a polydispersed system. Mathematically, the distribution can be affected by external variables, referring to the particle spatial location, and internal ones, referring to particles' intrinsic properties, such as mass and diameter.

In the problem addressed here, the distribution will be affected only by the internal variable particle diameter l. The population balance equation to be used here is presented in equation (S34). The deduction of that equation is not part of the scope of this work, but can be found in [211,212].

$$\frac{\partial n(l,t)}{\partial t} + \frac{\partial}{\partial l}\left(G' n(l,\mathrm{t})\right) = B - D \tag{S34}$$

In this equation, $n(l,\mathrm{t})$ is the function of particles numerical density distribution, G' is the particle growth rate, B is the particle nucleation rate and D is the rate of particle breakage and aggregation. That is, B - D is the net rate for particle birth and death.

Considering that there is no nucleation and neither breaking nor aggregation, the population balance is expressed by equation (S35).

$$\frac{\partial n(l,t)}{\partial t} + \frac{\partial}{\partial l}\left(G' n(l,\mathrm{t})\right) = 0 \tag{S35}$$

Here, the population balance objective is to calculate the growth molar rate, and consequently, the hydrate former consumption molar rate, of the solid phase by calculating the variation in the particulate phase volume obtained by the third-order moment, equation (S33).

The equation that expresses the growth kinetics in this work is linear. For this reason, the method chosen to solve the population balance was the most straightforward, the method of moments, in order to simplify the modeling and make the calculation faster. However, it is known that the method of moments does not allow the recovery of the system particle distribution, just the computation of the moments.

Applying the moment operator to a function $n(t,l)$, $\int n(t,l)l^j dl$, in equation (S35), we get to the equation (S36). The growth rate of the particles that will be proposed in this work does not depend on the size of the particles, that is $G' = G'(t)$. The definition of the moment of order j of the system particle distribution is given by equation (S37).

$$\frac{\partial}{\partial t}\left[\int_0^\infty l^j n(t,l)dl\right] + G'\int_0^\infty \frac{\partial}{\partial l}\big(n(L,\mathrm{t})\big)l^j dl = 0 \qquad \text{(S36)}$$

$$\mu_j = \int_0^\infty l^j n(t,l)dl \qquad \text{(S37)}$$

As the integral of the first term of equation (S36) is defined, the partial derivative becomes the total derivative. Replacing the definition of momentum, equation (S37), we arrive at equation (S38). Integrating the second term of equation (S36) by parts make it possible to obtain equation (S39).

$$\frac{\partial \mu_j}{\partial t} + G'\int_0^\infty \frac{\partial}{\partial l}\big(n(L,\mathrm{t})\big)l^j dl = 0 \qquad \text{(S38)}$$

$$\frac{\partial \mu_j}{\partial t} + G'\left[l^j n(l,t)\Big|_0^\infty - \int_0^\infty j\ n(l,\mathrm{t})l^{j-1}dl\right] = 0 \qquad \text{(S39)}$$

Because it represents a probability function, the numerical density distribution function of particles has the following properties: $n(0,\mathrm{t}) = 0$ e $\int_0^\infty n(l,\mathrm{t})dl \to 1$. From the first property it is concluded that the function applied to the zero size particles is null. Using both properties we can conclude that $\lim_{l\to\infty} n(l,\mathrm{t}) \to 0$, because the area under the curve $n(t,l)$ is finite. This conclusion cancels the first term contained in the brackets of equation (S39).

Therefore, when applying the definition of momentum, equation (S37), equation (S39) is now described by equation (S40).

$$\frac{\partial \mu_j}{\partial t} - jG'(t)\mu_{j-1} = 0 \tag{S40}$$

Therefore, the system of population balance equations necessary to compute the temporal variation of the third-order moment is given by the equations (S41), (S42), (S43) e (S44).

$$\frac{\partial \mu_0}{\partial t} = 0 \tag{S41}$$

$$\frac{\partial \mu_1}{\partial t} = G'(t)\mu_0 \tag{S42}$$

$$\frac{\partial \mu_2}{\partial t} = 2G'(t)\mu_1 \tag{S43}$$

$$\frac{\partial \mu_3}{\partial t} = 3G'(t)\mu_2 \tag{S44}$$

It then becomes necessary to define an appropriate model for the growth rate in order to obtain the temporal evolution of the particle size.

S.6.7 Numerical solution of dynamic

The integration of the system differential-algebraic equations (DAE) in time is accomplished through the computational code DASSL (Fortran). A system of differential equations can be generalized by a system differential-algebraic equations (DAE), rewriting the system algebraic-differential equations to be solved in the residual format, $res(N)$, as shown in equation (S45).

$$\begin{aligned} F\left(t, y, \dot{y}\right) &= 0 \\ y(t_0) &= y_0 \\ \dot{y}(t_0) &= \dot{y}_0 \end{aligned} \tag{S45}$$

Where $F, y\ e\ \dot{y}$ are the vectors of dimension N and *t* the independent variable.

The Differential-Algebraic System (DASSL) code were developed by Petzold [248] as an alternative of numerical solution for algebraic-differential equations (ADE), especially those whose solvers of systems ordinary differential equations (ODE) are not able to solve, such as:

a) Systems in which the derivative cannot be solved explicitly, rewriting it in the standard form of EDO, $\dot{y} = F(t, y)$, and;

b) When the derivative solution, $\dot{y}$, is impractical.

The numerical method applied consists of replacing the derivative by an approximate difference through discretization as a function of the independent variable t. The system, then, can be solved for the current time, t_{out}, using Newton's method. The advantage of DASSL is the possibility of using the retrograde differentiation formulas up to the fifth-order to replace the derivative at each time step, the program chooses the order and time interval, based on the solution behavior.

To solve the ADE system with the DASSL code, it is necessary to define the initial condition properly, both for the variables and their derivatives, which must obey equation (S45). For this purpose, only a few variables are provided as inputs to the system, while the other variables and derivatives are obtained by the DAE system or by differentiation by parts of the variable. The variables defined as inputs to the DAE system depend on the studied mixture and are presented together with their respective results. Besides, the relative and absolute tolerances must be provided by the user and in this work 10^{-12} and 10^{-14} were used for the absolute and relative tolerances, respectively.

S.7 System property variable profiles

S.7.1 System at 276 K and 70.9 bar with water activity in the driving force

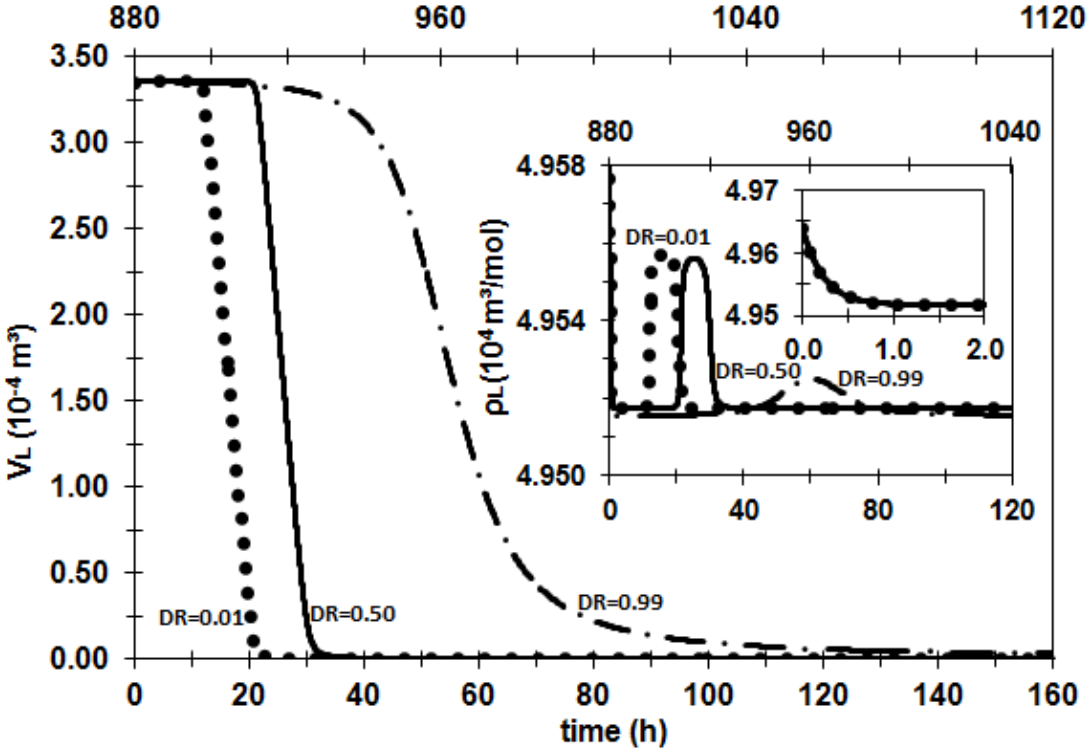

Figure S9 - The temporal profile of the liquid phase volume (V_L). The insertion shows the liquid density (ρ_L) profile with a zoom in the methane in water saturation (the first 2 hours). The dotted line describes the limited by diffusion profile (*DR*=0.01), the continuous line the diffusion-reaction coupling profile (*DR*=0.5), and the dotted-dashed line, in the 2nd time axis, the limited by reaction profile (*DR*=0.99). All profiles are at 276 K and 70.9 bar.

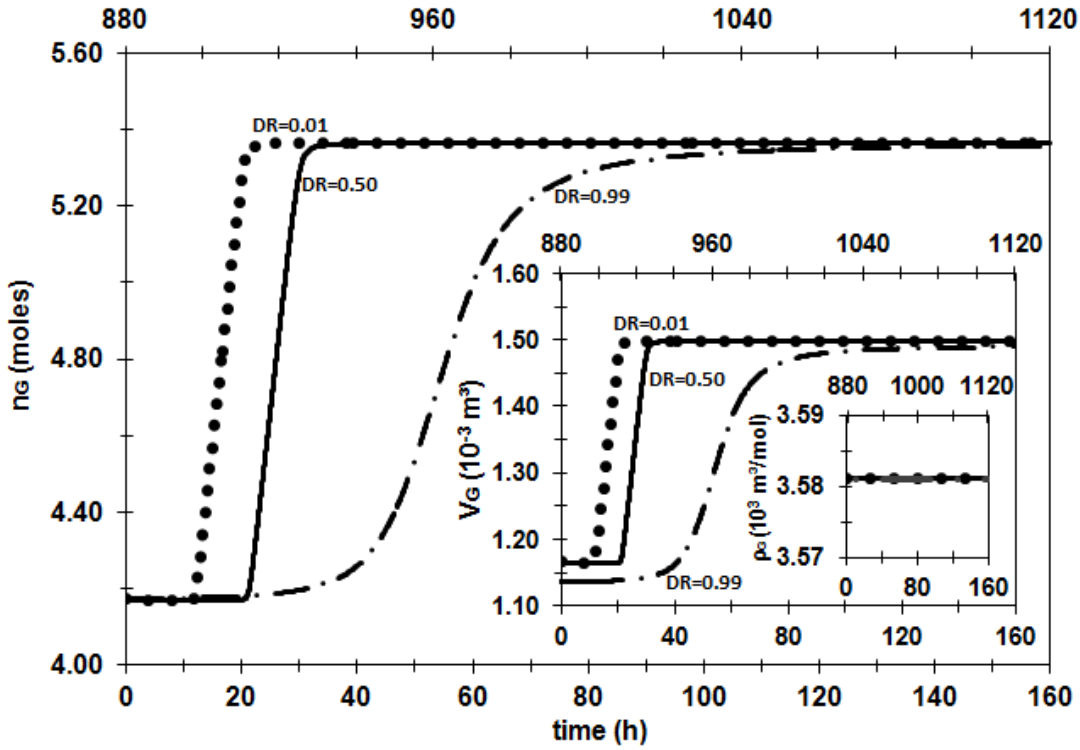

Figure S10 - The temporal profile of the methane number of moles in the pure vapor phase (n_G). The insertion shows the vapor phase volume (V_G) with the constant vapor density (ρ_G) profile. The dotted line describes the limited by diffusion profile (*DR*=0.01), the continue line the diffusion-reaction coupling profile (*DR*=0.5), and the dotted-dashed line, in the 2nd time axis, the limited by reaction profile (*DR*=0.99). All profiles are at 276 K and 70.9 bar.

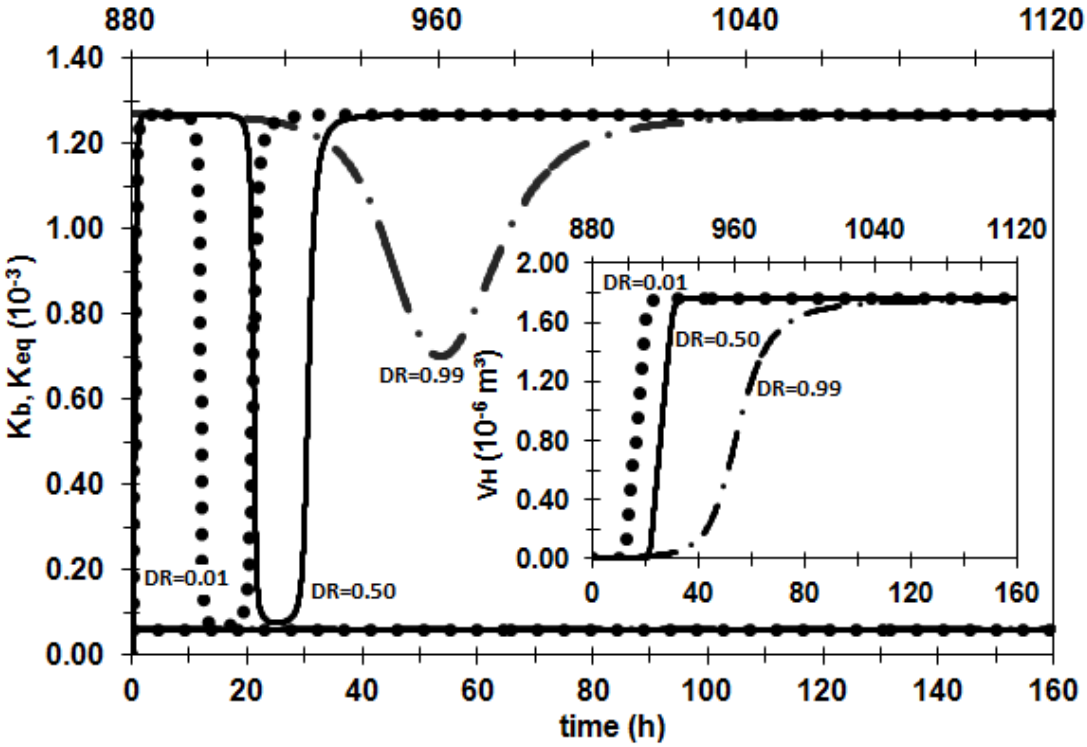

Figure S11 - The temporal profile of the product reagents' activities weighted by their stoichiometric coefficients in the bulk phase variable (K_b) and in the liquid-hydrate equilibrium interface variable (K_{eq}). The variable in the bulk liquid phase (K_b) is the one with the the highest value, while the variable in the liquid-hydrate equilibrium interface (K_{eq}) is the one constant. The insertion shows the hydrate phase volume (V_H). The dotted line describes the limited by diffusion profile (*DR*=0.01), the continuous line the diffusion-reaction coupling profile (*DR*=0.5), and the dotted-dashed line, in the 2nd time axis, the limited by reaction profile (*DR*=0.99). All profiles are at 276 K and 70.9 bar.

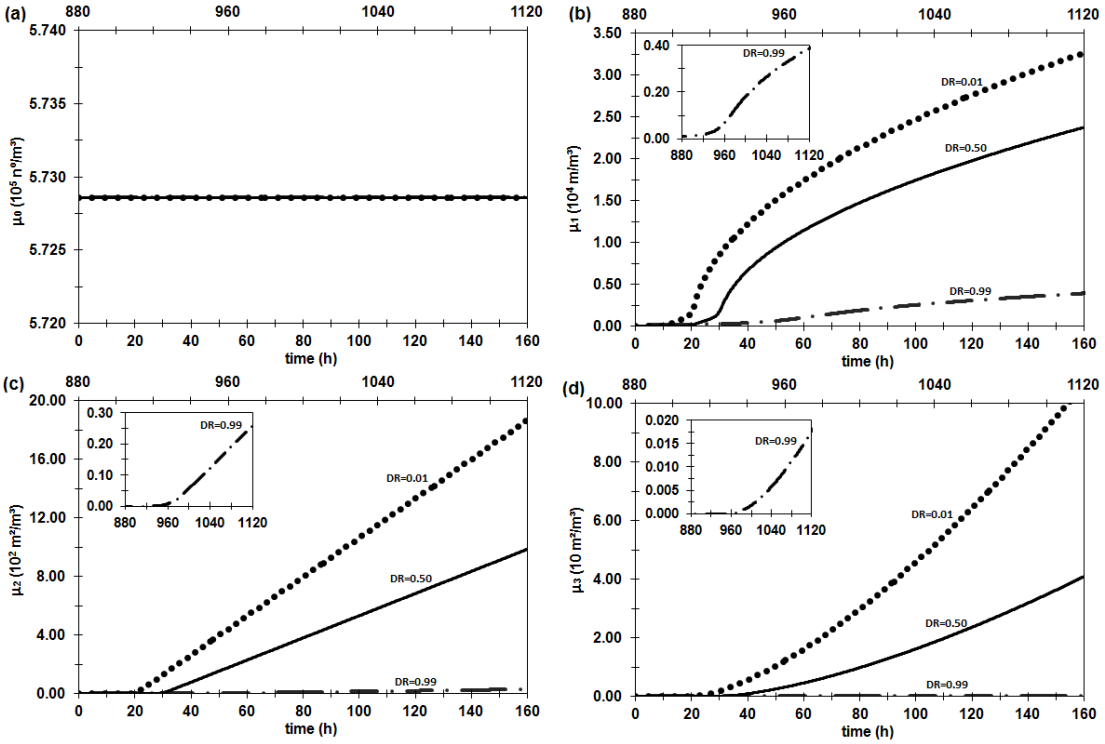

Figure S12 - (a) The temporal profile of the population balance moment of order zero, number of particles per liquid volume (μ_0), (b) moment of order one, particle diameter per liquid volume (μ_1), (c) moment of order two, particle surface area per liquid volume (μ_2) and (d) moment of order three, particle volume per liquid volume (μ_3). The inserts are a zoom in the limited by reaction profile. The dotted line describes the limited by diffusion profile (*DR*=0.01), the continue line the diffusion-reaction coupling profile (*DR*=0.5), and the dotted-dashed line, in the 2nd time axis, the limited by reaction profile (*DR*=0.99). All profiles are at 276 K and 70.9 bar.

S.7.2 System at 276 K and 48.6 bar with water activity in the driving force

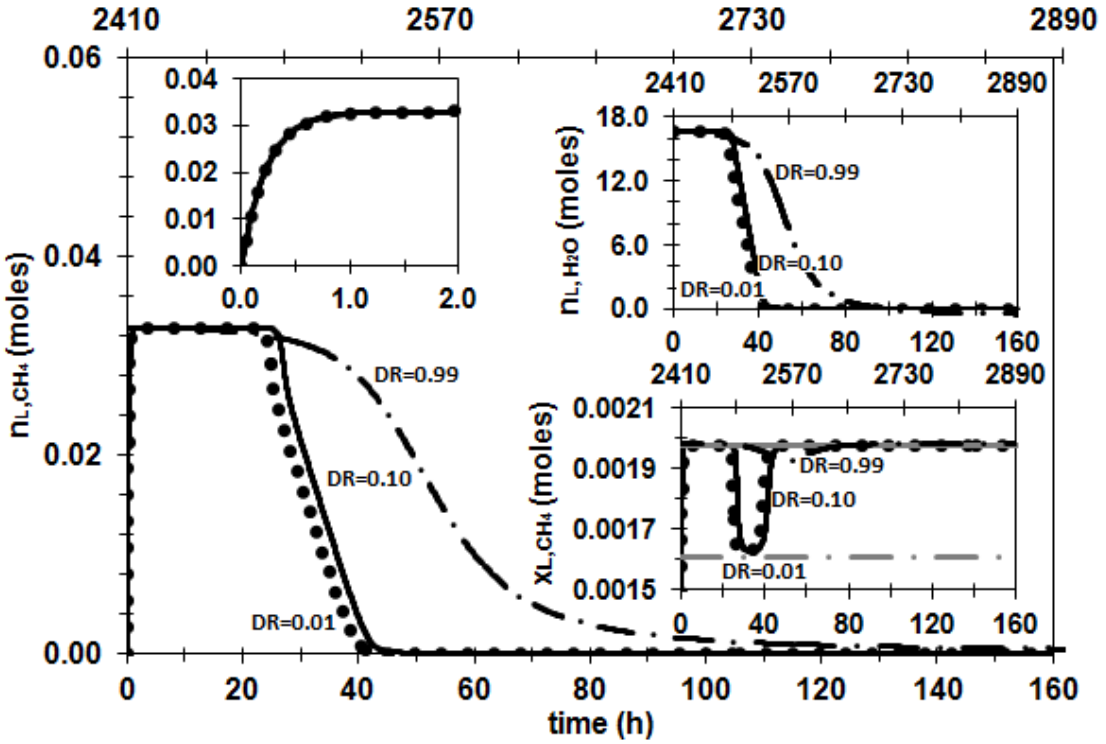

Figure S13 - The temporal profile of the methane number of moles in the bulk liquid phase ($n_{L,}CH_4$). The insertion on the left shows the methane in water saturation profile, the one in the bottom-right shows the methane mole fraction ($x_{L,}CH_4$) profile in the bulk liquid phase (dark lines), in the gas-liquid equilibria interface (continuous gray line), and the liquid-hydrate equilibrium interface (gray dotted-dashed line) and the one in the top right shows the water number of moles in the bulk liquid phase ($n_{L,}H_2O$). The dotted line describes the limited by diffusion profile (*DR*=0.01), the continuous line the diffusion-reaction coupling profile (*DR*=0.1), and the dotted-dashed line, in the 2nd time axis, the limited by reaction profile (*DR*=0.99). All profiles are at 276 K and 48.6 bar.

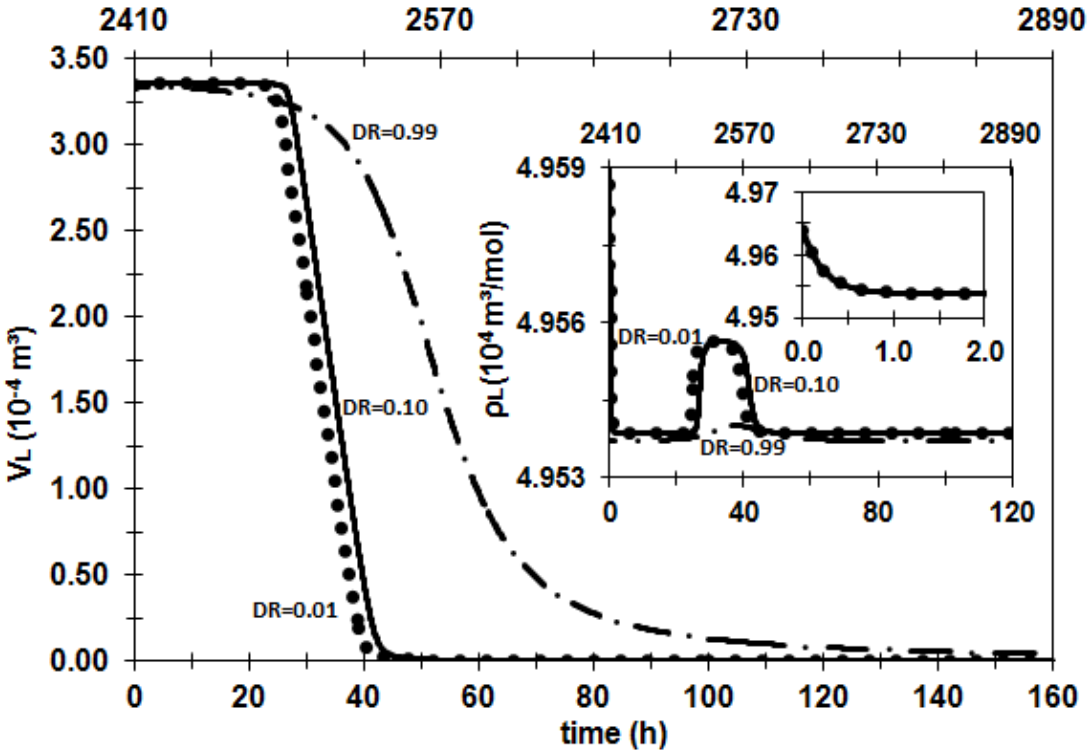

Figure S14 - The temporal profile of the liquid phase volume (V_L). The insertion shows the liquid density (ρ_L) profile with a zoom in the methane in water saturation (the first 2 hours). The dotted line describes the limited by diffusion profile (*DR*=0.01), the continue line the diffusion-reaction coupling profile (*DR*=0.1), and the dotted-dashed line, in the 2nd time axis, the limited by reaction profile (*DR*=0.99). All profiles are at 276 K and 48.6 bar.

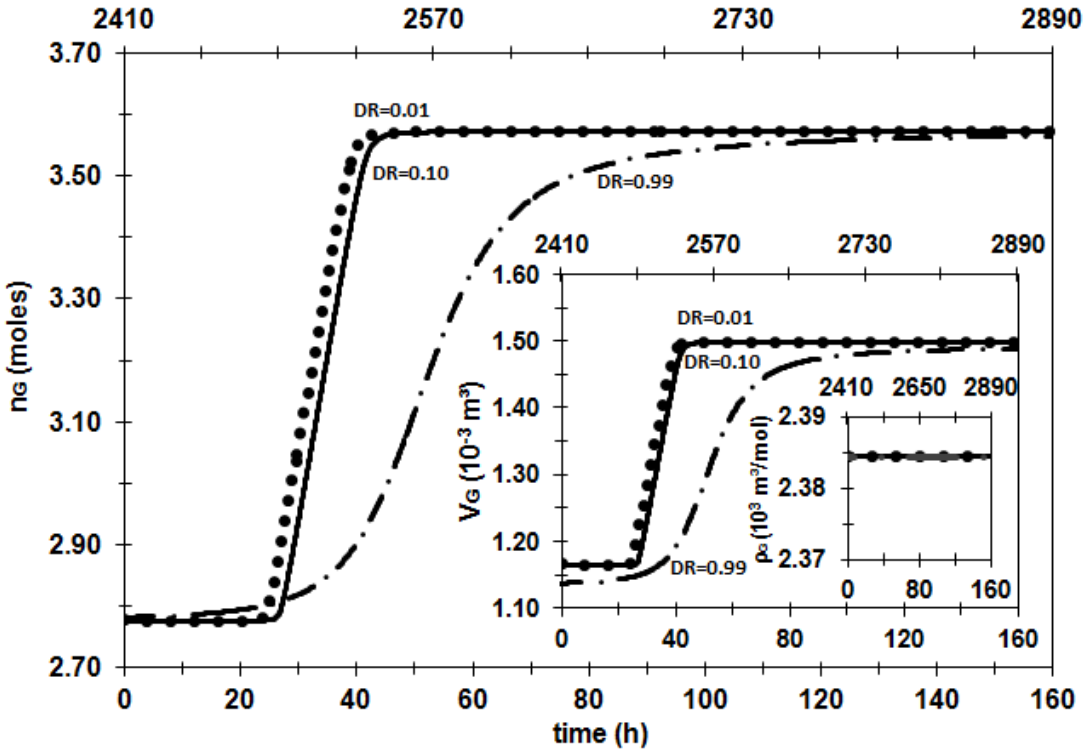

Figure S15 - The temporal profile of the methane number of moles in the pure vapor phase (n_G). The insertion shows the vapor phase volume (V_G) with the constant vapor density (ρ_G) profile. The dotted line describes the limited by diffusion profile (*DR*=0.01), the continuous line the diffusion-reaction coupling profile (*DR*=0.1), and the dotted-dashed line, in the 2nd time axis, the limited by reaction profile (*DR*=0.99). All profiles are at 276 K and 48.6 bar.

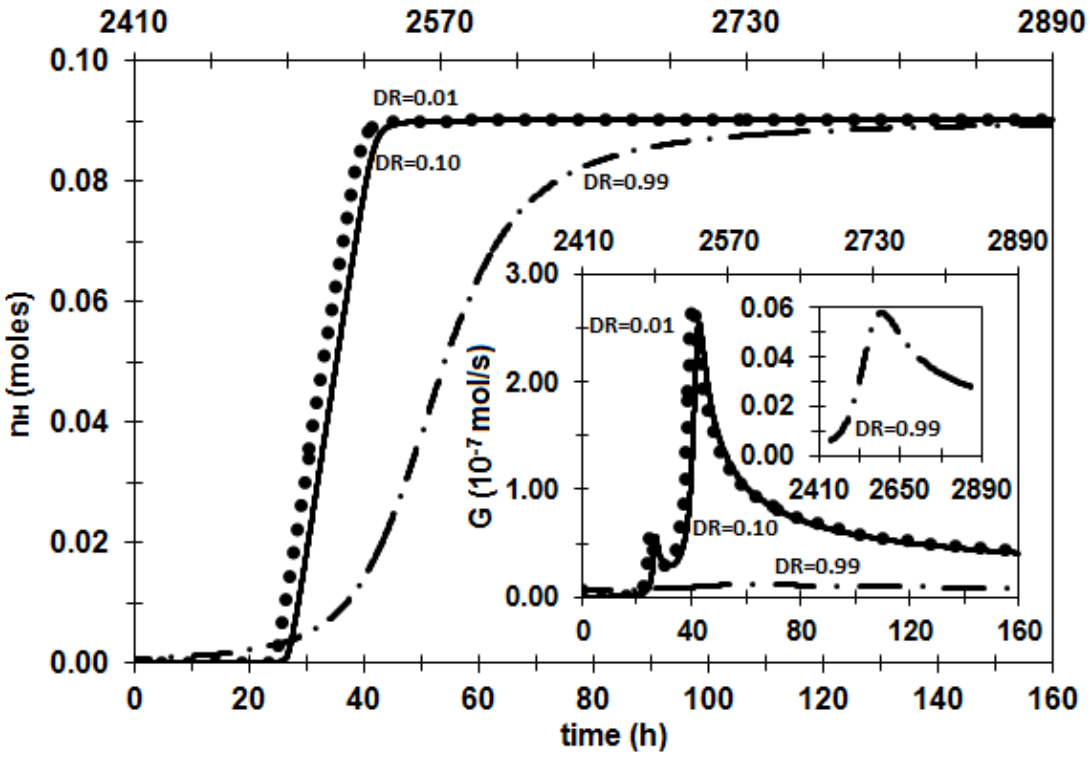

Figure S16 - The temporal profile of the hydrate number of moles (n_H). The insertion shows the hydrate growth rate (G) temporal profile with a zoom in the limited by reaction profile. The dotted line describes the limited by diffusion profile (*DR*=0.01), the continuous line the diffusion-reaction coupling profile (*DR*=0.1), and the dotted-dashed line, in the 2nd time axis, the limited by reaction profile (*DR*=0.99). All profiles are at 276 K and 48.6 bar.

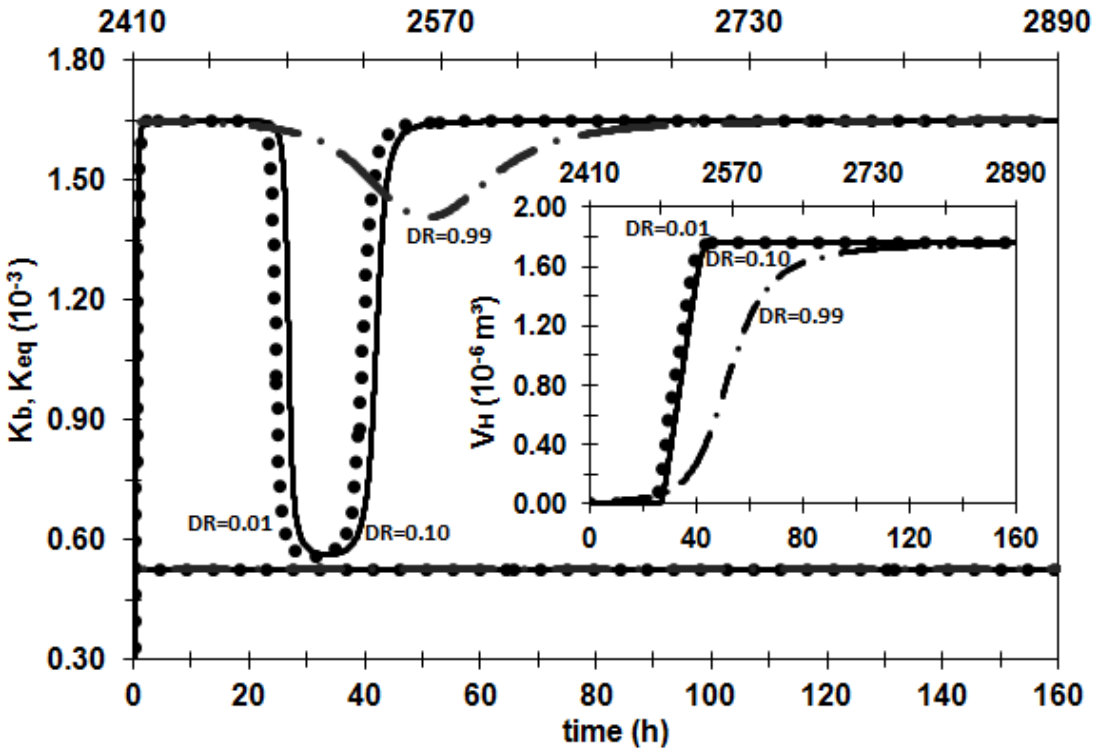

Figure S17 - The temporal profile of the product reagents' activities weighted by their stoichiometric coefficients in the bulk phase variable (K_b) and in the liquid-hydrate equilibrium interface variable (K_{eq}). The variable in the bulk liquid phase (K_b) is the one with the the highest value, while the variable in the liquid-hydrate equilibrium interface (K_{eq}) is the one constant. The insertion shows the hydrate phase volume (V_H). The dotted line describes the limited by diffusion profile (*DR*=0.01), the continuous line the diffusion-reaction coupling profile (*DR*=0.1), and the dotted-dashed line, in the 2nd time axis, the limited by reaction profile (*DR*=0.99). All profiles are at 276 K and 48.6 bar.

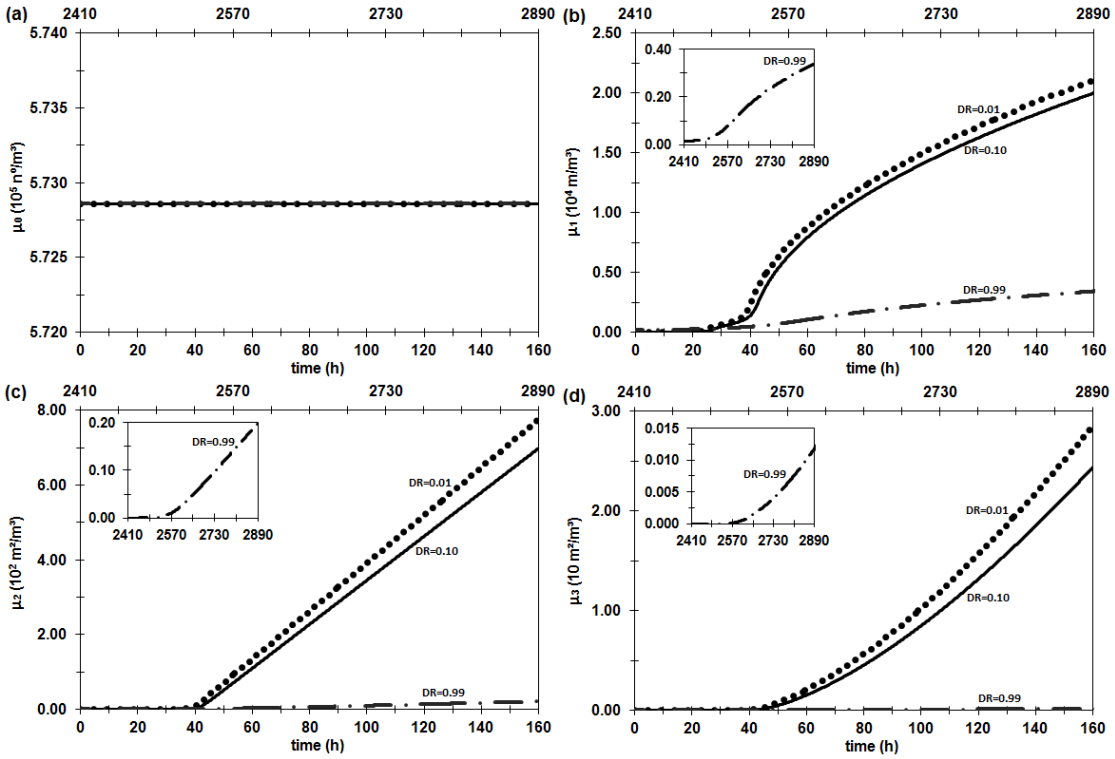

Figure S18 - (a) The temporal profile of the population balance moment of order zero, number of particles per liquid volume (μ_0), (b) moment of order one, particle diameter per liquid volume (μ_1), (c) moment of order two, particle surface area per liquid volume (μ_2) and (d) moment of order three, particle volume per liquid volume (μ_3). The inserts are a zoom in the limited by reaction profile. The dotted line describes the limited by diffusion profile (*DR*=0.01), the continuous line the diffusion-reaction coupling profile (*DR*=0.1), and the dotted-dashed line, in the 2nd time axis, the limited by reaction profile (*DR*=0.99). All profiles are at 276 K and 48.6 bar.

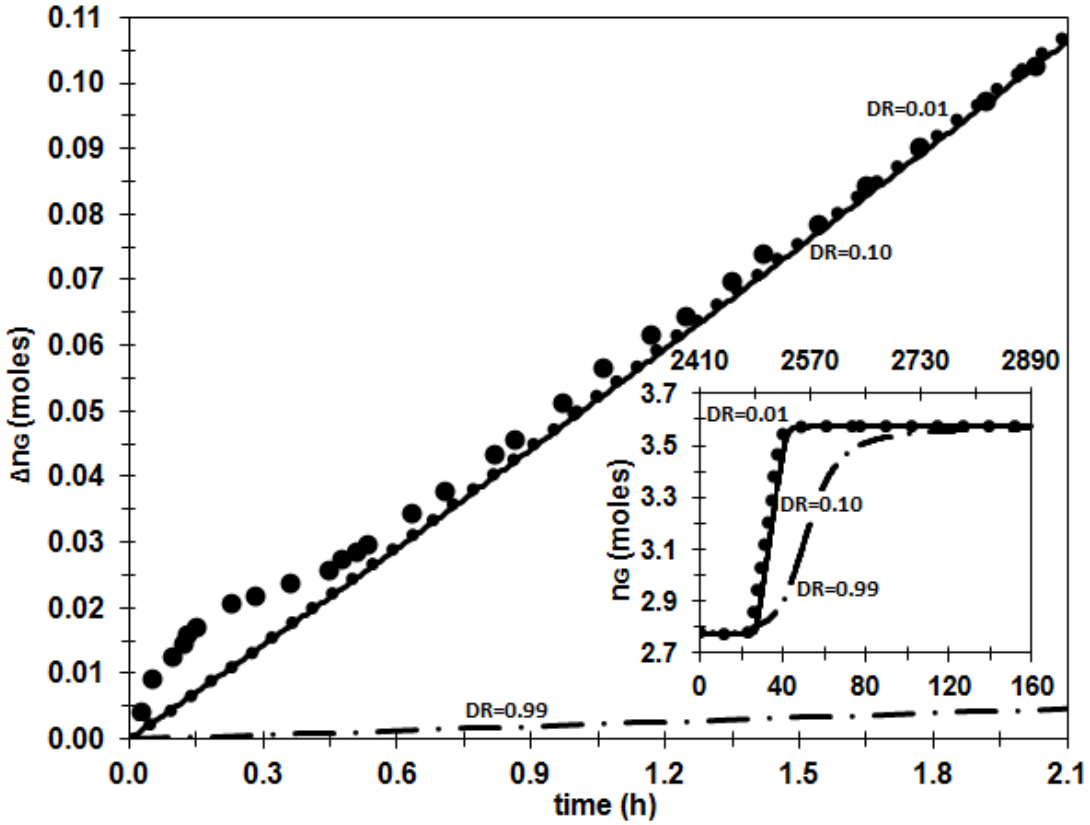

Figure S19 - The temporal profile of the methane molar consumption (Δn_G). The insertion shows the temporal variation of the methane number of moles in the gas phase (n_G). The dotted line describes the limited by diffusion profile (*DR*=0.01), the continue line the diffusion-reaction coupling profile (*DR*=0.1), and the dotted-dashed line, in the 2nd time axis, the limited by reaction profile (*DR*=0.99). All profiles are at 276 K and 48.6 bar. The black circles are the Englezos et al. [42] data also at 276 K and 48.6 bar.

S.7.3 System at 274 K and 76.0 bar with water activity in the driving force

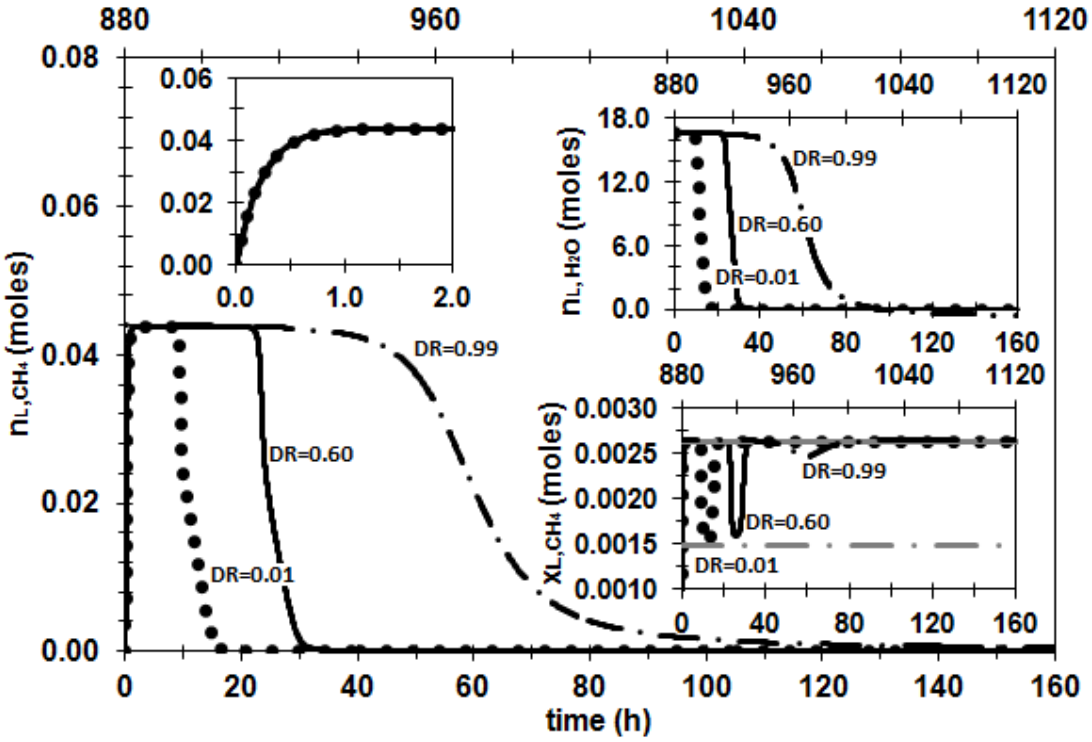

Figure S20 - The temporal profile of the methane number of moles in the bulk liquid phase ($n_{L,}CH_4$). The insertion on the left shows the methane in water saturation profile, the one in the bottom-right shows the methane mole fraction ($x_{L,}CH_4$) profile in the bulk liquid phase (dark lines), in the gas-liquid equilibria interface (gray continus line), and in the liquid-hydrate equilibrium interface (gray dotted-dashed line) and the one in the top right shows the water number of moles in the bulk liquid phase ($n_{L,}H_2O$). The dotted line describes the limited by diffusion profile (*DR*=0.01), the continuous line the diffusion-reaction coupling profile (*DR*=0.6), and the dotted-dashed line, in the 2nd time axis, the limited by reaction profile (*DR*=0.99). All profiles are at 274 K and 76.0 bar.

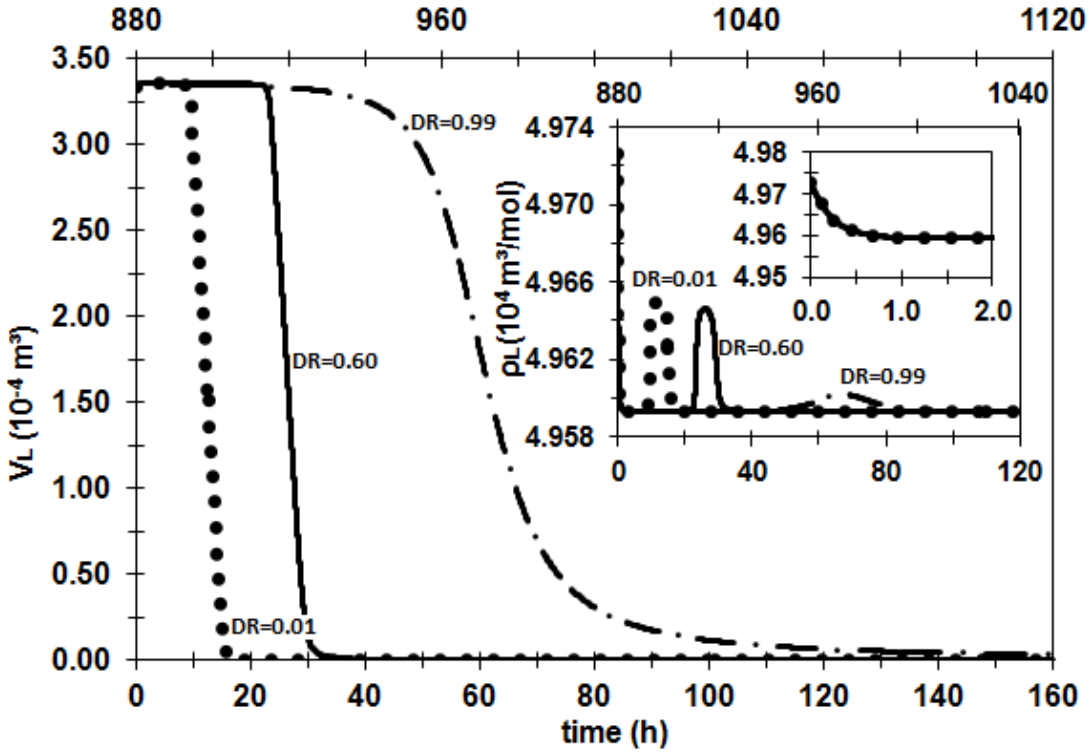

Figure S21 - The temporal profile of the liquid phase volume (V_L). The insertion shows the liquid density (ρ_L) profile with a zoom in the methane in water saturation (the first 2 hours). The dotted line describes the limited by diffusion profile (*DR*=0.01), the continuous line the diffusion-reaction coupling profile (*DR*=0.6), and the dotted-dashed line, in the 2nd time axis, the limited by reaction profile (*DR*=0.99). All profiles are at 274 K and 76.0 bar.

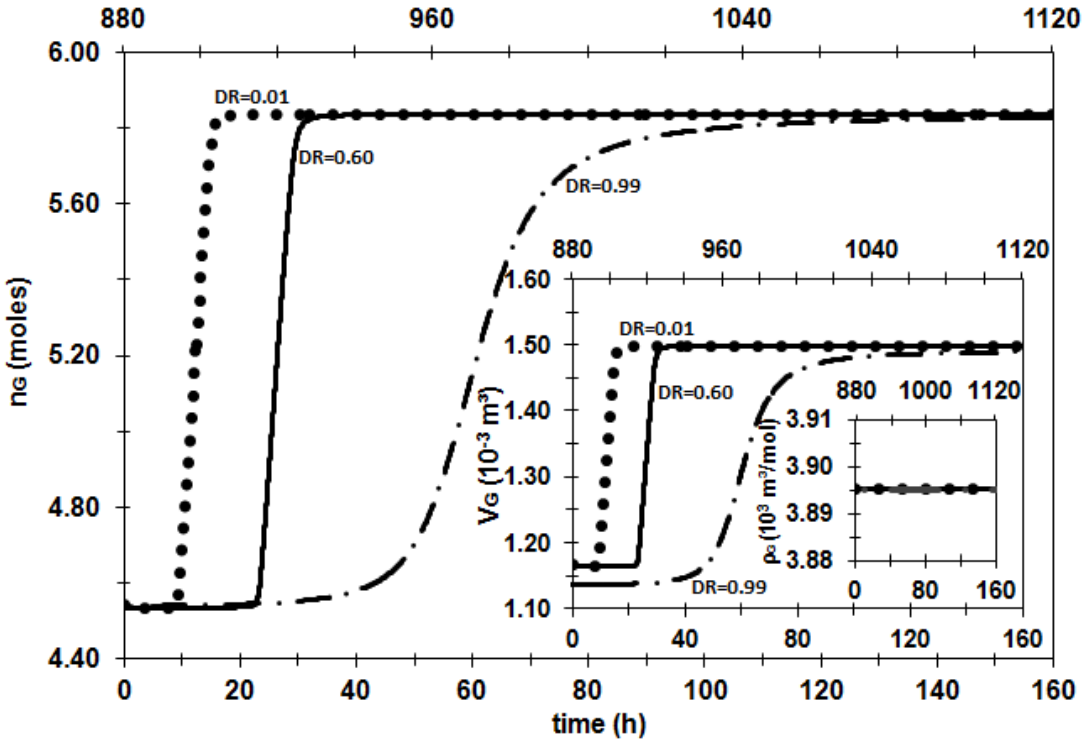

Figure S22 - The temporal profile of the methane number of moles in the pure vapor phase (n_G). The insertion shows the vapor phase volume (V_G) with the constant vapor density (ρ_G) profile. The dotted line describes the limited by diffusion profile (*DR*=0.01), the continuous line the diffusion-reaction coupling profile (*DR*=0.6), and the dotted-dashed line, in the 2nd time axis, the limited by reaction profile (*DR*=0.99). All profiles are at 274 K and 76.0 bar.

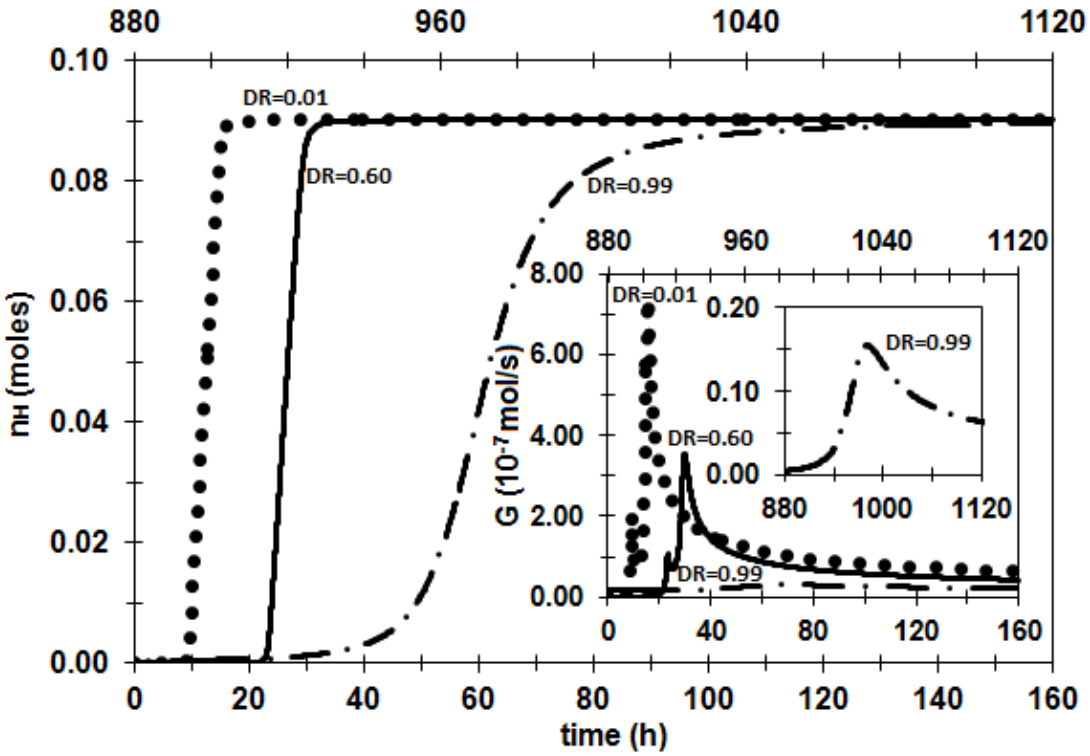

Figure S23 - The temporal profile of the hydrate number of moles (n_H). The insertion shows the hydrate growth rate (G) temporal profile with a zoom in the limited by reaction profile. The dotted line describes the limited by diffusion profile (*DR*=0.01), the continuous line the diffusion-reaction coupling profile (*DR*=0.6), and the dotted-dashed line, in the 2nd time axis, the limited by reaction profile (*DR*=0.99). All profiles are at 274 K and 76.0 bar.

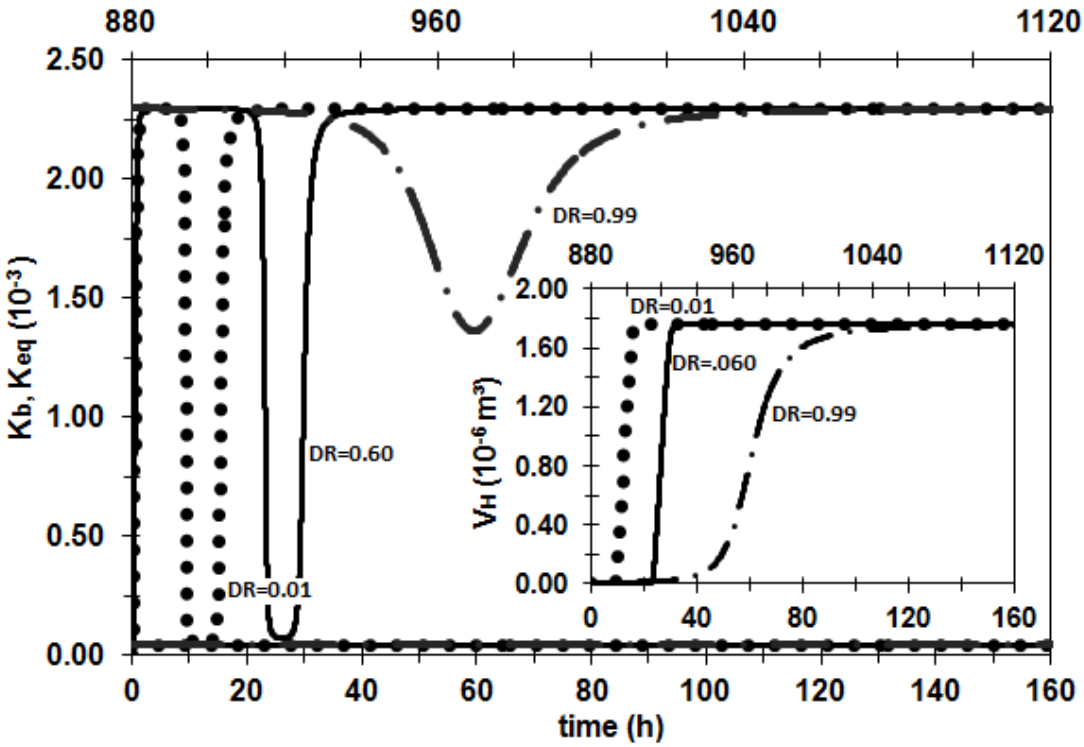

Figure S24 - The temporal profile of the product reagents' activities weighted by their stoichiometric coefficients in the bulk phase variable (K_b) and in the liquid-hydrate equilibrium interface variable (K_{eq}). The variable in the bulk liquid phase (K_b) is the one with the the highest value, while the variable in the liquid-hydrate equilibrium interface (K_{eq}) is the one constant. The insertion shows the hydrate phase volume (V_H). The dotted line describes the limited by diffusion profile (*DR*=0.01), the continuous line the diffusion-reaction coupling profile (*DR*=0.6), and the dotted-dashed line, in the 2nd time axis, the limited by reaction profile (*DR*=0.99). All profiles are at 274 K and 76.0 bar.

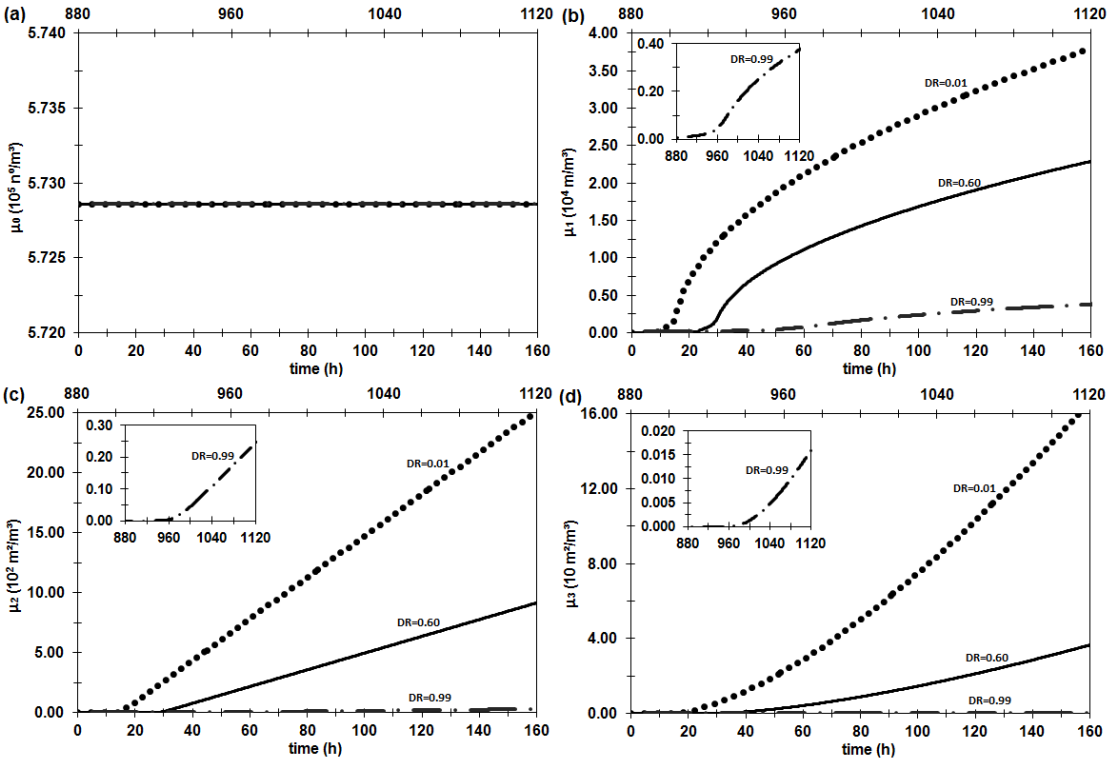

Figure S25 - (a) The temporal profile of the population balance moment of order zero, number of particles per liquid volume (μ_0), (b) moment of order one, particle diameter per liquid volume (μ_1), (c) moment of order two, particle surface area per liquid volume (μ_2) and (d) moment of order three, particle volume per liquid volume (μ_3). The inserts are a zoom in the limited by reaction profile. The dotted line describes the limited by diffusion profile (*DR*=0.01), the continuous line the diffusion-reaction coupling profile (*DR*=0.6), and the dotted-dashed line, in the 2nd time axis, the limited by reaction profile (*DR*=0.99). All profiles are at 274 K and 76.0 bar.

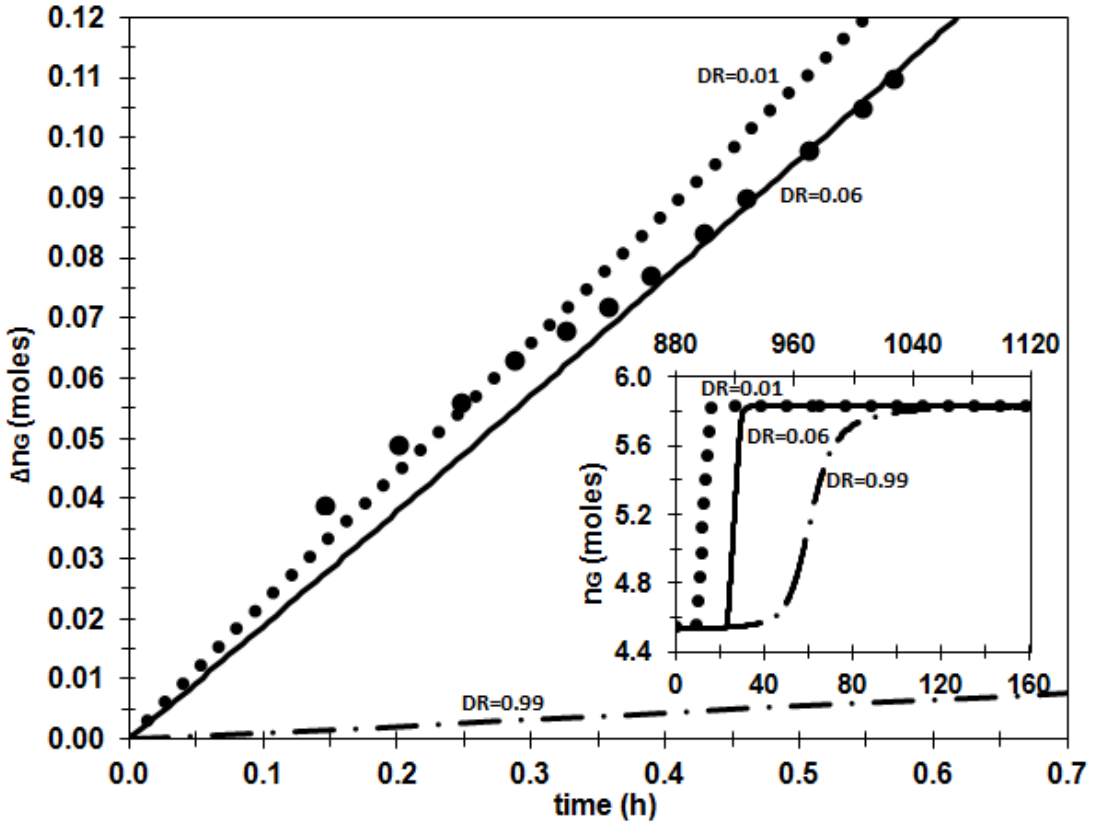

Figure S26 - The temporal profile of the methane molar consumption (Δn_G). The insertion shows the temporal variation of the methane number of moles in the gas phase (n_G). The dotted line describes the limited by diffusion profile (*DR*=0.01), the continuous line the diffusion-reaction coupling profile (*DR*=0.6), and the dotted-dashed line, in the 2nd time axis, the limited by reaction profile (*DR*=0.99). All profiles are at 274 K and 76.0 bar. The black circles are the Englezos et al. (1987) [42] data also at 274 K and 76.0 bar.

S.7.4 System at 276 K and 70.9 bar without water activity in the driving force

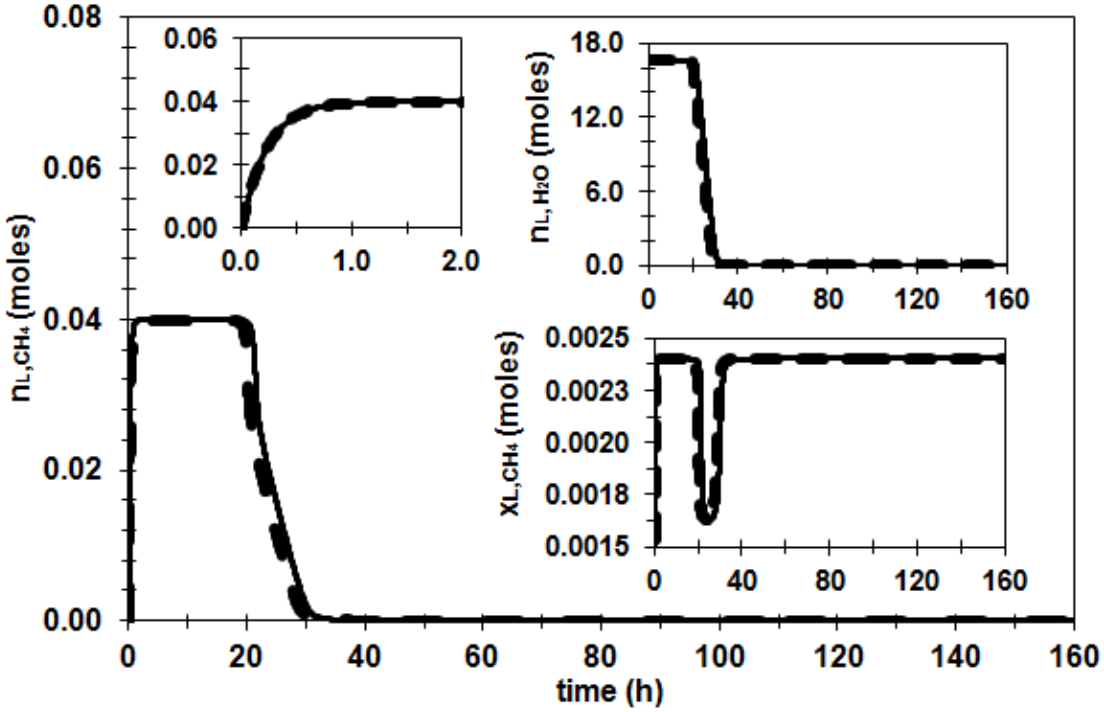

Figure S27 - The diffusion-reaction coupling (*DR*=0.5) temporal profile of the methane number of moles in the bulk liquid phase ($n_{L,}CH_4$). The insertion on the left shows the methane in water saturation profile, the one in the bottom-right shows the methane mole fraction ($x_{L,}CH_4$) profile in the bulk liquid phase (dark lines), in the gas-liquid equilibria interface (gray continus line) and in the liquid-hydrate equilibrium interface (gray dotted-dashed line) and the one in the top right shows the water number of moles in the bulk liquid phase ($n_{L,}H_2O$). The continuous line represents the profile with the water activity, while the dashed line represents the profile without the water activity in the growth rate driving force. All profiles are at 276 K and 70.9 bar.

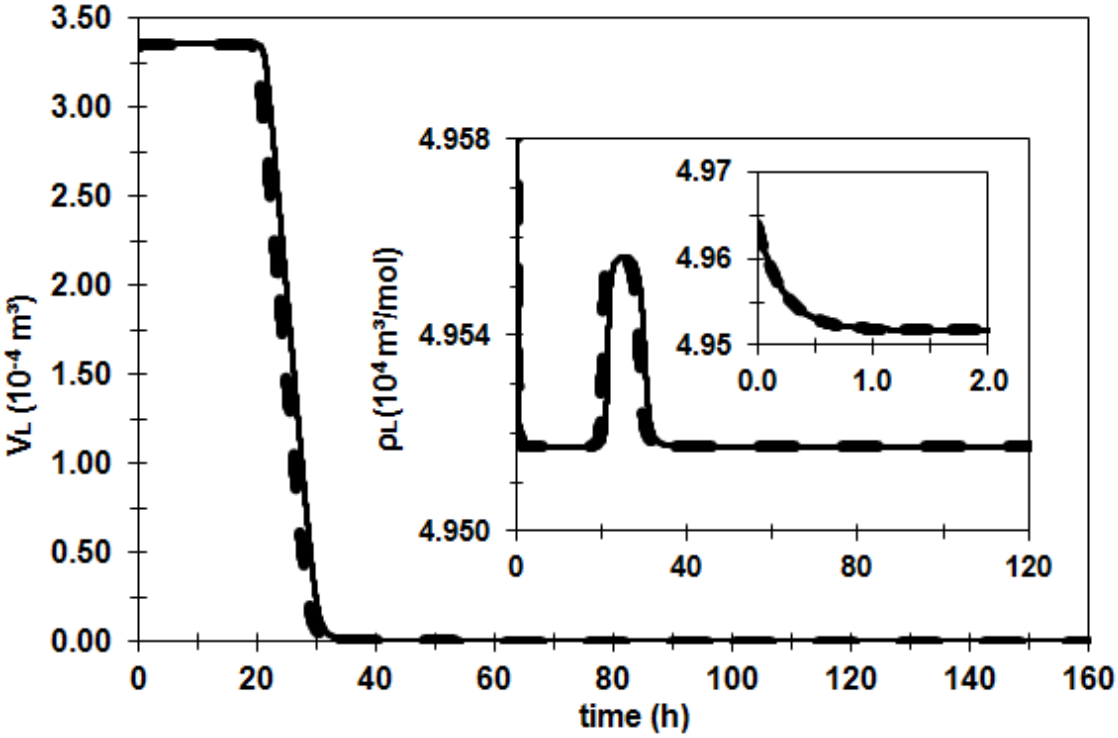

Figure S28 - The diffusion-reaction coupling (*DR*=0.5) temporal profile of the liquid phase volume (V_L). The insertion shows the liquid density (ρ_L) profile with a zoom in the methane in water saturation (the first 2 hours). The continuous line represents the profile with the water activity, while the dashed line represents the profile without the water activity in the growth rate driving force. All profiles are at 276 K and 70.9 bar.

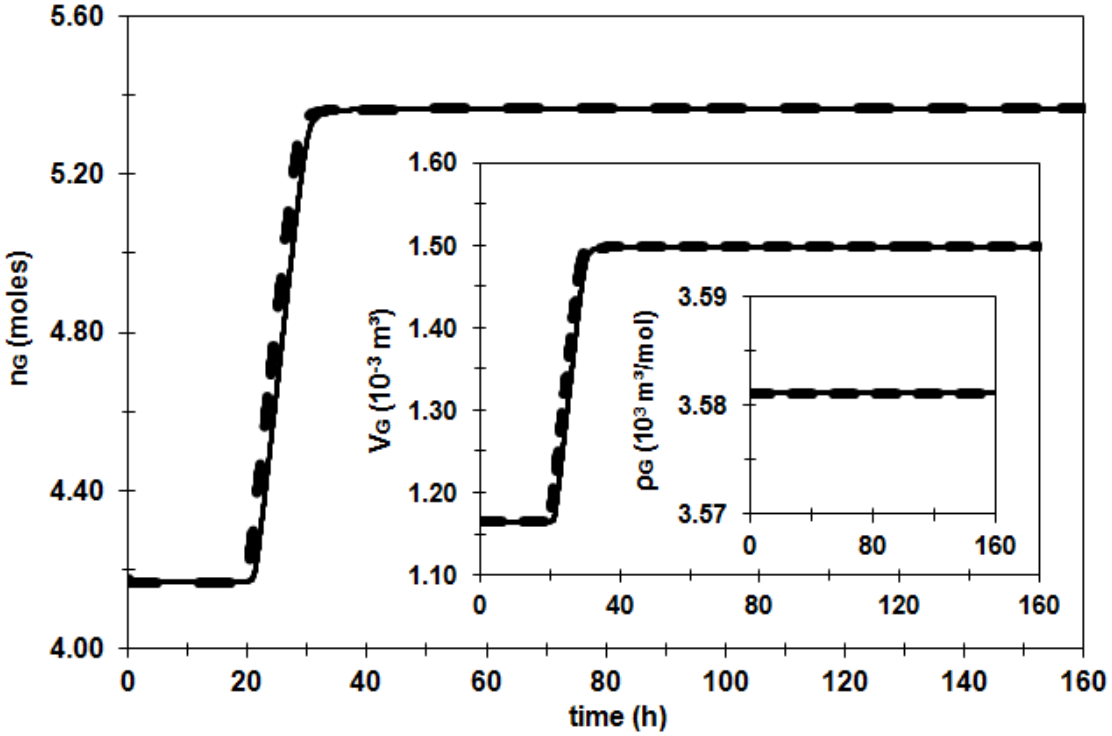

Figure S29 - The diffusion-reaction coupling (*DR*=0.5) temporal profile of the methane number of moles in the pure vapor phase (n_G). The insertion shows the vapor phase volume (V_G) with the constant vapor density (ρ_G) profile. The continuous line represents the profile with the water activity, while the dashed line represents the profile without the water activity in the growth rate driving force. All profiles are at 276 K and 70.9 bar.

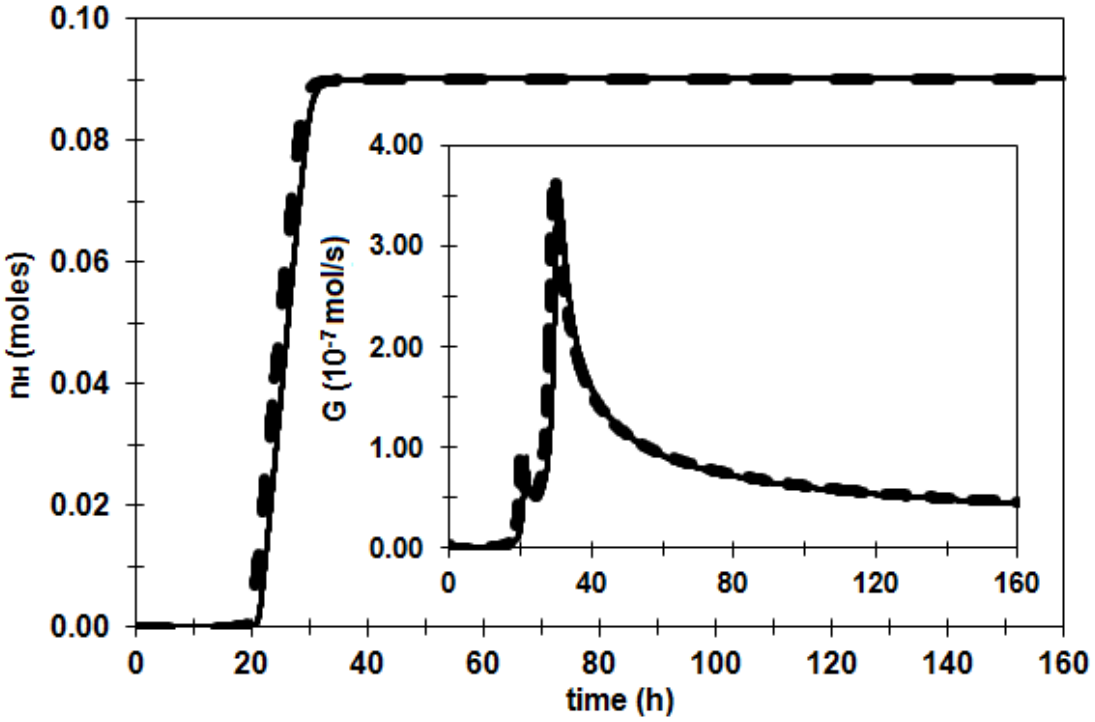

Figure S30 - The diffusion-reaction coupling (*DR*=0.5) temporal profile of the hydrate number of moles (n_H). The insertion shows the hydrate growth rate (G) temporal profile with a zoom in the limited by reaction profile. The continuous line represents the profile with the water activity, while the dashed line represents the profile without the water activity in the growth rate driving force. All profiles are at 276 K and 70.9 bar.

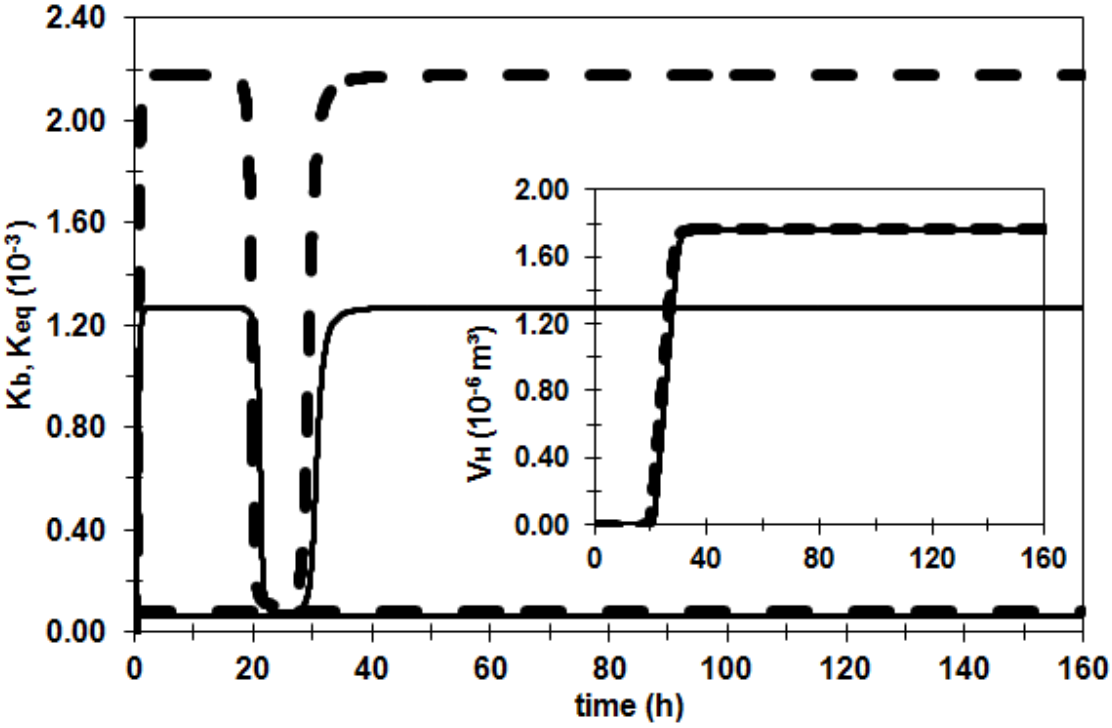

Figure S31 - The diffusion-reaction coupling (*DR*=0.5) temporal profile of the product reagents' activities weighted by their stoichiometric coefficients in the bulk phase variable (K_b) and in the liquid-hydrate equilibrium interface variable (K_{eq}). The variable in the bulk liquid phase (K_b) is the one with the the highest value, while the variable in the liquid-hydrate equilibrium interface (K_{eq}) is the one constant. The insertion shows the hydrate phase volume (V_H). The continuous line represents the profile with the water activity, while the dashed line represents the profile without the water activity in the growth rate driving force. All profiles are at 276 K and 70.9 bar.

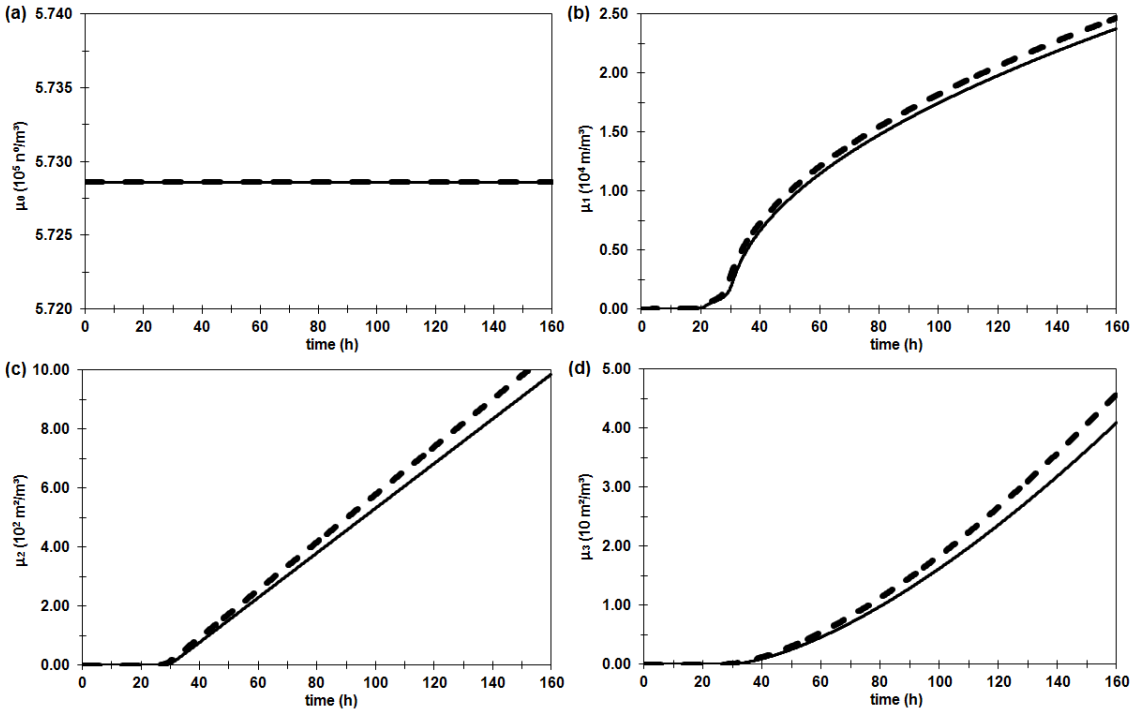

Figure S32 - (a) The diffusion-reaction coupling (*DR*=0.5) temporal profile of the population balance moment of order zero, number of particles per liquid volume (μ_0), (b) moment of order one, particle diameter per liquid volume (μ_1), (c) moment of order two, particle surface area per liquid volume (μ_2) and (d) moment of order three, particle volume per liquid volume (μ_3). The inserts are a zoom in the limited by reaction profile. The continuous line represents the profile with the water activity, while the dashed line represents the profile without the water activity in the growth rate driving force. All profiles are at 276 K and 70.9 bar.

S.8 System property derivative profiles

S.8.1 System at 276 K and 70.9 bar with water activity in the driving force

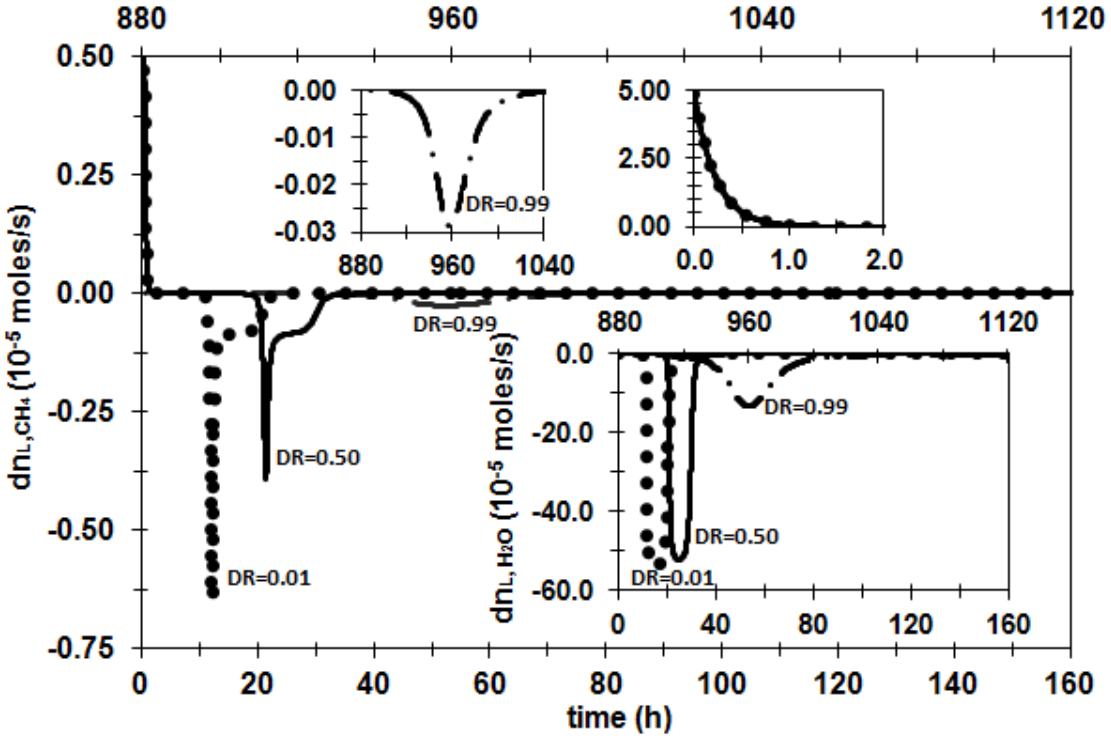

Figure S33 - The differential profile of methane number of moles in the bulk liquid phase ($dn_{L,}CH_4$). The insertion on the top-left shows a zoom in the limited by reaction profile, while the one in the top-right shows the methane in water saturation profile (the first 2 hours). The insertion in the bottom-right shows the differential profile of the water number of moles in the bulk liquid phase ($dn_{L,}H_2O$). The dotted line describes the limited by diffusion profile (*DR*=0.01), the continuous line the diffusion-reaction coupling profile (*DR*=0.5), and the dotted-dashed line, in the 2nd time axis, the limited by reaction profile (*DR*=0.99). All profiles are at 276 K and 70.9 bar.

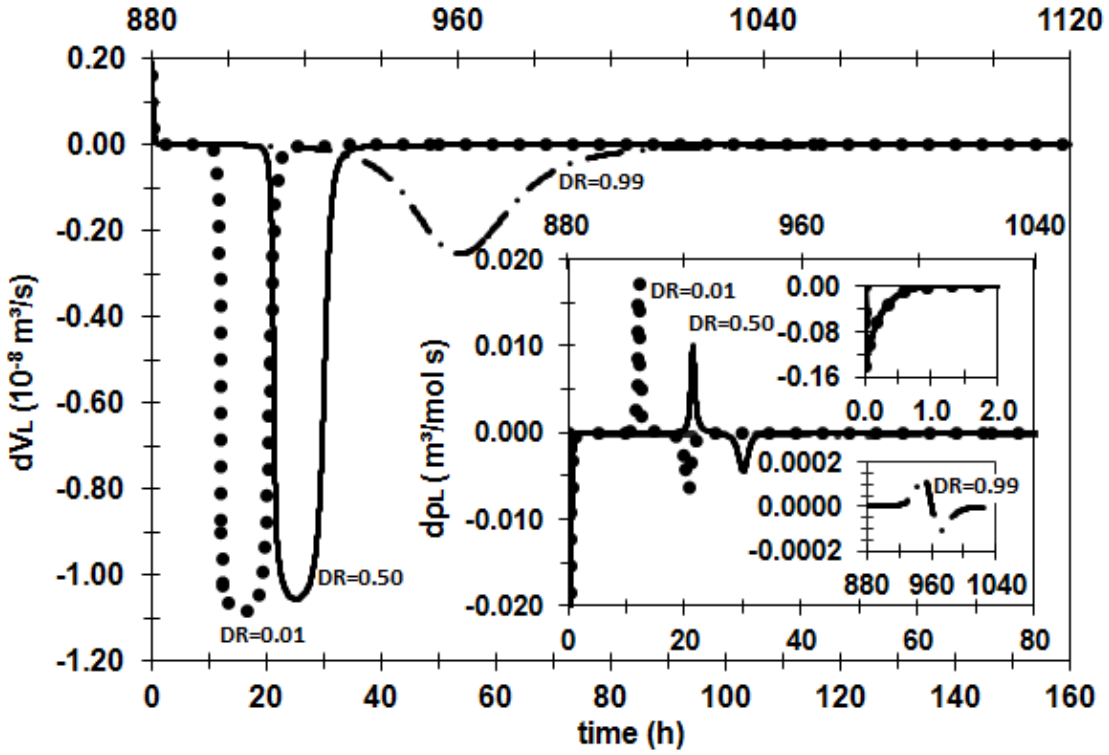

Figure S34 - The differential profile of the liquid phase volume (dV_L). The insertion shows the differential profile of the liquid density ($d\rho_L$) with a zoon in the methane in water saturation (the first 2 hours) and in the limited by reaction profile. The dotted line describes the limited by diffusion profile (*DR*=0.01), the continuous line the diffusion-reaction coupling profile (*DR*=0.5), and the dotted-dashed line, in the 2nd time axis, the limited by reaction profile (*DR*=0.99). All profiles are at 276 K and 70.9 bar.

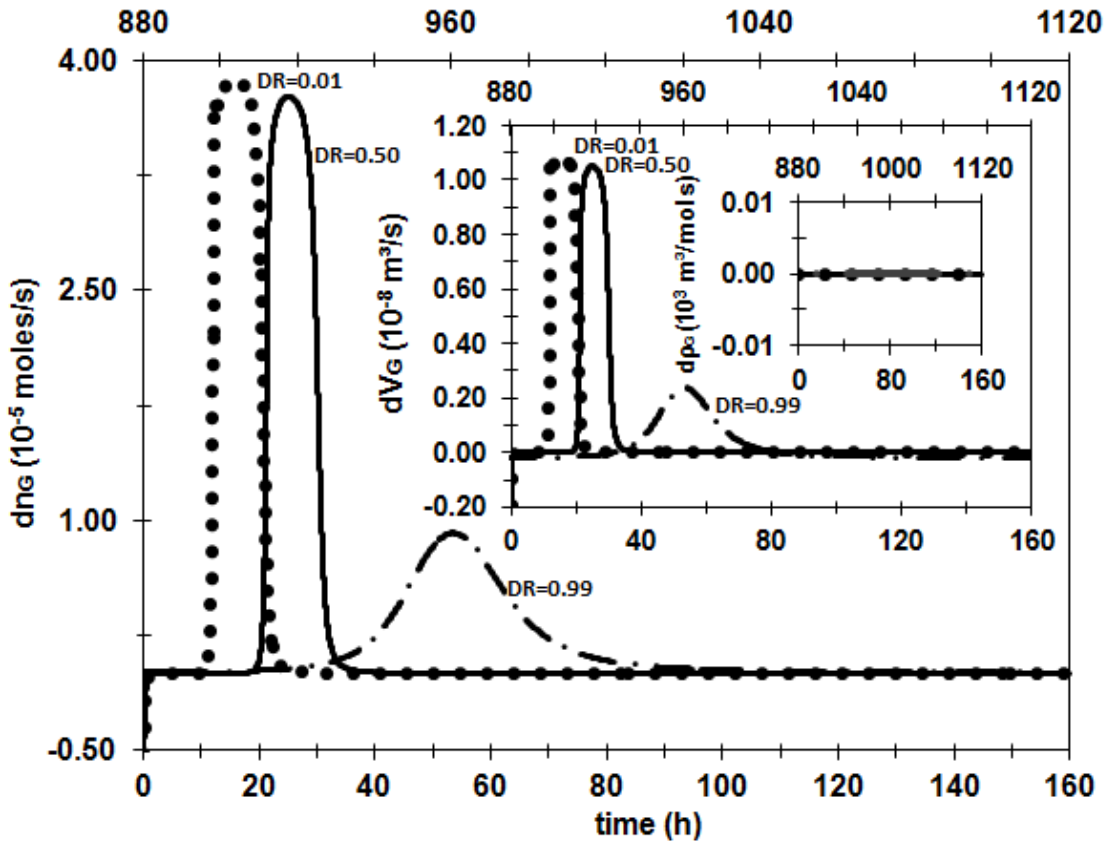

Figure S35 - The differential profile of the methane number of moles in the pure vapor phase (dn_G). The insertion shows the vapor phase volume (dV_G) with the constant vapor density ($d\rho_G$) differential profile. The dotted line describes the limited by diffusion profile (*DR*=0.01), the continuous line the diffusion-reaction coupling profile (*DR*=0.5), and the dotted-dashed line, in the 2nd time axis, the limited by reaction profile (*DR*=0.99). All profiles are at 276 K and 70.9 bar.

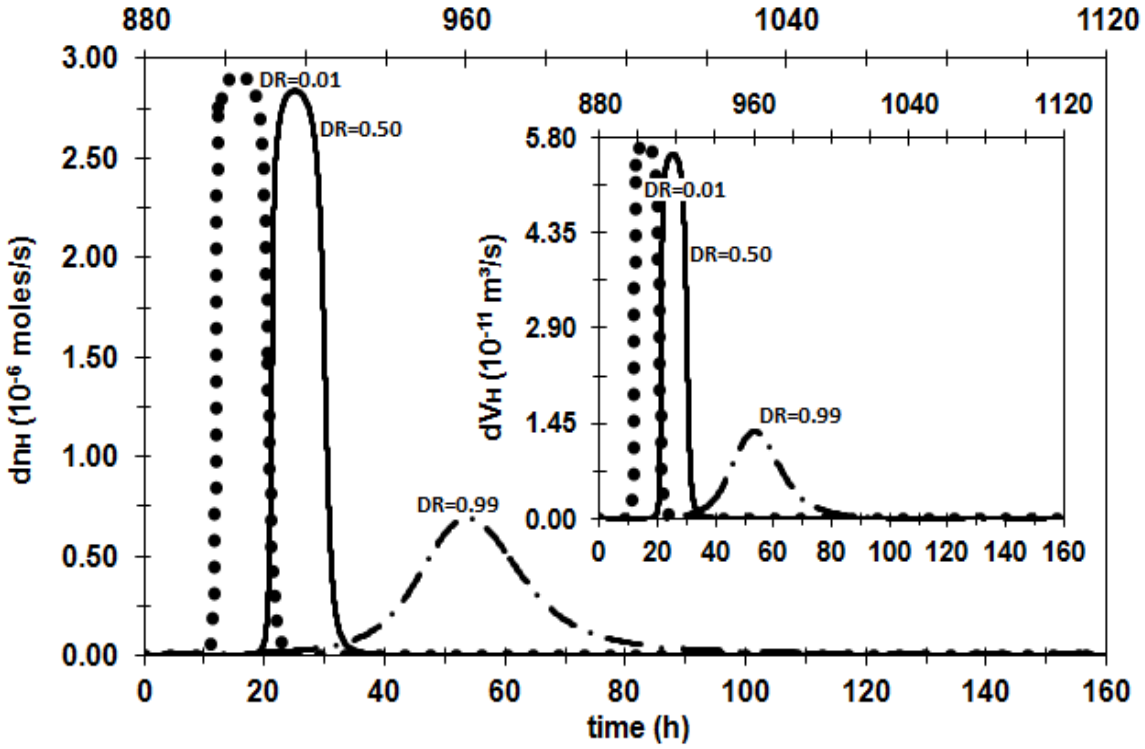

Figure S36 - The differential profile of the hydrate number of moles (dn_H). The insertion shows the hydrate phase volume (dV_H) differential profile. The dotted line describes the limited by diffusion profile (*DR*=0.01), the continuous line the diffusion-reaction coupling profile (*DR*=0.5), and the dotted-dashed line, in the 2nd time axis, the limited by reaction profile (*DR*=0.99). All profiles are at 276 K and 70.9 bar.

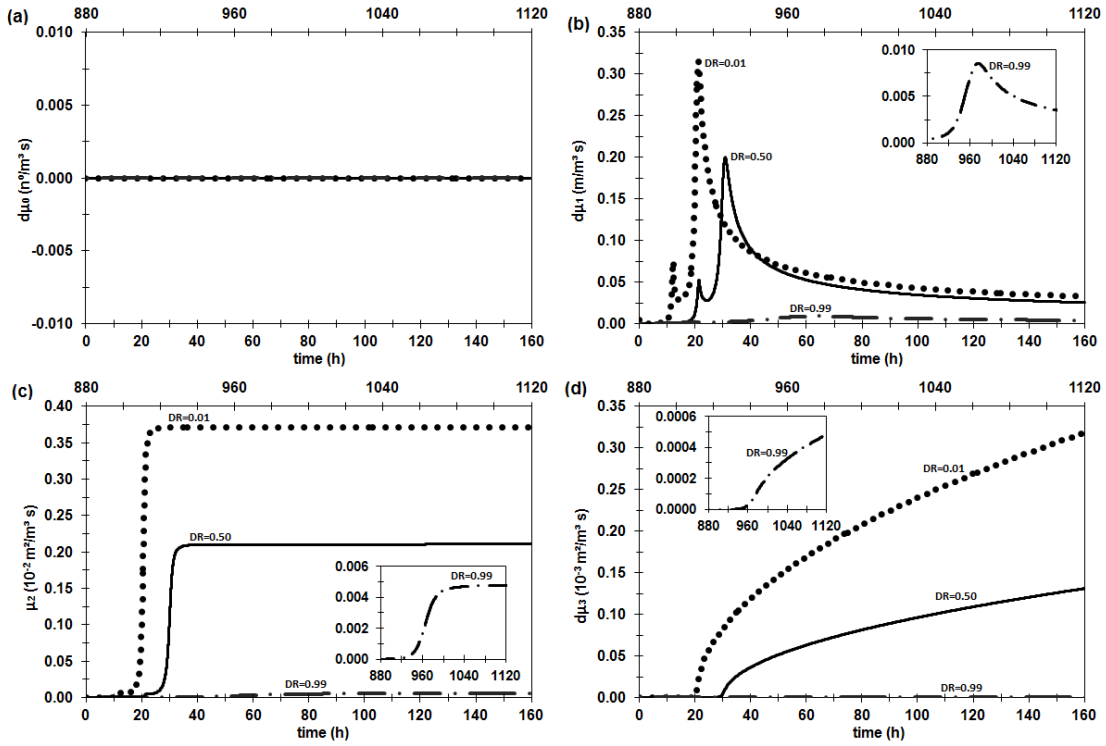

Figure S37 - (a) The differential profile of the population balance moment of order zero, number of particles per liquid volume ($d\mu_0$), (b) moment of order one, particle diameter per liquid volume ($d\mu_1$), (c) moment of order two, particle surface area per liquid volume ($d\mu_2$) and (d) moment of order three, particle volume per liquid volume ($d\mu_3$). The inserts are a zoom in the limited by reaction differential profile. The dotted line describes the limited by diffusion profile (*DR*=0.01), the continuous line the diffusion-reaction coupling profile (*DR*=0.5), and the dotted-dashed line, in the 2nd time axis, the limited by reaction profile (*DR*=0.99). All profiles are at 276 K and 70.9 bar.

S.8.2 System at 276 K and 48.6 bar with water activity in the driving force

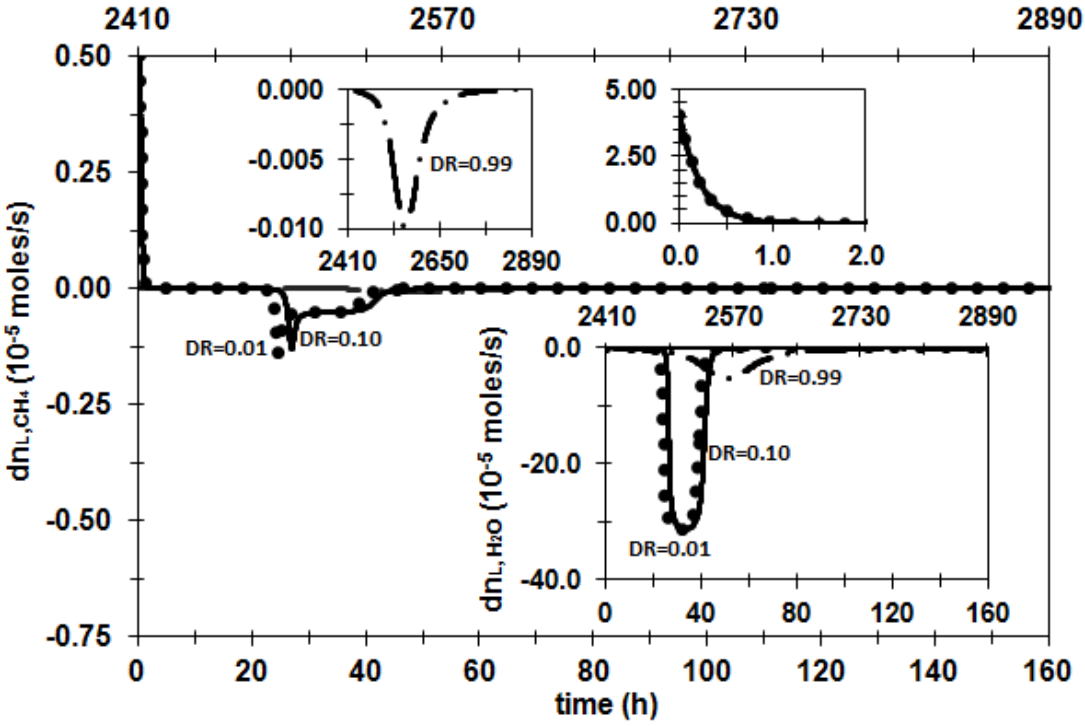

Figure S38 - The differential profile of methane number of moles in the bulk liquid phase ($dn_{L,}CH_4$). The insertion on the top-left shows a zoom in the limited by reaction profile, while the one in the top-right shows the methane in water saturation profile (the first 2 hours). The insertion in the bottom-right shows the differential profile of the water number of moles in the bulk liquid phase ($dn_{L,}H_2O$). The dotted line describes the limited by diffusion profile (*DR*=0.01), the continuous line the diffusion-reaction coupling profile (*DR*=0.1), and the dotted-dashed line, in the 2nd time axis, the limited by reaction profile (*DR*=0.99). All profiles are at 276 K and 48.6 bar.

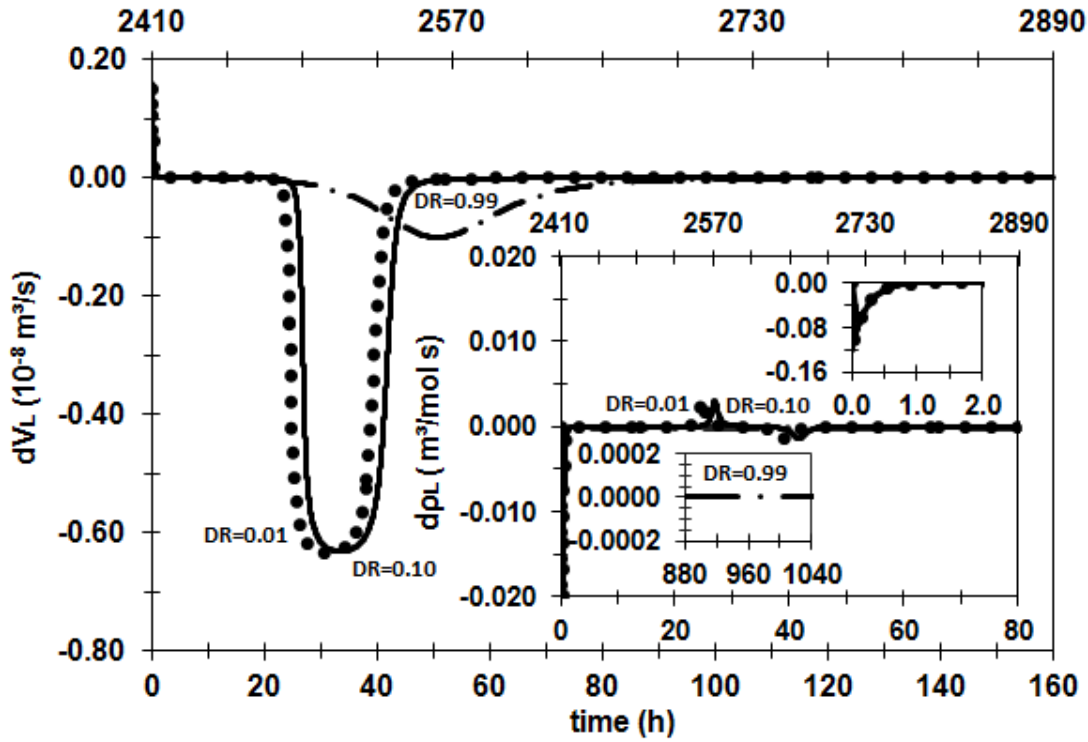

Figure S39 - The differential profile of the liquid phase volume (dV_L). The insertion shows the differential profile of the liquid density ($d\rho_L$) with a zoon in the methane in water saturation (the first 2 hours) and in the limited by reaction profile. The dotted line describes the limited by diffusion profile (*DR*=0.01), the continuous line the diffusion-reaction coupling profile (*DR*=0.1), and the dotted-dashed line, in the 2nd time axis, the limited by reaction profile (*DR*=0.99). All profiles are at 276 K and 48.6 bar.

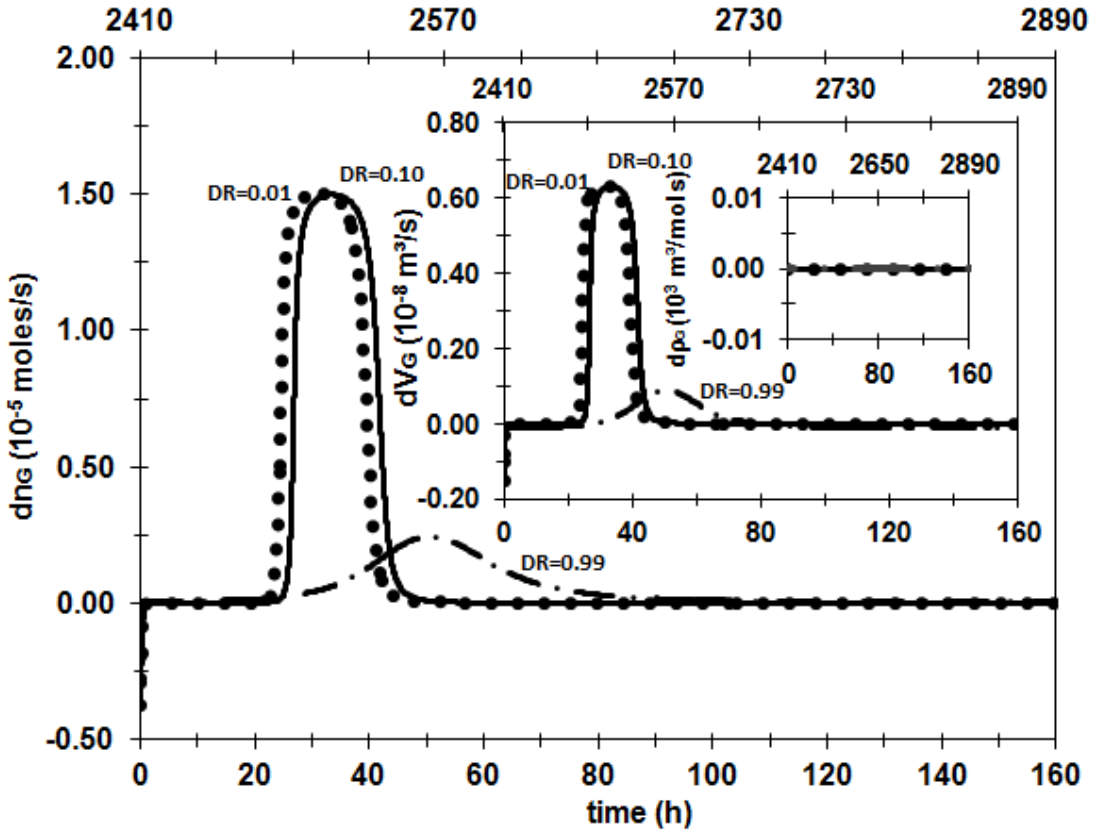

Figure S40 - The differential profile of the methane number of moles in the pure vapor phase (dn_G). The insertion shows the vapor phase volume (dV_G) with the constant vapor density ($d\rho_G$) differential profile. The dotted line describes the limited by diffusion profile (*DR*=0.01), the continuous line the diffusion-reaction coupling profile (*DR*=0.1), and the dotted-dashed line, in the 2nd time axis, the limited by reaction profile (*DR*=0.99). All profiles are at 276 K and 48.6 bar.

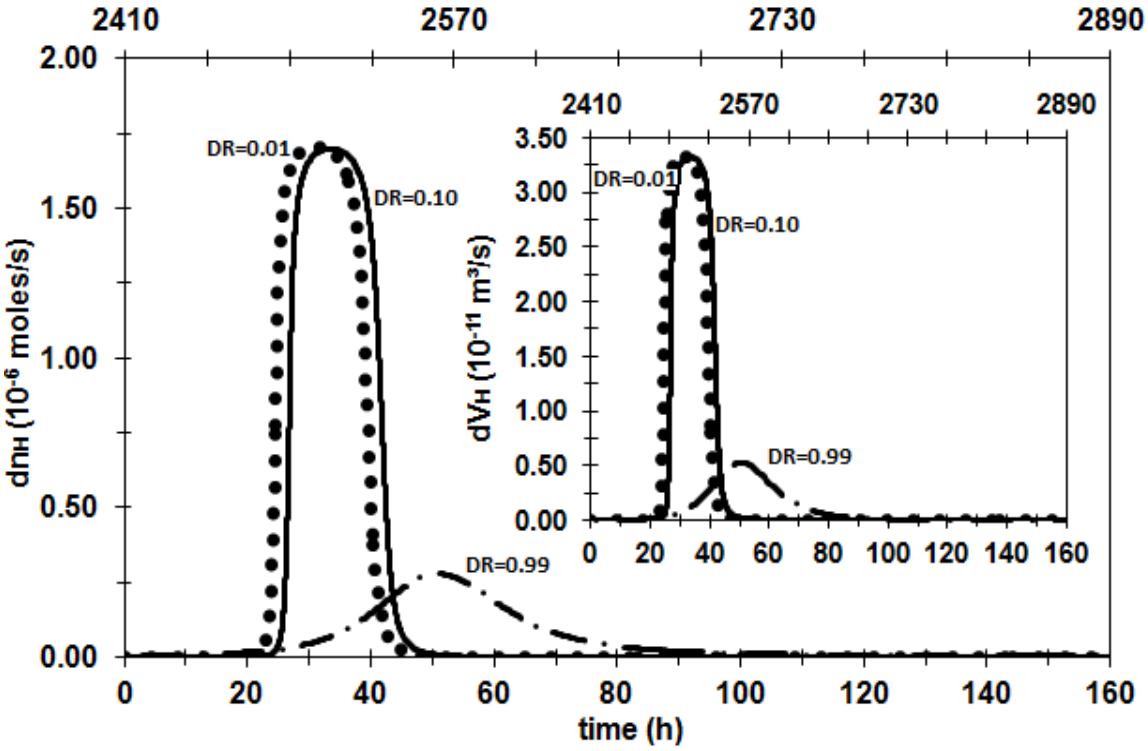

Figure S41 - The differential profile of the hydrate number of moles (dn_H). The insertion shows the hydrate phase volume (dV_H) differential profile. The dotted line describes the limited by diffusion profile (*DR*=0.01), the continuous line the diffusion-reaction coupling profile (*DR*=0.1), and the dotted-dashed line, in the 2nd time axis, the limited by reaction profile (*DR*=0.99). All profiles are at 276 K and 48.6 bar.

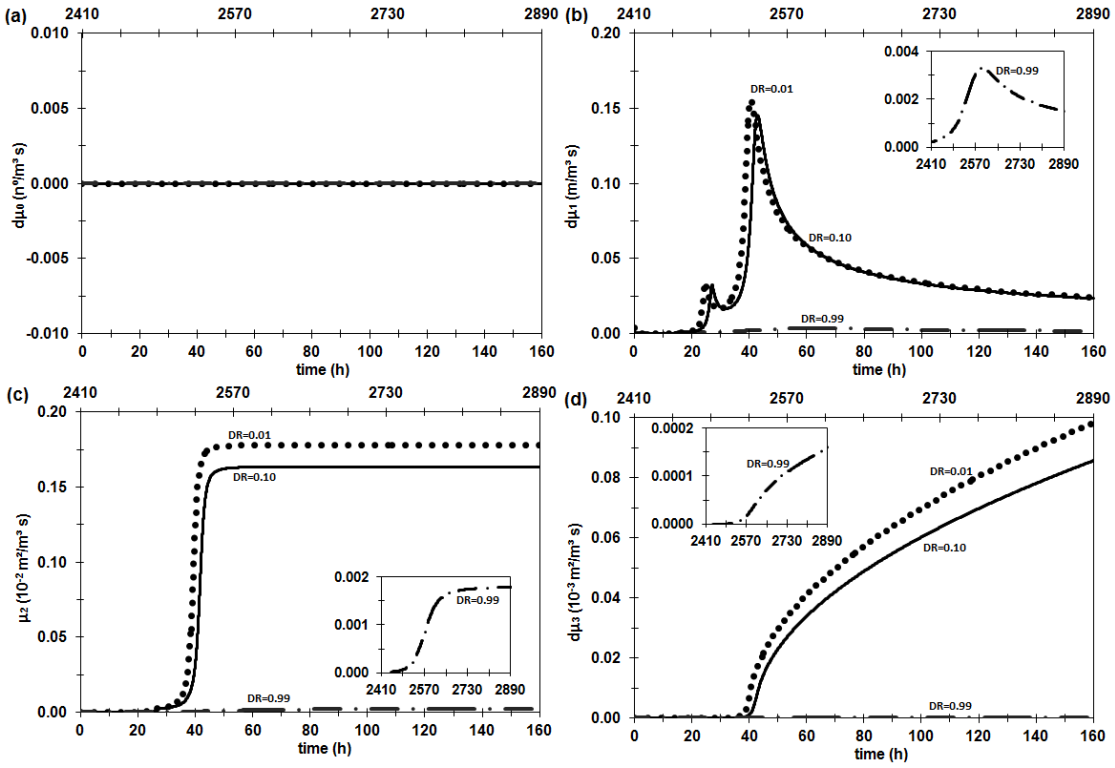

Figure S42 - (a) The differential profile of the population balance moment of order zero, number of particles per liquid volume ($d\mu_0$), (b) moment of order one, particle diameter per liquid volume ($d\mu_1$), (c) moment of order two, particle surface area per liquid volume ($d\mu_2$) and (d) moment of order three, particle volume per liquid volume ($d\mu_3$). The inserts are a zoom in the limited by reaction differential profile. The dotted line describes the limited by diffusion profile (*DR*=0.01), the continuous line the diffusion-reaction coupling profile (*DR*=0.1), and the dotted-dashed line, in the 2nd time axis, the limited by reaction profile (*DR*=0.99). All profiles are at 276 K and 48.6 bar.

S.8.3 System at 274 K and 76.0 bar with water activity in the driving force

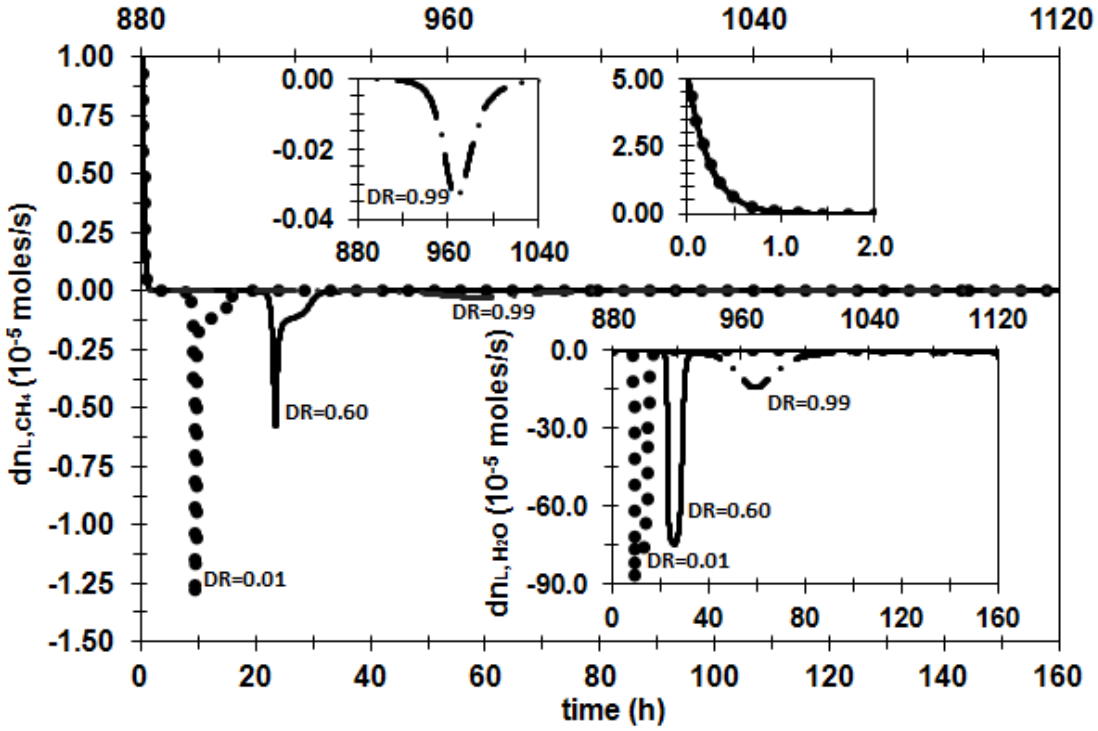

Figure S43 - The differential profile of methane number of moles in the bulk liquid phase ($dn_{L,}CH_4$). The insertion on the top-left shows a zoom in the limited by reaction profile, while the one in the top-right shows the methane in water saturation profile (the first 2 hours). The insertion in the bottom-right shows the differential profile of the water number of moles in the bulk liquid phase ($dn_{L,}H_2O$). The dotted line describes the limited by diffusion profile (*DR*=0.01), the continuous line the diffusion-reaction coupling profile (*DR*=0.6), and the dotted-dashed line, in the 2nd time axis, the limited by reaction profile (*DR*=0.99). All profiles are at 274 K and 76.0 bar.

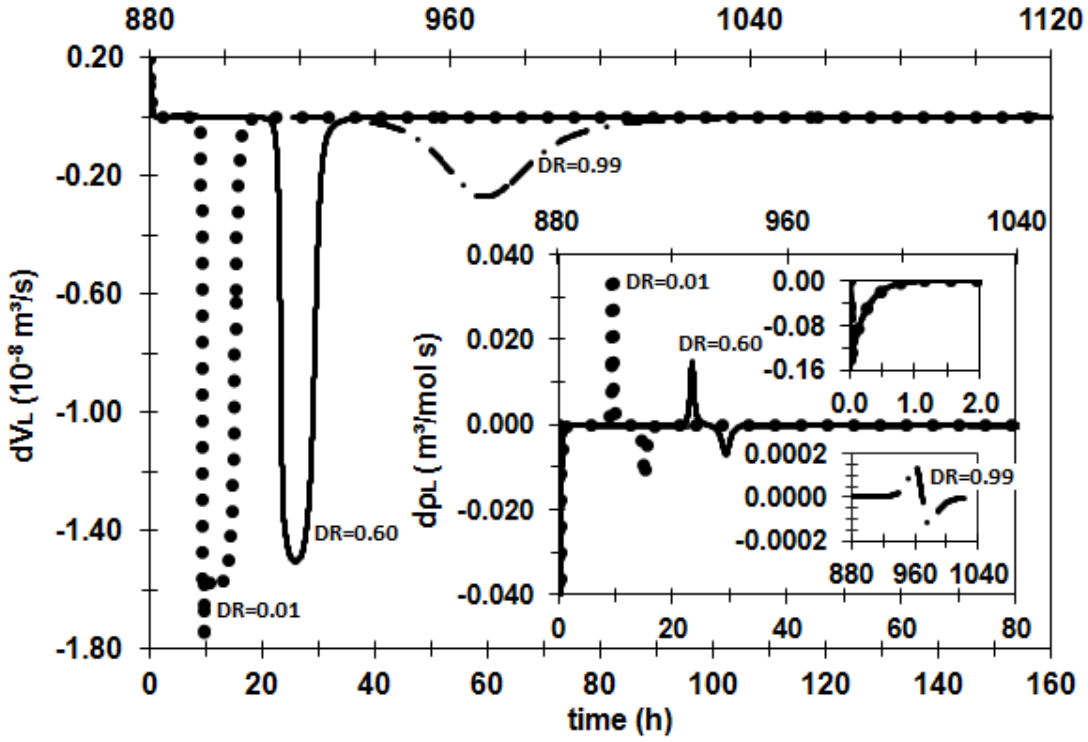

Figure S44 - The differential profile of the liquid phase volume (dV_L). The insertion shows the differential profile of the liquid density ($d\rho_L$) with a zoon in the methane in water saturation (the first 2 hours) and in the limited by reaction profile. The dotted line describes the limited by diffusion profile (*DR*=0.01), the continuous line the diffusion-reaction coupling profile (*DR*=0.6), and the dotted-dashed line, in the 2nd time axis, the limited by reaction profile (*DR*=0.99). All profiles are at 274 K and 76.0 bar.

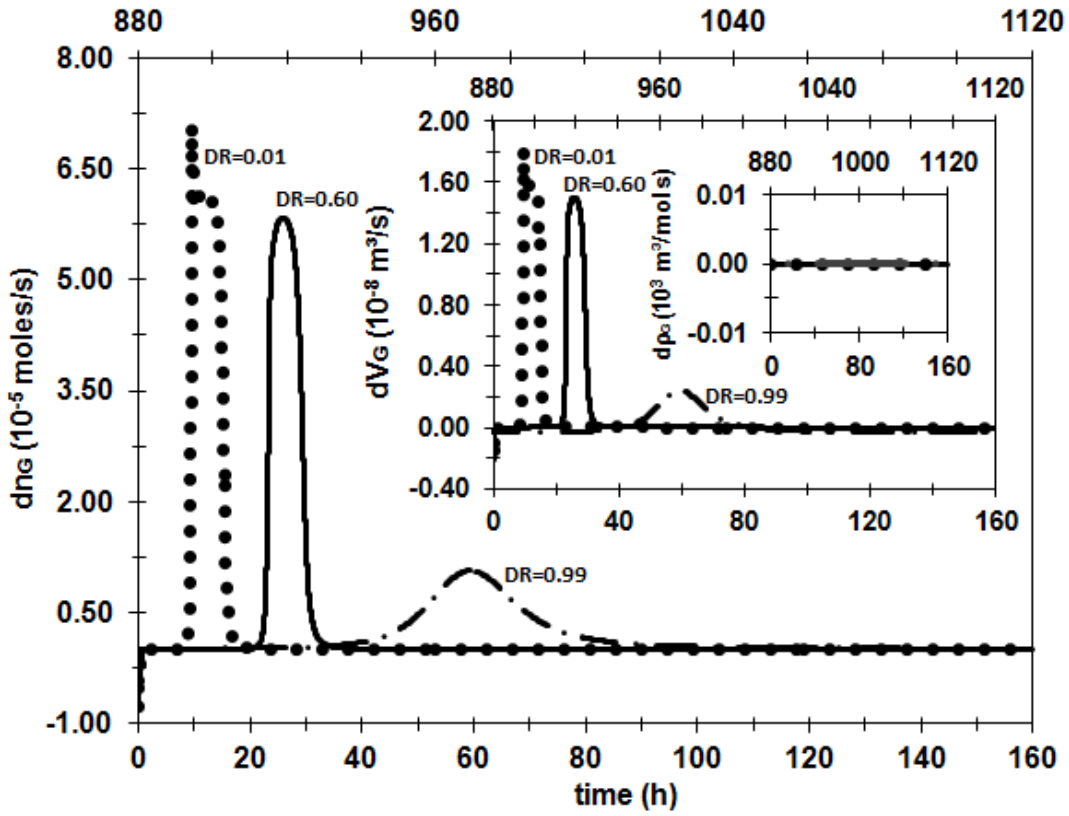

Figure S45 - The differential profile of the methane number of moles in the pure vapor phase (dn_G). The insertion shows the vapor phase volume (dV_G) with the constant vapor density ($d\rho_G$) differential profile. The dotted line describes the limited by diffusion profile (*DR*=0.01), the continuous line the diffusion-reaction coupling profile (*DR*=0.6), and the dotted-dashed line, in the 2nd time axis, the limited by reaction profile (*DR*=0.99). All profiles are at 274 K and 76.0 bar.

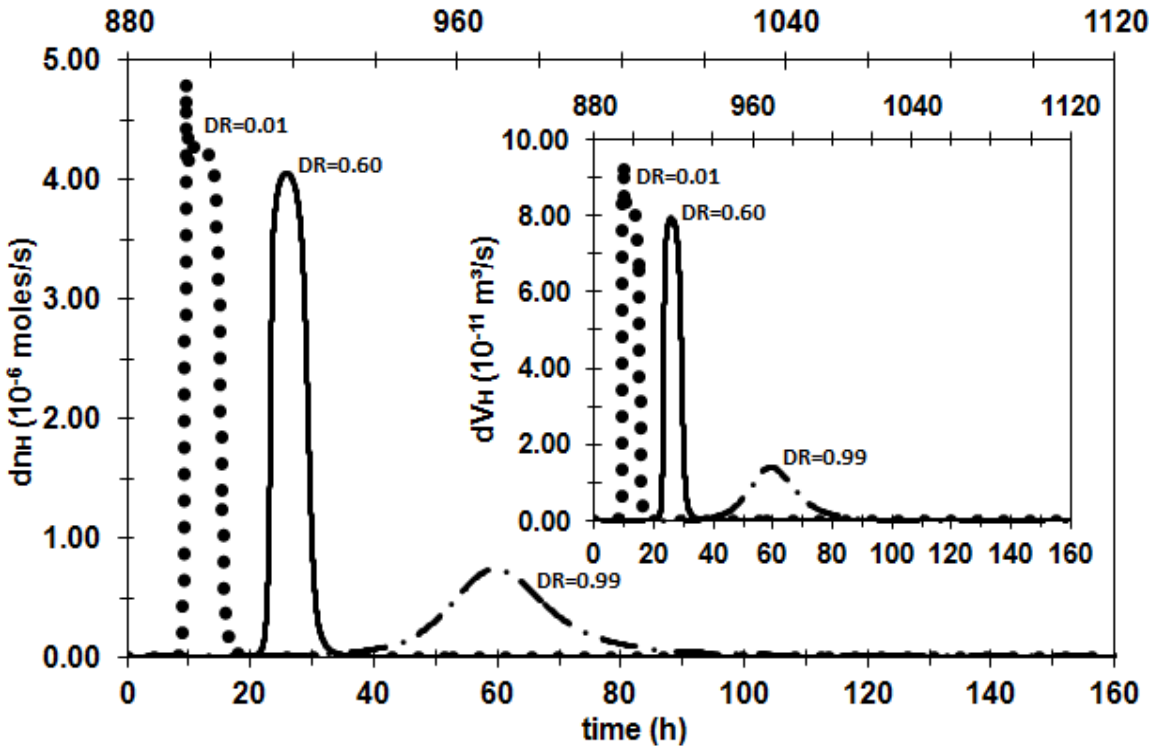

Figure S46 - The differential profile of the hydrate number of moles (dn_H). The insertion shows the hydrate phase volume (dV_H) differential profile. The dotted line describes the limited by diffusion profile (*DR*=0.01), the continuous line the diffusion-reaction coupling profile (*DR*=0.6), and the dotted-dashed line, in the 2nd time axis, the limited by reaction profile (*DR*=0.99). All profiles are at 274 K and 76.0 bar.

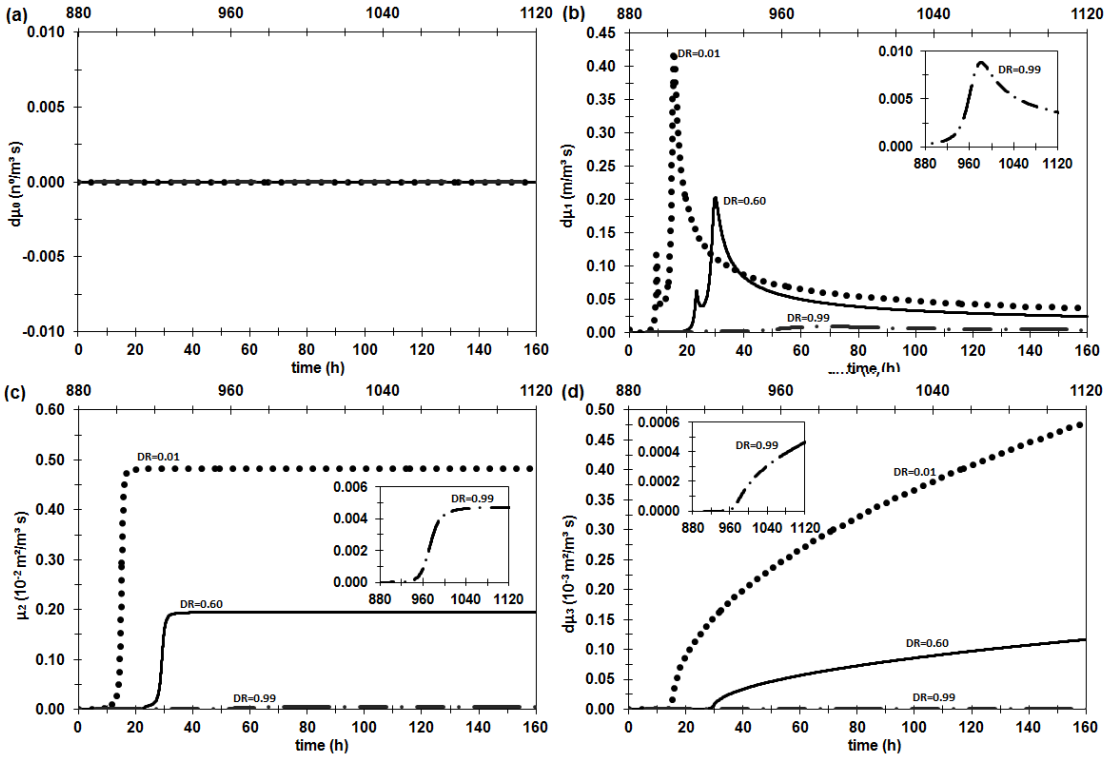

Figure S47 - (a) The differential profile of the population balance moment of order zero, number of particles per liquid volume ($d\mu_0$), (b) moment of order one, particle diameter per liquid volume ($d\mu_1$), (c) moment of order two, particle surface area per liquid volume ($d\mu_2$) and (d) moment of order three, particle volume per liquid volume ($d\mu_3$). The inserts are a zoom in the limited by reaction differential profile. The dotted line describes the limited by diffusion profile (*DR*=0.01), the continuous line the diffusion-reaction coupling profile (*DR*=0.6), and the dotted-dashed line, in the 2nd time axis, the limited by reaction profile (*DR*=0.99). All profiles are at 274 K and 76.0 bar.

S.8.4 System at 276 K and 70.9 bar without water activity in the driving force

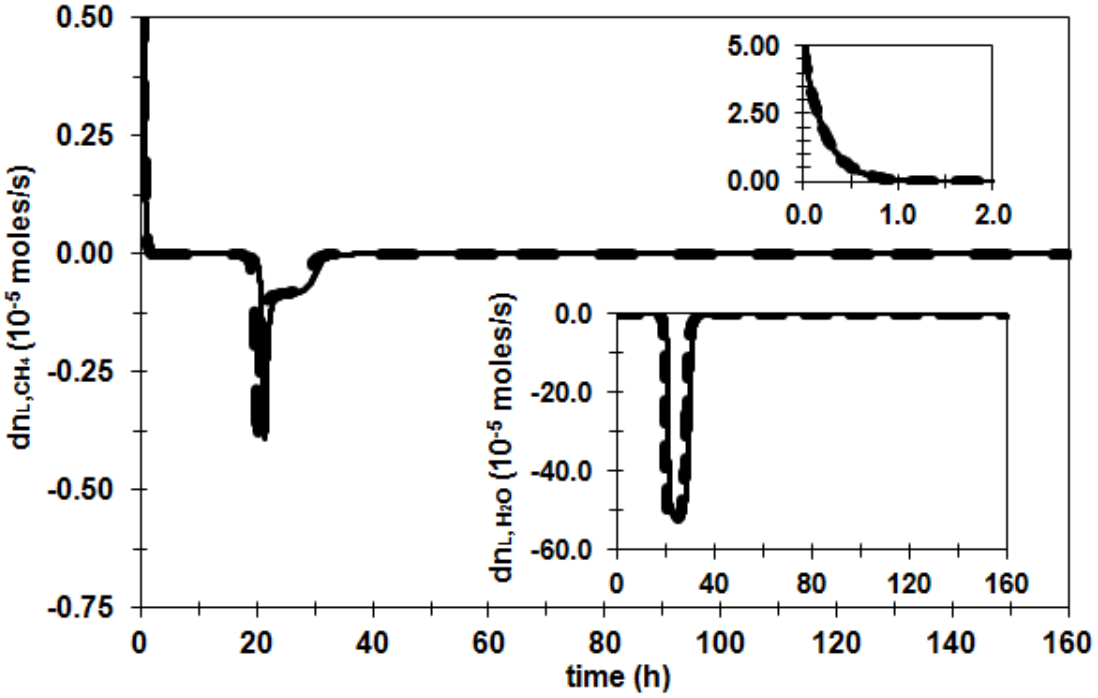

Figure S48 - The diffusion-reaction coupling (*DR*=0.5) differential profile of methane number of moles in the bulk liquid phase ($dn_{L,}CH_4$). The insertion on the top-left shows a zoom in the limited by reaction profile, while the one in the top-right shows the methane in water saturation profile (the first 2 hours). The insertion in the bottom-right shows the differential profile of the water number of moles in the bulk liquid phase ($dn_{L,}H_2O$). The continuous line represents the profile with the water activity, while the dashed line represents the profile without the water activity in the growth rate driving force. All profiles are at 276 K and 70.9 bar.

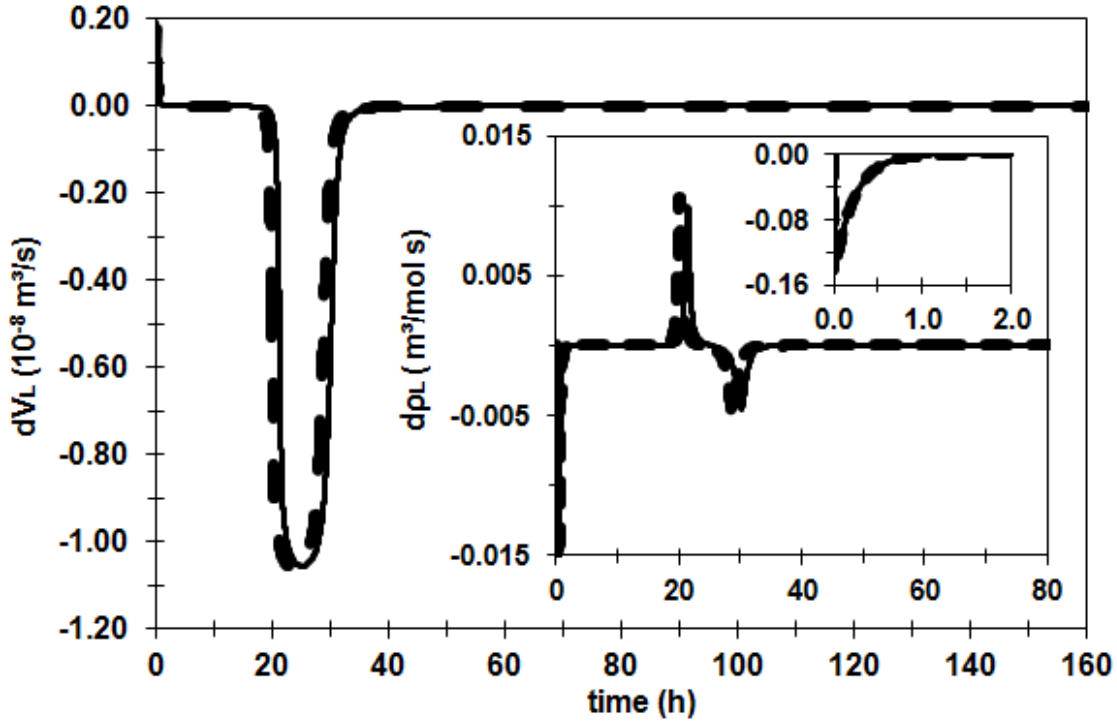

Figure S49 - The diffusion-reaction coupling (*DR*=0.5) differential profile of the liquid phase volume (dV_L). The insertion shows the differential profile of the liquid density ($d\rho_L$) with a zoom in the methane in water saturation (the first 2 hours) and in the limited by reaction profile. The continuous line represents the profile with the water activity, while the dashed line represents the profile without the water activity in the growth rate driving force. All profiles are at 276 K and 70.9 bar.

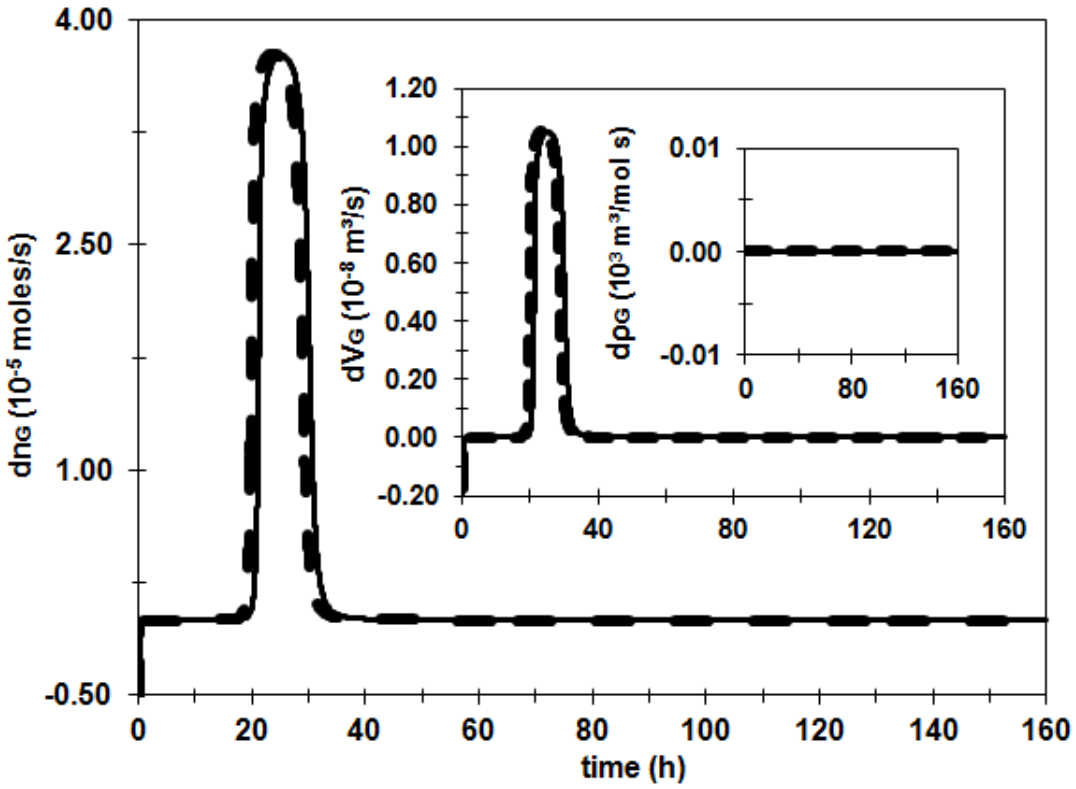

Figure S50 - The diffusion-reaction coupling (*DR*=0.5) differential profile of the methane number of moles in the pure vapor phase (dn_G). The insertion shows the vapor phase volume (dV_G) with the constant vapor density ($d\rho_G$) differential profile. The continuous line represents the profile with the water activity, while the dashed line represents the profile without the water activity in the growth rate driving force. All profiles are at 276 K and 70.9 bar.

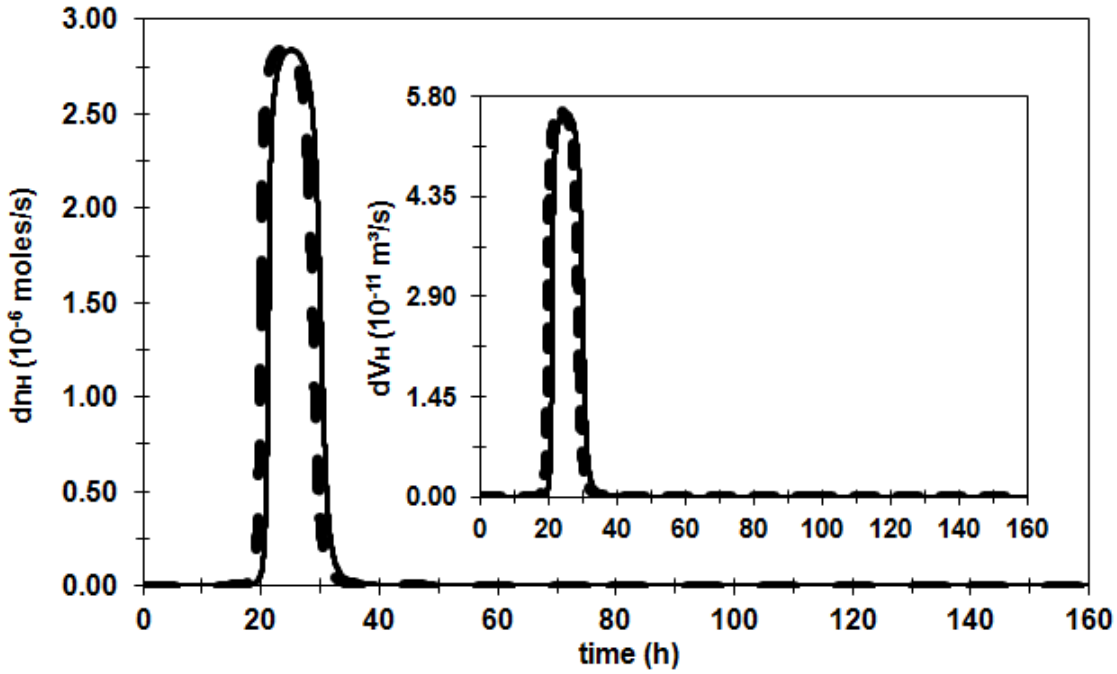

Figure S51 - The diffusion-reaction coupling (*DR*=0.5) differential profile of the hydrate number of moles (dn_H). The insertion shows the hydrate phase volume (dV_H) differential profile. The continuous line represents the profile with the water activity, while the dashed line represents the profile without the water activity in the growth rate driving force. All profiles are at 276 K and 70.9 bar.

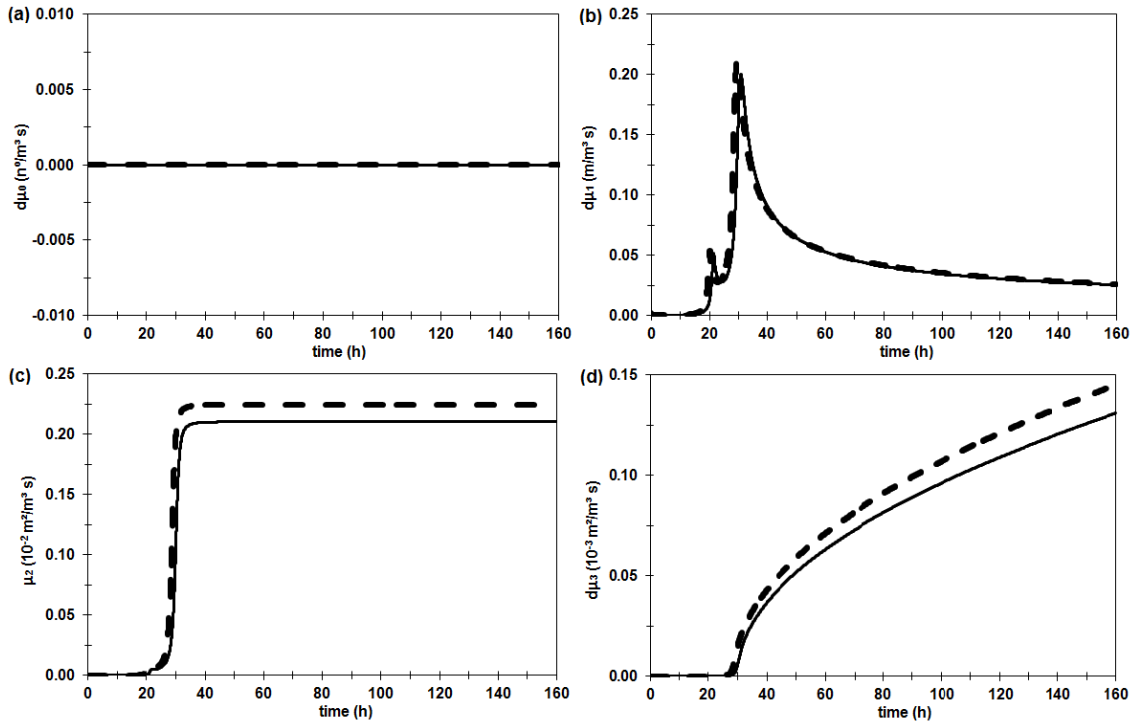

Figure S52 - (a) The diffusion-reaction coupling (*DR*=0.5) differential profile of the population balance moment of order zero, number of particles per liquid volume ($d\mu_0$), (b) moment of order one, particle diameter per liquid volume ($d\mu_1$), (c) moment of order two, particle surface area per liquid volume ($d\mu_2$) and (d) moment of order three, particle volume per liquid volume ($d\mu_3$). The inserts are a zoom in the limited by reaction differential profile. The continuous line represents the profile with the water activity, while the dashed line represents the profile without the water activity in the growth rate driving force. All profiles are at 276 K and 70.9 bar.

S.9 Correlation of the parameters A_{int}^{GL} e k_d^{GL}

The modeling of CH_4 solubilization in H_2O requires the description of the interfacial area of the continuous gas-liquid phases, $A_{\text{int}}^{GL}[m^2]$. For the calculation of this area, the model of Lemoine and Morsi [245], equation (S46).

$$A_{\text{int}}^{GL} = \left[\frac{1}{H} + \frac{1}{H_L} \frac{\text{Re}^{1.75} We^{3.0}}{Eu^{3.0}} \left(\frac{\overline{\rho_{susp.}}}{\overline{\rho^G}} \right)^{-2.67} \right] V^r \qquad \text{(S46)}$$

Where, $We = \text{D}_{ag}{}^3 \overline{\rho_{susp.}} s^2 \big/ \overline{\sigma}_{susp.}$ $Eu = P \big/ D_{ag}{}^2 \overline{\rho_{susp.}} MM_{susp.} s^2$, are the dimensionless numbers of Reynolds, Weber and Euler, respectively. And $H[m]$ is the height of the tank, $H_L[m]$ is the height of the liquid column, $\text{D}_{ag}[m]$ is the diameters of the stirrer, $s[rps]$ is the system agitation rate and $V^r[\text{m}^3]$ is the reactor volume.

The suspension molar density, $\overline{\rho_{susp.}}[mol/m^3]$, is obtained by the weighted average, by the number of moles of each phase, of the liquid and solid phases molar densities, as well as the molar mass of the suspension, $MM_{susp.}$, is given by the weighting, by the number of moles, of the the liquid and solid phases molecular masses.

The dynamic viscosity, $\overline{\eta_{susp.}}[mol/m\ s]$, s calculated by the model of Mooney (1951) [249], equation (S47).

$$\overline{\eta_{susp.}} = \overline{\eta_L} \exp\left(\frac{2.5\varphi_H}{1 - 1.43\varphi_H} \right) \qquad \text{(S47)}$$

Where, φ_H is the ratio between the solid phase volume and the reactor volume.

Considering that the gas-liquid interface is free of solid particles, it is assumed that the specific surface energy of the suspension, $\overline{\sigma_{susp.}}[\text{J/m}^2]$, is equal the specific surface energy of the gas-liquid interface, $\overline{\sigma_{GL}}[J/m^2]$.

According to the proposal of Firoozabadi and Ramey [250], it can be considered approximately equal to the surface tension, and it is obtained according to equation (S48).

$$\overline{\sigma_{GL}} = \left(2.848 \left(\Delta \overline{\rho^{GL}} \right)^2 - 8.056 \Delta \overline{\rho}^{GL} + \frac{8.530 \Delta \overline{\rho^{GL}}}{\left(\frac{T_L}{T_{c,CH_4}} \right)^{0.3125}} \right)^4 10^{-3} \qquad \text{(S48)}$$

where $\Delta\overline{\rho^{GL}}$ is the difference between the liquid and vapor phases molar densities.

To determine the diffusion coefficient of methane, $k_d^{GL}[m/s]$, the penetration model proposed by Taniguchi, Kawaguchi and Kikuchi [251] equation (S49) is used.

$$k_d^{GL} = 0.5\left(\bar{\varepsilon}\frac{\overline{\rho_{susp.}}}{\overline{\eta_{susp.}}}\right)^{\frac{1}{4}} D \tag{S49}$$

Where $D[m^2/s]$ is the diffusivity of the gas and $\bar{\varepsilon}[m^2/s^3]$ is the average energy input calculated according to the Spicer and Pratsinis [252] equation (S50).

$$\bar{\varepsilon} = \frac{N_{P_O} s^3 D_{ag}{}^5}{V^r} \tag{S50}$$

And N_{P_O}, $s[rps]$ and $D_{ag}[m]$ are the agitator power number, the agitator blade diameter and the system agitation rate, respectively.

S.10 - Krichevsky e Kasarnovsey (1935) correlation

The initial guess to calculate the CH_4 solubility in the liquid phase was obtained using the equation of Krichevsky and Kasarnovsey [246], equation (S51), with Henry's constant at infinite dilution calculated by a correlation in temperature, equation (S52).

$$x_{eq}^{GL} = \frac{\hat{\phi}_{CH_4}^{V}(T,P,\mathbf{y})P}{H_{CH_4}^{\infty}\exp\left(\frac{P\,\nu}{RT}\right)} \tag{S51}$$

$$H_{CH_4}^{\infty} = \exp\left(B_0 + \frac{B_1}{T}\right)101325 \tag{S52}$$

For CH_4, a light gaseous component, the parameters are B_0 = 15,826277, B_1 = -1559,063 [K] and ν = 32 10^{-12} [m^3/mol].

S.11 - Fugacity correlation of the light gases hypothetical liquid phase at 101.32 Pa

According to Prausnitz and Shair [244] the volatility of the solute hypothetical liquid phase at 101.32 Pa, being this a light gas, depends only on the temperature and properties of the solute, that is, it is independent of the solvent properties. It is possible, therefore, to apply the corresponding state theorem and show that the reduced fugacity of the hypothetical liquid solute is a universal function of the reduced temperature.

Prausnitz and Shair [244] correlated data on light gas solubility using an exponential function. However, as this function is not explicit in that work, the calculation of the hypothetical liquid phase fugacity in this work was performed using an exponential function, equation (S53), adjusted to the data obtained by the Prausnitz and Shair [244] work.

The adjustment is shown in Figure S53 and the parameters obtained are in Table S18.

$$f_{puro}^{L,0}\left(T,P_0\right)=\frac{D_1}{T_r}\exp\left(\frac{D_2}{T_r}+\frac{D_3}{T_r^2}\right) \qquad \text{(S53)}$$

Table S18 - Correlation parameters of the hypothetical liquid phase for light gases at 101.32 Pa and their respective deviations.

Correlation parameters		
D_1	D_2	D_3
44,490 ± 0,326	-1,445 ± 0,025	-2,688 ± 0,020

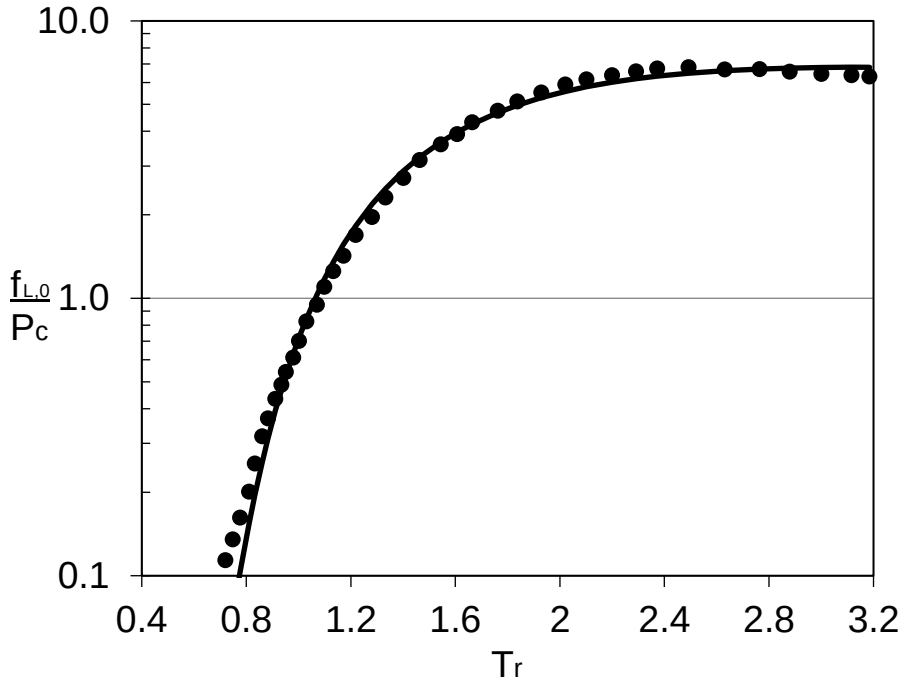

Figure S53 - Fugacy profile of the hypothetical liquid phase for light gases by the correlation of Prausnitz and Shair [244] with the temperature at 101.32 Pa. The points, ●, represent the calculation of the correlation and the curve the calculation performed by the function used in this work.

Since the critical temperature of CH_4 is 190.56 K and the occurrence of hydrate formation in the range of 266.15 to 280.15 K, we work in the reduced temperature range of 1.4 to 1.5, which was the range that showed the best agreement with the correlation of Prausnitz and Shair [244].

S.12 - NRTL model adjustment with LVE and solubility experimental data of the CH_4 + H_2O system

The parameters of the NRTL model were estimated by minimizing the sum of the quadratic residues of the output variables for each experiment (*l*), according to equation (S54).

$$F_1^{\text{obj}}\left(\underline{\beta}\right) = \sum_l^{N_{\text{exp}}} \left(\left(w\left(P_l^{\text{calc}}\left(\underline{\beta}\right) - P_l^{\text{exp}} \right) \right)^2 + \left(w\left(y_l{}^{\text{calc}}\left(\underline{\beta}\right) - y_l{}^{\text{exp}} \right) \right)^2 \right) \qquad \text{(S54)}$$

For each type of experimental data, the implemented routine allows different calculations with the NRTL model: for solubility data, only the equilibrium pressure is calculated; and for the liquid-vapor equilibrium data, the pressure and composition of the vapor phase in equilibrium are calculated using the temperature and composition of the liquid phase as input variables. $\underline{\beta}$ is the set of parameters to be estimated. For the NRTL model, it was defined as: $\underline{\beta} = (A_{1,2}, A_{2,1}, \mathrm{B}_{1,2}, \mathrm{B}_{2,1}\, \alpha)$. The inverse of the admitted weights for each output variable was 0.0001% of the measured variable. These weights were defined in order to establish similar deviations for all points.

The NRTL model parameters, Table S15, were estimated for liquid-vapor balance data of H_2O (2) + CH_4 (1) at the temperature of 283.89 K, 298.31 K, 313.11 K and 323.56 K, Figure S54, and solubility data between 275.11 K and 444.26 K, Figure S55, covered a pressure range of 0.0073 MPa to 68.95 MPa.

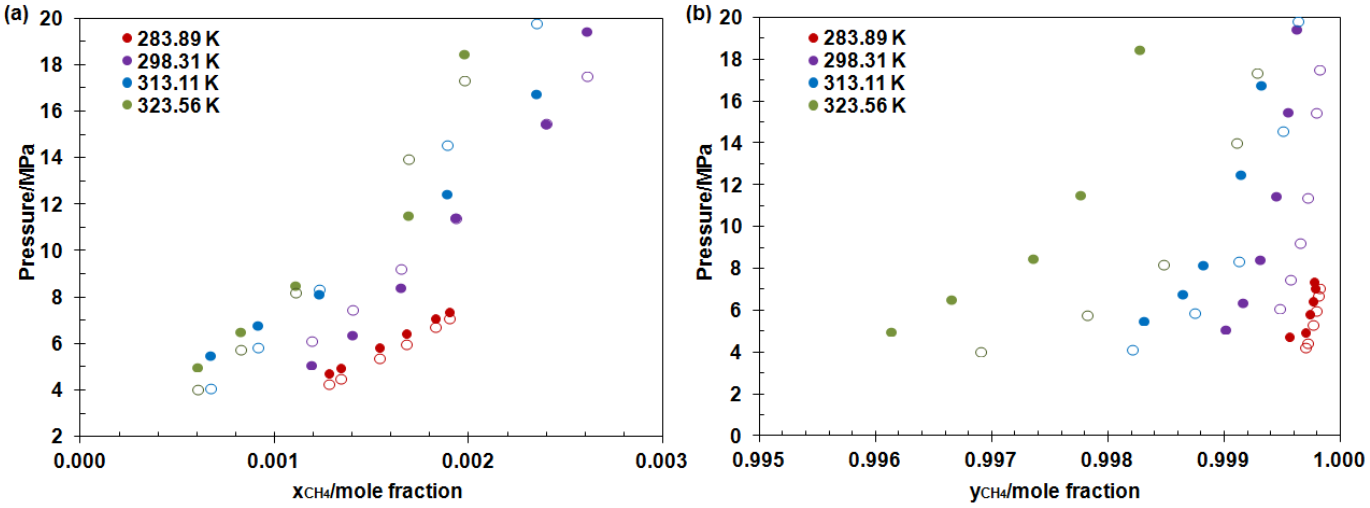

Figure S54 - H_2O+CH_4 liquid-vapor equilibrium isothermal curves. The experimental data are represented by the filled circles for (a) the dew point and for (b) the bubble point [234–236]. The empty circles represent the points calculated with the NRTL model.

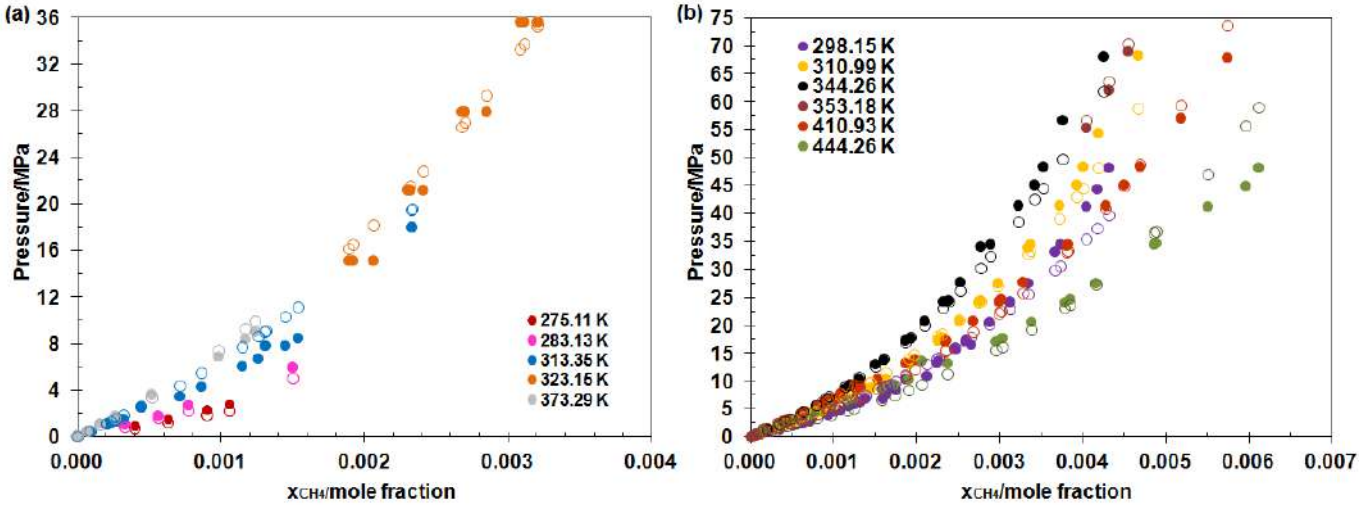

Figure S55 - Isothermal curves of CH_4 solubility in H_2O. The experimental data is represented by the filled circles [237–242]. The empty circles represent the points calculated with the NRTL model.

Here, the particle swarm method - PSO [233] was used as the stochastic method to achieve a good initial estimate to be provided to a Quasi-Newton type algorithm, a deterministic method that uses differential calculus techniques.

Calculations of absolute average deviations, equation (S55), are used to analyze the best adjustments.

$$AAD\left(\underline{\beta}\right) = \frac{\sum_{i}^{N_{exp}} \left| \frac{z_{i,j}^{calc}\left(\underline{\beta}\right) - z_{i,j}^{exp}}{z_{i,j}^{exp}} \right|}{N_{exp}}.100 \qquad \text{(S55)}$$

The values calculated for pressure and mole fraction were well adjusted and showed deviations of 0.08% and 10.51%, respectively.

Figure S54 shows the comparison between the calculation and the LVE data of the $CH_4 + H_2O$ system diagrams for which the NRTL model parameters were estimated, while Figure S55 shows this comparison for the solubility data diagrams of this same system used in parameter estimation. The correlation of the data used in the estimation was adequate and the model has predictive capacity within the studied temperature and pressure range.

Appendix 4. Supporting information for Chapter 5

S.13 Excess Gibbs Free Energy Model (NRTL)

In this work, we use the excess Gibbs energy model, NRTL, to describe the non-ideality of the liquid phase in both conditions in the bulk liquid phase and in the local equilibria of the gas-liquid and hydrate-liquid interfaces. The activity coefficients of the excess Gibbs free energy model, NRTL, for the ternary mixture of $H_2O(1) + CH_4(2) +$ EtOH(3) were calculated by equation (S56), for $n = 3$.

$$\gamma_i = \exp\left(\frac{\sum_{j=1}^{n} x_j \tau_{j,i} G_{j,i}}{\sum_{k=1}^{n} x_k G_{k,i}}\right) + \sum_{j=1}^{n} \frac{x_j G_{i,j}}{\sum_{k=1}^{n} x_k G_{k,j}} \left(\tau_{i,j} - \frac{\sum_{m=1}^{n} x_m \tau_{m,j} G_{m,j}}{\sum_{k=1}^{n} x_k G_{k,j}}\right) \quad \text{(S56)}$$

The NRTL model parameters were estimated by adjusting the binary systems ($H_2O + CH_4$; H_2O + EtOH; CH_4 + EtOH) in equilibrium. In our previous work, Oliveira et al. (2020, in submission process, Appendix 3) we used the liquid-vapor equilibrium (LVE) and CH_4 solubility in H_2O data to estimate the NRTL parameters of the pair $H_2O + CH_4$ (Dalton and Raoult laws). For the pair H_2O + EtOH the NRTL parameters were estimated in Oliveira et al. [124] using the liquid-vapor equilibrium (LVE) and infinite dilution of EtOH in H_2O data. The NRTL parameters for CH_4 + EtOH were estimated here using liquid-vapor equilibrium (LVE) data. The conditions for estimating these parameters were chosen according to the available experimental data from the respective systems. However, with the objective of estimating parameters under conditions other than hydrate formation conditions to obtain poorly correlated parameters of high transferability.

A set of experimental data on LVE [165,253,254] for the CH_4 + EtOH system has been drawn from the literature. The temperature-dependent binary interaction parameters in this work were described by equation (S57)(S1), for T_{ref} = 280.15 K. The coefficients of the binary interaction parameters and the non-randomness factor were estimated for the temperature range of 238.15 K to 333.40 K and pressure range of 0.33 MPa to 41.69 MPa.

$$\tau_{i,\mathrm{j}} = A_{\mathrm{i,j}} + B_{i,\mathrm{j}}\left(\frac{T_{ref}}{T} - 1\right) \qquad \text{(S57)}$$

The activity coefficients of the excess Gibbs free energy model, NRTL, for a binary mixture of CH_4(1) + EtOH(2) were calculated by equation (S56)(S2), for $n = 2$.

The non-randomness factor, α , was considered symmetric for each binary system and $G_{i,\mathrm{j}} = \exp(\alpha\tau_{i,\mathrm{j}})$. The parameters of the NRTL model are in Table S19 and the methodology and results of the estimation are in Item S.19.

Table S19 - Parameters of the ternary NRTL model for the system H_2O(1) + CH_4(2) + EtOH(3), and their respective errors, obtained by adjusting experimental data from binary systems.

Ternary NRTL Parameters					
$A_{1,2}$	-208.760 ± 0.007	$A_{1,3}$	3.078 ± 0.077	$A_{2,3}$	26.250 ± 0.019
$A_{2,1}$	879.302 ± 0.011	$A_{3,1}$	-1.577 ± 0.068	$A_{3,2}$	-2.013 ± 0.003
$B_{1,2}$	-41.891 ± 0.006	$B_{1,3}$	-11.387 ± 0.223	$B_{2,3}$	-146.893 ± 0.328
$B_{2,1}$	-430.631 ± 0.013	$B_{3,1}$	7.193 ± 0.161	$B_{3,2}$	-16.337 ± 0.037
$\alpha_{1,2} = \alpha_{2,1}$	0.00161 ± 0.00001	$\alpha_{1,3} = \alpha_{3,1}$	0.06097 ± 0.00197	$\alpha_{2,3} = \alpha_{3,2}$	0.08057 ± 0.00022
Tref $_{1,2}$ = Tref $_{2,1}$	330.15 K	Tref $_{1,3}$ = Tref $_{3,1}$	283.15 K	Tref $_{2,3}$ = Tref $_{3,2}$	280.15 K

The calculation of the hydrate-forming components activity in the liquid phase (H_2O and CH_4), both in the hydrate-liquid equilibrium and in the bulk liquid phase are obtained by equation (S58) for the H_2O + CH_4 + EtOH system.

$$a\left(T,\mathrm{P},\mathbf{x}\right)=\gamma_i^L\left(T,\mathrm{P},\mathbf{x}\right)x_i^L \tag{S58}$$

S.14 Calculation of the equilibrium composition at the H-L interface

The work approach by Oliveira et al. (2020, in submission process, Appendix 3) calculates the equilibrium methane composition in pure water at the hydrate-liquid interface through the minimization of the water chemical potential difference between the liquid phase and the hydrate phase. This modeling is based on Oliveira et al. [124] that use the van der Waals and Platteuw theory [98] with Holder et al.[105] model to describe the hypothetical phase of the empty hydrate.

In this system, the pressure and temperature are kept constant, and the equilibrium methane composition, $x_{CH_4}^{eqLH}$, is calculated iteratively. The equilibrium composition at the hydrate-liquid interface (H-L) is varied up to the minimum of the water chemical potential between the liquid and the hydrate phases. The bulk methane composition is used as the initial guess.

A similar methodology is applied for the system with the liquid phase composed of water and ethanol. The difference is that here the ternary NRTL (Item S.13) is used to calculate the non-ideal terms applied in the water potential between the liquid and the empty lattice phases and the methane fugacity in the liquid in equilibrium with the hydrate phase. The details of the equations used to calculate the water chemical potential in a non-ideal system are in the Appendix 2 [207]. Meanwhile, the details of the equations for calculating methane fugacity in the liquid phase are in the Item S.11 Appendix 3. However, as in this case, the system has three compositions to be obtained at the interface and only two equations: a) the equality of the water chemical potential and, b) the sum of the fractions equal to one. So, it is necessary to establish one more criterion to obtain the equilibrium composition on the interface.

In this case, it is possible to apply a flash calculation to obtain all the phase equilibrium composition; however, the flash calculation is a complex and robust interactive calculation [144]. As we are already performing an iterative temporal

calculation of the system variables, this flash would have to be executed several times for the temporal computation. Since the objective is to obtain a model capable of describing the dynamic behavior in a quick and functional way, we then chose to use one of the system hypotheses to define the methane composition at the H-L interface.

Considering that the ethanol is not consumed with hydrate growth is possible to establish a third criterion. In this criterion, the ethanol number of moles in the liquid phase does not suffer spatial or temporal variation. Ethanol has the same number of moles at the interfaces and in bulk, and is preserved over time, with null time derivative.

Therefore, for each iterative calculation of the methane composition at the H-L interface, an ethanol composition is defined. The number of moles of methane is equally distributed in the liquid phase, i.e., the ethanol composition is constant spatially, but it varies over time. Therefore, the methane and water are obtained from the water equal chemical potential between the hydrate and liquid phases and the molar sum equal to 1, receptively, while the amount of ethanol is kept constant.

Briefly, the calculation performed is the same as for the pure water system present in Oliveira et al. (2020, in submission process), Item S.5 Appendix 3; however, using the ternary NRTL to obtain the non-ideal properties of the liquid phase as activity and activity coefficient of the systems.

S.15 Growth Kinetics

Similar modeling applied for the H_2O+CH_4 system (Item S.6 Appendix 3) is applied for the H_2O+CH_4+EtOH system, including the ethanol in the balances. Here we present only the equations that changed or are included in the differential equation system due to the ethanol addition.

Using the hypotheses adopted to adapt the model to systems inhibited by ethanol, changes, and inclusions of differential equations will be presented in this topic.

S.15.1 Liquid phase mole balance

Applying the mole balance for the liquid phase with the hypotheses previously assumed, we get to equation (S59) for the ethanol. Given the considerations that ethanol does not participate in the solid structure, and at low temperatures, it practically does not evaporate into the gas phase, the ethanol molar derivative in the liquid phase will be null. Because of this non-participation of ethanol in the solid and vapor phase, the water

and methane mole balance in the liquid phase was still the same in Item S.6 Appendix 3 for the system with fresh water.

$$\frac{dn_{EtOH}^{L}}{dt} = 0 \tag{S59}$$

Therefore, the global mole balance in the liquid phase is given by equation (S60). The same one for the freshwater system.

$$\frac{dn^{L}}{dt} = \left[\frac{dn_{H_2O}^{L}}{dt} + \frac{dn_{CH_4}^{L}}{dt} + \frac{dn_{EtOH}^{L}}{dt} \right] = \dot{n}_{sol,CH_4} - \left(\frac{\tau}{\xi} + 1 \right) \dot{n}_{c,CH_4} \tag{S60}$$

Where, $\dot{n}_{sol,CH_4}$ is the methane solubilization rate in the liquid phase and $\dot{n}_{c,CH_4}$ is the hydrate growth rate in terms of the methane moles, Item S.15.40.

The index *"sol"* holds for entry or exit molar, $\dot{n}$, rates of the solubilization of methane in phase *j*, o "*e* "used for the methane input variables in the gas phase through the feed and the" *c* "for the input or output rates of component *i* due to the growth of the hydrate phase.

S.15.2 Gas-phase mole balance

Considering that there is no water and ethanol evaporation for the gas phase, the mass balance of the pure methane gas phase in molar terms does not modify by the addition of ethanol, i.e., is the same as the freshwater.

S.15.3 Solid-phase mole balance

With the hypotheses adopted for the solid phase, the ethanol only acts as a thermodynamic hydrate inhibiter. So, the hydrate crystal is a homogeneous solid without the ethanol participation in the structure and the mole balance is kept the same one used for freshwater.

S.15.4 Constitutive relations

The methane solubilization molar rate (methane molar rate entering in the liquid phase), $\dot{n}_{sol,CH_4}$, is defined by the methane diffusion from the gas-liquid interface into the liquid phase, equation (S61)(S24), as in Sampaio et al. [87] work, where $A_{\text{int}}^{GL}\left[m^2\right]$ is the gas-liquid interface area and $k_d^{GL}\left[m/s\right]$ is the mass transfer coefficient at the gas-

liquid interface. Both parameters are obtained by correlations founded in the literature [87,245], presented in Item S.18.

$$\dot{n}_{sol,CH_4} = \frac{A_{\text{int}}^{GL} k_d^{GL}}{V^L}\left(n_{\text{eq},CH_4}^L - n_{CH_4}^L\right) \tag{S61}$$

When using the equilibrium hypothesis at the gas-liquid interface, the methane mole fraction at the interface is obtained iteratively by the methane fugacity equality in the phases, equation (S62). The Peng-Robinson equation of state is applied to obtain the methane fugacity coefficient the CH_4 pure vapor phase $\phi_{CH_4}^V$. For this iterative calculation, the Krichevsky and Kasarnovsey [246] correlation is used as an initial guess.

$$f_{CH_4}^V = f_{CH_4}^L \rightarrow x_{CH_4}^{eqGL} = \frac{\hat{\phi}_{CH_4}^V\left(T,\mathrm{P},\mathbf{y}\right)P}{\gamma_{CH_4}^L\left(T,\mathrm{P},\mathbf{x}\right)f_{puro}^{L,0}\left(T,P\right)} \tag{S62}$$

The fugacity of pure CH_4 in the hypothetical liquid phase, $f_{CH_4}^{L,0}$, was calculated by the equation of Prausnitz, Lichtenthaler, and Azevedo [243], where P_0 = 101300 [Pa] and $v_{CH_4}^L$ = 5.21 10-5 [m³ / mol]. The same methodology is used to calculate the methane fugacity in the liquid phase in equilibrium with the hydrate phase $x_{CH_4}^{eqLH}$.

The fugacity of pure CH_4 in the condition P_0 $f_{puro}^{L,0}\left(T,P_0\right)$ was obtained by a T_r correlation presented by Prausnitz and Shair [244], adjusted for experimental data of solubility of several light gases H_2O. However, as this correlation is not explicit in the referenced work, a function similar to the one described by Prausnitz and Shair [244] was adjusted and correlated with the data presented in the article, as described in Item S.11 of the Appendix 3 above.

Therefore, the methane number of moles solubilized in the liquid phase, n_{eq,CH_4}^L, is given by $n_{\text{eq},CH_4}^L = x_{CH_4}^{eq} n^L$, where $n^L = \sum_i n_i^L = \overline{\rho}^L V^L$.

The methane molar rate consumed by the hydrate phase growth is obtained from the number of moles temporal variation in the particulate phase. The hydrate phase number of moles is equal to the product between the molar density and the phase volume in the same way as for the pure water system (Appendix 3).

The methane feed rate to maintain the system pressure can be obtained from the vapor phase mole balance. The methane gas number of moles in the reactor is given by the product between the molar density of the pure methane gas phase $\overline{\rho}_{CH_4}^G$ (Appendix 3).

S.15.5 Volumes and Molar Densities of the Phases

The vapor phase molar density, $\overline{\rho}^{G}$, is calculated with the Peng-Robinson EoS for pure substances, adopting pure CH_4 in the vapor phase. Meanwhile, the liquid phase molar density, $\overline{\rho}^{L}$, is calculated by the generalized Rackett equation [222,224–226,255]. Which in this case, includes the ethanol present in the liquid phase. In this work, the hydrate phase molar density, $\overline{\rho}^{H}$, is considered constant and is obtained by the product between the hydrate phase mass density of Sloan and Koh and the hydrate phase molecular mass, MM_H. It is obtained through the weighted sum of the component molecular masses by the number of water molecules and guests present in the hydrate phase.

The volumes of the gas, liquid, and solid are calculated in the same way as for the pure water system $\overline{\rho}^{G}_{CH_4}$ (Appendix 3). The gas-phase volume, the difference of the tank volume and the liquid, and solid volume phases. The liquid phase volume through the product between the number of moles and the molar density. And finally, the solid phase volume trough the characterization of the crystalline population size distribution through the use of the population balance of solid-phase [87,247].

S.15.6 Numerical solution of dynamic

The same computational code DASSL (Fortran) as the integrator of the system algebraic-differential equations (ADE) in time used previously for the freshwater system is applied in this work (Supporting Information of Oliveira et al., 2020, in submisson process). The Differential-Algebraic System (DASSL) code was developed by Petzold [248] as an alternative to numerical solution for algebraic-differential equations (ADE), especially those whose solvers of systems ordinary differential equations (ODE) are not able to solve, such as systems in which the derivative cannot be solved explicitly, and when the derivative solution is impractical. The numerical method applied consists of replacing the derivative by an approximate difference through discretization as a function of the independent variable. The system, then, can be solved for the current time using Newton's method.

To solve the ADE system with the DASSL code, it is necessary to define the initial condition properly, both for the variables and their derivatives. Only a few variables are provided as inputs, while the other variables and derivatives are obtained by the DAE

system or by differentiation by parts of the variable. The variables defined as inputs to the DAE system depend on the studied mixture and are presented together with their respective results. The user must provide the relative and absolute tolerances, and 10^{-10} and 10^{-12} were used for the absolute and relative tolerances, respectively.

S.16 System property variable profiles

In this topic, we will present the secondary system variables at the different temperature and pressure conditions, with or without the water activity in the driving force and for the four initial ethanol compositions studied, 0, 5, 10, and 15 wt% of EtOH.

Among these variables are the volume and molar density of the liquid phase, the number of moles, volume, and molar density of the gas phase. In addition to the moments used to describe the solid phase. Moment of order 0, 1, 2, and 3, which are proportional to the number of particles, particle diameter, the surface area of the particles, and volume of the particles.

The temporal profile of the variables obtained by the simulations carried out with the proposed model is following the expected behavior for each system and temperature, pressure, and composition condition.

S.16.1 The system at 276 K and 70.9 bar with water activity in the driving force for 0 and 5 wt%

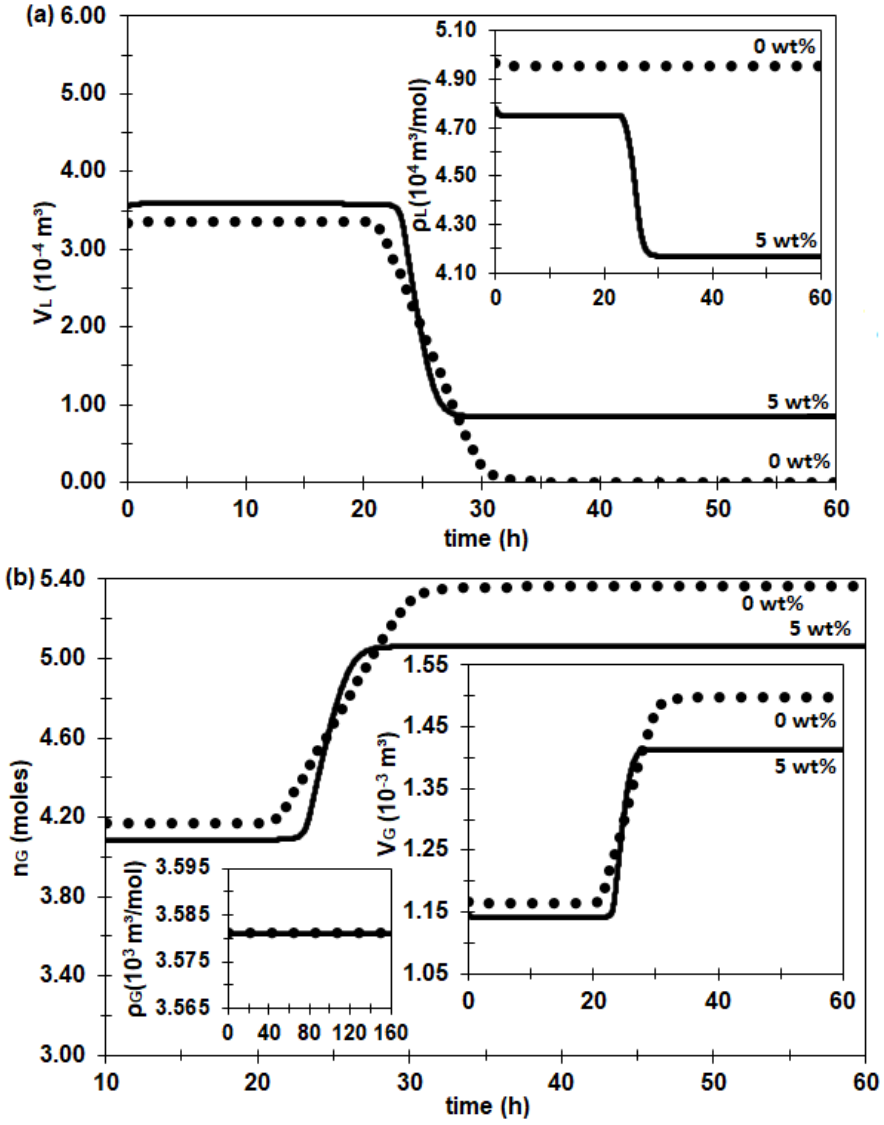

Figure S56 - (a) The liquid phase volume (V_L) and (b) the methane number of moles in the pure vapor phase (n_G) temporal profiles at 276 K and 70.9 bar (*DR* = 0.5). The insertion (a) shows the liquid density (ρ_L) profile. The insertion (b) in the left is the gas density (ρ_G) profile, and the one in the right is the vapor phase volume (V_G). The lines describe the time profiles for the following ethanol compositions of the initial liquid phase: 0 wt% (dotted line) and 5 wt% (continuous line) of EtOH.

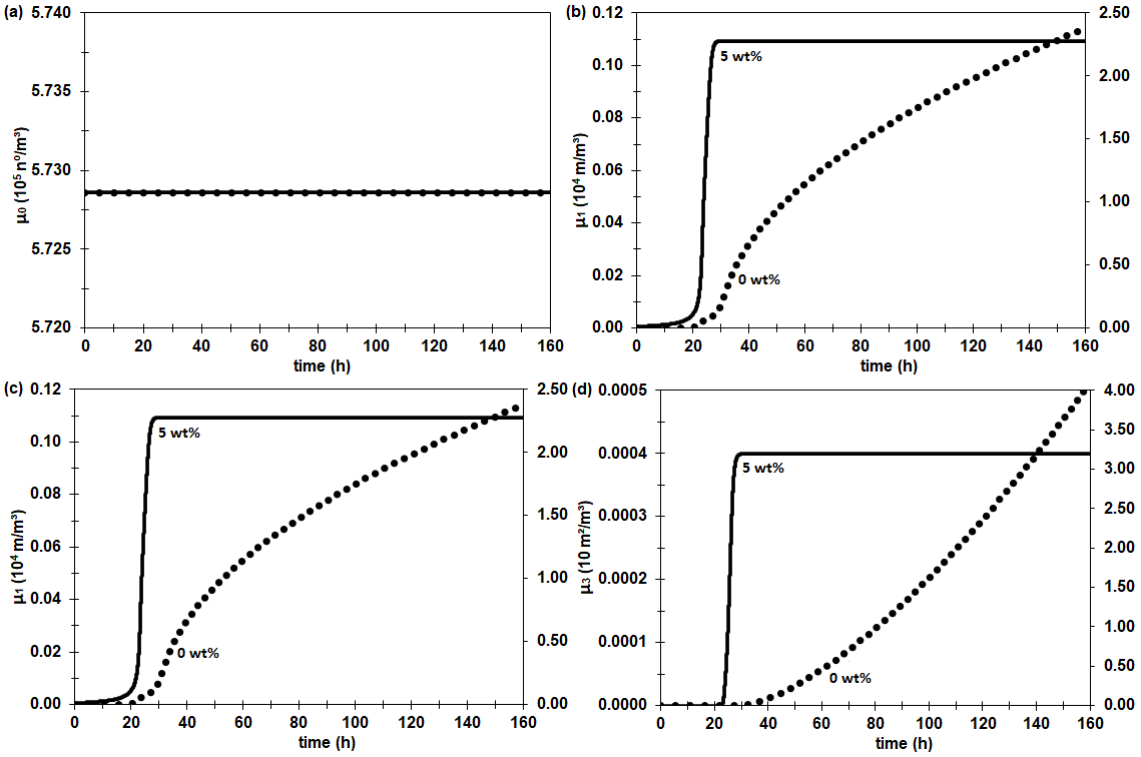

Figure S57 - (a) The temporal profile of the population balance moment of order zero, number of particles per liquid volume (μ_0), (b) moment of order one, particle diameter per liquid volume (μ_1), (c) moment of order two, particle surface area per liquid volume (μ_2) and (d) moment of order three, particle volume per liquid volume (μ_3) at 276 K and 70.9 bar (*DR* = 0.5). The lines describe the time profiles for the following ethanol compositions of the initial liquid phase: 0 wt% (dotted line) and 5 wt% (continuous line) of EtOH.

S.16.2 The system at 276 K and 70.9 bar with water activity in the driving force for 5, 10 and 15 wt%

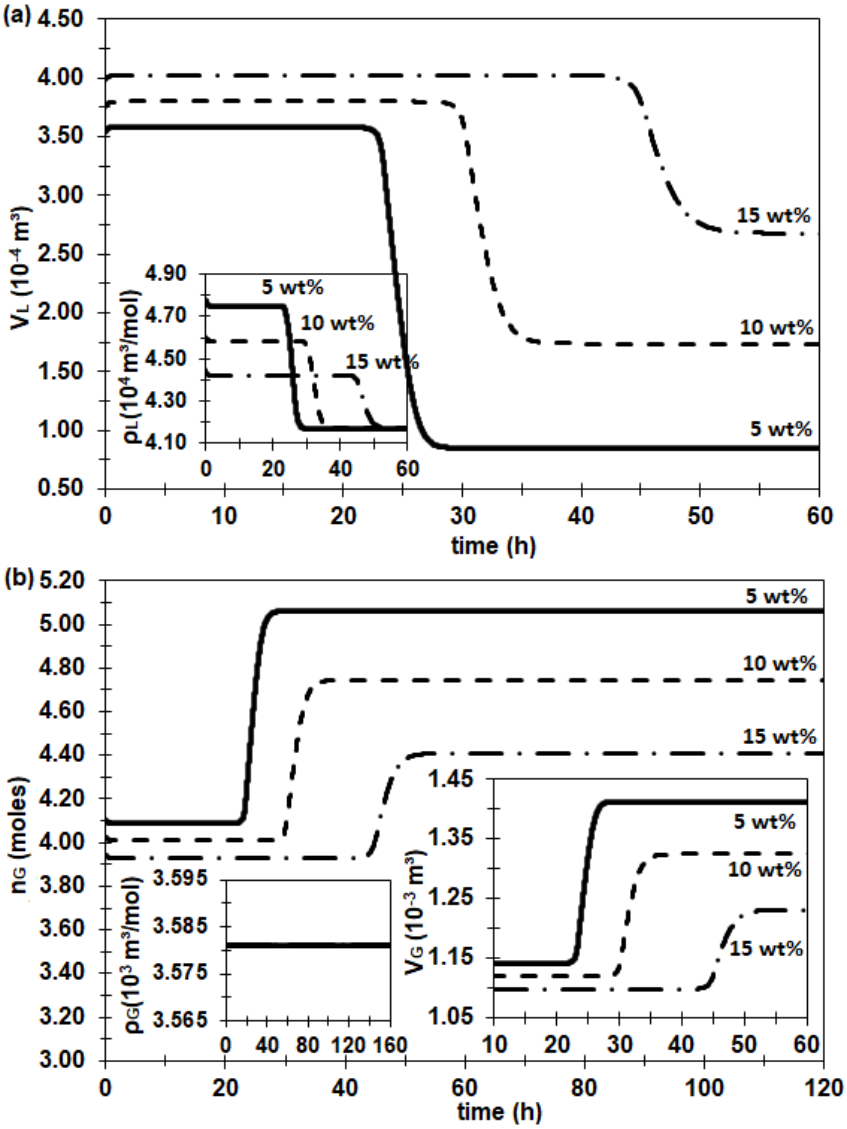

Figure S58 - (a) The liquid phase volume (V_L) and (b) the methane number of moles in the pure vapor phase (n_G) temporal profiles at 276 K and 70.9 bar (*DR* = 0.5). The insertion (a) shows the liquid density (ρ_L) profile. The insertion (b) in the left is the gas density (ρ_G) profile, and the one in the right is the vapor phase volume (V_G). The lines describe the time profiles for the following ethanol compositions of the initial liquid phase: 5 wt% (continuous line), 10 wt% (dashed line) and 15 wt% (dotted-dashed line) of EtOH.

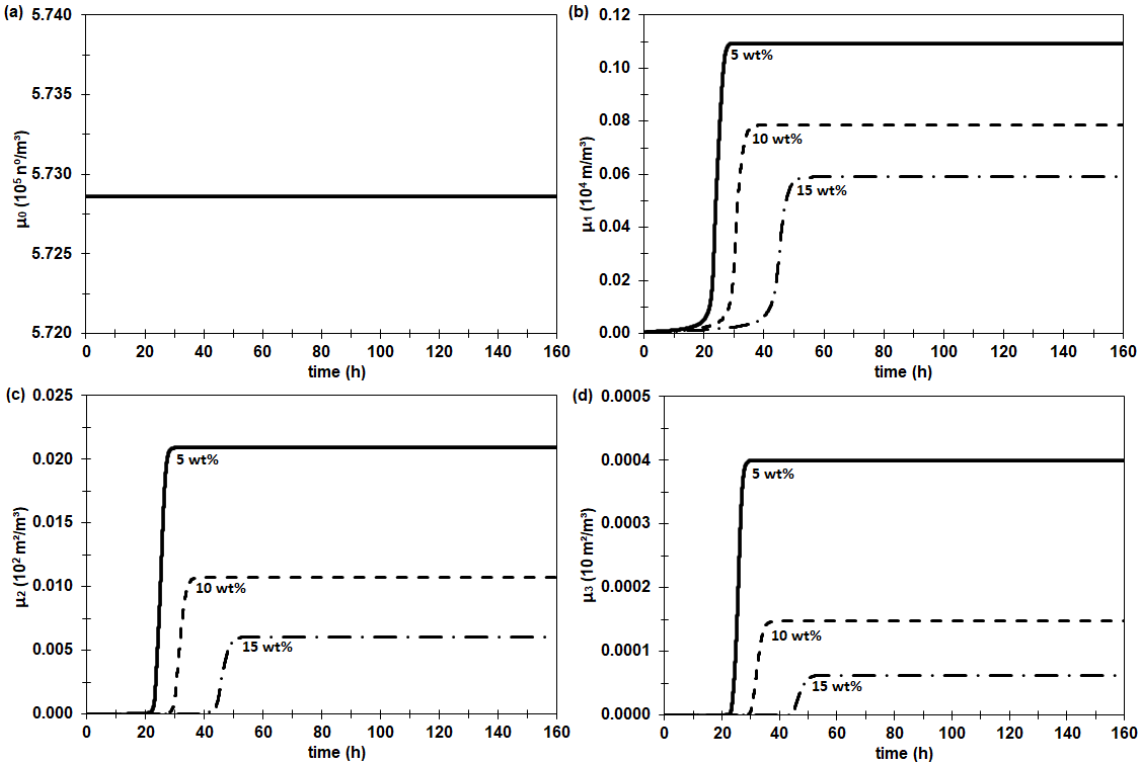

Figure S59 - (a) The temporal profile of the population balance moment of order zero, number of particles per liquid volume (μ_0), (b) moment of order one, particle diameter per liquid volume (μ_1), (c) moment of order two, particle surface area per liquid volume (μ_2) and (d) moment of order three, particle volume per liquid volume (μ_3) at 276 K and 70.9 bar (*DR* = 0.5). The lines describe the time profiles for the following ethanol compositions of the initial liquid phase: 5 wt% (continuous line), 10 wt% (dashed line) and 15 wt% (dotted-dashed line) of EtOH.

S.16.3 The system at 276 K and 70.9 bar without water activity in the driving force for 0 and 5 wt%

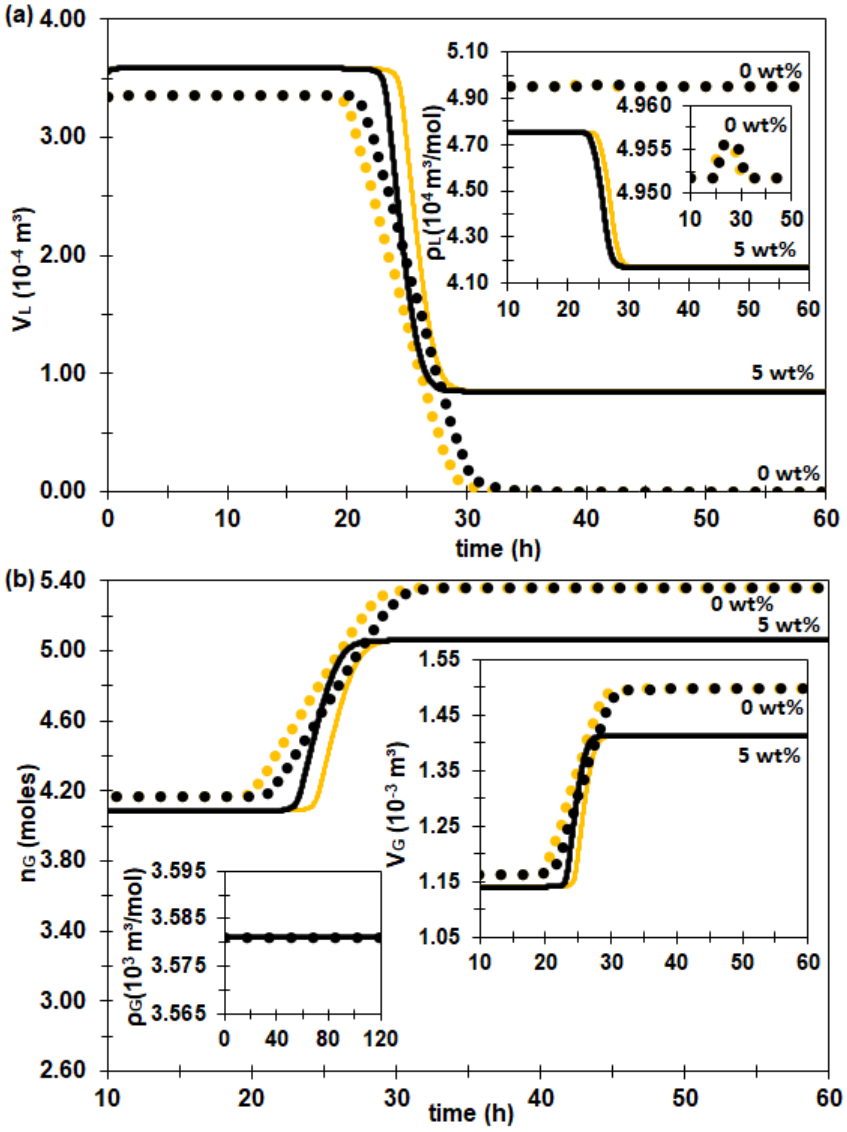

Figure S60 - (a) The liquid phase volume (V_L) and (b) the methane number of moles in the pure vapor phase (n_G) temporal profiles at 276 K and 70.9 bar (*DR* = 0.5). The insertion (a) shows the liquid density (ρ_L) profile. The insertion (b) in the left is the gas density (ρ_G) profile, and the one in the right is the vapor phase volume (V_G). The lines describe the time profiles for the following ethanol compositions of the initial liquid phase: 0 wt% (dotted line) and 5 wt% (continuous line) of EtOH, with (black) and without (yellow) water activity in the driving force.

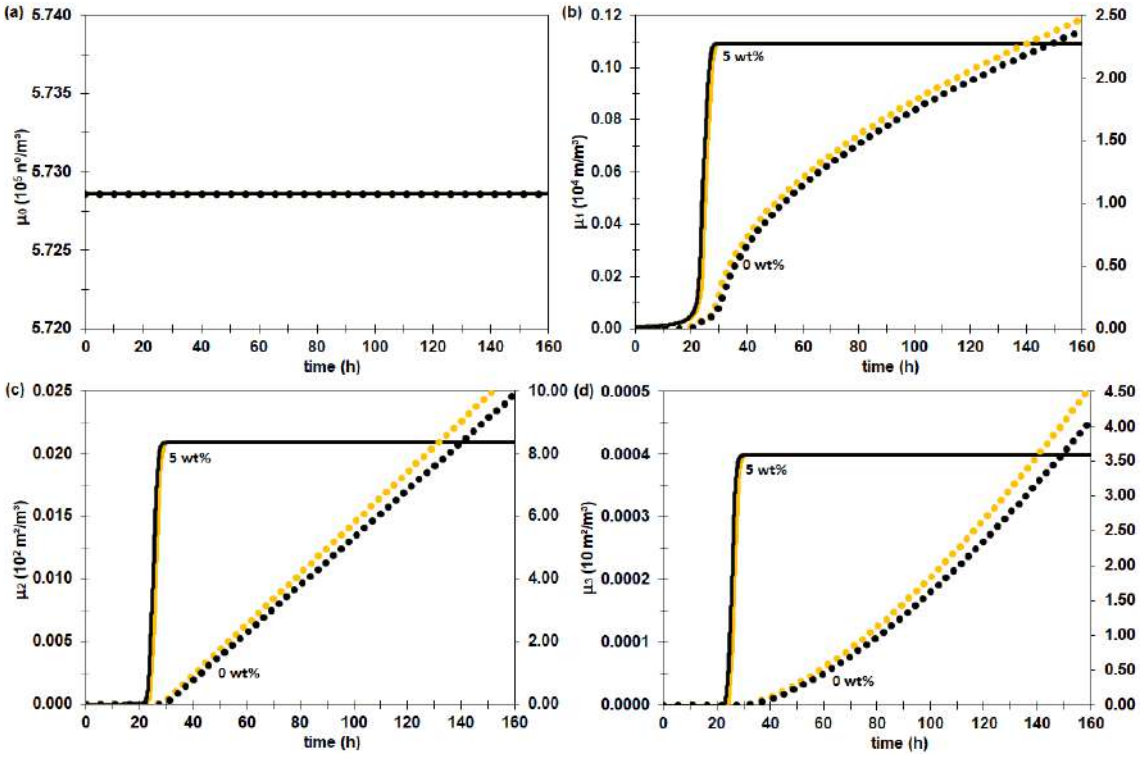

Figure S61 - (a) The temporal profile of the population balance moment of order zero, number of particles per liquid volume (μ_0), (b) moment of order one, particle diameter per liquid volume (μ_1), (c) moment of order two, particle surface area per liquid volume (μ_2) and (d) moment of order three, particle volume per liquid volume (μ_3) at 276 K and 70.9 bar (*DR* = 0.5). The lines describe the time profiles for the following ethanol compositions of the initial liquid phase: 0 wt% (dotted line) and 5 wt% (continuous line) of EtOH, with (black) and without (yellow) water activity in the driving force.

S.16.4 The system at 276 K and 70.9 bar without water activity in the driving force for 5, 10, and 15 wt%

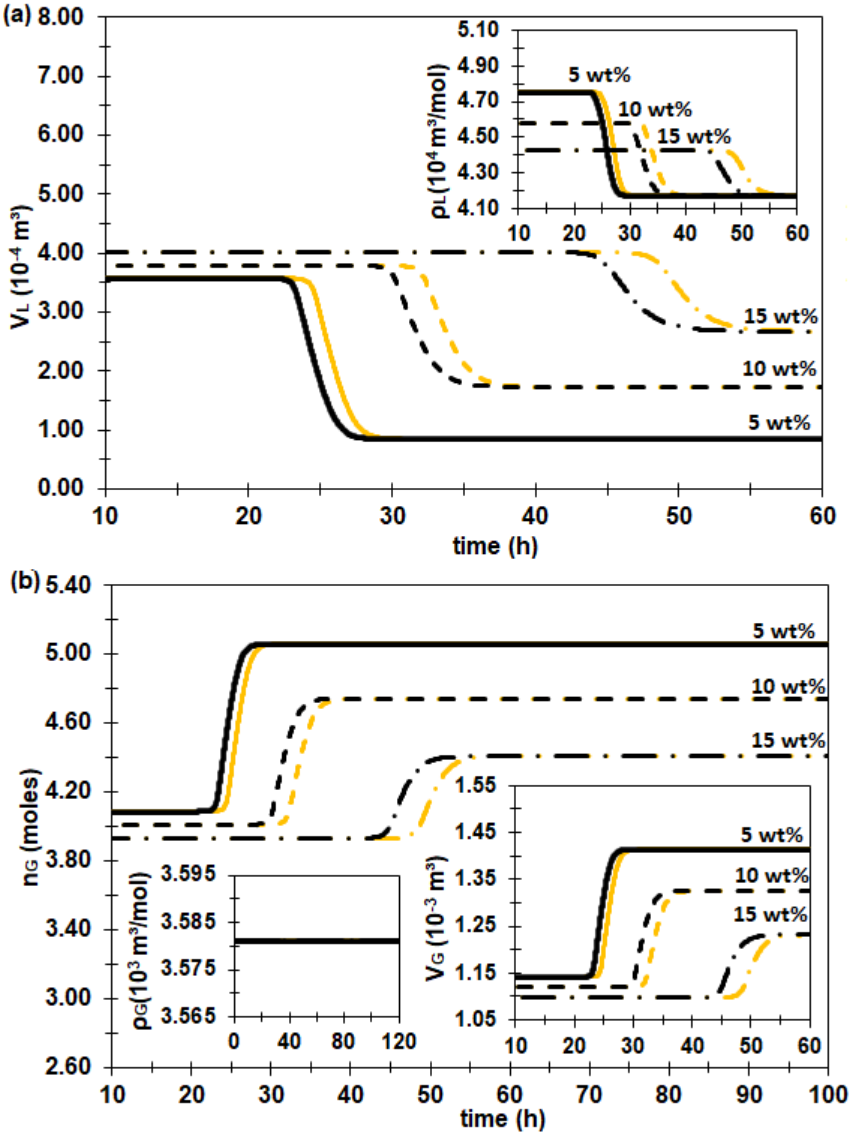

Figure S62 - (a) The liquid phase volume (V_L) and (b) the methane number of moles in the pure vapor phase (n_G) temporal profiles at 276 K and 70.9 bar (*DR* = 0.5). The insertion (a) shows the liquid density (ρ_L) profile. The insertion (b) in the left is the gas density (ρ_G) profile, and the one in the right is the vapor phase volume (V_G). The lines describe the time profiles for the following ethanol compositions of the initial liquid phase: 5 wt% (continuous line), 10 wt% (dashed line) and 15 wt% (dotted-dashed line) of EtOH, with (black) and without (yellow) water activity in the driving force.

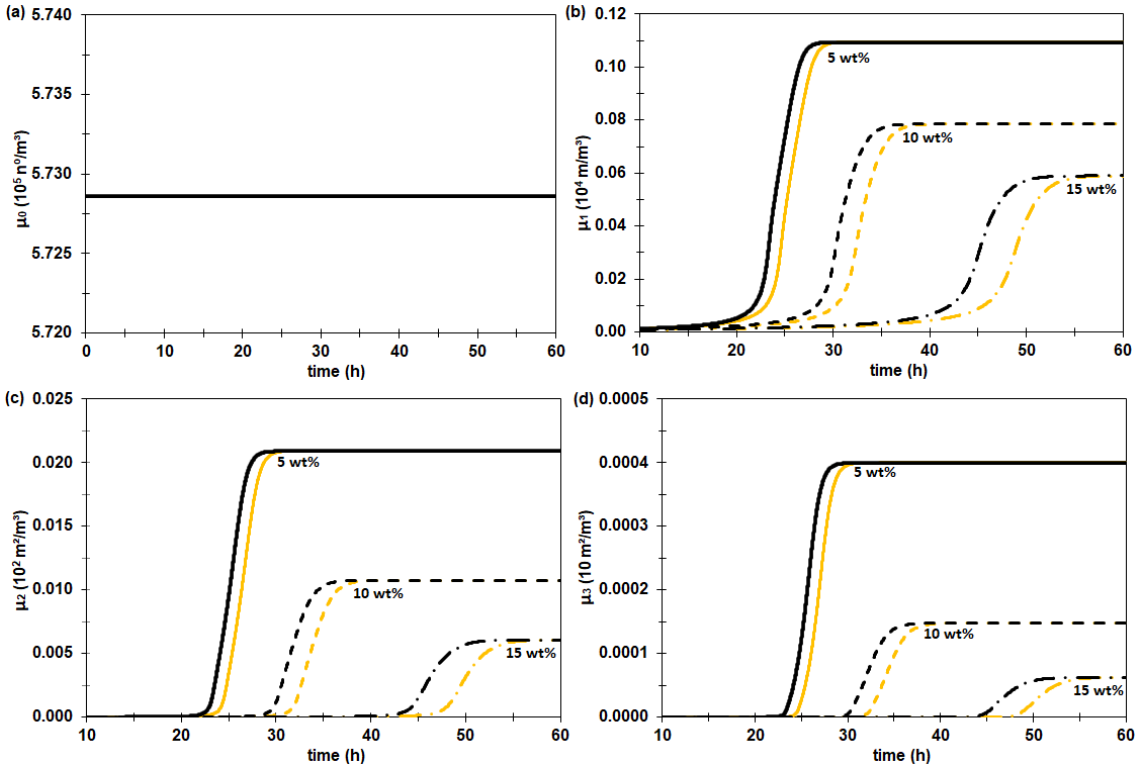

Figure S63 - (a) The temporal profile of the population balance moment of order zero, number of particles per liquid volume (μ_0), (b) moment of order one, particle diameter per liquid volume (μ_1), (c) moment of order two, particle surface area per liquid volume (μ_2) and (d) moment of order three, particle volume per liquid volume (μ_3) at 276 K and 70.9 bar (*DR* = 0.5). The lines describe the time profiles for the following ethanol compositions of the initial liquid phase: 5 wt% (continuous line), 10 wt% (dashed line) and 15 wt% (dotted-dashed line) of EtOH, with (black) and without (yellow) water activity in the driving force.

S.16.5 The system at 276 K and 74.9 bar with water activity in the driving force for 5, 10 and 15 wt%

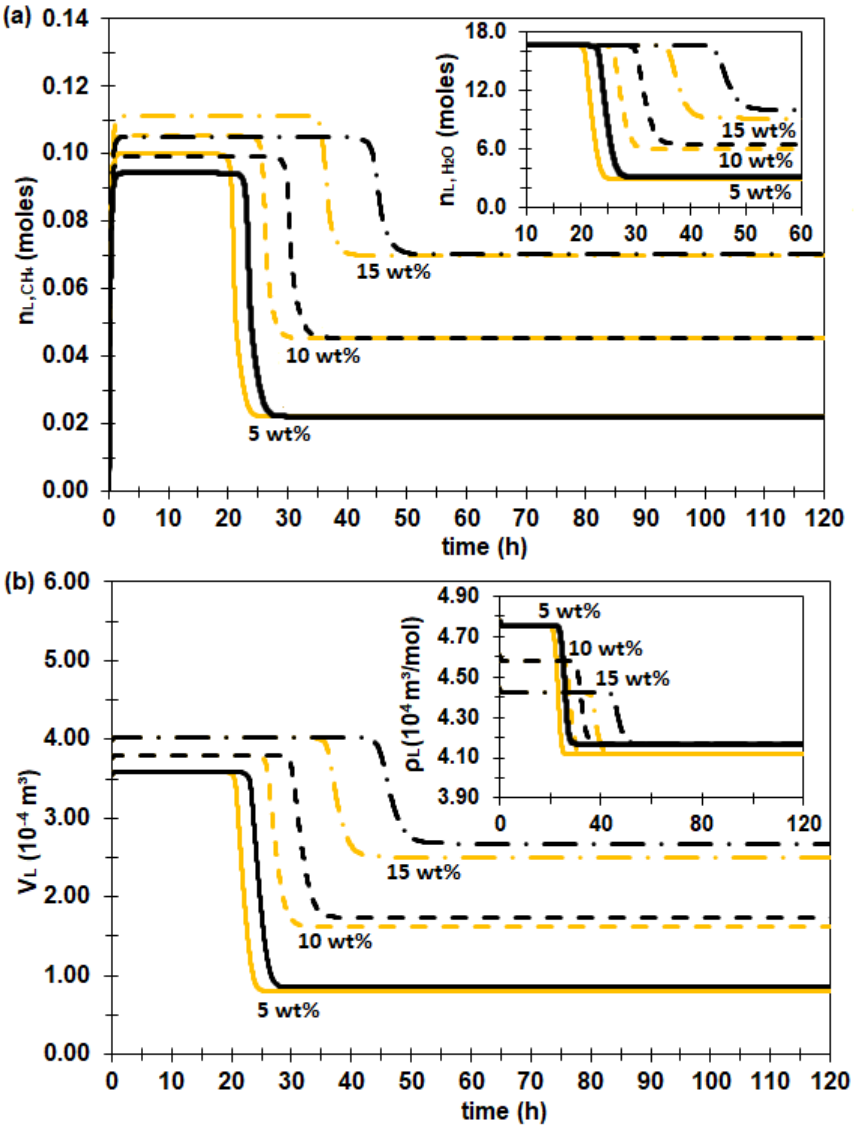

Figure S64 - (a) The number of moles of methane (n_L,CH_4) and (b) the liquid phase volume (V_L) temporal profiles at 276 K (*DR* = 0.5). The insertion (a) shows the number of moles of water (n_L,H_2O) profile in the bulk liquid phase. The insertion (b) shows the liquid density (ρ_L) profile. The lines describe the time profiles for the following ethanol compositions of the initial liquid phase: 5 wt% (continuous line), 10 wt% (dashed line) and 15 wt% (dotted-dashed line) of EtOH, at 70.9 bar, θ = 72% (black), and at 74.9 bar, θ = 75% (yellow).

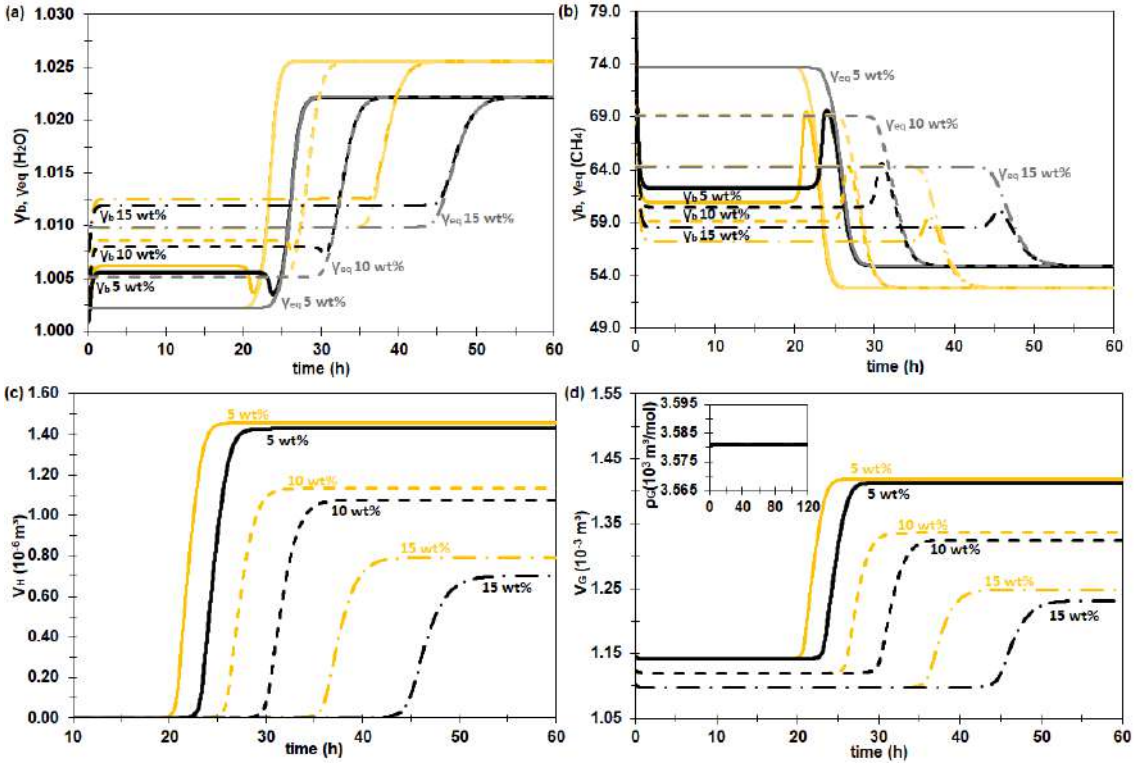

Figure S65 - The activity coefficient (γ) for (a) H_2O and (b) CH_4, (c) the hydrate volume temporal profile (V_H) and (d) the vapor phase volume (V_G) temporal profile at 276 K (*DR* = 0.5). The insertion (d) shows the the gas density (ρ_G) profile. The lines describe the time profiles for the following ethanol compositions of the initial liquid phase: 5 wt% (continuous line), 10 wt% (dashed line) and 15 wt% (dotted-dashed line) of EtOH, at 70.9 bar, θ = 72% (black), and at 74.9 bar, θ = 75% (yellow).

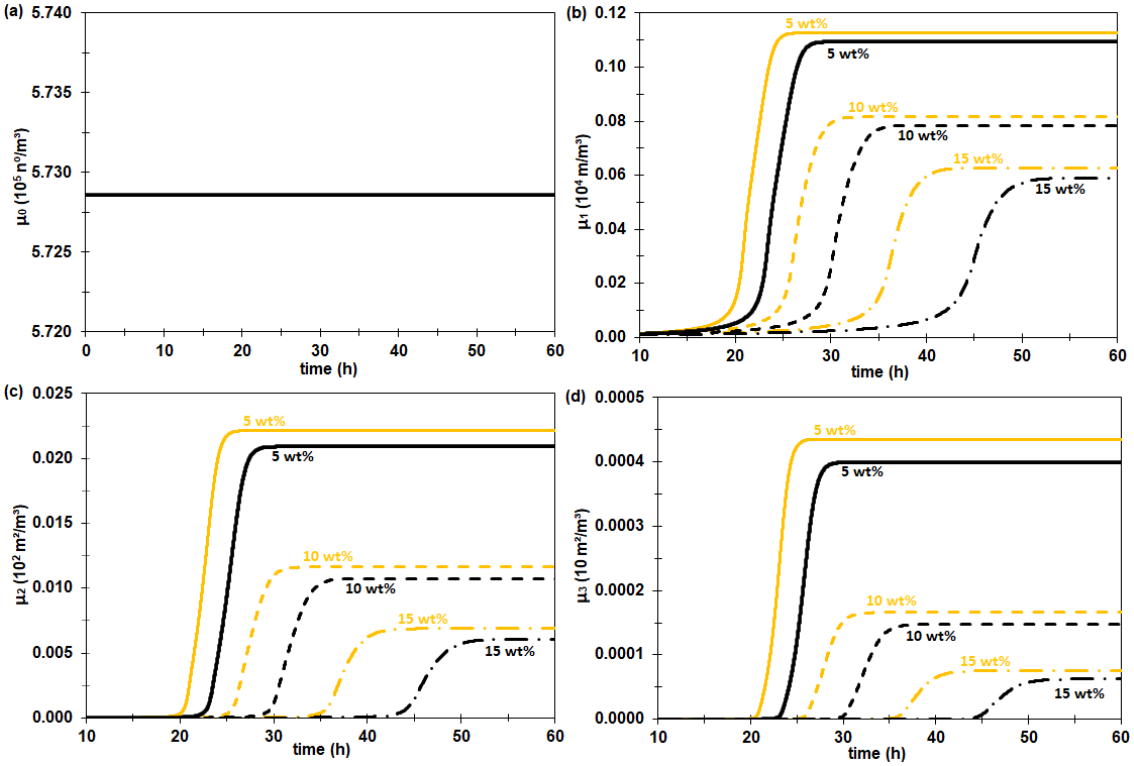

Figure S66 - (a) The temporal profile of the population balance moment of order zero, number of particles per liquid volume (μ_0), (b) moment of order one, particle diameter per liquid volume (μ_1), (c) moment of order two, particle surface area per liquid volume (μ_2) and (d) moment of order three, particle volume per liquid volume (μ_3) at 276 K (*DR* = 0.5). The lines describe the time profiles for the following ethanol compositions of the initial liquid phase: 5 wt% (continuous line), 10 wt% (dashed line) and 15 wt% (dotted-dashed line) of EtOH, at 70.9 bar, θ = 72% (black), and at 74.9 bar, θ = 75% (yellow).

S.16.6 The system at 274 K and 70.9 bar with water activity in the driving force for 5, 10, and 15 wt%

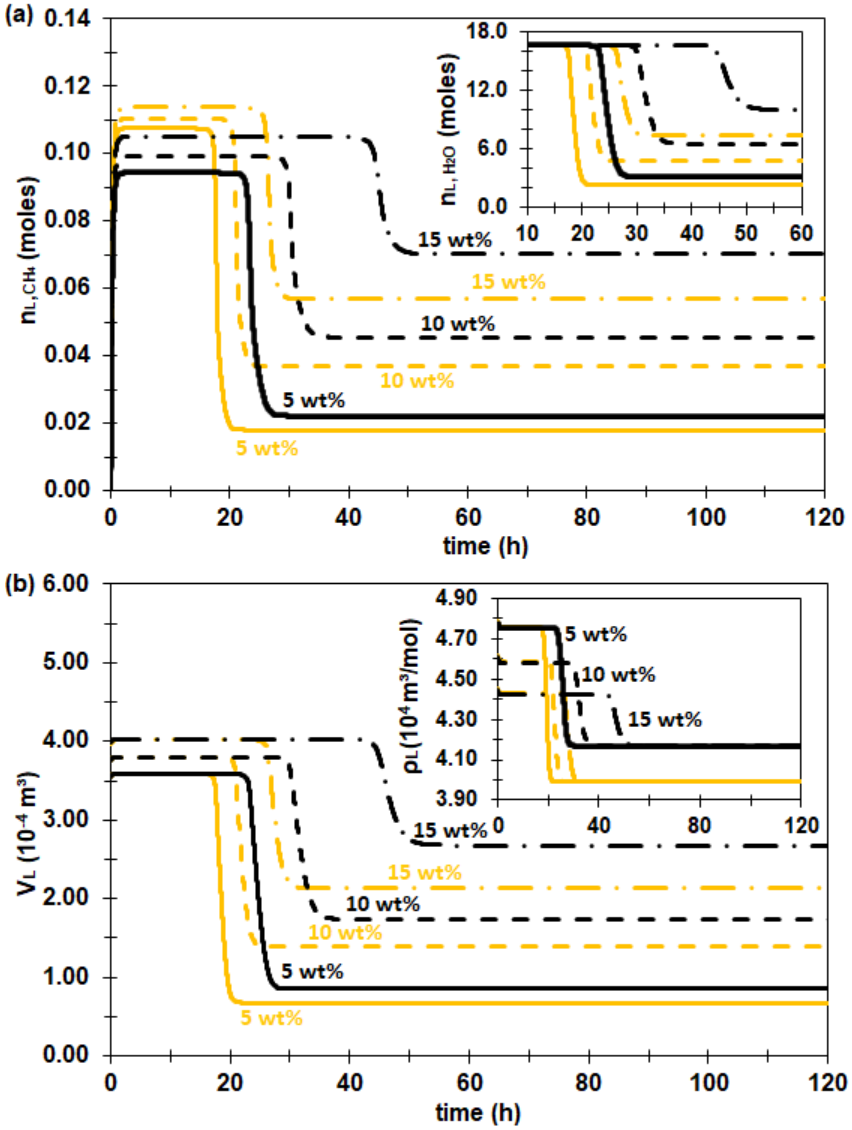

Figure S67 - (a) The number of moles of methane (n_L,CH_4) and (b) the liquid phase volume (V_L) temporal profiles at 70.9 bar (*DR* = 0.5). The insertion (a) shows the number of moles of water (n_L,H_2O) profile in the bulk liquid phase. The insertion (b) shows the liquid density (ρ_L) profile. The lines describe the time profiles for the following ethanol compositions of the initial liquid phase: 5 wt% (continuous line), 10 wt% (dashed line) and 15 wt% (dotted-dashed line) of EtOH, at 276 K, θ = 72% (black), and at 274 K, θ = 68% (yellow).

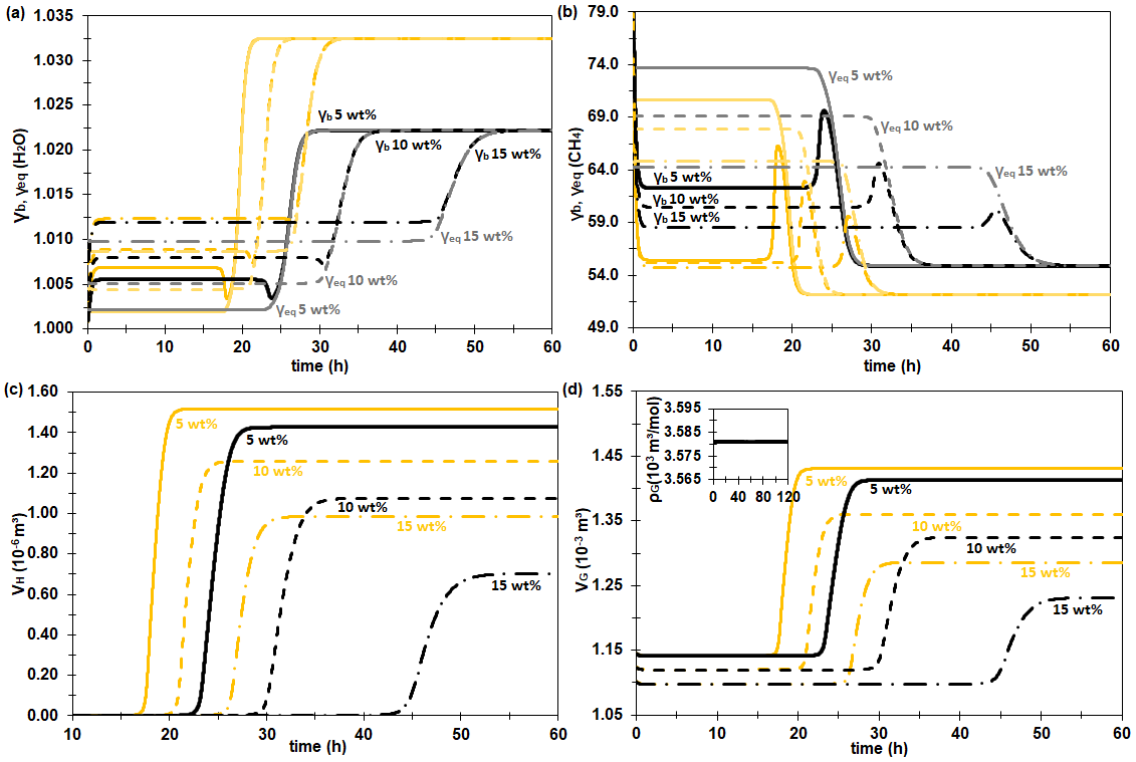

Figure S68 - The activity coefficient (γ) for (a) H_2O and (b) CH_4, (c) the hydrate volume temporal profile (V_H) and (d) the vapor phase volume (V_G) temporal profile at 70.9 bar (*DR* = 0.5). The insertion (d) shows the the gas density (ρ_G) profile. The lines describe the time profiles for the following ethanol compositions of the initial liquid phase: 5 wt% (continuous line), 10 wt% (dashed line) and 15 wt% (dotted-dashed line) of EtOH, at 276 K, θ = 72% (black), and at 274 K, θ = 68% (yellow).

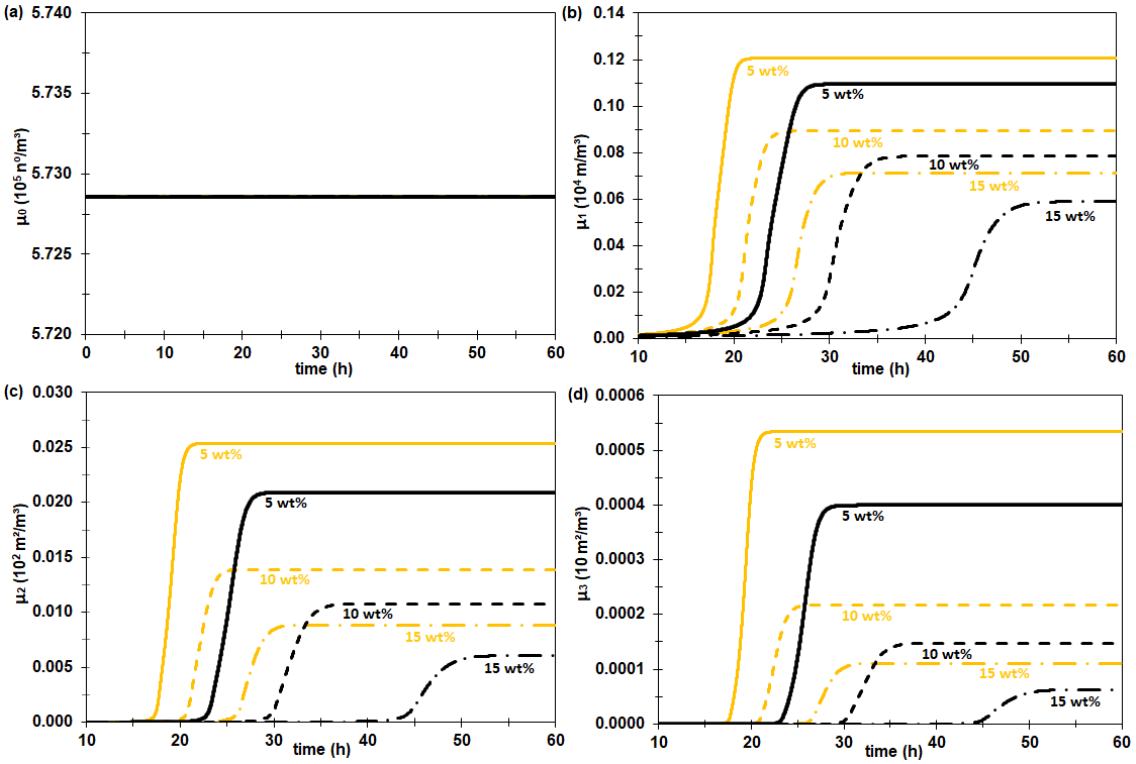

Figure S69 - (a) The temporal profile of the population balance moment of order zero, number of particles per liquid volume (μ_0), (b) moment of order one, particle diameter per liquid volume (μ_1), (c) moment of order two, particle surface area per liquid volume (μ_2) and (d) moment of order three, particle volume per liquid volume (μ_3) at 70.9 bar (*DR* = 0.5). The lines describe the time profiles for the following ethanol compositions of the initial liquid phase: 5 wt% (continuous line), 10 wt% (dashed line) and 15 wt% (dotted-dashed line) of EtOH, at 276 K, θ = 72% (black), and at 274 K, θ = 68% (yellow).

S.17 System property derivative profiles

The profile of the time derivatives of all variables calculated by the proposed model is presented in this topic. In all simulated conditions, of temperature, pressure, and composition, the derivatives presented the expected temporal behavior for all phases and components of the system.

S.17.1 The system at 276 K and 70.9 bar with water activity in the driving force for 0 and 5 wt%

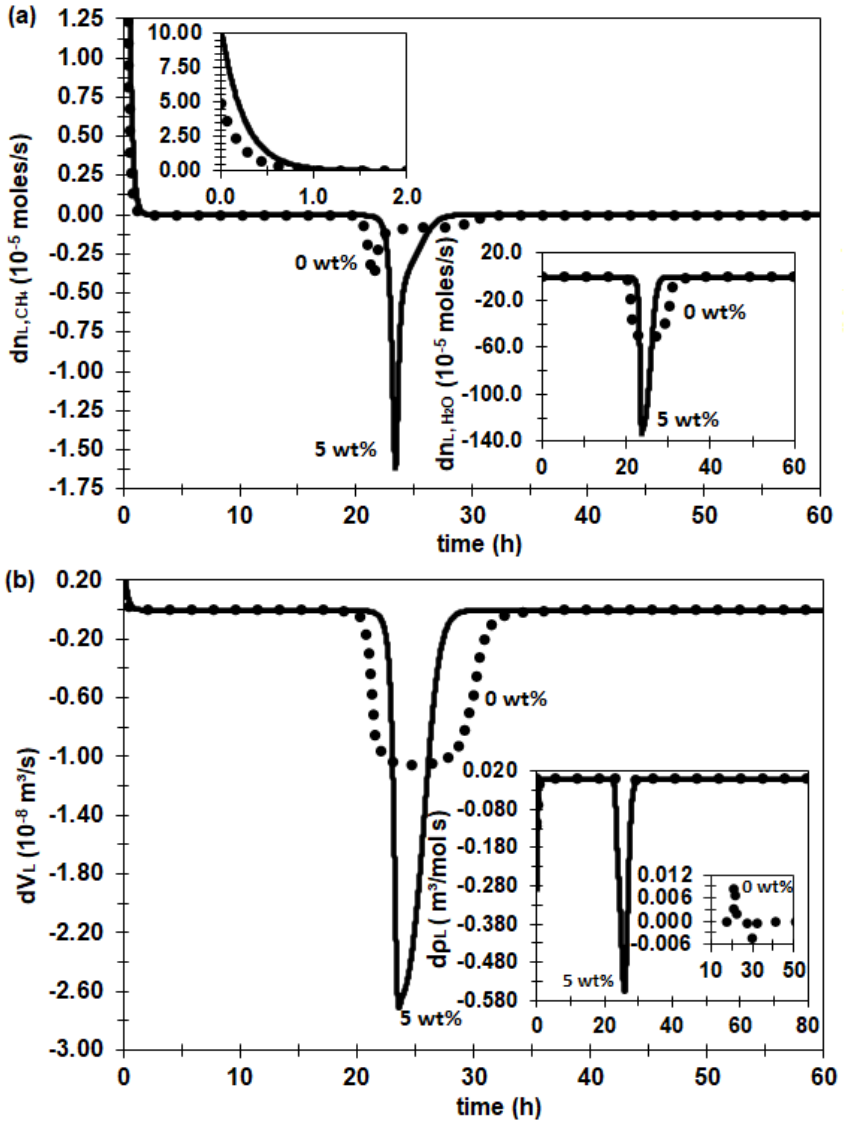

Figure S70 - The differential profile of (a) the methane number of moles in the bulk liquid phase (dn_{L,CH_4}) and (b) the liquid phase volume (dV_L) at 276 K and 70.9 bar (*DR* = 0.5). The insertion (a) in the left shows the methane saturation profile and the one in the right shows the water number of moles (n_L,H_2O) profile in the bulk liquid phase. The insertion (b) shows the liquid density (ρ_L) profile with a zoom in the profile at 0 wt% of EtOH. The lines describe the time profiles for the following ethanol compositions of the initial liquid phase: 0 wt% (dotted line) and 5 wt% (continuous line) of EtOH.

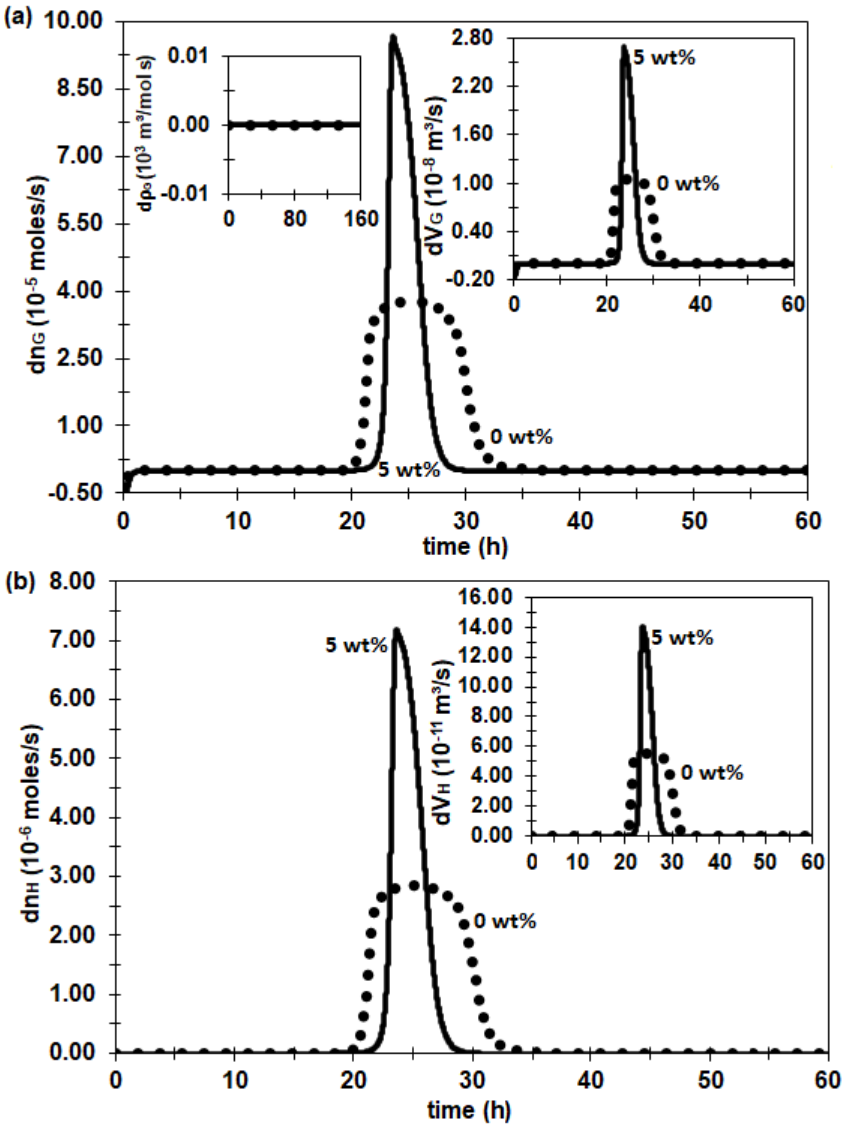

Figure S71 - The differential profile of (a) the methane number of moles in the pure vapor phase (dn_G) and (b) the hydrate number of moles (dn_H) at 276 K and 70.9 bar (*DR* = 0.5). The insertion (a) shows the vapor phase volume (dV_G) with the constant vapor density ($d\rho_G$) differential profile. The insertion (b) shows the hydrate phase volume (dV_H) differential profile. The lines describe the time profiles for the following ethanol compositions of the initial liquid phase: 0 wt% (dotted line) and 5 wt% (continuous line) of EtOH.

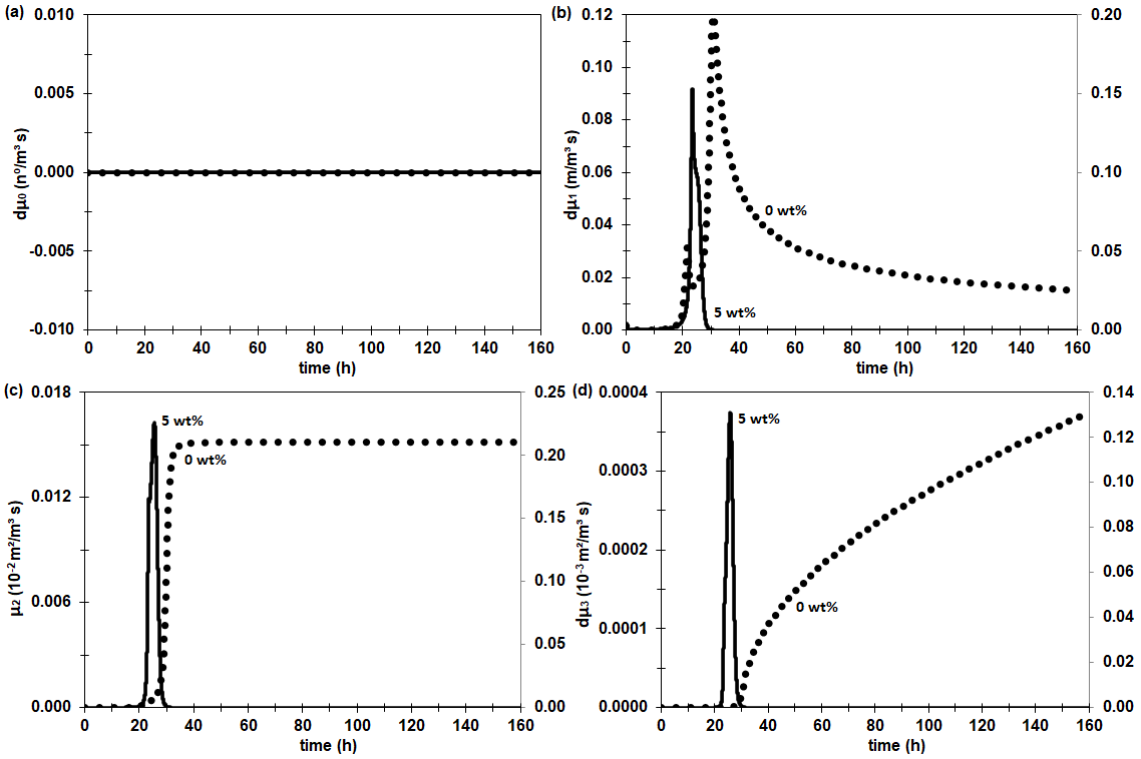

Figure S72 - (a) The differential profile of the population balance moment of order zero, number of particles per liquid volume ($d\mu_0$), (b) moment of order one, particle diameter per liquid volume ($d\mu_1$), (c) moment of order two, particle surface area per liquid volume ($d\mu_2$) and (d) moment of order three, particle volume per liquid volume ($d\mu_3$) at 276 K and 70.9 bar (*DR* = 0.5). The lines describe the time profiles for the following ethanol compositions of the initial liquid phase: 0 wt% (dotted line, 2nd axis) and 5 wt% (continuous line, 1st axis) of EtOH.

S.17.2 The system at 276 K and 70.9 bar with water activity in the driving force for 5, 10, and 15 wt%

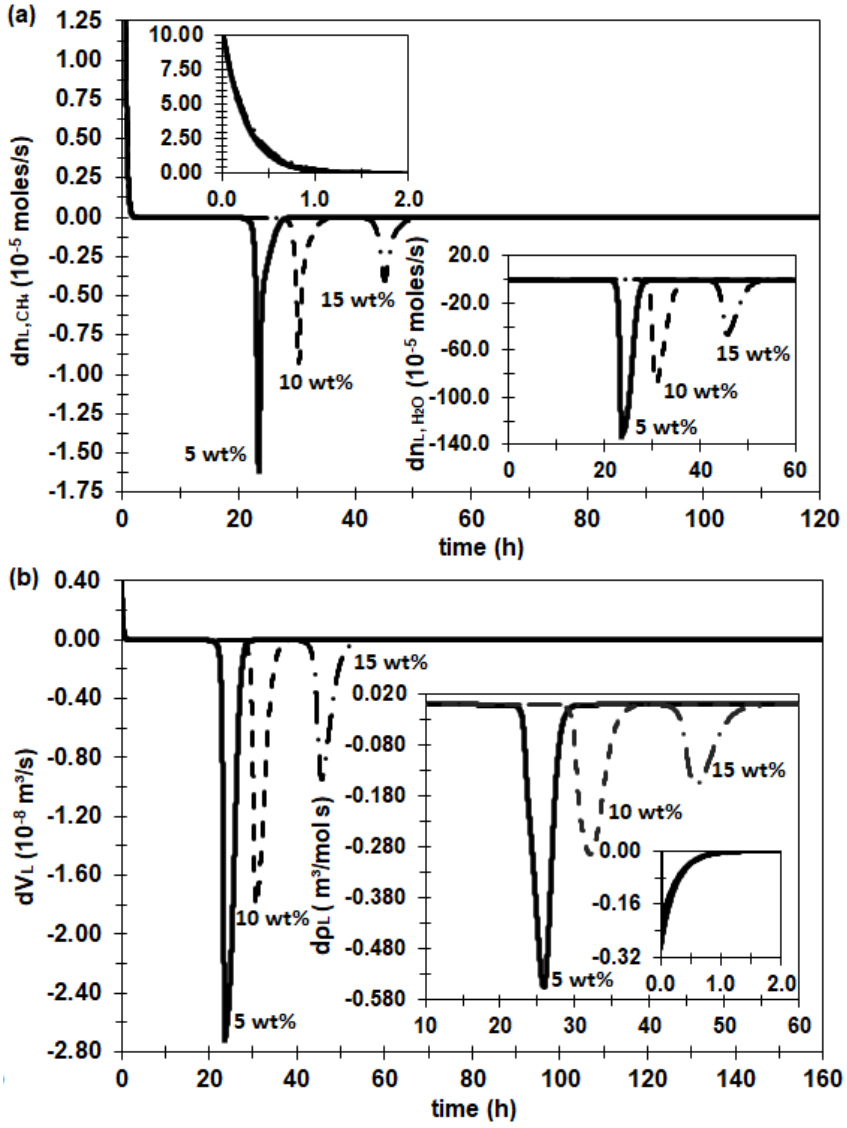

Figure S73 - The differential profile of (a) the methane number of moles in the bulk liquid phase (dn_{L,CH_4}) and (b) the liquid phase volume (dV_L) at 276 K and 70.9 bar (*DR* = 0.5). The insertion (a) in the left shows the methane saturation profile and the one in the right shows the water number of moles (n_L,H_2O) profile in the bulk liquid phase. The insertion (b) shows the liquid density (ρ_L) profile with a zoom in the methane saturation profile. The lines describe the time profiles for the following ethanol compositions of the initial liquid phase: 5 wt% (continuous line), 10 wt% (dashed line) and 15 wt% (dotted-dashed line) of EtOH.

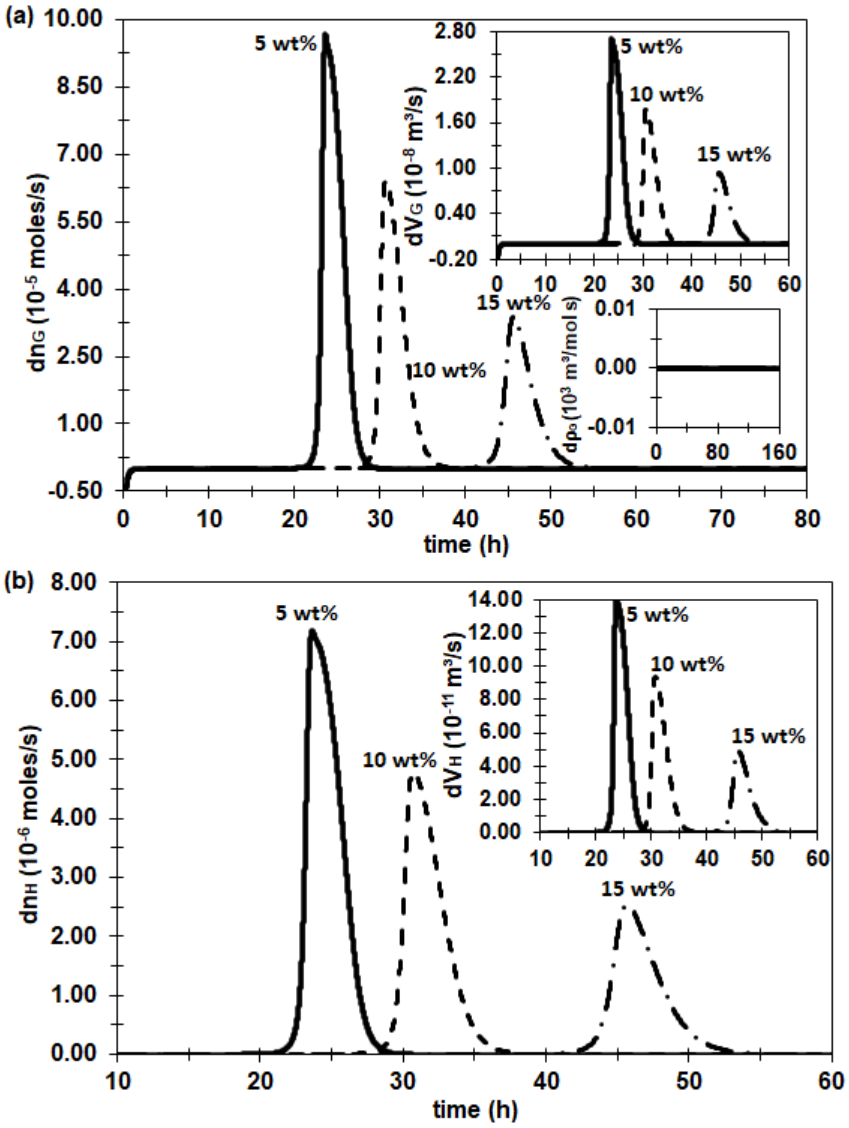

Figure S74 - The differential profile of (a) the methane number of moles in the pure vapor phase (dn_G) and (b) the hydrate number of moles (dn_H) at 276 K and 70.9 bar (*DR* = 0.5). The insertion (a) shows the vapor phase volume (dV_G) and the constant vapor density ($d\rho_G$) differential profile. The insertion (b) shows the hydrate phase volume (dV_H) differential profile. The lines describe the time profiles for the following ethanol compositions of the initial liquid phase: 5 wt% (continuous line), 10 wt% (dashed line) and 15 wt% (dotted-dashed line) of EtOH.

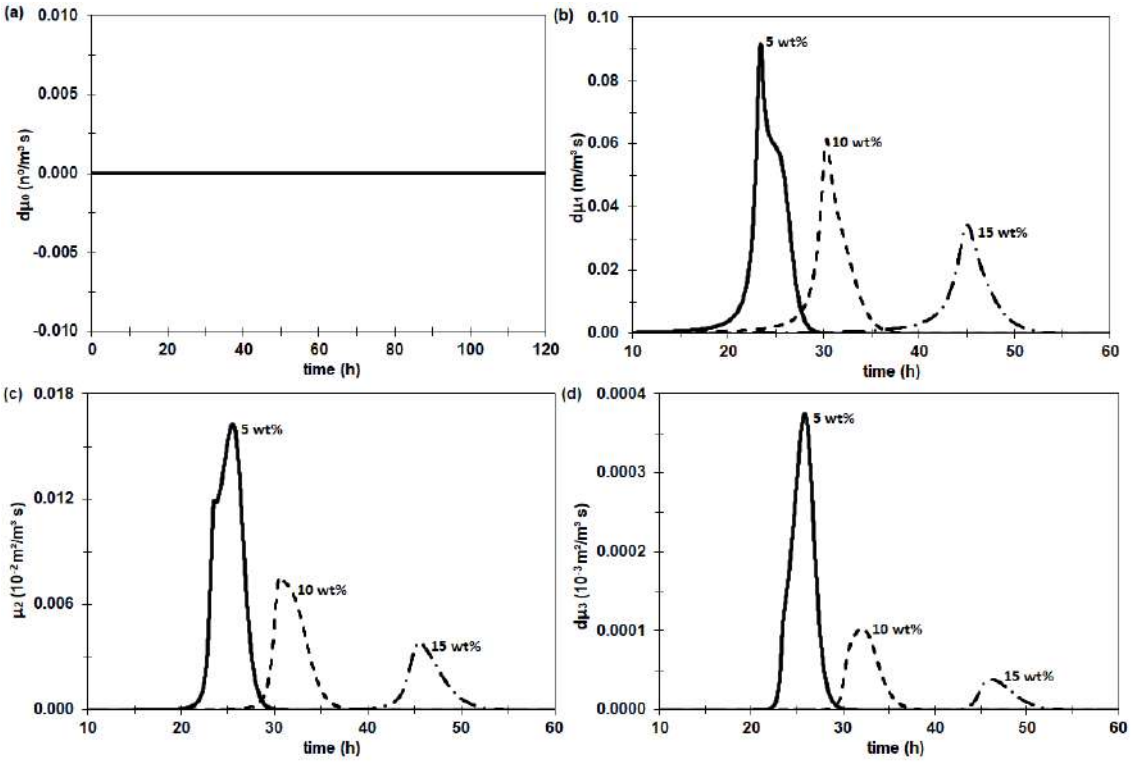

Figure S75 - (a) The differential profile of the population balance moment of order zero, number of particles per liquid volume ($d\mu_0$), (b) moment of order one, particle diameter per liquid volume ($d\mu_1$), (c) moment of order two, particle surface area per liquid volume ($d\mu_2$) and (d) moment of order three, particle volume per liquid volume ($d\mu_3$) at 276 K and 70.9 bar (*DR* = 0.5). The lines describe the time profiles for the following ethanol compositions of the initial liquid phase: 5 wt% (continuous line), 10 wt% (dashed line) and 15 wt% (dotted-dashed line) of EtOH.

S.17.3 The system at 276 K and 70.9 bar without water activity in the driving force for 0 and 5 wt%

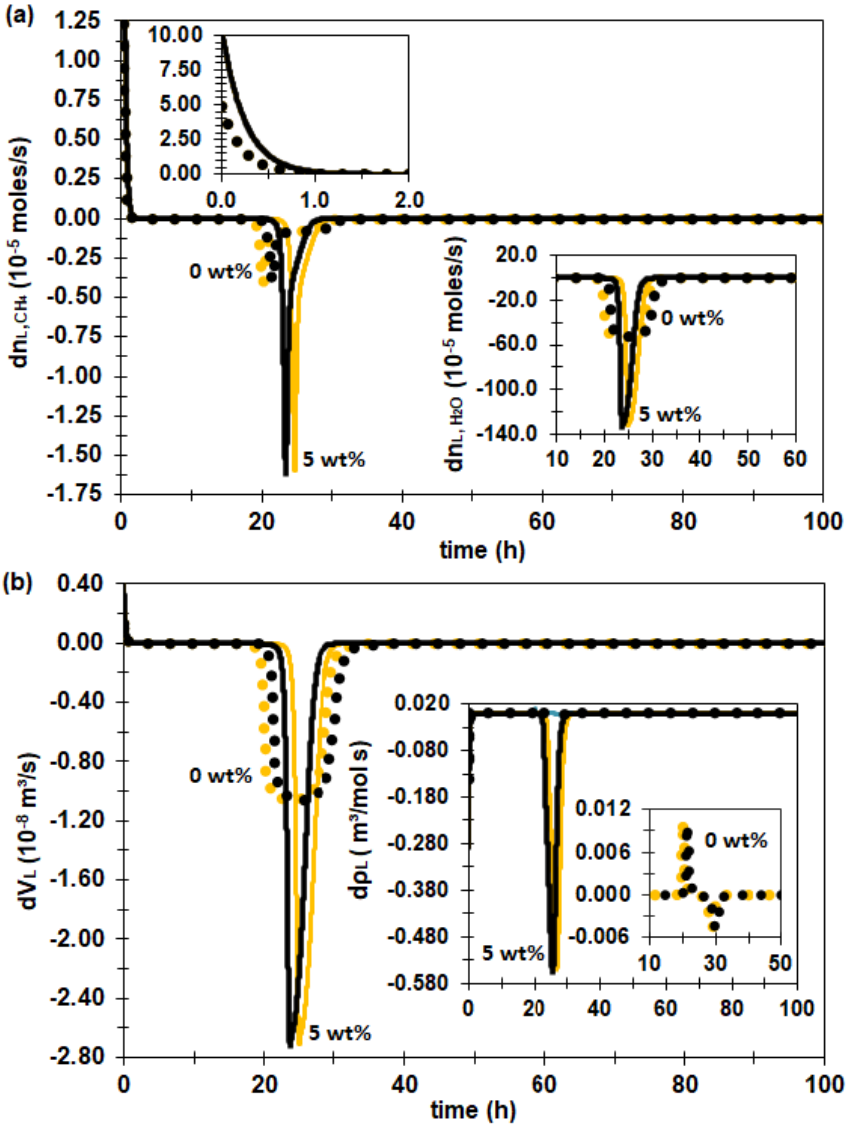

Figure S76 - The differential profile of (a) the methane number of moles in the bulk liquid phase (dn_{L,CH_4}) and (b) the liquid phase volume (dV_L) at 276 K and 70.9 bar (*DR* = 0.5). The insertion (a) in the left shows the methane saturation profile and the one in the right shows the water number of moles (n_L,H_2O) profile in the bulk liquid phase. The insertion (b) shows the liquid density (ρ_L) profile with a zoom in the profile at 0 wt% of EtOH. The lines describe the time profiles for the following ethanol compositions of the initial liquid phase: 0 wt% (dotted line) and 5 wt% (continuous line) of EtOH, with (black) and without (yellow) water activity in the driving force.

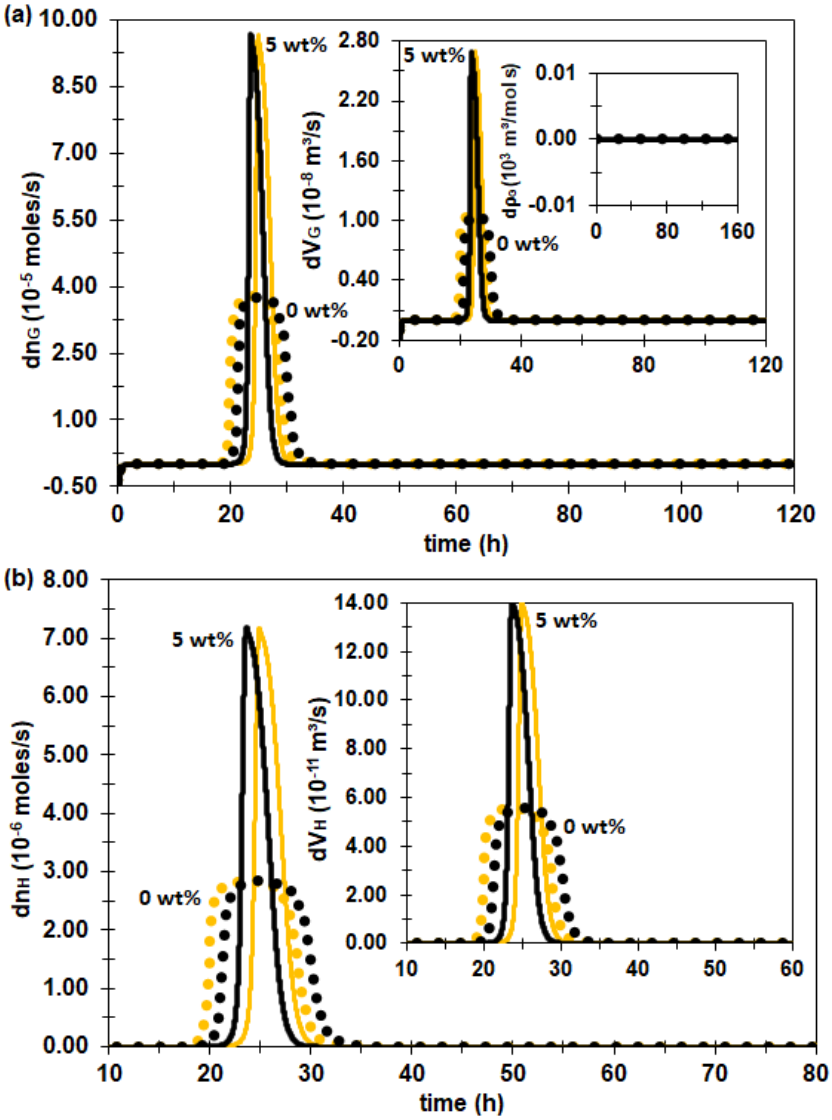

Figure S77 - The differential profile of (a) the methane number of moles in the pure vapor phase (dn_G) and (b) the hydrate number of moles (dn_H) at 276 K and 70.9 bar (*DR* = 0.5). The insertion (a) shows the vapor phase volume (dV_G) with the constant vapor density ($d\rho_G$) differential profile. The insertion (b) shows the hydrate phase volume (dV_H) differential profile. The lines describe the time profiles for the following ethanol compositions of the initial liquid phase: 0 wt% (dotted line) and 5 wt% (continuous line) of EtOH, with (black) and without (yellow) water activity in the driving force.

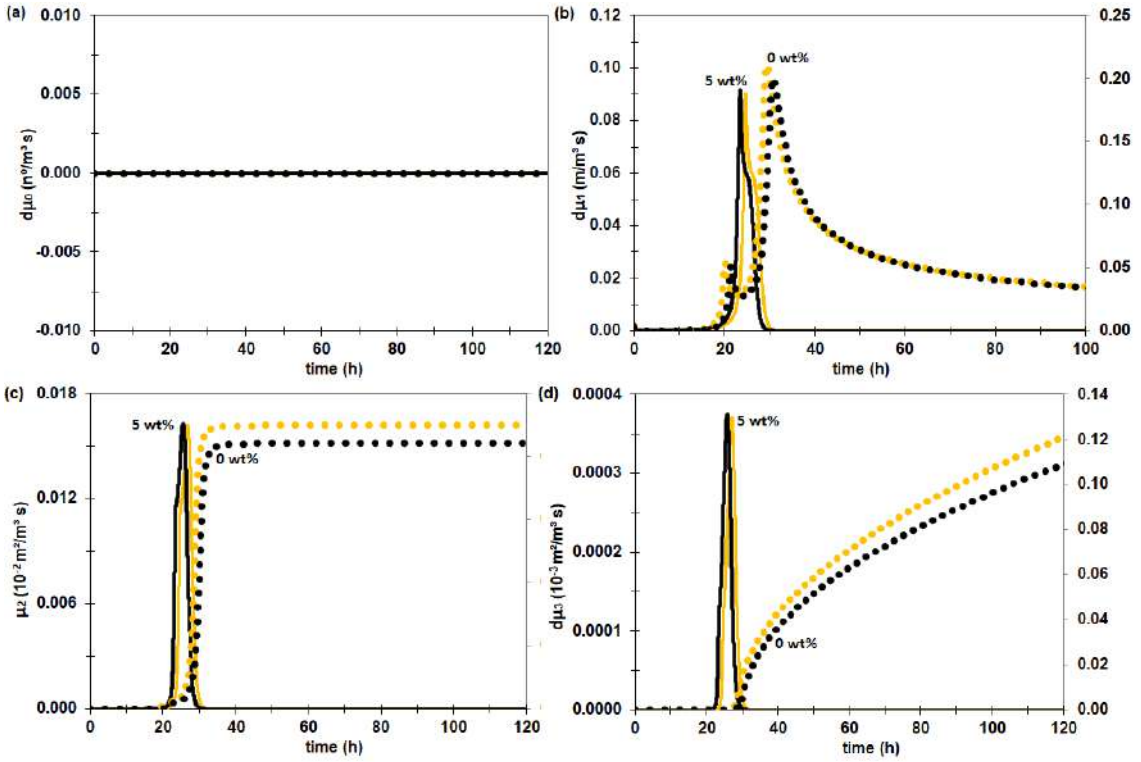

Figure S78 - (a) The differential profile of the population balance moment of order zero, number of particles per liquid volume ($d\mu_0$), (b) moment of order one, particle diameter per liquid volume ($d\mu_1$), (c) moment of order two, particle surface area per liquid volume ($d\mu_2$) and (d) moment of order three, particle volume per liquid volume ($d\mu_3$) at 276 K and 70.9 bar (*DR* = 0.5). The lines describe the time profiles for the following ethanol compositions of the initial liquid phase: 0 wt% (dotted line, 2nd axis) and 5 wt% (continuous line, 1st axis) of EtOH, with (black) and without (yellow) water activity in the driving force.

S.17.4 The system at 276 K and 70.9 bar without water activity in the driving force for 5, 10 and 15 wt%

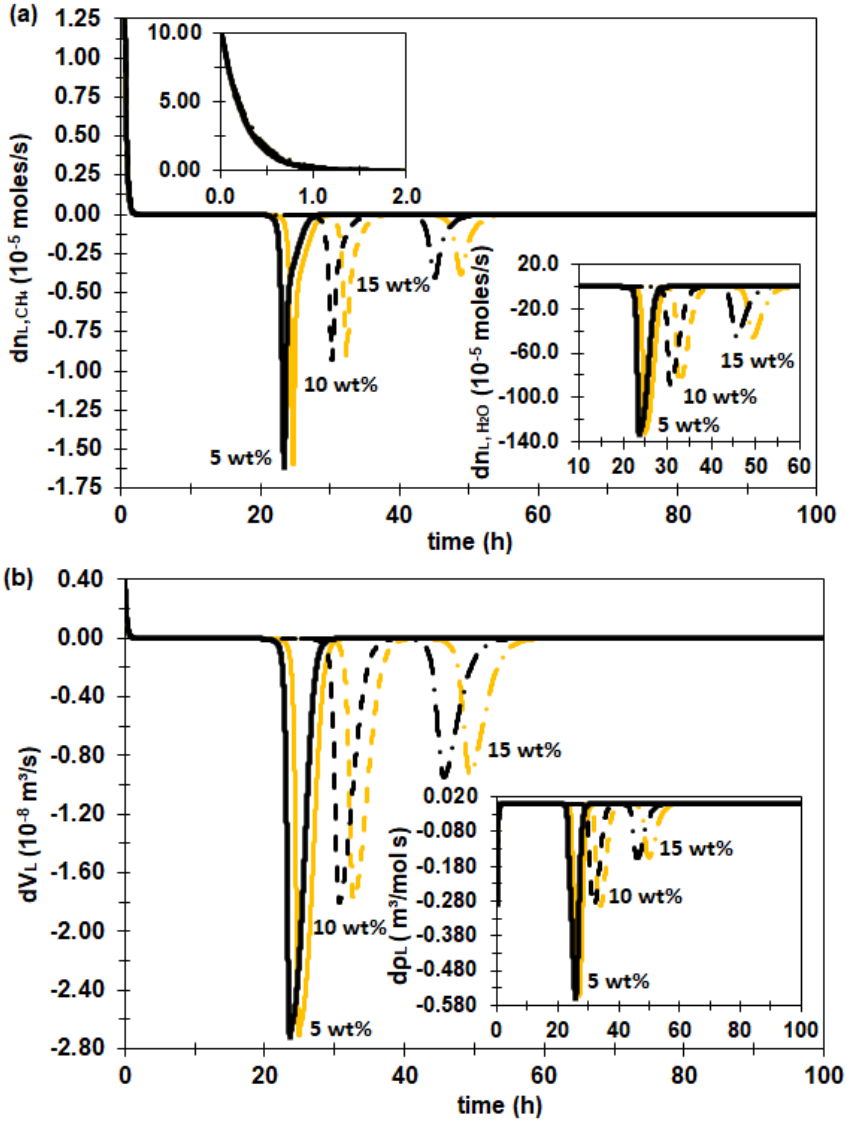

Figure S79 - The differential profile of (a) the methane number of moles in the bulk liquid phase (dn_{L,CH_4}) and (b) the liquid phase volume (dV_L) at 276 K and 70.9 bar (*DR* = 0.5). The insertion (a) in the left shows the methane saturation profile and the one in the right shows the water number of moles (n_L,H_2O) profile in the bulk liquid phase. The insertion (b) shows the liquid density (ρ_L) profile with a zoom in the methane saturation profile. The lines describe the time profiles for the following ethanol compositions of the initial liquid phase: 5 wt% (continuous line), 10 wt% (dashed line) and 15 wt% (dotted-dashed line) of EtOH, with (black) and without (yellow) water activity in the driving force.

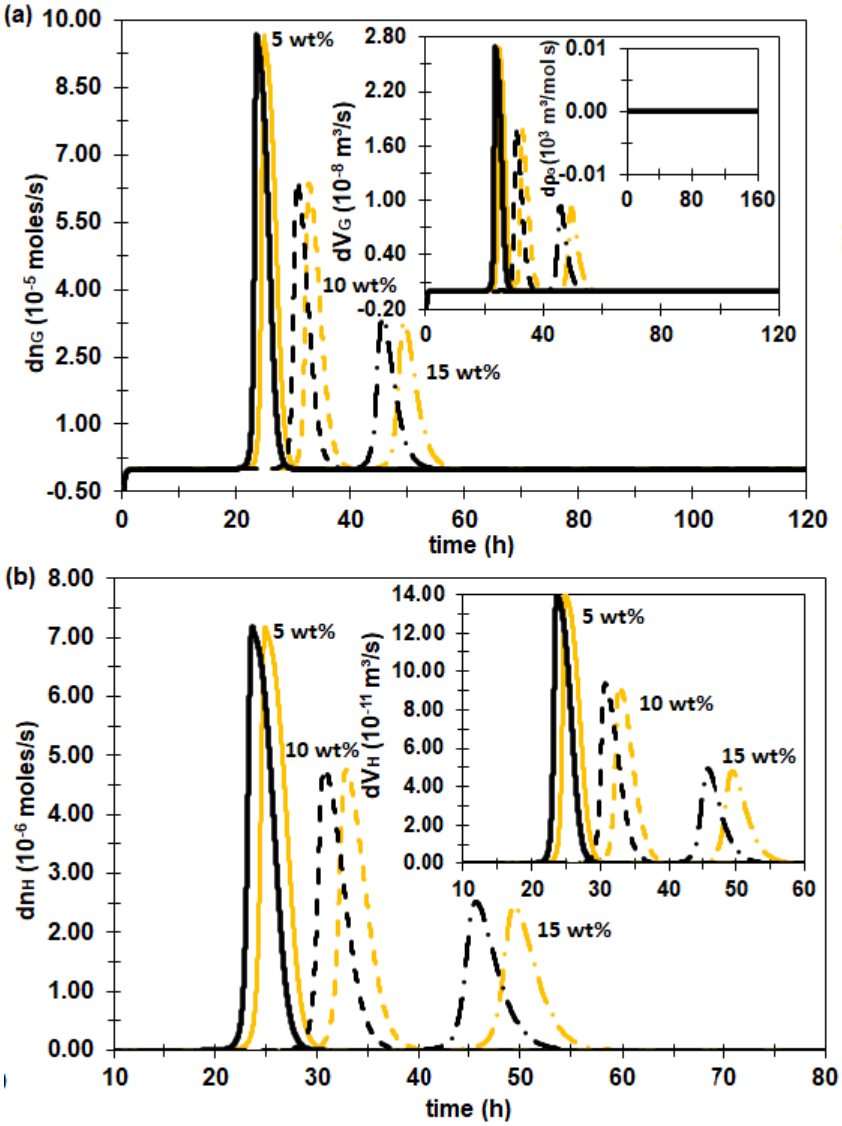

Figure S80 - The differential profile of (a) the methane number of moles in the pure vapor phase (dn_G) and (b) the hydrate number of moles (dn_H) at 276 K and 70.9 bar (*DR* = 0.5). The insertion (a) shows the vapor phase volume (dV_G) and the constant vapor density ($d\rho_G$) differential profile. The insertion (b) shows the hydrate phase volume (dV_H) differential profile. The lines describe the time profiles for the following ethanol compositions of the initial liquid phase: 5 wt% (continuous line), 10 wt% (dashed line) and 15 wt% (dotted-dashed line) of EtOH, with (black) and without (yellow) water activity in the driving force.

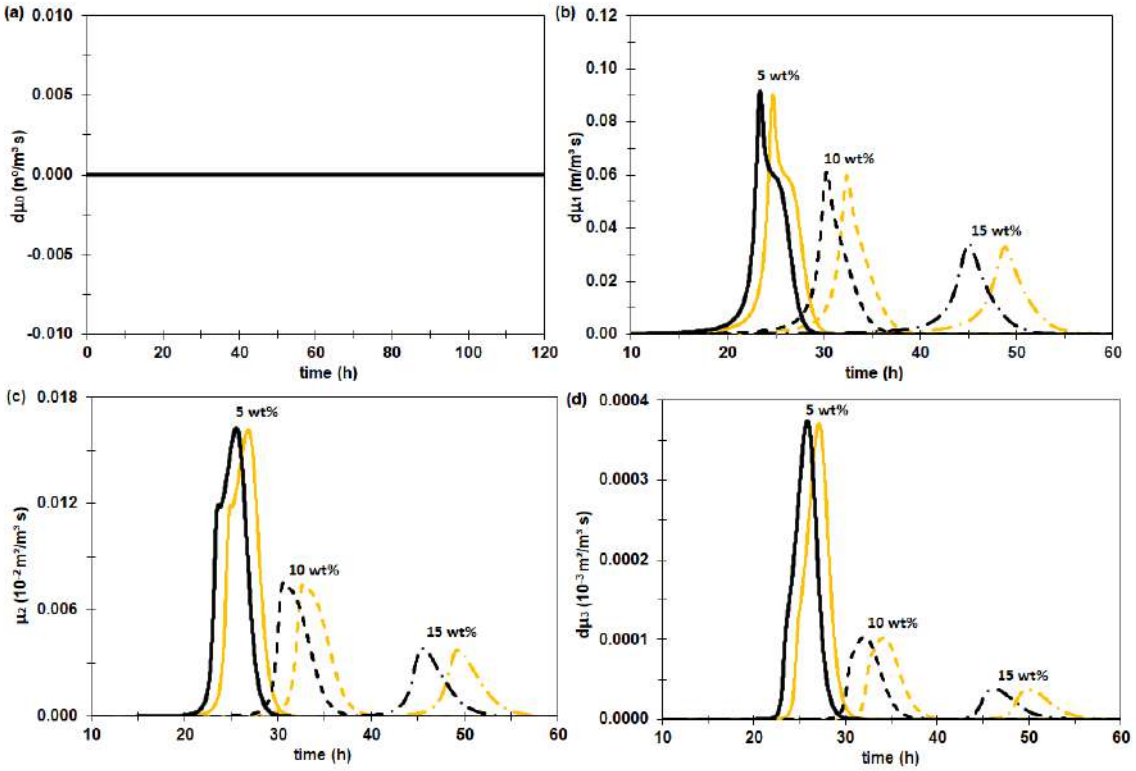

Figure S81 - (a) The differential profile of the population balance moment of order zero, number of particles per liquid volume ($d\mu_0$), (b) moment of order one, particle diameter per liquid volume ($d\mu_1$), (c) moment of order two, particle surface area per liquid volume ($d\mu_2$) and (d) moment of order three, particle volume per liquid volume ($d\mu_3$) at 276 K and 70.9 bar (*DR* = 0.5). The lines describe the time profiles for the following ethanol compositions of the initial liquid phase: 5 wt% (continuous line), 10 wt% (dashed line) and 15 wt% (dotted-dashed line) of EtOH, with (black) and without (yellow) water activity in the driving force.

S.17.5 The system at 276 K and 74.9 bar with water activity in the driving force for 5, 10 and 15 wt%

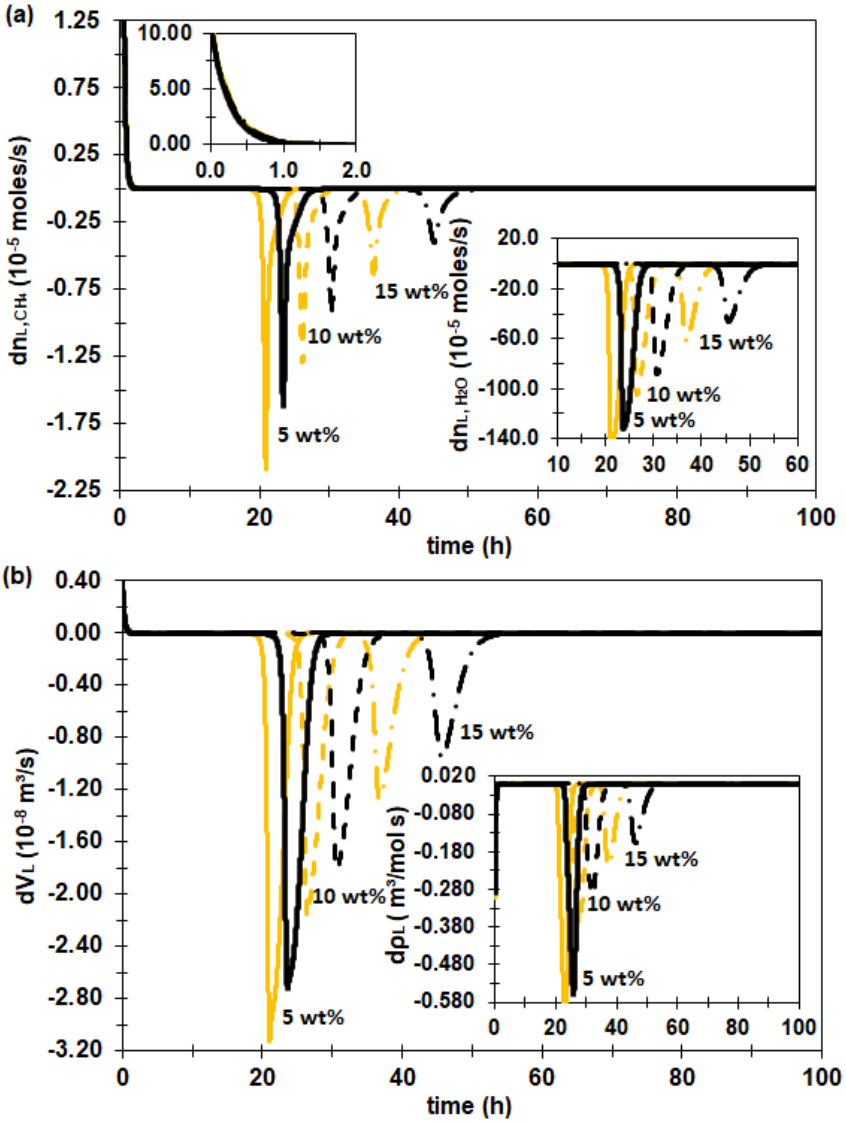

Figure S82 - The differential profile of (a) the methane number of moles in the bulk liquid phase (dn_{L,CH_4}) and (b) the liquid phase volume (dV_L) at 276 K (*DR* = 0.5). The insertion (a) in the left shows the methane saturation profile and the one in the right shows the water number of moles (n_L,H_2O) profile in the bulk liquid phase. The insertion (b) shows the liquid density (ρ_L) profile with a zoom in the methane saturation profile. The lines describe the time profiles for the following ethanol compositions of the initial liquid phase: 5 wt% (continuous line), 10 wt% (dashed line) and 15 wt% (dotted-dashed line) of EtOH, at 70.9 bar, θ = 72% (black), and at 74.9 bar, θ = 75% (yellow).

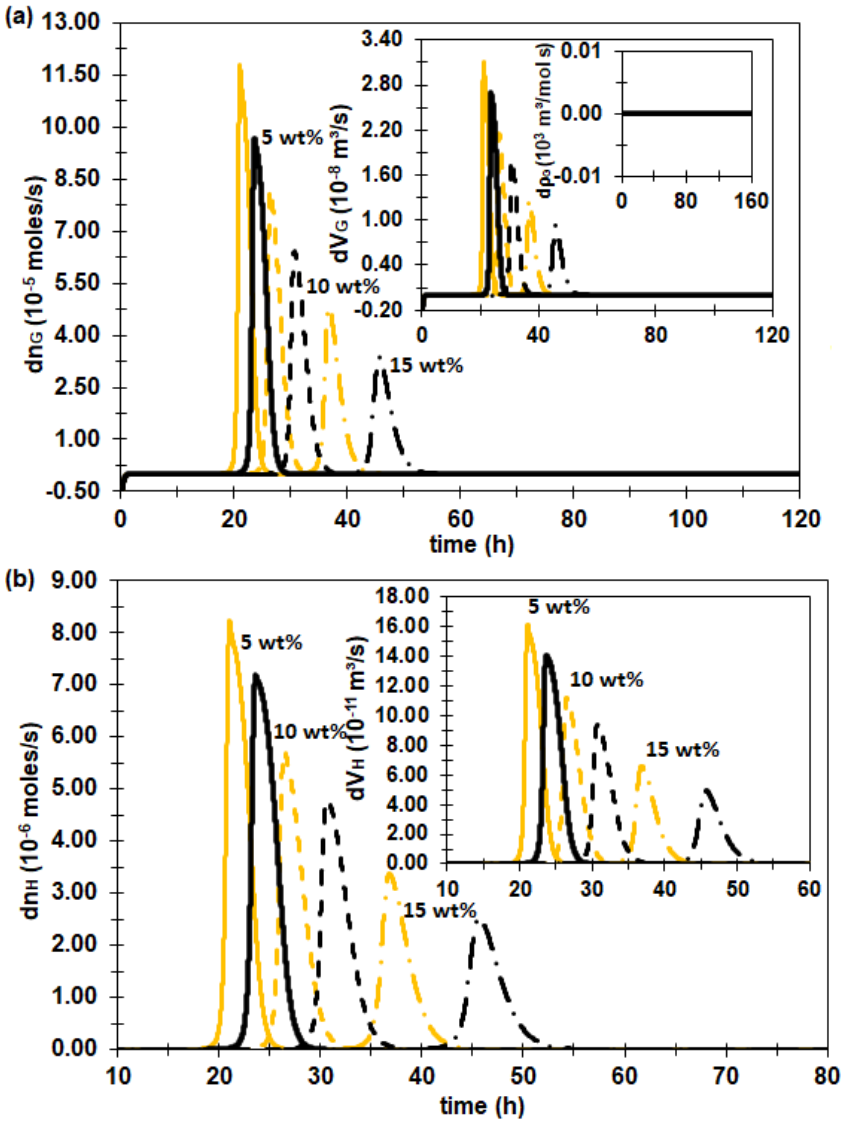

Figure S83 - The differential profile of (a) the methane number of moles in the pure vapor phase (dn_G) and (b) the hydrate number of moles (dn_H) at 276 K (*DR* = 0.5). The insertion (a) shows the vapor phase volume (dV_G) and the constant vapor density ($d\rho_G$) differential profile. The insertion (b) shows the hydrate phase volume (dV_H) differential profile. The lines describe the time profiles for the following ethanol compositions of the initial liquid phase: 5 wt% (continuous line), 10 wt% (dashed line) and 15 wt% (dotted-dashed line) of EtOH, at 70.9 bar, θ = 72% (black), and at 74.9 bar, θ = 75% (yellow).

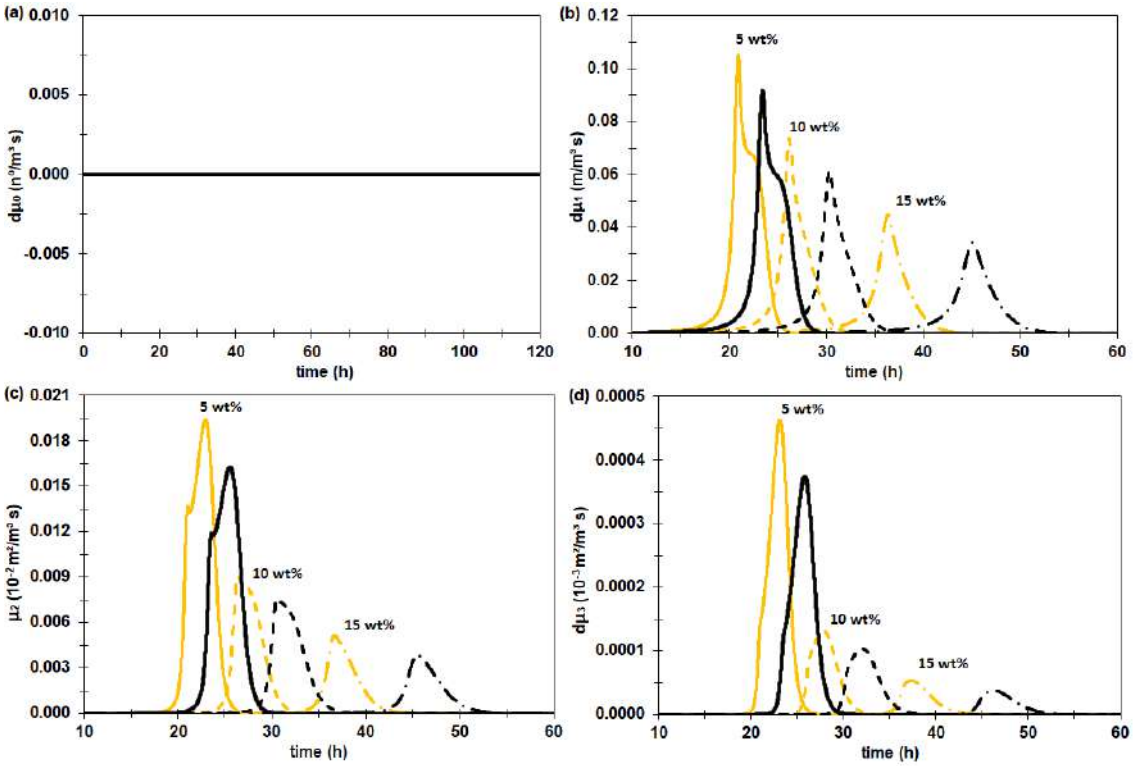

Figure S84- (a) The differential profile of the population balance moment of order zero, number of particles per liquid volume ($d\mu_0$), (b) moment of order one, particle diameter per liquid volume ($d\mu_1$), (c) moment of order two, particle surface area per liquid volume ($d\mu_2$) and (d) moment of order three, particle volume per liquid volume ($d\mu_3$) at 276 (*DR* = 0.5). The lines describe the time profiles for the following ethanol compositions of the initial liquid phase: 5 wt% (continuous line), 10 wt% (dashed line) and 15 wt% (dotted-dashed line) of EtOH, at 70.9 bar, θ = 72% (black), and at 74.9 bar, θ = 75% (yellow).

S.17.6 The system at 274 K and 70.9 bar with water activity in the driving force for 5, 10 and 15 wt%

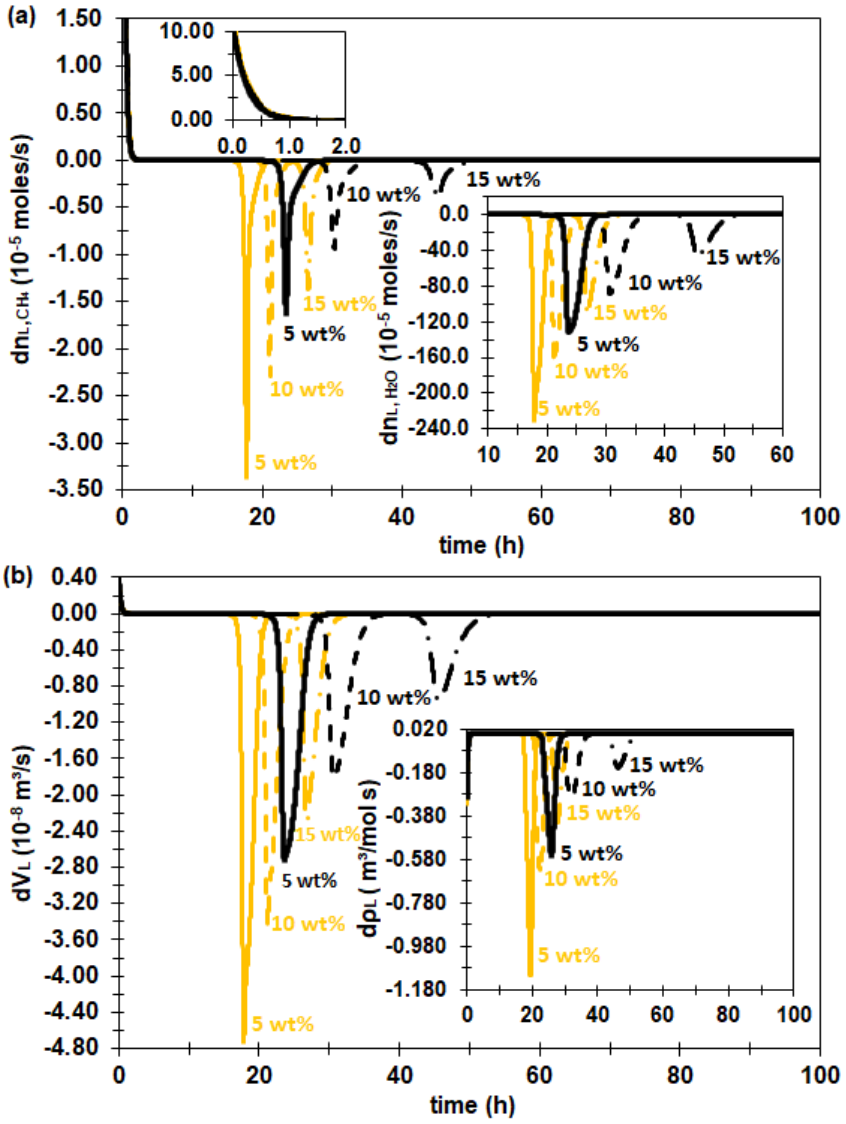

Figure S85 - The differential profile of (a) the methane number of moles in the bulk liquid phase (dn_{L,CH_4}) and (b) the liquid phase volume (dV_L) at 70.9 bar (*DR* = 0.5). The insertion (a) in the left shows the methane saturation profile and the one in the right shows the water number of moles (n_L,H_2O) profile in the bulk liquid phase. The insertion (b) shows the liquid density (ρ_L) profile with a zoom in the methane saturation profile. The lines describe the time profiles for the following ethanol compositions of the initial liquid phase: 5 wt% (continuous line), 10 wt% (dashed line) and 15 wt% (dotted-dashed line) of EtOH, at 276 K, θ = 72% (black), and at 274 K, θ = 68% (yellow).

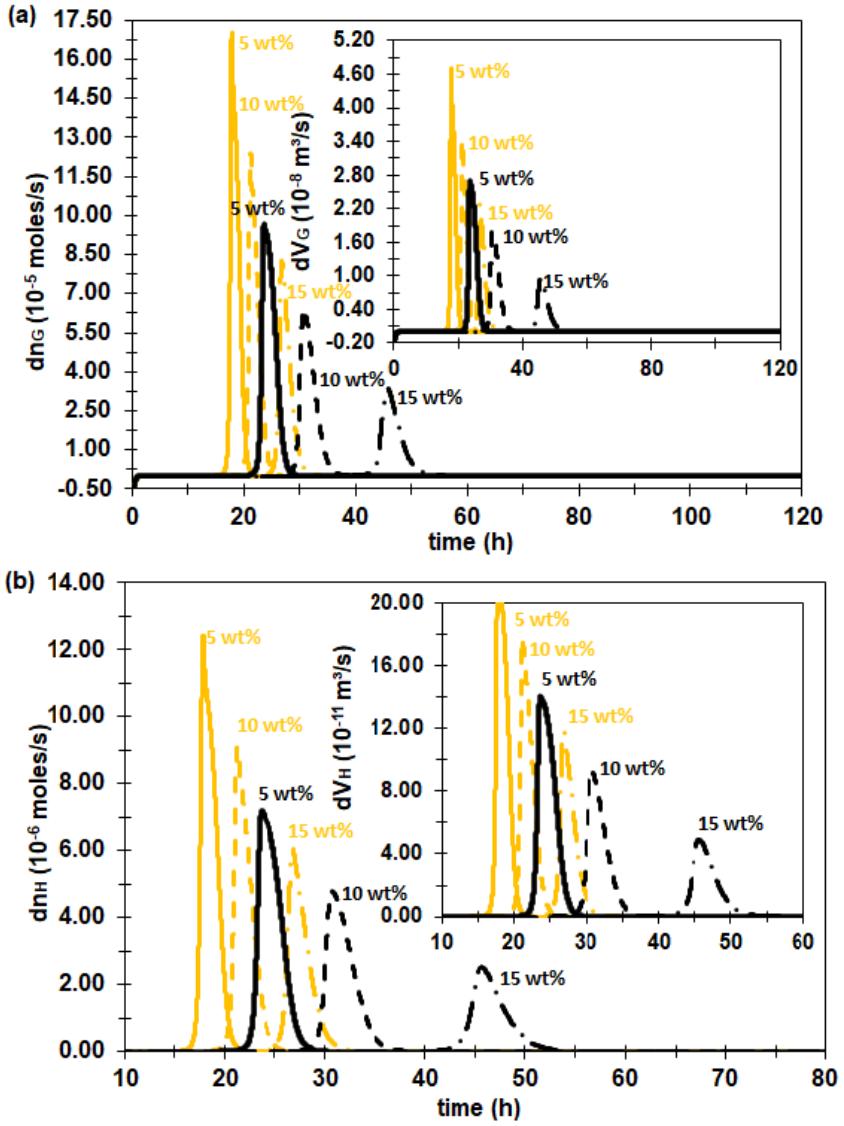

Figure S86 - The differential profile of (a) the methane number of moles in the pure vapor phase (dn_G) and (b) the hydrate number of moles (dn_H) at 70.9 bar (*DR* = 0.5). The insertion (a) shows the vapor phase volume (dV_G) and the constant vapor density ($d\rho_G$) differential profile. The insertion (b) shows the hydrate phase volume (dV_H) differential profile. The lines describe the time profiles for the following ethanol compositions of the initial liquid phase: 5 wt% (continuous line), 10 wt% (dashed line) and 15 wt% (dotted-dashed line) of EtOH, at 276 K, θ = 72% (black), and at 274 K, θ = 68% (yellow).

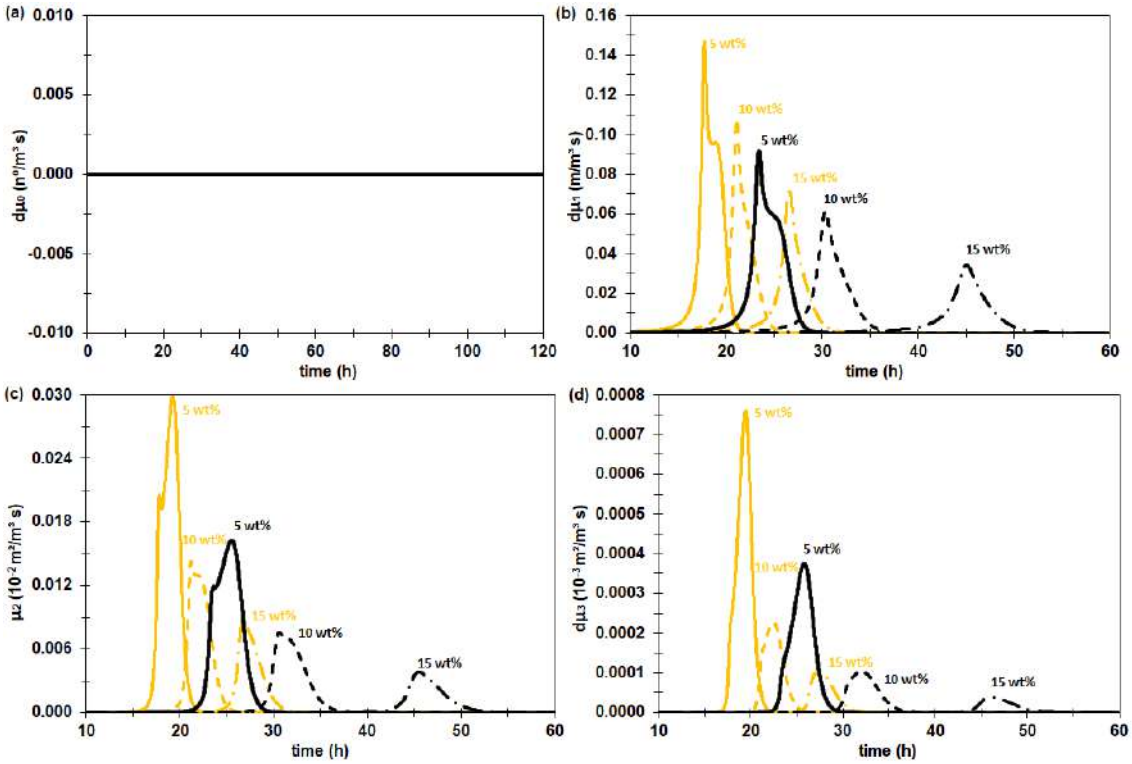

Figure S87 - (a) The differential profile of the population balance moment of order zero, number of particles per liquid volume ($d\mu_0$), (b) moment of order one, particle diameter per liquid volume ($d\mu_1$), (c) moment of order two, particle surface area per liquid volume ($d\mu_2$) and (d) moment of order three, particle volume per liquid volume ($d\mu_3$) at 70.9 bar (*DR* = 0.5). The lines describe the time profiles for the following ethanol compositions of the initial liquid phase: 5 wt% (continuous line), 10 wt% (dashed line) and 15 wt% (dotted-dashed line) of EtOH, at 276 K, θ = 72% (black), and at 274 K, θ = 68% (yellow).

S.18 Correlation of the parameters A_{int}^{GL} e k_d^{GL}

The modeling of CH_4 solubilization in H_2O with EtOH requires describing the interfacial area of the continuous gas-liquid phases $A_{\text{int}}^{GL}[m^2]$ and the methane diffusion coefficient $k_d^{GL}[m/s]$. For the calculation of this area, the same modeling used by Sampaio et al. [87] and in our previous work Oliveira et a (2020, in submission process), Item S.9 Appendix 3, is used.

Then, the suspension molar density, $\overline{\rho}_{susp.}[mol/m^3]$, the molar mass of the suspension, $MM_{susp.}$, the dynamic viscosity, $\overline{\mu}_{susp.}[mol/m\ s]$, and the specific surface energy of the suspension, $\overline{\sigma}_{susp.}[J/m^2]$ are given by models that pondered the properties of the solid phase and the liquid phase (Item S.9 Appendix 3). Thus, in calculating the properties of the liquid phase, which now has ethanol present, we now also include the properties of ethanol weighted through its mole fraction at that time in the system.

S.19 NRTL model adjustment with LVE experimental data of the CH_4 + EtOH system

The parameters of the NRTL model were estimated by minimizing the sum of the quadratic residues of the output variables, P_i, and the reconciliation of experimental data using the reported experimental errors of the input variables, T_i and x_i, for each experiment (l), according to equation (S63).

$$F_1^{\text{obj}}\left(\underline{\beta}\right)=\sum_l^{N_{\text{exp}}}\left(\begin{array}{l}\left(w\left(P_l^{\text{calc}}\left(\underline{\beta}\right)-P_l^{\text{exp}}\right)\right)^2+\\+\left(\text{desv}T\left(T_l^{\text{calc}}\left(\underline{\beta}\right)-T_l^{\text{exp}}\right)\right)^2+\left(\text{desv}x\left(x_l{}^{\text{calc}}\left(\underline{\beta}\right)-x_l{}^{\text{exp}}\right)\right)^2\end{array}\right) \quad \text{(S63)}$$

The equilibrium pressure, P_i, is calculated by the NRTL model using the equilibrium temperature, T_i, and liquid phase composition, x_i, as input variables, adjusting this input data according to the reported experimental deviations [165,253,254] through data reconciliation. $\underline{\beta}$ is the set of parameters to be estimated. For the NRTL model, it was defined as: $\underline{\beta}=(A_{2,3},A_{3,2},\text{B}_{2,3},\text{B}_{3,2},\alpha_{3,2=3,2})$. The inverse of the admitted weights for the output variable was 0.1% of the measured variable, $w=1/_{0.001P}$. While the deviation used in the reconciliation data process was the inverse of the quadratic error of each experimental point $desv=1/_{error^2}$.

In this work, the particle swarm method - PSO [233] was used as the stochastic method to achieve a good initial estimate for a Quasi-Newton type algorithm, a deterministic method uses differential calculus techniques.

Calculations of absolute average deviations, equation (S64), are used to analyze the best adjustments.

$$AAD\left(\underline{\beta}\right)=\frac{\sum_i^{N_{\text{exp}}}\left|\frac{z_{i,j}{}^{\text{calc}}\left(\underline{\beta}\right)-z_{i,j}{}^{\text{exp}}}{z_{i,j}{}^{\text{exp}}}\right|}{N_{\text{exp}}}.100 \quad \text{(S64)}$$

The parameter estimation procedure used data reconciliation in order to obtain parameters with low correlation and high transferability. Using this methodology, we obtained the lowest coefficient correlation between the parameters, Figure S88. The methane composition in the liquid phase presented the Absolute Average Deviation (AAD), equation (S64), of 0.57%, and as the Figure S88 (a) shows, the experimental

and the reconciliation data has total linearity with each other. On the other hand, the reconciled temperature showed AAD of 2.59% and did not present total linearity with the experimental data; however, the deviation was low, and the variation was within the error range of 5 K, Figure S88 (b). Using the data reconciliation technique, the AAD of the pressure calculated with the NRTL model was 0.0014% and showed total linearity with the experimental pressure, Figure S88 (c). Then, as the pressure was calculated by the model with high precision using data reconciliation despite the 5 K deviation in temperature, the adjustment was considered adequate.

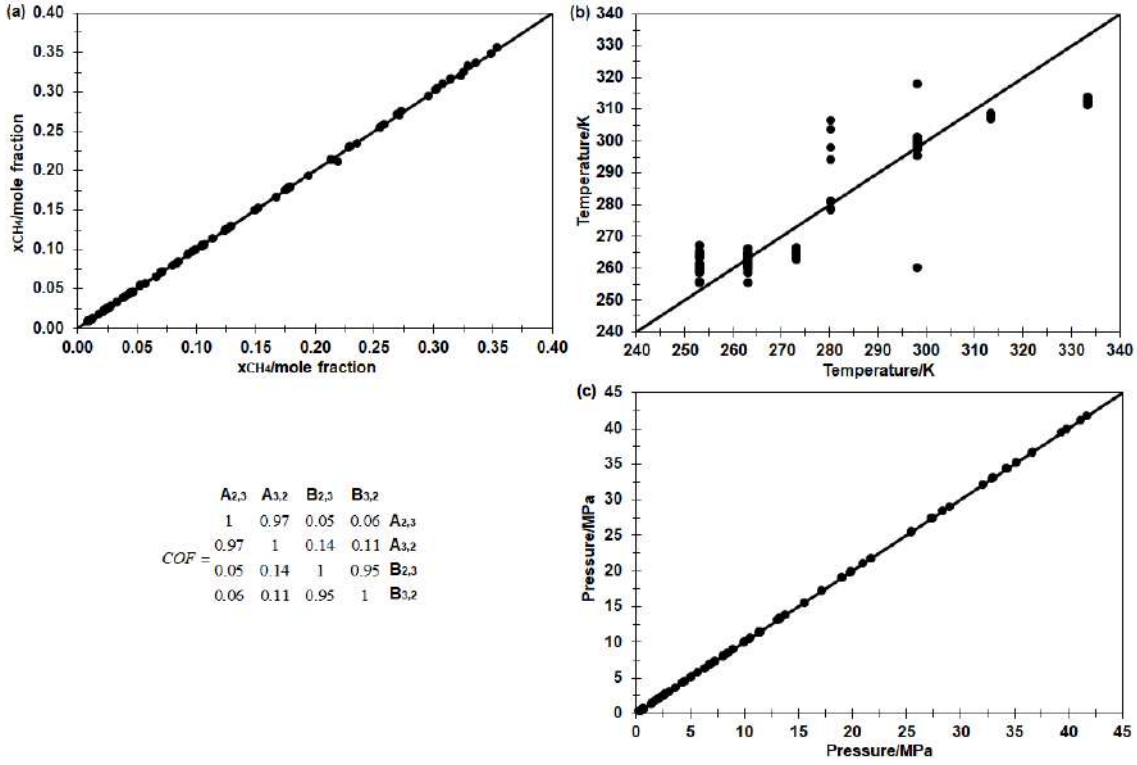

$$COF = \begin{array}{c} \\ 1 \\ 0.97 \\ 0.05 \\ 0.06 \end{array} \begin{array}{cccc} A_{2,3} & A_{3,2} & B_{2,3} & B_{3,2} \\ 0.97 & 0.05 & 0.06 & A_{2,3} \\ 1 & 0.14 & 0.11 & A_{3,2} \\ 0.14 & 1 & 0.95 & B_{2,3} \\ 0.11 & 0.95 & 1 & B_{3,2} \end{array}$$

Figure S88- Comparison between experimental values, y-axis, and calculated values, x-axis, in the estimation of NRTL model parameters using data reconciliation for the CH_4+EtOH system [165,253,254] and the matrix of the parameters correlation coefficients. The input variables reconciled using the reported experimental errors were (a) the methane composition in the liquid phase, x_{CH_4}, and (b) the equilibrium temperature. The output variable calculated through the NRTL model in the estimation process was (c) the pressure.

The NRTL model parameters for the pair CH_4(2) + EtOH(3), Table S19, were estimated for liquid-vapor equilibrium data at the temperature of 253.15 K, 263.15 K, 273.15 K, 280.15 K, 298.15 K, 313.4 K, and 333.4 K, Figure S89, covered a pressure range of 0.33 MPa to 41.69 MPa. The methane concentration range in the liquid phase

is 0.008 to 0.353 molar, and for all the range, the equilibrium pressure was calculated precisely by the model with the adjusted parameters Figure S89.

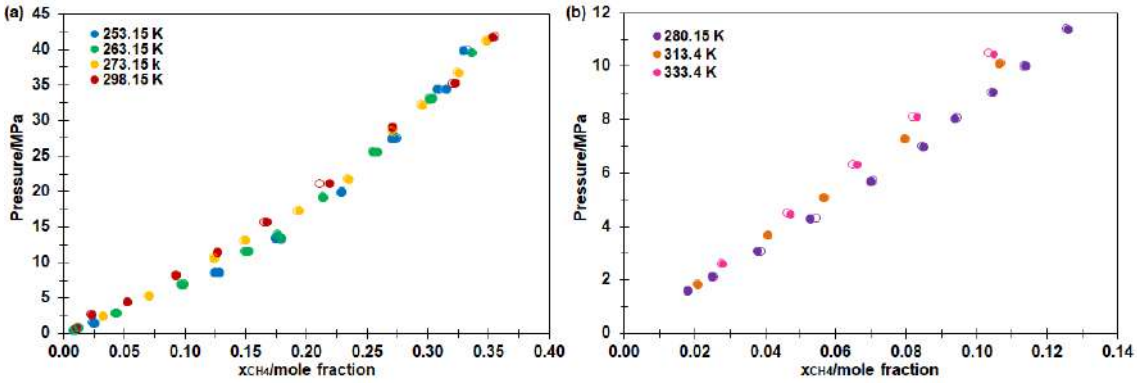

Figure S89 - CH_4(2) + EtOH(3) liquid-vapor equilibrium isothermal curves. The experimental data are represented by the filled circles for (a) 253.15 K, 263.15 K, 273.15 K, 298.15 K, and (b) 280.15 K, 313.4 K, and 333.4 K. The empty circles are calculated with the NRTL model.

With the sets of the NRTL parameters for the pair CH_4+EtOH we have all the parameters necessary for the ternary NRTL to calculate both the hydrate reagents and the equilibrium composition at the hydrate-liquid and liquid-gas interfaces for the H_2O+CH_4+EtOH system. Using also the parameters for the pairs H_2O+EtOH, estimated in Oliveira et al. [124], and H_2O+CH_4, estimated in Oliveira et al. (2020, in submission process), Item S.12 Appendix 3.